Thesis submitted for the degree of
Doctor of Philosophy

Petrogenesis of the phonolitic rocks of the Velay oriental, France

by

Sean Patrick Hodges

Department of Earth Sciences
Oxford University
Trinity 1991

ABSTRACT

Sean Hodges
St. Edmund Hall

D.Phil.
Trinity 1991

Petrogenesis of the phonolitic rocks of the Velay oriental, France

The Velay oriental (Massif Central, France) is a basaltic plateau with abundant viscous phonolite extrusions. The plateau lavas grade from alkali basalt to mugearite, but intermediate compositions are volumetrically scarce. Pyroclastics are absent. The most complete plateau sections are in the south, while in the north intermediate lavas appear only as viscous, phenocryst-rich extrusions.

The plateau lavas were erupted between 11.7Ma and 7.6Ma, the southern phonolites 8.5Ma-6.5Ma and new data show that the northern phonolites were erupted between 13.3Ma and 10.5Ma. Basement uplift occurred during the plateau-building stage, due to the emplacement of magma chambers. Intermediate lavas are scarce because they remained in the magma chambers due to their density, whereas phonolite was able to rise hydrostatically. The magma chambers were within 5km of the surface.

Phonolites are divided into miaskitic and agpaiitic types on the basis of their chemistry and petrography. They evolved from the basalt by crystal settling in the magma chambers, whereas the aphyric plateau lavas evolved by plating crystals onto their conduit walls as they flowed towards the surface.

Sr-isotopes show that the basalt-phonolite series is uncontaminated, whereas the northern intermediate lavas evolved by assimilation-fractional-crystallisation.

A suite of cumulate nodules was recovered from a pyroclastic unit, which is probably younger than the Velay Miocene lavas. They are related to the northern intermediate lavas, and belong to the "Group II" class of nodules.

Geothermobarometry suggests that both the cumulates and the northern intermediate lavas crystallised at a depth of 15-20km and probably became contaminated due to the smaller temperature difference between the geotherm and granite solidus at that depth.

The vast majority of the Velay lavas are identical to alkalic ocean-island lavas, geochemically unaffected by their passage through the lithosphere, but with their relative proportions at the surface controlled by the density contrast between the basalt and basement granite.

Contents

Acknowledgements 1

Long Abstract 2

Chapter 1
Volcanology, chronology and structure of the Velay oriental

1.1 Geography 8

1.2 Volcanic activity 12
1.2.1 Summary 12
1.2.2 Historical work 18

1.3 Chronology 18
1.3.1 Field relations 18
1.3.2 Sedimentary stratigraphy 19
1.3.3 Potassium-Argon dating 20
1.3.3.1 Previous work 20
1.3.3.2 New K-Ar data 20
1.3.3.3 Discussion 23

1.4 Main features to be explained 25
1.4.1 Bimodality of lava compositions 25
1.4.2 Lack of explosivity 26

1.5 The structure of the Velay oriental 27
1.5.1 Evidence of uplift 27
1.5.2 Timing of uplift 31
1.5.3 Comparison with other areas 32

1.6 Integrated model of uplift and magmatism 35
1.6.1 Cause of uplift 35
1.6.2 Form of magma chambers 36
1.6.3 The Daly gap and scarcity of pyroclastics explained 36

1.7 Summary 40

Chapter 2
History, volcanism and structure of the Massif Central

2.1 General history 44
2.1.1 Palaeozoic and Mesozoic 45
2.1.2 Cenozoic 45
2.1.3 Cenozoic volcanism in the rest of Europe 47

2.2 Deep structure 49

2.3 Interpretation 55
2.3.1 Mantle diapir 55
2.3.2 Hotspot model 56
2.3.3 Mantle metasomatism 57
2.3.4 Magma sources 58
2.3.5 Conclusions 59

Chapter 3
Petrography and mineral chemistry of the Velay oriental lavas

3.1 Lava types 61
3.1.1 Introduction 61
3.1.2 Alkali basalts *(sensu lato)* 63
3.1.3 Hawaiite 64
3.1.4 Mugearite and Benmoreite - Intermediate lavas 64
3.1.4.1 Southern Intermediate lavas 65
3.1.4.2 Northern Intermediate lavas 66
3.1.4.3 Comparison between northern intermediate lavas and cumulates 70
3.1.5 Phonolites 71
3.1.5.1 Miaskitic phonolites 71
3.1.5.2 Agpaiitic phonolites 75
3.1.6 Quartz-trachytes 76

3.2 Petrography and mineral chemistry of phenocrysts 76
3.2.1 Introduction 76
3.2.2 Olivine 77
3.2.3 Clinopyroxene 77
3.2.4 Ti-magnetite 83
3.2.5 Pleonaste 86
3.2.6 Feldspar 86
3.2.7 Amphibole 90
3.2.8 Biotite 93
3.2.9 Sphene 95
3.2.10 Apatite 97
3.2.11 Zircon 97
3.2.12 Aenigmatite 98
3.2.13 Mosandrite 101
3.2.14 Feldspathoids 101
3.2.15 Carbonate 103

Chapter 4
Field relations, petrography and mineral chemistry of the cumulate blocks

4.1 Field relations 104

4.2 Petrography of clasts in the pyroclastics 108
4.2.1 Granite/gneissic fragments 108
4.2.2 Trachyte fragments 109
4.2.3 Welded blocks 109
4.2.4 Coarse-grained blocks 111

4.3 Composition of the magma involved in the pyroclastic eruption 111

4.4 Sequence of events 113

4.5 Petrography of the coarse-grained blocks 113
4.5.1 Introduction 113
4.5.2 Evidence for cumulate origin 118
4.5.3 Subdivision of the cumulates 120

4.6 Mineral descriptions and chemistry 127
4.6.1 Clinopyroxene 127
4.6.2 Amphibole 131
4.6.3 Feldspar 136
4.6.4 Ti-magnetite 138
4.6.5 Ilmenite 142
4.6.6 Pleonaste (spinel-hercynite) 146
4.6.7 Biotite 149
4.6.8 Apatite 152
4.6.9 Sphene and Zircon 152
4.6.10 Pyrrhotite 154
4.6.11 Glass and Carbonate 154

4.7 Other Occurrences of Cumulate Nodules 158
4.7.1 Introduction 158
4.7.2 Comparison with the Velay Nodules 161

Chapter 5
Geochemistry of the lavas and cumulates

5.1 Previous work 164

5.2 Sampling for this study 167

5.3 Choice of Fractionation Index 167
5.3.1 Lavas 167
5.3.2 Cumulates 183

5.4 Petrogenesis of the evolved rocks 186
5.4.1 Partial melting 186
5.4.2 Contamination 186
5.4.3 Magma mixing 188
5.4.4 Crystal-liquid fractionation 188
5.4.5 Other processes 189
5.4.6 Conclusion 190

5.5 Calculation of parental liquid 190

5.6 Fractionation in the Velay lavas 196
5.6.1 Qualitative analysis 196
5.6.1.1 Details of fractionation steps 196
5.6.1.2 Summary 199
5.6.2 Quantitative analysis 199
5.6.2.1 Problems encountered 200
5.6.2.2 Input Compositions 200
5.6.2.3 Interpretation 200
5.6.2.4 Comparison with cumulates 209
5.6.2.5 Constraint from incompatible elements 209
5.6.2.6 Agpaicity of the Velay phonolites 211
5.6.2.7 Conclusions 213

5.7 Bulk chemistry of the cumulates 213
5.7.1 Interpretation of major and trace element behaviour 213
5.7.2 Interstitial glasses and lavas associated with the cumulates 230
5.7.3 Conclusions 234

5.8 Sr-isotope data for the lavas and cumulates 234
5.8.1 Introduction 234
5.8.2 Lavas 237
5.8.3 Cumulates 239
5.8.4 Assimilation Fractional Crystallisation (AFC) 241
5.8.5 Conclusions 244

5.9 Phase relations 245
5.9.1 The CMAS-system 245
5.9.1.1 MS - CS – A 246
5.9.1.2 M_2S - C_2S_3 - A_2S_3 246
5.9.1.3 C_3A - M – S 250
5.9.1.4 CAS_2 - M_2S - CMS_2 250
5.9.1.5 Conclusions 251
5.9.2 Other phase relations 251

5.10 Thermometry and barometry 253
5.10.1 Coexisting Ti-magnetite and ilmenite thermometer 253
5.10.2 Al^{IV} in amphibole thermobarometer 254
5.10.3 Ca in olivine and clinopyroxene thermobarometer 257
5.10.4 Conclusions 260

5.11 Summary and conclusions 263

Chapter 6
Synthesis

6.1 The Massif Central 266

6.2 Velay oriental volcanism 267

6.3 Petrography of the Velay lavas 268

6.4 Geochemistry of the Velay lavas 268

6.5 Cumulate blocks 270

6.6 Summary of events 271

References and Appendices

References 272

Appendix A - Specimen localities 282

Appendix B - Specimen petrography 289

Appendix C - Whole-rock and mineral analyses 297
- C.1 Whole-rock analysis 297
  - C.1.1 Details of XRF spectrometer 297
  - C.1.2 Sample preparation 297
  - C.1.3 Bead and pellet manufacture 297
  - C.1.4 Precision and accuracy 298
  - C.1.5 Problems encountered 298
- C.2 Mineral analyses 300
  - C.2.1 Details of microprobe 300
  - C.2.2 Sample preparation 300
  - C.2.3 Operating conditions 300

Appendix D - Sr-isotope determination 321
- D.1 Strontium extraction 321
- D.2 Measurement of the Sr-isotope ratio 321
- D.3 Measurement of Rb and Sr concentrations 321
- D.4 Calculation of $(^{87}Sr/^{86}Sr)_{initial}$ 321

Appendix E - K-Ar age determination 325
- E.1 Theory 325
- E.2 Potassium determination 326
- E.3 Argon determination 326
  - E.3.1 Specimen preparation 326
  - E.3.2 Argon extraction 326
  - E.3.3 Isotopic measurement 329
- E.4 Age calculation 330

Acknowledgements

I would like to thank my supervisor, **Dr David Bell**, for his friendship, enthusiasm, support and tolerance as my ideas progressed from the ludicrous to the (I hope) reasonable, **Jean Mergoil**, of Université Blaise-Pascal, Clermont-Ferrand, for his generosity in showing me around "his" area, for explaining its problems to me in the clearest French I have heard since O-level, and with his wife **Juliette**, for showing me the best of French hospitality, **Dr Keith Cox**, for providing a voice of sanity at a few crucial points, and for being kind enough to say that, although I had been an obnoxious undergraduate, I had turned out alright in the end, **Jean-Marie Cantagrel**, for the use of the K-Ar laboratory at Clermont-Ferrand, and **Dion Vickers**, of the Oxford Polytechnic, for allowing me to use their large-scale digitising table.

Many technical and secretarial staff have provided enormous amounts of help over the years, and in particular I would like to thank **Phil Jackson, Jeremy Hyde, Keith Parish, Steve Wyatt, Norman Charnley, Roy Goodwin, John Payne, Steve Baker, Richard McAvoy, Joan Morrall, Nina Phipps, John O'Sullivan, Derek Preston, Kath Webb and Mary Cronin.** I am also indebted to **Colette Jamond**, who showed me how to measure Ar^{40} in Clermont, and pretended to understand my French.

Many of my fellow postgrads deserve thanks, especially **Giles** "voice of reason" **Rodway**, **Neil** "great white" **Mitchell** and **Martin** "plums" **Shepley**, for making 28 Cowley Road habitable, **Andy Whittingham**, for the use of several programs and for providing my weekly fix of gossip, **David Feltham**, for advice on all things computational and **Grant Wach, Sriyanee de Silva, Steve Hart, Ed Thorogood, Jon Bass, Pam Sansom, Elaine Scott and Jane Scarrow** for accompanying me on my five year mission. Thanks to everyone else who kept life interesting. Last, and particularly not least, **Marita** - thanks for making sure my final year was one of the best.

I gratefully acknowledge a grant from the Natural Environment Research Council, a weekly contribution from the NHS, and additional government support.

This thesis is dedicated to
my **Mum**, for kindling my interest in geology
and **Dad**, for firing my imagination with his love of science and history.

Petrogenesis of the phonolitic rocks of the Velay oriental, France

(Long Abstract)

Velay oriental volcanism

The Velay oriental is a basalt plateau with abundant phonolite hills dotted over its surface, with forms that show they were erupted as viscous lavas. The Velay lies to the south-east of the Massif Central volcanic province and is one of its eight main volcanic districts.

The plateau of the Velay oriental reaches a maximum thickness of 200m, with the most basic alkali basalts at the base, then a random sequence of more evolved lavas, up to and including hawaiite, and is capped by thin flows of mugearite and benmoreite. The volume proportion of these intermediate lavas is small compared with that of the basaltic lavas and the phonolite, giving a classic "Daly gap" for this district.

The thickest and most complete plateau sections are found in the southern half of the Velay, while in the north the plateau often consists of only two basaltic flows, and intermediate compositions are represented by viscous, phenocryst-rich extrusions.

K-Ar dating shows that the plateau sequence was erupted between 11.7Ma and 7.6Ma, and the phonolites in the south of the Velay between 8.5Ma and 6.5Ma. New work in this thesis confirms these age ranges and establishes that the phonolites of the north were distinctly older than the other Velay lavas, with an age range of 13.3Ma to 10.5Ma.

A contour map of the basement-basalt contact demonstrates the degree of basement uplift, which is deduced to have occurred between about 10Ma and 8Ma. Comparison of the Velay basement uplift with those of other districts strongly suggests that it was caused by the emplacement of a magma chamber, which elevated its roof hydrostatically.

Two chambers were formed, at different times in the north and south. The southern chamber had a volume in excess of 100km^3 and could easily have produced all the phonolite seen at the surface by fractional crystallisation alone. The distribution of trace elements in the phonolites and their varied petrography suggest that the chambers were zoned, with irregular roofs.

The scarcity of intermediate lavas, and the virtual absence of explosive volcanism, despite the highly viscous nature of the evolved phonolite magmas, are the two main features which need to be explained in the Velay. Both are probably due to the contrast in the densities of the basement granite and primitive alkali basalt magma. Initial extension allowed the basalt to rise to the surface via fissures and to build the plateau. As extension weakened the later basalt magma became trapped in a crustal magma chamber as a consequence of its high density compared with the country rock, and proceeded to differentiate. Eventually the density of the evolved magma fell sufficiently below that of the basement granite to enable it to rise under hydrostatic (rather than gas-exsolution) pressure, and to extrude passively onto the surface as viscous domes.

The calculated hydrostatic pressure, combined with the eruptive height of the phonolite domes,

shows that the magma chambers were about 5km below the surface.

The hydrostatic pressure can also be combined with calculated magma viscosity to estimate eruption rates through conduits of various sizes, although the degree of uncertainty renders this rather inconclusive.

The Massif Central

The Massif Central is a 300km-diameter area of elevated Hercynian crust in south central France, which suffered extension and graben formation in the Oligocene and major alkaline volcanism from the mid-Miocene to the present. Geophysical work has shown that anomalously low density, low seismic velocity mantle, probably containing a small proportion of melt, underlies the volcanic areas, and mantle xenoliths show pervasive deformation, due either to asthenospheric diapirism or to extensional shear of the lithospheric mantle. Various lines of evidence suggest that the source material for the basic lavas was garnet-lherzolite, at depths of at least 100km.

The cause of the volcanism is harder to determine. A hotspot seems unlikely due to the small size of the volcanic area and the lack of a geographical age progression. Mantle metasomatism may provide a more suitable explanation but it is difficult to assess, and most of the supposed metasomatised xenoliths are probably fragments of the lithospheric mantle.

The similarity of the Massif Central basic lavas to those of the ocean island basalts strongly suggests that continental lithosphere cannot have been a major source. Similarly the exclusion of the hotspot model seems to rule out a lower mantle source. This leaves the convecting upper mantle (including the asthenosphere) as the only suitable source for the Massif lavas. However, the asthenosphere is thought to be highly depleted due to the extraction of MORB, raising the problem of how it can produce the incompatible-element enriched alkali basalts. Possible explanations include the presence of trace-element enriched streaks (small scale heterogeneity) or the extraction of extremely small (< 0.5%) partial melts.

Petrography of the Velay lavas

The basalts and other lavas of the Velay oriental plateau are generally aphyric, with only a few microphenocrysts of olivine in the basalts, and Ti-magnetite, amphibole and apatite in the hawaiites and mugearites. The exceptions are the ankaramites, with olivine and clinopyroxene megacrysts, with Ti-magnetite and occasional pleonaste. None of these lavas contain feldspar phenocrysts.

The intermediate extrusions of the northern Velay have abundant phenocrysts, including apatite, Ti-magnetite, sphene, amphibole, biotite, clinopyroxene, plagioclase and K-feldspar. These are similar in composition, appearance and crystallisation sequence in most examples. Some reaction relationships show decreasing oxygen fugacity. These lavas are unique in the Velay in showing a weak trend towards silica saturation.

The phonolites can be divided into two groups, both mineralogically and chemically. The miaskitic phonolites are less evolved, have sphene and zircon as their Ti,Zr-silicates and nosean as

their characteristic feldspathoid. Agpaiitic phonolites are more evolved, have exotic Ti,Zr-silicates such as aenigmatite and mosandrite, and are characterised by the feldspathoid nepheline. They are largely aphyric, with only a few phenocrysts of K-feldspar.

Agpaiitic phonolites are more common in the south than in the north, demonstrating that the division of the phonolites geographically and chronologically into northern and southern groups also extends to the petrography.

Geochemistry of the Velay lavas

Almost the entire suite of lavas in the Velay oriental can be shown to have formed by simple crystal-liquid fractionation. Evidence in favour of this includes the close match between phenocryst assemblages inferred from the whole-rock geochemical trends and those observed in thin section. The observed curved and kinked trends are also much easier to explain with crystal-liquid fractionation. Partial melting models cannot explain the observed range in the concentrations of compatible elements, and contamination and melting models are excluded due to the absence of suitable contaminants or end-member magmas. Only crystal-liquid fractionation provides a suitable mechanism to produce the evolved lavas of the Velay, with the separation of crystals from the melt being achieved by flow crystallisation in the plateau lavas and by crystal settling in the phonolites.

Various attempts were made to calculate the parent liquid of the Velay volcanic series, with the conclusion that they were unlikely ever to have been in equilibrium with mantle olivine. This suggests some degree of mantle metasomatism, since the basalts have low $^{87}Sr/^{86}Sr$ and are unlikely to have been contaminated by lithospheric material. The most primitive Velay basalts are therefore probably primary.

Fractionation of the lavas was assessed both qualitatively, by examination of major and trace element trends and phenocryst assemblages, and quantitatively, using a least-squares method. It was found possible to model the entire Velay lava series as the result of phenocryst removal from a basalt melt. The steps were, with phenocrysts in order of decreasing proportion:

primitive to evolved basalt	*cpx, olivine, Ti-magnetite, pleonaste*
evolved basalt to hawaiite	*amphibole, cpx, olivine, Ti-magnetite*
hawaiite to intermediate lava	*amphibole, plagioclase, Ti-magnetite, apatite, cpx*
intermediate lava to miaskitic phonolite	*plagioclase, amphibole, Ti-magnetite, cpx, apatite, sphene*
miaskitic to agpaiitic phonolite	*K-feldspar, amphibole, Ti-magnetite, apatite, sphene*
(intermediate lava to quartz-trachyte	*plagioclase, biotite, Ti-magnetite, apatite, cpx)*

Phonolites were shown independently to be 6 - 20% of the parental alkali basaltic magma.

The Velay lavas form two series, the first, from basalt to agpaiitic phonolite, is overwhelmingly the most voluminous and seems to represent the normal low-pressure fractionation sequence. The second series diverges at the level of the benmoreites towards quartz-trachyte and rhyolite, and is marked by the appearance of biotite instead of K-feldspar. It is not clear at this stage whether the appearance of biotite is the cause, or a symptom of, the trend to silica-saturation.

Sr-isotopes show mantle values (0.7033 - 0.7035) for almost all the Velay basalt-phonolite

series lavas, which are presumed to be uncontaminated, and to have a sub-lithospheric source. The lavas of the silica-saturated trend (the northern intermediate lavas and a quartz-trachyte from the south) have elevated $^{87}Sr/^{86}Sr$-values which show a slight correlation with SiO_2 and with Pb, both of which are more abundant in the basement granite than the lavas. Contamination by a process of simple mixing was rejected in favour of assimilation-fractional-crystallisation (AFC), which is discussed in the next section.

In an attempt to assess the depth at which the Velay basalt originated, they were projected into the CMAS system. The results suggest that they last equilibrated at 15 - 20kbar before eruption. Thermometry and barometry was attempted for the ankaramites and northern intermediate lavas. The ankaramites gave only poor results, which suggest that their phenocrysts formed at or below the base of the crust (10-15kbar). The northern intermediate lavas are considered with the cumulates in the next section.

Cumulate blocks

The cumulate blocks occur in a small pyroclastic unit in a valley just to the south-east of Mt Mézenc, in the southern Velay. The pyroclastics are being eroded rapidly by a small stream, suggesting that they were erupted relatively recently, but carbon-14 dating of fossil wood showed that it was older than the maximum measurable by this method (35,000 years). One of the cumulate blocks yielded a K-Ar age of 8.5Ma, but this seems to be too high.

The blocks were deduced to be cumulates of the magma which produced the pyroclastics since its phenocrysts are the same as those in the most evolved cumulates. Evidence for the cumulus nature of the blocks includes the presence of intercumulus glass, modal and grain-size layering and adcumulus overgrowth on originally euhedral grains. The frequency distribution of the cumulate blocks shows that the least-evolved blocks are three times as abundant as the most-evolved.

Minerals in the blocks show continuous compositional variation over a wide range, and are used to divide the blocks into four suites, with Suite 1 the least evolved and Suite 4 the most evolved. The criteria are:

Suite 1 - *no feldspar present*
Suite 2 - *feldspar and amphibole present, biotite absent*
Suite 3 - *feldspar, amphibole and biotite all present*
Suite 4 - *feldspar and biotite present, amphibole absent or < 2%*

There is strong resemblance between the minerals of the cumulates and the phenocrysts of the intermediate lavas from the north of the Velay, both showing a trend towards silica-saturation and elevated values of $^{87}Sr/^{86}Sr$. The parental lava of the cumulates is deduced to be an alkali basalt.

The geochemistry of the cumulates matches that which would be predicted for the cumulates of a body of magma evolving mainly by crystal-liquid fractionation, with no gap at intermediate compositions. The interstitial glasses of the blocks show strong silica-enrichment, possibly due to loss of other components to nearby minerals, but emphasising the trend of the blocks as a whole.

The evolved cumulates have elevated $^{87}Sr/^{86}Sr$, suggesting that they were formed from a liquid

undergoing AFC, as previously concluded for the northern intermediate lavas. Modelling both lavas and cumulates is difficult since there are so few data, but results suggest that only small degrees of contamination, up to a maximum of 11%, are needed to account for the observed values of $^{87}Sr/^{86}Sr$.

Geothermobarometry was used to determine the depth at which the cumulate blocks formed. The coexisting FeTi-oxides thermometer, combined with the Al^{IV}-in-amphibole thermobarometer, shows that the cumulates probably equilibrated at 5 - 7kbars (15 - 20km). This is supported by the abundance of basement granite fragments and the absence of lower crustal or mantle material in the pyroclastics. The northern intermediate lavas are presumed to have formed at a similar depth.

Comparison of the Velay cumulate nodule suite with others from around the world shows that those of the Velay belong to the established "Group II" type, with a continuous range from wehrlite to the rare apatite/amphibole type. This has not been reported previously in the literature.

Summary of events

Partial melting of garnet-lherzolite in the asthenosphere beneath the Velay produced an alkali basalt parent magma. Lithospheric extension, which probably caused the melting by decompression, allowed the melt to rise towards the surface, and to erupt from fissures to form the Velay plateau. Some of this magma was trapped at or below the base of the crust and crystallised olivine and cpx before subsequent eruption as ankaramite. The other plateau lavas are aphyric, and probably evolved by flow crystallisation, plating crystals onto the walls of their conduits on the way to the surface. If they had evolved in a magma chamber they would contain phenocrysts and would also have had no reason to rise towards the surface.

When the extensional force decreased, ascending dense basaltic magma became trapped within the lower density granite basement and formed a $100km^3$ magma chamber which elevated its roof. Differentiation of this liquid by crystal settling produced successively more evolved liquids until the density of the remaining phonolite magma was low enough to allow it to rise under hydrostatic pressure alone and to extrude at the surface as viscous domes.

Old, parental basalt has not been identified for the phonolites of the northern Velay. Possibly extension in this area was too weak to allow the primary basalt to reach the surface, or the Boutières graben may have affected its rise. Pre-phonolite basalts may yet be found.

The intermediate lavas of the north appear to have evolved by AFC at mid-crustal levels (by analogy with the cumulates) and are probably related to the phonolites only in having a similar alkali basalt parent magma. The reason why the intermediate lavas were contaminated, whereas the phonolites were not, may have been due to the increased temperature of the crust at 15-20km depth, requiring a smaller input of heat to reach its solidus. At 1kbar the temperature of the crust must be raised by about 900°C for anhydrous melting to occur, whereas at depth a rise of only 600°C is required.

The cumulates are probably much more recent than the other Velay lavas. A small ($< 1km^3$) body of alkali basalt was emplaced at mid-crustal levels, and differentiated with simultaneous

wallrock contamination (AFC) to give a biotite-trachyte. Build-up of CO_2 eventually caused an explosive eruption, which ripped up the roof, walls and cumulates of the chamber. This process, like that which formed the northern intermediate lavas, is insignificant when compared with that which formed the Velay phonolites.

Chapter 1

Volcanology and structure of the Velay oriental

1.1 Geography

The Velay oriental volcanic district is so named because it forms the eastern half of an extensive basalt plateau in the Velay region of the French Massif Central. The Velay *occidental* to the west is usually referred to as the Devès, to avoid confusion. In this thesis "Velay" will be used synonymously with "Velay oriental".

Figure 1.1.1 is a general map of France showing the Massif Central and other areas of exposed Hercynian crust, together with their associated Tertiary and Quaternary volcanics. Figure 1.1.2 shows the Massif Central in more detail, with the names of the volcanic districts. The Velay oriental lies towards the eastern margin. Figure 1.1.3 is the last in this map series, showing the geology of the Velay oriental. It is a compilation from the published 1:250 000 map sheets Lyon-29 (Chiron and Kerrian 1979) and Valence-34 (Rouire and Chiron 1980) and the map provided in Mergoil (1980). The 1:80 000 geological map of the area was first published in 1893 and the present third edition (Goguel 1967) is of very poor quality.

The lavas of the Velay oriental extend to a maximum of 50km north-south and 30km east-west, covering at least 500km^2. The Velay plateau slopes gently down to the north, south and west

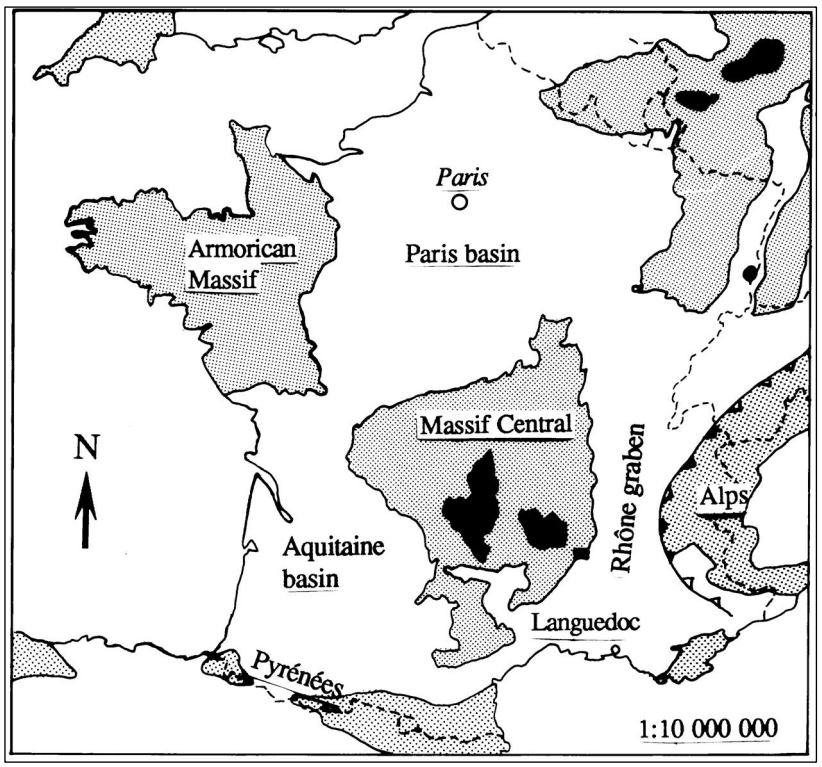


Figure 1.1.1. Map of France showing major geological elements.
White - Mesozoic and Tertiary basinal sediments
Shaded – Hercynian and other pre-Mesozoic basement
Black – Tertiary and Quaternary volcanics

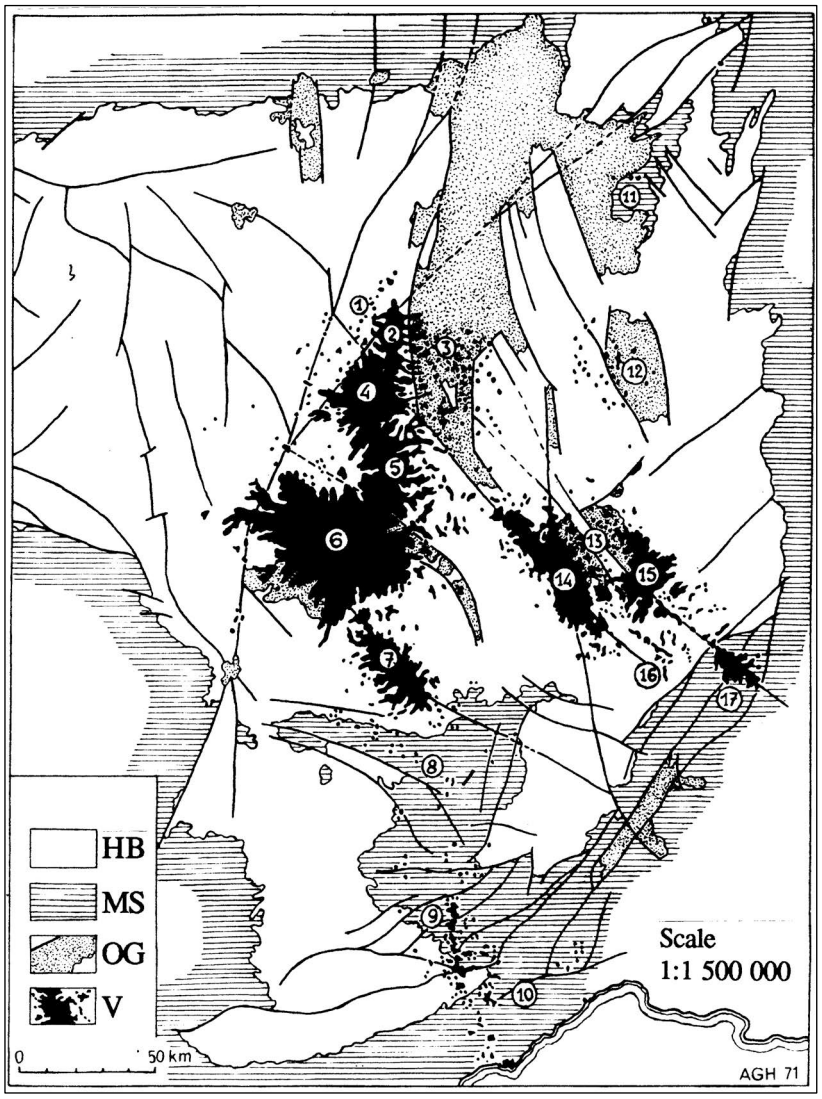


Figure 1.1.2. Simplified map of Massif Central geology, showing commonly used names of the volcanic regions (from de Goer and Mergoil 1971).
HB – Hercynian basement
MS – Mesozoic basin sediments
OG – Oligocene sediments in grabens
V – Tertiary and Quaternary volcanics

1 Chaîne de la Sioule
2 Chaîne des Puys
3 Limagne, Compté, Livradois
4 Mont-Dore
5 Cézallier
6 Cantal
7 Aubrac
8 Causses
9 Escandorgue
10 Bas-Languedoc
11 Bourgogne
12 Forez
13 Puy and Emblavès basins
14 Devès
15 Velay Oriental
16 Bas-Vivarais
17 Coiron

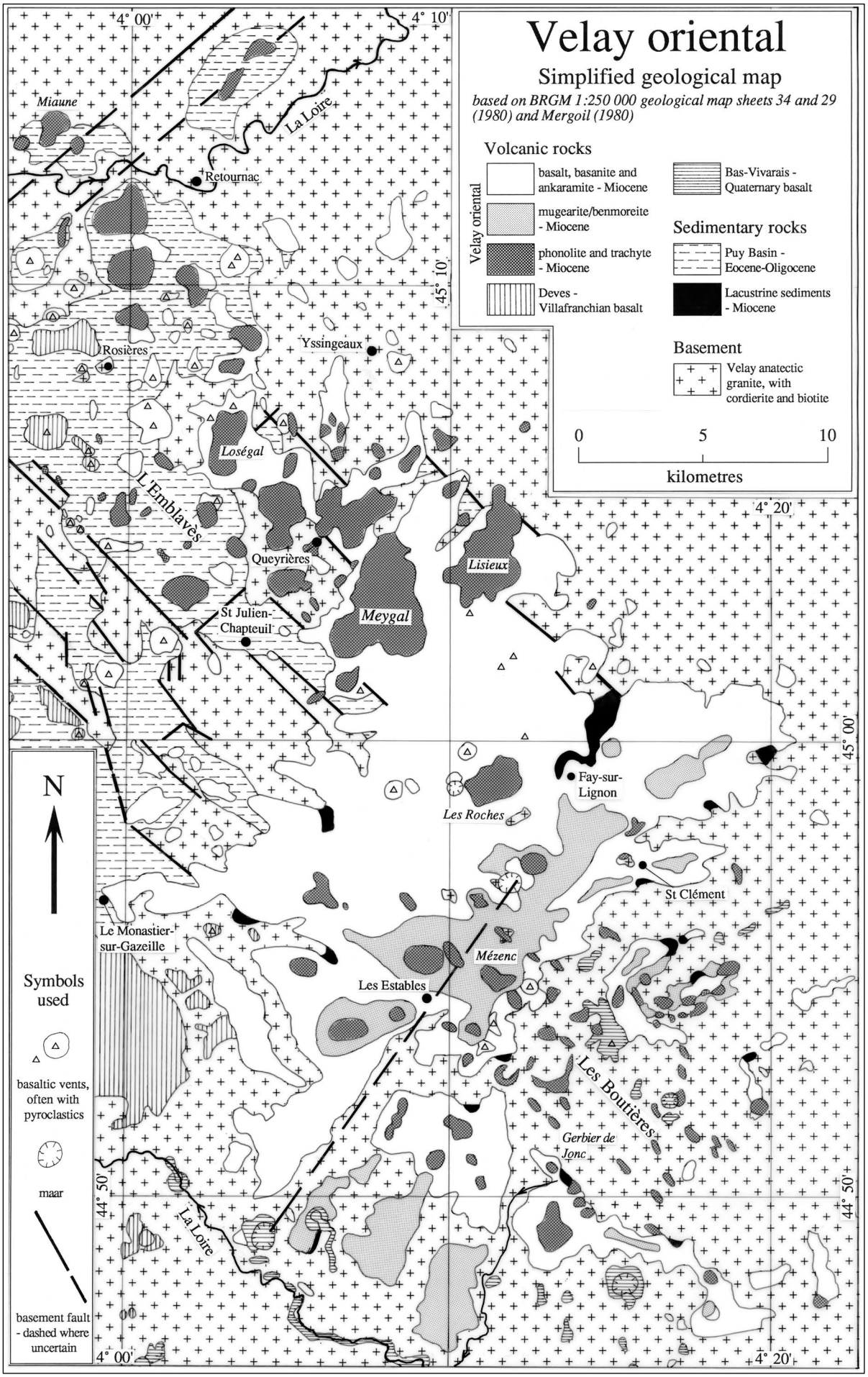

Velay oriental
Simplified geological map
based on BRGM 1:250 000 geological map sheets 34 and 29 (1980) and Mergoil (1980)
Volcanic rocks
Velay oriental
basalt, basanite and ankaramite - Miocene
mugearite/benmoreite - Miocene
phonolite and trachyte - Miocene
Deves - Villafranchian basalt
Bas-Vivarais - Quaternary basalt
Sedimentary rocks
Puy Basin - Eocene-Oligocene
Lacustrine sediments - Miocene
Basement
Velay anatectic granite, with cordierite and biotite
0
5
10
kilometres
4° 00'
4° 10'
4° 20'
45° 10'
45° 00'
44° 50'
Miaune
La Loire
Retournac
Rosières
Yssingeaux
Loségal
L'Emblavès
Queyrières
St Julien-Chapteuil
Meygal
Lisieux
Fay-sur-Lignon
Les Roches
St Clément
Le Monastier-sur-Gazeille
Mézenc
Les Estables
Les Boutières
Gerbier de Jonc
N
Symbols used
basaltic vents, often with pyroclastics
maar
basement fault - dashed where uncertain

Figure 1.1.3

from a maximum elevation of about 1500m in the area of Mézenc, down to 1000m. These relatively gentle slopes are part of the catchment area of the River Loire. To the east and south-east the plateau is sharply truncated by the downcutting tributaries of the Ardèche river, which have produced deep gorges separated by jagged ridges or "serres".

Scattered across the plateau are the numerous rounded hills of the phonolites. They take a variety of forms, from the huge Meygal with its shallow forested slopes, to the small rocky steep-sided domes or "sucs", exemplified by Gerbier de Jonc (see Figure 1.2.1). The highest point in the Velay is the phonolite peak of Mézenc at 1753m, overlooking the gorges of the Ardèche nearly 1000m below. Figure 1.1.4 is a view from Mt Mézenc towards the south-east into the dissected area known locally as Les Boutières. The three prominent peaks in the foreground are all phonolite extrusions. Figure 1.1.5, from the same point, shows the view to the south.

The north of the Velay consists of a large number of small basalt remnants that may once have formed a continuous plateau. Much of the area is also underlain by Eocene-Oligocene sediments of the Puy basin, which may have allowed the more rapid erosion of the basalt plateau. Phonolite hills are as abundant in the north as in the south of the Velay, and include the huge bulk of Meygal and Lisieux.

The granite basement of the Velay is important since there is evidence that it exerted a structural control on the sites of lava emission. Bout (1966) and de Göer de Hervé and Mergoil (1971) noted that on the basis of linear trends in valleys, combined with volcanic evidence, the basement appears to have been faulted into rectangular blocks elongated NW-SE, probably during the Tertiary. One of these blocks subsided to form the Emblavès graben, part of the Puy basin, which contains most of the phonolites in the north of the Velay.

1.2 Volcanic activity

1.2.1 Summary

The most recent description of the Velay volcanism appears in Mergoil (1980), as part of a general review of the geology of the area. The following is a summary of that paper, and other modern literature.

The Velay lavas were erupted onto a peneplain of Hercynian basement granite during the Miocene. Preserved under some of the lowest basalt flows are small pockets of detrital lacustrine sediments, sometimes containing lignite, which indicates a stable depositional environment. They are discussed in section 1.3.2.

The Velay oriental is unusual in the Massif Central in its abundance of phonolites and its paucity of quartz-normative lavas. There is also a marked bimodality between basalt and phonolite, as shown by



Figure 1.1.4. View to the south-east from Mt Mézenc. The three phonolite extrusions of (left to right) Roche de Borée, an unnamed 1290m peak and Suc de Touron, are visible in the foreground. Behind them the dissected landscape of Les Boutières contains the eroded roots of many other phonolite extrusions.



Figure 1.1.5. View to the south from the peak of Mt Mézenc. Horizontally stacked basalt flows are exposed in the wall of this glacial cirque, which has also exposed some strombolian pyroclastics beneath the plateau (in shadow). In the distance lie the phonolite flow-domes of (left to right) le Sépous, Suc de Séponet, Suc de la Lauzière and Suc de Taupernas.

the mapped surface areas of the various lava types (Mergoil 1980):

basalt, basanite, hawaiite	80%
mugearite, benmoreite, sub-alkaline trachyte	7%
phonolite, alkaline trachyte	13%

The bimodality is even more pronounced if volume proportions are calculated, the volume of phonolite being similar to that of the basaltic lavas (J. Mergoil *pers. comm.*).

The phonolites were erupted, without explosive activity, as viscous extrusions. They can be classified as:

"aiguilles" (needles) -	Roche de Borée, Gerbier de Jonc (Figure 1.2.1), unnamed 1290m peak near Touron (Figure 1.2.2)
endogenous domes -	Mt. Signon, La Tortue (Figure 1.2.3)
complex domes cut by dykes -	Mont d'Alambre, Mont Mézenc
flow-domes -	Lisieux, Testavoyre (Meygal)
short, blocky flows -	plateau NE of Le Béage

In the Boutières area of the southern Velay, where erosion has exposed the intrusive roots of phonolites, Mergoil (1968) identified ring-dyke intrusions of coarse-grained phonolite, or tinguaite. These vary from a few hundred metres in diameter (Rocher des Pradoux) to 2.5km (Suc de Sara - Figure 1.2.4). The outer contact of Sara is marked by minor fenitisation of the country rock. Other intrusive phonolites exposed in Les Boutières are elongated NW-SE, aligned with the general "grain" of the Hercynian basement.

Petrographically the phonolites are quite variable from one extrusion to another and sometimes within one extrusion. They cover the whole range from aphyric to phenocryst-rich, and their phenocrysts indicate a range from alkaline to peralkaline lava compositions, confirmed by bulk analysis. Any model of phonolite petrogenesis in the Velay must take into account the independent evolution of each of the phonolite extrusions, which led Göer de Hervé and Mergoil (1971) to suggest late-stage fractionation in small apophyses from larger magma chambers.

Most of the extrusive phonolites are set on a basalt plateau comprising up to ten stacked flows, each 8-12m thick. They are predominantly aphyric or sparsely phyric, but occasional ankaramites contain abundant olivine and clinopyroxene phenocrysts up to 1cm in diameter. In the south of the Velay the plateau flows grade from alkali basalts and basanites at the base, through hawaiite, to thin (4-6m) flows of mugearite and benmoreite at the top. The best locality to observe these features is the edge of the plateau to the south-east of St. Clément, as shown in Figure 1.2.5.

In the north the plateau often consists of only two basalt flows, with mugearite and benmoreite being represented by viscous extrusion domes. Although these evolved lavas have a similar bulk composition to those in the south, there are many other differences between them. To distinguish them, Mergoil (1980) used the terms "aphanitic alkaline trachyte" for the southern benmoreites and mugearites, and "porphyritic sub-alkaline trachyte" for those of the north. The phonolites were divided into northern and southern groups by de Göer de Hervé and Mergoil (1971) on the basis of



Figure 1.2.1. The “needle”extrusion of Le Gerbier de Jonc (literally “the stack of rushes”) showing the characteristic radial expansion joints, formed as the extrusion was forced out of its conduit. The fissility of the phonolite, sub-parallel to the surface, is also clearly visible.



Figure 1.2.2. The unnamed 1290m peak 500m NE of Suc de Touron (seen on the left). This is an exceptionally well-formed “needle” extrusion, which in contrast to Le Gerbier de Jonc, emphasizes the formation of prismatic columns. The prisms are horizontal and oriented radially at the base, changing to vertical towards the top, indicating that they formed as a result of cooling.



Figure 1.2.3. Mont de la Tortue (literally “Tortoise Hill”) is clearly appropriately named! It formed in a similar fashion to the aiguilles of Figures 1.2.1 and 1.2.2, but was able to flow outwards slightly to produce an endogenous dome. Radial expansion joints are visible on the left side of the larger mass. The whole hill is covered with scree, which is typical for Velay phonolites.

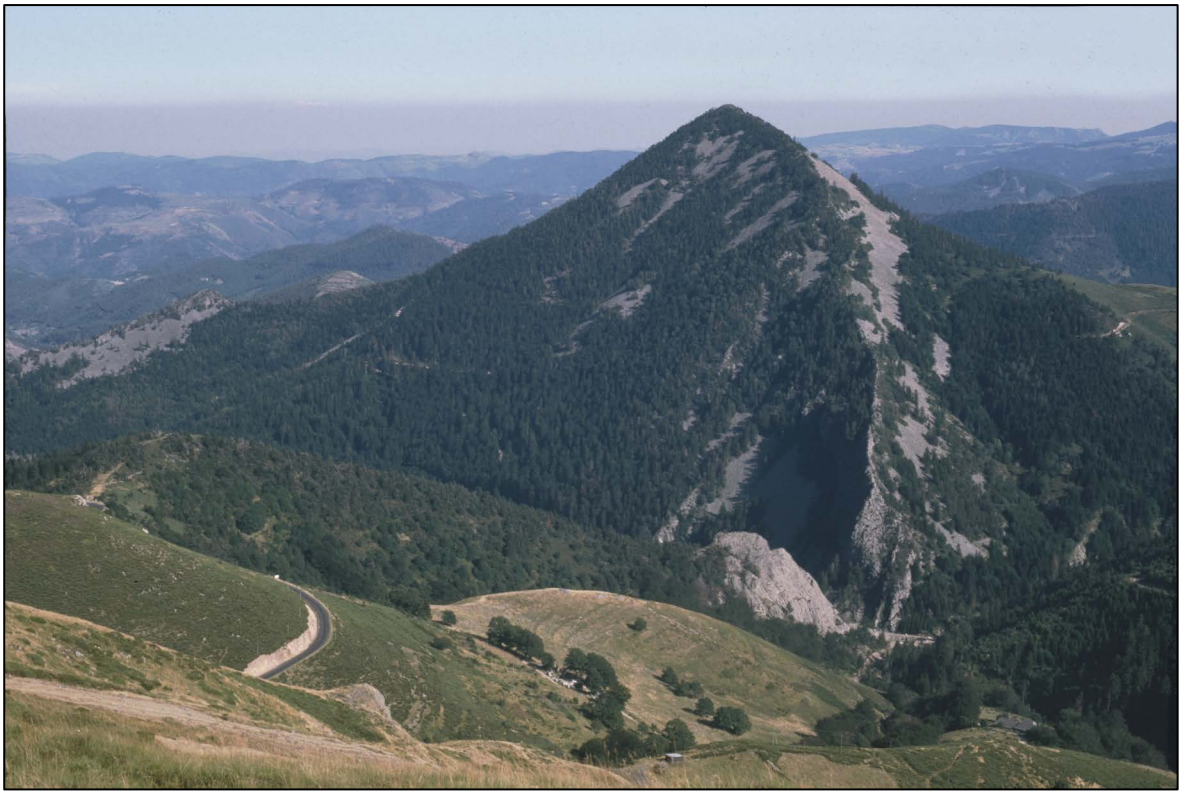


Figure 1.2.4. The ring-dyke of Suc de Sara. This intrusion of agpaiitic phonolite is not a complete ring, but forms a “horse-shoe” of about 270º. The prominent ridge to the right of the picture marks the outer contact of the intrusion, which can be picked up again on the left of the photograph, at the top of the scree-covered slope. Huge piles of scree obscure most of the contacts. The granite basement is visible in the road cutting in the foreground.



Figure 1.2.5. The plateau edge near St Clément, seen from Rocher de Soutron. In the distance the horizontally stacked flows of the plateau can be seen at their thickest, with at least nine flows visible. In the foreground, the ridge is capped by another basalt sheet. Originally all these isolated fragments formed a continuous plateau covering the whole area.

their association with these different types of intermediate lavas, their physical separation and the fact that peralkaline phonolites are more common in the south than in the north (de Göer de Hervé and Mergoil 1971).

The original volcanic structures of the plateau-building phase were buried by the successive flow-sheets of the basalt plateau but some have been exposed by erosion of the plateau edge. The best example is at Les Boutières (Figure 1.1.5), 2km south of Mont Mézenc, where strombolian cones of bedded hawaiite to mugearite pyroclastics are cut by dykes which fed the mugearites and benmoreites of the upper plateau flows. The area was studied in detail by Olives *et al* (1976) who were able to deduce the order of eruption of the various elements and also to correlate some flows across the southern wall of the cirque.

The most recent activity in the Velay was dominantly phreatomagmatic, producing prominent maars, often containing circular lakes, for example Lac de St. Front, Lac d'Issarlès. The basalt flows of the Bas-Vivarais, often rich in spinel-lherzolite nodules, are preserved in the valleys of the Ardèche, for example the St. Martial and Ray-Pic flows. They are only a few tens of thousands of years old.

1.2.2 Historical work

Most of the conclusions summarised above were reached by earlier workers in the Velay, with Boule (1892) as a notable example. An exception to this was G. Poulett Scrope's "The Geology and extinct volcanoes of Central France", first published in 1826 and reprinted in 1858. He described the Velay oriental, the Devès and the Coirons (see Figure 1.1.2) as products of a single volcano, but forming plateaux rather than a central cone. This was attributed to a low frequency of eruptions and also to the relative abundance of basalt and "clinkstone" (phonolite), both of which he regarded as being highly fluid lavas compared with the "granular or common trachyte" (trachybasalt) of the other Massif Central volcanoes.

Scrope concluded that "Mezen" (Mont Mézenc) was the source of all the lavas of the region by virtue of its elevation, which allowed the lavas to travel great distances downslope. In this light, he interpreted the phonolites of the northern and southern Velay as being eroded fragments of two gigantic phonolite lava flows. The dimensions he gave for the northern flow imply a volume of at least 54km^3. He also noted that local French geologists believed the phonolites to be individual extrusions, an interpretation now known to be correct.

1.3 Chronology

1.3.1 Field relations

The relative ages of the basaltic plateau flows can be determined using the assumption that the area was completely covered by successive sheets of lava, with those at the base obviously being erupted earliest. The absence of any interbedded sediments indicates that the successive plateau flows were erupted quite rapidly.

The ages of the phonolite extrusions relative to the plateau lavas are much more difficult to determine, due to the extensive piles of boulders and scree obscuring their bases. Many authors have attempted to solve this problem, trying to infer the age relations by other means. Bout (1968) and Bobier and Macle (1967) described a breccia with phonolite clasts beneath a basalt flow at Combevieille, on the D18 4km east of Queyrières, on the northern edge of Meygal, as evidence for the eruption of phonolites before the basalts. They also presented various lines of evidence suggesting that many phonolites were erupted after the plateau flows.

Later authors tended to the view that the phonolites were extruded after the plateau lavas, especially on the basis of fieldwork in the southern Velay and the K-Ar dates obtained by Cantagrel and Mergoil (1970).

1.3.2 Sedimentary stratigraphy

After being peneplaned at the end of the Permian, the Massif Central preserved virtually no sedimentary record from the Triassic to the early Eocene. In the Lutetian (M. Eocene) arkoses were deposited in the Puy basin, followed by lacustrine sediments, with gradual expansion of the area of subsidence and deposition until the lower Oligocene.

In the Velay, discontinuous thin lacustrine sediments are found beneath the oldest basalt flows at a few localities, such as Gourgouras, Aubépin, Clauzelles, Vacheresse, Meyzous and St. Clément. These localities are marked on Figure 1.1.3, and named on the large-scale location maps in the back pocket of this volume.

The sediments consist of fine homogeneous sands, sometimes with reworked "chailles" (Jurassic siliceous concretions), clays rich in plant material, lignite layers (towards the top of the sequence) and occasionally reworked volcanic material, which is one of the earliest signs of volcanism in the Velay.

The fossil plants of Gourgouras were studied by Grangeon (1953) who dated them as late Miocene to early Pliocene, with a mediterranean climate. At Aubépin, near the village of Moudeyre, in the old lignite mine, two teeth of *Hipparion gracile* were found in 1917, and later identified by Depéret (mentioned in Bout 1966). Elsewhere, near Fay-sur-Lignon, Boule (1892) found gastropod shell debris in a siliceous carbonate horizon. These fossil data, together with regional correlation, allow the sediments to be dated as Upper Miocene.

In the Villafranchian fluvio-lacustrine sediments of the Puy basin, Boule (1892) found pebbles of all the different lavas of the Velay oriental, suggesting that at this time most of the volcanism in the area had ceased. The age of these sediments is well constrained by the abundant mammalian fauna they contain, which led to their being named "the Mastodon sands".

The lavas of the Velay are thus stratigraphically constrained to lie between the Upper Miocene and the Villafranchian.

1.3.3 Potassium-Argon dating

1.3.3.1 Previous work

G.H. Curtis (*in* Bout 1966) published the first K-Ar date for the Velay: 13.6Ma for the trachyte "sous la Vierge", immediately to the north of the village of St. Pierre Eynac.

The first proper study of K-Ar ages for the Velay was presented by Cantagrel and Mergoil (1970). They dated thirteen specimens, five of which showed the plateau lavas to have been erupted between 11.7Ma and 7.6Ma. Four phonolites and a trachyte from the south had ages in the range 9.0Ma to 6.5Ma, and two trachytes from the north gave 10.8Ma and 9.75Ma. The remaining two specimens related to more recent volcanism.

Prévot and Dalrymple (1971) attempted to combine palaeomagnetic data with K-Ar dates to produce a detailed chronostratigraphy for part of the southern half of the area, but the resolution of the palaeomagnetic timescale proved insufficient for good correlation. They provided nine K-Ar dates, of variable quality, all of which were within the age ranges established by Cantagrel and Mergoil.

More recently Féraud (1981) measured the ages of seven dykes in the area, with compositions from hawaiite to mugearite. Two of these were from a more recent period of basalt volcanism, and the remaining five again all fit into the age ranges of Cantagrel and Mergoil.

All of the data described in this section have been recalculated using modern constants and are presented in Table 1.3.1.

1.3.3.2 New K-Ar data

The key discovery made in this thesis was that the phonolites in the north of the Velay were erupted at about 13Ma, before any other previously dated lava from the Velay. This unexpected result demonstrates that evolved lavas can be erupted without any precursor basalts.

Sixteen samples were K-Ar dated for this study, including ten phonolites, two alkali basalts and one each of basanite, hawaiite and benmoreite, using the techniques described in Appendix E. A cumulate block from a pyroclastic eruption was also dated and this is discussed in section 4.4. The results are given in Table 1.3.2.

The four most basic lavas, with compositions from alkali basalt to mugearite, fall in the established range of 11.7Ma to 7.6Ma. The lava lake of La Chaud de la Croix, dated 7.95Ma, shows that there was at least some eruption of basic lava in the north during the plateau-building stage. The Monastier flow rests on the granite, and was dated as 8.6Ma, which is 3Ma younger than the earliest basalts. It demonstrates the long duration of plateau building, and the increase in its area with time. The flow at Machabert is older and less evolved than that at Le Monastier, but rests on another basalt flow. Thus this locality was probably nearer to the site of the first plateau eruptions, and was covered earlier. At Fay-sur-Lignon a flow of mugearite lies at the top of the succession, dated 8.6Ma. This is 1Ma older than the youngest benmoreite, and is less evolved, demonstrating the continuity of the sequence, even if such compositions are rare

Table 1.3.1

Summary of published K-Ar data

Location	Reference	K%	^{40}Ar (rad) (10^{-9} g/g)	atmospheric argon %	Age using modern constants (Ma)	error (Ma)	Comments
St. Pierre Eynac - trachyte immediately to north of village	G.H.Curtis *in* Bout 1966 Rev. d'Auvergne v.80 p55-67	n.d.	n.d.	n.d.	13.6	±0.3	oldest date obtained for Velay - may not be reliable
1) Basalt flow - near Bonnevialle, SE of D43	Cantagrel & Mergoil 1970 C.R.Acad.Sci. v.271 p760-763	1.07	0.56	84	7.6	±0.2	too young - due to alteration/carbonates
			0.59	91	8.0	±0.2	
2) Basalt flow - bed of stream of Les Merles. 600m upstream of D154	"	1.46	1.18	20	11.7	±0.35	good quality
3) Basalt flow - base of plateau stack on D247, S of St Clément	"	1.06	0.77	78	10.5	±0.3	good quality
4) Basalt flow - immediately above 3)	"	2.29	1.16	39	7.3	±0.2	too young - due to alteration/carbonates
			0.86	46	5.4	±0.2	
5) Basalt flow - W edge of plateau of Huche Plate	"	1.76	0.15	75	1.23	±0.04	good quality
6) Basalt flow - St Martial area, near Le Chambon, on D215	"	0.90	0.23	31	4.0	±0.1	too high - due to presence of granite feldspars
7) Benmoreite flow - La Freydeyre, quarry near N500	"	3.17	1.68	27	7.65	±0.2	good quality
			1.67	17	7.60	±0.2	
8) Trachyte dome - 200m N of Montusclat	"	3.81	2.72	31	10.3	±0.3	good quality
			3.00	16	11.3	±0.3	
9) Phonolite - Les Roches, 1km S of Roffiac	"	4.91	2.12	30	6.3	±0.2	good quality
			2.60	20	7.65	±0.2	
10) Quartz trachyte - Dents du Mézenc, N of Mézenc	"	4.37	2.72	7	9.0	±0.3	good quality
11) Trachyte ?dyke - Riou Frei, W flank of Mont Loségal	"	4.75	3.22	13	9.75	±0.3	good quality
12) Phonolite ring intrusion - Suc de Sara near Borée	"	4.16	1.85	57	6.5	±0.2	good quality
13) Phonolite dome - Mont Mézenc	"	4.38	2.27	13	7.5	±0.2	good quality
			2.43	22	8.0	±0.2	
1) Benmoreite flow - 1554m peak, south of Rochers de Cuzet	Prévot and Dalrymple 1971 Ann. Géophys. v.27 p423-427	3.84 3.88	2.33	60.6	8.7	±0.3	good quality
2) flow beneath 1)	"	3.38	2.08	56.4	8.8	±0.3	good quality
3) basalt flow beneath 2)	"	0.86 0.88	0.44	20.9	7.3	±0.4	too low on strat. basis
4) basalt flow beneath 3)	"	0.96	0.57	41.3	8.5	±0.3	age probably too low, due to alteration
5) basalt flow - immediately to south of Mézenc	"	1.28 1.33	0.88	5.6	9.7	±1.6	poor quality due to alteration
6) Mézenc phonolite	"	4.23 4.25	2.29	47.6	7.8	±0.2	good quality
7) Mézenc phonolite	"	4.25	2.29	34.4	7.8	±0.3	good quality
8) Phonolite dyke in Mézenc	"	4.52 4.51	2.56	57.0	8.2	±0.2	good quality
9) Phonolite dyke in Mézenc	"	4.52 4.51	2.57	33.5	8.2	±0.3	good quality
1) Intermediate dyke - near Croix de Boutières	Féraud 1981 thesis University of Nice	1.34	0.82	57.6	8.8	±0.3	good quality
2) Intermediate dyke - 600m south of 1)	"	1.34	0.79	17.7	8.4	±0.2	good quality
3) Intermediate dyke - 200m SE of 2)	"	2.64	1.61	14.7	8.8	±0.2	good quality
4) Hawaiite dyke - 1km SE of Molines	"	1.68	0.68	21.3	5.8	±0.2	^{40}Ar-^{39}Ar gives 6Ma - so quite good quality
5) Hawaiite dyke - 200m SE of 4)	"	1.24	0.41	28.8	4.8	±0.1	too young - ^{40}Ar-^{39}Ar gives 6Ma
6) Hawaiite dyke - near Freycenet-la-Tour	"	2.05	1.34	33.1	9.4	±0.3	confirmed by ^{40}Ar-^{39}Ar, which gives 8.8Ma
6) Hawaiite dyke - near Freycenet-la-Tour	"	2.43	1.64	77.3	9.7	±0.5	probably the same age as 6)
7) dyke - near Le Pertuis	"	2.67	2.04	40.6	11.0	±0.2	good quality

Table 1.3.2
Results of K-Ar dating

	Name, location and exposure type	Co-ordinates	Petrographic description	Clermont analysis / Specimen number	Rock name	K%	40Ar (ng/g)	Atmos-pheric 40Ar %	Age (Ma)	error (Ma)
			Plateau lavas							
1)	La Chaud de la Croix - quarry in 1229m hill, near D15, 4.5km ENE of Boussoulet Lava lake	04°10'48" east 45°02'10" north	Phenocrysts: zoned cpx with some green cores,olivine,resorbed amphibole,opaques groundmass: cpx,olivine,opaques, plag An60,glass with dendritic opaques texture: porphyritic hypocrystalline	RT 12427 88/29	alkali basalt/ hawaiite boundary	1.86	1.02	25.7	7.95	±0.15
2)	Railway cutting, just north of D535 running SE from Le Monastier-sur-Gazeille. 1.5km from village centre Flow resting on basement	04°00'32" east 44°55'58" north	Zoned cpx,olivine,opaques,plagioclase - a) euhedral-An55 b) interstitial-zoned. texture: holocrystalline seriate	RT 12428 88/30	basanite	1.76	1.046	49.2	8.6	±0.2
3)	Quarry 200m north of D39 running W from St. Front 1.5km W of Machabert village Flow - 2nd or 3rd above basement	04°06'14" east 44°58'45" north	Zoned cpx,olivine,plagioclase An60, opaques texture: medium-grained holocrystalline seriate	RT 12429 88/31	alkali basalt	0.871	0.589	90.6	9.7	±1.0
4)	Road cutting on D500 500m SSW of Fay-sur-Lignon Flow near top of plateau	04°13'24" east 44°59'00" north	Phenocrysts: corroded plag An32,opaques, brown apatite,tr. resorbed amphibole groundmass: plag An60,opaques,cpx texture: trachytic	RT 12430 88/32	mugearite	2.27	1.36	47.1	8.6	±0.2
			Northern evolved lavas							
5)	Suc de Pertuis - road cutting on D28, running SE from Le Pertuis, 500m from junction with N88 Extrusion dome	04°03'47" east 45°05'37" north	Aphyric. groundmass: sanidine,cpx,nepheline aenigmatite,opaques,tr. amph,tr. apatite texture: trachytic	RT 12424 88/26	phonolite	4.50	4.12	22.8	13.2	±0.2
6)	Mont Loségal - quarry beside D35 running W from Le Pertuis, 1.5km from junction with N88 Flow dome	04°02'31" east 45°06'03" north	Aphyric. groundmass: sanidine,cpx,opaques, nepheline,aenigmatite texture: trachytic	RT 12425 88/27	phonolite	4.78	4.29	7.9	12.9	±0.2
7)	Miaune - quarry beside D35, 0.8km SE of Roche-en-Regnier, 7km WNW Retournac Flow dome	03°57'21" east 45°13'19" north	Phenocrysts: Anorthoclase,resorbed amphibole,opaques,sphene,zircon,tr. cpx groundmass: sanidine,aegirine,opaques, feldspathoid,apatite,tr. sphene texture: weakly trachytic	RT 12426 88/28	phonolite	5.22	4.84	7.7	13.3	±0.2
8)	Montagne du Meygal - Lac bleu quarry on SE edge, north of D15 1.3km ENE of Boussoulet Flow dome	04°09'24" east 45°02'18" north	Microphenocrysts: sanidine,opaques groundmass: sanidine,cpx,opaques, nepheline,aenigmatite texture: trachytic	RT 12435 86/15	trachyte/ phonolite boundary	4.98	4.35	7.9	12.6	±0.2
9)	La Dent, 970m peak.Road cutting near top. Peak is 2.8km SW of Beauzac and 6km NNE of Retournac Flow dome or thick flow	04°04'00" east 45°15'08" north	Microphenocrysts: plag An60,cpx,opaques groundmass: plag An60,?sanidine,opaques, cpx,tr. brown apatite texture: trachytic	RT 12604 87/11	benmoreite	3.17	2.77	16.6	12.6	±0.2
10)	Exposure 250m S of 869m hill, 1km ESE of St. Pierre Eynac and 1.5km NW of St. Julien Chapteuil Dyke	04°02'50" east 45°02'43" north	Microphenocrysts: tr. sanidine groundmass: sanidine,feldspathoid,cpx, tr. opaques,tr. sphene texture: trachytic	RT 12605 87/67	phonolite	4.56	3.33	54.3	10.5	±0.25
11)	Mt. Chanis - SW edge,300m NW of Montchanis and 2.5km NE of St. Julien Chapteuil Extrusion dome	04°04'58" east 45°03'18" north	Phenocrysts: plag An30-40,sanidine/ anorthoclase,resorbing amphibole,opaques, tr.cpx. groundmass: sanidine,cpx, opaques,tr. biotite texture: porphyritic holocrystalline	RT 12606 87/70	phonolite	3.58	2.77	18.8	11.1	±0.2
			Southern evolved lavas							
12)	Le Gerbier de Jonc - near the source of the Loire, at the junction of the D378 and D116 Rigid spine extrusion	04°13'18" east 44°50'38" north	Phenocrysts: sanidine groundmass: sanidine,nepheline,aegirine, aenigmatite texture: trachytic	RT 12607 87/76	phonolite	4.46	2.54	17.8	8.2	±0.15
13)	Suc de Touron - road cutting on southern edge, N of D378, 2km SW of Borée Extrusion dome	04°13'15" east 44°53'26" north	Phenocrysts: zoned anorthoclase, amphibole,nosean,opaques,sphene,zircon, apatite,tr. corroded cpx groundmass: K-feldspar,cpx,opaques, nosean,sphene. texture: trachytic	RT 12431 88/33	phonolite	4.79	2.82	32.2	8.5	±0.2
14)	Chabrières - uppermost part of landslip on SE edge. 2km W of Borée Extrusion dome	04°13'01" east 44°54'00" north	Phenocrysts: sanidine,tr. amphibole, tr. cpx,tr. opaques,tr. sphene groundmass: sanidine,amphibole,opaques, feldspathoid. texture: trachytic	RT 12432 88/34	phonolite	4.71	2.62	48.3	8.2	±0.2
15)	Quarry beside D122 running SE from Mézilhac, 3km ESE of Gerbier de Jonc Extrusion dome	04°21'47" east 44°47'44" north	Phenocrysts: sanidine,resorbing amphibole,cpx,opaques,tr. apatite groundmass: sanidine,cpx,opaques, tr. amphibole. texture: trachytic	RT 12433 88/35	trachyte/ phonolite boundary	4.54	2.42	24.6	7.7	±0.15
			Cumulate specimen							
16)	Chabrières - slightly lower in landslip on SE edge. 2km W of Borée Cumulate sampled by more recent pyroclastic eruption	04°13'01" east 44°54'00" north	Plag An22-31,biotite,corroding pale-green cpx,opaques, apatite,glass,carbonate,zircon texture: coarse granular	RT 12434 88/14b	amphibole cumulate	2.24	1.32	56.7	8.5	±0.2

The most northerly dated specimen is the aphyric benmoreite of La Dent, which lies outside the main area of northern phonolites. It was erupted at 12.6Ma and formed the short, thick flow of La Madeleine, 2km to the SW, which now stands on a pedestal of Oligocene sediments. It appears to be unrelated to the other benmoreites of the north, which are phenocryst-rich and form steep-sided domes.

The ages of the six phonolites from the north range from 13.3Ma to 10.5Ma, with Miaune, Loségal and Le Pertuis being the oldest, towards the NW of the group. They represent all types, from large flow domes to small plugs, with a wide range of phonolitic compositions. The phonolite dyke at St. Pierre Eynac had previously been presumed to be Villafranchian (Bout 1968, Mergoil *et al* 1979), but the age of 10.5Ma obtained in this study shows that it was contemporaneous with the intermediate lavas of the north.

The four southern phonolites are aged between 8.5Ma and 7.7Ma, which is within the established range. Suc de Touron gave an age of 8.5Ma, significantly different from that of Suc de Sara, at 6.5Ma (Cantagrel and Mergoil 1970). Mergoil (1968) interpreted these as two parts of a single ring intrusion, despite differences in their petrography. The age difference shows that they were not emplaced in a single event, although they may have exploited the same ring fault.

1.3.3.3 Discussion

These results clearly establish that the phonolites of the northern and southern groups were erupted in two separate episodes, with those in the north appearing before the earliest dated basalts. This implies that they rest directly on the sediments of the Puy basin or its underlying basement.

Figure 1.3.3 plots the age of the evolved lavas against their distance along a line joining Miaune in the NW and Mézilhac in the SE. The two groups are clearly separated and within each group the distribution is random. This demonstrates that the northern and southern phonolites were erupted as two independent groups and not as a result of a locus of activity migrating continuously from north-west to south-east.

As a melt fractionates, the concentration of incompatible trace elements increases. A correlation between the age of the phonolites and their Zr concentrations would therefore be expected for a single magma chamber differentiating with time. Figure 1.3.4 shows that no such correlation exists, either in the area as a whole, or within the two groups. This could be due either to repeated cycles of differentiation in the same chamber, a single zoned chamber that existed for a long time, or many independent small chambers.

Whatever their source, it is proposed that the northern phonolites be called the Emblavès group and those of the south the Boutières group, in view of the nomenclature adopted for the area by de Goër de Hervé and Mergoil (1971).

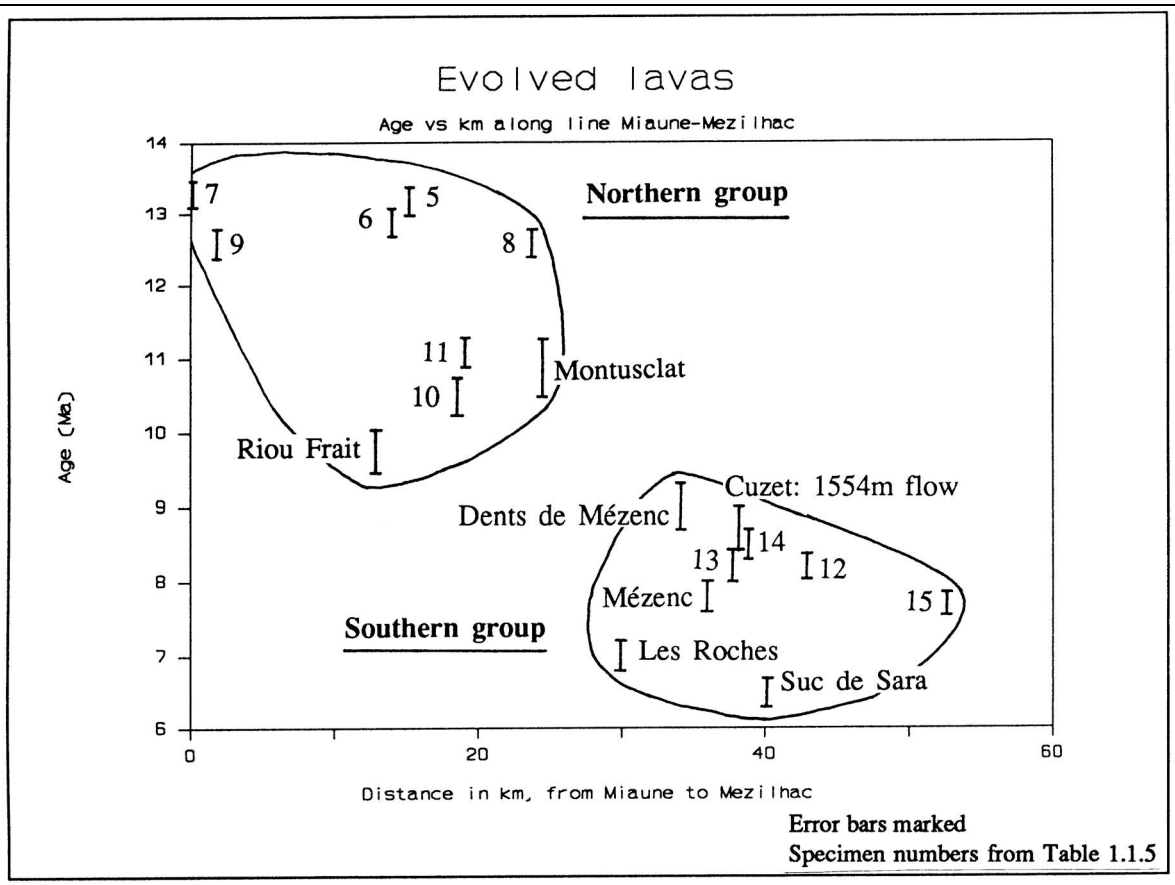


Figure 1.3.3. Age plotted against distance along the line joining Miaune to Mézilhac, showing no age progression, either as a whole or within each group.

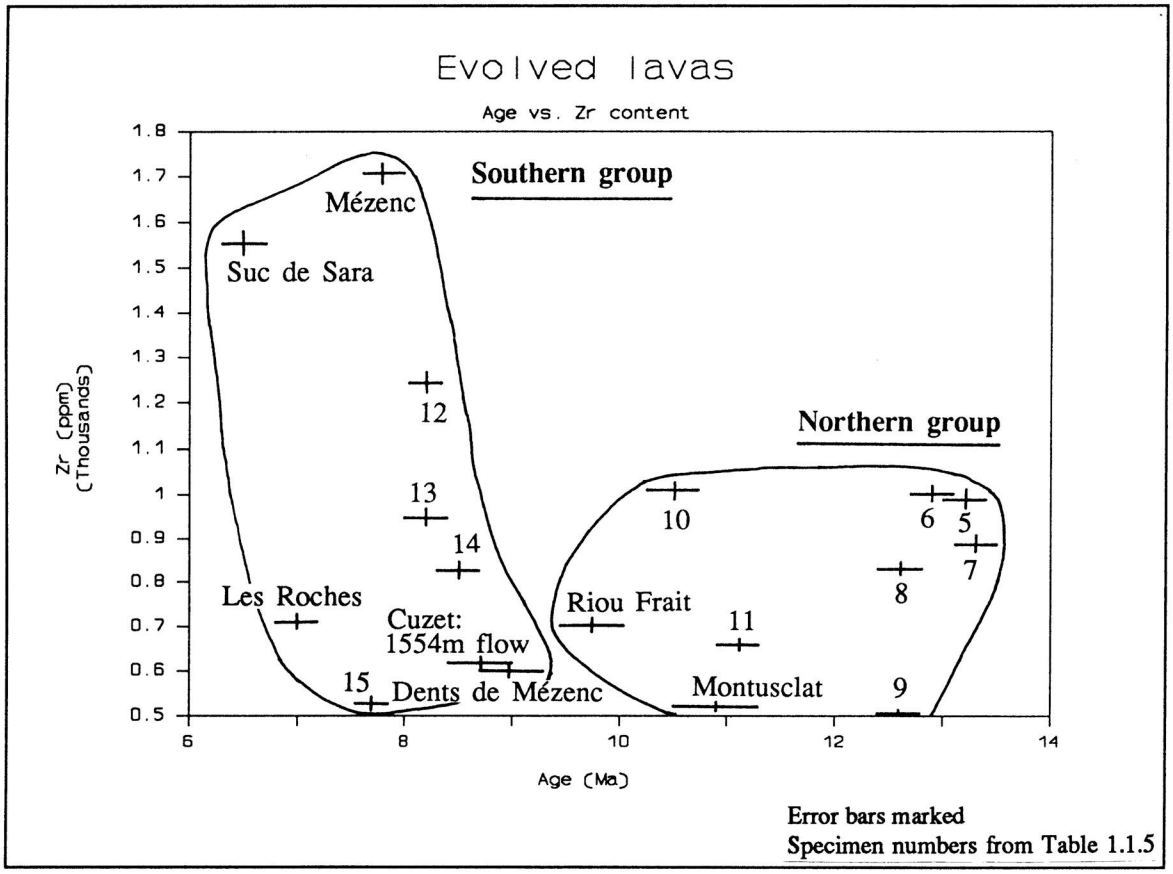


Figure 1.3.4. Age plotted against zirconium content, showing no correlation, either in the area as a whole, or within each group.

1.4 Main features to be explained

As shown in Chapters 3 and 5, the Velay oriental is a simple undersaturated differentiated series, with an alkali basalt parent fractionating to form all of the evolved lavas, including the phonolites.

Two features of the Velay volcanism remain unexplained, however. The first is the marked bimodality of the lava compositions between basalt and phonolite and the second is the virtual absence of evidence for explosive activity during the eruption of the phonolites. These features are discussed in detail below.

1.4.1 Bimodality of lava compositions

If a single batch of basalt magma differentiates at a continuous rate, and all the lava types produced have a roughly equal chance of being erupted, then the volume of each lava type that reaches the surface will be proportional to the amount in the chamber. Since the volume of magma decreases with evolution, this translates as large volumes of basalt, less abundant intermediate lavas and only small quantities of evolved lavas such as phonolite.

In the Velay by contrast, phonolites are almost as voluminous as basalts (see section 1.2.1), whereas intermediate lavas such as hawaiite, mugearite and benmoreite appear only in small amounts, based on the estimated volumes of mapped and analysed units of the plateau flows and extrusive lavas. Göer de Hervé and Mergoil (1971) also noted the bimodality on the basis of mapped areas of lava types. Graphs of bulk composition of the Velay lavas (Figure 5.3.1a-z) show the bimodality despite the deliberate oversampling of the intermediate lavas for this study.

The first observations of basalt-trachyte bimodality were by Daly (1925, 1927), for the lavas of Ascension and St. Helena islands. The paucity of intermediate lavas he noted came to be called "the Daly gap", after Chayes (1963) confirmed the bimodality of samples from oceanic islands all over the world. He pointed out that the existence of a gap is not incompatible with the mechanism of fractional crystallisation since, as stated at the start of this section, many assumptions need to be made in order to predict a progressive decline in lava volumes with evolution, some or all of which may be invalid. For example, different magma types may have a different probability of being erupted.

Baker (1968) however, showed that not only was there no gap on St. Helena, the volumes of lavas were exactly as predicted by fractional crystallisation. Cann (1968) emphasised that sampling bias was capable of generating an apparent Daly gap, but also suggested that natural processes might produce a gap in surface exposure. Hill (1974) subscribed to such a cause for the Daly gap in the Aden volcanics. He noted that the early part of the volcanic cycle produced only basalts and trachytes, whereas the subsequent caldera-filling event was dominantly of intermediate lavas. He concluded that simple fractionation operated in the magma chamber, but that physical processes such as volatile build-up controlled the proportions of lava types that reached the surface.

Detailed field mapping by J.D. Bell (*pers. comm.*) has established that Ascension island has a

true Daly gap, based on volumetric proportions observable at the surface, but makes the point that only a tiny fraction of the lava pile lies above sea level, rendering a true assessment of erupted volumes of lava types impossible. This problem will always face workers on oceanic islands.

A final significant point was made by Clague (1978) who showed that the commonly used measures for lava type such as SiO_2 and CaO were in fact poor indices of evolution when compared with an incompatible element (see section 5.3). This is true for the Velay, as Figure 5.3.1b illustrates, with a rapid increase in SiO_2 up to about 61% where it remains constant, despite the continued fractionation in the phonolites. However, even taking this factor into account, there is still strong bimodality in the volumes of the Velay lavas, which must be explained, and this point is pursued in section 1.6.3.

1.4.2 Lack of explosivity

Whereas the basaltic lavas form thin sheets covering large areas, it is clear from their forms that the phonolites were extruded as highly viscous lavas, which either remained at their source or travelled only a short way from it. High viscosities are also predicted from melting experiments on similar rocks. Despite these high viscosities, however, there are no phonolitic pyroclastics in the Velay (de Göer de Hervé and Mergoil 1971). The only example of pyroclastic material with an evolved composition is a rare quartz-trachyte (discussed in Chapter 4), which has only a small volume.

Normally a basalt magma starts its journey to the surface because it has a lower density than the mantle in which it forms. It rises up its conduit until it reaches the level at which the surrounding rock has the same density, at which point the force propelling it to the surface is entirely due to the magma column beneath it. Upon reaching the surface, the exsolution of dissolved gases forces it out of the conduit, like the contents of a freshly opened bottle of fizzy drink. In basalt magmas, with low viscosity, the process is fairly passive as the gas bubbles escape from the magma immediately it emerges from its conduit, causing fire-fountaining. Viscous lavas, especially rhyolites, are able to resist the expansion of the bubbles until they have enough force to cause a single catastrophic eruption, blasting the magma out of its chamber as tiny shards, which fall to the ground as pyroclastics.

In the Laacher See, in the Eifel volcanic district of Germany, exactly the same mechanism occurred in a zoned magma chamber, producing the Laacher See Tephra (Wörner and Schmincke 1984a,b). Elsewhere there are examples of phonolitic ignimbrites, all of which demonstrate that explosive phonolite eruptions are possible.

If the phonolites of the Velay were forced to the surface by internal gas pressure, their apparent lack of explosivity needs to be explained. If gas pressure was not the driving force another mechanism must be found to bring the abundant viscous phonolites to the surface. This is considered further in section 1.6.3.

1.5 The structure of the Velay oriental

1.5.1 Evidence of uplift

Figure 1.5.1 shows contours on the base of the Velay basalt plateau. These were constructed using the elevation of the base of the plateau edge, combined with extra data from the occasional basement "windows" in the plateau. The result is a map of the topography of the basement plus its overlying sediments, on which the contours define a small basement high in the south of the Velay, with a diameter of 20km and a maximum elevation of 300-400m. The northern Velay is also slightly elevated, but over a much wider area.

The basement elevation was probably formed by uplift of an originally sub-horizontal surface. The main line of evidence for this is the nature of the Miocene sediments preserved under the basalt plateau. As described in section 1.3.2, these consist of fine homogeneous sands with occasional lignites, which have been interpreted as being deposited in small lakes on a peneplaned surface with low relief.

The southern basement high is centred on the southern group of phonolites, whereas there is no clear relationship between elevation and phonolite distribution in the north. The association between the elevated area and phonolite volcanism in the south implies that both uplift and volcanism had a common cause.

Figure 1.5.2 is a contour map of the *top* of the basalt plateau. It has roughly the same form as the previous map, albeit simpler, with a height difference of 600m between lowest and highest areas. Post-eruption erosion is not thought to have had a major influence on its form since it is based on the planar tops of interfluvial plateau remnants in areas of erosion. The maximum elevation lies at almost exactly the same point as that of the basement uplift map in the south, but there is no sign of a maximum in the north.

Figure 1.5.1 can be subtracted from Figure 1.5.2 to give basalt thickness. Figure 1.5.3 shows the resultant isopach map. The most notable feature of this diagram is the appearance of two maxima, where the plateau is >175m thick. These correspond to the "Gazeille" and "St. Clément" sections (marked on the maps in the back pocket), from which many samples were collected. An attempt to produce a basalt stratigraphy by correlating flows between these two sections was not successful.

Figure 1.5.4 shows contours of phonolite height, using the peaks of only the highest phonolites in each area. It is a crude map and in areas of erosion is of little use. Nevertheless, a roughly concentric pattern appears in both the northern and southern Velay. Combining this map with the basement uplift map to give phonolite heights above basement shows that most of the phonolites of the north are less than 200m above the basement plus Oligocene sediments, whereas those of the south reach 300-400m. This difference is due to the time of phonolite eruption relative to the basalt plateau in each area. The northern phonolites were erupted directly onto the basement whereas those of the south were extruded onto a thick pile of basalt, adding at least 100m to their heights.

Figure 1.5.5 uses all the information from the preceding contour maps, together with K-Ar ages and geological map data to produce two cross-sections of the Velay, one roughly north-south,

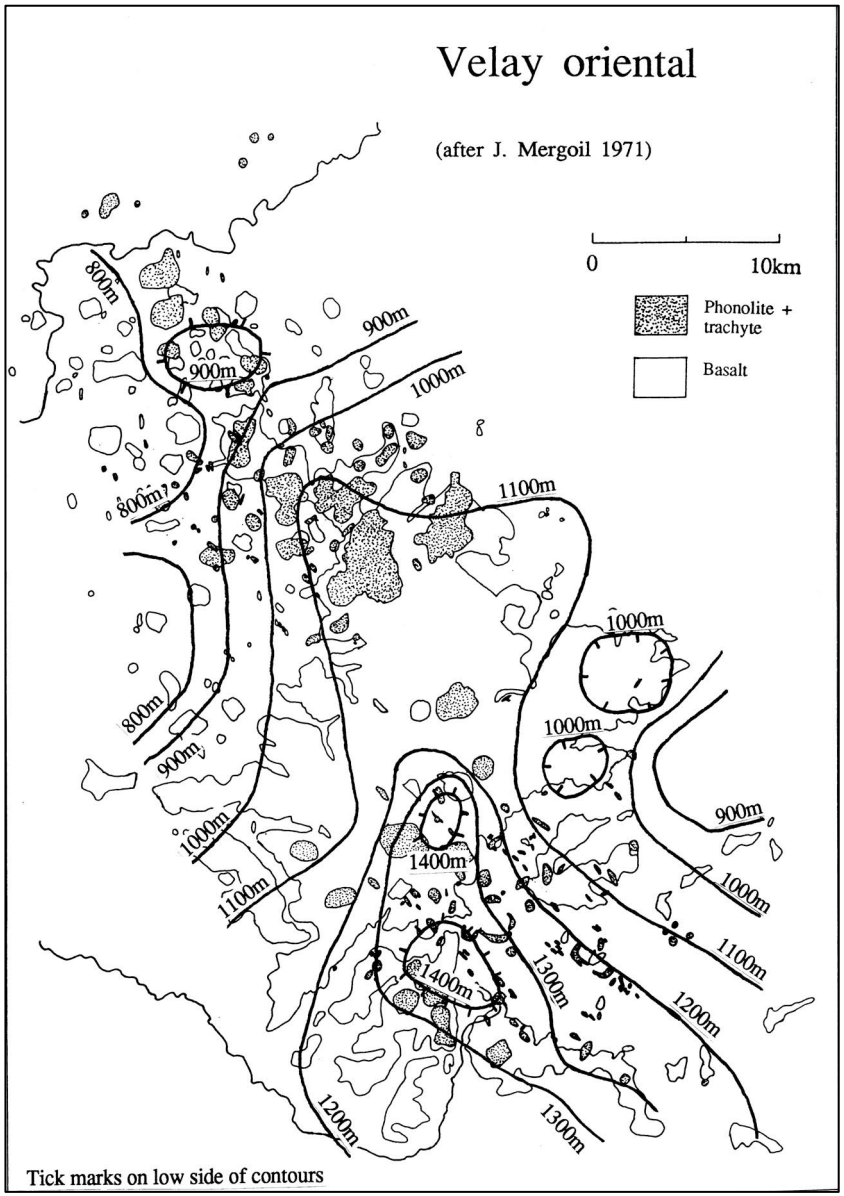


Figure 1.5.1. Contours on base of lowest basalt flow (basement height)

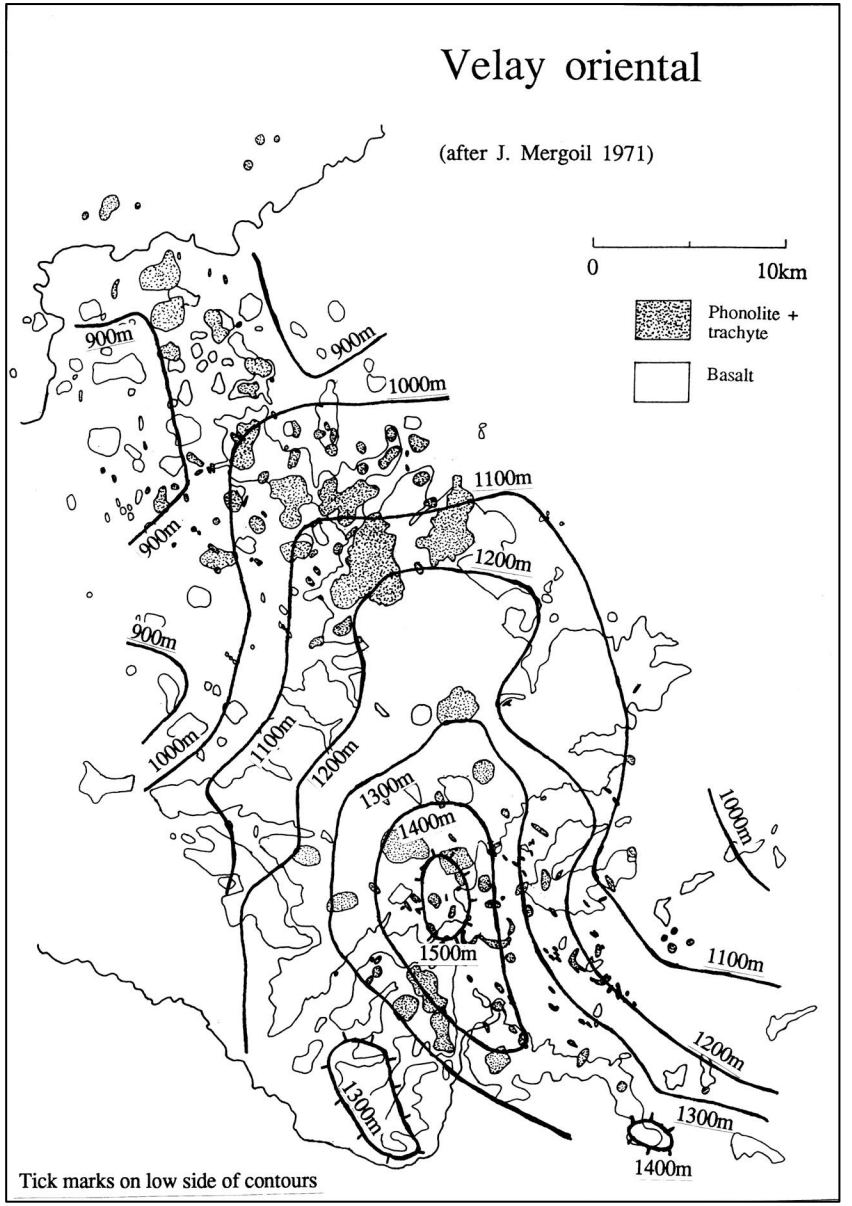


Figure 1.5.2. Contours on basement plateau upper surface.

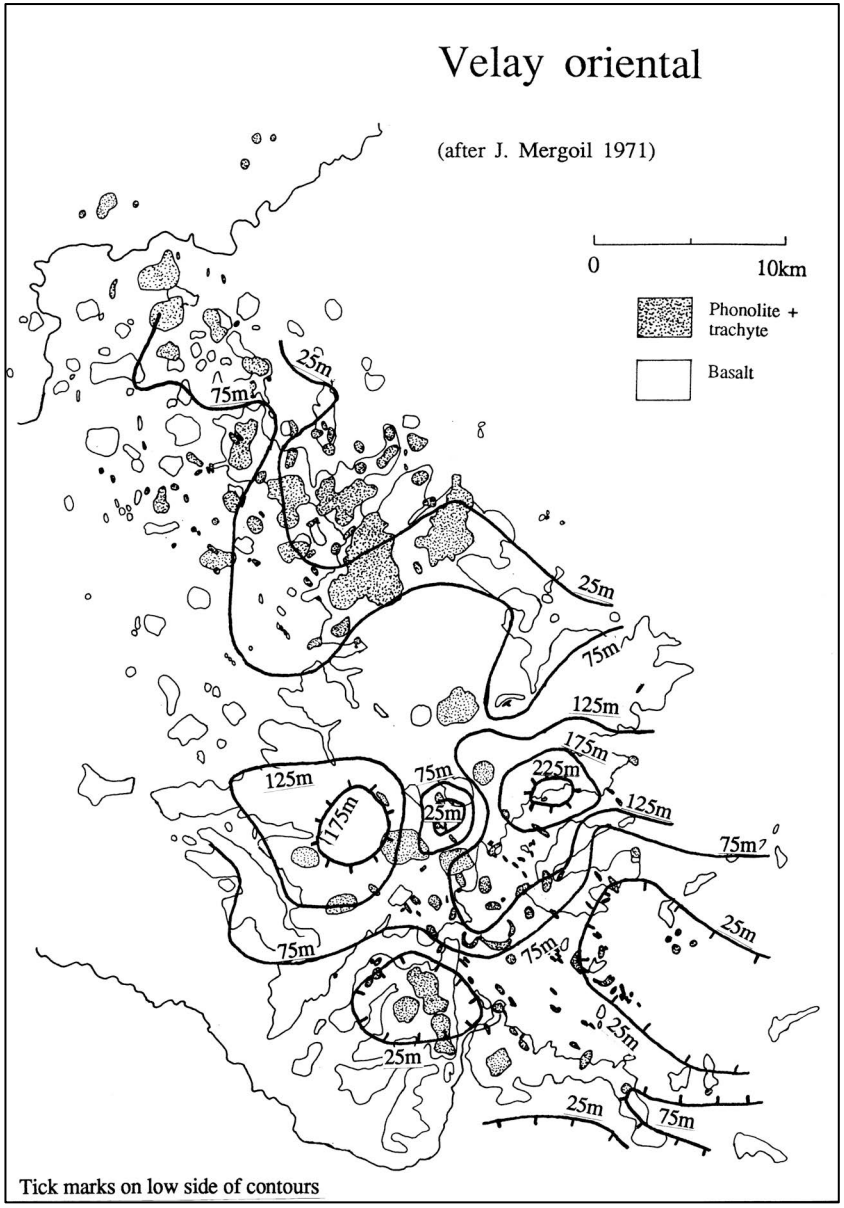


Figure 1.5.3. Isopach map of basalt plateau

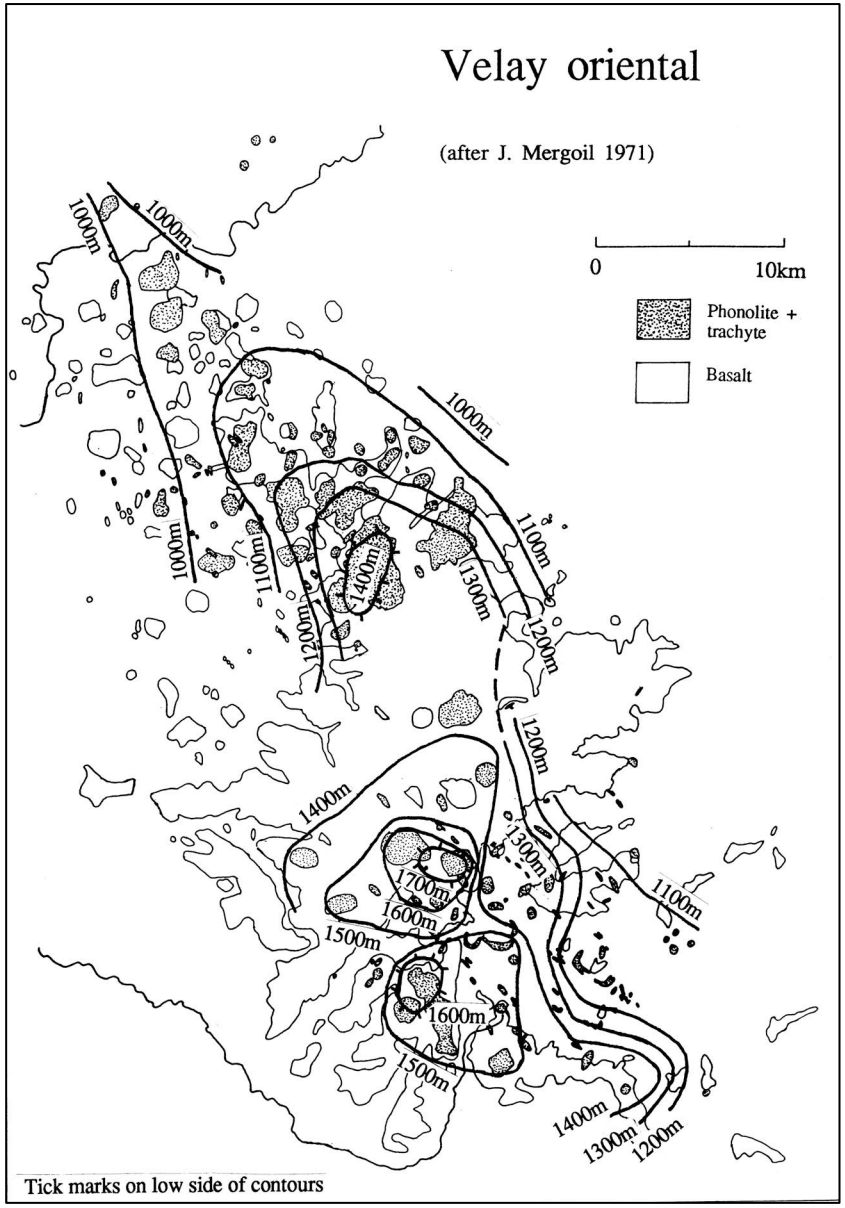


Figure 1.5.4. Contours on maximum heights of phonolites

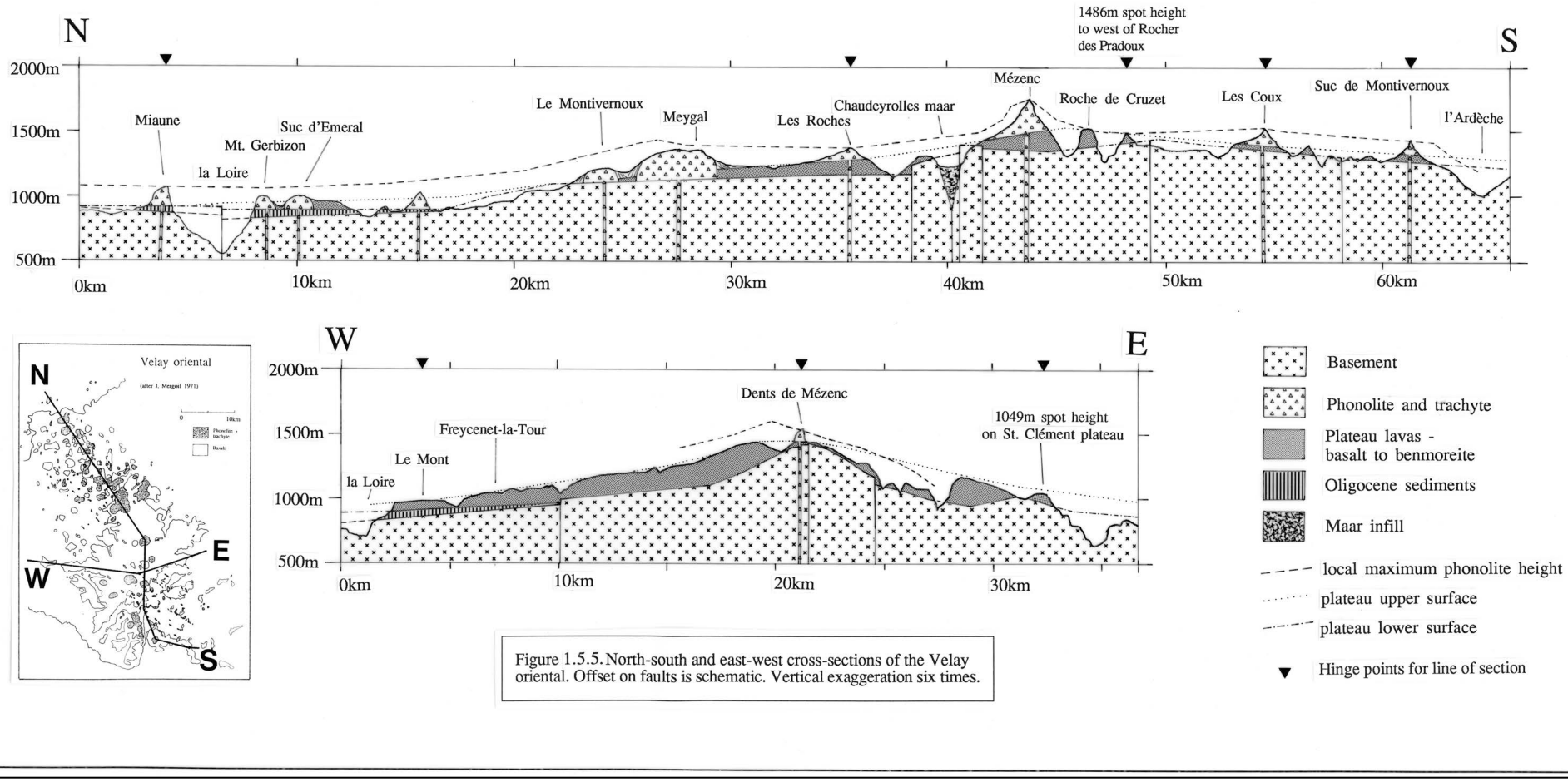


Figure 1.5.5. North-south and east-west cross-sections of the Velay oriental. Offset on faults is schematic. Vertical exaggeration six times.

the other east-west. The north-south section reveals the shape of the basement as it rises towards Mézenc, the variation in plateau thickness, the variation in peak phonolite height and also the sediments of the Oligocene Emblavès basin. The distinction in the relationship between the basalts of the plateau and the northern and southern phonolites is also shown. The line of the east-west section was chosen to illustrate the variation in basalt plateau thickness across the southern Velay, as well as the steepness of the basement uplift. It should be noted however, that the vertical exaggeration is six times on both sections.

1.5.2 Timing of uplift

In the north of the Velay, after the subsidence and consequent sedimentary infilling of the Emblavès graben there has apparently been little disturbance.

In the south the basement uplift was noted as long ago as 1892 by Boule, who concluded that it took place immediately before the formation of the main basalt plateau. Bout (1966) envisaged the basement as a "toit à double pente" or double-pitched roof, formed by two outwardly tilted blocks, with their elevated common edge running from Mézenc to the Coirons massif. Göer de Hervé and Mergoil (1971) also deduced the uplift to have occurred just prior to the main period of basaltic volcanism.

All of these authors noted that the Miocene lacustrine sediments preserved beneath the basalt plateau appear at varying heights within the area. For example, those at Gourgouras are at about 1050m whereas those near Gerbier de Jonc are nearer 1400m. These sediments would rapidly have been removed by erosion unless the basalt covered them before uplift occurred.

In Figures 1.5.3 and 1.5.5 the basalt isopachs define thick sequences lying to the east and west of the area with the most elevated basement, which is only covered with a thin layer of basalt. This suggests that the uplift of the basement had taken place before or during the outpouring of the basalts, causing them to build up their greatest thicknesses at the base of the slopes of the basement swell. An alternative explanation, that the thick sequences mark the main sources of basalt, is not supported by any field evidence.

Finally, the lavas of the plateau sequence seem to have flowed away from a central NW-SE axis, as previously noted by Bout (1966). Near this axis the basalts lying on the basement are more than 10Ma old and are relatively primitive (Cantagrel and Mergoil 1970), for example; Les Merles 11.7Ma, St Clément basal flow 10.5Ma (Cantagrel and Mergoil 1970), Rocher de Cuzet basal flow 10.9Ma (J. Mergoil *pers. comm.*). Towards the edges younger, more evolved lavas rest on the basement, for example; Le Monastier 8.6Ma (this thesis). The flows of the upper benmoreite, which have given ages of 7.6-8.4Ma at many localities, overlap onto the basement in SW Velay (Figure 1.1.3).

The pattern shown by the age data is of a continuous spread of the plateau with time, more recent lavas overstepping onto the basement further from the lava source.

The evidence in this section shows that the uplift of the southern Velay was initiated after the

extrusion of the earliest basalts at about 10Ma, and before the final eruptions of the benmoreite and the southern phonolites, at about 8Ma.

1.5.3 Comparison with other areas

Figures 1.5.6, 1.5.7 and 1.5.8 demonstrate that the uplift and its relationship to phonolite distribution, described in the previous sections, are not restricted to the Velay. Figure 1.5.6 shows basement contours for the Mont Dore volcano, also in the Massif Central. The basement has been uplifted by 300m, over a diameter of about 20km, similar to that in the Velay. The phonolites and trachytes of the Mont Dore are also mainly on the most elevated basement.

The Aïr Tertiary volcanic district, illustrated in Figure 1.5.7, also has lavas distributed like those of the Velay. Black and Girod (1970) noted that the basement under the volcanics has been uplifted by 500m (not shown). Few further details of this province are available.

Figure 1.5.8 is a map of the Atakor volcanic province in the Hoggar of Algeria, taken from Girod (1968). Apart from being much larger than the Velay oriental, it is otherwise an exact analogy. As the map shows, it has a very similar pattern of basement uplift and phonolite distribution. Girod (1968) provided a detailed description of the district. It has a basement of Precambrian to Cambrian granite and gneiss, which has undergone extensive normal faulting. The alkali basalt plateau was erupted during the Miocene and was capped at the end of this epoch by small-volume flows of hawaiite and mugearite.

Basement uplift took place in the Pliocene, followed by the extrusion of the phonolites, with a range of compositions up to and including peralkaline. The most recent activity was Quaternary, with small basalt flows channelled into valleys cut in the earlier material.

The types of lavas and their eruptive sequence are identical to those of the Velay oriental, in which the equivalents of the late-stage basalts are the "valley basalts" of the Bas-Vivarais. The basement uplift and its relative timing are also analogous. Girod (1968) calculated the *volume* proportions of the lava types:

alkali basalt	80%
hawaiites and mugearites	2%
phonolites and trachytes	18%

These show a "Daly gap" very similar to that in the Velay. The Atakor has no rhyolites, but a few rare quartz trachytes appear, also just as in the Velay.

Many of the Tertiary volcanoes of Eastern Australia have uplifted sub-volcanic basement similar to that in the Velay. These are described in the next section.

The close similarity between the Velay and the provinces described above strongly suggests a link between the volcanism and the uplift, with the phonolites lying nearest to the uplifted area. Thus their association in the southern Velay is not coincidental and must be included in any petrogenetic model.

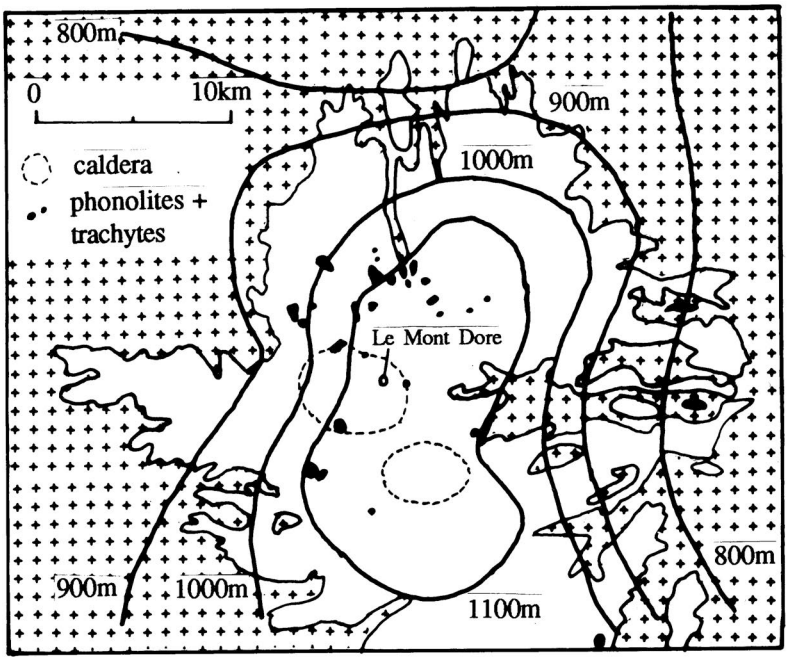


Figure 1.5.6. Basement contours on Mont Dore volcano (Massif Central, France), showing updoming associated with phonolites at highest point. Same scale as Figure 1.5.1. Figure taken from Vincent (1980)

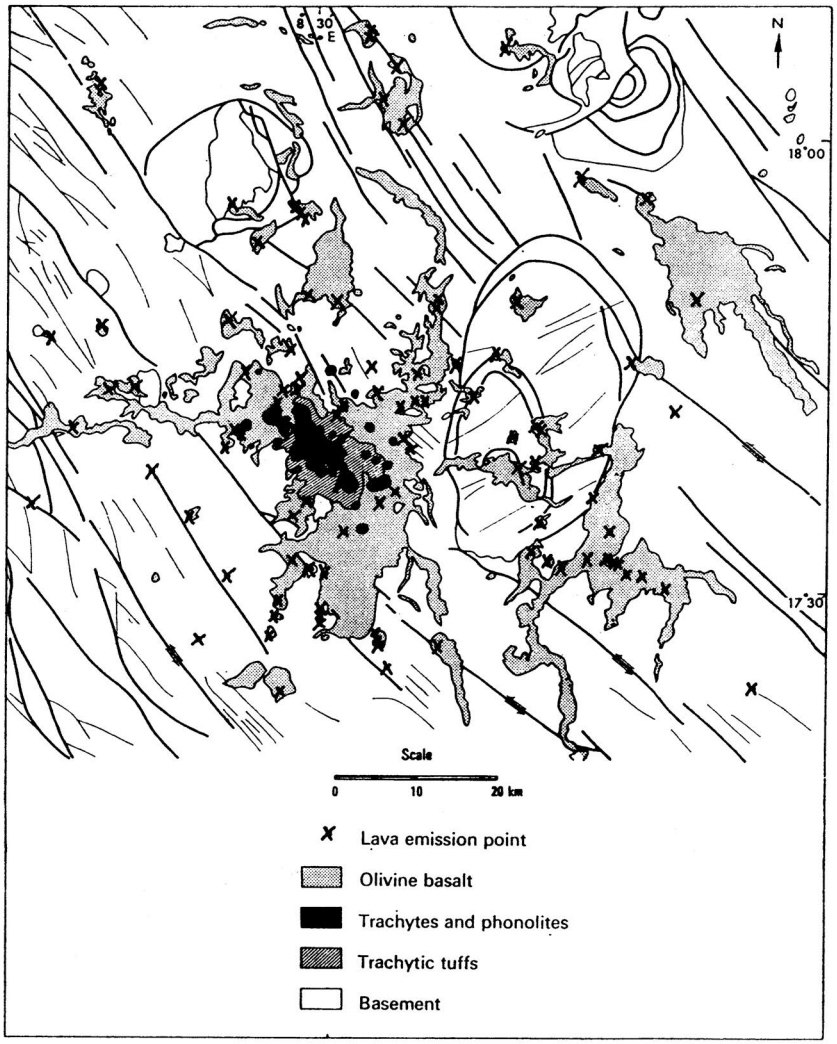


Figure 1.5.7. Map of southern Aïr (Niger) showing Tertiary volcanism, and basement faulting. Basement is elevated by 500m beneath volcanics. Figure taken from Black and Girod (1970).

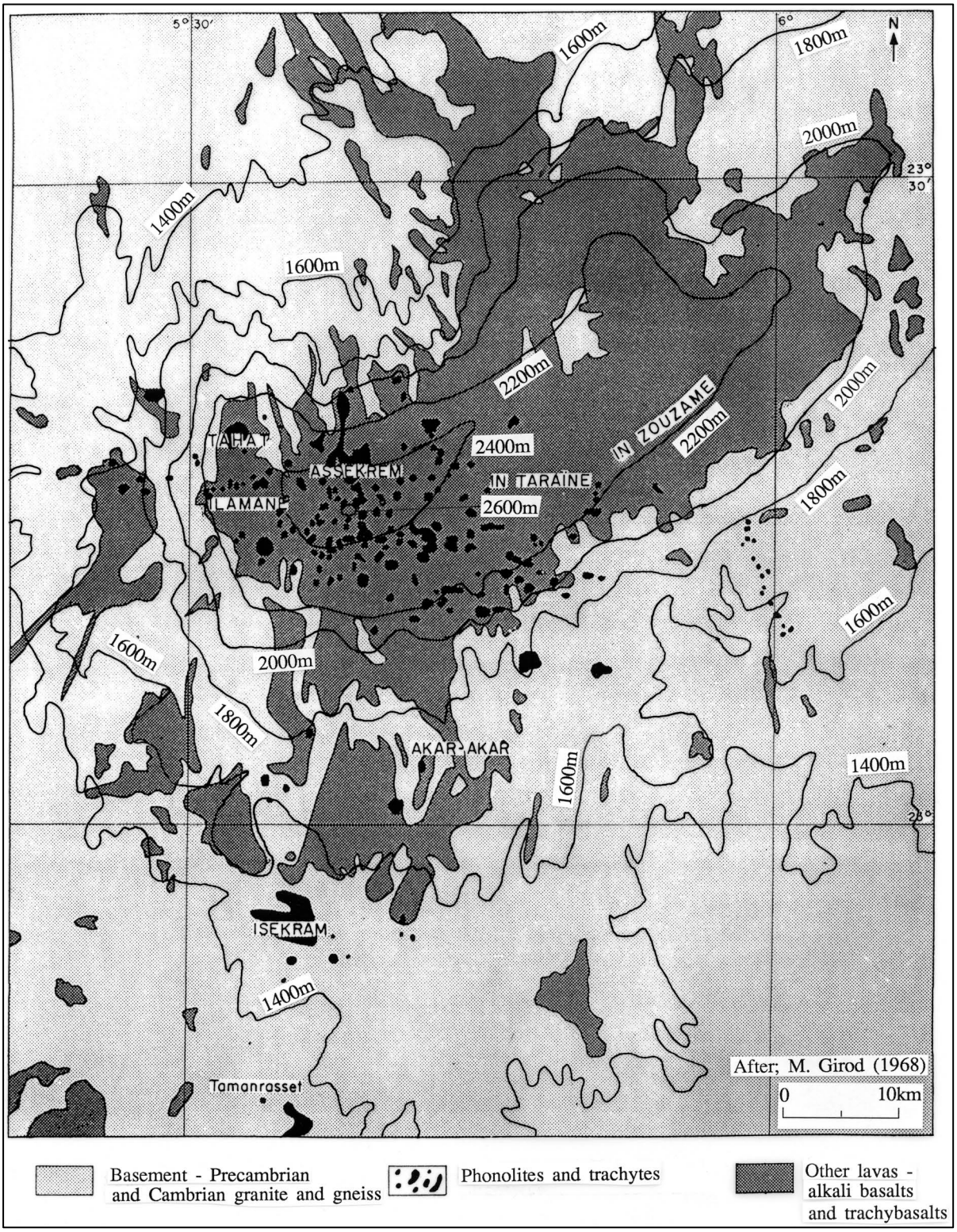


Figure 1.5.8. The Atakor alkaline volcanic province (Algeria), showing basement contours. Phonolites and trachytes are concentrated into the areas with most elevated basement.

1.6 Integrated model of uplift and magmatism

1.6.1 Cause of uplift

Possible causes of uplift include thermal expansion, expansion due to metasomatism, lithospheric flexure, thrust stacking and magma emplacement.

Thermal and/or metasomatic expansion of the mantle could cause uplift, but the scale on which they occur is much greater than that of the Velay. In addition a thermal uplift would decay with time and its present size, 8Ma after first forming, would imply an improbably large original uplift.

Lithospheric flexure can also be rejected as there is no appropriate load on the crust near the Velay. The scale of the Velay is again too small for this mechanism, a constraint which also applies to glacial rebound. Thrust stacking can be ruled out due to the absence of any geological evidence for either thrusting or even major compression in the area.

Magma emplacement is a suitable mechanism for localised uplift because basaltic magma is denser than the basement and can form magma chambers at quite small scales. Göer de Hervé and Mergoil (1971) described the Velay as a "volcano-tectonic horst", a concept introduced by Rittman (1962) to describe the island of Ischia, near the Italian coast, where dense basic magma was intruded into the crust to form a chamber which raised its roof hydraulically. In the Velay, Bout (1966) suggested that uplift of the basement was by reactivation of the faults which divide the basement into NW-SE blocks.

Wellman (1989) reported that in the alkaline volcanic province of Eastern Australia there were many centres with radially uplifted basement. Investigation showed that the pre-volcanic surfaces had low relief, and that the presently observed uplift was caused entirely by the volcanic activity. The diameters of the uplifts, at half the maximum amplitude, are 8-20km, with 300-600m uplift. All of these parameters compare well with those of the Velay. Deep erosion of some of the Australian volcanoes has exposed major intrusive complexes, lying beneath the volcanic piles. Wellman (1989) inferred that the basement uplift was due solely to the intrusion of magma. Using gravity and magnetic anomalies, and assuming that the volume of uplift was equal to the volume of the intrusion, Wellman calculated that the intrusions were 4-10km in diameter and lay at a depth of 6-8km, so that a range of 4-13km would bracket their depth within the upper crust.

The uplift in the southern Velay is rather asymmetrical, but has a diameter of roughly 20km (at half the maximum amplitude) and a volume in excess of $100km^3$. A similarly rough estimate for the volume of phonolite in the south gives $6km^3 \pm 2km^3$. Section 5.4 concludes that the phonolites were produced by fractional crystallisation and if $100km^3$ of alkali basalt differentiated to give 10-20% phonolite (on the basis of incompatible element concentrations - section 5.6.2.5) there would be $10\text{-}20km^3$ phonolite magma available. The differentiation model can also explain the continued elevation of the basement, after volcanism has ceased, as being due to the residual cumulate stack. This may be detectable as magnetic and positive Bouguer anomalies.

1.6.2 Form of magma chambers

The new K-Ar age data obtained in this study show that the northern and southern groups of phonolites were erupted at distinctly different times, from two separate sources rather than one source that migrated (Figure 1.1.6). Similarly, they were not formed by the simple differentiation of a single batch of magma, since there is no correlation between phonolite evolution and age (Figure 1.1.7). From this constraint it can be concluded that each group of phonolites formed either from many small independent chambers, or one zoned and/or multiply refilled chamber.

Agpaiitic phonolites (see section 5.6.2.6) are commoner in the south than in the north of the Velay, and also reach greater degrees of incompatible trace element enrichment. Figure 1.6.1 shows that the incompatible element enriched phonolites lie towards the centre of the two phonolite groups, whereas those with lower concentrations of incompatibles are found throughout both areas. This strongly suggests large zoned chambers were the source for the two groups, since multiple independent small chambers would give a random distribution of phonolite types.

Variation in phonolite petrography and chemistry was used by Göer de Hervé and Mergoil (1971) as evidence that the phonolites evolved either in multiple independent chambers or in apophyses from a single, large chamber.

The evidence summarised here suggests that the northern and southern phonolites of the Velay formed in two separate, probably zoned, chambers with very irregular roofs, which allowed some degree of independent evolution of liquids in various parts. This model is very similar to that proposed by Rittmann (1962) for the magma chamber inferred to lie beneath Ischia (Figure 1.6.2).

The northern group does not lie on a localised basement uplift and its phonolites are less evolved. This could be due its magma chamber being much flatter, distributing uplift more widely. The surface distribution of phonolites supports this. The chamber may also have had a smaller volume than that in the south, so that its phonolites were erupted before fractionation had reached such an extreme degree as in the south. These factors would reduce basement uplift.

1.6.3 The Daly gap and scarcity of pyroclastics explained

At this stage it has been established that the two groups of phonolites in the Velay were the products of large zoned magma chambers, which elevated their roofs, probably by exploiting faults in the overlying basement. This arrangement can explain the bimodality of the Velay lavas, using the model proposed by Gill (1973). He noted that continental alkaline provinces frequently had a Daly gap, whereas on oceanic islands such bimodality was often found to be weak or absent, requiring an explanation which incorporates some aspects of the differences between the continental and oceanic environment.

Gill (1973) suggested that the relationship between magma density and that of its enclosing rock controlled its eruption. Extensional episodes of dyke emplacement would allow "normal" fissure eruptions of basaltic lava, but ponding of the dense basalt within the crust would occur during periods with weak extension. Differentiation of the magma in these chambers would give residual liquids of

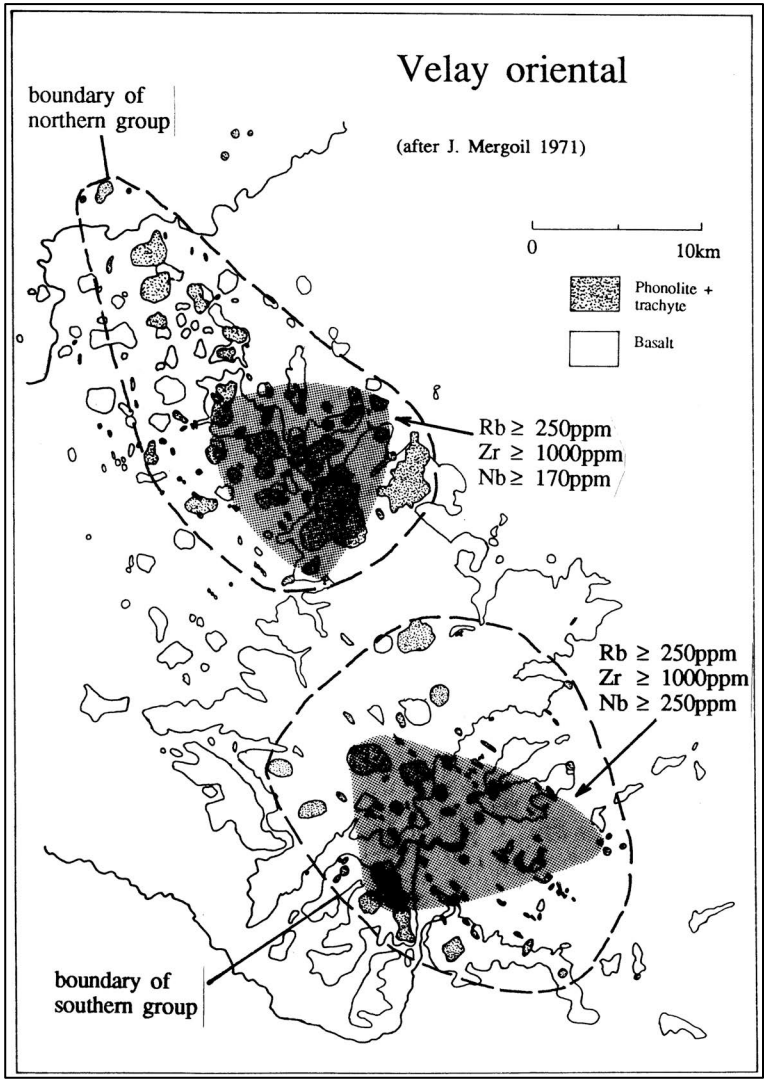


Figure 1.6.1. The shaded areas include all agpaïtic phonolites, with incompatible trace element concentrations in excess of the values marked. Miaskitic phonolites, with less incompatible trace element enrichment, occur throughout the two areas.

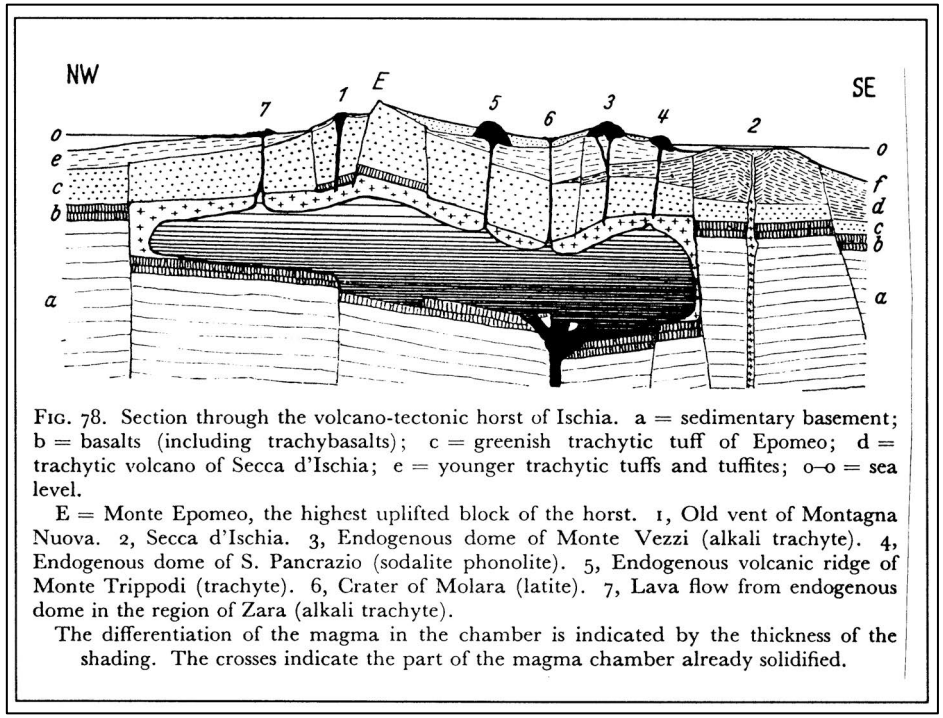


FIG. 78. Section through the volcano-tectonic horst of Ischia. a = sedimentary basement; b = basalts (including trachybasalts); c = greenish trachytic tuff of Epomeo; d = trachytic volcano of Secca d'Ischia; e = younger trachytic tuffs and tuffites; o–o = sea level.

E = Monte Epomeo, the highest uplifted block of the horst. 1, Old vent of Montagna Nuova. 2, Secca d'Ischia. 3, Endogenous dome of Monte Vezzi (alkali trachyte). 4, Endogenous dome of S. Pancrazio (sodalite phonolite). 5, Endogenous volcanic ridge of Monte Trippodi (trachyte). 6, Crater of Molara (latite). 7, Lava flow from endogenous dome in the region of Zara (alkali trachyte).

The differentiation of the magma in the chamber is indicated by the thickness of the shading. The crosses indicate the part of the magma chamber already solidified.

Figure 1.6.2. Cross section of the Italian island of Ischia, drawn by Rittmann (1962). The magma chamber beneath the southern Velay was probably of this type.

successively lower densities until the liquid was able to make its way to the surface due to hydrostatic pressure alone. In oceanic islands, by contrast, there is no low density crust to act as "density filter" so no Daly gap would be expected.

This is supported by several examples, including the oceanic islands of Tristan da Cunha (Le Roex *et al* 1990), São Tomé (Fitton 1987) and St Helena (Baker 1968) on which careful fieldwork has shown no Daly gap in *volumetric* lava proportions. Atakor (Girod 1968) and the Velay oriental (Mergoil 1980) both have true Daly gaps.

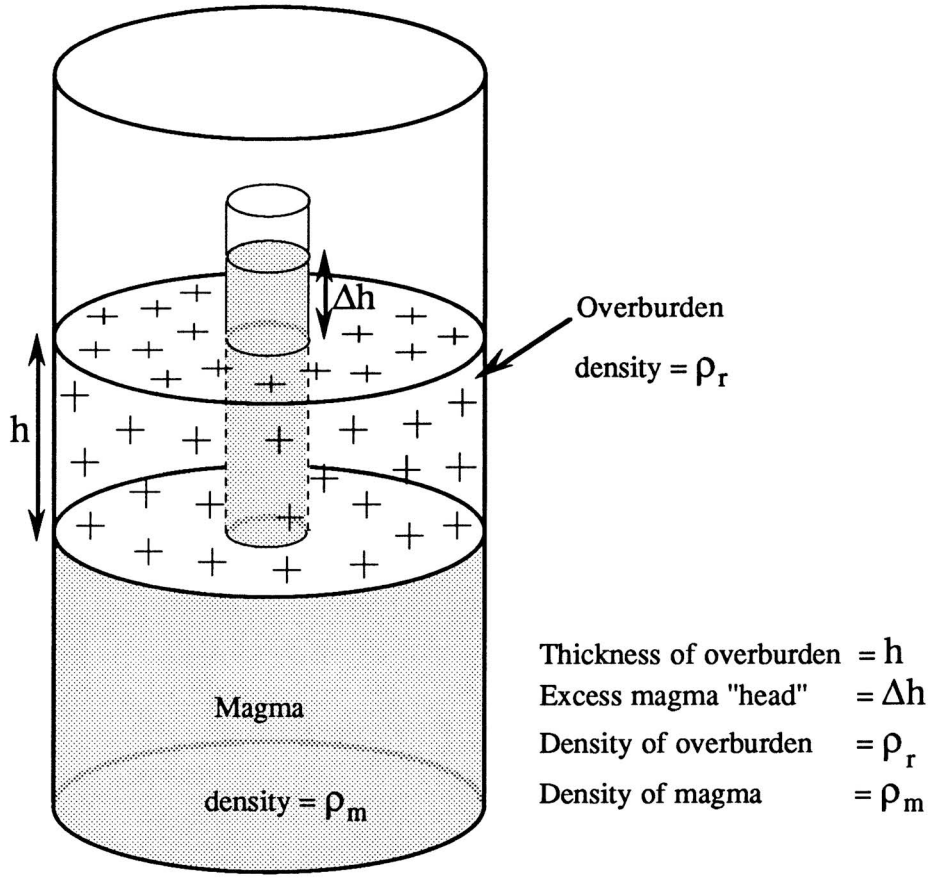
In the Velay, Gill's model would predict that early dyke-fed fissure volcanism built the basaltic plateau, with some compositional evolution due to flow crystallisation (see section 5.4.4). Extension then ceased and the later basalt magma became trapped in large chambers, which elevated their roofs. The ponded magma then fractionated until its density became low enough to force its way to the surface entirely under the influence of hydrostatic pressure, with no need for gas exsolution to force it out rapidly. This explains the scarcity of phonolite pyroclastics, since there were no explosive eruptions. It might be asked why the magma was not erupted the moment its density fell below that of the crust. The explanation is probably that a certain degree of overpressure was needed to force open the conduits and push the rapidly chilled initial batch of magma to the surface. Similarly, when most of the phonolite had been erupted, it would have built thick piles over the outlets at the surface, blocking the rise of less fractionated lavas.

Figure 1.6.3 shows, in schematic form, the situation after the phonolite had formed, with the relationships expressed as equations (from Suppe 1985). The overburden in the Velay is the Velay anatectic granite. The densities of the five freshest basement samples collected during this study were measured as 2430, 2430, 2510, 2470 and 2490 $kg.m^{-3}$. The mean of these is 2470 $kg.m^{-3}$, which was used as the bulk density, without thermal or pressure correction since the magma chamber was expected to be quite shallow.

The density of the phonolite melt was rather more difficult to determine. Gill (1973) cites densities of 2370-2450 $kg.m^{-3}$ for trachyte and rhyolite glasses at room temperature, reasoning that a hot phonolite liquid would have even lower density. This was confirmed using the theoretical density calculations of Bottinga and Weill (1970) and Bottinga *et al* (1982). The phonolites of the Velay give densities which cluster around 2340 $kg.m^{-3}$ at 800°C. This value was assumed to be representative.

The maximum height to which a magma can rise above the surface of the crust controls the maximum height of its volcanoes and is referred to as its hydrostatic "head". In the Velay, as mentioned in section 1.5.1, the maximum height of phonolites above the surface onto which they were erupted is 200m. If it is assumed that this is equivalent to Δh in the second equation of Figure 1.6.3, it is possible to calculate the depth to the roof of the magma chamber (h):

$$h = \Delta h/(\rho_r/\rho_m - 1)$$
$$= 200/(2470/2340 - 1)$$
$$= 3600m$$



The diagram shows a body of magma overlain by a mass of solid overburden. The block of overburden is free to move vertically and is pierced by an open-ended tube, into which the magma can flow, as shown.

The pressure on the magma due to the weight of the overburden is $\rho_r gh$. To balance this pressure the magma will rise to a height of $h+\Delta h$. Thus:

$$\rho_r gh = \rho_m g(h+\Delta h)$$

$$\therefore \quad \Delta h = (\rho_r/\rho_m - 1)h$$

The excess pressure of magma at the level of the upper surface of the overburden is:

$$P_{excess} = \rho_m g\Delta h = gh(\rho_r - \rho_m)$$

(from Chapter 7, Suppe 1985)

Figure 1.6.3. The effect of density contrast between low density magma and relatively high density overburden. This model can be equated to the situation in the Velay, as described in the text.

Considering the approximations involved this is certainly no more reliable than about ± 0.5km, so the depth to the top of the Velay magma chambers is probably around 3-4km. This is reasonable considering the presence of the Suc de Sara and Rocher des Pradoux ring-dykes (Mergoil 1968), which have a diameter of ≤ 2km. The subsidence of an upward-tapering cone of granite is required for their formation, and with a surface diameter of 2km the depth to the top of the chamber seems unlikely to exceed about 5km.

The third equation of Figure 1.6.3 gives the excess pressure of the magma. This can be rearranged to give the pressure gradient:

$$P_{excess} = gh(\rho_r - \rho_m)$$

$$\therefore \quad \text{Pressure gradient} = g(\rho_r - \rho_m)$$

$$= 1275 \text{ Pa.m}^{-1}$$

The pressure gradient is needed for the equation of flow of a viscous liquid through a cylindrical conduit:

$$V_{average} = (r^2 /12\eta) \times P_{excess} /h$$

$V_{average}$ is the mean velocity of the liquid, r is the conduit radius and η is the liquid viscosity. The equation of flow through a fracture of infinite width was not used since magma flow rapidly stabilises into a roughly cylindrical form for reasons of thermal and mechanical efficiency.

Few data have been published on the properties of phonolite liquids but the equations of Shaw (1972) allow the viscosity can be calculated. The results are highly dependent on the water content and the temperature of the melt, but temperatures of 800-900°C and H_2O 1-2% give viscosities of 5×10^4 to 5×10^5 Pa.s, which are reasonable for lavas which were apparently very viscous when erupted. Figure 1.6.4 is a graph of conduit radius versus the time needed to erupt $10^8 m^3$ phonolite, roughly the volume of Mt Mézenc. Lines of constant viscosity are drawn as a guide, together with dotted lines of constant mean liquid velocity. The shaded area shows the most probable field in which the Velay phonolites lie. Thus the viscosity is the main constraint, and ten days is chosen as the shortest possible time of eruption. This represents an eruption rate of $100 m^3 s^{-1}$, which is the maximum recorded rate for any eruption of viscous lava.

The time that Mt Mézenc took to form is not necessarily the same as shown on the graph since the graph assumes continuous lava eruption, whereas most domes form episodically. The best estimate available for the episodic rate is 0.35 $m^3 s^{-1}$ for the Mount St Helens dacite dome (Dzurisin 1987), which gives nine years as the time taken to erupt Mt Mézenc.

1.7 Summary

The Velay is an alkali basalt - phonolite volcanic province formed in the latter half of the Miocene. The basalts make up an extensive plateau composed of stacked sub-horizontal sheets, whereas the phonolites were erupted as viscous extrusions. There is a marked bimodality in the lava compositions, with only a small proportion of intermediate lavas, such as mugearite and benmoreite.

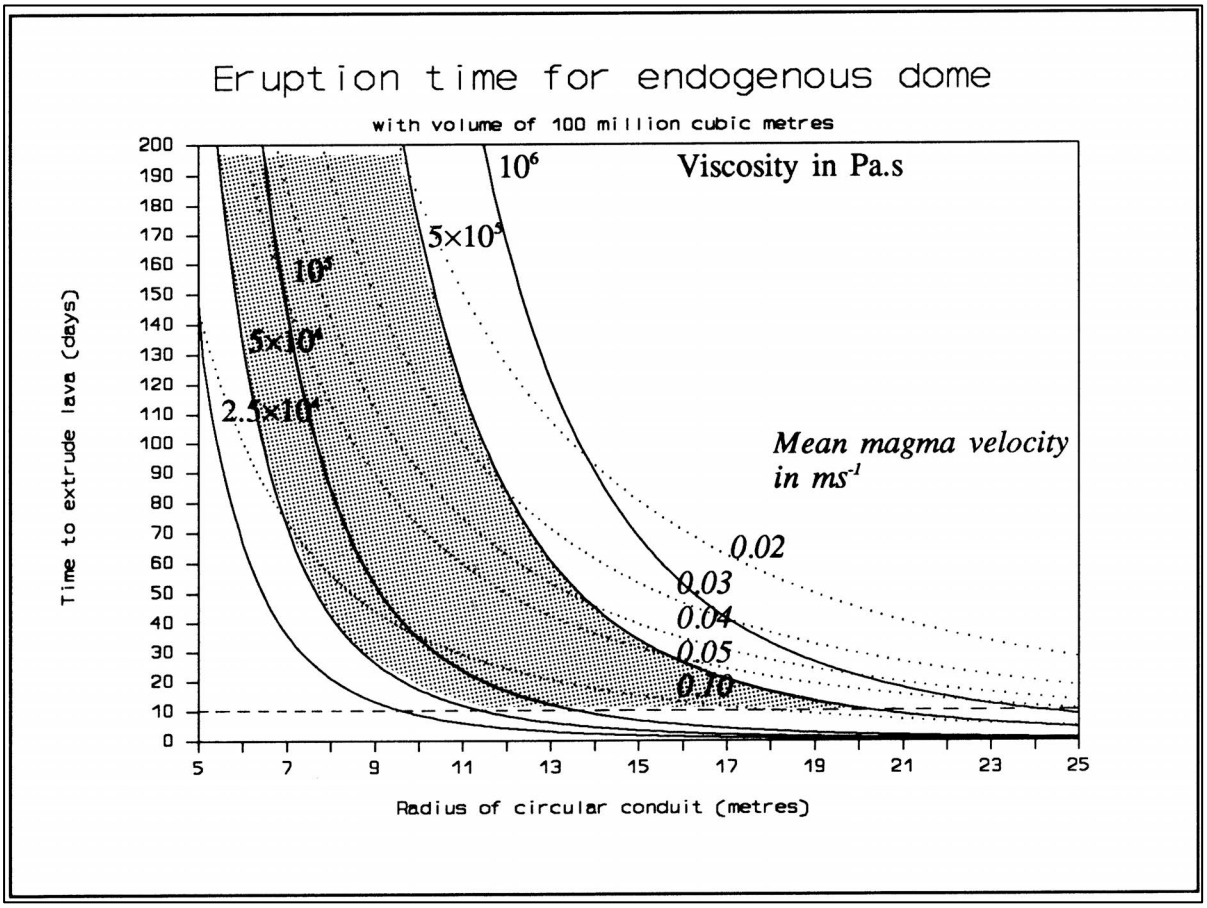


Figure 1.6.4. Graph of conduit radius versus time taken to erupt $10^8 m^3$ vicous phonolite lava. The volume chosen is roughly equivalent to a dome the size of Mt Mézenc. The shaded area covers the likely range of eruption rates and viscosities. The equation used and the values of parameters are discussed in the text.

Despite the high viscosity of the phonolite lavas pyroclastics are scarce.

K-Ar dates, including sixteen new determinations, show an early period of phonolite volcanism in the north (13-10Ma) during which the construction of the basaltic plateau began. Plateau eruptions lasted from 12Ma to about 8Ma, when the phonolites of the south began to be extruded. Phonolite activity ceased at about 6.5Ma. These results are supported by field relations and sedimentary stratigraphy.

Contour maps drawn on the base of the basalt plateau show a marked basement uplift in the south. Various lines of evidence show that this uplift took place during the construction of the plateau, and was caused by the emplacement of a large ($100km^3$), probably zoned, magma chamber which elevated its roof as a volcano-tectonic horst.

Differentiation of the alkali basalt filling the magma chamber led to the formation of $10\text{-}20km^3$ phonolite magma. This had a lower density than that of the basement and was therefore able to force its way to the surface under hydrostatic pressure alone. Magma with lower densities than phonolite remained trapped in the chamber due to this "density filter" effect, which explains both the bimodality and the scarcity of pyroclastics.

Calculations using the densities of magmas and basement, phonolite melt viscosity and maximum phonolite dome heights show that the depth to the top of the magma chambers was 3 - 4km and allow the eruption rates and size of conduit to be constrained.

Figure 1.7.1 shows a sequence of four sketch sections through the Velay which summarise what has been established in this chapter.

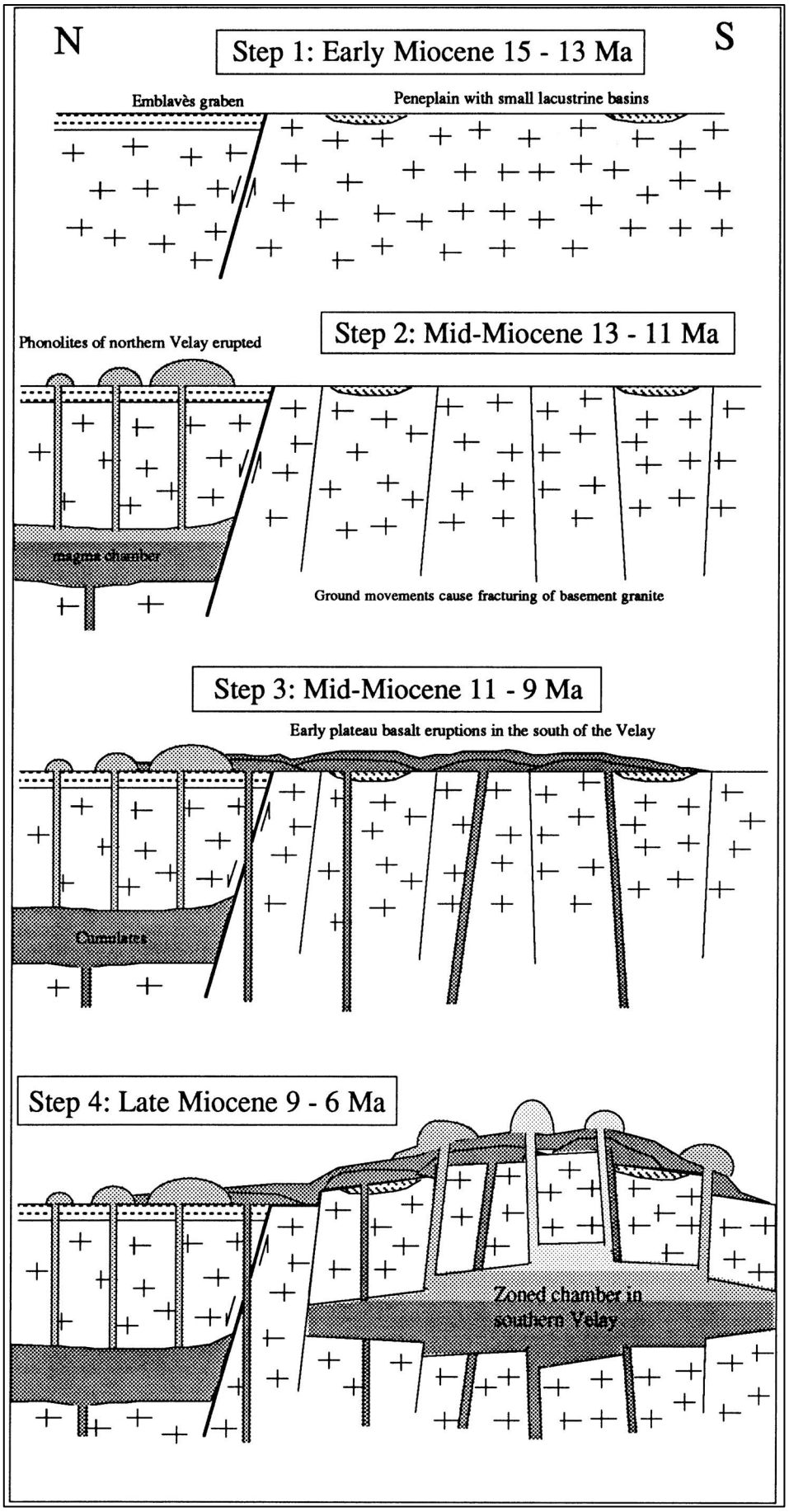


Figure 1.7.1. Four sketch sections showing the evolution of the Velay volcanism:
Step 1 – early pre-volcanic peneplain,
Step 2 – phonolite volcanism of the Emblavès graben,
Step 3 – formation of the main basalt plateau,
Step 4 – uplift of the basement and formation of the zoned magma chamber in the south.

Chapter 2

History, volcanism and structure of the Massif Central

2.1 General history

The Massif Central is an area of elevated Hercynian crust in south-central France, bounded to the north, west and south-west by the Mesozoic Paris and Aquitaine basins and to the south by the Jurassic Causses basin. Its eastern margin is defined by the Tertiary Bresse/Rhône graben (see Figures 1.1.1, 1.1.2 and 2.1.2).

The crust of the Massif is a complex assemblage of schists and granitoids, which has been strongly faulted. The Tertiary grabens of the Limagne and Forez cut deep into the Massif from the north.

The Cenozoic volcanism of the Massif Central is mainly confined to the south, with little in the grabens.

In the following summary the pre-Cenozoic history of the Massif Central is derived from Lapadu-Hargues (1971) and the Alpine chronology and that of the Corsica-Sardinia microplate, is from Dewey *et al* (1989). The details of the Massif Central volcanism are from Autran and Peterlongo (1980).

2.1.1 Palaeozoic and Mesozoic

The crust of the Massif Central was formed during the Devonian and Carboniferous as a result of the Hercynian orogeny. Widespread metamorphism and abundant granite emplacement ensued from this continental collision, including that of the Velay anatectic granite, which covers 6000km^2 in the eastern Massif Central. This heterogeneous granite forms the basement in the Velay oriental.

Some Carboniferous and Permian lavas and sediments are preserved in downfaulted blocks, but severe erosion during the Triassic subsequently reduced the area to a peneplain, with some marginal arkose deposits. During the Jurassic a rise in sea-level allowed deposition on the margins of the Massif, including that of the Causses in the south. Traces preserved by fault blocks show that a slightly larger area was covered originally than at present. Two marine transgressions occurred during the Cretaceous, but probably failed to cover the Massif as no traces of sediments of this age are preserved.

2.1.2 Cenozoic

Palaeocene

The earliest volcanism in the Massif Central occurred in the extreme north and south, in the Bourgogne and the Causses (see Figures 1.1.2 and 2.1.1). In the north the activity consisted of small volume scattered eruptions of highly undersaturated nephelinites, and less-undersaturated alkali basalts in the south.

Eocene

The Massif had a dry tropical climate at this time. The earliest Tertiary sediments are the Blavozy arkoses, deposited in the Puy basin, showing evidence of active basement erosion. Minor volcanism continued in the Bourgogne, and there is also evidence of some activity in the Forez.

Alpine deformation began in this epoch, with the emplacement of the Austro-Alpine and Penninic nappes.

Oligocene

At the start of the Oligocene the Massif Central formed a peneplain, with a low rate of erosion. A major period of crustal extension subsequently caused the formation of the Limagne, Forez and other minor grabens, which came to dominate sedimentation in the Massif. The continuation of compression in the Alps makes it difficult to explain the extension as a related phenomenon.

Volcanism in the Massif Central virtually ceased during this epoch, suggesting that the graben extension and the magmatism shared a common cause.

Miocene

During the early Miocene, between 23Ma and 19Ma, Corsica and Sardinia were rifted away from the coast of southern France and rotated into their present positions, creating the Ligurian sea. Continued Alpine compression led to the emplacement of the Helvetic nappes. In the Massif Central, movement on the Oligocene grabens continued.

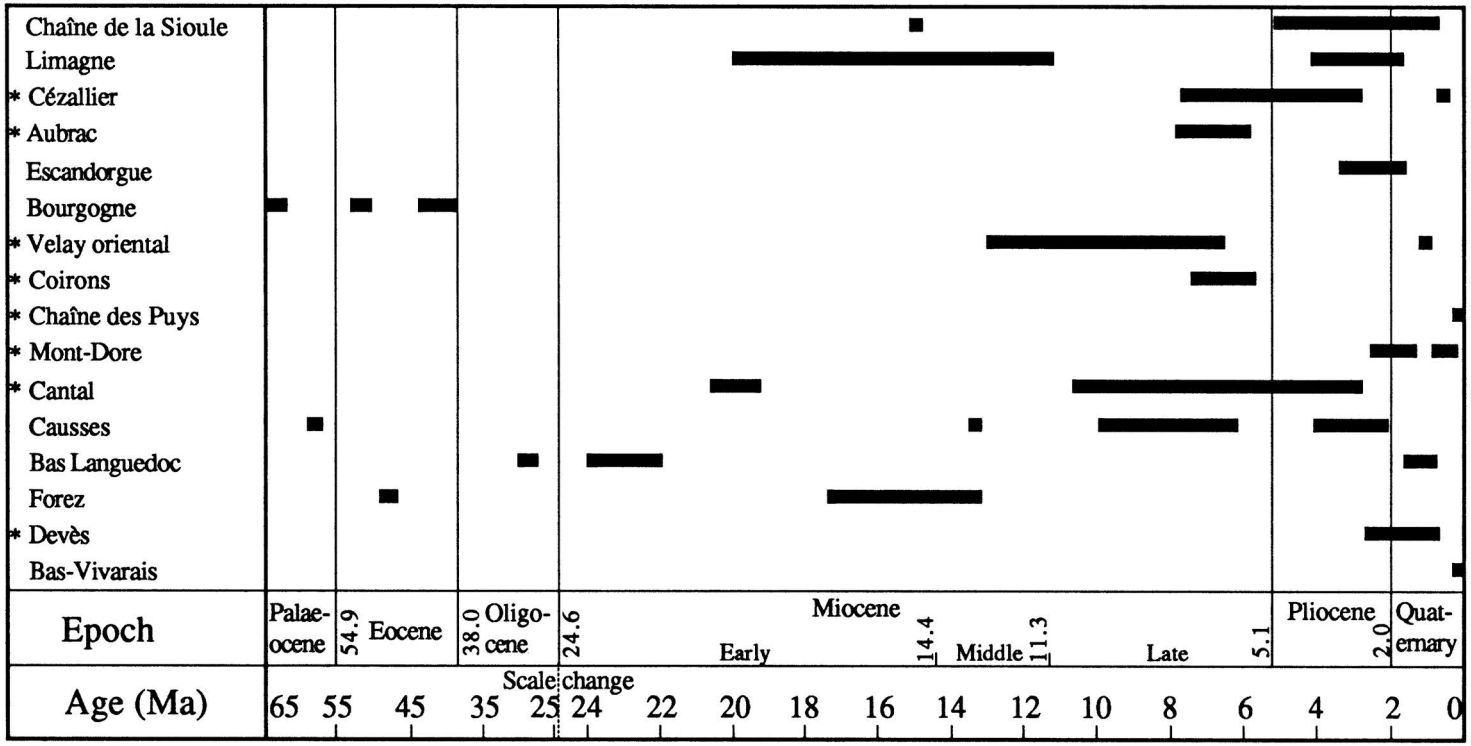


Figure 2.1.1. Age determinations for alkaline volcanism in the Massif Central. Locations of these volcanic districts are given in Figure 1.1.2. The main areas of voluminous lava production are marked with an asterisk (*). Figure modified from Maury and Varet (1980), Downes (1987a) and using data presented in this thesis for the Velay oriental.

Volcanism in the Massif reached a peak in the late Miocene (see Figure 2.1.1), during which the huge Cantal central volcano was constructed, together with the basalt plateaux of Aubrac, Cézallier, Velay oriental and Coirons. Many other smaller-volume volcanic districts were also active during the Miocene, for example, those of the Limagne and Forez grabens. The basic lavas of these districts were almost exclusively alkali basalt and basanite, and differentiated lavas were also abundant, including hawaiite, trachybasalt, trachyandesite, trachyte, rhyolite and phonolite.

Events outside the Massif Central at the end of the Miocene include the formation of the "thin-skinned" Jura fold and thrust belt, and the "Messinian crisis", in which the Mediterranean Sea became isolated from the Atlantic and was evaporated dry more than once.

Pliocene

Large volumes of lavas continued to be produced, with activity continuing in the Cézallier and Cantal, and commencing in the Mont-Dore central volcano and the Devès basalt plateau. Activity began or continued in many other minor districts (see Figure 2.1.1). This volcanism was essentially a continuation of the late Miocene peak.

During the Villafranchian (end Pliocene) the whole of the Massif Central was uplifted to form the dome-shape that it has today (Derruau 1971).

Quaternary

Volcanism has continued almost until the present, with the construction of the Mont-Dore volcano and the Devès plateau, and the recent activity of the Bas-Vivarais valley-filling basalt flows and the Chaîne des Puys differentiated series. The latter contains the Pavin trachytic pumice, which at 3450 years is the most recent lava yet dated in the Massif.

2.1.3 Cenozoic volcanism in the rest of Europe

The Cenozoic was a period of volcanic activity in other parts of Europe as well as the Massif Central. Figure 2.1.2 shows the distribution of this volcanism.

The volcanic districts of the Bohemian Massif were emplaced during the Oligocene and early Miocene. Those of the Rhenohercynian/Ardennes Massif, at the northern end of the Rhine graben, were mainly erupted between the late Miocene and the Pliocene. The Eifel district was still active as recently as 10 000 years ago.

These volcanic districts comprise a broad spectrum of alkaline lavas. Alkali basalts are ubiquitous, with the addition of variants such as melilitite and nephelinite. Evolved undersaturated lavas, including phonolite, are also abundant.

The southern end of the Rhine graben divides the Vosges/Black Forest Massif and contains the Kaiserstuhl volcanic district. This was erupted in the early Miocene and includes a wide range of lava types, from basic to evolved, and even a carbonatite.

The distribution of the volcanism shown in Figure 2.1.2 seems to be related to the formation of

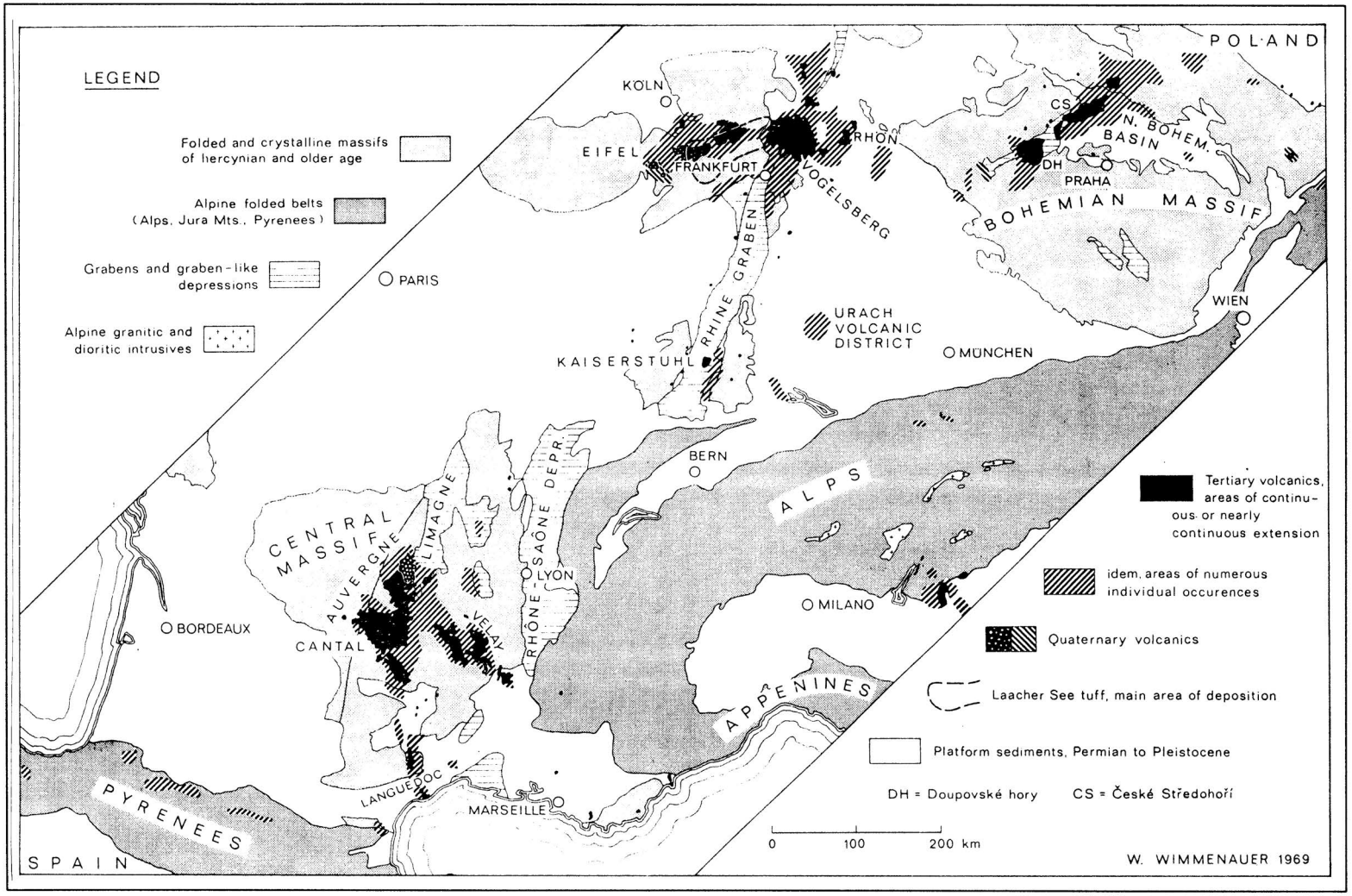


Figure 2.1.2. Cenozoic volcanism of France and central Europe (from Wimmenauer 1974).

the Oligocene rift system, including the Limagne, Bresse/Rhône and Rhine grabens. The relationship is not clear, however, since the volcanic districts are not spatially very close to the grabens, and the Bresse/Rhône graben has no volcanism. This is discussed in the following sections on the structure of the Massif Central.

2.2 Deep structure

Figure 2.2.1, from Lucazeau and Bayer (1982), shows that the averaged topography of the Massif Central forms a dome with a diameter of about 300km and an amplitude of 1km (using a reference level of 150m from the Brittany Hercynian basement). The same authors estimate that the grabens of the Massif represent an extension of 7-13% at the crest of the dome. Derruau (1971) showed that most of the uplift was produced in the Villafranchian (late Pliocene) based on erosion rates and the ages of lava flows in gorges which were cut in response to the uplift.

Le Bas (1980) recognised three scales of domes found in association with continental alkaline volcanism:

1) Lithospheric -	very large area, ≥1km uplift e.g. East Africa dome with 1500km long axis.
2) Crustal -	200-500km diameter, ~1km uplift, with rifting at the crest e.g. Kenya dome, Rhine dome. Underlain by "pillow" with density intermediate between crust and mantle. Often associated with alkaline volcanism.
3) Sub-volcanic -	1-20km diameter, caused by cone sheet (or magma chamber) emplacement.

Le Bas (1980) interprets the low-density "pillow" found beneath these domes as being due to the presence of 5-10% melt. The Massif Central is clearly a crustal dome in this scheme, showing most of the features described.

The deep structure of the Massif Central is summarised in Figure 2.2.2. The "gravity contours" are Bouguer anomaly lines, showing a large, roughly circular negative anomaly over the Massif, reaching values of -60mgals. This is characteristic of mountain belts, with their deep roots of low-density crustal rocks. However, given that the Massif has been found to have normal or thinned crust, underlain by low-velocity mantle (from seismic studies described later in this section), it must be concluded that this anomalous mantle must also have lower density than normal mantle material. Perrier and Ruegg (1973) calculated that a density contrast of 0.03 gcm^{-3} at 50km depth would be needed to account for the gravity data. Such a density contrast is also in accord with the presence of a partial melt.

Also shown on Figure 2.2.2 is the "limit of mantle deformation" from Coisy and Nicolas (1978a, 1978b), who used the wide geographical distribution of ultramafic nodules in the Massif Central to build up a picture of the mantle. They found that nodules could be divided into three main

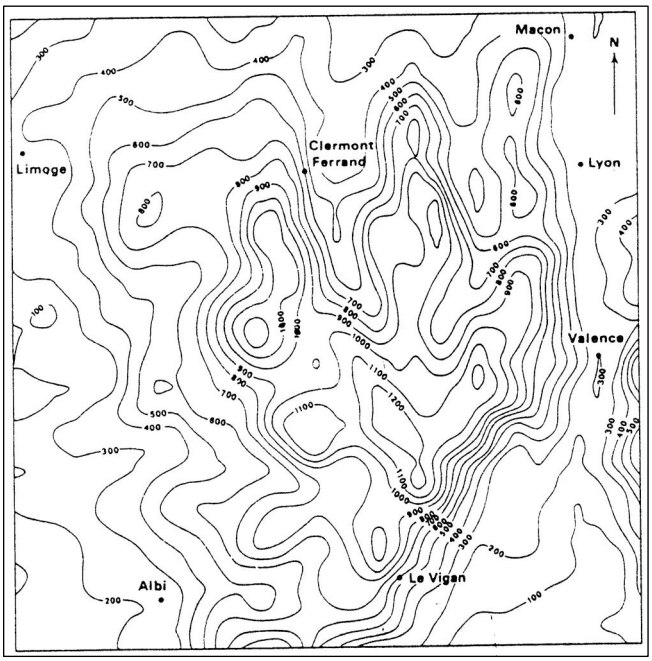


Figure 2.2.1. Averaged topography of the Massif Central using a 10 × 10km grid (taken from Lucazeau and Bayer 1982).

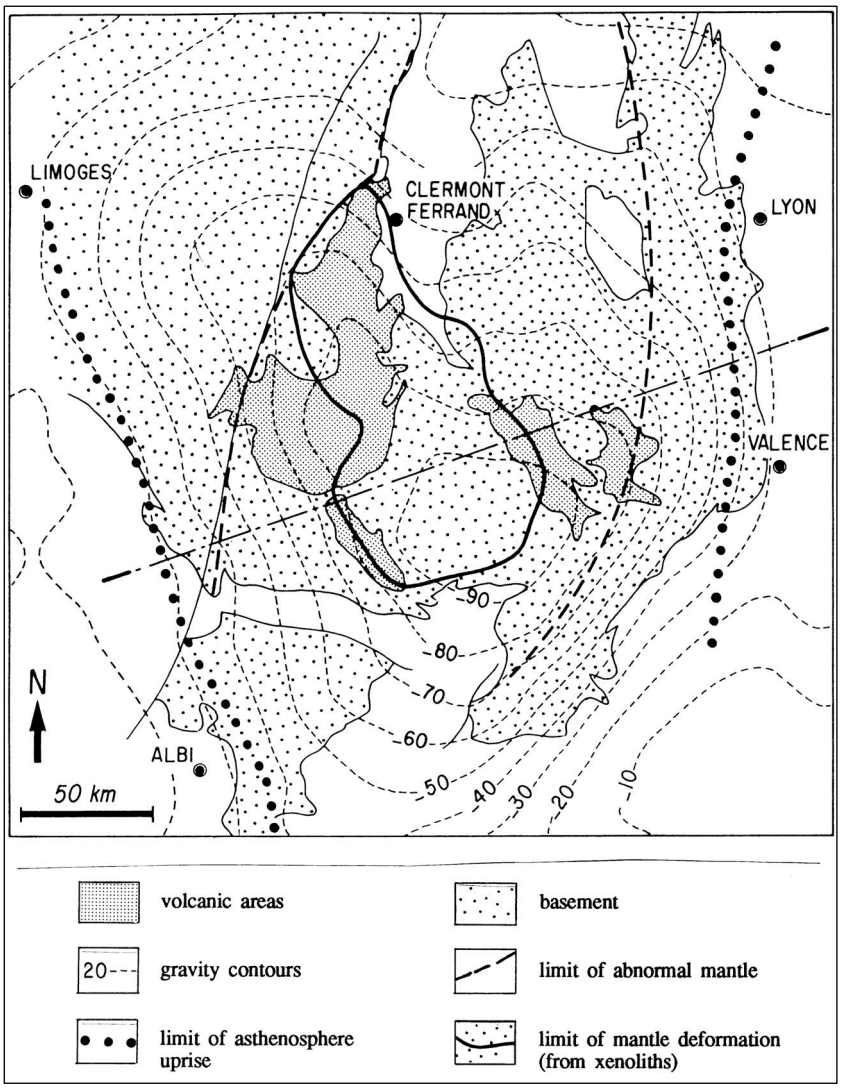


Figure 2.2.2. Summary map of the deep structure of the Massif Central (taken from Nicolas *et al* 1987)

groups on the basis of their crystalline fabric:

1) Coarse - 4mm grain size, no deformation.

2) Porphyroclastic - Bimodal size distribution of olivines, smaller grains are neoblasts. Olivines and spinels may show foliation.

3) Mosaic - 1mm grain size, high degree of recrystallisation, all olivines are neoblasts.

The first of these groups was interpreted as undeformed spinel lherzolite, and examples were found in volcanic rocks of all ages in the Massif. The second and third groups had suffered some deformation, sometimes severe, and were found only in rocks younger than 5.5Ma. Calculations of stress from olivine substructures and neoblast grain-size gave values of 300-400 bars for group 1 nodules, 400-1150bars for group 2 nodules and 300-700bars for group 3. Group 2 nodules also indicate elevated strain rates, up to $10^{-13}s^{-1}$.

The geographical distribution of the nodules was the key to their interpretation, with the undeformed group 1 nodules occurring predominantly towards the periphery of the volcanic province, and the mosaic nodules being concentrated in a central elliptical zone, with irregular margins (boundary marked on Figure 2.2.2). The porphyroclastic group 2 nodules tended to lie along the boundary between these two areas. Coisy and Nicolas (1978a,b) interpreted the group 3 mosaic nodules as having suffered pervasive strain and substantial recrystallisation, due to upward flow in the mantle by creep. The high stress and strain rates shown by some of the group 2 porphyroclastic nodules, together with their location marginal to the central area of deformation, led Coisy and Nicolas to the conclusion that they represent shear zones in the mantle, with relatively rapid movement of 1-5mm yr^{-1}.

In contrast to this model, Downes (1990) suggested that the distribution of nodule types was not sufficiently regular to delineate a mantle diapir, but was more easily explained by analogy with peridotite massifs exposed at the surface in the Red Sea, in which numerous shear zones pervade the material as a result of extension. Fluid/melt metasomatism would be concentrated in these shear zones.

Apart from the "limit of asthenosphere uprise", from Coisy and Nicolas' diapir calculations (see section 2.3.1), the remaining boundary on Figure 2.2.2 is that of "abnormal mantle". This is derived from deep seismic analyses conducted by Perrier and Ruegg (1973), Hirn and Perrier (1974) and Sapin and Hirn (1974). Their collective results are presented in Figures 2.2.3. Figure 2.2.4 shows a map of Moho depth produced using these and other seismic sections. The main point of interest in these seismic sections is that a zone of anomalously low-velocity mantle lies beneath the volcanic areas of the Massif. Figure 2.2.4 shows that the crust above this anomalous mantle has been thinned from the normal 30km to about 24km.

The anomalous mantle, with seismic velocities of 7.2 - 7.6 kms^{-1} (normally 8.2 kms^{-1}), probably contains a small proportion of interstitial melt, as suggested by the gravity anomaly. This

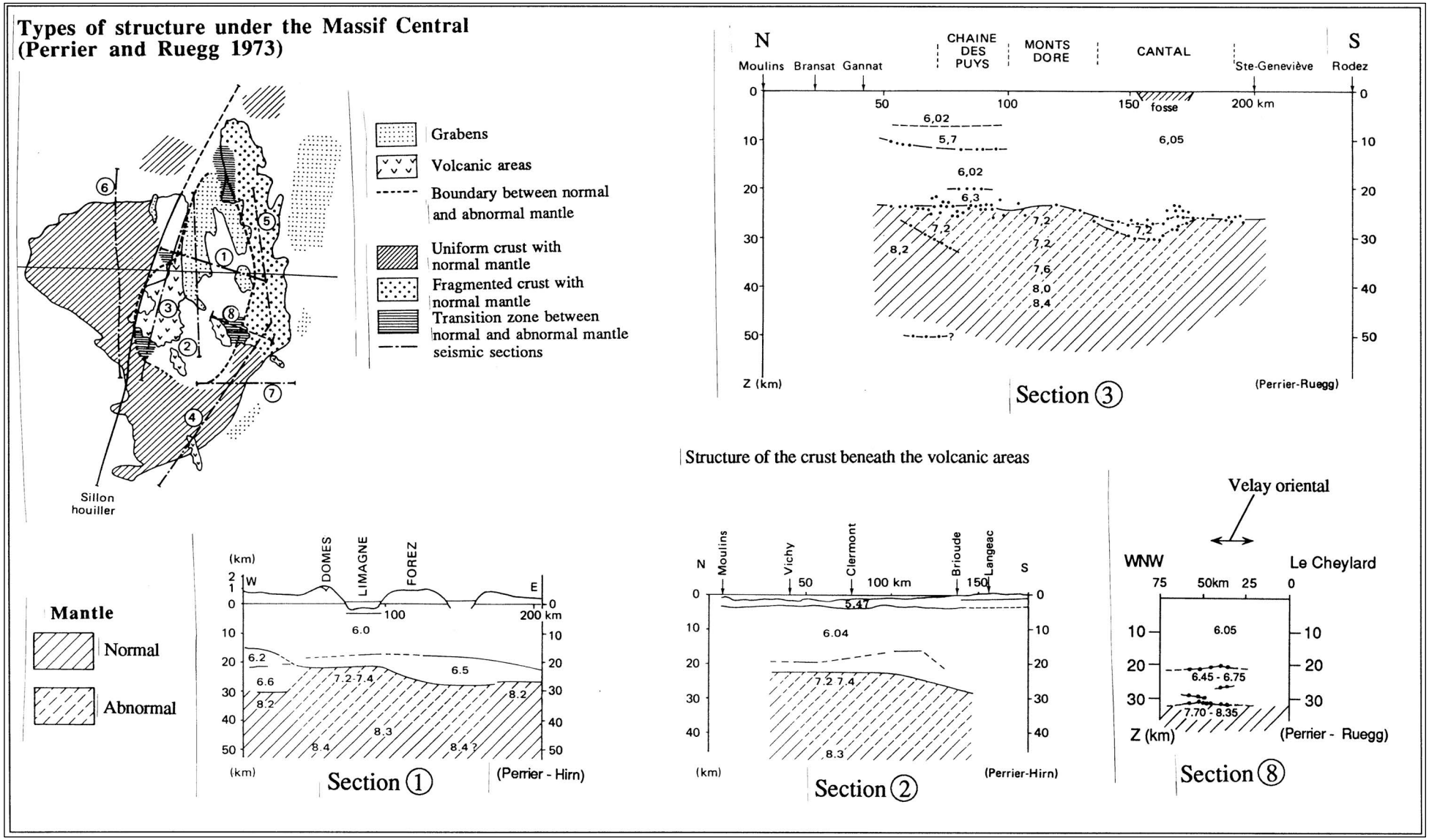


Figure 2.2.3. Deep seismic sections through the Massif Central (taken from Autran and Aubert 1980, using data in… [continued overleaf]

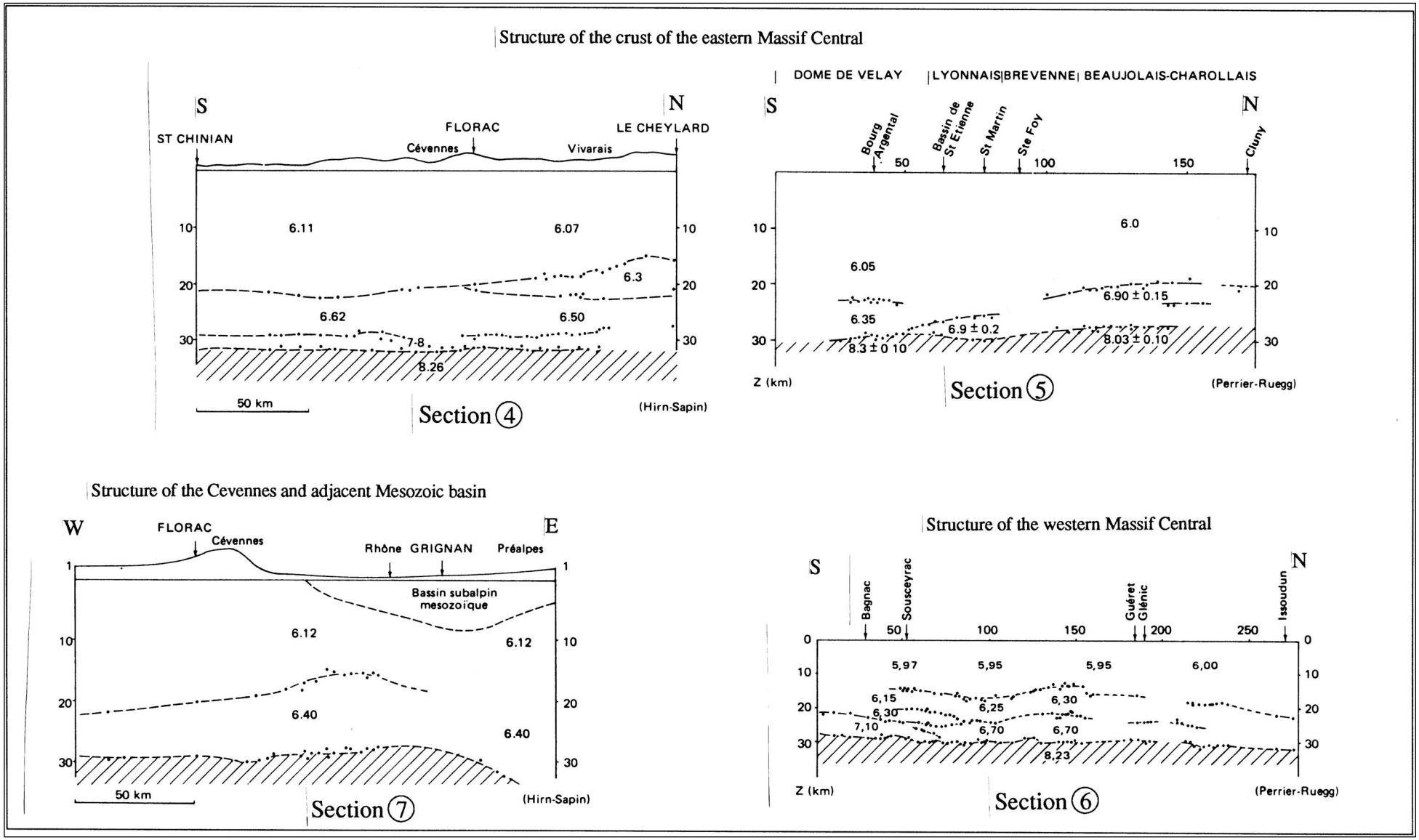


Figure 2.2.3. [continued from previous page] …Perrier and Ruegg 1973, Sapin and Hirn 1974 and Hirn and Perrier 1974)

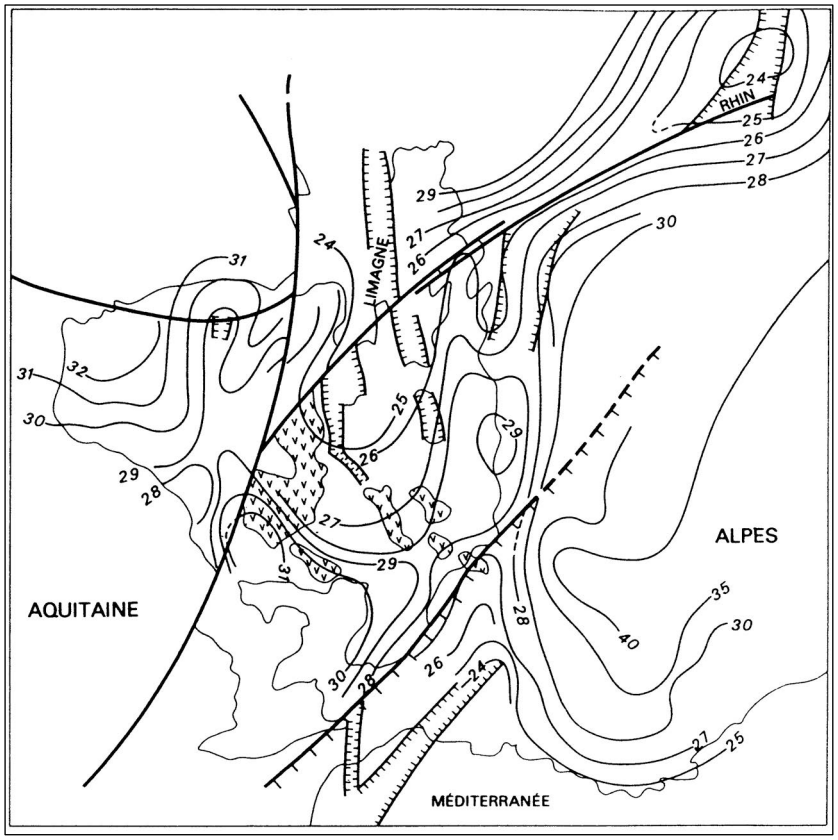


Figure 2.2.4. Map of depth (in kilometres) to the base of the crust (Moho). Recent volcanism and grabens are also shown. Figure taken from Autran and Aubert (1980).

interpretation was supported by analysis of deep (70 - 240km) Rayleigh waves (Souriau *et al* 1980) which also suggests that the lithosphere is reduced to a thickness of 50km, compared with the normal lithospheric thicknesses of over 100km.

A study of heat flow in the Massif Central (Lucazeau *et al* 1984), with the radioactive heat production of the surface rocks removed, showed that there is a high residual heat flow of 25 - 30 mW m^{-2} over the volcanic and graben areas.

The residual magnetic anomaly map of the Massif shows only near-surface structures, such as masses of basement amphibolite, and shallow igneous bodies beneath some of the volcanic areas.

2.3 Interpretation

2.3.1 Mantle diapir

The hypothesis that a mantle diapir could explain all of the data described above was tested in Lucazeau and Bayer (1982), Lucazeau *et al* (1984), Lucazeau (1986) and Nicolas *et al* (1987). In the first of these, a two-dimensional model was constructed to represent a vertical section through a radius of the diapir, assuming it to be symmetrical. Other constraints were;

1) no motion in the mantle in the Oligocene,
2) the diapir was initiated at a given depth, and affected higher zones with time,
3) the diapir rose with a vertical speed which is taken to be the maximum,
4) the crust suffered no internal deformation, and stopped all vertical movement of the diapir,
5) the extraction of magma involved insignificant volumes compared with the size of the diapir.

Using finite element modelling, with mass and energy balance constraints, and taking into account the flexural rigidity of the crust, the flow of the hypothetical diapir was used to predict patterns of Bouguer anomaly, heat flow, topography and degree of partial melting. For different combinations of diapir velocity and starting depth the best fit was obtained with a depth of initiation of 150km, a maximum velocity of 1cm.yr^{-1} (corresponding to an average velocity of 1mm.yr^{-1}), and a diameter of 40km. The effect on the result of using the anhydrous mantle solidus, as opposed to the 0.1%-H_2O solidus, was found to be small. Comparison with data from the Baikal rift area, The Rhine graben, the Bohemian massif, the Rio Grande rift and the Basin and Range province showed that they were similar to the Massif Central in most respects, with the exception of the diameter of the area affected, which was mainly controlled by diapir width.

Lucazeau *et al* (1984) described the same model, but with the addition of new heat flow data. They also clearly stated their view that the diapir was initiated by rifting of the lithosphere, which they regarded as being related to the Tertiary Alpine tectonic movements. Lucazeau (1986) left the question slightly more open, pointing out that rifting could either be passive, caused by plate motions generating extension of the lithosphere, or active, where mantle convection generates the stresses which cause the lithosphere to be rifted. However, he still preferred to explain the European rift system (Limagne-Rhône-Rhine-Bohemia) as a consequence of the Alpine continental collision, despite the difficulty involved in explaining how a major system of grabens could be formed sub-

parallel to the main compressional front.

Nicolas *et al* (1987) proposed the additional refinement of many small diapirs with diameters <10km, instead of one large diapir. They based this on the original work on nodule deformation, in which it was noted that in detail the data might fit smaller diapirs lying within the central area. This refinement allows a closer fit to the timing of volcanism due to the faster thermal relaxation of the smaller intrusions.

As mentioned in section 2.2, Downes (1990) disagreed with the diapir model, preferring a model of pervasive extensional shear in the lithosphere, coupled with asthenospheric uprise.

2.3.2 Hotspot model

A hotspot (Wilson 1963, 1965, Morgan 1972) is generated when a supply of excess heat deep in the mantle lowers the density of the local mantle material by thermal expansion, causing it to rise as a plume. The rate of conductive heat loss from the plume is several orders of magnitude lower than the speed at which it is able to flow, especially since the elevated temperature of the plume material lowers its viscosity, i.e. the hot, low-density plume rises much faster than it loses heat. Decompression may subsequently produce partial melting of the plume, since it rises essentially adiabatically.

As a lithospheric plate moves over a hotspot, it collects a trail of lavas which become progressively older with distance from the hotspot. Froidevaux *et al* (1974) attempted to demonstrate such an age-progression in the lavas of the Massif Central. He concluded that there were three independent branches leading away from the centre of the Massif. These branches are neither convincing, nor evidence for a hotspot.

One way to explain the absence of an age-progression is to propose that the European plate was stationary with respect to a hotspot during the volcanism. Duncan *et al* (1972) examined the Central European volcanic province (see Figure 2.1.2) and concluded that there was an absolute plate motion of 2.3cm.yr^{-1} from west to east. Minster and Jordan (1978) attempted independently to correlate all data on plate motions and to relate them to a hotspot-based absolute frame of reference. Their results for Europe were very poorly constrained and gave 0.3 ± 0.45 cm.yr^{-1} to the east i.e. the error bars exceed the plate motion, and direction is virtually meaningless. However, more recently Morgan (1981) and Livermore *et al* (1983) obtained more precise results, giving an absolute plate motion of 1.6cm.yr^{-1} to the SE over the last 10Ma, and 1.2cm.yr^{-1} to the ESE, averaged over the last 30Ma.

Morgan (1981) calculated from fossil hotspot trails that hotspots were able to move relative to one another at speeds of up to 0.5cm.yr^{-1}, although Duncan and Richards (1991), using the most recent data, were able to show that the maximum possible relative motion is 0.2-0.5cm.yr^{-1} and may actually be zero. If hotspot relative motion *is* as large as 0.5 cm.yr^{-1} it further confuses the picture, since this is a significant fraction of the absolute plate speed.

Morgan (1981) estimated that hotspots have a life of about 100-200Ma, but there is no evidence in the Massif for continuous pre-Palaeocene magmatism, and significant volumes of magma were not produced until the beginning of the Miocene. Either the postulated hotspot migrated from elsewhere to its present location, or the Massif Central volcanism represents the first 25Ma of the life of a new hotspot. If this were the case, and absolute plate motion was of the same magnitude as hotspot relative motion, the lack of an age-progression would not be a problem.

The consensus seems to be that the European plate is moving roughly from west to east, with an absolute (relative to hotspots) speed of around 1.2cm.yr^{-1}. This would require a trail of lavas about 300km long for the last 25Ma, leading east from the Massif Central, its age increasing with distance.

According to White and McKenzie (1988) the diameter of the uplifted area over a hotspot is 1000-2000km, due to the deflection of the plume head into a large mushroom-shape. Melting under such a swell is mainly controlled by lithospheric rifting. Since the hotspot raises the temperature of the plume mantle almost to the solidus even before rifting and decompression take place, the resultant magmatism can be both rapid and voluminous. Although their model was intended to account for the generation of continental flood basalt (CFB) provinces, they state that small degrees of rifting ($ß \leq 2$) will produce alkali basalt. The Massif Central has been stretched by a ß-factor of about 1.25, but the model predicts that magmatism should be simultaneous with rifting, and in the Massif it was at a minimum during rifting. Another problem for the White and McKenzie (1988) model is the apparent absence of significant extension associated with some CFB provinces, for example the Siberian Traps.

Wilson and Downes (in press), in a study of the chemistry of the sources of the European Cenozoic volcanism, evaluated the White and McKenzie (1988) hotspot model for all of the European Cenozoic volcanism. A 2000km diameter circle encompasses all of the volcanism, but the geochemical diversity of lavas leads them to prefer smaller, independent hotspots, or magma generation due to lithospheric flexure.

2.3.3 Mantle metasomatism

Mantle metasomatism is a process of selective enrichment of the mantle in some elements. It was postulated by Sun and Hanson (1975) and Lloyd and Bailey (1975) to explain high concentrations of large ion lithophile (LIL) elements in alkali basalts compared with relatively depleted MORB, since both basalt types were thought to come from a sub-lithospheric source. In addition, alkali basalts often have $^{143}Nd/^{144}Nd$ too high and $^{87}Sr/^{86}Sr$ too low to have been generated by the inferred Sm/Nd and Rb/Sr ratios of their mantle source rocks. To explain this a relatively recent addition of Rb and Nd was postulated, either by means of a low percentage partial melt, or by a percolating fluid phase, which could lower the liquidus and thus both increase the amounts and enrich the compositions of subsequent partial melts. The process is supported by the presence of apparently metasomatic minerals, such as kaersutite, apatite and phlogopite, in some mantle xenoliths carried by alkali basalts.

Menzies and Murthy (1980) showed that the $^{87}Sr/^{86}Sr$ of amphiboles in spinel-lherzolite nodules from Alaska and South Yemen was the same as that of the basanite in which they were carried, suggesting that the amphibole melted to produce the basanite. They also demonstrated petrographically that the amphibole had formed by reaction of the spinel *before* the nodules were entrained by their host lavas.

As described in the following section, Fitton and Dunlop (1985), Fitton and James (1986) and Fitton (1987) proposed an alternative to mantle metasomatism, dismissing metasomatised mantle xenoliths as accidental samples of the continental lithosphere and claiming that very small degrees of partial melting could provide suitable LIL-enrichment in alkali basalts.

Downes (1983) noted that the primitive lavas of the Massif Central were enriched in light rare earth elements (LREE) and Rb, while their low $^{87}Sr/^{86}Sr$ and high $^{143}Nd/^{144}Nd$ indicated a source depleted in these elements for a long time. She also noted the presence of apparently metasomatic amphibole, phlogopite and apatite in spinel-lherzolite nodules. Chauvel and Jahn (1984) tested several models of metasomatism for the Massif and demonstrated that the most likely mechanism was infiltration by a LREE, Rb-enriched fluid, followed by 10-20% partial melting.

Downes (1987a) further demonstrated that garnet-lherzolite was a more suitable source material for the Massif Central basalts, so that most of the spinel-lherzolite nodules brought to the surface were accidental, probably lithospheric, samples of conduit walls.

Downes (1987b) investigated the geochemistry of the ultramafic nodules from some of the same localities used by Coisy and Nicolas (1978a, 1978b). She found that the deformed nodules were depleted in a basaltic component and had higher K_2O/TiO_2 and LREE, compared to the coarse-grained, undeformed nodules. The deformed nodules also had lower E_{Nd} and higher E_{Sr} than those with no deformation, possibly due to an enrichment in LREE >200Ma ago.

In the Velay, the basalts analysed for this study never have Mg/Fe^{2+} high enough to be in equilibrium with mantle olivine (Fo_{90-92}). This is discussed in more detail in section 5.5, with the conclusion that at most only a small degree of fractionation has affected the most basic lavas. This is in accord with Downes (1983), who concluded that lavas with $Mg/Fe^{2+} > 2.1$ were primary (compared with $Mg/Fe^{2+} = 2.70$-3.45 for liquids in equilibrium with Fo_{90-92}). This suggests that metasomatic minerals were melted preferentially to produce the primary magmas in the Massif Central.

2.3.4 Magma sources

The source of alkali basalts has been the subject of speculation ever since they were recognised. Fitton and Dunlop (1985), Fitton and James (1986) and Fitton (1987) investigated the Cameroon line in an attempt to provide some constraints. The Cameroon line is a linear alkali basalt province in equatorial west Africa, and is unique in that it straddles the ocean-continent boundary, allowing comparison between lavas that have been erupted through widely different types of

lithosphere. Fitton and Dunlop (1985) demonstrated that the basic lavas from both oceanic and continental sectors were identical in all respects, thus eliminating the continental lithosphere as a potential source. A hotspot source was ruled out, due to the absence of any age-progression, leaving only the convecting upper mantle. Fitton and Dunlop (1985) and Fitton and James (1986) noted that metasomatised peridotite xenoliths were rare in oceanic basalts, but abundant in the continental basalts. They used this distribution as evidence that the continental xenoliths were samples of the lithospheric mantle, and as such took no part in the generation of the magmas.

As an alternative to mantle metasomatism, Fitton and Dunlop (1985) and Fitton and James (1986) suggested that very small (< 1%) partial melts of the depleted upper mantle, possibly with the involvement of small-scale, LILE-rich heterogeneities, could give the enrichment required by the lavas. These heterogeneities could be the streaked-out remains of subducted oceanic plates.

In the Massif Central, several lines of evidence have given clues about the origin of the basaltic lavas. Nicolas *et al* (1987) suggested that the basalts were partial melts of garnet + olivine, after comparing rare garnet-peridotite and spinel-lherzolite xenoliths. They suggested that small clusters of tiny opx + cpx + spinel crystals that commonly occur in spinel-lherzolite xenoliths represented pockets of melt, formed on the sites of garnets, that were quenched before being able to escape. The equilibration conditions of the garnet-bearing xenoliths (32kbar, 1400°C) would then show that the basalts were formed at depths of at least 100km. Downes (1987a) independently deduced a garnet-lherzolite source for the Massif Central basalts, on the basis of isotopes and trace elements.

In this thesis, the CMAS-projection of O'Hara (1968) was used to assess the phase relations of the Velay basalts (section 5.9). The results suggest that they were equilibrated with spinel-lherzolite, at about 15kb (40-50km). This was probably not their depth of formation, but merely a stage in their journey to the surface. Also in this study, the low $^{87}Sr/^{86}Sr$ of the undersaturated Velay lavas (section 5.8) is used as evidence that they are uncontaminated, and had a source in the convecting upper mantle, like those of the Cameroon line.

Wilson and Downes (in press) made a complete isotopic analysis of the basic lavas of the Massif Central and other European Cenozoic volcanic provinces. They concluded that the source of all these lavas was a mixture of two components, which they termed A and B. Component A was a mixture of depleted (MORB-source) mantle and HIMU (St Helena-type) mantle. HIMU may be recycled subducted oceanic lithosphere. Component B was subordinate to A, and had isotopic values appropriate for enriched mantle. It probably represented a lithosphere component, either the lower crust or the lithospheric mantle.

The relative proportions of depleted mantle, HIMU and enriched mantle in the source of the Velay lavas were not determined in this study since a complete suite of isotopic measurements was not made.

2.3.5 Conclusions

Some mantle nodules from beneath the Massif Central show high strain rates, which indicate

either pure shear in the lithosphere, diapiric flow in the asthenosphere, or both. There is evidence for diapirism from geophysical studies, but it remains difficult to assess whether it was generated by a hotspot or by lithospheric extension as a result of plate motions. The absence of a clear age-progression in the Massif Central, or the European Cenozoic volcanic province as a whole, and the small scale of volcanism in general, militate against the hotspot model.

Mantle metasomatism has been suggested to explain the apparent decoupling of isotopes and trace elements in the basalts of the Massif, but the alternative explanation of very small partial melts as the cause of trace element enrichment, cannot easily be dismissed. The basalts were probably decompression melts of garnet lherzolite, formed at a depth of at least 100km due to diapiric uprise, which equilibrated with spinel-lherzolite before being erupted.

In the Massif Central, the sequence of Oligocene rifting, Miocene and early Pliocene magmatism and late Pliocene uplift seems to provide the only simple evidence that lithospheric extension and rifting caused the diapirism and volcanism, since the uplift and volcanism would be expected to occur at the same time as rifting if a diapir was the cause.

Chapter 3

Petrography and mineral chemistry of the Velay oriental lavas

3.1 Lava types

3.1.1 Introduction

For this study, the lavas of the Velay are classified by their bulk composition, or by their mineralogy if not analysed. The basis for the compositional classification is the SiO_2 vs Na_2O+K_2O diagram (Cox *et al* 1979), shown in Figure 3.1.1. As this graph shows, the basic lavas straddle the boundary between basalt and basanite, and no simple petrographic criterion distinguishes them. For this reason they are referred to as alkali basalts (with the suffix *sensu lato* implicit). The trachybasalt divisions of hawaiite and mugearite+benmoreite (the latter pair referred to as "intermediate") are used as in the diagram, plus a few trachytes and phonolites that are petrographically similar to the intermediate lavas.

The most evolved lavas straddle the trachyte and phonolite fields, causing the same problem as in the basic lavas. All these lavas were thus called phonolites. The two remaining lavas are both quartz-trachytes.

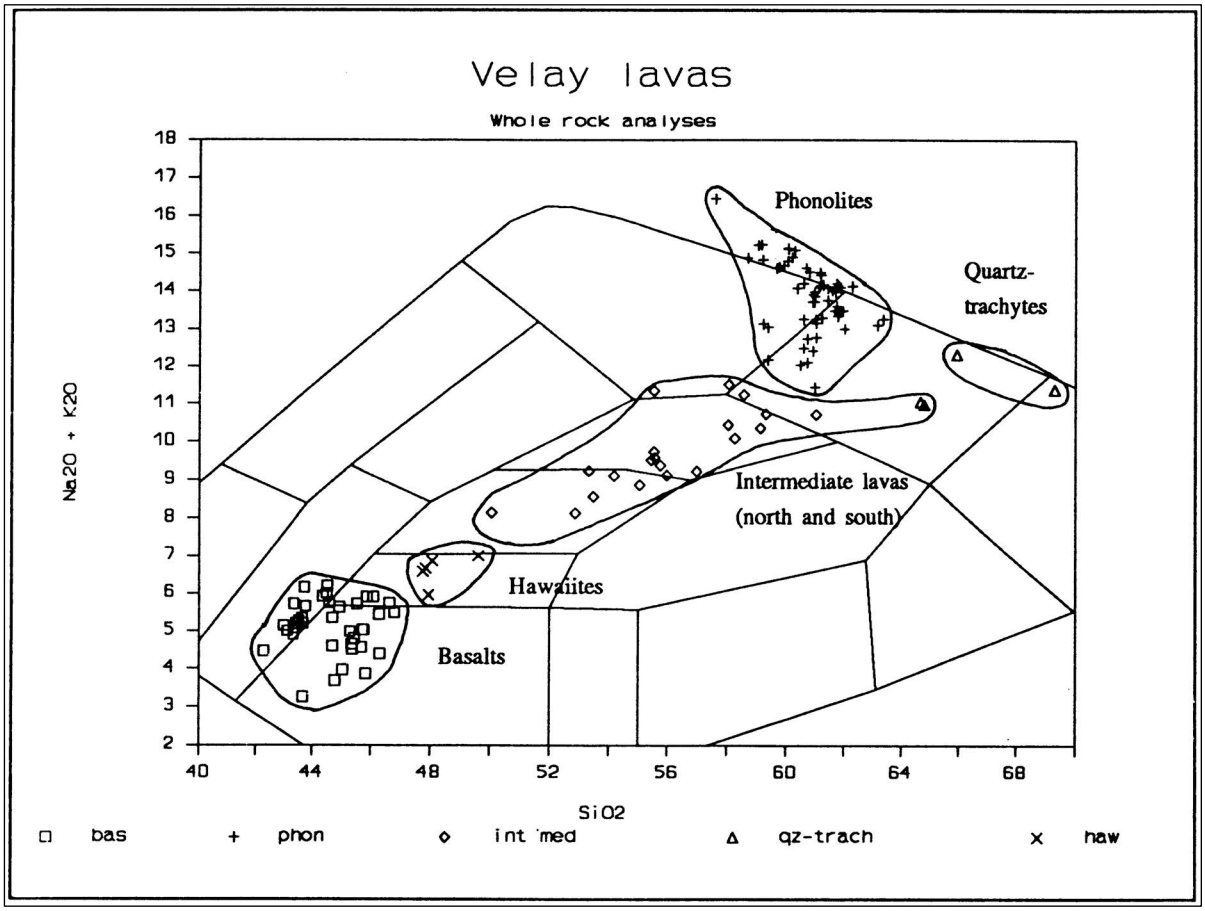


Figure 3.1.1. Graph of silica against total alkalis, showing the classification of lavas. The grid is from Cox *et al* (1979)

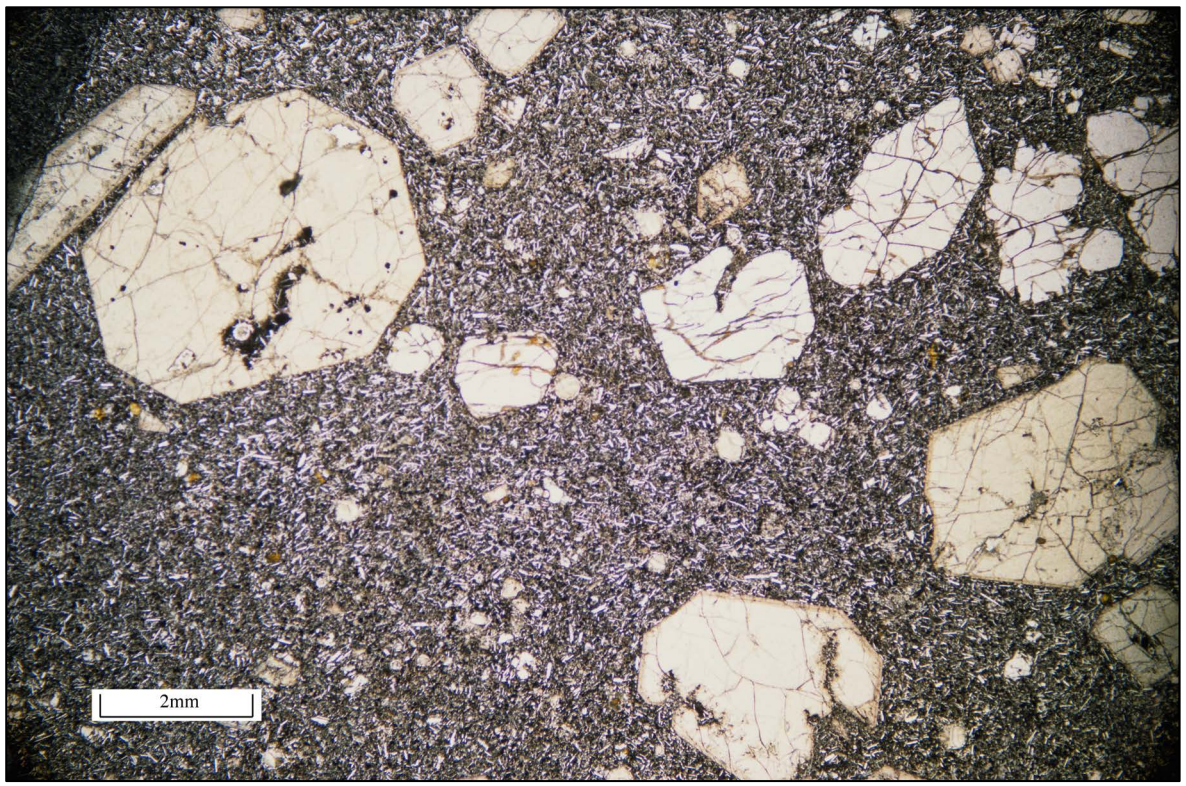


Figure 3.1.2. The Bonnevialle ankaramite (87/43) contains large phenocrysts of clourless olivine and pale pink clinopyroxene. The brown rim on the cpx crystals is the same as the groundmass cpx. (Plane polarised light).

All specimens are listed in Appendices A and B, which give their locations and mineralogy, respectively. The location maps in the back pocket should be consulted for named locations.

3.1.2 Alkali basalts *(sensu lato)*

The basalts occur as horizontal sheets, stacked vertically on an originally sub-horizontal peneplain surface to form the Velay oriental plateau. Sampling has shown that the most basic lavas are found at the base of this pile and the most evolved at the top.

Most of the basalts are almost aphyric, with only a few eu-subhedral microphenocrysts of olivine (Fo_{71-86}, most Fo_{80}) and Ti-magnetite (22-24% TiO_2). Their groundmasses are composed of plagioclase An_{63-70}, clinopyroxene, Ti-magnetite, olivine and occasionally brown glass. The presence of glass is not related to the bulk composition of the lava, but is probably related to rapid cooling. It is often found in the flows resting on the basement and is exemplified by specimen 84/40b, the lowest flow at St Clément.

The ankaramites contain euhedral clinopyroxene phenocrysts, up to 2cm in diameter and usually larger than the accompanying olivines. The best examples of ankaramite are specimens 84/43 (St Clément), 86/53 (near Machabert), 86/63 (near Champagnac) and 87/43 (near Bonnevialle). Figure 3.1.2 shows a thin section of the Bonnevialle sample. 84/43 has accessory Ti-magnetite phenocrysts (11-22% TiO_2) and 86/53 has Ti-magnetite and trace amphibole, while 86/63 and 87/43 have phenocrysts of pleonaste.

The order of crystallisation in the ankaramites is:

a) pyrrhotite + pleonaste + Ti-magnetite ⇒ olivine + cpx — 84/43, 86/63, 86/53, 87/43

b) olivine ⇒ Ti-magnetite ⇒ cpx ⇒ amphibole — 87/29, 87/49

The shapes of some of the macrocrysts, their compositions and occasional partial resorption, suggest that they are re-entrained cumulate crystals. The unusually-shaped minerals would represent interstitial minerals that have been broken into fragments within the melt. Specimen 87/88 (la Besseyre-basse) contains euhedral clinopyroxene and a suite of partially resorbed crystals; amphibole, Ti-magnetite, olivine, pleonaste, apatite and plagioclase (An_{54}). It is probably younger than those of the Velay oriental and is included only to demonstrate the phenomenon of re-entrainment.

Some Velay basalts contain partially resorbed amphibole. 86/53 has already been mentioned, but one of the best examples is specimen 87/29, from Chaud de la Croix. This contains large, relict "ghost" amphiboles composed only of reaction products (cpx + Ti-magnetite + plagioclase + brown amphibole), as well as clinopyroxene, olivine and Ti-magnetite. The resorption does not necessarily mean that the amphiboles are xenocrysts, since amphibole is stable only at pressures greater than 2-10kb for basaltic melt temperatures of 1000-1100°C (Merrill and Wyllie 1975), so if there is enough time for equilibration at the surface, in this case in a lava lake, the amphibole will be resorbed.

Biotite/phlogopite is present in the groundmasses of a few specimens: 86/63 (Champagnac), 87/47 (near Les Estables) and 87/49 (Machabert quarry). It is always associated with small vesicles and alteration minerals and is probably the product of high temperature hydrothermal alteration during the cooling of the lava flow.

There is no evidence for plagioclase crystallisation in the basalts, except in the groundmass where its anorthite content can be used to assess how "primitive" the basalt is, varying from An_{70} to An_{63}. In both of the continuous sequences sampled - Gazeille and St Clément - the flows with An_{70} plagioclase are at the base. However, above this there is no gradual decline towards the An_{45} of the upper benmoreite, but a random variation between An_{69} and An_{63}.

3.1.3 Hawaiite

Hawaiite is characterised by having a much smaller proportion of olivine than the basalts, either as phenocrysts or in the groundmass. The largest volume of hawaiite appears as a flow sheet near the top of the St Clément sequence, below the uppermost benmoreite.

Six specimens were examined and of these 84/44, 84/45 and 86/55 all came from the St Clément flow sheet. They have Ti-magnetite (17-22% TiO_2) and augite microphenocrysts (similar composition to those in basalts), and their groundmasses consist of plagioclase An_{64}, augite, Ti-magnetite and rare olivine. Specimen 86/55 contains a single microphenocryst of Cr-rich magnetite (15% Cr_2O_3), but no other examples were found. Specimen 85/17 (near Echamps) has essentially the same mineralogy as the St Clément samples but with An_{61} plagioclase in the groundmass.

Specimen 87/75, from Yssingeaux in the north of the Velay, resembles a basalt with microphenocrysts of olivine. The presence of apatite, with an olivine inclusion, shows that the rock is slightly more evolved, and this is confirmed by its bulk composition. Specimen 87/32, from a small neck in the centre of Queyrières, is similar in composition and groundmass to the other hawaiites, but also contains a unique suite of phenocrysts. Its groundmass is plagioclase An_{56-59}, augite, Ti-magnetite with traces of olivine and brown apatite. The phenocrysts include partially resorbed amphibole, pale pink-brown zoned augite, some with greenish rims, partially resorbed plagioclase An_{48-52}, Ti-magnetite and partially resorbed olivine (Fo_{71-83}). The resorption of the plagioclase may indicate that the phenocryst suite is xenocrystic or part of a re-entrained early cumulate. The crystallisation sequence is:

$$\text{apatite} \Rightarrow \text{Ti-magnetite + olivine} \Rightarrow \text{cpx} \Rightarrow \text{amphibole + plagioclase}$$

3.1.4 Mugearite and Benmoreite - Intermediate lavas

Lavas of these compositions from the northern and southern parts of the Velay oriental are treated separately here since they form two distinct groups. The intermediate lavas in the south occur as thin aphyric (4-6m) flows over the top of the basaltic plateau and usually lie above a prominent red

bole (Mergoil 1980). In the north their equivalents occur as extrusion domes, suggesting that on eruption they were rather more viscous than those of the south, and are often phenocryst-rich, up to 23% by volume. The total volume of the southern intermediate lavas is about 0.25km^3 (50km^2 x 5m). That of the northern lavas is more difficult to assess, but the volume of all the extrusions except Mont Chanis and Mont Gerbizon, with about 0.04km^3 and 0.15km^3 respectively, is very small. These two are also slightly more evolved than the others, lying on the phonolite/benmoreite boundary.

The bulk compositions of the lavas from both areas cover a wide range, but almost all lie on the same general trend from hawaiite towards trachyte. The southern intermediates fall mainly in the field of mugearite or just within the benmoreite field. The northern lavas are mainly benmoreites and trachytes.

3.1.4.1 Southern Intermediate lavas

Nine specimens were examined, of which three - 84/23, 84/46 and 86/56 - came from the summit flow, within 500m of St Clément, and consequently have similar petrography. All nine specimens are aphyric, with only a few microphenocrysts of Ti-magnetite (21-27% TiO_2) and pink-brown apatite (see Figure 3.2.22). Some samples also have "ghost" amphibole and plagioclase An_{36-44}. The order of crystallisation of the microphenocrysts, deduced from examination of several sections, is:

apatite ⇒ Ti-magnetite ⇒ plagioclase + amphibole

The groundmass of the least evolved specimen, 87/8 (Fay-sur-Lignon), consists of plagioclase An_{64}, Ti-magnetite and augite, with a trace of apatite. In the more evolved specimens it becomes progressively harder to determine the groundmass plagioclase composition optically, and results obtained range from An_{60} to An_{45}, sometimes with sanidine/anorthoclase. A more reliable compositional range for the upper benmoreite flow was obtained by Batard (1974) using a microprobe. She found it to be oligoclase-andesine with 10-20% orthoclase component, forming 80-85% of the rock.

Other specimens from the upper plateau flow sheet are 87/23 (near Pailhès, NE of St Clément), 86/47 (near Chaudeyrolles) and 88/1 (Freydeyre). All have similar petrography and compositions to the St Clément samples.

Specimen 88/23 is from a mugearite dyke near Borée and has similar mineralogy to that of the other mugearites, albeit slightly coarser-grained. It has a single zircon microphenocryst, and groundmass biotite, which may be due to secondary hydrothermal action. A possible origin related to the cumulates is outlined in section 4.3.

Specimen 87/51 is from the short, thick flow at the top of the Rochers de Cuzet. It has the composition of a trachyte, although it lies close to the benmoreite boundary and has similar petrography to the other intermediate lavas of the south, with Ti-magnetite and apatite microphenocrysts and a groundmass of K-feldspar laths.

The presence of apatite as microphenocrysts in all of these lavas reflects the increase in P_2O_5 concentration from basalt to benmoreite. None contain olivine.

3.1.4.2 Northern Intermediate lavas

The intermediate lavas of the northern Velay oriental differ in many respects from their southern equivalents, particularly in their phenocryst content. Table 3.1.3 gives a detailed account of the petrography of the twelve extrusions studied. The Dents de Mézenc extrusion from the south (shown in Figure 3.2.20) has been included in the northern group because it is very similar to them petrographically. It is also quartz-normative, unlike the southern lavas.

With the exception of the St Pierre Eynac, Mont Gerbizon, La Madeleine and La Dent lavas the northern intermediate lavas are phenocryst-rich. It is particularly striking that the assemblage of minerals and their order of crystallisation is virtually the same in each of them *despite their occurrence in independent extrusions, with varied bulk compositions*. Even the compositions of the phenocrysts are frequently similar. Only their relative proportions and degree of resorption vary significantly.

The relative proportions of phenocrysts do not provide a framework for subdividing the group, although the three least evolved phenocryst-rich extrusions: Suc de Monac, Montusclat and Veyrines, have the greatest proportion of kaersutite amphibole.

Kaersutite is the characteristic amphibole in the Velay, and is abundant in most of the northern intermediate lavas. In most cases it is partly resorbed to a mixture of green clinopyroxene and opaques along surfaces exposed to the liquid (see Figures 3.1.4 and 3.2.18), although in Montusclat it is virtually pristine (Figure 3.1.5). The reason for this resorption is not clear, but one possibility is that the amphibole re-equilibrated during a slow passage to the surface, where at low pressure it becomes unstable. However, the time it would take the melt to reach the surface does not seem to be enough for such an extensive equilibration, as some of the lavas show almost no trace of the original amphibole. A more likely explanation is a fall in oxygen fugacity, which would increase the Fe^{2+}/Fe^{3+} ratio and promote the growth of FeO-rich phases at the expense of Fe_2O_3-rich phases. This would also explain the Ti-magnetite overgrowth of sphene that appears in these lavas (see section 3.2.9 and Figure 3.2.21).

Kaersutite also shows replacement by biotite (8.3% TiO_2 - single analysis), as shown in Figure 3.2.18. It usually grows *within* the amphibole and could be mistaken for an inclusion.

Clinopyroxene is the next phase to appear after amphibole, displaying marked zoning, both in colour and birefringence. The birefringence zoning is oscillatory, but the colour zoning records more important changes. Pale green clinopyroxene with yellow end-sections is the most common, showing zoning in the intensity of the green colour. Another distinct type of clinopyroxene, with pale pink/pale grey-green/pale yellow pleochroism, is also occasionally present, either as separate phenocrysts or as cores to the pale green/pale yellow clinopyroxene. This sequence is very rarely

Specimen location and number	P H E N O C R Y S T S P R E S E N T									Comments	Sections * = probed	Normative nepheline, quartz and hypersthene	87Sr/86Sr orig	Age (Ma)
	Apatite	Ti-magnetite	Sphene	Amphibole - Kaersutite	Biotite	Clinopyroxene - Salite	Plagioclase	K-feldspar	Zeolites, carbonates and others					
Suc de Monac 84/19a, 87/30	Euhedral, grey inclusion-rich.Most assoc. with amph. 0.6mm long max tr.	Sub-anhedral, except those in resorbing amph 0.5mm max 0.4%	Euhedral, with overgrowing opaques 0.7mm max tr.	greeny brown-red brown-clear Strongly resorbed to cpx + opaques. Originally Eu-subhedral, now anhedral 3.5mm long max 8.3%	red brown-clear Eu-subhedral Within margins of resorbing amph max 0.3mm 0.1%	pale green-pale yellow Eu-anhedral. Some zoning to paler green at edge of phenocrysts 1.2mm max 0.2%	Eu-subhedral, some strongly zoned, cores strongly corroded with much carbonate An47-57 (probe) at least 4mm long max 10.3%	Thin rim of K-feldspar as overgrowth on plagioclase 2.1%	Carbonate abundant in cores of plag phenocrysts. Zircon in coarse-grained inclusions.	The subject of a paper: Batard *et al.* (1977) Phenocrysts often in glomerocrysts	2*	0.08 Qz	0.703424	-
Montusclat 88/16	Euhedral, pale grey few inclusions. Quite thick stubby crystals 0.4mm long max 0.05%	An-subhedral 0.7mm max 1.0%	Eu-subhedral diamonds. Some overgrowth by opaques 0.7mm max 0.2%	greeny brown-red brown-clear Hardly any resorption Eu-subhedral 3.0mm long max 8.8%	_____	pink-grey green-pale yellow, zoned. Eu-subhedral 1.7mm max 0.8%	Eu-subhedral laths, strongly zoned, resorbing. Often with K-feldspar overgrowth. An40 max. (optical) 9.0mm long max 8.2%	Anorthoclase - as overgrowth on plag cores (0.8mm thick max). Also a few anhedral phenos 1.0mm max 4.1%	Zeolites in cores of resorbing plagioclases	Lack of resorption of amphibole in this rock clearly correlates with near absence of strongly green cpx	1	0.03 Qz	0.703751	10.8
Veyrines 87/74	Euhedral, pale grey inclusion-rich. In amphibole 0.2mm long max tr.	Anhedral, some with blobby groundmass overgrowth 0.6mm max 0.3%	_____	greeny brown-red brown-clear partly resorbed. Originally eu-subhedral 3.5mm max 10.3%	_____	pale green-pale yellow or pale pink. Zoning in either direction. Euhedral 1.2mm max 1.3%	Subhedral laths,with some zoning. An23-34 (probe) 3.5mm long max 0.5%	_____			2*	5.42 Neph.	0.703745	-
Glavenas 87/72	Sub-euhedral, pale grey, inclusion-rich 0.2mm long max tr.	An-subhedral 0.3mm max tr.	Eu-subhedral diamonds 0.5mm max tr.	Totally resorbed originally sub-euhedral 1.0mm max 0.4%	_____	pale green-pale yellow Eu-subhedral. No zoning 1.1mm max 0.5%	Eu-subhedral laths, strongly zoned. Cores often corroded with carbonate present An46 (optical) 2.4mm long max 1.0%	Thin K-feldspar overgrowth on plagioclase 0.4%	Carbonate abundant in plag. cores - as in Suc de Monac Carbonate + zeolites in gloms		1	0.96 Neph.	----	-
Queyrières 87/33	Euhedral, grey inclusion-rich.Much assoc. with amph. 0.3mm long max 0.1%	Sub-anhedral 0.5mm max 0.4%	Eu-subhedral diamonds 0.7mm max 0.1%	greeny brown-red brown-clear partly to strongly resorbed. Originally eu-subhedral 2.5mm max 3.4%	red brown-clear anhedral. Within amph 0.1mm max tr.	green-yellow Eu-subhedral. Some have clear cores 1.2mm max 0.8%	Eu-subhedral laths, zoned. Some with K-feldspar rims. An60 (optical) max 4.0mm long max 8.3%	Sub-anhedral Clusters of anorth/sanidine phenos. Little zoning 2.0mm max 5.1%		Rock contains xenocrysts from granite	2	0.47 Qz	0.703899	-
Mont Chabrier 87/31	Euhedral, grey inclusion-rich. 0.6mm long max 0.3%	An-subhedral 0.4mm max 0.7%	Euhedral diamonds 0.5mm max 0.2%	greeny brown-red brown-clear partly resorbed to cpx + opaques. Originally euhedral 3.0mm long max 2.5%	red brown-clear Subhedral, within amph 0.2mm max tr.	pale green-pale yellow Eu-subhedral. Some faintly zoned to darker green at edge, one has darker green core 0.8mm max 0.5%	Eu-anhedral, strongly resorbed, often as anhedral cores to K-feldspar phenocrysts Zoned An32 (optical) max 2.6mm max 3.0%	Anorthoclase - euhedral laths to large, rounded, anhedral crystals, w. resorbed margins 5.3mm max 14.5%			1	1.26 Hyp	0.704128	-
Mont Chanis 87/70	Euhedral, pale grey inclusion-rich. Often assoc. w. amph 0.3mm long max tr.	An-subhedral one 3.5mm xenocryst 0.4mm max 1.5%	_____	greeny brown-red brown-clear Strongly resorbed. Orig. sub-euhedral 2.5mm max 10.2%	red brown-clear Sub-anhedral. Assoc. with resorbing amph 0.2mm max tr.	pale green-yellow green Sub-anhedral. Largest has clear core 1.3mm max 0.8%	Sub-anhedral laths, strongly zoned. Range at least An27-44 (probe). Cores occ. replaced by zeolites 3.5mm max 7.3%	Possibly some as thin overgrowth on plagioclase tr.	Zeolites abundant; clear, brown, green Usually in interstices. Carbonate w. opaque xeno 2.5%		2*	13.16 Neph	0.703456	12.6
St Pierre Eynac under La Vierge 87/68	Sub-anhedral clear to pale grey some inclusions 0.2mm max tr.	An-subhedral 0.3mm max 0.3%	_____	one pheno - completely resorbed to cpx + opaques anhedral 0.5mm tr.	_____	pale green - one ragged anhedral phenocryst 0.4mm tr.	one crystal - subhedral lath, rounded with thin overgrowth of K-feldspar 2.1mm tr.	two crystals - both probably xenocrysts One is anorthoclase anhedral, other is ?orthoclase 2.1mm, 3.5mm 1.2%	Carbonate moat around ?orthoclase pheno. Also carbonate in plag core 0.4%	Virtually aphyric	1	3.33 Qz	----	13.6
Mont Gerbizon 86/27	Euhedral, dark grey. Very inclusion-rich 0.5mm long max 0.1%	Anhedral 0.6mm max 0.6%	Euhedral diamonds pale brown 0.9mm max 0.2%	greeny brown-red brown-clear Nearly all completely resorbed. Orig sub-anhedral 1.5mm long max 3.4%	_____	green-greeny yellow or pink-pinkish green. Some have pink core,green rim Others are all green, and are sieved 1.2mm max 1.0%	_____	Anorthoclase, anhedral, sieved Or40-55 (probe) 1.2mm max tr.	Lots of zeolites in cracks 1.8% one 0.1mm zircon anhedral in zeolites.		1*	4.93 Neph	0.703654	-
La Madeleine 87/10	N O S E C T I O N									See below	0	0.38 Neph	----	-
La Dent 87/11	Euhedral, grey inclusion-rich 0.5mm long max tr.	Sub-anhedral 0.5mm max tr.	_____	_____	_____	pale pink-pale green Euhedral, filled with small opaques 0.9mm long max tr.	Euhedral laths, some zoning An59 (optical) - same as groundmass 1.4mm long max tr.	_____	Zeolites - interstitial	Possibly the same flow as La Madeleine	1	4.62 Neph	0.703722	11.1
Dents de Mézenc (Roche Pointue) 86/8, 87/58 88/17	Euhedral, dark grey-pale brown. Very inclusion-rich 0.6mm long max tr.	Anhedral 0.7mm max 0.4%	_____	greeny brown-red brown-clear partly resorbed. Original outlines sub-anhedral 3.0mm max 0.3%	red brown-clear partly resorbed to opaque needles Orig sub-anhedral 2.0mm max 1.1%	pale green-v pale yellow and pink-grey green, both euhedral. Pink occ. forms cores to green cpx 1.5mm max 0.2%	Eu-subhedral laths, strongly zoned, often partly resorbed. Usually have K-spar overgrowth An71-15 (probe) 2.0mm max 0.8%	Anorthoclase, most in clusters, up to 5mm, of intergrown xtals. Rest as anhedral phenos Or13-42 (probe) 4.0mm max 18.1%	Zircon, pre-opaque Eu-subhedral 0.18mm max tr.	The subject of a paper; Berger *et al* (1978) 21% phenocrysts	4*	7.12 Qz	0.704782	9.0

Table 3.1.3. Phenocryst petrography of the intermediate lavas of the north of the Velay oriental, and Dents de Mézenc from the south. Bulk analyses have been made of all of these. Order of crystallisation is left to right, with apatite earliest and K-feldspar last. Percentages were obtained by point-counting, with 1000 to 9000 points for each lava.



Figure 3.1.4. Mt Chanis (87/70) intermediate lava, with abundant plagioclase and partially resorbed amphibole phenocrysts. Pale green cpx can be seen replacing the amphiboles. (Plane polarised light).

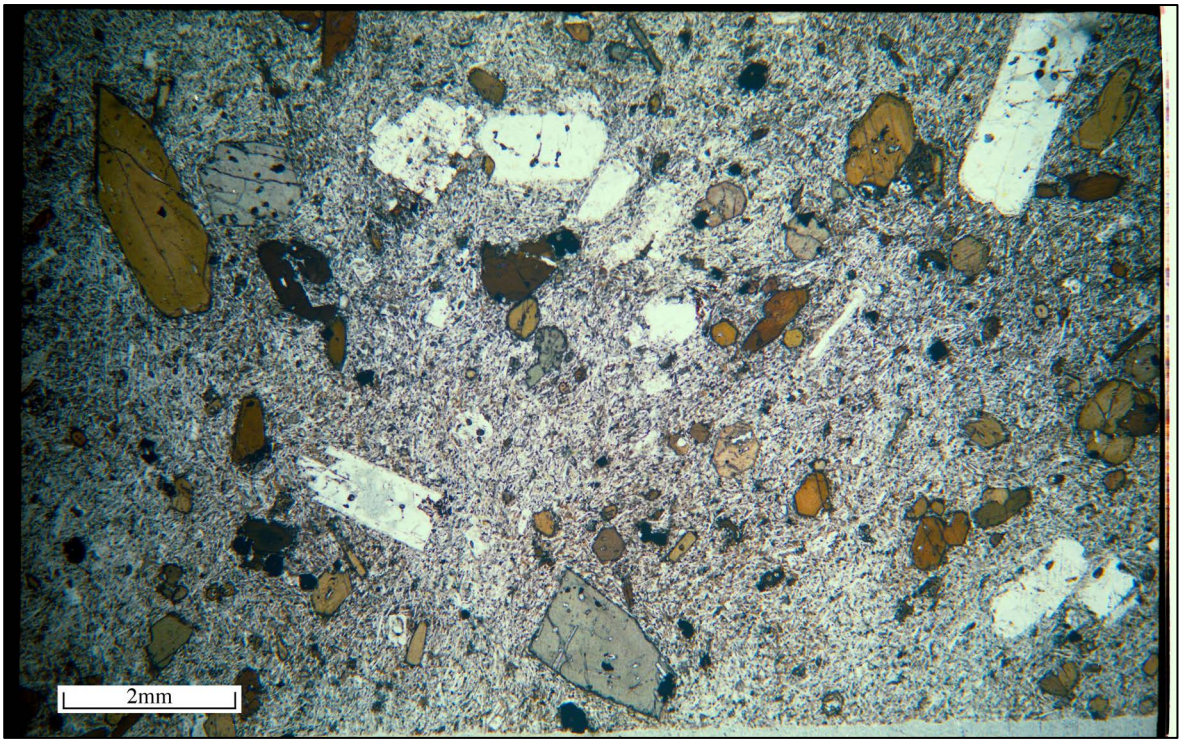


Figure 3.1.5. The Montusclat (88/16) lava has equally abundant plagioclase and amphibole phenocrysts to that shown in Figure 3.1.4, but the amphibole in this rock shows no sign of resorption. In addition, the cpx in this lava is pink/grey-green, as opposed to the green/yellow cpx of Mt Chanis. (Plane polarised light).

reversed, showing that the pink clinopyroxene predates the green. Two further observations are crucial to the interpretation of these data:

a) the cpx which replaces the resorbed amphiboles is invariably pale green/yellow (see Figure 3.2.18)

b) only the pale pink cpx is present in the Montusclat lava, with its unresorbed amphiboles (see Figure 3.1.5), and only the green/yellow cpx occurs in the Queyrières lava, which has strong amphibole resorption.

The kaersutite resorption is clearly linked to the change in the equilibrium clinopyroxene.

Most elements show fairly random variation between the two types of clinopyroxene, the exceptions being Fe, Mg and to a lesser extent Al. The green/yellow clinopyroxene is characterised by $FeO^{total}/MgO > 1$ and $Al_2O_3 < 6\%$, the pinkish clinopyroxene by $FeO^{total}/MgO < 1$ and $Al_2O_3 > 6\%$. There is at most only a weak correlation between green colour and Na_2O-content (see section 3.2.3). The FeO^{total}/MgO ratio appears to determine the colour of the clinopyroxene, but the chemical basis for the connection between kaersutite resorption and the appearance of green clinopyroxene is not clear. FeO^{total}/MgO for the kaersutites averages about 1.2, but the clinopyroxene which replaces it is accompanied by Ti-magnetite, which has very high FeO^{total}/MgO. Thus the resorption of kaersutite should not raise the FeO^{total}/MgO ratio of the bulk liquid significantly, nor that of the equilibrium clinopyroxene.

One possible explanation is that a decrease in oxygen activity, already suggested as an explanation for the resorption of the kaersutite and the sphene, raised the $FeO/(FeO+Fe_2O_3)$ of the liquid. Thus the FeO/MgO of the liquid would be raised, causing more Fe^{2+} to enter the clinopyroxene structure. Other minerals, such as feldspar and apatite would not be affected by the change in oxygen activity.

The feldspars of these lavas were described by Batard (1974) as composite, zoned from Ca-rich plagioclase cores to anorthoclase rims. This study confirms her results, with a range of $An_{60\text{-}23}$ for the plagioclases, which have anorthoclase and sometimes sanidine overgrowths. Feldspars in Dents de Mézenc have a range of $An_{71\text{-}15}$, $Or_{13\text{-}42}$, with zoning from calcic to sodic, showing that the melt composition changed more rapidly than the feldspar phenocrysts were able to equilibrate. Since phenocryst proportions are so high -up to 23% - it may be that fractionation was taking place predominantly by this zoning, with Ca-rich plagioclase being isolated from the liquid by the (Na,K)-rich overgrowths.

Zeolites and carbonate are also present in unusual abundance in these lavas, compared with the other rocks of the series. Batard *et al* (1977) noted that the carbonate in Suc de Monac was concentrated in the plagioclase cores of the composite feldspar phenocrysts. This, and the associated corrosion of the plagioclase, led them to postulate a process of CO_2-autometasomatism, where CO_2-corrosion of the plagioclase released Na_2O into the liquid, leaving $CaCO_3$ and Al_2O_3 in the cores. There is the same relationship in the Glavenas lava.

The groundmasses of these lavas are predominantly of fine-grained feldspar, from plagioclase ($\approx An_{50}$) to sanidine, with pale green clinopyroxene and Ti-magnetite. Small amounts of apatite and sphene are occasionally present.

The normative silica saturation of these lavas varies from 13% nepheline for Mont Chanis to 3% quartz for St Pierre Eynac, whereas in the south the intermediate lavas are all nepheline normative, apart from the anomalous Dents de Mézenc, with 7% quartz. For the calculation, FeO/Fe_2O_3 was calculated by the method of LeMaître (1976) but even using different ratios the silica-saturation remains.

3.1.4.3 Comparison between northern intermediate lavas and cumulates

The phenocryst assemblage of the northern intermediate lavas, described in the previous section, has a close parallel in the minerals of the cumulate blocks, discussed in Chapter 4. As described in section 4.5.3 the order of crystallisation in Suites 3 and 4 is:

apatite ⇒ Ti-magnetite + ilmenite ⇒ cpx ⇒ kaersutite ⇒ biotite ⇒ feldspar ⇒ sphene/zircon ⇒ glass + carbonate

which compares well with that of the phenocrysts of the northern intermediate lavas:

apatite ⇒ Ti-magnetite ⇒ sphene ⇒ kaersutite (+ biotite) ⇒ cpx ⇒ plagioclase ⇒ K-feldspar ⇒ zeolites + carbonate

Notable differences include the absence of ilmenite and the early crystallisation of sphene in the lavas. It should also be pointed out that the crystallisation order of clinopyroxene and kaersutite in both the lavas and the blocks is difficult to determine, which may account for their reversed order. Clinopyroxene is present in both the blocks and the lavas in two forms:

1) pinkish Ti-rich, Mg-rich salite, which may have crystallised before the amphibole in the lavas

2) green/yellow, Ti-poor, Fe-rich salite, present as both phenocrysts and as a reaction product of the kaersutite in the lavas.

In the *blocks*, 1) is pre-kaersutite and 2) follows, but rarely co-exists with, the kaersutite. In the *lavas*, 1) is pre-kaersutite and 2) replaces the kaersutite, as a mixture of small crystals accompanied by Ti-magnetite, as well as forming phenocrysts.

Biotite also replaces the kaersutite, both in the blocks (Figure 4.6.25), where biotite is abundant, and in the lavas, where only trace amounts occur (see Figure 3.2.18). Feldspar in the lavas covers the range An_{71} to Or_{42}, and that of the blocks ranges from An_{82} to Or_{36}, again showing strong similarity between the two groups. Carbonate is also abundant in both groups.

Finally, both blocks and lavas show a trend towards increasing silica saturation, becoming quartz-normative in the most evolved blocks, and a few of the lavas. There is also a weak correlation between SiO_2-content and $(^{87}Sr/^{86}Sr)_{initial}$ (see section 5.8 for details).

The similarities between the blocks and the northern intermediate lavas suggest a genetic link, the most obvious being that the blocks represent samples of cumulates formed from similar lavas. The fact that the blocks came from the southern area need not be a problem since there is already one example of this lava-type in the south - Dents de Mézenc.

3.1.5 Phonolites

Phonolites are by far the most abundant evolved rock and dominate the landscape in the Velay oriental in the form of endogenous extrusion domes, flow domes and spines. Each extrusion is characterised by its petrography as well as by its geochemistry, and this section summarises the petrographical variation and its significance.

Phonolites can be divided into miaskitic and agpaiitic types according to their geochemistry and petrography. Table 3.1.6 summarises the differences between the two groups. Batard (1974) pointed out that many of the Velay phonolites with values of (Na+K)/Al > 1 are not simply agpaiitic but show mixed characters, with miaskitic phenocrysts and agpaiitic groundmasses. Other phonolites show consistent miaskitic characteristics and are easier to categorise.

In this study, the presence of poikilitic aenigmatite, euhedral nepheline and rare or absent opaques in the groundmass was used to classify a phonolite as agpaiitic. The presence of zircon, kaersutite, salite and Ti-magnetite phenocrysts, sphene in the groundmass and the *absence* of aenigmatite or euhedral nepheline was used to classify the miaskitic phonolites.

Azambre and Girod (1966) found the agpaiitic Zr/Ti-silicates eudialyte, mosandrite and låvenite in the groundmass of Suc de Montfol. Mosandrite was found in the lava of Les Roches (86/54) in this study.

In the following two sections, only those phonolites with relatively clear miaskitic or agpaiitic affinities have been described.

3.1.5.1 Miaskitic phonolites

Most of these are quite phenocryst-rich, with >10% by volume. Figure 3.1.7 illustrates this with a photomicrograph of the Reynaud dyke sample (85/18). The crystallisation sequence and mineralogy are remarkably consistent, with most variation in the relative proportions of minerals.

The order of crystallisation of phenocrysts is (starting with the earliest formed):

Apatite - euhedral, grey, inclusion-rich ⇒

Ti-magnetite - subhedral, 10-16% TiO_2 ⇒

Sphene + zircon - brown euhedral sphene; subhedral zircon sometimes present ⇒

Kaersutite - euhedral, red brown/greeny brown/clear-yellow, 4-5% TiO_2. Resorbing to various degrees, from edges only (rare) to completely resorbed "ghosts" (common). Traces of biotite sometimes present ⇒

Clinopyroxene - Two types; early pinkish, late green/yellow. All euhedral, total range salite to ferrosalite (with trace aegirine augite). Crystals are often zoned with darker green edges. Na_2O 1.0-4.0% ⇒

Table 3.1.6

Summary of the geochemistry and petrography of miaskitic and agpaiitic phonolites. Compiled from Azambre and Girod (1966), Varet (1969) and Sørensen (1974)

	Miaskitic	**Agpaiitic**
Geochemistry	K + Na < Al Na > K CaO, MgO important Fe low FeO > Fe_2O_3 ⇒ low oxygen fugacity low: Zr, Nb, Ce, La, REE, Rb, Zn, Th, U, Be, Li OH, F, Cl low CO_2 high	K + Na > Al (peralkaline) often K > Na CaO, MgO low Fe significant Fe_2O_3 > FeO ⇒ high oxygen fugacity high: Zr, Nb, Ce, La, REE, Rb, Zn, Th, U, Be, Li OH, F, Cl high
Petrography		
feldspar	sanidine/anorthoclase (with oligoclase-andesine cores)	sanidine/anorthoclase
clinopyroxene	Ti-augite to salite (may have sodic rims)	aegirine-augite to aegirine
amphibole + *biotite*	Ti-rich kaersutite (resorbing to cpx + opaques) Fe-rich biotite (also resorbing)	Na-rich amphiboles: F-arfvedsonite riebeckite katophorite barkevikite
feldspathoid	nosean	nepheline, sodalite, analcite
oxides	Ti-magnetite, ilmenite	no oxides
apatite	present	absent
Zr/Ti-silicates	zircon, sphene	aenigmatite, eudialyte, catapleite, astrophyllite, mosandrite, låvenite etc
Crystallisation sequence	normal: magnetite, ilmenite ⇒ apatite, sphene, zircon ⇒ pyroxene, plagioclase ⇒ amphibole, plagioclase ⇒ K-feldspar ⇒ feldspathoid	reversed: feldspathoid ⇒ K-feldspar ⇒ Zr/Ti-silicates ⇒ alkali pyroxene
	ferromagnesian minerals euhedral, K-feldspars have oxide inclusions	ferromagnesian minerals poikilitic, K-feldspars inclusion-free

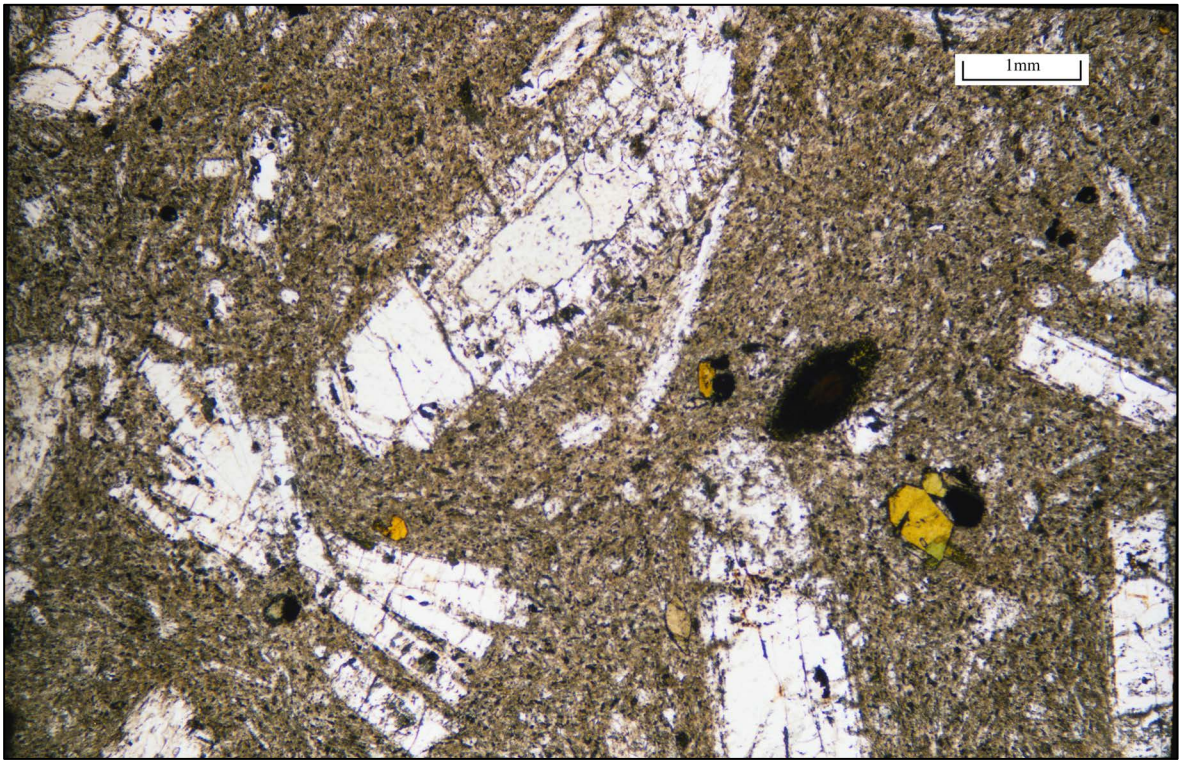


Figure 3.1.7. The miaskitic phonolite dyke of Reynaud (85/18), showing the distinctive “rosettes” of sanidine glomerocrysts, dark brown partially resorbed amphiboles and bright green/yellow clinopyroxene microphenocrysts. (Plane polarised light).

Plagioclase - sometimes as euhedral phenocrysts but more often as an-euhedral cores to K-feldspar. Often corroded, with zeolite replacement. Probed compositional range An_{26-46} ⇒

Nosean - Eu-anhedral, clear (rarely pale blue), isotropic with opaque "needle" inclusions. Appears as phenocrysts in Suc de Touron (86/33, 88/33) and Rocher de Pradoux (86/40) ⇒

K-feldspar - Usually sanidine, occasionally some anorthoclase. Main range Or_{41-57}. Usually euhedral, simple-twinned, often as "rosette" clusters (see Figure 3.1.7). Occasionally absent, or present only as a thin rim on plagioclase phenocrysts.

Differences between this sequence and that of the northern intermediate lavas (section 3.1.4.2) include a smaller proportion of apatite, sphene and Ti-magnetite (with lower TiO_2) in the phonolites. In addition, kaersutite in the phonolites is often present only as "ghost" relicts after total reaction/resorption, biotite is rarer, and zircon is occasionally present. The clinopyroxene in the phonolites is almost all of the green/yellow type, ranging towards aegirine-augite, with only rare cores of the pink clinopyroxene. Plagioclase is relegated to the cores of K-feldspars in most cases, and plays only a minor role. K-feldspar is mainly sanidine with subordinate anorthoclase, linked probably to the K_2O/Na_2O ratios of these rocks, which are among the highest in the Velay.

The groundmasses of these phonolites consist of sanidine, aegirine-augite, Ti-magnetite and sphene, in decreasing order of abundance. A feldspathoid, usually nosean, is often detectable, and when present is second in abundance to the sanidine. The order of crystallisation is more difficult to characterise, but the basic sequence is:

Ti-magnetite ⇒ sphene ⇒ aegirine-augite ⇒ nosean ⇒ sanidine

A small amount of apatite is occasionally present, crystallising before the Ti-magnetite. Sphene sometimes appears in a poikilitic, post-K-feldspar form. The sequential order of the nosean is hard to determine, but clearly varies from rock to rock. It is always pre-K-feldspar, and in Suc de Touron, Suc d'Eyme and Pic du Lisieux it is pre-clinopyroxene.

The extrusions which are most clearly miaskitic are:

Rocher de Pradoux (84/31, 86/40), the phonolite dyke near Reynaud (85/18, 88/36), Miaune (86/25, 87/13, 88/28), Pic du Lisieux (86/20), Suc de Touron (86/33, 88/33), Suc de Montivernoux (86/41), phonolite near Bourges (86/43), Peyre de Bard (86/45), La Chau de Carle (87/7a), Roche-en Régnier (87/12), Orselas Bas (87/22), le Rand (87/34), Suc de Saussac (87/36), Suc d'Eyme (87/40), Suc de Jalore (87/46), Dornas (87/62), Rocher de Soutron (87/81), phonolite flow in SW of Velay (88/6) and Mézilhac (88/35).

3.1.5.2 Agpaiitic phonolites

Most of these are virtually aphyric or have only sparse phenocrysts of sanidine. An unusual sample from the base of Suc de Touron (88/22), with a coarse-textured appearance in hand specimen, contains euhedral phenocrysts of nepheline and sanidine, the nepheline crystallising before the sanidine. This is characteristic of agpaiitic phonolites.

The phenocrysts in the phyric agpaiitic lavas appear to be residual from an earlier miaskitic stage, and have the crystallisation sequence:

Apatite - trace ⇒

Ti-magnetite - an-subhedral, 12.5% TiO_2 in Les Roches ⇒

Sphene - trace ⇒

Cpx + Amphibole - cpx: green/yellow, some euhedral, 1.7-1.8% Na_2O in Les Roches.

- amphibole: only as "ghost" relicts ⇒

K-feldspar - sanidine/anorthoclase, euhedral. Or_{18-29} in Les Roches.

Of these only the K-feldspar is ever present in significant amounts.

Rare phenocrysts of aenigmatite are present in the Suc de Sara tinguaite (hypabyssal phonolite), and Les Roches phonolite (86/54) contains mosandrite in glomerocrysts.

The last observation, of a peralkaline mineral confined to glomerocrysts in 86/54, is an example of a phenomenon particularly well displayed in this thin section, but also seen in others. That is, the development of extremely peralkaline micro-environments within glomerocrysts. The effect is to allow the growth of relatively large crystals of peralkaline minerals which are not in equilibrium with the main body of melt. In 86/54, apart from the mosandrite already mentioned, there are also relatively large crystals of aenigmatite and aegirine (3.0-10.6% Na_2O), shown in Figure 3.2.24. This micro-environment is caused by the restricted access that the melt has to the cores of the glomerocrysts, which slows the rate of interchange between the melt in the core and the main body of melt, allowing a compositional gradient to develop. Since the melt in the core of the glomerocrysts is usually supplying K_2O, SiO_2 and Al_2O_3 to the K-feldspar phenocrysts surrounding it, it becomes depleted in these components and relatively enriched in Na_2O and TiO_2. This gives ideal conditions for the crystallisation of the minerals observed in 86/54, and potentially for others of the esoteric agpaiitic minerals listed in Table 3.1.6.

The groundmass mineralogy of the agpaiites is the main feature which characterises them. The general sequence is:

Ti-magnetite - an-subhedral, quite rare, 12.5-13.8% TiO_2 ⇒

Nepheline - euhedral; squares and hexagons, very rare Ti-magnetite inclusions ⇒

K-feldspar - eu-subhedral, usually sanidine but some anorthoclase ⇒

Aegirine-augite - from subhedral to extremely poikilitic, 1.7-10.6% Na_2O ⇒

Aenigmatite - poikilitic, as overgrowth on opaques (if present). 4.7-7.9% TiO_2 ⇒

Zeolites - in voids and cracks. Quite evenly disseminated.

For the most part this is the expected reversed crystallisation sequence for the agpaiitic lavas, in contrast to the normal sequence of the miaskitic rocks. However, the presence of groundmass opaques in some of the agpaiites, coupled with the presence of a few phenocrysts with a normal crystallisation sequence, shows that they are only just agpaiitic. This is borne out by their peralkalinity indices (see section 5.6.2.6), which reach a maximum of only 1.05. Figures 3.2.27, 3.2.23 and 3.2.24 illustrate various features of the petrography of the agpaiitic phonolites.

The extrusions which are most clearly agpaiitic are:

Mont Loségal (84/17, 88/27), Meygal (84/20, 86/15), Suc de Sara (84/26-29, 84/32, 87/55), phonolite NE of Borée (85/15, 85/16), Roche du Bachat (86/6), Mont Signon (86/9), dyke SE of Les Estables (86/32), Suc de Pertuis (86/44, 88/26), Mont de la Tortue (86/46), Les Roches (86/54), phonolite near Hennes (86/64), Mont Mézenc (87/48), Gerbier de Jonc (87/76), Suc de Touron coarse-facies (88/22).

3.1.6 Quartz-trachytes

These are known only from four localities in the Velay. One of these, the extrusion of Dents de Mézenc, was classified with the northern intermediate lavas due to its strong petrographical similarity with them. The other three are Domaine de Faurie (near St-Etienne-Lardeyrol in the north - J. Mergoil *pers. comm.*), Riou Frait and one at the col just south of Sommet de la Farre. Domaine de Faurie was not sampled for this study.

Riou Frait (87/44) is poorly exposed and deeply weathered. It is aphyric and has a groundmass dominated by sanidine laths, with pale green clinopyroxene and Ti-magnetite making up about 10% of the rock. The order of crystallisation is:

Ti-magnetite ⇒ clinopyroxene ⇒ sanidine

The Sommet de la Farre quartz-trachyte (85/8, 87/24) is also deeply weathered. It appears to lie under a basalt flow, as an earlier small extrusion. Sanidine forms a few phenocrysts and also the bulk of the groundmass. The remainder of the groundmass consists of aegirine, arfvedsonite, aenigmatite and Ti-magnetite. The order of crystallisation is:

Ti-magnetite ⇒ aegirine ⇒ sanidine ⇒ arfvedsonite + aenigmatite

The presence of the last two minerals shows that this lava is agpaiitic, using the same criteria as for the phonolites.

3.2 Petrography and mineral chemistry of phenocrysts

3.2.1 Introduction

185 thin-sections of 160 lavas from the Velay were examined. The following sections describe the variation in petrography and chemistry of their minerals.

3.2.2 Olivine

Olivine appears in the basalts and ankaramites as phenocrysts, microphenocrysts and groundmass crystals. In the hawaiites it is restricted almost entirely to small groundmass grains. No other lavas contain equilibrium olivine, although Batard (1974) reported the presence of xenocrysts in two phonolites.

In all cases, olivine phenocrysts are colourless in plane polarised light, eu-subhedral and either equant or as elongated hexagons. Some crystals are embayed or skeletal, especially the largest. Size range is 0.5 - 3.0mm, with the largest in the ankaramites, coexisting with even larger clinopyroxenes (see Figure 3.1.2). These olivines have rare inclusions of Ti-magnetite and pleonaste. The basalts have smaller inclusion-free microphenocrysts (< 1.0mm). Both basalts and ankaramites have 0.05-0.2mm, sub-anhedral groundmass olivine. Phenocryst compositions range from Fo_{71} to Fo_{86}, but there is no correlation with the Fe/Mg of the host lava.

The hawaiites from St Clément show only a trace of groundmass olivine, as rare diamond or swallowtail crystals. Specimen 87/75 from Yssingeaux is slightly less evolved and olivine forms a few microphenocrysts and is abundant in the groundmass. Specimen 87/32 from Queyrières has a few microphenocrysts of olivine with similar compositions to those of the basalts (as shown in Figures 3.2.1 and 3.2.2), and these are usually overgrown by cpx.

The olivine structure permits little major-element substitution beyond the ($Mg \Leftrightarrow Fe^{2+}$) and ($Fe^{2+} \Leftrightarrow Mn$) exchanges. The first of these is illustrated in Figure 3.2.1, in which all the analyses lie close to $Fe^{2+} + Mg = 2$. Only small amounts of Mn are present in olivine, and as Figure 3.2.2 shows, it is taken into the olivine structure in proportion to the amount of Fe^{2+} incorporated. This relationship is common in silicate minerals.

3.2.3 Clinopyroxene

Clinopyroxene (cpx) is present throughout the Velay lava series, but varies enormously in both appearance and chemistry. In the ankaramites, it occurs in roughly equal proportions to olivine. Phenocrysts in these lavas are pale pink-brown/pale yellow, with a darker brown rim like the groundmass cpx (see Figure 3.1.2). Most are sub-euhedral, some show zoning, fragmentation and even pale green/yellow cores. Most are less than 5mm in diameter, but the few that reach 10mm are usually strongly embayed, with many rounded holes. In all cases the groundmass cpx is dark pink-brown, eu-subhedral and 0.1-1.0mm long.

There is a continuous range from phenocryst-rich ankaramite to aphyric basalt, with no clear division between the two. Cpx phenocrysts in the basalts are identical in appearance to those in the ankaramites, although smaller. Groundmass cpx in the basalts is also darker brown than the phenocrysts and 0.05-0.3mm long. When the groundmass is glassy its cpxs are perfectly euhedral.

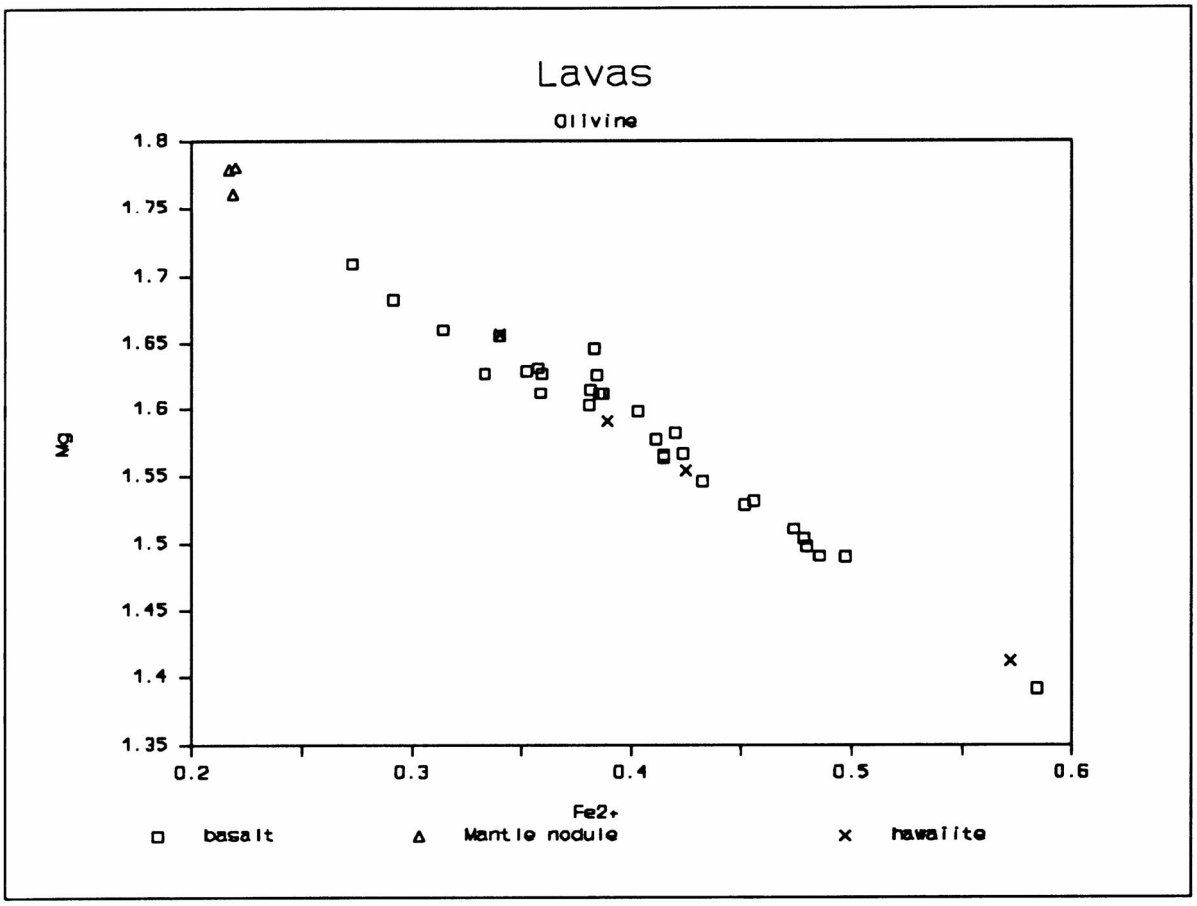


Figure 3.2.1

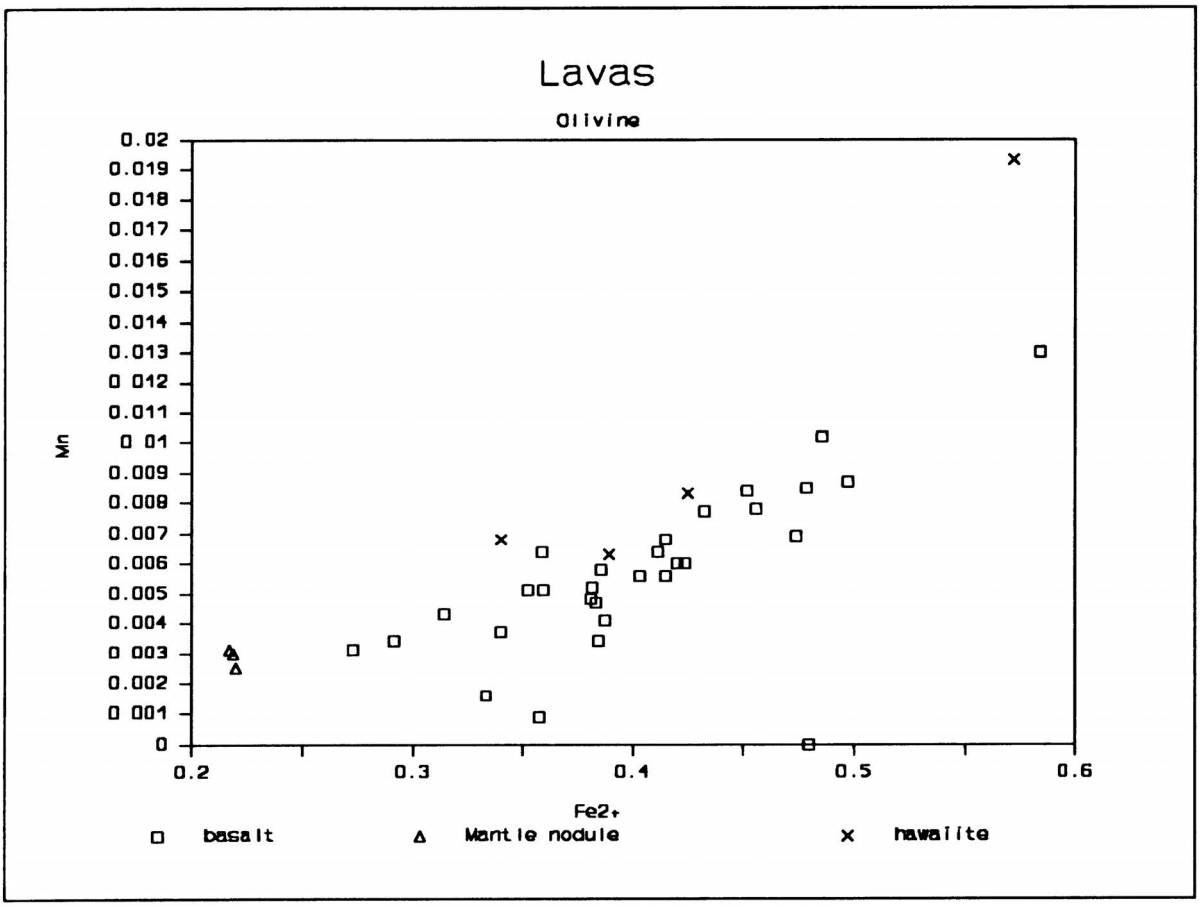


Figure 3.2.2

In the south of the Velay the mugearites and benmoreites of the upper plateau are entirely aphyric, with only rare, tiny cpxs in the groundmass. The most evolved specimen, from the Rocher de Cuzet flow (87/51), has very pale green cpx laths in its groundmass.

The phenocryst-rich intermediate lavas of the north have cpxs showing quite a complex history. They are eu-subhedral, the smallest having only green/yellow/clear pleochroism, whereas the larger crystals (max 1.7mm) also have pink/grey-green cores. As described in section 3.1.4.2, the green/yellow cpx appears at the same time that the amphibole starts to be resorbed, the change being mainly due to increased Fe^{2+}/Mg in the cpx, rather than $NaFe^{3+}$-substitution. The groundmasses of these lavas include 0.1-0.2mm needles of the green/yellow cpx.

The miaskitic phonolites have similar cpxs to the northern intermediate lavas, with emerald-green/yellow/muddy-brown pleochroism (see Figure 3.1.7), sometimes with pale pink or clear cores. Crystals are eu-subhedral and reach 2.5mm in diameter. Green/yellow cpx appears in the groundmass.

The agpaiitic phonolites are almost aphyric, occasionally with an isolated green/yellow cpx phenocryst. In the groundmass however, the cpx varies from green/yellow/greeny-brown laths to extremely poikilitic, aegirine-rich crystals, with diameters up to 3.0mm in the Suc de Touron coarse-facies (87/22). These aegirines have dark blue-green/muddy-green/yellow-brown pleochroism. Figures 3.2.23 and 3.2.27 show examples of the poikilitic groundmass aegirine.

Two diopside analyses from the Mont Peylenc lherzolite (86/14) have also been plotted on the graphs, using triangle symbols.

The basic clinopyroxene formula is $Ca_{0-1}(Fe^{2+},Mg)_{2-1}Si_2O_6$ and Figure 3.2.3 shows that the Ca-content of the cpxs of all the lavas varies little, except in the agpaiitic phonolites. Figure 3.2.4 shows the large extent of Al-substitution in these cpxs. Probable substitutions involved are:

end member	$CaTiAl_2O_6$	(CaTi)	$TiAl_2 \Leftrightarrow (Fe^{2+},Mg)Si_2$
end member	$Ca(Al,Fe^{3+})AlSiO_6$	(FaTs)	$(Al,Fe^{3+})Al \Leftrightarrow (Fe^{2+},Mg)Si$

The first of these is confirmed by the correlation of Al and Ti, shown in Figure 3.2.5, up to a maximum of 12% CaTi. There is still a surplus of $Al+Fe^{3+}$ above that needed to balance the Ti, which gives 15% (max) FaTs substitution. These two substitutions are the same as those found in the clinopyroxenes of the cumulates, which reach 23% FaTs and 11% CaTi (see section 4.6.1).

In the phonolites, Ca is progressively replaced by Na, as shown in Figure 3.2.3, but there is no correlation between Na and Al, which rules out jadeite substitution. Figure 3.2.6 shows the strong correlation between Na and Fe^{3+}, demonstrating that the end member for these cpxs is aegirine, reaching a maximum of 80%.

Figure 3.2.7 plots Ca vs Mn. Mn, substituting for Fe^{2+}, is very low in the early Mg-rich cpxs. As Fe^{2+}-content rises, so does Mn, although Ca remains virtually constant. Eventually aegirine substitution takes over, and as the $NaFe^{3+}Si_2O_6$ component starts to dominate, the amount of Mn decreases, with Ca decreasing at the same time.

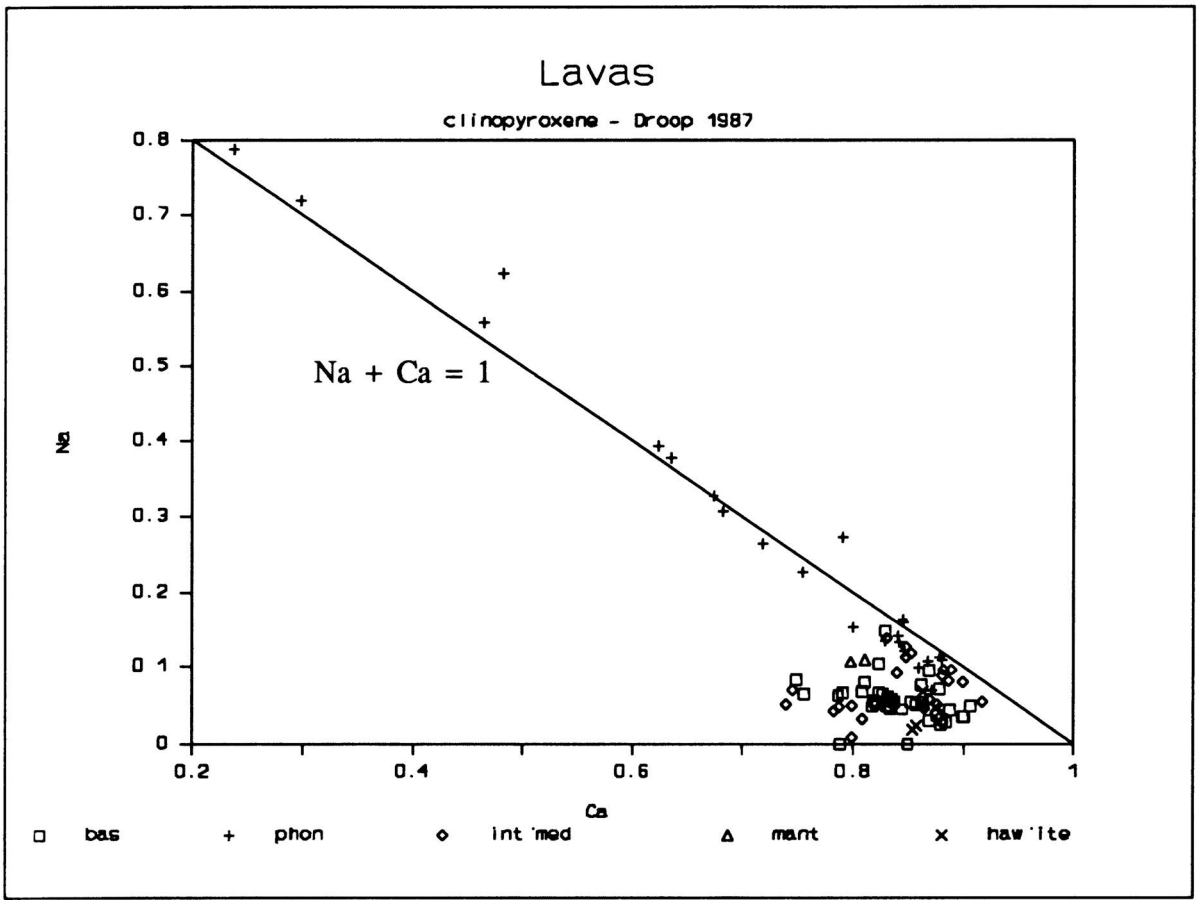


Figure 3.2.3.

Key to symbols: bas = basalt, phon = phonolite, int'med = intermediate lavas, mant = mantle nodule and haw'ite = hawaiite

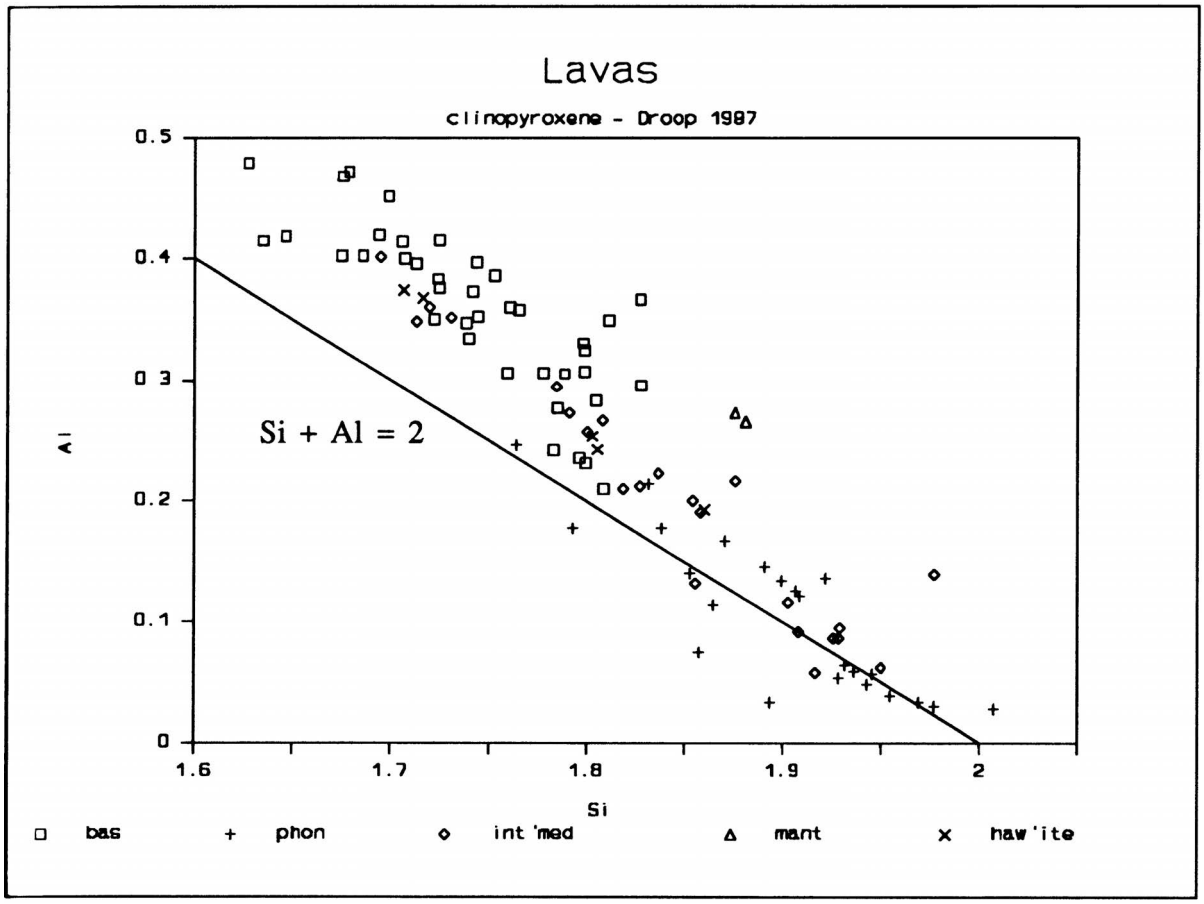


Figure 3.2.4

(Symbols as given in Figure 3.2.3)

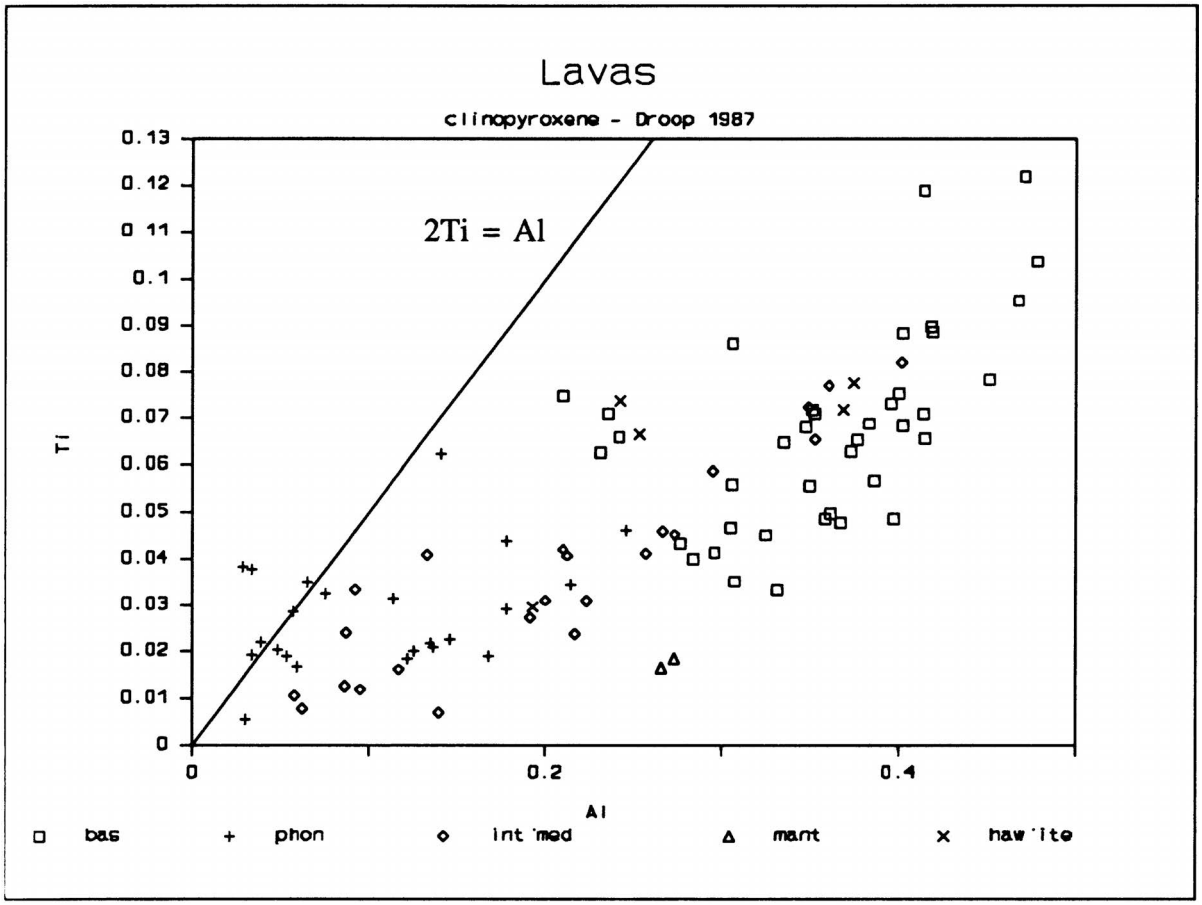


Figure 3.2.5
(Symbols as given in Figure 3.2.3)

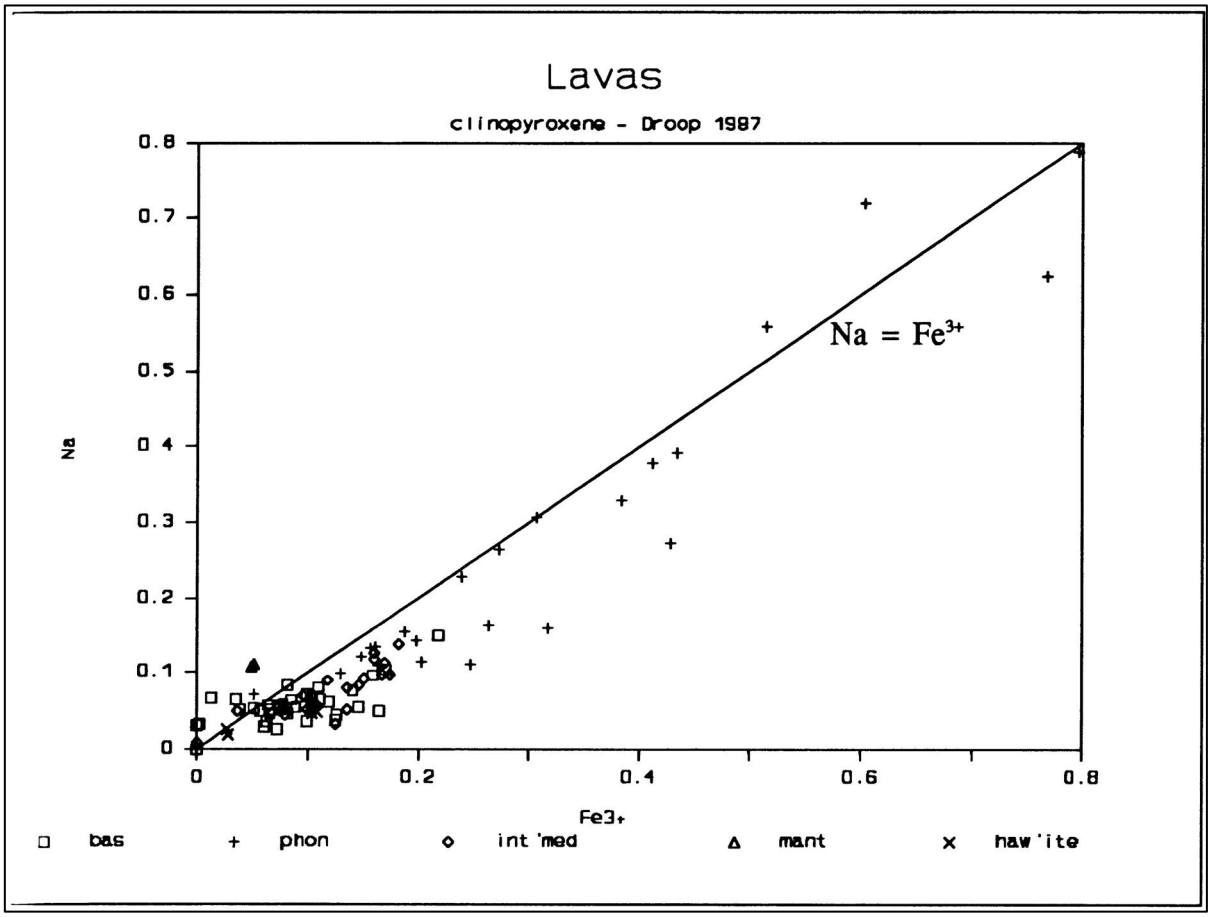


Figure 3.2.6
(Symbols as given in Figure 3.2.3)

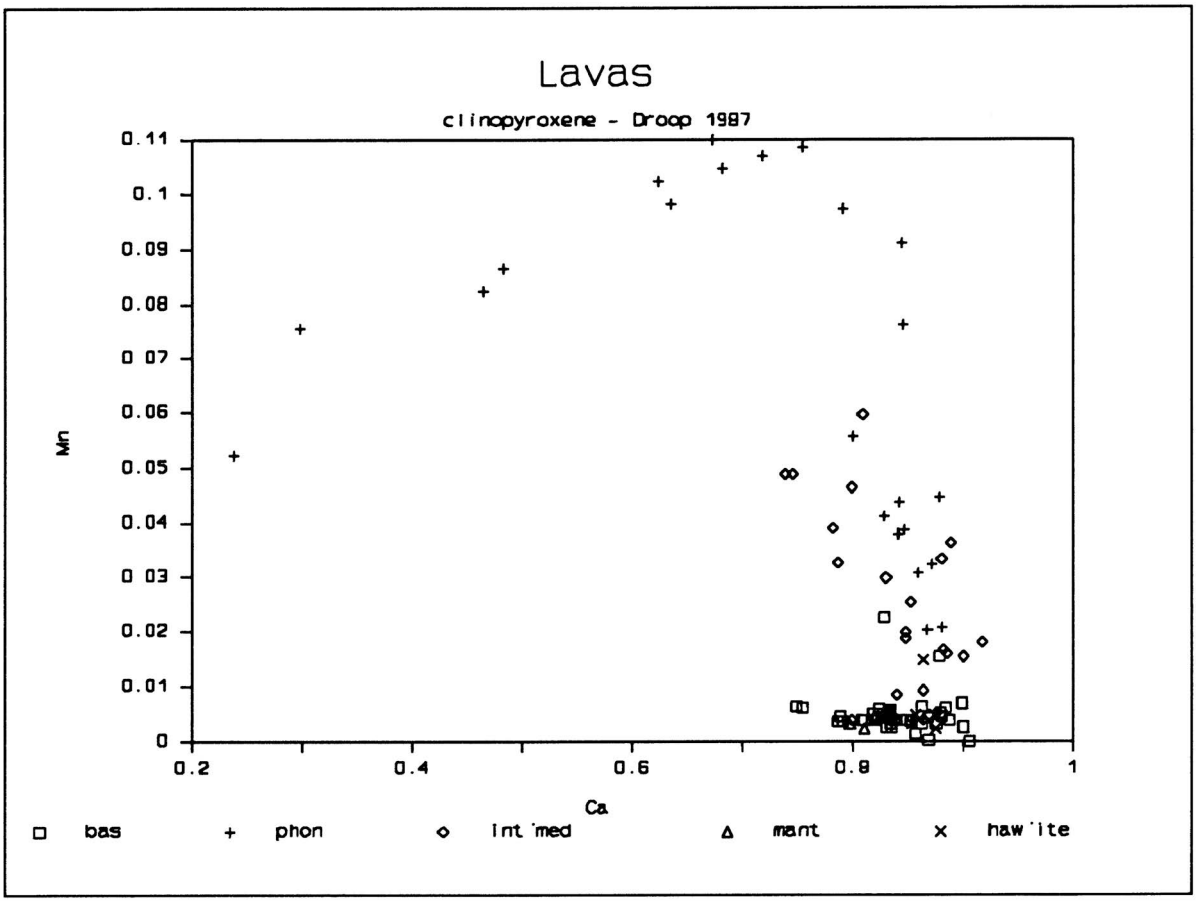


Figure 3.2.7
(Symbols as given in Figure 3.2.3)

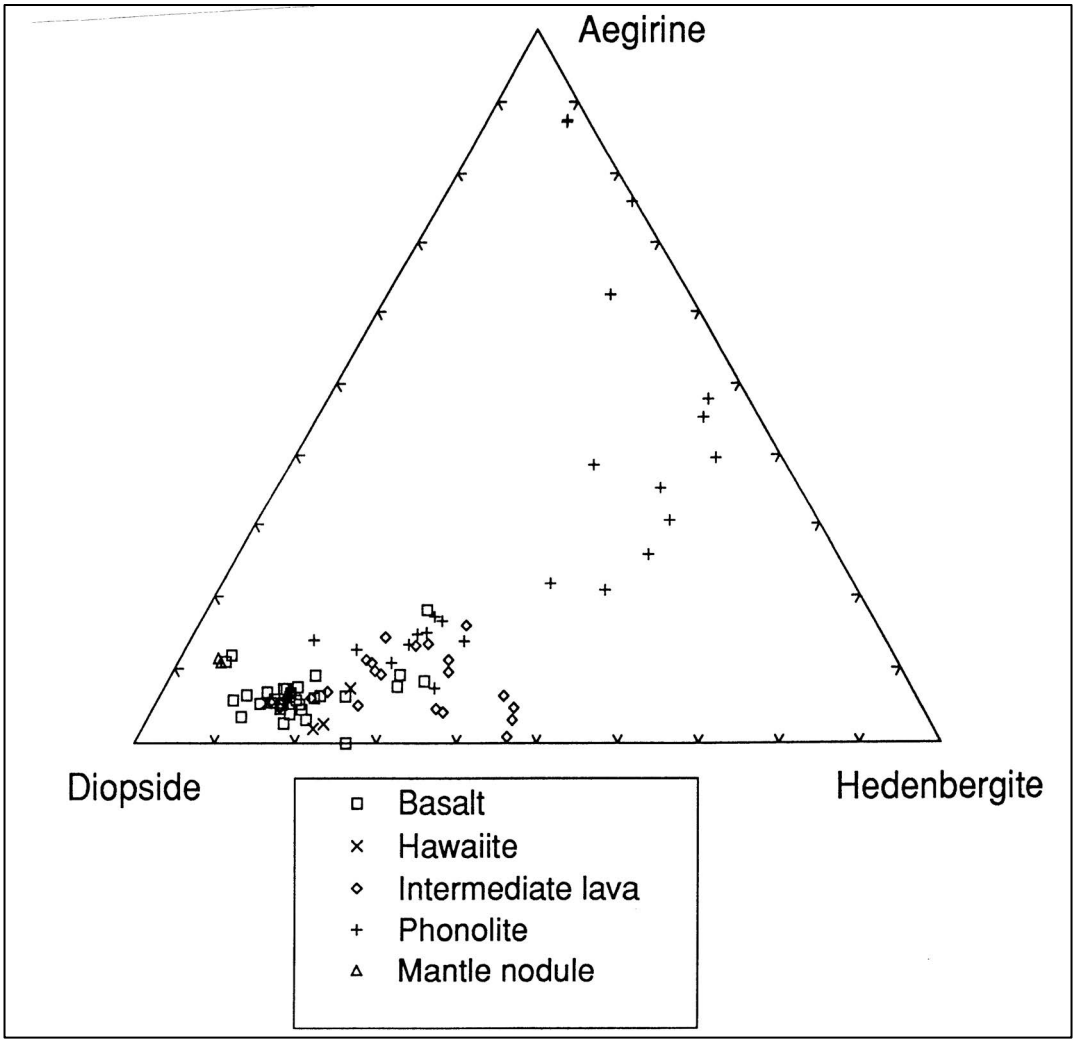


Figure 3.2.8

Figure 3.2.8 shows the evolution from Mg-rich to more Fe^{2+}-rich cpxs within the less evolved lavas, then to aegirine in the most evolved phonolites. This pattern has been documented from many evolved undersaturated volcanic provinces.

3.2.4 Ti-magnetite

In the ankaramites Ti-magnetite phenocrysts are either absent or appear as 0.3-0.6mm anhedral microphenocrysts and as inclusions in olivine and clinopyroxene. Prévot and Mergoil (1973) investigated the compositions of Ti-magnetites in an ankaramite from the St Clément series and found no significant difference between the inclusions and the microphenocrysts.

The basalts tend to have smaller, more subhedral microphenocrysts, 0.1-0.5mm in diameter, although specimen 86/66 (Freycenet-La-Tour) contains extremely irregular 2.0mm fragments which may be from a re-entrained cumulate.

Hawaiites have eu-subhedral microphenocrysts up to 0.5-1.1mm in diameter, with many peripheral embayments. The mugearites/benmoreites of the south have similarly embayed euhedral grains, 0.2-0.7mm in diameter. The northern intermediate lavas have sub-euhedral crystals 0.1-0.6mm in diameter, again with many edge-embayments. Those of the miaskitic phonolites are similar but less abundant. The agpaiitic lavas have only a few tiny specks of Ti-magnetite in the groundmass, with aenigmatite overgrowths obscuring their shapes.

The groundmass Ti-magnetites of all the lavas have a size range of 0.01-0.4mm, sometimes with a bimodal distribution suggesting two phases of solidification.

Up to six end-members are involved in the solid solution of these Ti-magnetites; magnetite, ulvöspinel, spinel, hercynite, magnesioferrite and jacobsite. Figure 3.2.9 shows Fe^{2+} vs Ti, with the ulvöspinel line added. It can be seen from this that there is excess Fe^{2+}, with ulvöspinel varying from 25% to 70%. Figure 3.2.10 shows Al vs Mg, with the line of spinel solid solution marked. It is clear that there is too much Mg for the available Al and some must be combined with Fe^{3+} to form magnesioferrite.

The highest degrees of solid solution are:- 0.7 Ti atoms per formula unit (apfu), 0.35 Mg apfu, 0.45 Al apfu, 0.2 Mn apfu. The maximum amount of spinel component (23%) occurs in the ankaramite phenocrysts, which have only 0.28-0.44 Ti apfu, whereas maximum ulvöspinel solid solution appears in their groundmass grains and the Ti-magnetites of the basalts, with 0.48-0.68 Ti apfu.

Thus the basaltic Ti-magnetites approach the composition of ulvöspinel, whereas the phenocrysts of the ankaramites have a strong spinel-content, and also occasionally carry spinel-hercynite (pleonaste) phenocrysts (see section 3.2.5). This may be due to high-pressure crystallisation in the ankaramites, the deepest giving true spinel-hercynites, shallower examples giving spinel solid solution in Ti-magnetite.

Figure 3.2.11 shows Fe^{2+}- 2Ti (i.e. Fe^{2+} minus the Fe^{2+} used in forming ulvöspinel) vs Fe^{3+}. The line of magnetite solid solution is also given. The trend is reasonably linear, with a slight surplus

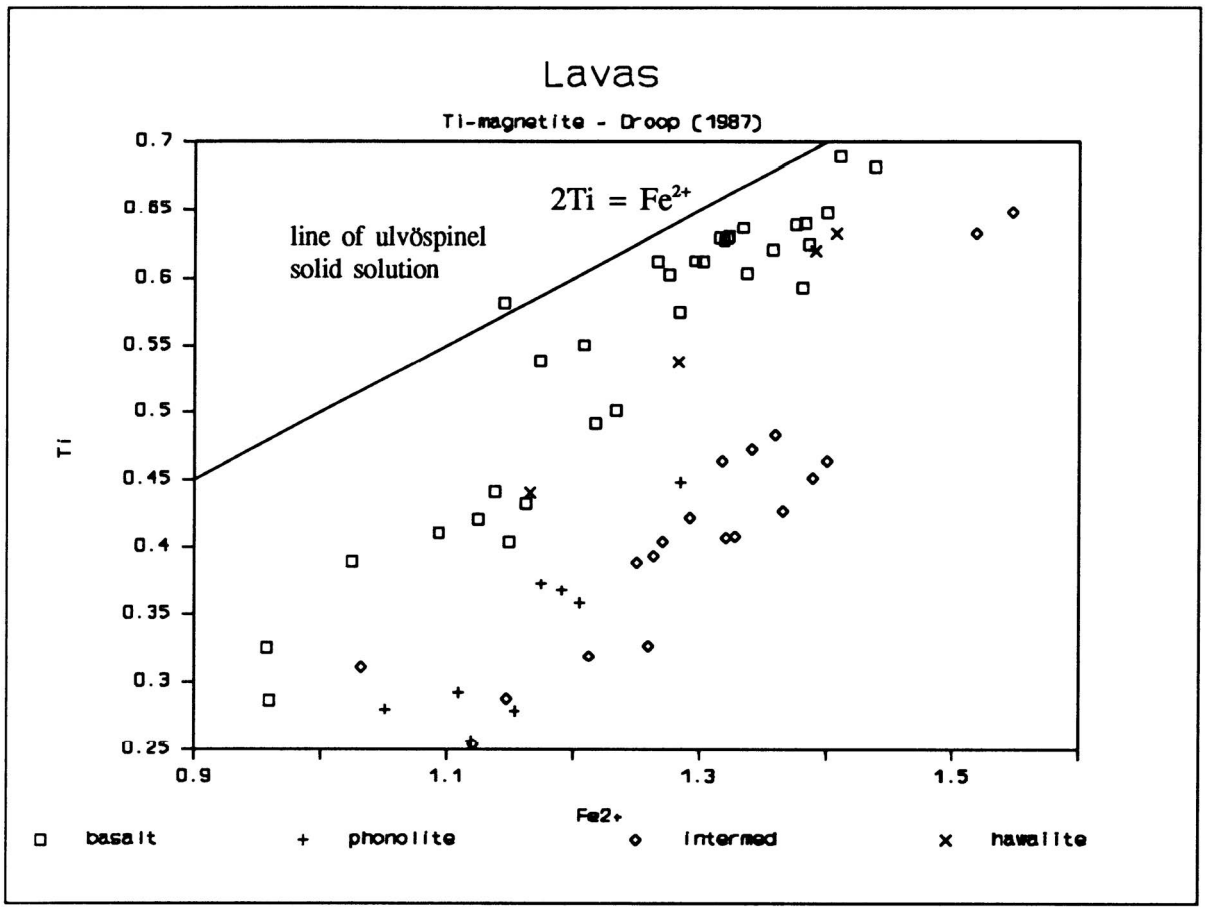


Figure 3.2.9
(intermed = intermediate lavas)

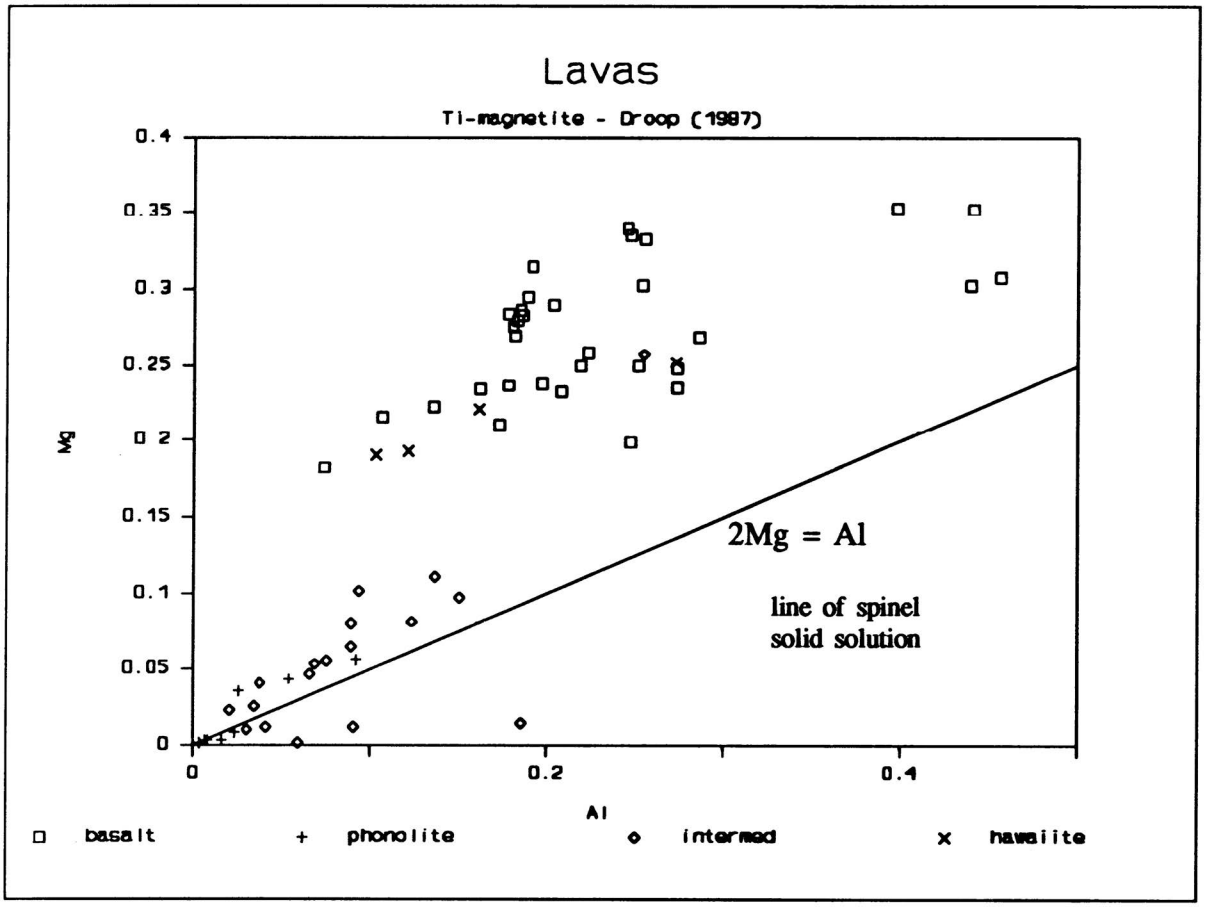


Figure 3.2.10
(intermed = intermediate lavas)

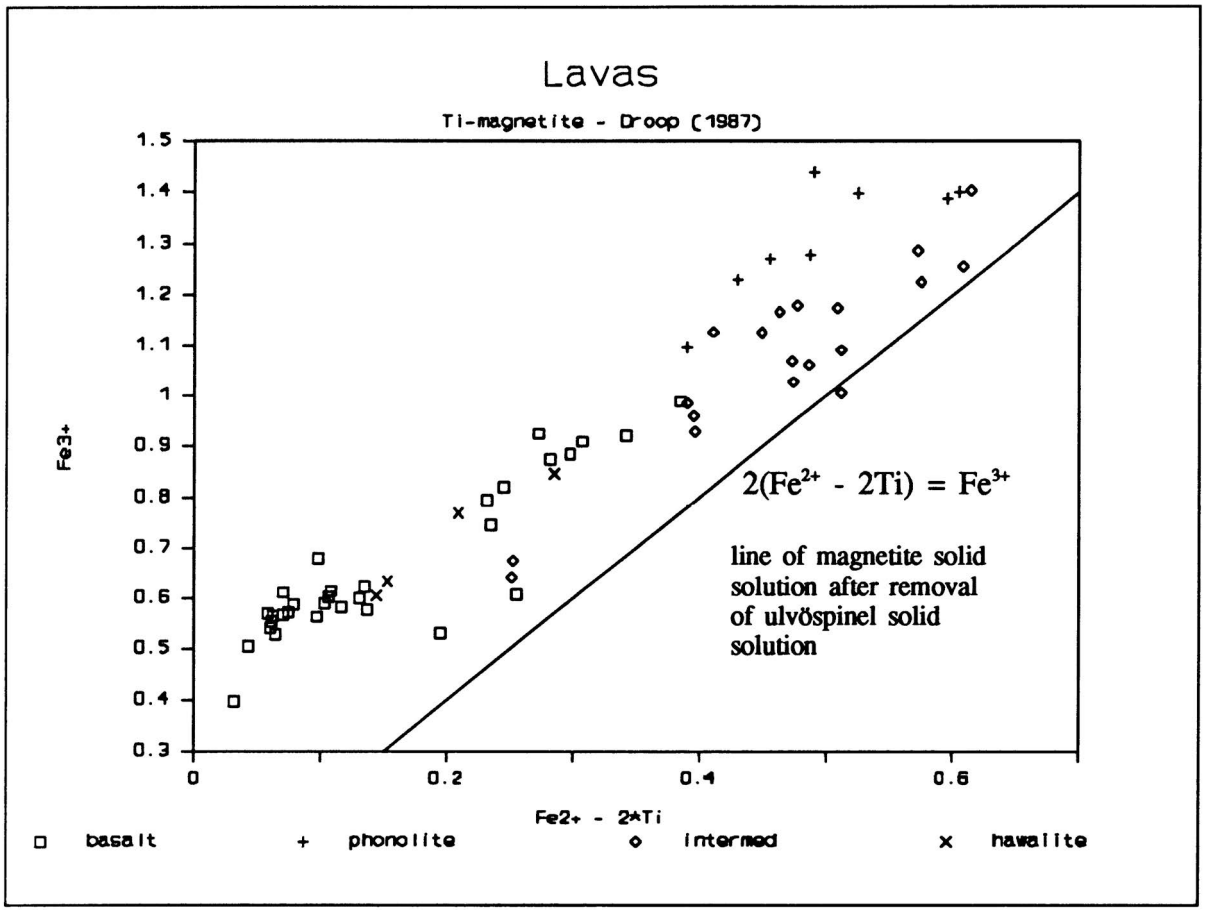


Figure 3.2.11
(intermed = intermediate lavas)

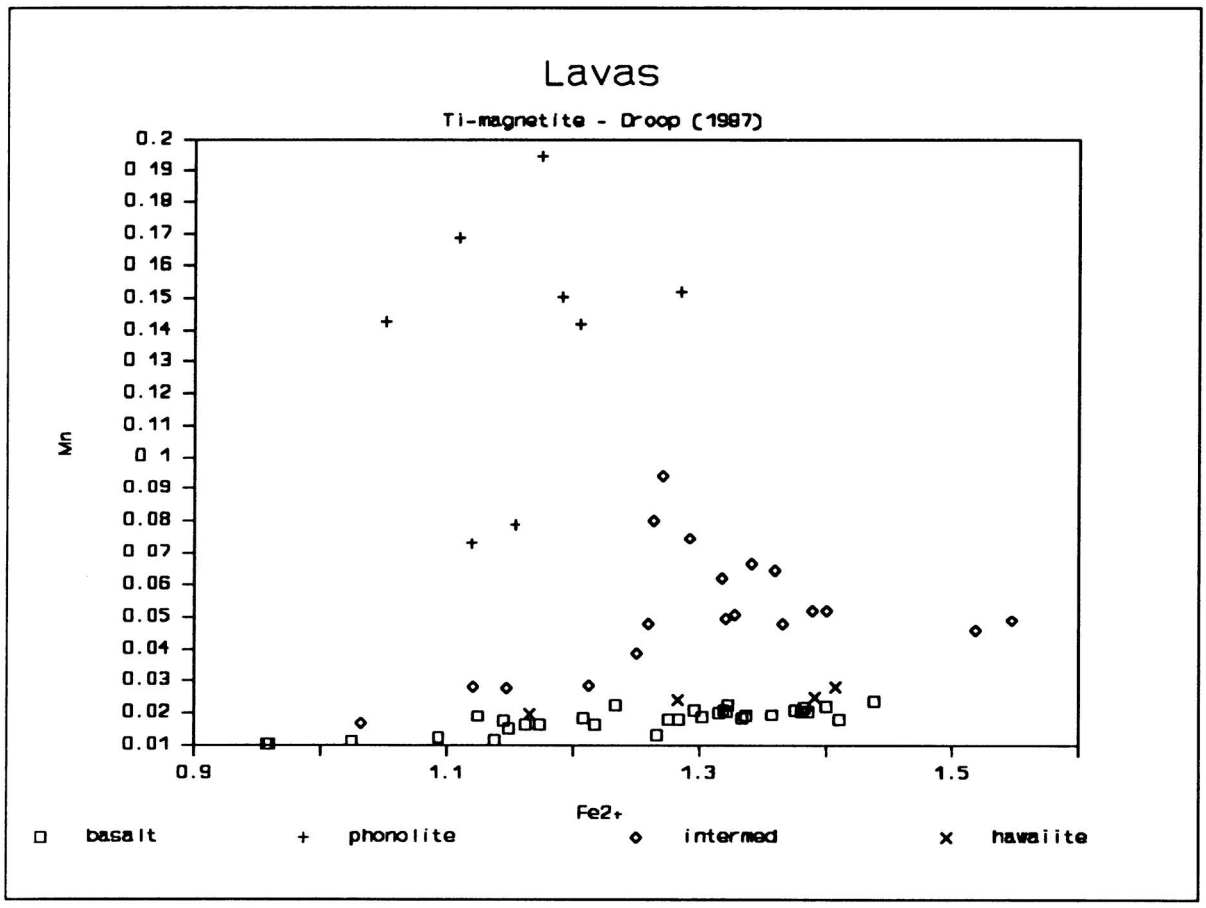


Figure 3.2.12
(intermed = intermediate lavas)

of Fe^{3+} forming magnesioferrite in the Mg-rich Ti-magnetites of the basalts and ankaramites, and jacobsite ($MnFe^{3+}_2O_4$) in the Mn-rich Ti-magnetites of the phonolites.

Figure 3.2.12 plots Fe^{2+} vs Mn. Mn substitutes for Fe^{2+} and Mn/Fe^{2+} usually increases as Fe^{2+}-content increases. This is the pattern shown by the Ti-magnetites of the cumulates in section 4.6.4. Those of the lavas however, show less of a clear pattern, with a rise in Mn from 0.01 to 0.02 apfu as Fe^{2+} increases in the basaltic Ti-magnetites, followed by a large increase in Mn-content in the intermediate and phonolitic Ti-magnetites, with no correlation with Fe^{2+}. This is unlikely to be due to increased MnO in the bulk rocks, as basalts and phonolites have 0.2% and 0.25% respectively.

Prévot and Mergoil (1973) found the same pattern for their ankaramite as in this study, with higher Al and Mg in the phenocrysts and inclusions and higher Ti and Mn in the groundmass grains. They explained the increase in Ti-content as being due to decreasing oxygen fugacity caused by degassing of the lava during eruption. However, the same trend is seen in the cumulates (see section 4.6.4) which casts doubt on this mechanism. High pressure crystallisation, coupled with increasing TiO_2-content of the lavas may be a more consistent explanation.

3.2.5 Pleonaste

Ferrian-pleonaste (spinel-hercynite) occurs only in the ankaramites from le Petit Champagnac (86/63), a dyke near Bonnevialle (87/43) and la Besseyre-basse (87/88). The last of these is probably younger than the Miocene Velay lavas but was included to extend the sample range.

Specimen 86/63 contains pleonaste both as phenocrysts and as rounded inclusions in the olivines and clinopyroxenes. The inclusions are usually circular and reach 0.6mm diameter. The largest phenocryst is 1.1mm. Ti-magnetite is restricted to the groundmass.

In sample 87/43 pleonaste is present only as inclusions in olivines, up to 0.3mm diameter. The olivines also contain circular inclusions of pyrrhotite and rarely Cu,Fe-sulphide (33% Cu) up to 0.1mm. Ti-magnetite is again restricted to the groundmass.

The basalt from la Besseyre-basse (87/88) contains rounded fragments of both Ti-magnetite (up to 4mm) and pleonaste (up to 1.1mm). The olivines and cpxs in this lava have pleonaste inclusions, but the amphiboles, Ti-magnetites and apatites do not.

Pleonastes in all of these lavas have 60-70% spinel component, 20-15% hercynite component and 20-15% magnetite component. Figure 3.2.13 shows Al vs Mg, although the line of spinel solid solution lies outside the graph area.

The presence of this mineral in the Velay lavas, as in the cumulates (described in section 4.6.6) suggests crystallisation at high pressure, probably several kilobars.

3.2.6 Feldspar

There are no feldspar phenocrysts in any of the ankaramites or basalts studied. A few rare xenocrysts occur but these are always anhedral and strongly resorbed. Groundmass plagioclase is

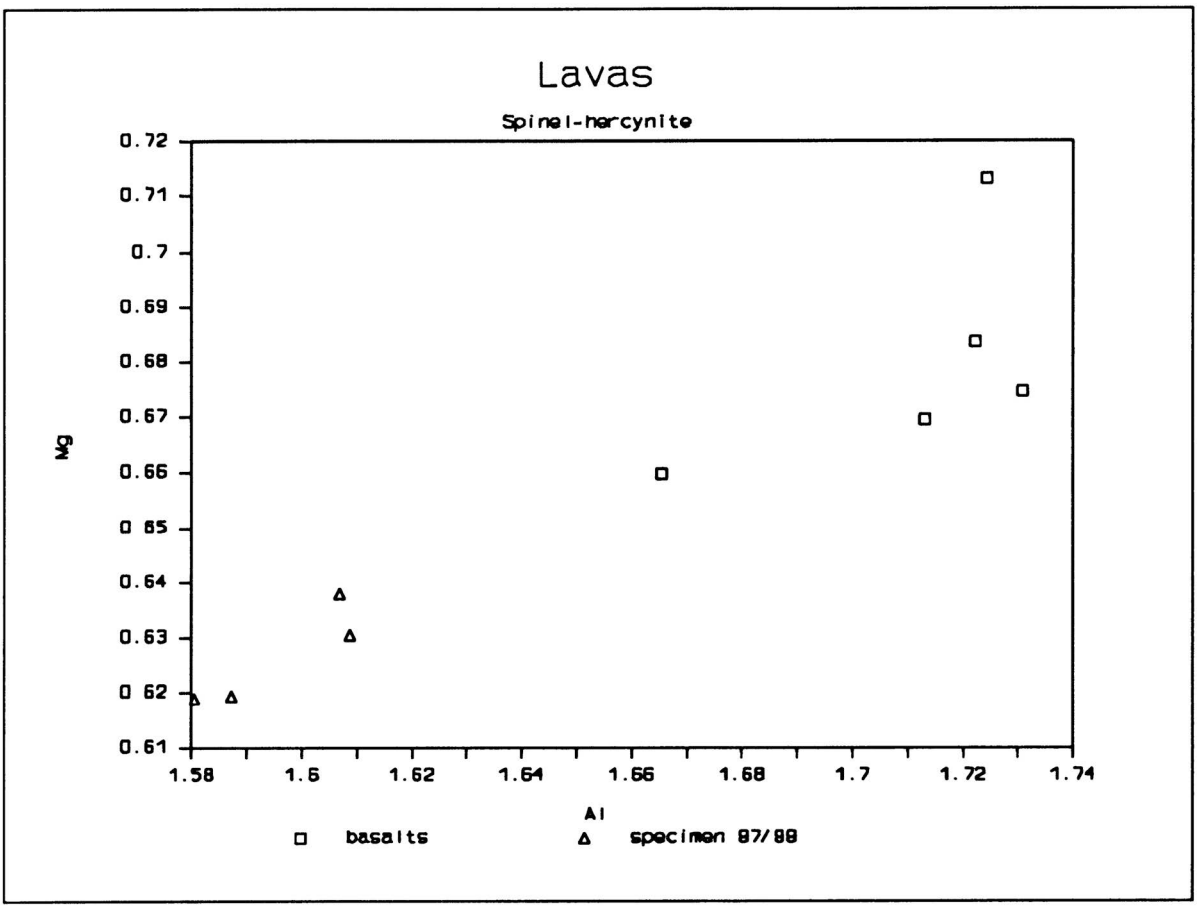

Lavas
Spinel-hercynite
0.72
0.71
0.7
0.69
0.68
0.67
0.66
0.65
0.64
0.63
0.62
0.61
Mg
1.58
1.6
1.62
1.64
1.66
1.68
1.7
1.72
1.74
Al
basalts
specimen 87/88

Figure 3.2.13

abundant as 0.1-0.4mm long eu-subhedral laths, and optical determinations give An_{72-54}. The hawaiites follow the same pattern, with no phenocrysts and only a few partially resorbed xenocrysts of plagioclase, even in the phenocryst-rich 87/32 (Queyrières). Their groundmasses consist of small laths of An_{64-56} plagioclase. The southern intermediate lavas also have only xenocrysts of plagioclase, up to 2mm long. Groundmass feldspars range from 0.05-0.5mm long, with a compositional range of An_{64-45} and probably some K-feldspar, especially in the evolved Rocher de Cuzet flow (87/51).

The intermediate lavas of the north, with the addition of Dents de Mézenc, have up to 18% feldspar phenocrysts (see Figures 3.1.4 and 3.1.5). Their compositional range, measured by microprobe, is An_{71} to Or_{55}, with most of the plagioclase in the range An_{23} to An_{60}. Plagioclase phenocrysts in the least evolved extrusions 87/74 (Veyrines), and 88/16 (Montusclat) reach 3.5-9.0mm long, with only a thin overgrowth of K-feldspar. In the rest of these lavas plagioclase reaches 2.1-4.0mm, with K-feldspar overgrowths and phenocrysts reaching 5.3mm. Plagioclase phenocrysts in all the northern intermediate lavas are eu-subhedral but some of the K-feldspars also have anhedral plagioclase cores. Plagioclase phenocrysts are often strongly zoned, occasionally without twins, and are often severely corroded and replaced by zeolites and carbonate, which Batard *et al* (1977) interpreted as being due to CO_2-flux through the magma.

K-feldspar in these lavas forms euhedral laths and anhedral intergrown glomerocrysts. Plagioclase cores are often optically continuous with K-feldspar, but those with a sharp discontinuity and anhedral shape suggest that a period of resorption preceded K-feldspar overgrowth. Identification of the type of K-feldspar present is difficult due to the absence of either simple twinning or cross-hatching, probably due to their compositions intermediate between anorthoclase and sanidine. Groundmass feldspars vary from euhedral plagioclase in 87/74 (Veyrines), to euhedral sanidine in 84/19a (Monac).

The feldspar phenocrysts of the miaskitic phonolites resemble those in the northern intermediates, with a few K-feldspars having plagioclase cores. These cores are usually anhedral, <0.5mm diameter and with compositions of An_{43} to An_{26}. They are often corroded and replaced by zeolites and carbonate. The host K-feldspars are optically unzoned, eu-subhedral laths, reaching a length of 4.0mm (see Figure 3.1.7). Sanidine is occasionally indicated by simple twinning, and anorthoclase by weak cross-hatching, but in most cases no identification can be made. The groundmasses are of 0.1-1.0mm long eu-anhedral K-feldspar laths.

Most of the agpaiitic phonolites are aphyric, but a few have euhedral sanidine phenocrysts up to 4.0mm long (see Figure 3.2.24). Some of these even have relict plagioclase or anorthoclase as fragments or cores to sanidines. The groundmasses are always composed of euhedral sanidine laths, 0.1-2.0mm long, depending on the specimen.

The two quartz-trachytes 85/8 (Sommet de la Farre) and 87/44 (Riou Frait) are both composed of euhedral sanidine laths, 0.1-1.2mm long, with a continuous size range.

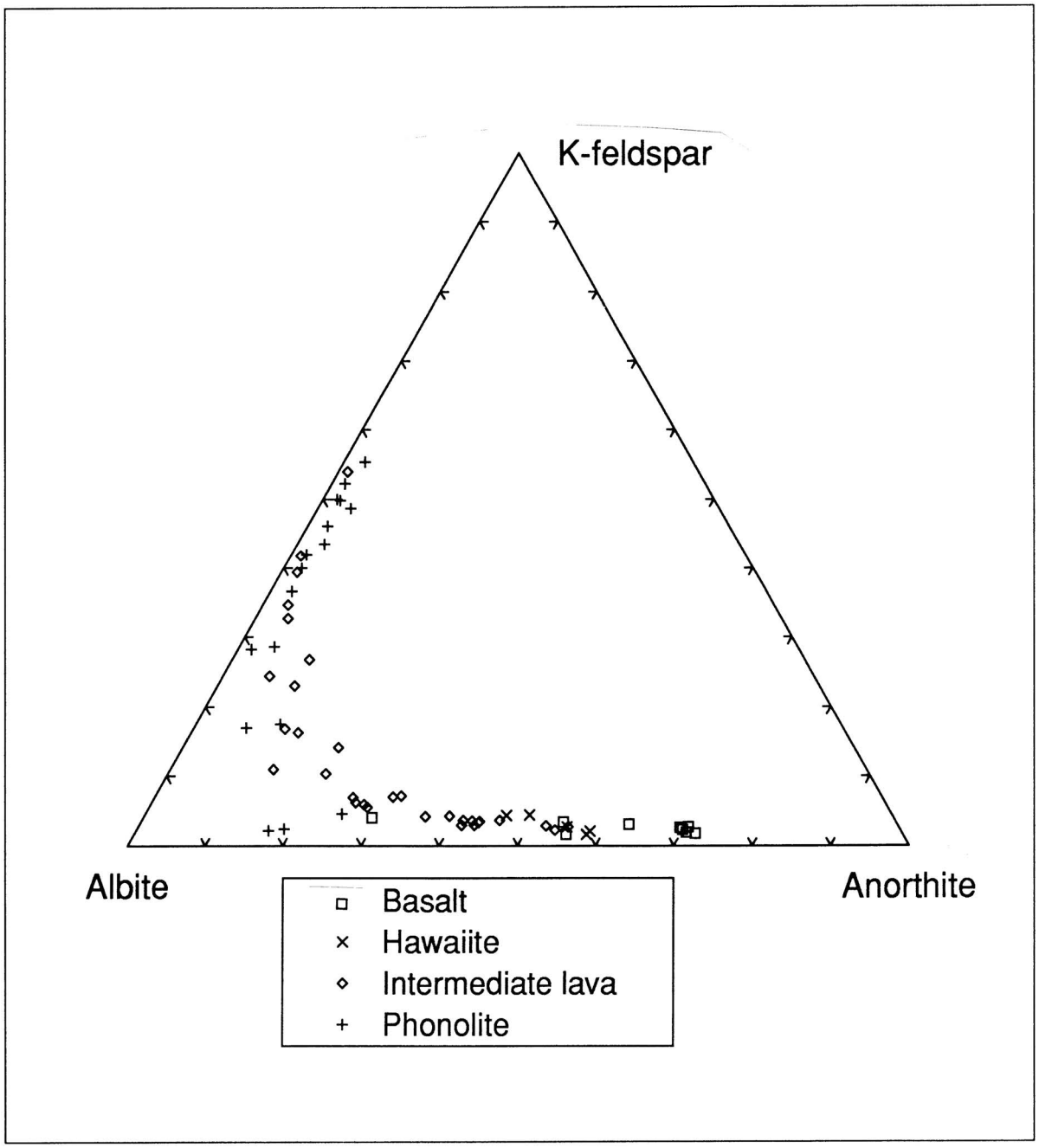


Figure 3.2.14. Triangular plot of feldspars in the Velay lavas, showing the progression from calcic groundmass plagioclase in the basalts and hawaiites, through sodic plagioclase and anorthoclase in the intermediate lavas, to sanidine in the phonolites.

To summarise, the feldspar phenocryst sequence of the Velay lavas starts with calcic plagioclase in the least evolved northern intermediates and progresses through sodic plagioclase to anorthoclase in the most evolved. The miaskitic phonolites have anorthoclase and some sanidine, the agpaiites ending the series with sanidine alone.

Feldspars have a very simple range of solid solution, from $CaAl_2Si_2O_8$ to $(Na,K)AlSi_3O_8$, with little substitution of other elements. This is illustrated by Figure 3.2.14.

3.2.7 Amphibole

Kaersutite amphibole is quite common in the Velay, although it is rarely present in the ankaramites or basalts. The Machabert ankaramite (86/53) has a trace of red-brown/yellow kaersutite and the basalt of la Chaud de la Croix (87/29, 88/29) is filled with the relicts of completely resorbed an-subhedral amphibole phenocrysts, up to 5mm in diameter. The only hawaiite with amphibole is 87/32 from Queyrières, with 5-10% relict outlines of originally euhedral phenocrysts, up to 2.5mm long.

The southern intermediate lavas have anhedral relicts of completely resorbed amphiboles, up to 1.4mm long. Sample 86/56 (St Clément) has one partly resorbed phenocryst with red brown/greeny brown pleochroism. In the northern intermediate lavas kaersutite is occasionally the dominant phase, reaching 9% in the Montusclat trachyte (88/16) (see Figures 3.1.5 and 3.1.4). Phenocrysts in these lavas have red brown/greeny brown/pale yellow pleochroism and vary from pristine to relicts of totally resorbed crystals. Figure 3.2.18 shows partially resorbed kaersutite phenocrysts in Suc de Monac (87/30) which illustrate their reaction to a mixture of green cpx and Ti-magnetite, subsequent overgrowth by biotite, and their original euhedral shapes. The unresorbed parts also show little optical zoning, and had a maximum original length of 3.5mm.

The miaskitic phonolites see the last of the kaersutite, which is absent in the agpaiites. Phenocrysts are usually strongly resorbed (often leaving only reaction products) and have the same pleochroic scheme as those of the northern intermediates. Rocher de Pradoux (84/31, 86/40) however, has olive green/dark greeny-brown/yellow brown phenocrysts, probably reflecting increased Fe/Mg. Maximum size reached in these lavas is 4.0mm and most were originally euhedral and unzoned.

There is no groundmass amphibole in the phonolites, but the quartz-trachyte near Sommet de la Farre (85/8, 87/24) has groundmass arfvedsonite. It was the last mineral to crystallise and is thus interstitial to poikilitic. It has brown/indigo blue/clear pleochroism. This is the only recorded occurrence of this mineral in the Velay.

Attempts to calculate the Fe^{3+}-content of these amphiboles using variations on the method of Droop (1987) were unsuccessful (see section 4.6.2 for details). The compositions of the amphibole phenocrysts in the lavas lie between kaersutite and Ti-rich ferrohastingsite (formulae given in section 4.6.2). The Ti range is 0.44-0.68 apfu, so most are kaersutite *sensu stricto*. The range in (Na+K) is 0.9-1.2 apfu and Ca is 1.8-2.0 apfu, neither showing correlation with other elements.

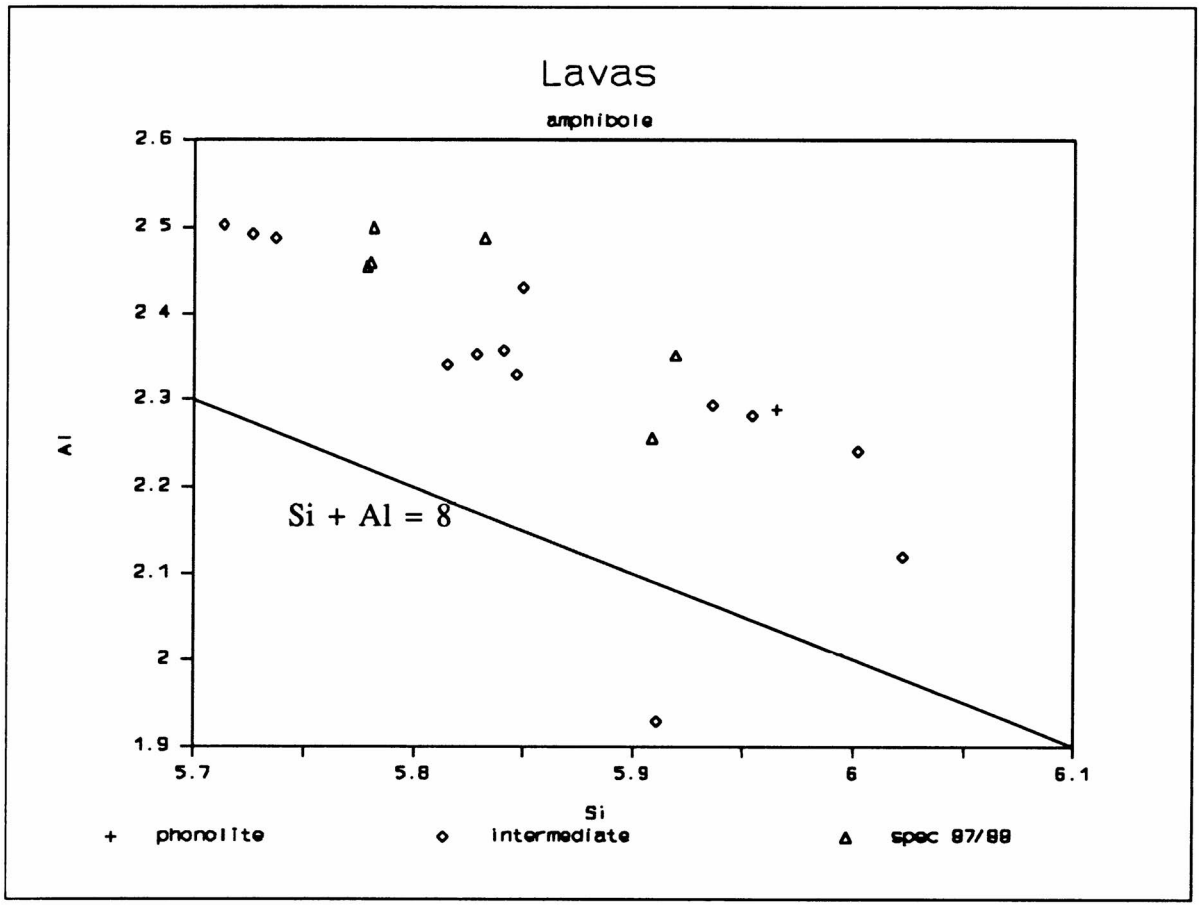


Figure 3.2.15
(intermediate = intermediate lavas, spec 87/88 = la Besseyre-basse ankaramite 87/88)

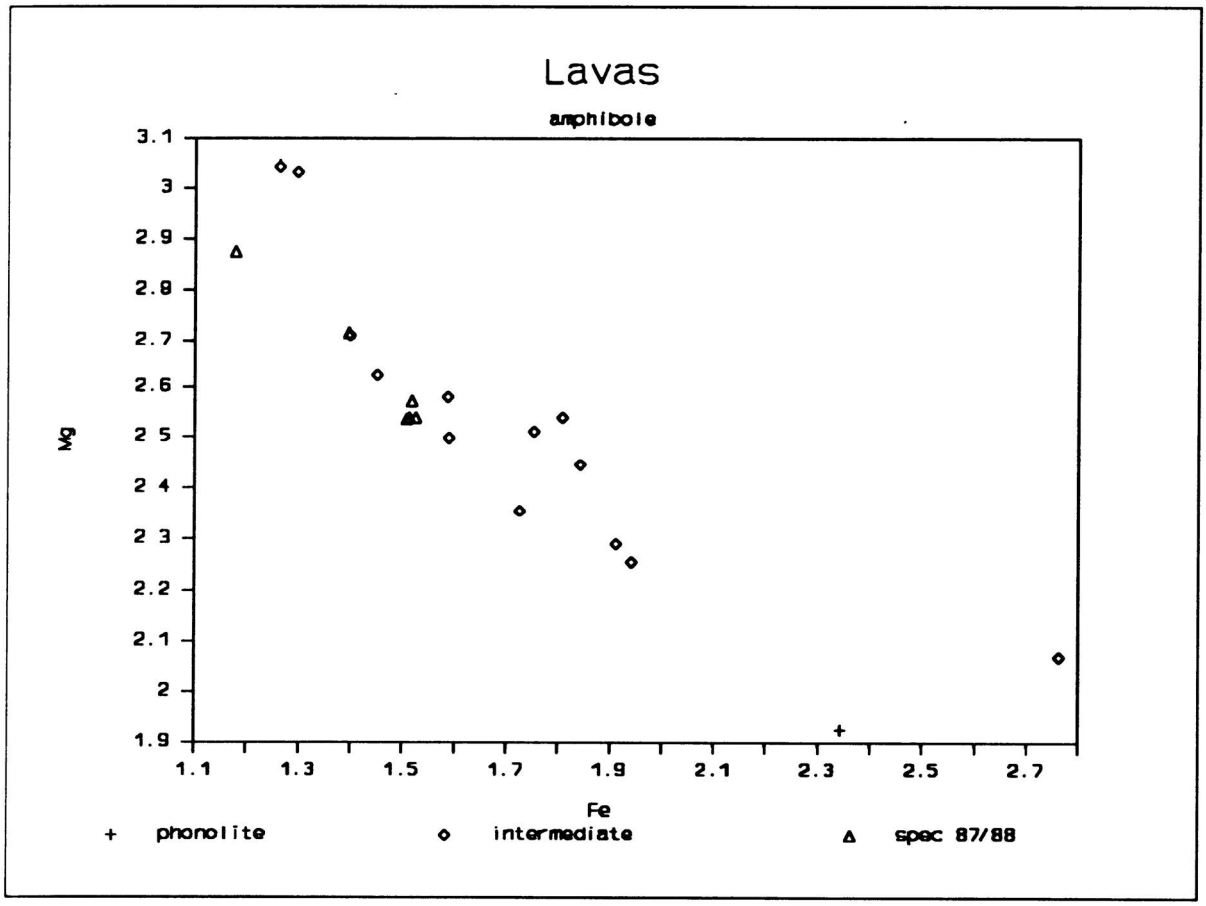


Figure 3.2.16
(intermediate = intermediate lavas, spec 87/88 = la Besseyre-basse ankaramite 87/88)

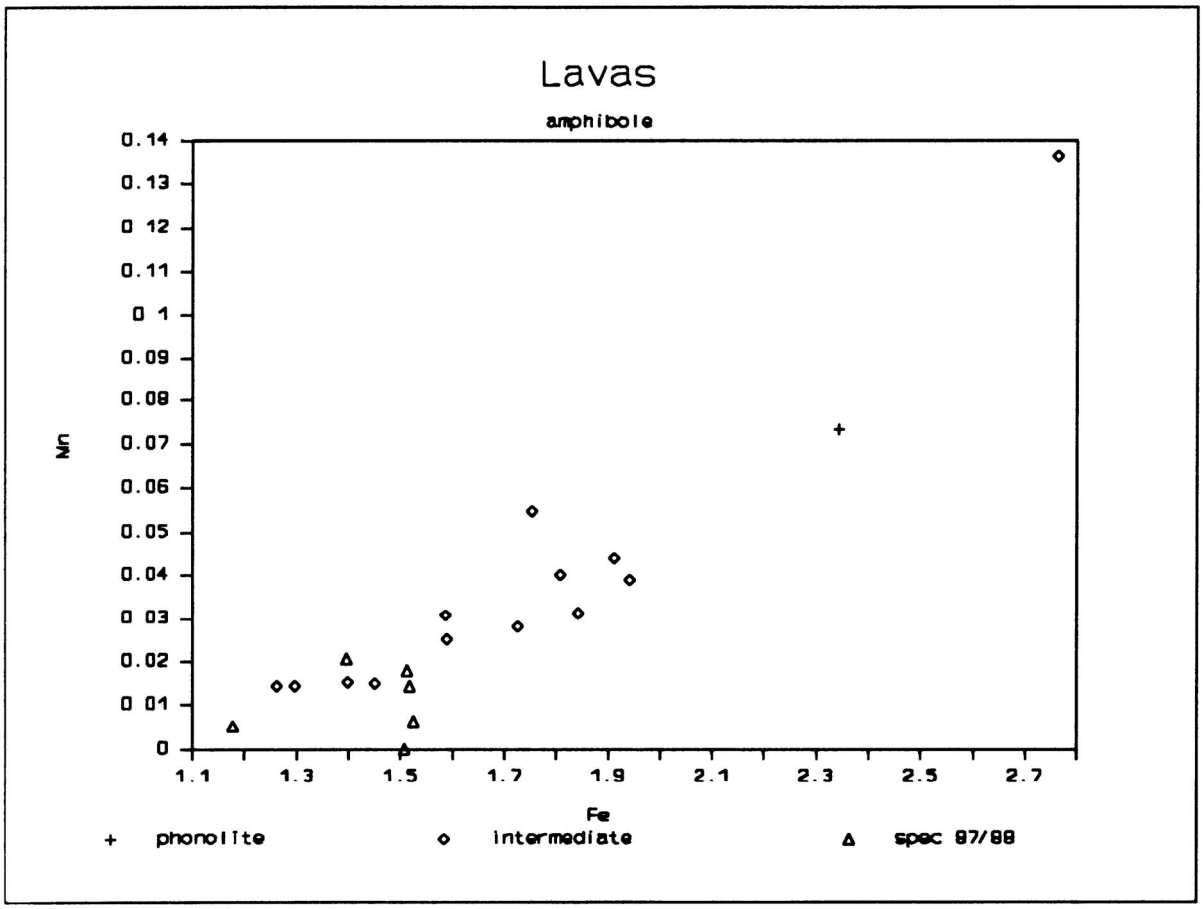


Figure 3.2.17
(intermediate = intermediate lavas, spec 87/88 = la Besseyre-basse ankaramite 87/88)

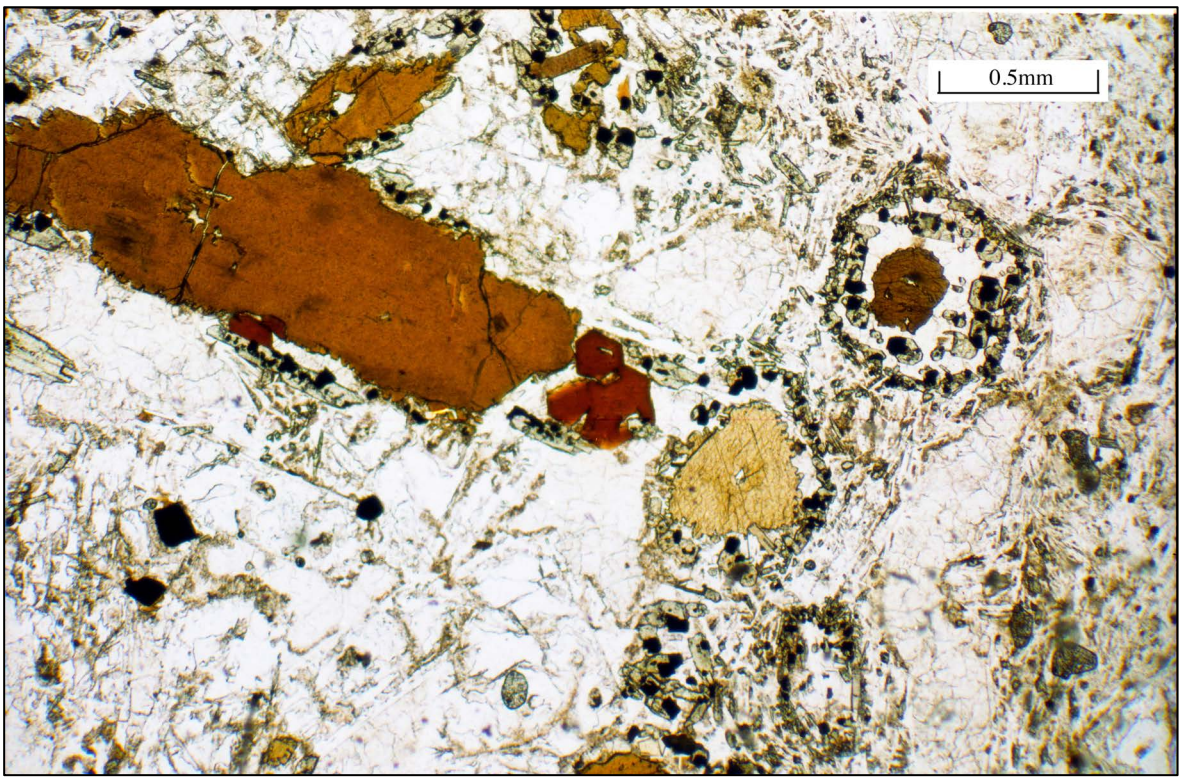


Figure 3.2.18. Partially resorbed amphibole phenocrysts in Suc de Monac (87/30). The original euhedral shapes of the amphiboles have been preserved by the green clinopyroxene and Ti-magnetite by which they were replaced. A subsequent reaction has caused the growth of euhedral biotites (inclusions of cpx show they were more recent). (Plane polarised light).

Figure 3.2.15 shows Si vs Al, with the Si + Al = 8 line marked. There is a good correlation, but one analysis plots a considerable distance from the others. This is a small Fe-rich partially resorbed crystal in Dents de Mézenc. It has a deficit of Al and may have Fe^{3+} proxying for Si, although this is not a normal feature of amphiboles and the analysis should be regarded as suspect.

Figure 3.2.16 shows Fe vs Mg, with good correlation except for the same anomalous analysis. This reflects the strong diadochy between these two elements. Figure 3.2.17 plots Mn vs Fe, showing that Mn increases with Fe. The range in Fe is 1.2 - 2.3 apfu (discounting the anomalous analysis) which exceeds the limit of 1.5 apfu cited by Deer *et al* (1966), although they do not state whether this is a miscibility limit or a restriction on the use of the name kaersutite.

The graphs presented here show more scatter than those for the cumulate amphiboles (section 4.6.2). This is due to the multiple origins of the lavas, with varied pressure, temperature and host liquid compositions, in contrast to the monogenetic cumulates.

In addition to the microprobe analyses, the H_2O-content of one amphibole was measured. This was a kaersutite phenocryst from the pyroclastics beneath the Besseyre-basse ankaramite (87/88), which was analysed in a Carlo-Erba CHN analyser, a furnace gas-chromatograph, run at 1000˚C for the analysis. The sample contained 0.27-0.36% H_2O and insignificant nitrogen and carbon. The low H_2O-content is due either to the presence of another anion such as fluorine in the structure, or an extra oxygen ion, to give oxykaersutite. A low hydroxyl content is common in basaltic hornblendes, and Deer *et al* (1966) suggest this is due to oxidation during eruption.

3.2.8 Biotite

Biotite is uncommon in the Velay, appearing in basalts from Les Estables (87/47) and Champagnac (86/63) as tiny anhedral groundmass grains associated with zeolites in cavities. These have red-orange brown/clear pleochroism and a maximum length of 0.7mm. The association with zeolites suggests that they were formed by high temperature hydrothermal circulation, probably while the lava was cooling.

In the Borée mugearite dyke (88/23) and the Mézilhac phonolite (88/35) there is a trace of groundmass biotite, again reddish in colour, anhedral with a maximum size of 0.1mm. The Mézilhac sample also has a 0.2mm subhedral grain in the core of a resorbed amphibole. The phonolite of Mézenc (87/48) contains a cluster of biotite fragments, maximum length 0.8mm, within an anorthoclase phenocryst.

In the northern intermediate lavas, red-brown/clear sub-anhedral biotite sometimes appears in the cores of partially resorbed amphiboles, with a maximum size of 0.3mm in Suc de Monac (84/19a, 87/30). Figure 3.2.18 illustrates this replacement, with small biotite crystals replacing kaersutite phenocrysts. Rocher de Pradoux (86/40) has a similar biotite-amphibole phenocryst. This relationship, where biotite grows within and on the edges of amphiboles, is identical to that seen in the cumulates (see sections 4.6.2, 4.6.7 and Figure 4.6.25). In the cumulates the biotite replacing the

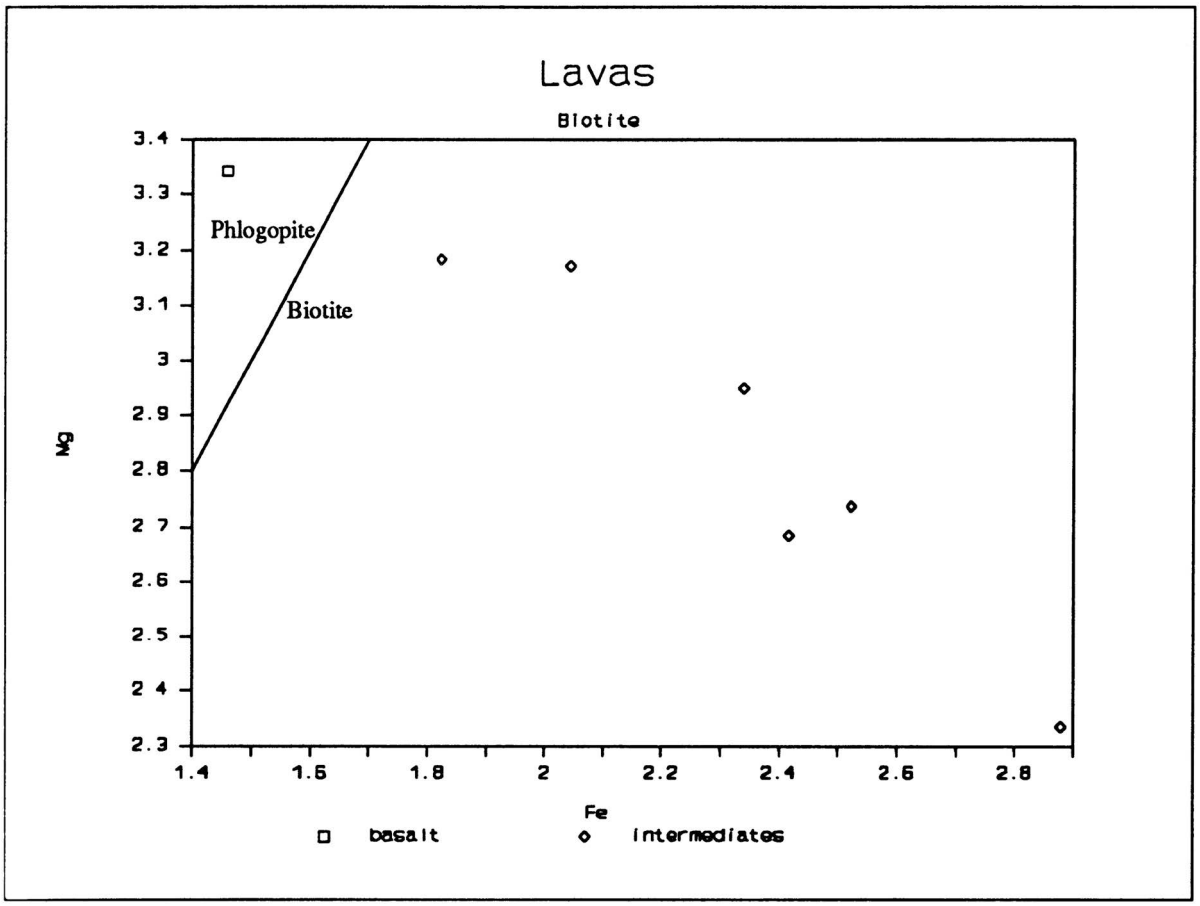


Figure 3.2.19
(intermediates = intermediate lavas)

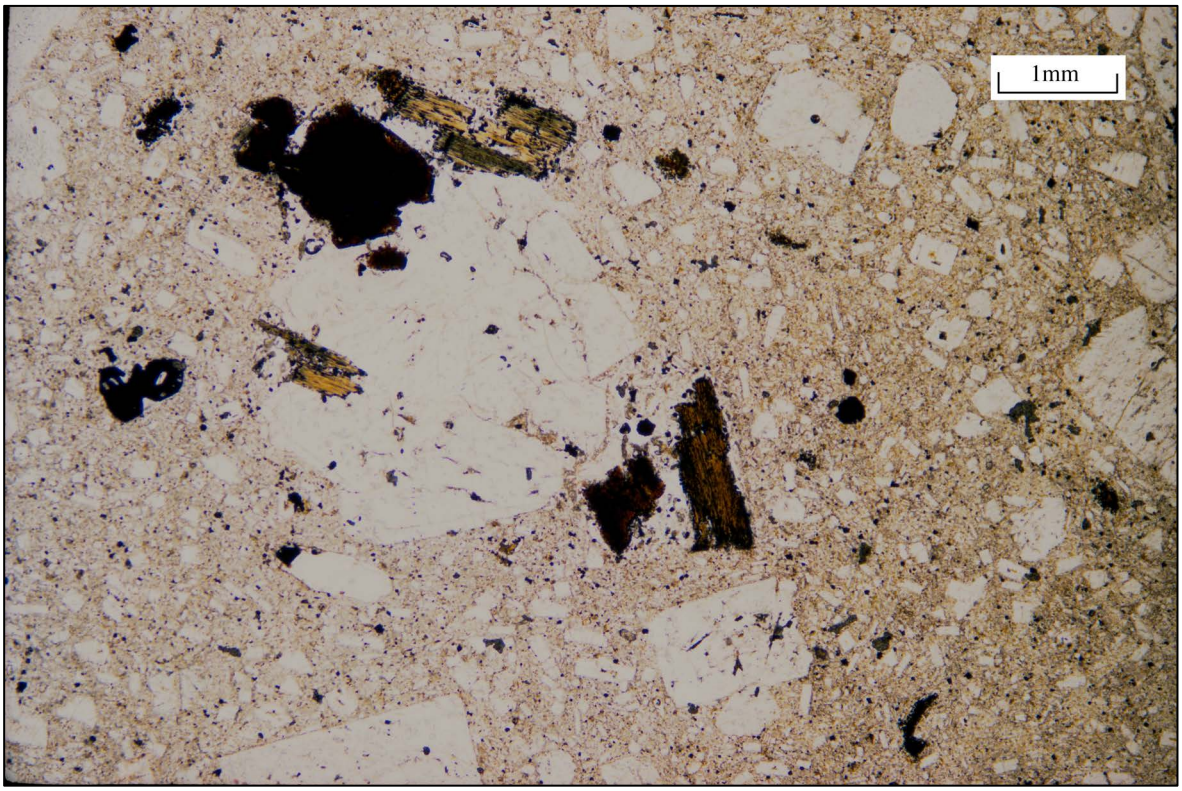


Figure 3.2.20. The Dents de Mézenc (87/58) quartz-trachyte, with partially resorbed biotite and amphibole phenocrysts associated with larger anorthoclase glomerocrysts. This is the only lava in the Velay with biotite phenocrysts and seems to be most closely related to the northern intermediate lavas. (Plane polarised light).

amphiboles has exactly the same appearance as that in the lavas, and leads eventually to the crystallisation of euhedral phenocrysts of biotite.

Red-brown/clear sub-anhedral biotite phenocrysts appear in the Dents de Mézenc lava, overgrowing kaersutite. Both the amphibole and the biotite are partially resorbed, the biotite being replaced by opaque needles (see Figure 3.2.20).

Only seven analyses of biotite were made, so the trends they show may not be particularly representative. The formula of biotite is:

$$K_2(Mg,Fe^{2+})_{6-4}(Fe^{3+},Al,Ti)_{0-2}[Si_{6-5}Al_{2-3}O_{20}](OH,F)_4$$

with Na substituting for K and Mn for (Fe^{2+},Mg). Attempts to determine Fe^{2+}/Fe^{3+} using Droop (1987) not successful. The best correlation is between Fe and Mg, as shown in Figure 3.2.19, which has the dividing line of phlogopite and biotite marked, showing that the single basaltic biotite is phlogopite *sensu stricto*.

Weaker correlations exist between Fe and Mn, K and Na (K + Na ≈ 1). Ca is absent from the structure, and Ti has a range of 0.75 - 1.15 apfu but shows no correlation with other elements. Al does not correlate with Si, and there is always excess Al beyond that needed to give Al + Si = 8.

3.2.9 Sphene

Sphene first appears in the northern intermediate lavas. It is eu-subhedral, pale brown with occasional sector twinning, and reaches a maximum size of 0.5-0.9mm. Its margins are occasionally overgrown by small Ti-magnetite grains, as shown in Figure 3.2.21. Groundmass sphene is also occasionally present.

The miaskitic phonolites have euhedral brown sphene microphenocrysts which reach a maximum size of 1.0mm, with occasional sector twins. They are occasionally found overgrowing Ti-magnetite phenocrysts - the reverse of the previous relationship. Sphene is usually present in the groundmass.

The agpaiitic phonolites either contain no sphene, or have rare isolated crystals, eu-anhedral, maximum 0.7mm. Some appear to be partially resorbed. Sphene is always absent from the groundmass.

Carmichael and Nicholls (1967) noted the absence of sphene from rhyolites, its sporadic appearance in trachytes as phenocrysts coexisting with amphibole or biotite, and its common coexistence with Na-pyroxene (but not amphibole or biotite) in phonolites. They suggested that this distribution was due to the effect of alkalis on the oxygen fugacity in the melt, since a high concentration of alkalis gives higher oxygen fugacity, which stabilises sphene. This is due to the increase in Fe^{3+}/Fe^{2+}, which promotes the formation of magnetite at the expense of ulvöspinel, leaving the Ti available to form sphene. The overgrowth of Ti-magnetite grains on sphene crystals in the northern intermediate lavas, and vice versa in the miaskitic phonolites, shows that the liquid with which they were in equilibrium had varying oxygen fugacity during its crystallisation. Other effects are described in section 3.1.4.2. The reasons for this change in oxygen fugacity are not clear.

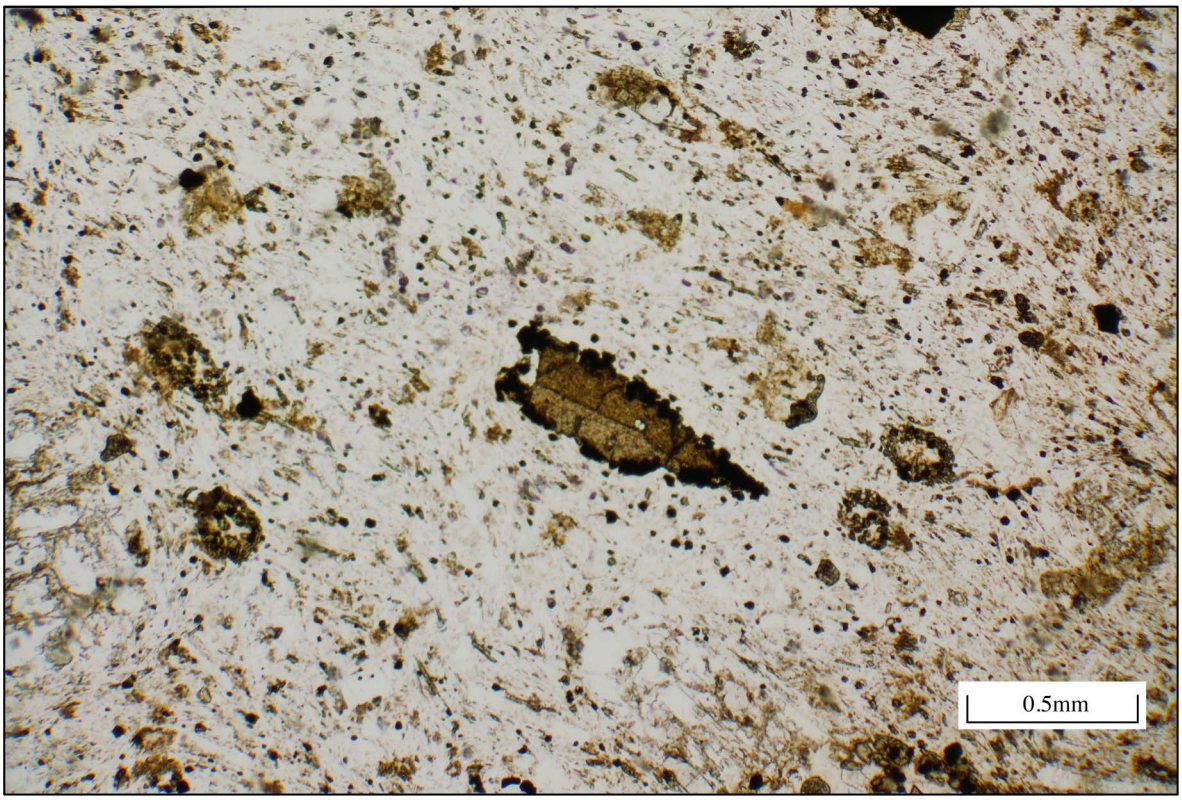


Figure 3.2.21. Ti-magnetite overgrowing sphene microphenocryst in the intermediate lava of Suc de Monac (87/30), indicating a reduction in oxygen fugacity. A few “ghost” relicts of resorbed amphibole are also visible. (Plane polarised light).

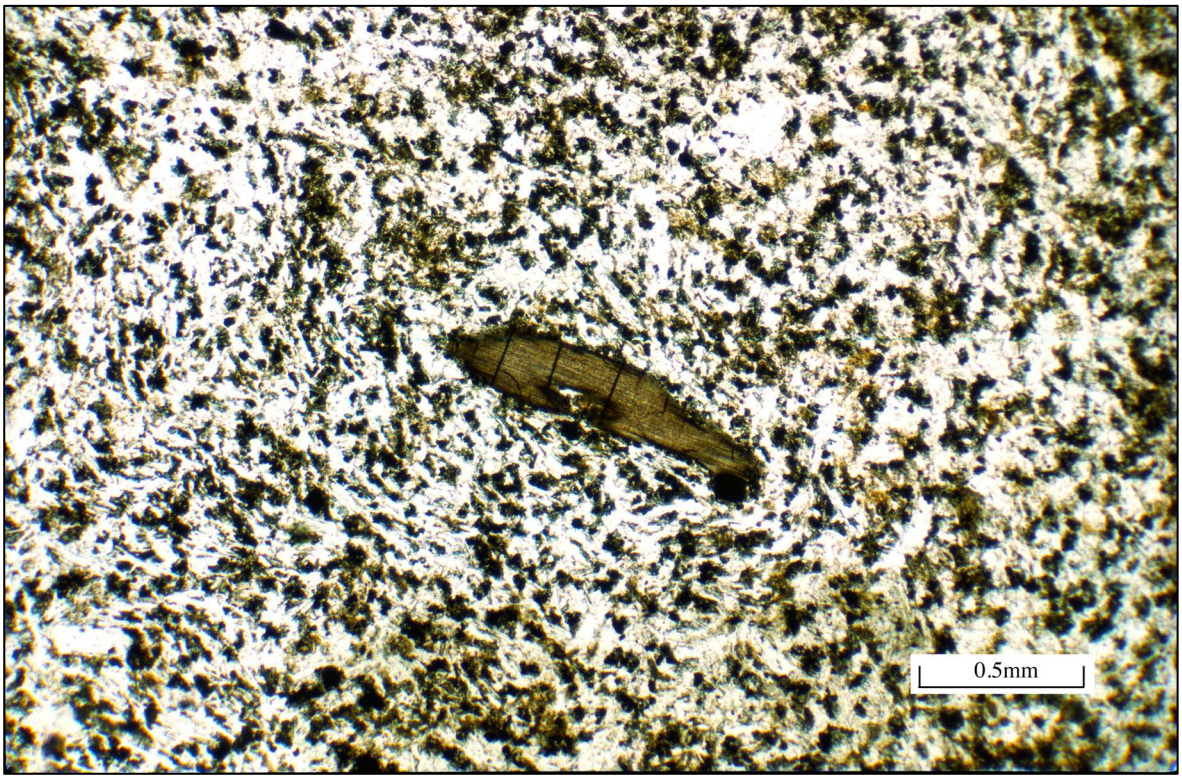


Figure 3.2.22. “Apatite bronze” (brown apatite) in the mugearite flow (southern intermediate lava) of Pailhès (87/23). Most apatites in these lavas are euhedral. (Plane polarised light).

Four test analyses of sphene were made, in which Al_2O_3 reached 1.8% and FeO 1.9%. Totals were 89.8-94.7%, but the effect of the OH/F anion on the total gives, at most, a reduction to 98.5%. This leaves 3.8-8.7% unaccounted for. Deer *et al* (1966) presented three analyses, one of which contains 4.5% REE. Further probe analyses should be made to test for the presence of such elements.

3.2.10 Apatite

Apatite is probably present in all the lavas, but in the basalts the groundmass crystals are too fine to be detectable. Only two of the hawaiites contain apatite, Queyrières (87/32) with a few subhedral brown/grey pleochroic sections, reaching 0.2mm long, and Yssingeaux (87/75) with two microphenocrysts, including a colourless euhedral 0.34mm crystal with an olivine inclusion, showing that it crystallised post-olivine.

In the intermediate rocks apatite is important both as a fractionating phase and as a means of distinguishing the lavas of north and south. In the south it appears as eu-anhedral pale brown/grey pleochroic sections, as in 87/32. Cleavages are length-parallel and intersect at 60° on some of the hexagonal end-sections. Maximum length is 0.6mm and crystals have some fluid inclusions. This type of apatite was called "apatite bronzé" by Olives *et al* (1976) and an example is shown in Figure 3.2.22.

In the north the intermediate lavas contain grey, euhedral, inclusion-rich apatites, reaching a maximum length of 0.6mm. They are found particularly within amphiboles. Mt Chabrier (87/31) has the highest proportion with 0.3%, although true amounts may be higher since apatite also appears as 0.05mm crystals in the groundmass.

The miaskitic phonolites also contain grey inclusion-rich apatites like the northern intermediates, but they are far less abundant and reach a maximum length of only 0.35mm. Apatite is largely absent from the agpaiitic phonolites, but a few grey, inclusion-rich crystals (maximum length 0.1mm) appear in Mt Mézenc (87/48), and the coarse-facies of Suc de Touron (88/22) contains a single 1.2mm grain filled with 0.01mm fluid inclusions, which may be a xenocryst.

There is a common association between inclusion-rich apatite and amphibole phenocrysts in the Velay lavas. One possible explanation for this is that the crystallisation of kaersutite uses all the major oxides, except P_2O_5, to some extent. Thus P_2O_5 would tend to become concentrated in the liquid adjacent to the growing amphibole phenocrysts, favouring apatite nucleation and growth.

Three test analyses showed only minor levels of elements other than CaO and P_2O_5. SiO_2 was the most significant, with 0.67%. The brown colour of the "apatite bronzé" does not seem to be caused by any particular major element.

3.2.11 Zircon

Zircon is a rare accessory mineral in the Velay, first appearing in a few of the intermediate lavas. Mont Gerbizon (86/27) bears a single 0.12mm anhedral grain, the dyke near Borée (88/23)

likewise and a coarse-grained inclusion from Suc de Monac (84/19b) has a few grains, although there are none in the host lava.

Dents de Mézenc, the anomalous quartz-normative extrusion from the south of the Velay, has abundant zircons, 0.03-0.16mm in diameter, which crystallised post-apatite, pre-opaque. They form elongated prisms with a square section and pyramidal ends.

Zircon also appears in a few miaskitic phonolites and helps to separate the group from the agpaiites, in which other Zr-silicates appear. The size range is similar to that in the intermediate lavas; 0.06-0.16mm, but the zircons are rarely euhedral, usually rather rounded and often have a rim of zeolites. The phonolites with zircon are Miaune (86/25), Roche-en-Régnier (87/12) and Meygal (86/18). Suc d'Eyme (87/39) contains a single rounded inclusion-rich zircon 0.42mm in diameter with a brownish altered-looking rim, which may be a xenocryst.

The only agpaiitic phonolite with zircon is that at Provenchères (88/24a), with a single 0.28mm rounded grain surrounded by zeolites. The rock has abundant basement xenoliths and examination of thin-sections of these and other Velay granite samples shows them to contain zircons, which reach a maximum size of 0.3mm. The zircon in the phonolite is therefore probably a xenocryst.

It should be noted that six of the occurrences of zircon are in the north, and that the three southern examples are all anomalous rock types or xenocrysts. This is a useful division between the evolved lavas of the north and south.

3.2.12 Aenigmatite

Aenigmatite is a pyroxene-like mineral characteristic of peralkaline rocks. It has been used as an indicator of agpaiicity in the Velay lavas and so by definition occurs almost exclusively in the agpaiitic phonolites.

Suc de Sara (87/55) has rare phenocrysts of aenigmatite (section loaned by M.Rourke and P.Law), but the mineral is confined to the groundmass of all other agpaiites in which it occurs. Due to late crystallisation it is always *extremely* poikilitic, covering areas of up to 0.4mm diameter with a very thin tracery of interconnected branches, as shown in Figure 3.2.23. It is often nucleated on early-formed Ti-magnetite grains. Its blood-red/dark brown/clear pleochroism is highly distinctive and the very strong colours obscure its birefringence.

The ideal formula of aenigmatite is $Na_2Fe^{2+}{}_5TiSi_6O_{20}$, but in practice substantial substitution is encountered. Al^{3+} and occasionally Fe^{3+} can replace Si^{4+}, and K^+ and Ca^{2+} can proxy for Na^+, all other cations filling the remaining sites. In four analyses of aenigmatites from Mont de la Tortue (86/46) and Les Roches (86/54) this scheme is followed, albeit with low Ti (0.46-0.84 apfu) and high Mn (0.57-0.68 apfu). One problem is an excess of (Na+K) above 2.0 apfu, which requires the surplus Na to go into an Fe^{2+}-site. Na^+ is difficult to accommodate in these sites due to both charge and ionic radius discrepancy, but may be accepted due to two factors. The first is the high concentration of Na_2O which would develop in the core of a K-feldspar glomerocryst, which would tend to increase

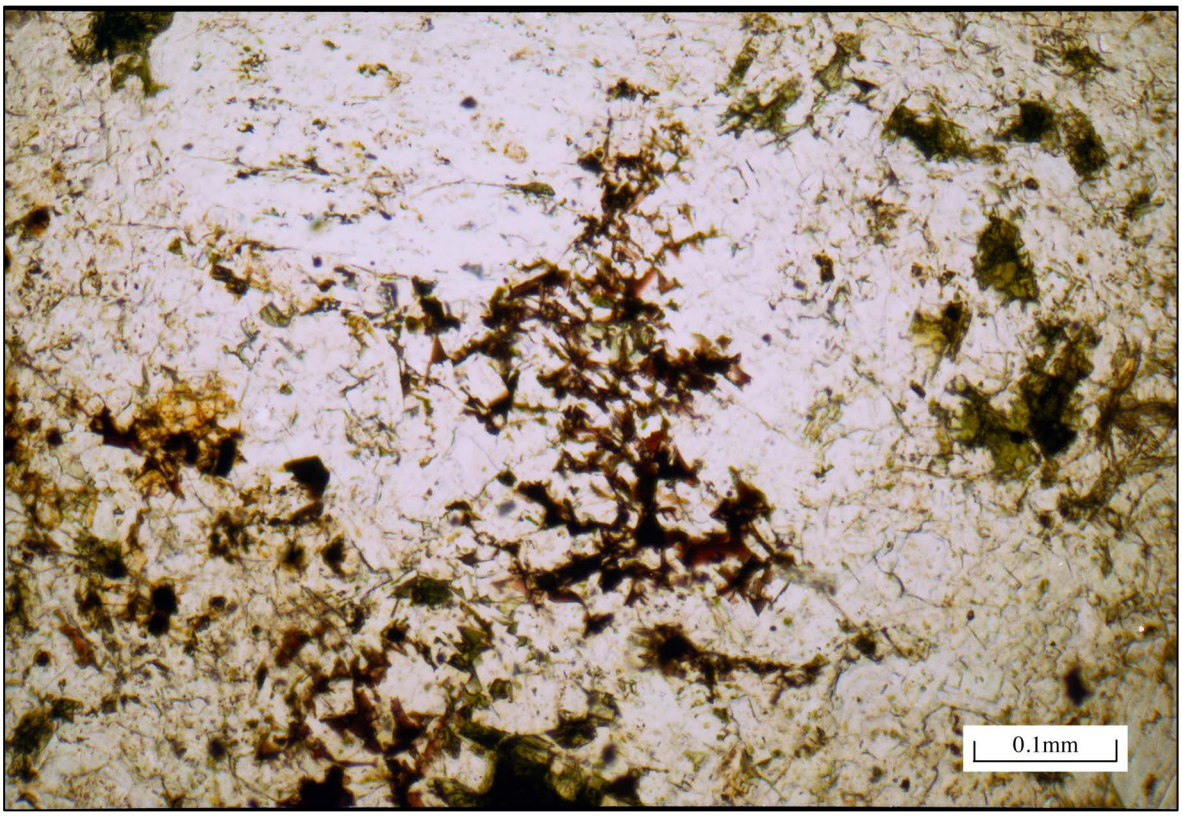


Figure 3.2.23. Extremely poikilitic aenigmatite in the groundmass of Mont de la Tortue (86/46). Euhedral K-feldspar laths are enclosed by the dark red aenigmatite. The green aegirine also has the same form, but less extreme. (Plane polarised light).

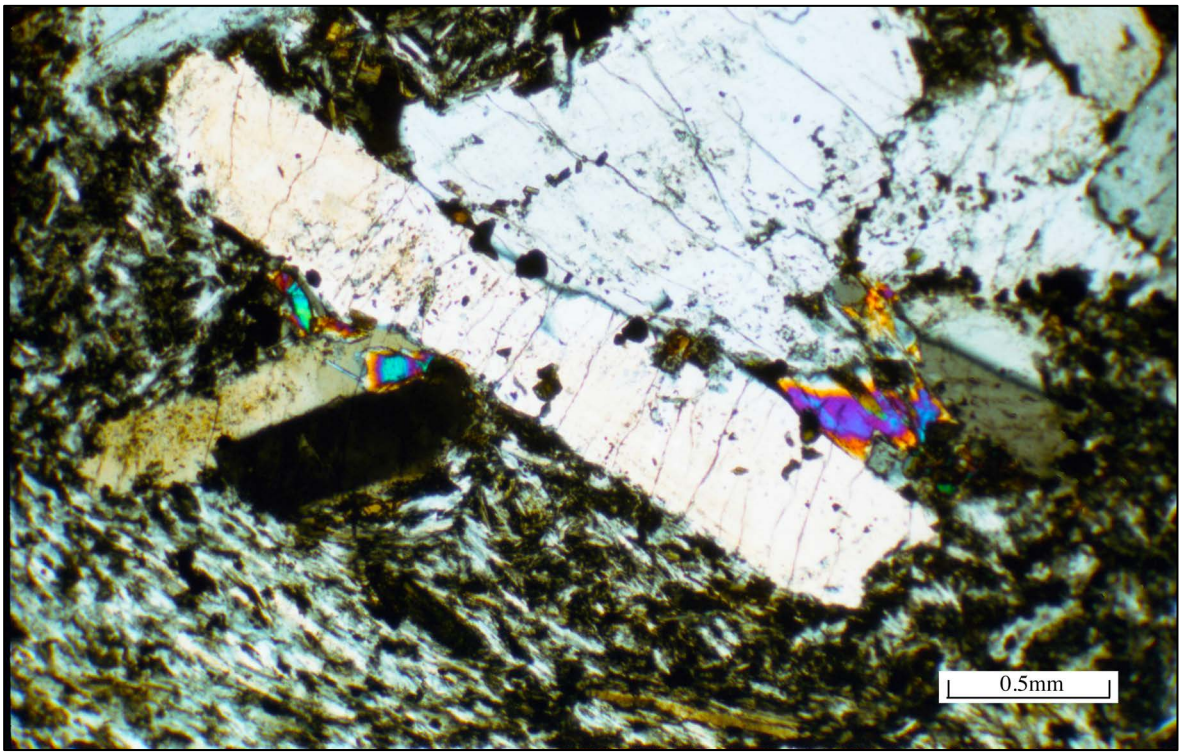


Figure 3.2.24. Mosandrite in the interstices of a sanidine glomerocryst in the phonolite of Les Roches (86/54). The mosandrite shows moderate birefringence and the dark spots in the K-feldspars are aegirine. (Crossed polarisers).

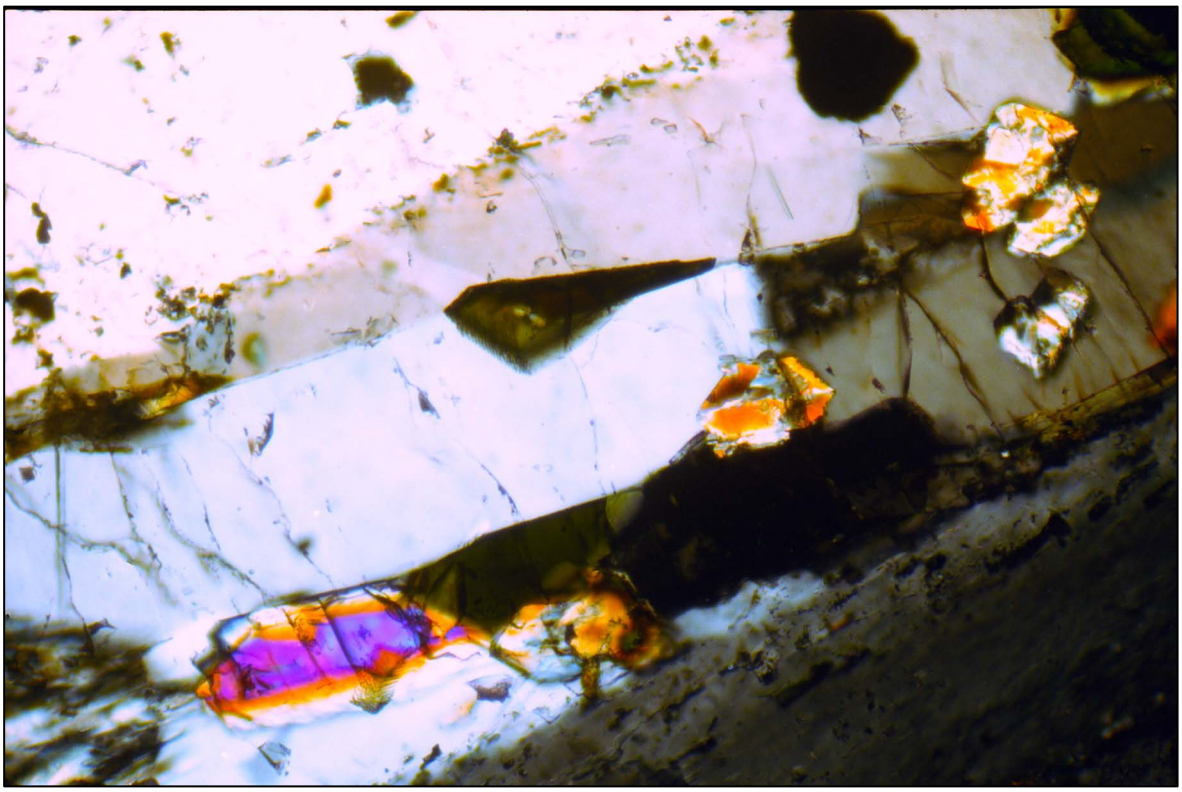


Figure 3.2.25. Mosandrite in Les Roches (86/54), with crossed polarisers. The mosandrite is within a large sanidine phenocryst and shows moderate birefringence. This is its only occurrence as euhedral crystals.

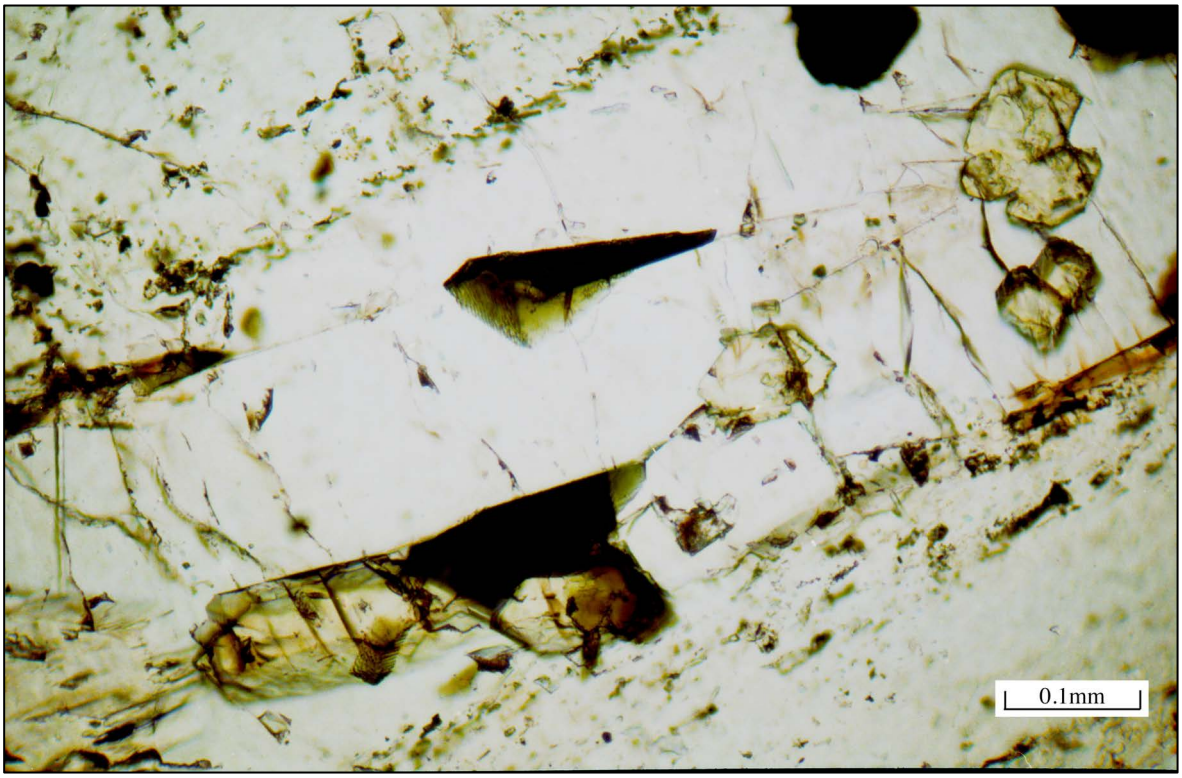


Figure 3.2.26. Mosandrite in Les Roches (86/54), with plane polarised light. This is the same view as above, showing the very pale yellow colour of the mosandrite and its lack of cleavage. The green mineral is aegirine.

its incorporation into the aenigmatite structure. The second is that rapid crystallisation may have occurred, forcing the lattice to tolerate the distortion that results from accepting such a large cation.

The observed reaction of Ti-magnetite to aenigmatite is normal for peralkaline magmas. Marsh (1975) suggested that the reaction:

$$2(Fe_3O_4 + Fe_2TiO_4) + 2Na_2Si_2O_5 + 8SiO_2 \Rightarrow 2Na_2Fe_5TiSi_6O_{20} + O_2$$

ß-phase solid solution glass glass aenigmatite gas

was responsible, with low oxygen fugacity causing the formation of aenigmatite.

3.2.13 Mosandrite

As shown in Table 3.1.6, mosandrite is characteristic of the agpaiitic phonolites. In the Velay it occurs within K-feldspar glomerocrysts in Les Roches (86/54) and Roche du Bachat (86/6), both of which are agpaiitic. It is usually anhedral and reaches a maximum size of 0.3mm. Its maximum birefringence is 0.013-0.015 and a low-∂ section gave a biaxial positive interference figure, with $2V_\gamma \geq 60^\circ$. Its pleochroism is weak, with γ clear, α pale yellow, ß clear/very pale yellow. Some tiny euhedral crystals, shown in Figures 3.2.25 and 3.2.26, have 45° and 90° interfacial angles. Extinction angles are 0-5° from cleavage traces, but cleavage is weak. The mineral has medium relief. All of these optical data are concomitant with its identification as mosandrite.

The most recently published formula of mosandrite (Aleph/CSIRO 1989) is:

$$(Ca,Na,Ce)_{12}(Ti,Zr)_2Si_7O_{25}(OH)_6F_4$$

Preliminary microprobe analyses which excluded Zr and Ce gave totals of 82%. Subsequent analyses included these elements and gave totals of 89-90%. A program (courtesy of K.Parish) was used to re-calculate the analyses for H_2O and F-content. The recalculated totals are close to 100%, with 4% H_2O and 5.7% F, supporting the identification of the mineral as mosandrite.

3.2.14 Feldspathoids

Feldspathoids appear only in phonolites in the Velay. As Table 3.1.6 shows, the type of feldspathoid present in a phonolite helps to determine whether it is miaskitic or agpaiitic. Those of the Velay fit the model well, with nosean appearing only in the miaskites and nepheline, sodalite and analcite mainly in the agpaiites.

To aid in their identification the feldspathoid staining method described by Shand (1939) was tested on a few sections (see Appendix B). The effect was weak for nepheline, but strong for zeolites, making it almost as hard to identify the nepheline as without the stain, as shown in Figure 3.2.27. For this reason staining was not used in general.

Nepheline

Nepheline was identified on the basis of its shape and uniaxial negative character. Phenocrysts are rare but the Suc de Touron coarse-facies (88/22) has euhedral microphenocrysts up to 1.1mm, and Pot à Chard (87/65a) has a few anhedral crystals, reaching a maximum size of 1.0mm.

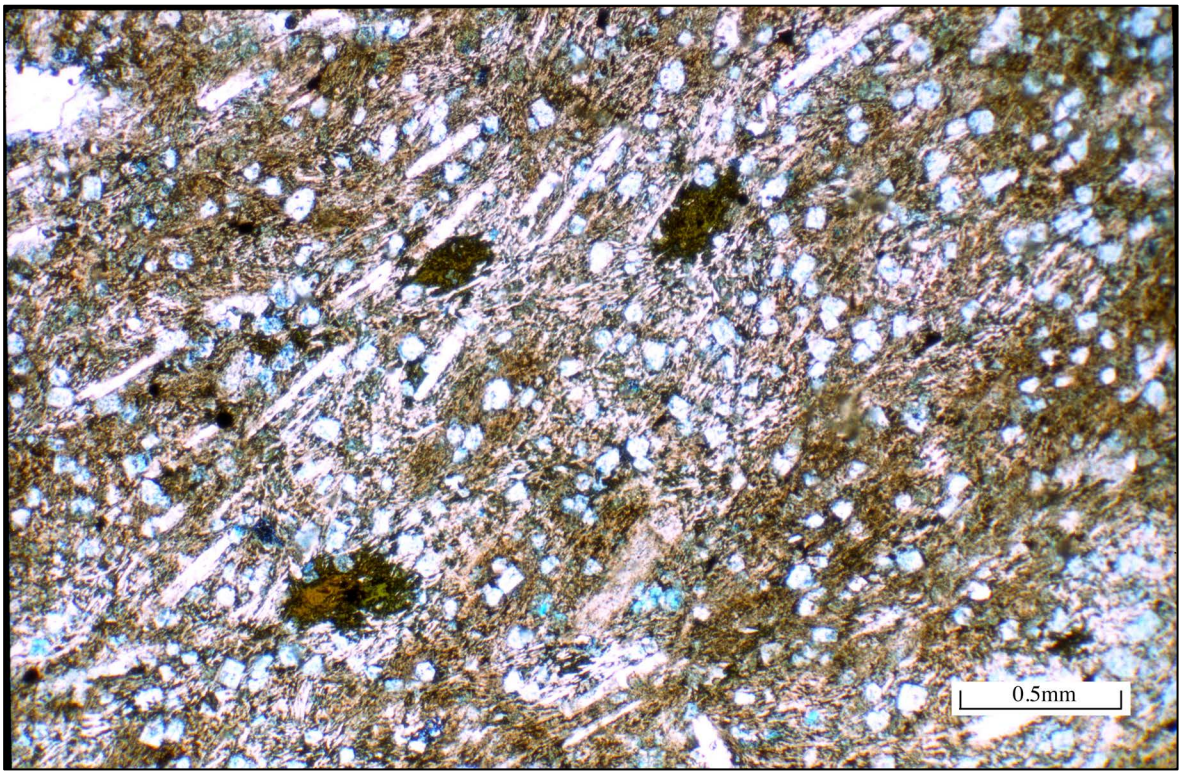


Figure 3.2.27. The medium-grained agpaiitic phonolite (tinguaite) of Suc de Sara (87/55), showing the effect of blue-staining on the groundmass nepheline. Inspection of this photograph illustrates the reversed crystallisation in this rock, with euhedral nepheline first, then sanidine laths, and finally poikilitic aegirine. (Plane polarised light).

Groundmass nepheline is more widespread, occurring in 20 phonolites. It is usually sub-euhedral and reaches 0.1mm, except in the Suc de Sara intrusion (84/29) where euhedral crystals reach 0.2mm (see Figure 3.2.27).

Nosean

Nosean is isotropic and forms rectangular sections with abundant opaque inclusions. It appears as phenocrysts in Suc de Touron (86/33, 88/33) with sub-euhedral grains up to 1.8mm, Rocher de Pradoux (phenocryst-rich sample 86/40) with completely altered an-euhedral grains up to 0.4mm, Suc de Chabrières (86/37) with two altered euhedral crystals reaching 1.0mm and Pot à Chard (87/65a) with a single altered hexagon 0.36mm in diameter. Pot à Chard also contains nepheline, as described above.

Nosean was positively identified in the groundmasses of eight phonolites, ranging from anhedral to euhedral and reaching 0.2mm in diameter. In Pot à Chard (87/65a) it forms elongated euhedral crystals reaching 0.28 x 0.1mm.

Sodalite

Sodalite is hard to distinguish from nosean, except by the absence of opaque inclusions. In the Hennes outcrop (86/64) it forms poikilitic an-euhedral crystals up to 0.4mm in diameter. An inclusion from Roche de Borée (86/70) contains sodalite.

Analcite

This label is applied, by default, to an isotropic anhedral groundmass phase with no opaque inclusions. It is found in the phonolite dyke near St Pierre Eynac (87/67) and in the Dornas phonolite (87/62).

3.2.15 Carbonate

Carbonate is present in amygdales and in the groundmasses of many of the Velay lavas. It seems to be an alteration product in most cases, as shown by its abundance in the basalts with glassy groundmasses.

If lavas with clear signs of weathering are discounted, all those that remain have carbonate within phenocrysts or glomerocrysts. In the case of Suc de Monac (84/19a, 87/30) Batard *et al* (1977) concluded that the carbonate in the plagioclase cores of composite feldspar phenocrysts was calcite formed by CO_2-corrosion of the plagioclase, which released Na into the liquid. Most of the other phenocryst-rich intermediate lavas also have corroded plagioclase phenocrysts, but the carbonate is restricted to the cores in only a few of them.

The miaskitic phonolites occasionally contain carbonate, usually within sanidine phenocrysts or in the cores of glomerocrysts. The feldspars show little evidence of corrosion and the carbonate forms uniform patches. This does not seem to be in accord with the model outlined above.

Chapter 4

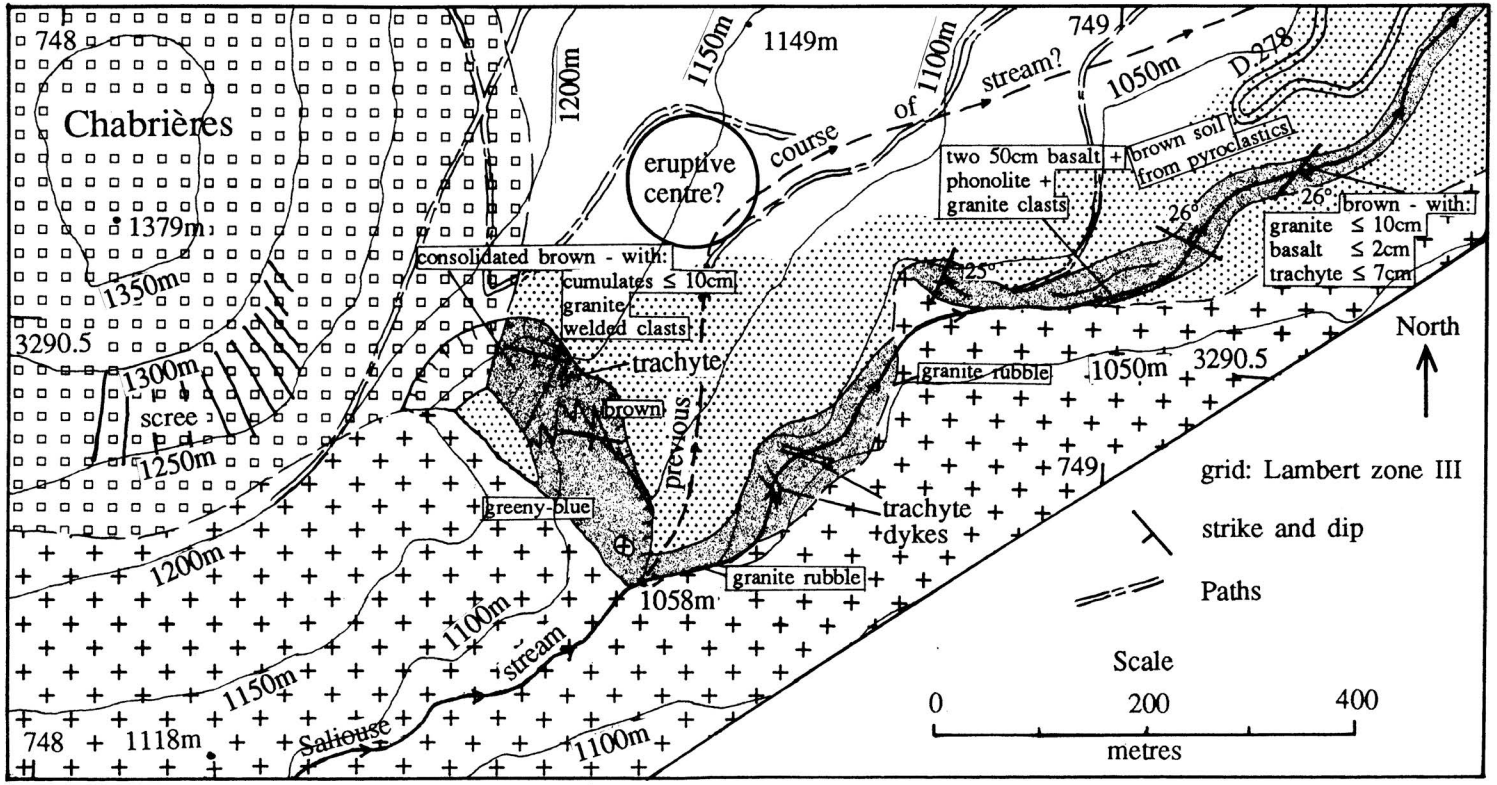
Field relations, petrography and mineral chemistry of the cumulate blocks

4.1 Field relations

The cumulates are found as coarse-grained blocks in a pyroclastic unit near the phonolite of Chabrières, which lies 2km SE of Mt Mézenc in the south of the Velay. Previously published literature has made little or no mention of this unit, and this study includes only a reconnaissance study of the pyroclastics, with the main emphasis on the included coarse-grained blocks.

The pyroclastics are exposed in the stream of la Saliouse, from just south-east of Chabrières to more than 1km downstream. The largest area of exposure lies closest to Chabrières, resulting from severe erosion by small streams and landslides. Figure 4.1.1 is a geological sketch map of the area and Figure 4.1.2 shows a view of the landslip from the east.

The pyroclastics appear to be more recent than the Velay basalts, since the valley in which they



Pyroclastics

Inferred pyroclastics

Basement - granite and gneiss

Phonolite

Figure 4.1.1. Geological sketch map of the pyroclastic deposit to the east of the phonolite of Chabrières.

Spot heights and contours in metres, contour interval 50m



Figure 4.1.2. View of Chabrières phonolite from the east, with the pyroclastics exposed in the landslip. The white material on the left of the landslip is the basement granite, grey phonolite appears in the centre and brown pyroclastics to the right.



Figure 4.1.3. Weak layering in the consolidated brown pyroclastics at the highest level in the landslip. This material is the source of the cumulate blocks.

occur cuts deeply into the granite which underlies the Velay basalt plateau. Uplift of the area took place in the upper Miocene and again in the Villafranchian (2-4Ma) and would have led to rapid downcutting of the rivers. The carbon-14 age of some fossil wood preserved in the flow was greater than the maximum that this technique can measure - 35,000 years (J. Mergoil *pers. comm.*).

The main centre of eruption was probably just to the east of Chabrières, with the pyroclastics flowing or falling further down the valley. The stream runs roughly along the southern contact between the granite and the pyroclastics, suggesting that the palaeo-valley, into which the pyroclastics were deposited, once followed a meander which curved slightly further to the north, as shown on Figure 4.1.1.

The blocks carried by the pyroclastics can be divided into five groups:

1) *Granite/gneissic fragments* - single grains to 10cm blocks.

2) *Trachyte fragments* - variable in appearance, with biotite. Max 10cm.

3) *Welded blocks* - similar to the pyroclastics, but with abundant streaks of glass. Quite rare, ≤10cm in diameter.

4) *Coarse-grained blocks* - individual grains + megacrysts, and nodules ≤15cm.

5) *Lava fragments* - weathered basalt and phonolite. Fragments of bole show that some surface basalt was included.

The granite and trachyte fragments are more common in the stream and lower levels and the welded fragments and coarse-grained blocks appear only in the highest parts of the landslip exposure.

Other evidence of trachyte magmatism, in addition to the trachyte fragments in the pyroclastics, includes patches of white lava visible in the upper parts of the cliffs of the landslip area, and a 6m-wide white trachyte dyke (sample 88/13) cutting the pyroclastic material in the stream. This dyke contains K-feldspar, plagioclase, biotite, opaques and apatite phenocrysts, as well as abundant granite xenoliths.

The pyroclastics themselves can be divided into two types. The lowest, found in the Saliouse stream, has a light brown colour, caused by weathering of the matrix, and ultimately forms the brown soil of the farmed terraces. Fresh samples have a greeny-blue colour and consist of fragments of granite and trachyte, from sand-sized grains to 1cm fragments. Biotite crystals are easily distinguishable, and their euhedral shape suggests that they were derived from the trachyte. This material is exposed from the NE corner of the area shown in Figure 4.1.1 to the landslip area, where it forms greeny-blue cliffs in the lower parts, with the more weathered brown material overlying and interfingering with it.

The second type of pyroclastic material lies above the light brown/greeny-blue material. It is dark brown and appears to be more resistant to erosion than the lower material, standing out as distinct layers, as shown in Figure 4.1.3. In thin section it contains about 50% crystals + lithics, with trachyte phenocrysts, granite minerals and crystals from the coarse-grained blocks. The groundmass is brown devitrified glass.

4.2 Petrography of clasts in the pyroclastics

4.2.1 Granite/gneissic fragments

Two samples were examined, the first (86/38c), which differs most from a normal granite, is described below:

K-feldspar - orthoclase, with similar appearance to those in normal Velay granite. ≤ 5mm, with turbid alteration and dusty appearance, poikilitically encloses smaller grains of plagioclase, quartz, biotite, zircon, opaques.

Plagioclase - sodic, euhedral, ≤ 6mm. Dusty appearance, slightly altered.

Quartz - equant, uniform size (0.2 - 0.5mm) with 120° grain boundaries, typical metamorphic texture. Apart from a few small patches within feldspars, none show shadowy extinction, subgrain formation, or fine dusty inclusions, attesting to their recrystallisation under strain-free conditions.

Biotite - greenish-brown/red-brown/pale yellow pleochroism, compared to the deep red/orange/clear pleochroism of biotite in the normal granite. Also far fewer pleochroic haloes around the abundant included zircons than the normal granite, probably as a result of annealing and recrystallisation. Ragged margins due to the growth of smaller biotite crystals, which often penetrate into the earlier crystals.

Grey mica - Unidentified mica with clear/grey-green/pale brown pleochroism, apparently grading into biotite in some places. In association with another, high-relief low-birefringence mineral, it forms irregular masses of fine crystals.

In hand specimen this material is hard, grey and microcrystalline and forms diffuse patches throughout the rock.

Zircon - abundant, maximum 0.2mm, most 0.05mm. Earliest crystallising.

Opaques - rare, present in the recrystallised quartz.

Both the plagioclase and the K-feldspar are generally present as isolated crystals surrounded by the recrystallised quartz. There is no trace of muscovite in this rock, unlike most of the normal Velay granites examined.

The other sample (86/38d) is much less affected by recrystallisation. Its feldspar crystals are still mainly in contact, and much of the quartz is like that normally seen in the Velay granite, with irregular shape, dusty inclusions, shadowy extinction and sub-grain formation. Some recrystallisation has taken place, apparently by continuation of subgrain formation until separate grains formed. Biotite has lost all pleochroic haloes, probably by annealing rather than by recrystallisation, and the clear/grey-green/pale brown mica is not present.

The texture of the minerals in these two specimens is quite different from those in the normal Velay granite. The recrystallised minerals show few indications of strain, which means that the most recent change in their structure was caused by high temperature alone. From their association with the pyroclastics, the granite blocks must have formed part of the magma chamber wall which was heated by the magma until the quartz and biotite recrystallised.

4.2.2 Trachyte fragments

Two specimens were examined (88/10, 88/10b), both of which contain abundant calcite. There is no external source of carbonate, so the most likely explanation is that it was present in the original melt. Phenocrysts in these rocks are, in decreasing order of abundance:

Plagioclase - sub-euhedral stubby tabular crystals, about An_{38}. Often embayed, or with marginal sieve texture. Clustered in glomerocrysts. (0.5 - 3.0mm).

K-feldspar - usually strongly zoned, often as overgrowth on plagioclase. Signs of resorption on margins. (0.5 - 2.0mm).

Biotite - an-euhedral, pale yellow/reddish brown/greenish brown pleochroism. (0.3 - 2.0mm).

Clinopyroxene - pale green, euhedral, often extensively altered/resorbed. (1.5mm).

Amphibole - brown, almost always totally resorbed with only tiny traces remaining within a rim of opaques. Sub-euhedral. (0.5 - 3.0mm).

Opaques - anhedral, ragged outlines, with rare euhedral squares. (0.1 - 0.5mm).

Apatite - 88/10 has abundant pinkish-brown euhedral crystals. (0.1 - 0.5mm).
88/10b has much smaller (0.1mm), colourless crystals within other phenocrysts.

The order of crystallisation is:

Apatite ⇒ opaques ⇒ clinopyroxene + amphibole ⇒ plagioclase ⇒ biotite ⇒ K-feldspar

As described in section 4.1 the dyke cutting the pyroclastics contains similar phenocrysts (although cpx and amphibole were absent from the section examined) with the same order of crystallisation. It is almost certainly from the same liquid batch.

4.2.3 Welded blocks

This material includes grains of all the minerals available in the eruption, with K-feldspar, plagioclase and biotite from the granite, trachyte and coarse-grained blocks, quartz, muscovite and zircon from the granite, and amphibole, clinopyroxene, apatite and opaques from the trachyte and coarse-grained blocks. Some lithic clasts are also present, including basalt and more evolved lavas. A homogeneous dark brown glass makes up the groundmass, with a weak fabric of parallel streaks. In hand specimen this fabric is quite strong, with parallel streaks of glass reaching 3cm long. Figure 4.2.1 shows a thin-section of a welded block.

The welded material seems to form isolated blocks within the pyroclastics, but closer examination shows that the edges of the welded material grade into the pyroclastics by progressive alteration of the glass. Thus the glassy welded rock is probably the unweathered version of the brown consolidated pyroclastics found in the highest part of the landslip area.

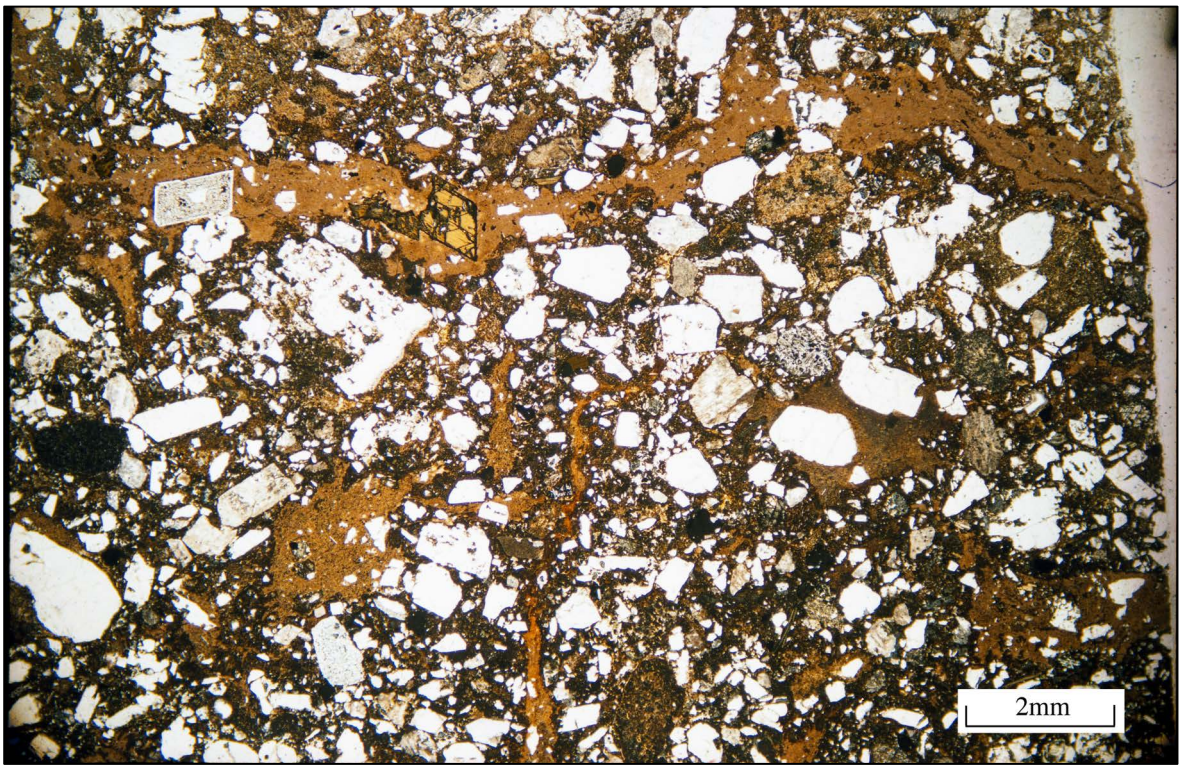


Figure 4.2.1. Thin section of a welded block from the pyroclastics. The euhedral feldspar from the granite shows sieve-texture, due to reaction with the glass. This contrasts with the euhedral amphibole, apparently in equilibrium. (Plane polarised light).

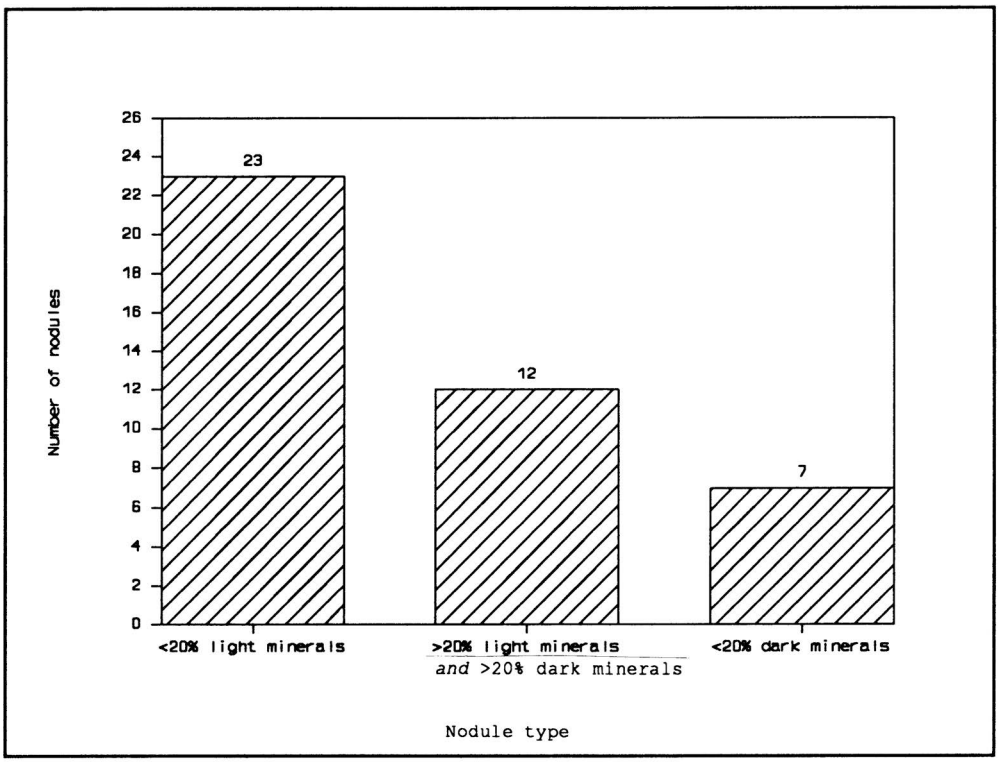


Figure 4.2.2. Bar chart of the numbers of cumulate nodules in each of the three categories, which represent different degrees of fractionation.

4.2.4 Coarse-grained blocks

These are found weathered out of the brown pyroclastics in the highest part of the landslip area. They vary in hand specimen from a dense black coarsely-crystalline rock, with no feldspar, to a lower density, feldspar-rich rock, with few dark crystals. Their grain size is highly variable, from 0.5mm to 10.0mm, with occasional megacrysts up to 10cm.

Forty two blocks were collected and Figure 4.2.2 shows a bar chart of three categories of nodule type, distinguished by examination of hand specimens. The size range is about the same in each of the categories, so the trend shown in the diagram represents a true decrease in volume from mafic to felsic material. This is the pattern which would be produced by the cumulate stack of a closed-system fractionating magma chamber.

The detailed petrography of these rocks is described in sections 4.5 and 4.6, but it is important to note that the most evolved examples consist of anorthoclase, biotite, clinopyroxene, opaques and apatite, all of which are present as phenocrysts in the trachyte.

4.3 Composition of the magma involved in the pyroclastic eruption

The composition of the pyroclastic magma can be deduced from the compositions of the trachyte dyke, glass from the welded clast, the trachyte fragments, and the most evolved cumulates, although it must be borne in mind that they may not all be cogenetic. The glass in the welded clast was analysed by microprobe and several experimental runs were made to determine the best analytical conditions (see Appendix C, section C.2.3). The results, when normalised, show that the composition of the glass is homogeneous. The average of the best four analyses was therefore taken as the composition.

The trachyte fragments present a problem because they contain abundant calcite, giving an unrealistically high CaO-content. To overcome this all the compositions were normalised with CaO fixed at 1.85%, as measured in the glass. The glass was assumed to be unaltered since it shows no signs of devitrification. The results given in Table 4.3.1 show that the compositions of the different rocks and glass are quite similar after normalisation. Figure 4.3.2 plots them on a silica-alkalis graph, where they all lie in the trachyte field.

Another possible candidate for liquid from the chamber is the dyke (bearing 300°) near Borée (88/23), which is orientated radially to the landslip and lies 1.5km to the SE. It has Ti-magnetite, apatite and zircon microphenocrysts and its groundmass contains biotite and carbonate, unusually for the Velay lavas. Unlike the other "liquid candidates" however, it is a mugearite and even after normalising to 1.85% CaO it still does not match them. If it *was* from the same magma chamber as the pyroclastics it must have been emplaced when the liquid was less evolved, possibly at the time the cumulate 86/38g was forming.

normalised	SH88/10	SH88/10b	SH88/13	SH88/15
SiO2	51.88	59.97	66.49	63.09
TiO2	0.84	0.89	0.32	0.62
Al2O3	16.25	19.90	17.22	19.01
Fe2O3T	4.68	4.11	3.14	3.54
MnO	0.22	0.13	0.21	0.17
MgO	0.63	0.77	0.09	0.50
CaO	**15.93**	**3.09**	**0.78**	**1.85**
Na2O	4.86	5.38	6.03	6.43
K2O	4.34	5.41	5.64	4.79
P2O5	0.36	0.33	0.07	n.d.
Total	99.99	99.98	100	100
sum alks	9.20	10.79	11.67	11.22
Normalised to **CaO = 1.85**				
	SH88/10	SH88/10b	SH88/13	SH88/15
SiO2	60.57	60.74	65.77	63.09
TiO2	0.98	0.90	0.32	0.62
Al2O3	18.97	20.15	17.03	19.01
Fe2O3T	5.46	4.16	3.11	3.54
MnO	0.26	0.13	0.21	0.17
MgO	0.74	0.78	0.09	0.50
CaO	**1.85**	**1.85**	**1.85**	**1.85**
Na2O	5.67	5.45	5.96	6.43
K2O	5.07	5.48	5.58	4.79
P2O5	0.42	0.33	0.07	n.d.
Total	99.99	99.97	99.99	100
sum alks	10.74	10.93	11.54	11.22

Table 4.3.1. Compositions of different lavas from pyroclastic flow. SH88/10 and SH88/10b are trachyte clasts, SH88/13 is the dyke and SH88/15 is the glass in the welded clast. n.d. = not determined.

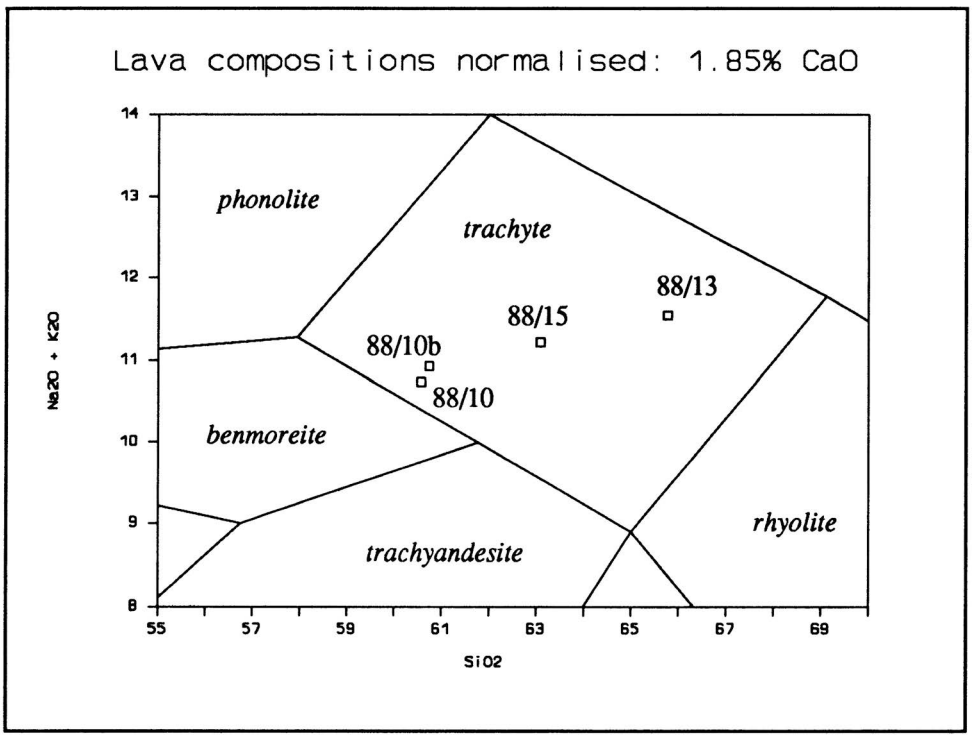


Figure 4.3.2. Silica-alkalis graph of calculated lava compositions. Grid is from Cox *et al* (1979).

4.4 Sequence of events

The following is a simple model to account for all the data available:

1) The emplacement of basalt into a magma chamber in the crust and its subsequent differentiation to a biotite-trachyte. During this differentiation the granite walls of the chamber were recrystallised, and trachyte dykes were emplaced in and above the chamber roof.
2) A violent explosive eruption, probably caused by a build-up of CO_2, fragmented the remaining liquid and the overlying granite and trachyte dykes. These fragments were all incorporated into the ejected pyroclastics.
3) Towards the end of the eruption the cumulates at the base of the chamber were disrupted and ejected.
4) The final stage was the intrusion of some late-stage melt into the pyroclastics, either from an undisturbed part of the original magma chamber, or by remobilisation of liquid from within the pyroclastics.

The mineralogy of the coarse-grained blocks supports this model, since the most evolved nodules are made of anorthoclase, biotite and clinopyroxene, all of which are seen as phenocrysts in the trachytes. The cumulus nature of these blocks is described in section 4.5.2.

A K-Ar age of 8.5Ma was obtained for one of the cumulate blocks (see section 1.3.3.2), similar to much of the Velay phonolite volcanism in this area (8.5 - 6.5Ma). In addition, 4km to the NW there is another biotite-trachyte, that of Dents de Mézenc, with an age of 9.0Ma. The incorporation of excess ^{40}Ar from the melt into the cumulate minerals seems unlikely, since the addition of a random amount of argon would not be expected to give an age so close to that of the nearby Velay phonolites. If the eruption *did* take place at 8.5Ma, the valley that it filled must have been formed in response to the upper Miocene uplift (see section 1.5). If, however, as field relations suggest, the pyroclastic eruption is more recent than the late Miocene, then the 8.5Ma cumulate blocks would represent an older cumulate stack. The similarity between the biotite-trachyte of the eruption and the most evolved cumulate strongly suggests that they are cogenetic, thus making the K-Ar age suspect.

The true age of the pyroclastic eruption might be found by a K-Ar date on a good quality sample of either the trachyte dyke, or a trachyte block (with very little carbonate replacement) from the pyroclastics.

4.5 Petrography of the coarse-grained blocks

4.5.1 Introduction

Forty one sections of twenty nine coarse-grained blocks were examined and the results are given in Table 4.5.1. This includes a brief description of the minerals present, their appearance and modal proportion from point-counting (500 or 1000 points per section).

Table 4.5.1. Petrography of the coarse-grained blocks

Specimen number	Minerals present								Comments	number of thin sections	sample micro-probed	sample XRF bulk analysis
	clinopyroxene - salite	opaque phases	amphibole - kaersutite	biotite	feldspar	apatite	glass and carbonate	sphene/zircon/ other				
SH88/14a	pale green, strongly corroded and partly overgrown by biotite An-subhedral. 0.5-2mm 4.5%	Ti-magnetite, 1.5% Ilmenite 1.5% rounded, anhedral, within biot,cpx 0.1-1mm	_____	pale yellow/greeny brown /dark red brown. Sub-euhedral. Often over-growing cpx. Usually assoc. with glass 0.2-3mm 8%	Anorthoclase - roughly equant, anhedral. Commonly shows tartan twinning, lots of glass-filled holes. Or15-36 (probe) 0.5-6mm 76%	euhedral, earliest crystallising 0.04-0.3mm 0.5%	glass - pale brown,adjoining minerals have sharp edges. Patches up to 2mm. 7% carbonate - anhedral blobs in glass, up to 0.5mm 1%	zircon - 2 crystals, <0.1-0.2mm anhedral. tr.	Most evolved block. Texture most like adcumulate.	2	yes	yes
SH88/14b	pale green, strongly corroded along cleavage, overgrown by biotite. An-subhedral. (orig. euhedral), rare pinkish cpx cores. 0.1-4mm 7%	Ilmenite 0.35% Ti-magnetite 0.15% blobby, anhedral, within cpx 0.2-0.6mm	_____	pale yellow/greeny brown /dark red brown. Sub-euhedral. Sometimes overgrowing cpx. 0.1-2mm 13.5%	Plagioclase - eu-anhedral, intergrown laths, narrow or absent twins. Interstitial glass blebs, some zoning to calcic cores. An31-22 (probe) 0.5-4mm 66.5%	euhedral, earliest crystallising inclusion-rich cores. one 1.2mm crystal 0.02-0.3mm 1%	glass - pale brown,adjoining minerals have sharp edges. Patches up to 2mm. 11% carbonate - an-euhedral, usually as rounded blobs in glass. 0-0.3mm 0.5%	zircon - 9 crystals. An-subhedral. Post-feldspar 0.1-0.4mm tr.	This block has been K-Ar dated at 8.5 ±0.2 Ma.	2	yes	yes
SH88/14c	pale green, anhedral, in core of resorbing amph. 0.4-0.7mm tr.	Ilmenite - single grain Ti-magnetite - an-subhedral, altered with cross-hatching pattern 0.1-0.2mm 1.5%	yellow/red brown/olive green. strongly corroded anhedral - orig. euhedral overgrown by biotite 0.5-3mm 1%	yellow/red brown/red black. sub-euhedral, roughly equant, over-grows amph. 0.1-4mm 17%	Plagioclase - an-subhedral intergrown crystals, little interstitial glass, weak zoning. An34-Or22 (probe) 1-9mm 69%	euhedral, earliest crystallising 0.04-0.4mm 1%	glass - altered, adjoining minerals have sharp edges Patches up to 4mm. 10.5%	zircon - one subhedral crystal 0.4mm tr.		1	yes	yes
SH88/14d	pale yellow/pinkish/ bluish. Anhedral, equant unzoned, little twinning 0.2-5mm 77%	Ti-magnetite - altered, overgrows spin-herc, anhedral 0-1.2mm 16% Spinel-hercynite - rounded 0.3-0.5mm 4.5% Pyrrhotite - circular blobs in cpx <0.1mm tr.	_____	_____	_____	_____	glass - altered to brown material. Interstitial patches up to 0.9mm. 1.5% carbonate - sheaves of max. 0.2mm crystals in round patches within glass 1%	_____		1	yes	no
SH88/14e	v. pale green, anhedral always within amph. 0.1-0.5mm 0.5%	Ti-magnetite - altered, an-subhedral 0-0.6mm 1% Ilmenite - sub-anhedral 0-0.7mm 1.5%	pale yellow/red brown/ olive green. Sub-euhedral 0.5-7mm 54%	pale yellow/greeny brown /dark red brown. Anhedral within amph, Sub-anhedral outside amph. 0.1-2mm 2.5%	Plagioclase - eu-anhedral. Clear twins, weak zoning, little grain boundary glass An21-51 (probe) 0.2-7mm 33%	Eu-subhedral, slightly rounded, inclusion-rich 0.1-3mm 3%	glass - pale brown,adjoining minerals have sharp edges. Patches up to 6mm. 3.5% carbonate - euhedral crystals up to 0.1mm in round patches in glass up to 0.6mm 0.5%	sphene - clear, sub-anhedral usually in glass. 0.2-4mm 0.5%		1	yes	yes
SH88/14f	_____	Ti-magnetite - an-euhedral 0-1mm 0.5% Ilmenite - an-euhedral 0-0.8mm 0.5%	_____	pale yellow/greeny brown /red black. Eu-subhedral 0.1-1.6mm 12%	Plagioclase/anorthoclase - an-subhedral, v. fine twins or cross-hatching. Zoning from calcic cores to K-spar. An56-Or26 (probe) up to 5mm 71.5%	euhedral, earliest crystallising 0-0.5mm 1%	glass - all altered to fine material. Regular equant outlines of patches suggests resorbed cpx. Up to 2mm 11% carbonate - fine crystals in glass <0.1mm 3.5%	zircon - eu-anhedral, clear. Most about 0.1mm 0.1-0.4mm. tr.		2	yes	yes
SH88/14g	pale: yellow/pinkish/ bluish. Anhedral, equant unzoned, untwinned 0.3-7mm 78%	no polished section anhedral equant blobs 0-2mm 21%	tiny quench crystals in glass. clear/brown, euhedral max. 0.1mm tr.	_____	_____	_____	glass - altered to brown material, with quench crystals. Patches up to 0.3mm 1%	_____		1	no	yes
SH88/14h	pale: yellow/pinkish/ bluish. Anhedral, equant unzoned, few twins 0.3-5mm 70.5%	Ti-magnetite - altered, overgrows spin-herc, anhedral 0-1mm 9% Spinel-hercynite - equant, anhedral 0-1.6mm 14% Pyrrhotite - round blobs in other minerals 0.15mm tr.	clear/reddish brown/ greenish brown. Eu-sub-hedral quench crystals. Always in glass patches, sometimes with parallel opaque needles 0-0.2mm incl. with glass	_____	_____	_____	glass - brown, often altered to fine material. Contains quench crystals of amph and opaques. Patches 1-3mm 6.5%	_____		1	yes	yes

Table 4.5.1 (continued)

Specimen number	Minerals present								Comments	number of thin sections	sample micro-probed	sample XRF bulk analysis
	clinopyroxene - salite	opaque phases	amphibole - kaersutite	biotite	feldspar	apatite	glass and carbonate	sphene/zircon/ other				
SH88/14i	pale green, remnants in amph cores. Resorbing 0-0.5mm 0.5%	Ti-magnetite - altered anhedral 0-0.5mm 1.5% Ilmenite - unaltered, an-subhedral 0.1-0.8mm 1.5%	pale yellow/red brown/ olive green. An-subhedral edges corroding, over-grown by biotite 0.2-5mm 54%	pale yellow/red brown/ dark red black. Anhedral replacing amph 0-3.5mm 6.5%	Plagioclase - anhedral, chaotic intergrowth. Some zoning An62-38 (probe) 0.2-6mm 31.5%	euhedral, earliest crystallising max diam 0.5mm length 1.5mm 2.5%	glass - altered to fine material. Adjoining minerals have sharp edges. Patches up to 2mm 3%	sphene - one crystal. An-hedral 0.4mm tr.		2	yes	yes
SH88/14j	pale: yellow/pinkish/ bluish. Anhedral blobs enclosed by amph 0-6mm 62.5%	Ti-magnetite - anhedral, 0-1.2mm 5.5% Ilmenite - one 2mm-long anhedral crystal. tr. pyrrhotite - small circular blobs. tr.	pale yellow/red brown/ greenish brown. Large poikilitic crystals enclosing cpx max 10mm 27.5%	_____	Plagioclase - anhedral, inter-stitial patches, often assoc. with glass. Poor twins An82-72 (probe) 0-1.6mm 1%	_____	glass - altered to fine material. Interstitial. Patches up to 2mm, most <0.3mm 3.5%	_____		1	yes	no
SH88/14k	pale green/yellow an-subhedral, slightly corroded 0-2.2mm 2.5%	no polished section Anhedral, second mineral to crystallise 0-1.4mm 2%	pale yellow/red brown/ olive green. Eu-subhedral some replacement by biot. 1) 0.1-2mm 2) 0.1-4mm (+11x7mm Xtal) 3) 0.1-12mm needles (see comments) 17.5%	pale yellow/red brown/ red black. Anhedral, usually replacing amph 0-3mm 8%	Plagioclase - anhedral, poikilitic, strongly zoned with calcic cores An55-26 (optical method) 0-14mm 66%	euhedral, earliest crystallising most 0.1mm 0-0.5mm 1%	glass - altered to fine material. Adjoining minerals have sharp edges. Patches up to 3mm 3%	zircon - an-subhedral. 7 grains 0.1-0.4mm tr. sphene - an-hedral. Often overgrowing opaques 0.1-2mm tr.	Section shows pronounced layering: 1) plag-rich 2) amph-rich 3) plag + amph needles with no cpx	1	no	yes
SH88/14l	pale: yellow/pinkish/ bluish. Anhedral, equant no zoning, some twins 0.2-7mm 72%	Ti-magnetite - anhedral, altered, interstitial 0-3.5mm 19% Spinel-hercynite - rounded blobs 0-0.8mm 5% pyrrhotite - small round blobs tr.	_____	_____	_____	_____	glass - altered to fine material. Adjoining minerals embayed - no sharp edges patches reach 1mm 3% carbonate - round patches in glass. Crystals up to 0.3mm mainly anhedral 1%	_____		1	yes	yes
SH88/14m	pale: yellow/pinkish/ bluish. An-subhedral, equant. Some twinning, little zoning 0.2-10mm 43%	Ti-magnetite - subhedral near glass, anhedral as inclusions. 0-1.4mm 13% pyrrhotite - round blobs up to 0.15mm diam. tr.	pale yellow/red brown/ greenish brown. Anhedral, equant but slightly poikilitic. Large patches prob. nucleated on settled crystals 0.8-7mm 25.5%	_____	_____	_____	glass - brown, adjoining minerals have sharp edges. Contains quench crystals of amph + opaques. Forms an emulsion with carbonate. Patches up to 9mm carbonate - round blobs mixed in with glass. max 1.5mm total glass + carb. 18.5%	_____	Block shows best evidence for presence of carbonate immiscible liquid.	1	yes	no
SH88/14n	pale: yellow/pinkish/ bluish. Anhedral, equant intimately intergrown with amph, some twinning. max 4mm 32%	Ti-magnetite - an-euhedral altered. 0-1mm 13.5% Pyrrhotite - round blobs and some larger squares - ?fragmental. max 0.5mm tr.	pale yellow/red brown/ greenish brown. highly poikilitic, equant patches max 5mm 38.5%	_____	Plagioclase - anhedral, some zoning, poikilitically encloses all minerals. Wide twins, occ. lath shape shows orig. shape An64-57 (probe) 0.1-5mm 10%	_____	glass - always assoc. with carbonate, altered to fine material. Scarce. 1.5% carbonate - interstitial or large 4mm patches of euhedral 0.9mm crystals in concentric zones. 4.5%	_____	Block has abundant carbonate, as crystals on conduit walls, to the exclusion of glass.	1	yes	no
SH88/14p	pale: yellow/pinkish/ bluish. Anhedral, equant All intergrown. Some twinning. 0.3-14mm 57%	Ti-magnetite - anhedral, altered, non-equant, patches up to 7mm 27% Pyrrhotite - completely altered. 0-3mm tr.	pale yellow/red brown/ greenish brown. Anhedral blobs in cpx. 0.1-1.2mm tr.	_____	_____	_____	glass - brown, some altered to fine material. Quench crystals of amph, opaques and occ. plag. Adjoining minerals have sharp edges patches up to 10mm 16%	_____	Shows the earliest appearance of plagioclase as quench crystals in melt. One section has pyroclastic rind attached.	2	yes	no

Table 4.5.1 (continued)

Specimen number	Minerals present								Comments	number of thin sections	sample micro-probed	sample XRF bulk analysis
	clinopyroxene - salite	opaque phases	amphibole - kaersutite	biotite	feldspar	apatite	glass and carbonate	sphene/zircon/ other				
SH88/14q	_____	no polished section An-euhedral squares and diamonds - hence prob. Ti-magnetite 0-0.8mm 1) 3% 2) 2% 3) 5.5% - see comments section	_____	pale yellow/red brown/ greenish brown. Sub-euhedral. 0-6mm 1) 10.5% 2) 2% 3) 38.5% - see comments section	Anorthoclase - completely anhedral, fine cross-hatching, some zoning, rare plag-type twins. No probe values obtained 0.3-9mm 1) 79.5% 2) 93.5% 3) 26.5% - see comments section	euhedral, earliest crystallising max 1.1mm most 0.1mm 1) 1% 2) tr. 3) 2.5%	glass - altered to fine material, adjoining minerals have sharp edges. Patches up to 2mm. 1) 6% 2) 2.5% 3)27% - see comments section	red mineral - often over-growing opaques - possibly rutile derived from ilmenite	Section shows layering: 1) plag + biot 2) plag only 3) biot only	1	no	yes
SH88/14r	single large megacryst no colour scheme due single orientation. Weak zoning confirmed by probe. 30mm (whole section) 100%	anhedral, tiny in glass pockets, or as inclusions max 0.4mm tr.	clear/red brown quench crystals in glass Euhedral max 0.1mm tr.	_____	_____	_____	glass+carbonate-mostly altered patches in holes up to 0.6mm diameter tr.	_____	megacryst, seems to be simply a large single cpx from the same cumulate series	1	yes	no
SH88/14s	pale green/pale yellow an-euhedral, strongly resorbing, esp. near glass. Equant. Some have pink cores. 0.1-5mm 6.5%	Ilmenite - an-subhedral, unaltered. 0-0.9mm 1% Ti-magnetite - an-sub-hedral, max 0.5mm, usually smaller. 0.5% Pyrrhotite - trace	_____	pale yellow/red black/ greenish brown. Sub-euhedral. Encloses cpx 0-2.6mm 14%	Plagioclase - sub-euhedral, equant, some zoning. An31-21 (probe) 0-7mm 68%	euhedral, earliest crystallising Largest have inclusion-rich cores. 0-0.4mm 1%	glass - pale brown, unaltered Adjoining minerals have sharp edges. Contains small euhedral crystals of other phases. Patches up to 2.5mm carbonate - rounded blobs in glass, some euhedral. up to 0.3mm. total glass + carb. 9%	zircon - 4 crystals. An-subhedral. 0.1-0.4mm	Section shows clear evidence that plag was cumulate in origin before adcumulate overgrowth.	2	yes	yes
SH88/14t	pale green/clear once euhedral, now strongly altered, ragged with overgrowth by amph. occurs in clusters. Max 1.6mm 14%	no polished section anhedral 0-0.6mm 1.5%	clear/red brown/ greenish brown. An-subhedral, as overgrowth on cpx, being overgrown by biotite. 0.1-5mm 33.5%	pale yellow/dark red brown/greenish brown replacing amph max 1.3mm 2%	Plagioclase - an-subhedral, intergrown equant laths. Medium twins, quite strong zoning An60 (optical) 0-3.5mm 46.5%	euhedral, earliest crystallising 0-0.6mm 0.5%	glass - altered to fine material, adjoining minerals have sharp edges. Patches up to 0.8mm. 2%	_____		1	no	no
SH88/14u	clear, anhedral, equant intergrown in clusters max 2mm. Single grains <0.06mm 0.5%	Ilmenite - anhedral max 0.9mm 1% Ti-magnetite - an-euhedral max 0.2mm 0.5%	pale yellow/red brown/ olive green. Sub-euhedral 0.2-5mm 47%	pale yellow/red black/ greenish brown. An-sub-hedral, replacing amph. max 3.5mm 9%	Plagioclase - anhedral but may have started euhedral, inter-grown equant laths, strongly zoned with calcic cores An45-21 (probe) max 4mm 35.5%	euhedral, earliest crystallising 0-0.5mm 2.5%	glass - pale brown, unaltered, with holes. Adjoining minerals have sharp edges. Patches up to 2mm 4% tr.	sphene - 6 crystals an-euhedral 0.4-2.2mm		2	yes	yes
SH88/14v	pale: yellow/pinkish/ bluish. Anhedral, equant orig. euhedral? max 4.5mm 73%	Ti-magnetite - anhedral, non-equant, interstitial to cpx. Altering. max 2.4mm 15.5% Spinel-hercynite - anhedral equant blobs in ti-mag. max 2.2mm 6.5% pyrrhotite - blobs and fragments up to 0.5mm. tr.	brown/clear. Single blob in cpx, anhedral, round 0.1mm tr.	_____	_____	_____	glass - altered to fine material. Always with carb. patches up to 0.4mm. 2% carbonate - round blobs up to 0.9mm, occ. embaying other minerals. 3%	_____		1	yes	no
SH88/14w	pale green, aggregates up to 5.5mm diam, and single crystals in amph. max 0.1mm 1%	Ti-magnetite - anhedral, altered. max 0.3mm 1.5% Ilmenite - an-subhedral, unaltered. max 0.7mm 1% pyrrhotite - blobs up to 0.04mm in Ilm. tr.	yellow-clear/red brown/ olive green. Sub-anhedral max 5mm 55%	pale yellow/red black/ greenish brown. An-subhedral max 2.4mm 5%	Plagioclase - anhedral, equant laths, intergrown. Strong zoning from calcic cores, variable twin size An49-26 (probe) max 4mm 30%	euhedral, earliest crystallising max 0.3mm (one crystal 5 x 2mm) 2%	glass - pale brown, unaltered adjoining minerals have sharp edges. Patches up to 2.4mm 4.5%	_____		2	yes	yes

Table 4.5.1 (continued)

Specimen number	Minerals present: clinopyroxene - salite	opaque phases	amphibole - kaersutite	biotite	feldspar	apatite	glass and carbonate	sphene/zircon/ other	Comments	number of thin sections	sample micro-probed	sample XRF bulk analysis
SH88/25	pale: yellow/pinkish/ bluish. Anhedral, equant daylight view shows cumulate texture max 4mm 72.5%	Ti-magnetite - anhedral, equant, altered. max 1.8mm 25% Ilmenite - anhedral, equant, rounded max 0.7mm 2.5% pyrrhotite - blobs 0.1mm tr.	one tiny blob in cpx, brown 0.1mm tr.	_____	_____	_____	glass - altered to fine material. Adjoining minerals have sharp edges 0.6mm tr.	_____		1	no	no
SH86/38a	pale: yellow/pinkish/ bluish. Anhedral, equant max 4mm 54.5%	Ti-magnetite - anhedral, non-equant, altered, interstitial max 5mm 14.5% Spinel-hercynite - equant, anhedral, often enclosed by ti-mag. max 6mm 6.5% Ilmenite - anhedral, non-equant, unaltered max 5mm 3.5% pyrrhotite - blobs up to 0.15mm tr.	clear/red brown/ greenish brown. Anhedral, blobby sub-poikilitic max 2mm 18.5%	_____	_____	_____	glass - altered to fine material. Adjoining minerals sometimes show sharp edges patches up to 1mm 2.5%	_____		1	yes	yes
SH86/38b	pale green/pale yellow An-subhedral, strongly corroded, equant. Some have pink cores. max 2.1mm 7%	Ilmenite - an-subhedral rounded, unaltered max 0.7mm 1.5% Ti-magnetite - an-subhedral, altered max 0.3mm 0.5%	greeny brown/red brown one crystal, anhedral being replaced by biotite 4mm 2%	pale yellow/red black/ greenish brown. Sub-euhedral, equant max 1.7mm 30%	Plagioclase - sub-euhedral,not enough overgrowth to obscure cumulus texture, v. narrow twins, strongly zoned An31-21 (probe) max 4mm 50.5%	euhedral, earliest crystallising inclusion-rich cores max 0.14mm 2%	glass - pale brown, unaltered Adjoining minerals have sharp edges. Patches up to 1.4mm 6.5% carbonate - an-euhedral, always in glass max 0.3mm tr.	_____		1	yes	yes
SH86/38e	pale: yellow/pinkish/ bluish. Intimately intergrown with amph, opaques, plag. 0.8-30mm (whole section) 32.5%	Ti-magnetite - anhedral, blobby, non-equant, intergrown, skeletal max 11mm 14% Spinel-hercynite - blobs, anhedral. max 0.6mm 1% pyrrhotite - blobs up to 0.18mm tr.	clear/red brown/ greenish brown. Extremely intergrown with cpx, opaques, plag 1.4-30mm+ (whole section) 47.5%	_____	Plagioclase - extremely inter-grown with cpx, amph, opaques. Interstitial, poor twins. An79-67 (probe) 0.2-6mm 2.5%	_____	glass - in small patches, altered to fine material max 1.2mm 2.5%	red mineral - see SH88/14q		2	yes	no
SH86/38f	pale green/pale yellow anhedral, in intergrown groups of 0.2mm crystals + some larger crystals; sub-euhedral 0.3-1.2mm 0.5%	Ilmenite - an-subhedral, unaltered max 0.7mm 0.35% Ti-magnetite - an-euhedral altered. max 0.4mm 0.15%	clear/red brown/ olive green. Sub-euhedral Slightly corroded max 4mm 35%	pale yellow/red black/ greenish brown. Sub-anhedral. Replacing amph 0-4mm 7.5%	Plagioclase - anhedral, but prob. orig. euhedral, inter-grown laths, very fine twins An40-17 (probe) max 5mm 49.5%	euhedral, earliest crystallising Largest have inclusion-rich cores. max 0.5mm 0.5%	glass - pale brown,unaltered Contains plag quench xtals. Adjoining minerals have sharp edges, except plag with sieved margins. Patches up to 3mm 6% carbonate - euhedral xtals in glass. max 0.4mm 0.5%	sphene - an-euhedral 0.2-2.4mm tr.	Unusual in that the glass is not in equilibrium with the plagioclase, and has caused sieving of its margins.	2	yes	no
SH86/38g	pale green, anhedral only as cores in amph 0.1-1mm tr.	Ti-magnetite sub-anhedral max 0.2mm 7% Ilmenite - anhedral, usually larger than the ti-mag. 0-2.4mm 0.5%	pale yellow/red brown/ greenish brown. An-subhedral max 6.5mm 48.5%	_____	Plagioclase - an-subhedral, intergrown laths, some strong zoning, medium twins An56.5-42 (probe) max 4.5mm 30.5%	euhedral, earliest crystallising max diam 0.4mm length 1mm 6%	glass - altered to fine material, quench crystals of plag. Adjoining minerals have sharp edges. Patches up to 6mm 7.5%	_____		2	yes	no
SH86/38h	pale: yellow/pinkish/ bluish. Anhedral, some-times as cores in amph Rare subhedral max 0.7mm (coarse) 0.5% max 0.5mm (fine) 1%	Ti-magnetite - anhedral, non-equant, angular, interstitial coarse; max 1.1mm 9.5% fine; max 0.6mm, elongated parallel to layering 12.5%	pale yellow/red brown/ greenish brown. Anhedral coarse; max 2.3mm, most >0.3mm 71% fine; max 2.7mm, most <0.3mm 75%	_____	Plagioclase - poikilitically enclosing amph + cpx, less poikilitic in coarse grained area, but similar size. An60.5-59 (probe) max 1.6mm 1.5% (coarse) 3% (fine)	euhedral, earliest crystallising max diam 0.4mm length 1mm 9% (coarse) 4.5% (fine)	glass - altered to fine material. Some adjoining amph crystals have sharp edges, others less so ?resorbing. Patches up to 1mm 8.5% (coarse) 4% (fine)	_____	Section shows pronounced layering, with grain size defining layers, with similar mineralogy. Fine grained layer has long axes of amph and opaques parallel to grain size boundary.	2	yes	no

4.5.2 Evidence for cumulate origin

Various lines of evidence lead to the interpretation of the coarse-grained blocks as cumulates. Two of the most compelling are the presence of layers, graded by both grain size and by mode, and interstitial glass which is clearly not a partial melt.

Layering

Layering is seen most clearly in 88/14q, 88/14k and 86/38h. In 88/14q there are three distinct modal layers:

1) *plagioclase + biotite + some apatite*

2) *plagioclase only*

3) *biotite + resorption products + minor plagioclase + apatite*.

and 88/14k also has three layers:

1) *plagioclase-rich [+ amphibole + biotite + minor cpx]*

2) *amphibole-rich [+ plagioclase + biotite + minor cpx]*

3) *plagioclase + amphibole as elongate crystals [+ biotite]* *(cpx absent)*

The grain size does not vary systematically between layers in either of these specimens. In 86/38h, by contrast, there are two layers distinguished only by a prominent change in grain size, with almost identical modes; 73% amphibole, 11% Ti-magnetite, 7% apatite, 6% glass, 2% plagioclase and 1% cpx. Most amphibole grains are <0.3mm in the fine layer and >0.3mm in the coarse layer, but the size of the largest grain is similar in both layers (2.3mm coarse, 2.7mm fine) suggesting that sorting alone produced the layers. The block is also laminated, with elongate amphibole and Ti-magnetite crystals aligned parallel to the grain-size boundary. All these features are clearly visible in Figure 4.5.2.

Interstitial glass

Almost all the blocks have some interstitial glass, although frequently altered to fine breakdown products. Where unaltered the glass is uniform in colour and minerals adjacent to it show sharp facets, as shown in Figure 4.5.3. The presence of the latest formed minerals as phenocrysts in the glass patches, for example, zircon and sphene (see Figure 4.6.28), shows that crystallisation continued until the glass was quenched, presumably at eruption. If this glass was a partial melt it would have caused sieving and rounding of the adjacent crystals. Although clinopyroxene is partially resorbed where adjacent to glass patches, no other minerals are affected. If the glass was injected from the host liquid that carried the nodule to the surface it would all have the same composition, even in different blocks. Analyses show that this is not the case, and the variation in glass composition is described in section 5.7.2.

Many minerals which are normally seen only as anhedral sutured grains are euhedral in the glass, suggesting that they were originally euhedral before overgrowth. Examples are cpx, amphibole and Ti-magnetite in 88/14m (Figure 4.6.30), and biotite and anorthoclase in 88/14a (Figures 4.5.8 and 4.5.9).

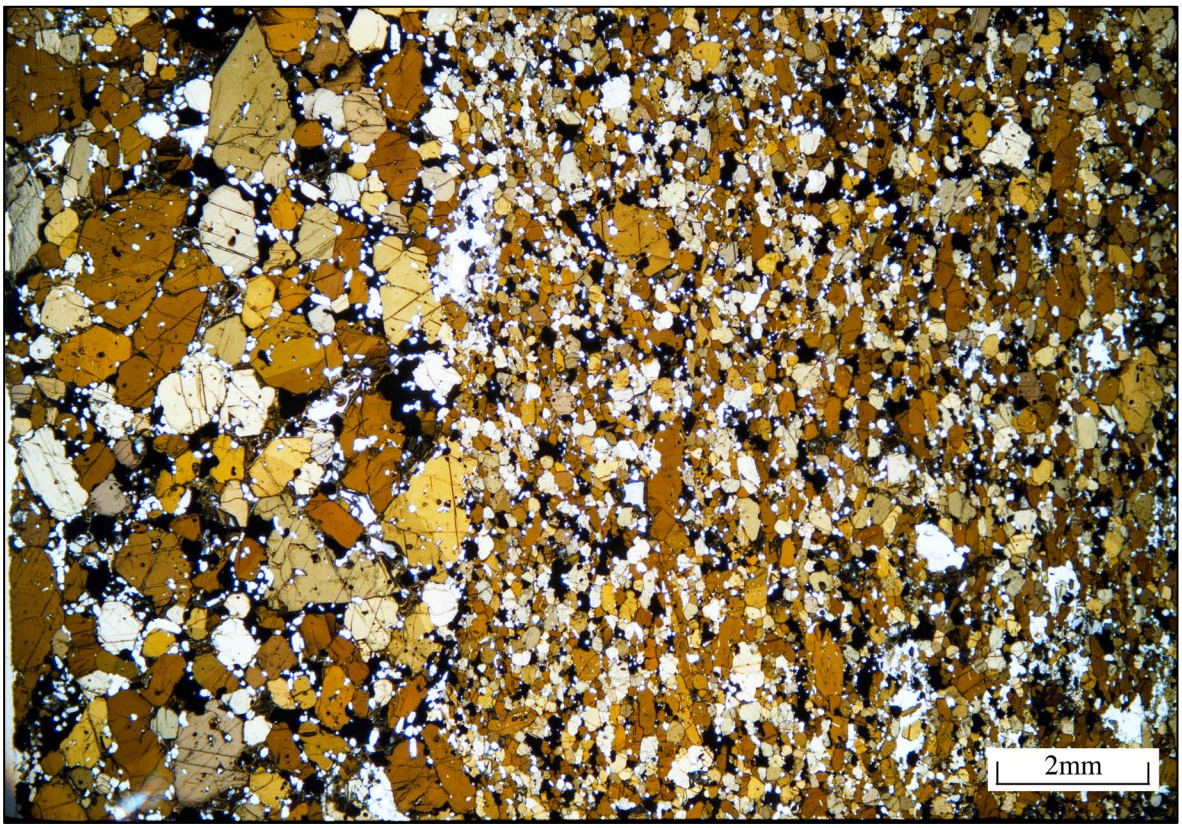


Figure 4.5.2. Grain-size layering in specimen 86/38h. Most of the field of view is filled with brown kaersutite, with numerous colourless apatite inclusions. The few larger, anhedral colourless patches are plagioclase. Ti-magnetite and cpx, although present, are hard to identify in this photograph. (Plane polarised light).



Figure 4.5.3. Brown to olive-green kaersutite crystals in specimen 88/14u, with euhedral shapes where in contact with the light brown glass, show that the glass represents an intercumulus liquid. The large area of colourless material is sodic plagioclase, and apatite is ubiquitous. The glass also contains blobs of an immiscible carbonate melt (see section 4.6.11). (Plane polarised light).

The evidence shows that the glass represents intercumulus liquid, which enabled crystal growth to fill all interstices, in many cases to produce an adcumulate.

Other evidence

Some sections show classic orthocumulate texture, with euhedral cumulus crystals, and sub-poikilitic post-cumulus material filling the interstices. Examples include 88/14e with cumulus amphibole, apatite, sphene, biotite and Ti-magnetite and postcumulus plagioclase, and 88/14g with cumulus amphibole, apatite and opaques and postcumulus plagioclase (shown in Figure 4.5.7). The least evolved blocks have cumulate textures visible with the naked eye, with cpx crystals apparently earliest, and opaques growing in the interstices.

However, as with the feldspars in the most evolved blocks, these cpx crystals are completely sutured together (see Figure 4.5.5).

The wide range of minerals and assemblages displayed by the series of blocks, with a continuous range of compositions, is also evidence that they are cumulates produced by fractional crystallisation of a single batch of parent magma. The best example of this is the feldspar compositional trend (Figure 4.6.11) which shows very little scatter from An_{82} to Or_{26}. This contrasts with that of the lava phenocrysts (Figure 3.2.14). The same pattern was found by Harris (1982) for the Ascension Island lavas and the NASA-facies cumulates. The phenocrysts of the lavas show this scatter probably because they crystallised polybarically from a wide range of magma compositions.

Summary

The coarse-grained blocks were all part of a single cumulate stack produced by the differentiation of a single parent body of magma. Using the terminology of Wager *et al* (1960), the least-evolved blocks are adcumulates and all others are meso- to orthocumulates, with more or less postcumulus overgrowth. Normal zoning in the postcumulus minerals shows that the connection with the main magma body lasted long enough to record its changing composition. The complete overgrowth of clinopyroxenes in the least-evolved blocks, with no zoning, suggests that overgrowth during this period was rapid, or that the liquid composition changed only slowly during their crystallisation.

4.5.3 Subdivision of the cumulates

A summary of the progression from least to most evolved block is presented in Figure 4.5.4, based on the assumption that Na_2O increases with fractionation. The mineralogy follows much of the sequence of phenocrysts seen in the extrusive rocks of the Velay, with the notable exception of olivine, which is never found in these blocks. Spinel-hercynite (pleonaste) is present in the most primitive blocks and is also found in the ankaramites of the Velay lavas (see section 3.1.5), which may themselves have swept up cumulus crystals from the base of a magma chamber.

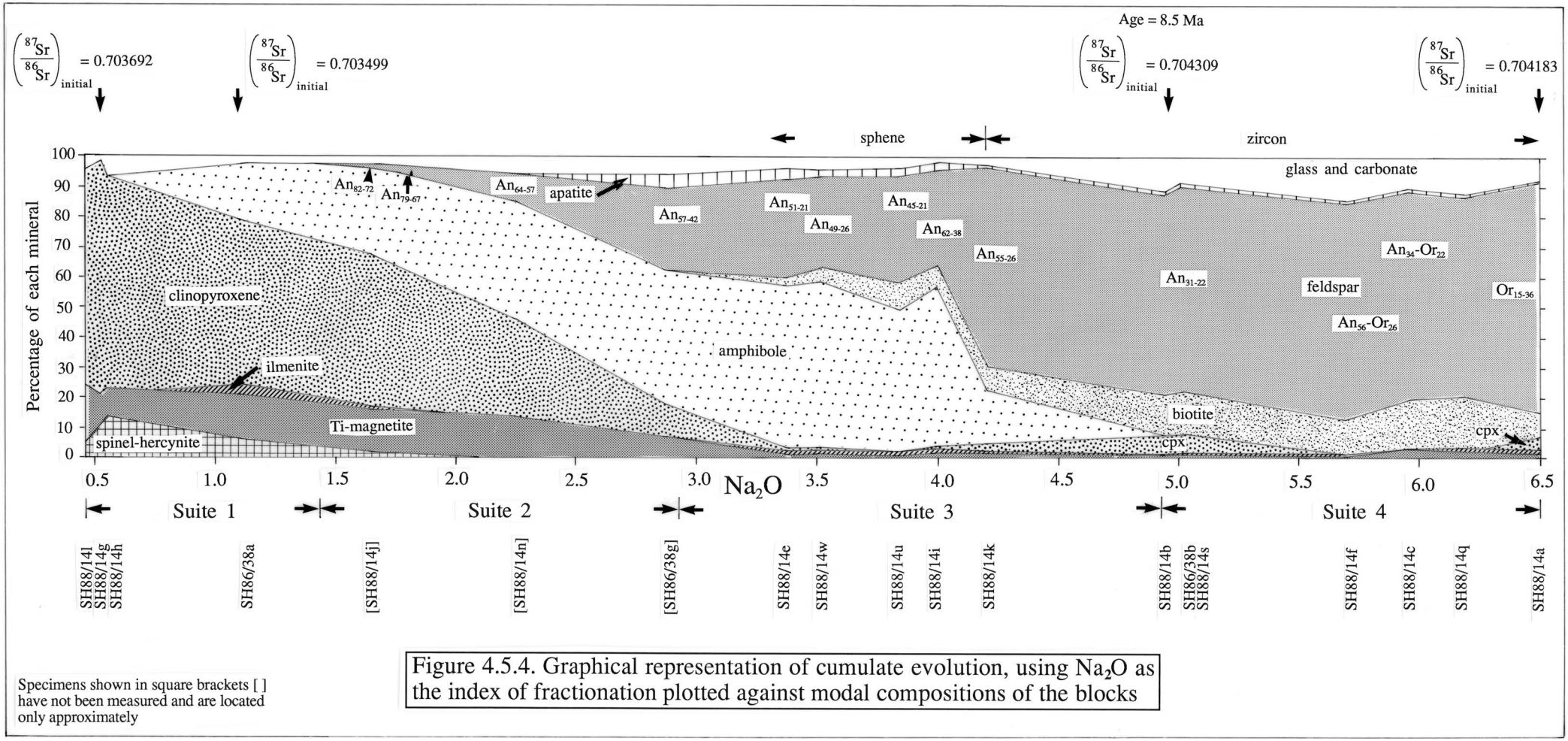


Figure 4.5.4. Graphical representation of cumulate evolution, using Na_2O as the index of fractionation plotted against modal compositions of the blocks

Specimens shown in square brackets [ ] have not been measured and are located only approximately

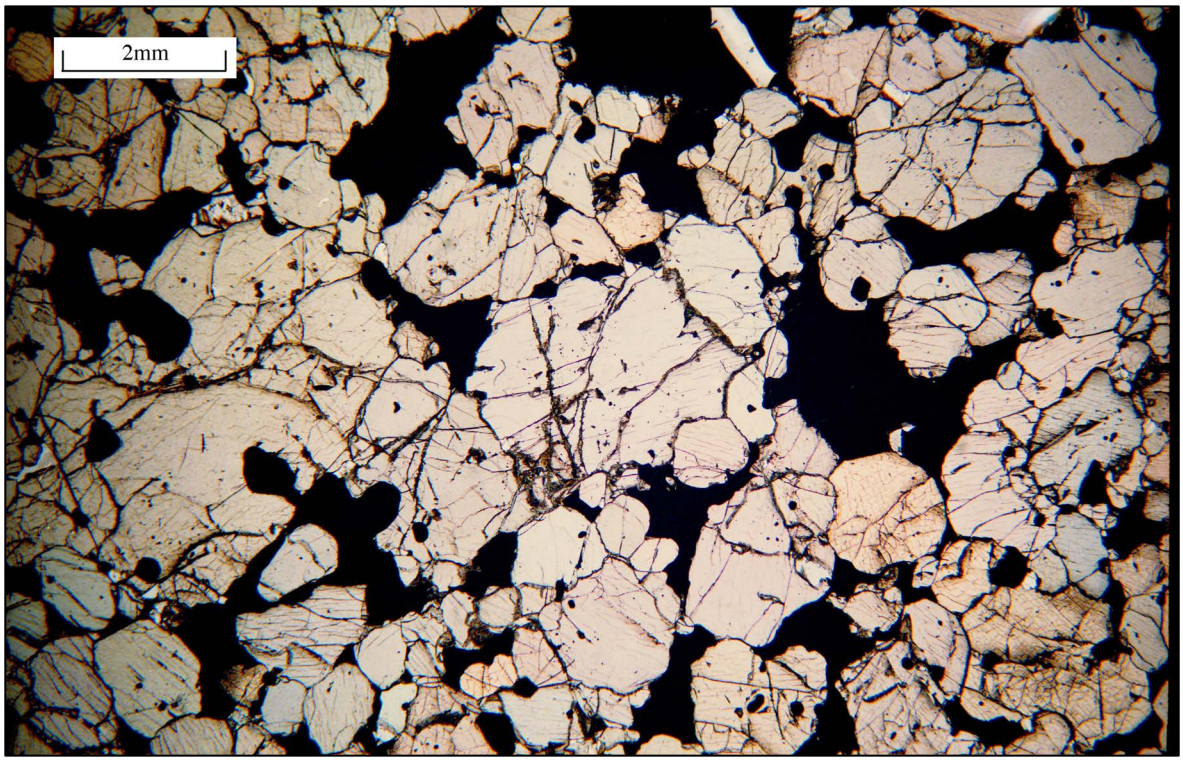


Figure 4.5.5. Sample 88/14v is one of the more basic blocks of Suite 1. It is composed mainly of equant pinkish clinopyroxene, with interstitial opaques (Ti-magnetite, pleonaste and ilmenite). The clinopyroxenes and the centres of the larger opaque patches were probably eu-subhedral before adcumulus overgrowth. (Plane polarised light).

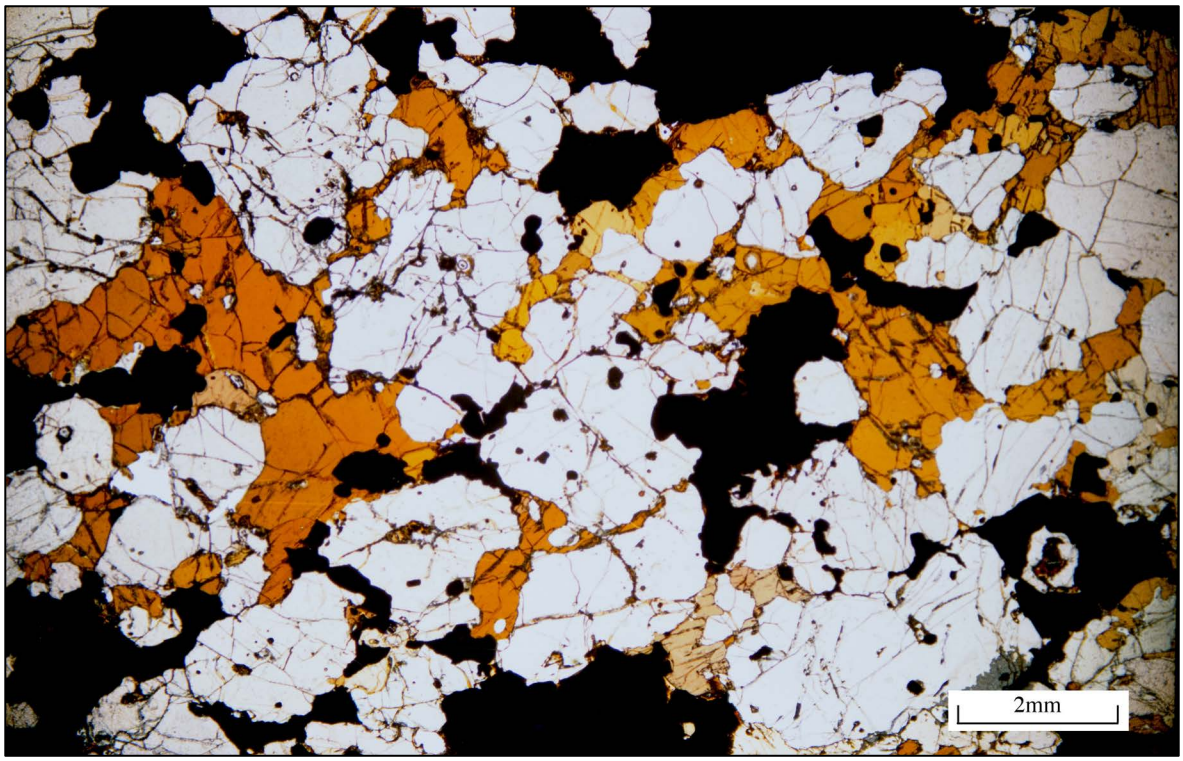


Figure 4.5.6. Sample 86/38a, also in Suite 1, is slightly more evolved than 88/14v (above). It has the same minerals, with the addition of interstitial kaersutite, which suggests that an intercumulus liquid more evolved than that in 88/14v fed their growth. The kaersutites in Suites 2 and 3 are sub-euhedral, indicating that they formed by crystal settling (see Figure 4.5.7). (Plane polarised light).

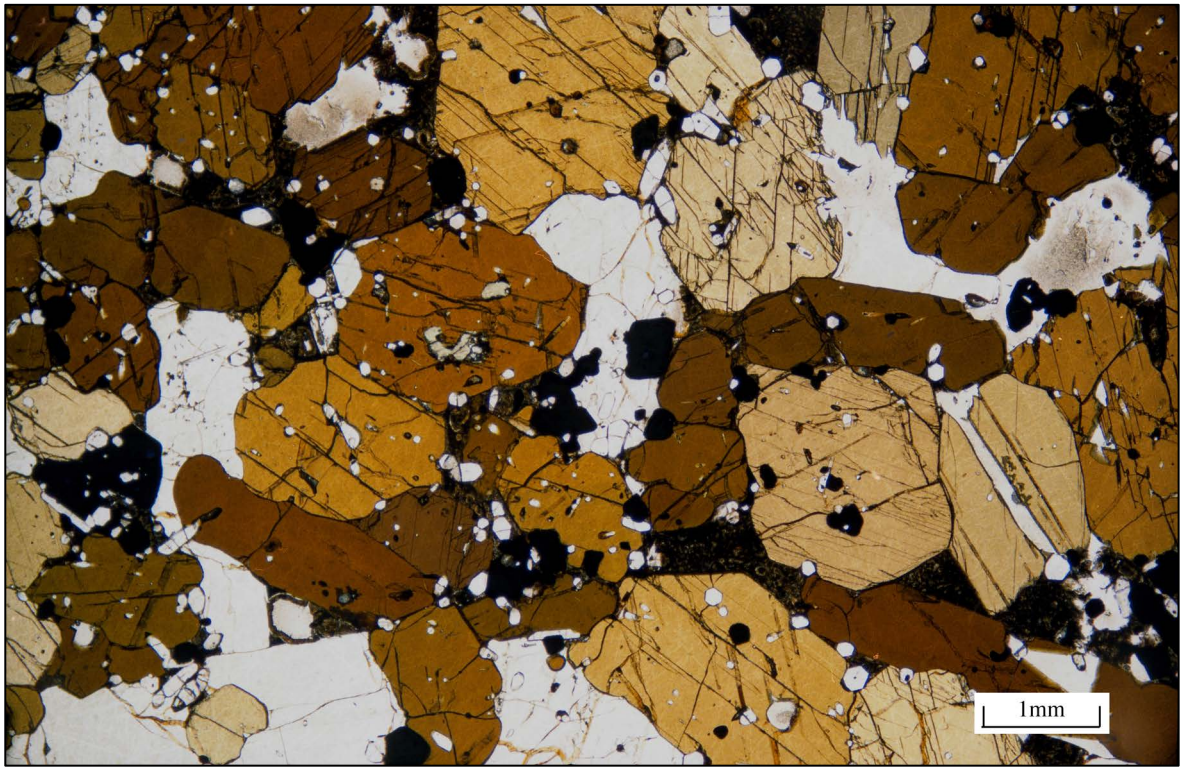


Figure 4.5.7. Suite 2 is represented here by block 86/38g. Minerals are sub-euhedral brown/yellow kaersutite, colourless anhedral plagioclase and, within the other minerals, colourless euhedral apatite. In this block the apatite and kaersutite probably settled from the melt, possibly with minor plagioclase, then adcumulus growth of the plagioclase filled in the interstices. There are also some dark areas of altered glass in this section, against which the amphiboles show sharp crystal faces. (Plane polarised light).

The blocks can be divided into four suites, as marked on Figure 4.5.4. They are defined as follows:

Suite 1 - no feldspar present

Suite 2 - feldspar and amphibole present, biotite absent

Suite 3 - feldspar, amphibole and biotite present

Suite 4 - feldspar and biotite present, amphibole < 2% (only as remnant crystals)

Suite 1

(Blocks 88/14d, 14g, 14h, 14l, 14m, 14p, 14v, 25 and 86/38a)

Pyrrhotite droplets and fragments are the earliest phase, followed by equant, anhedral clinopyroxene and rounded pleonaste, which crystallised together. Ti-magnetite apparently filled the interstices left after the accumulation of the earlier minerals (see Figure 4.5.5). The most primitive blocks have no amphibole, and glass and carbonate fill interstices, the glass occasionally containing quench crystals of amphibole. More evolved blocks contain ilmenite, which crystallised at the same time as the pleonaste. Amphibole is more abundant in these blocks and forms interstitial crystals enclosing the other minerals (see Figure 4.5.6).

The sequence of crystallisation is:

pyrrhotite ⇒ cpx + pleonaste + ilmenite ⇒ Ti-magnetite ⇒ amphibole ⇒ carbonate + glass

Suite 2

(Blocks 88/14j, 14n and 86/38e, 38g, 38h)

The most primitive blocks of this suite resemble those of Suite 1, with the addition of plagioclase. Pyrrhotite droplets are again the earliest phase, sometimes followed by a small proportion of ilmenite or pleonaste. Clinopyroxene and Ti-magnetite follow, apparently crystallising at the same time. Poikilitic amphibole appears next and interstitial plagioclase (An_{82-72}) is the last phase. Glass fills any remaining interstices.

Blocks with slightly more evolved compositions have distinct characteristics. Pleonaste and ilmenite are still occasionally present and the cpx and amphibole are intimately intergrown, with originally equant cpx crystals enclosed, and sometimes patchily replaced by the amphibole. This replacement requires the addition of Na, Al, K, Ti, and Fe from the liquid. The seamless transition between the two phases suggests that the change in structure from single to double-chain silicate is easily accommodated. The proportion of amphibole continues to increase in the more evolved blocks, with some showing complete intergrowth/replacement of cpx, amphibole, opaques and plagioclase.

In the most evolved blocks of this suite cpx is present only as tiny fragments in the cores of amphibole crystals. Amphibole and plagioclase (An_{64-42}) become cumulus phases at this stage, with traces of an originally euhedral shape visible in their zoning patterns. Apatite also appears towards the evolved end of this suite (see Figure 4.5.7), at roughly the same point as pleonaste disappears. It rapidly reaches a maximum of 4% before declining. Glass and occasionally carbonate are present

throughout this suite, as remnants of the original adcumulus liquid. The crystallisation sequence in this suite is:

pyrrhotite ⇒ pleonaste + ilmenite ⇒ cpx + Ti-magnetite ⇒ amphibole ⇒ plagioclase ⇒ glass + carbonate
(in the most primitive blocks)

pyrrhotite + apatite ⇒ cpx + Ti-magnetite ⇒ amphibole ⇒ plagioclase ⇒ glass + carbonate
(in the most evolved blocks)

Suite 3

(Blocks 88/14e, 14i, 14k, 14t, 14u, 14w and 86/38f)

These blocks have fairly uniform mineralogy. Apatite is always the first to crystallise, followed by Ti-magnetite and ilmenite in roughly equal proportions. Rare traces of cpx are found in most blocks, either in the cores of amphiboles, or as clusters of small crystals surrounded by biotite. Euhedral kaersutite appears after the cpx, with partial replacement by biotite, either as small patches growing within the kaersutite (see Figure 4.6.25), or as euhedral overgrowths. The conversion of kaersutite to biotite involves the removal of Na and Ca, and the addition of K and Fe by the adcumulus liquid. The boundary between the two phases is much less gradational than between the cpx and amphibole, appearing as a sharp transition, the biotite usually showing at least some crystal faces against the amphibole. Thus it seems that the change from the double-chain structure of amphibole to the sheet structure of biotite is much less easily accommodated than that of cpx to amphibole.

Plagioclase appears after the biotite, initially as cumulus crystals of An_{50-60}, with later adcumulus overgrowth reaching An_{20} and producing clearly visible zoning. Patches of interstitial glass are commonly preserved, often with sphene crystals growing within it, sometimes by reaction with opaques (see Figures 4.6.28 and 4.6.29). An increase in oxygen fugacity, combined with Ca-release from the resorbed amphiboles, is probably the cause of this reaction (see section 3.2.9). Specimen 88/14k contains both sphene and zircon, and more evolved blocks have only zircon.

The crystallisation sequence in this suite is:

apatite ⇒ Ti-magnetite + ilmenite ⇒ cpx ⇒ amphibole ⇒ biotite ⇒ plagioclase ⇒ sphene/zircon ⇒ glass + carbonate

Suite 4

(Blocks 88/14a, 14b, 14c, 14f, 14q, 14s and 86/38b)

Figures 4.5.8 and 4.5.9 show ppl and xpl views of 88/14a, the most evolved block. In this suite, as in Suite 3, apatite is the first mineral to form, followed by Ti-magnetite and ilmenite in roughly equal proportions. Cpx reappears in significant quantities in these blocks, as a pale green salite, occasionally with cores of a pinkish colour. It is not in equilibrium with the glass and shows varying degrees of resorption, from virtually none to total, so it is difficult to estimate the proportion originally present. The blocks with least resorption have 5 - 7% cpx, and as Figure 4.5.4 shows, blocks which have less cpx than this often have a higher proportion of glass. Biotite is present as

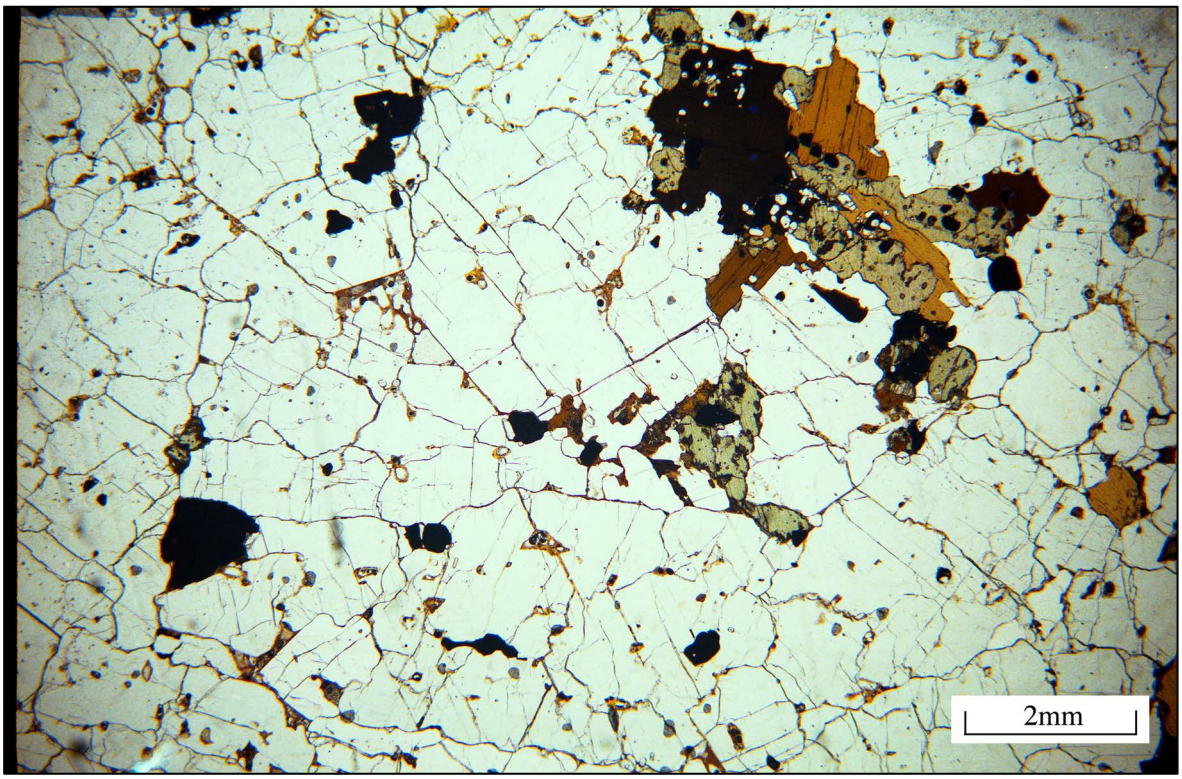


Figure 4.5.8. Block 88/14a is one of the most evolved in Suite 4, mainly composed of alkali-feldspar. This view, in plane polarised light, shows the biotite (brown to black) and the pale green clinopyroxene, which shows signs of reaction. Apatite is also visible as inclusions in the other minerals. The feldspar contains numerous small patches of brown interstitial glass, showing how thoroughly adcumulus growth has filled in the structure.

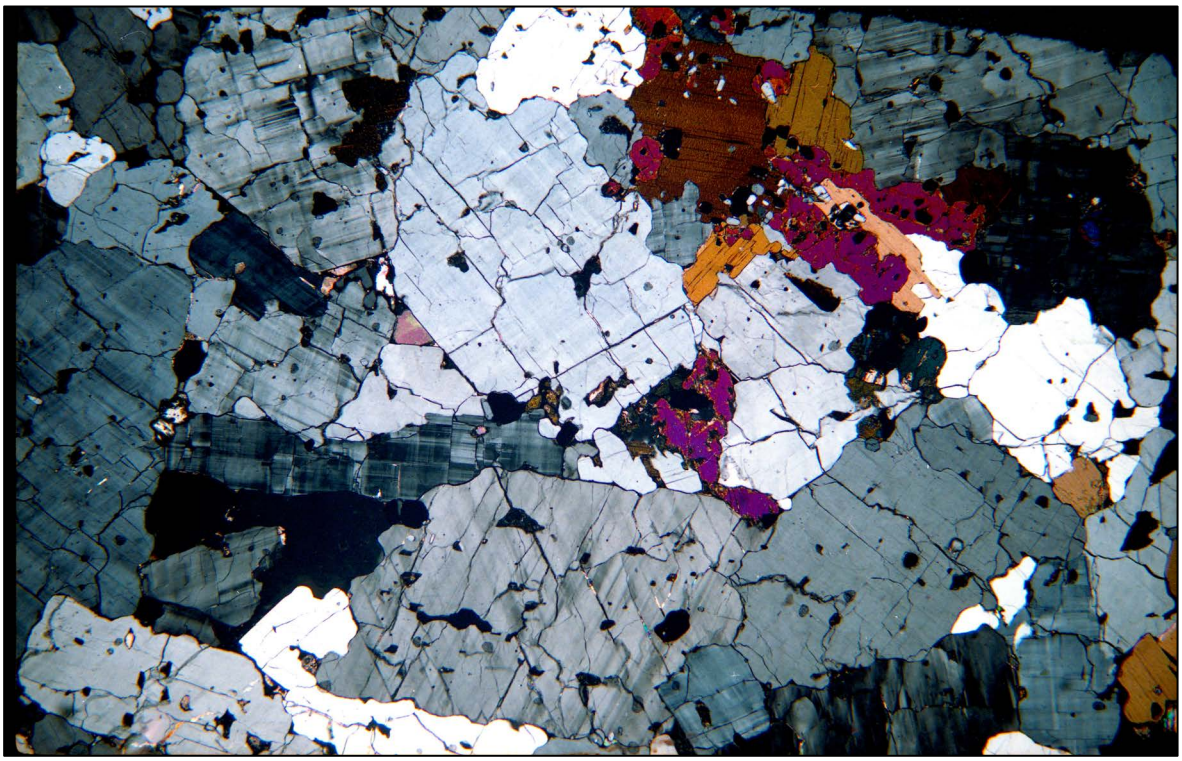


Figure 4.5.9. This photograph shows the same area of 88/14a as above, but with crossed polarisers. The clinopyroxene and biotite can be distinguished more easily and the outlines of the feldspars are revealed, with their anorthoclase “cross-hatching”. The feldspar crystals were probably euhedral and settled from the melt to form this rock. The small interstitial patch with high birefringence (pink/green), slightly to the left of centre, is carbonate.

euhedral crystals and was clearly a cumulus phase in this suite. Feldspar appeared shortly after the biotite and adcumulus overgrowth on the originally euhedral cumulus crystals resulted in strong zoning, with a range of An_{31-22} at the start of the suite, reaching Or_{15-36} (anorthoclase) in the most evolved example, with continuous variation. Carbonate and zircon appear in the glass. The crystallisation sequence is:

apatite ⇒ Ti-magnetite + ilmenite ⇒ cpx ⇒ amph ⇒ biotite ⇒ feldspar ⇒ zircon ⇒ glass + carbonate

These minerals and their order of crystallisation resemble the phenocrysts in the trachyte blocks (section 4.2.2).

4.6 Mineral descriptions and chemistry

4.6.1 Clinopyroxene

Clinopyroxene (cpx) is present in almost all of the blocks of the cumulate series. In Suite 1 it forms 78-43% of the rock and is anhedral, equant and unzoned with very faint pink/yellow/bluish pleochroism. Grain size is ≤ 14mm, twins are occasionally present, and the only inclusions are rounded opaque blobs. From the texture of these blocks, especially 88/25, it seems likely that the clinopyroxene crystallised early, with later overgrowth and interstitial crystallisation of Ti-magnetite obscuring what were probably originally euhedral forms. Figure 4.5.5 shows an example.

At the start of Suite 2, blocks 88/14j, 14n and 86/38e have 62.5-32% clinopyroxene with the same appearance as in Suite 1. Samples 88/14j and 88/14n have grains up to 6mm, but 86/38e is composed of very large intimately intergrown crystals of cpx (> 30mm), amphibole, opaques and plagioclase. 86/38h has only 0.75% of the same pink/yellow/blue cpx. At the end of the suite, 86/38g has a few anhedral 0.1-1.0mm grains of a pale green cpx in the cores of amphiboles.

Suite 3 blocks contain small (< 0.5mm) grains of pale green/yellow cpx, usually in the cores of amphibole crystals. A few larger (≤ 2.2mm) crystals are present as phenocrysts and although these are corroded and anhedral, their outlines suggest they were once euhedral. Proportions vary from 0.5% to 2.5%. Block 88/14t is an exception with 14%, but its clinopyroxenes are more like those in Suite 1 than the pale green cpx and are probably re-entrained fragments of an earlier cumulate.

At the end of the series, in Suite 4, the pale green/yellow cpx occasionally forms as much as 7% of a given block, although it is always strongly corroded and clearly not in equilibrium with the melt (see Figure 4.5.8). Maximum size is 5mm, and some grains have pinkish cores, suggesting, as in 88/14t, the re-entrainment of earlier formed cpx. Blocks 88/14f and 88/14q have no cpx, but the shapes of alteration patches show that it was originally present. Most of the cpx in these blocks is an-subhedral, but the shapes of the areas of cpx + alteration products sometimes indicate that they were originally euhedral, and probably settled from the melt.

A 30mm cpx megacryst (88/14r) was also found in the pyroclastics. It has the same pleochroism as the cpx in Suite 1, and contains pockets of glass + carbonate with tiny quench crystals of clear/brown amphibole. Three analyses of this cpx are marked on the graphs presented in this section (using diamond symbols) and they fall roughly on the boundary between Suite 1 and Suite 2

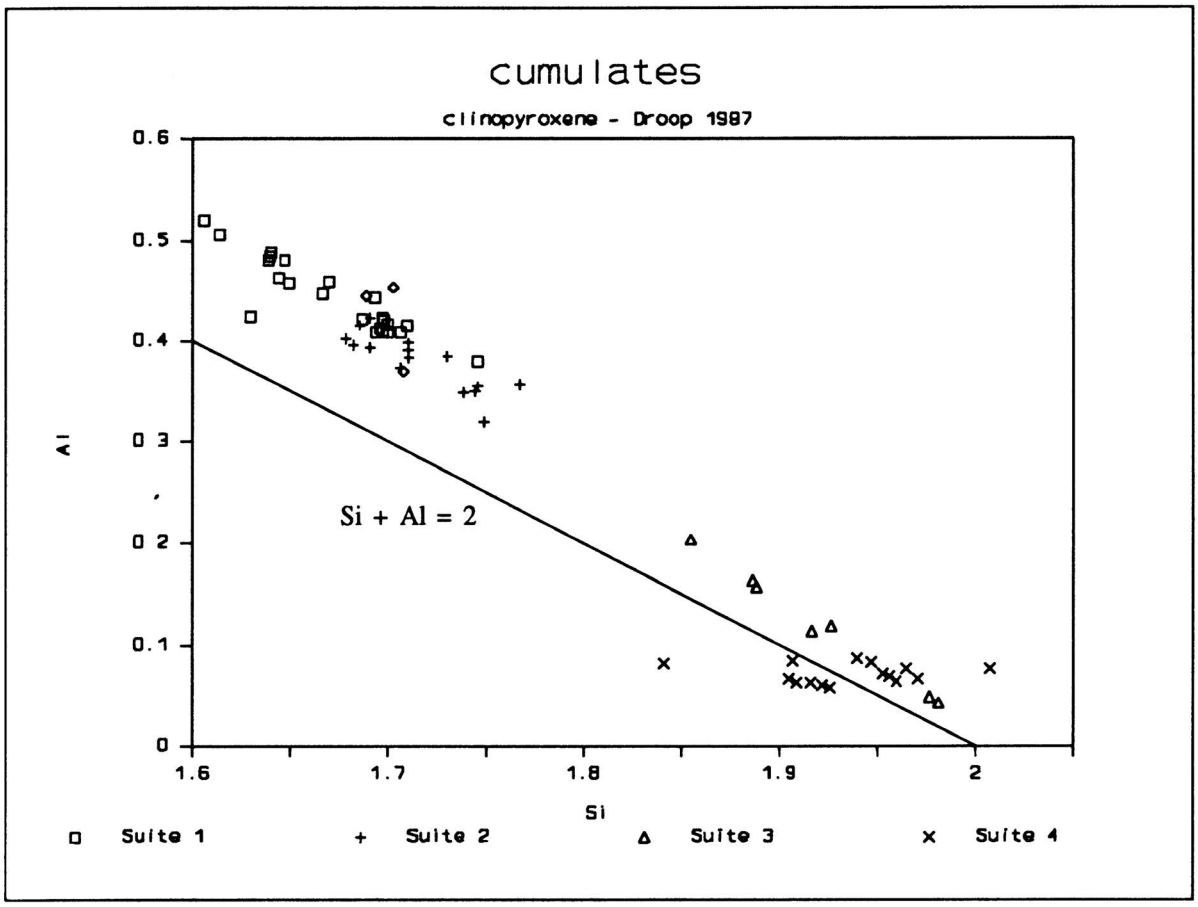


Figure 4.6.1
(diamonds are analyses of cpx megacrysts)

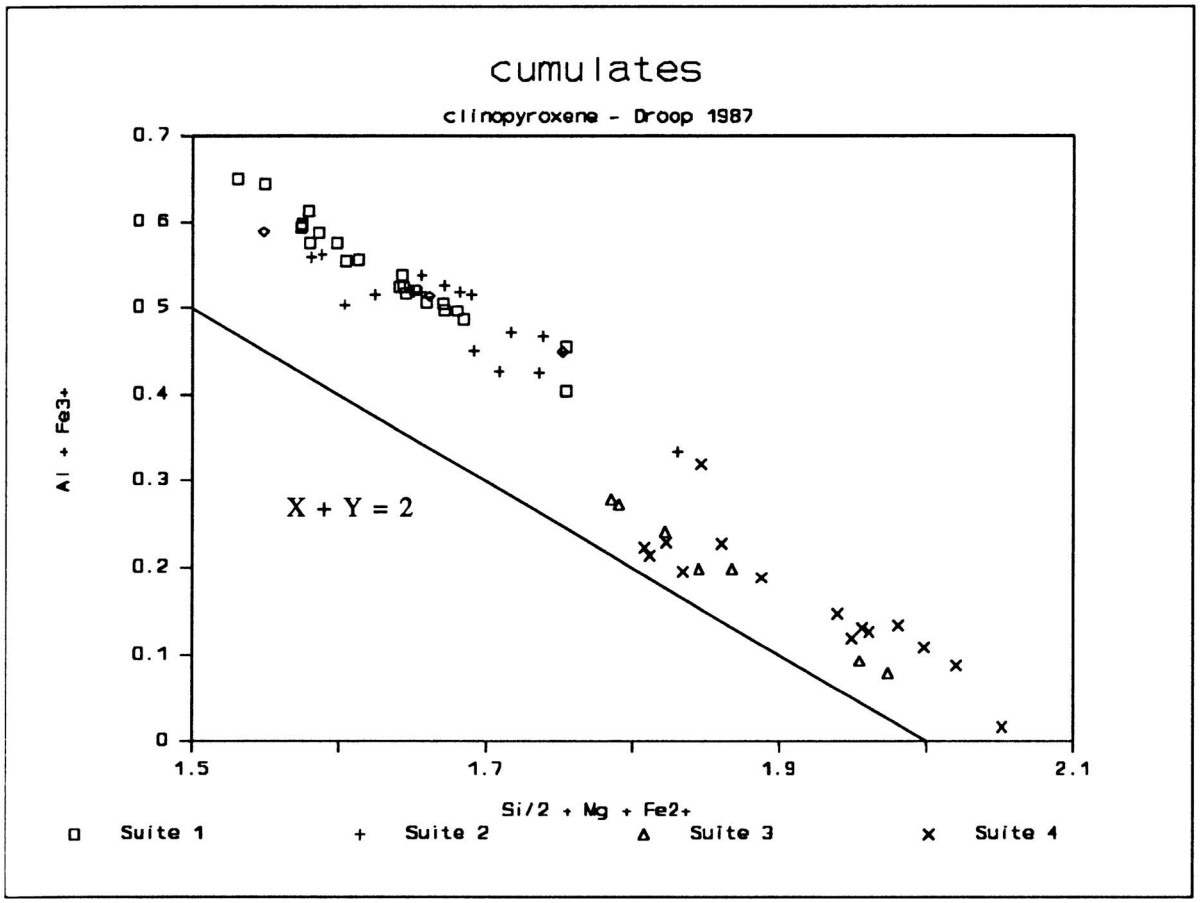


Figure 4.6.2
(diamonds are analyses of cpx megacrysts)

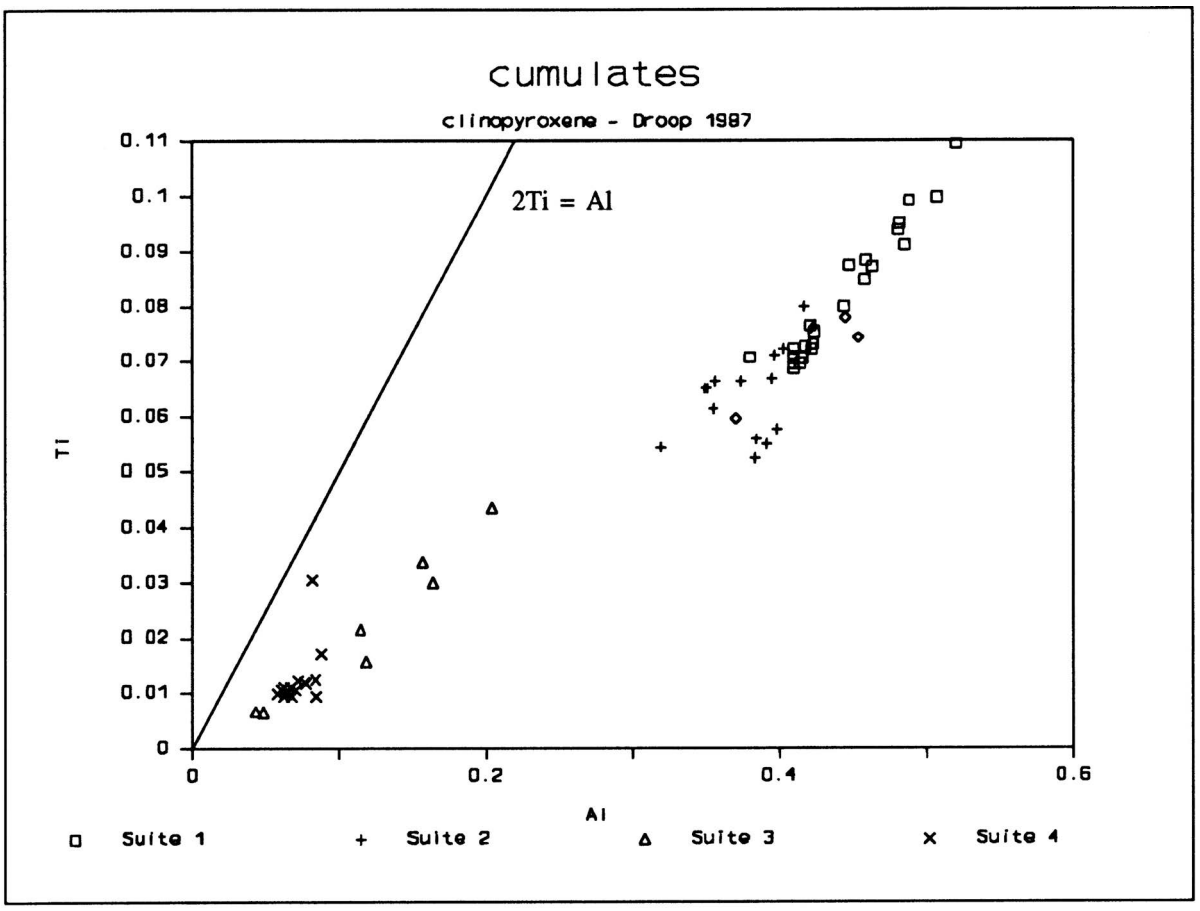


Figure 4.6.3
(diamonds are analyses of cpx megacrysts)

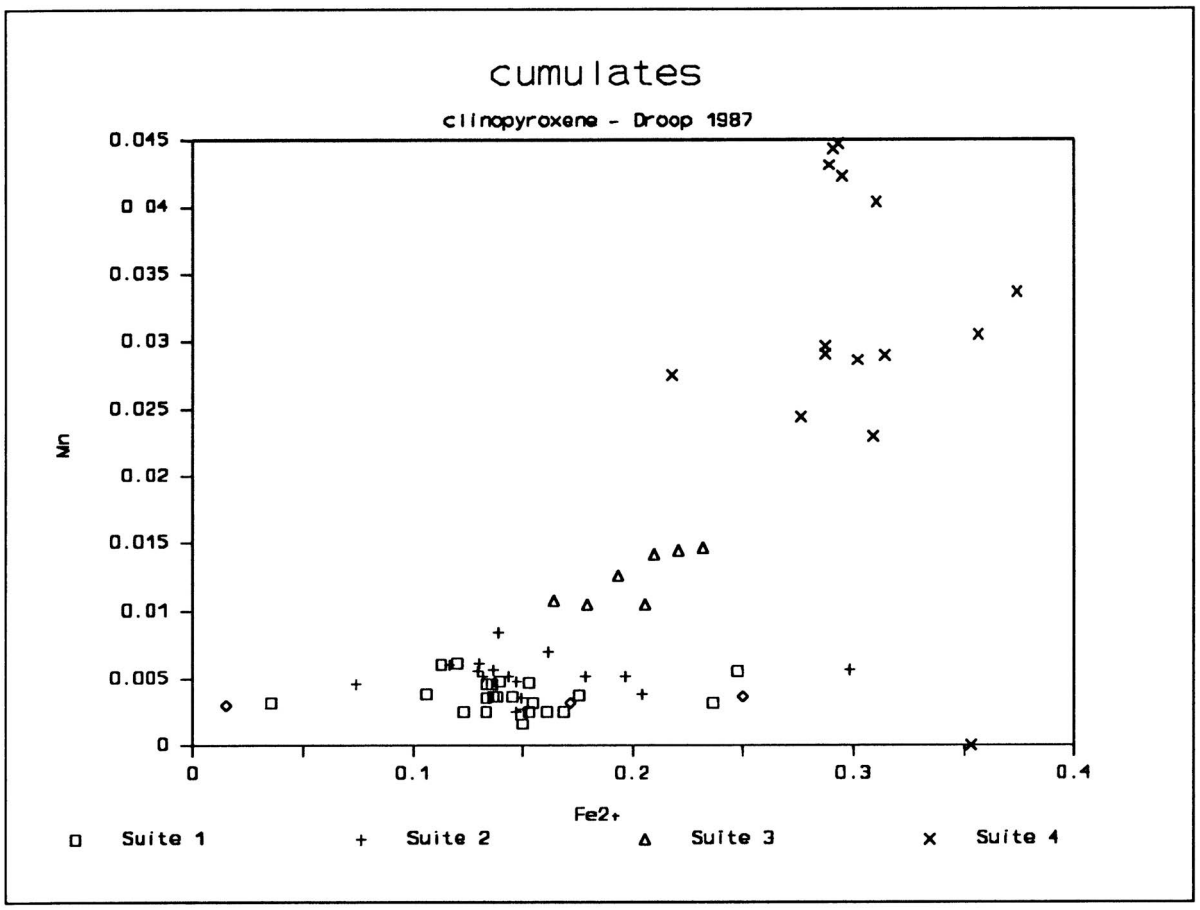


Figure 4.6.4
(diamonds are analyses of cpx megacrysts)

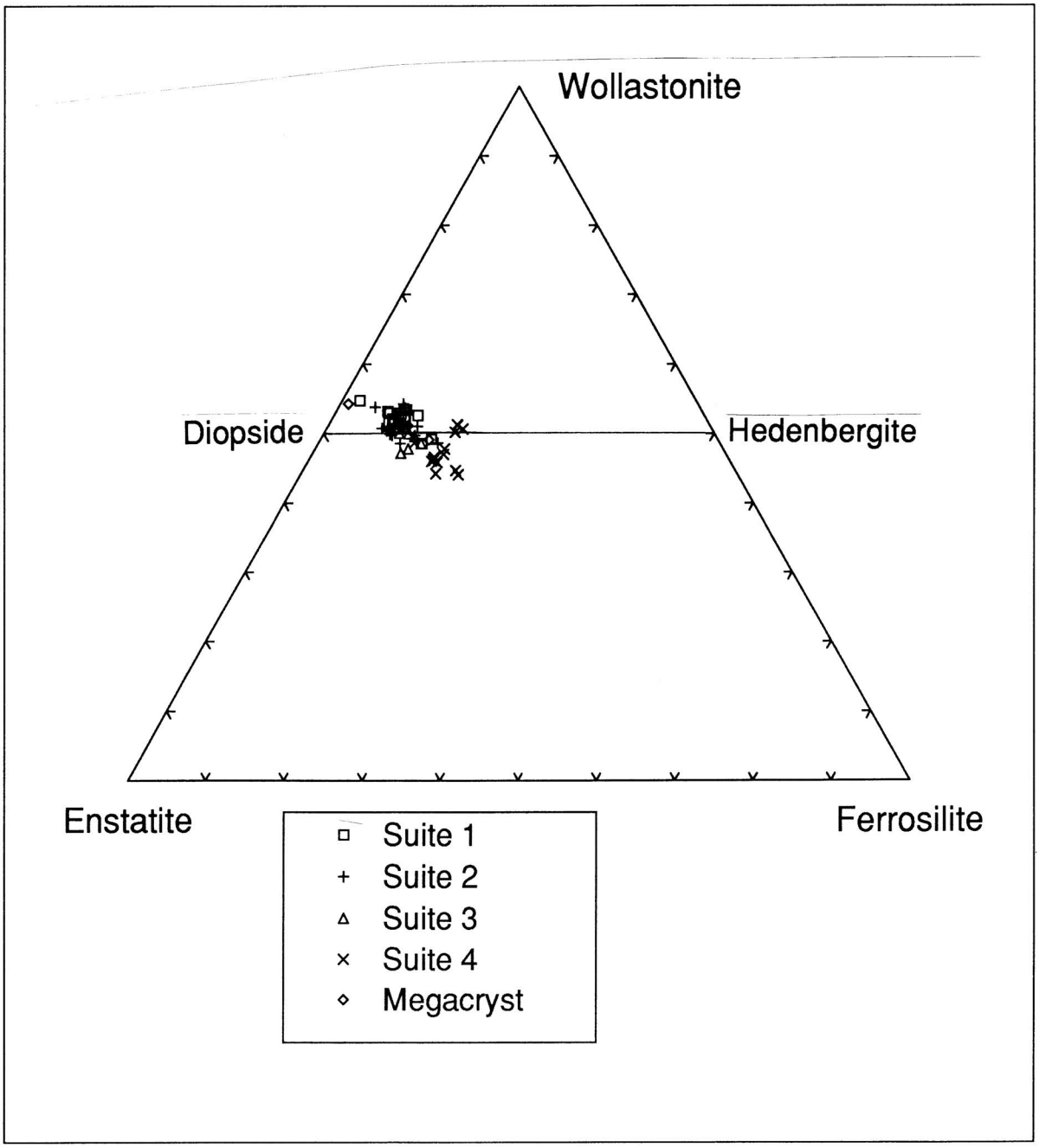


Figure 4.6.5. Triangle diagram of clinopyroxenes from the cumulate blocks. Almost all lie outside the area of the "pyroxene quadrilateral" (<50% wollastonite), probably due to overestimation of the Fe^{3+}-content. Despite this, it is clear that the compositions of the cpxs are all quite similar, except for those of Suite 4, which show a slight Fe-enrichment and a change in colour, from the pale pink of Suites 1 and 2, to pale green.

clinopyroxenes. This is the composition of the cpx in 86/38e, with its large-scale intergrowth. Although 88/14r shows no intergrowth, it is interpreted here as a single disaggregated crystal from a giant-grain cumulate.

The composition of the common pyroxenes is:

$$Ca_{0-1}(Mg,Fe^{2+})_{1-2}Si_2O_6$$

However, this neglects the other components that may be present, such as Al, Fe^{3+}, Ti, Na and Mn, which reach maximum values of 0.5, 0.25, 0.11, 0.11 and 0.05 atoms per formula unit (apfu) respectively in the pyroxenes of the cumulates.

Figure 4.6.1 shows that Al substitutes for Si, with a slight surplus of Al. The main solid solution involved is towards the $Ca(Al,Fe^{3+})AlSiO_6$ (FaTs) end member, by the exchange $(Mg,Fe^{2+})Si \Leftrightarrow (Al,Fe^{3+})_2$. Figure 4.6.2 demonstrates this exchange, with a surplus of $Al+Fe^{3+}$. Most of this surplus can be accounted for by solid solution towards the $CaTiAl_2O_6$ (CaTi) end member as shown in Figure 4.6.3.

Mn is weakly correlated with Fe^{2+} (Figure 4.6.4), and is probably accepted by the lattices of the later formed cpxs. Na does not show any correlation with Fe^{3+} (aegirine) or Al (jadeite).

The highest levels of solid solution reached are 23% FATs and 11% CaTi, both of which occur in the Suite 1 pyroxenes, the Suite 4 pyroxenes having only normal quadrilateral components. The pyroxene quadrilateral is shown in Figure 4.6.5.

The green colour of the Suite 3 and 4 pyroxenes is not due to aegirine solid solution but to their higher Fe^{2+}/Mg compared with those of Suites 1 and 2. The faint purplish pleochroism of the Suite 1 and 2 pyroxenes is probably due to their TiO_2-content (up to 3.8%). The decline of the $CaAl_2SiO_6$ Ca-Tschermak's component (CaTs) is probably due to the increase in a_{SiO_2}, causing the reaction:

$$CaAl_2Si_2O_6 + SiO_2 \Rightarrow CaAl_2Si_2O_8 \text{ (anorthite)}$$

The Suite 1 and 2 clinopyroxenes are typical of the "Type II" class of nodules (Frey and Prinz 1978) and are commonly referred to as Al-augites. They are discussed further in section 4.7.

4.6.2 Amphibole

Amphibole appears in trace amounts in Suite 1, as small (< 0.2mm) euhedral quench crystals (not analysed) in interstitial glass, with clear to pale yellow/reddish-brown/greenish-brown pleochroism. Later in Suite 1, interstitial growth gives anhedral sub-poikilitic crystals 0.8 - 7.0mm in diameter, forming up to 25.5% of the rock (see Figure 4.5.6).

At the start of Suite 2, the amphiboles are highly poikilitic, enclosing, replacing or intergrown with cpx, reaching a maximum of at least 30mm in diameter and forming 27.5 -47.5% of the rock. The end of this suite is characterised by equant, sub-anhedral crystals, reaching 6.5mm and forming 48.5 - 73% of the assemblage (see Figure 4.5.7).

Suite 3 amphiboles have pale yellow/red-brown/olive-green pleochroism and are eu-subhedral, with the appearance of having settled out of the liquid. They make up 55 - 17.5% of each block, with

a maximum size of 7mm. Reaction with the liquid has caused resorption and biotite overgrowth, as it became the stable hydrous phase (see Figure 4.6.25).

In Suite 4 only 88/14c has cogenetic amphibole, with the same pleochroism as in Suite 3, size 0.5 - 3.0mm, showing severe corrosion, leaving only 1% by volume. Crystals were originally euhedral but are now anhedral. 86/38b has an amphibole grain with biotite overgrowth, but analyses show it to have the same composition as those in Suite 2, and was probably derived from an earlier cumulate.

The amphiboles of the cumulates lie in the solid solution range:

Kaersutite $(Na,K)Ca_2(Mg,Fe^{2+},Fe^{3+})_4Ti[Si_6Al_2O_{22}](O,OH,F)_2$ to

Ti-rich ferrohastingsite $(Na,K)Ca_2Fe^{2+}{}_4(Al,Fe^{3+},Ti)[Si_6Al_2O_{22}](O,OH,F)_2$

Most have sufficient Ti (> 0.5 apfu) to be classed as kaersutites. Attempts to recalculate the formula for Fe^{3+} using the method of Droop (1987) with 23 oxygens and either all 16 cations, or subsets of cations, were unsuccessful, producing negative quantities of either Fe^{2+} or Fe^{3+} for many analyses. All Fe was left as Fe^{2+} for this reason.

Fe is inversely correlated with Mg, as shown in Figure 4.6.6, with the Fe-rich crystals at the evolved end of the series. This Fe-enrichment is probably the cause of the change in colour to more strongly green at the end of the series. Figure 4.6.7 shows that Mn is positively correlated with Fe and is preferentially concentrated in the last formed crystals. Deer *et al* (1966) state that kaersutite is invariably Mg-rich, with a maximum of 1.5 Fe apfu. The amphiboles of the cumulates have a range of 1.2 - 2.3 Fe apfu, and 2.6 Fe apfu (with 0.4 Ti apfu) in 88/14c. Thus the range of solid solution is considerably wider than previously recorded.

Figure 4.6.8 shows the strong correlation between Si and Al, with the Si + Al = 8 line added for reference. Whereas the $Mg \Leftrightarrow Fe^{2+}$ substitution involves no charge problem, the $Si \Leftrightarrow Al$ exchange leaves a charge deficiency. The excess Al over and above that needed to give 8 cations in the Z position goes into the Y position as Al^{VI} and helps to balance this charge deficiency, as does the filling of the A position, and the presence of Fe^{3+} and Ti in the Y position. Figure 4.6.9 shows that Ti correlates well with Al^{VI} and Figure 4.6.10 shows that (Na + K) has a weak correlation with Al. Ca remains roughly constant at 1.8 apfu.

The presence of amphibole (and biotite) in significant proportions suggests that the melt crystallised under high P_{H_2O}, although this assumption should be viewed with caution in view of the common replacement of OH^- anions by O^{2-} in kaersutite, and the low measured H_2O content (0.3%) of a volcanic kaersutite from the Velay (section 3.2.7).

Kaersutite is ubiquitous in the volcanic rocks of the Auvergne, and abundant in evolved alkaline rocks around the world. It is a characteristic mineral of "metasomatised" mantle nodules, and appears to have a broad paragenesis both in P, T range and in parental melt composition. Its presence in the Velay cumulates suggests a depth of crystallisation of at least a few kilometres, since it is unstable at low pressures.

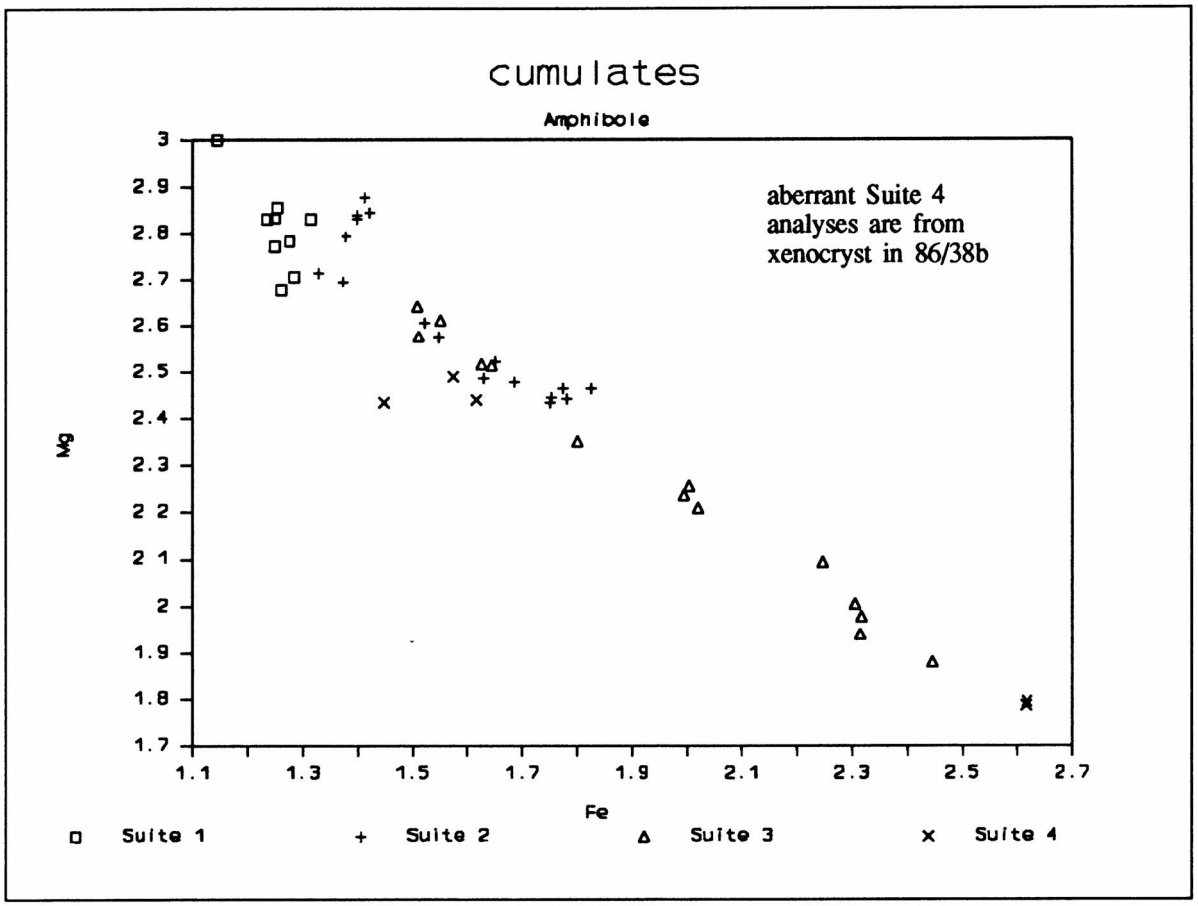


Figure 4.6.6

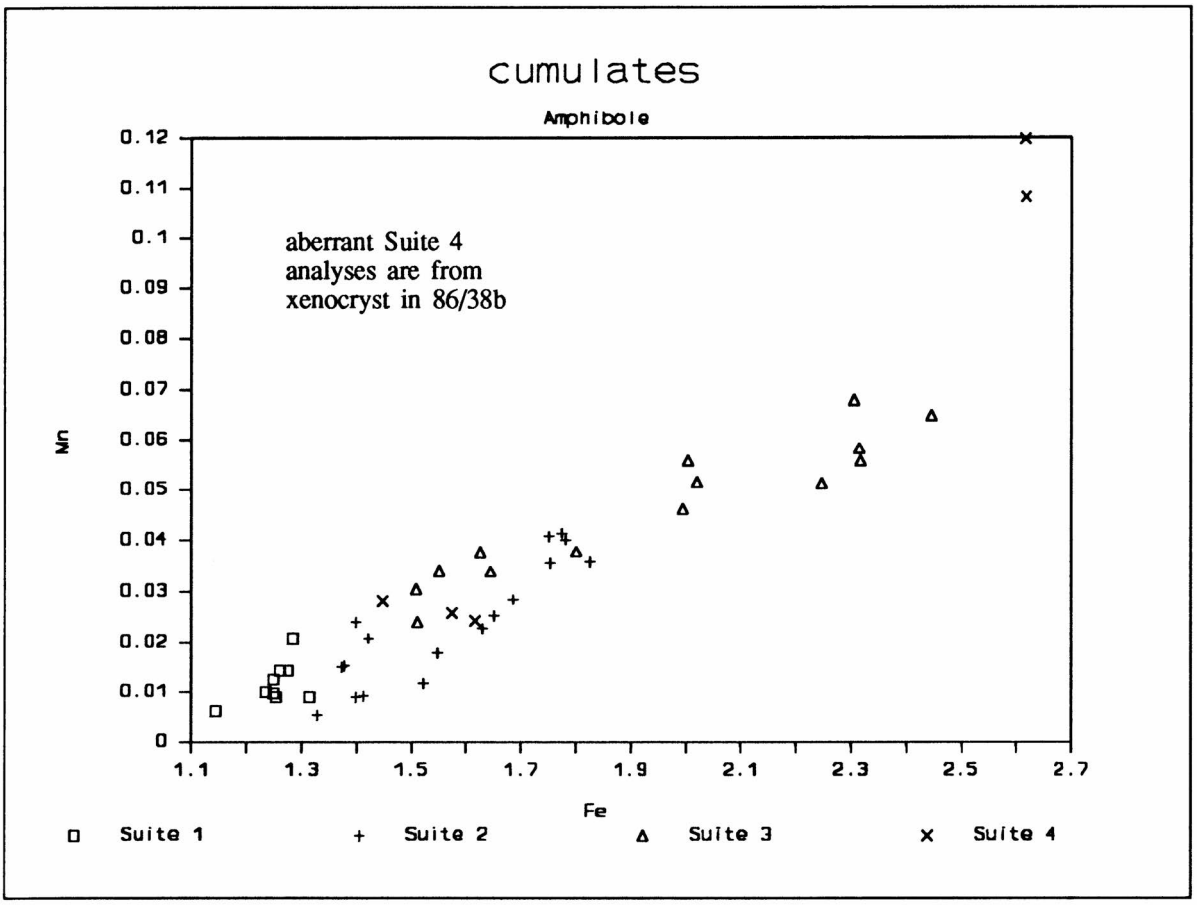


Figure 4.6.7

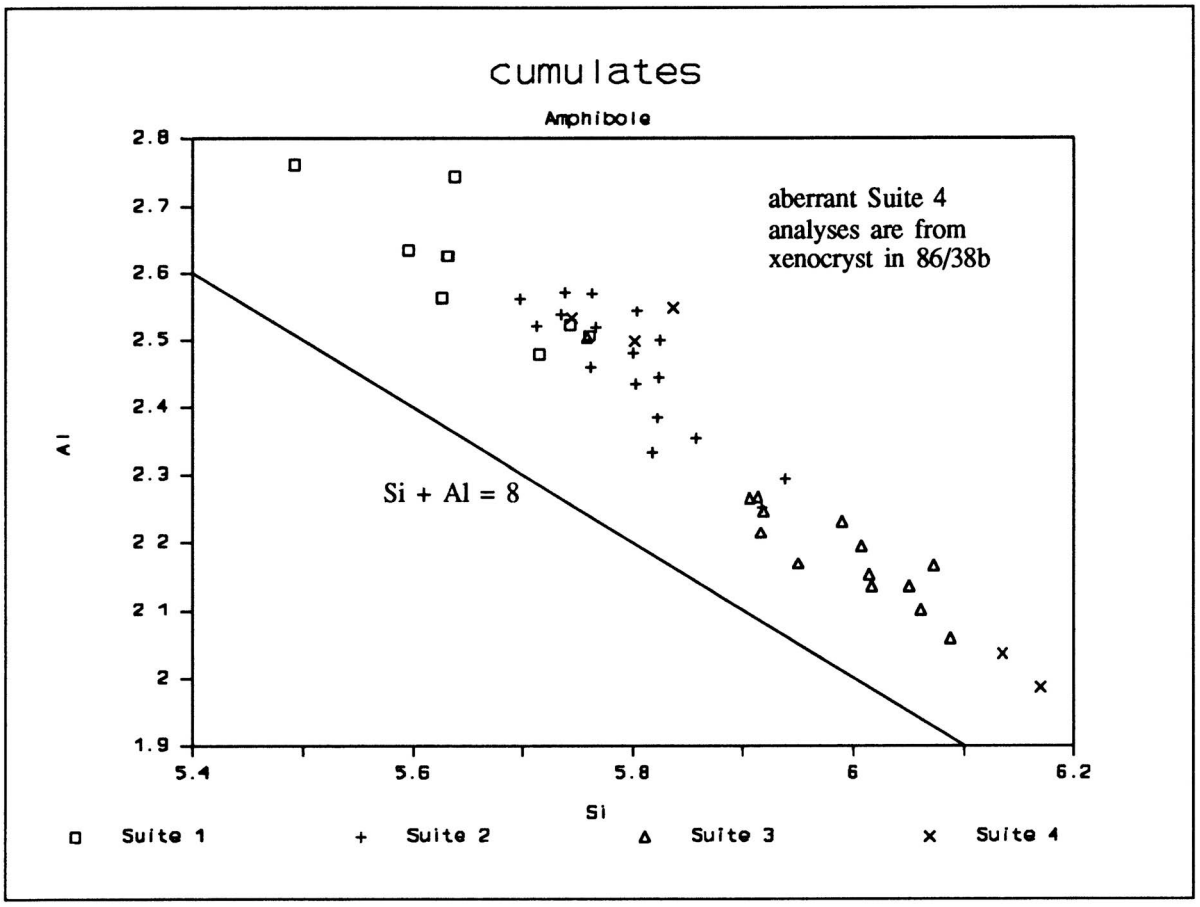


Figure 4.6.8

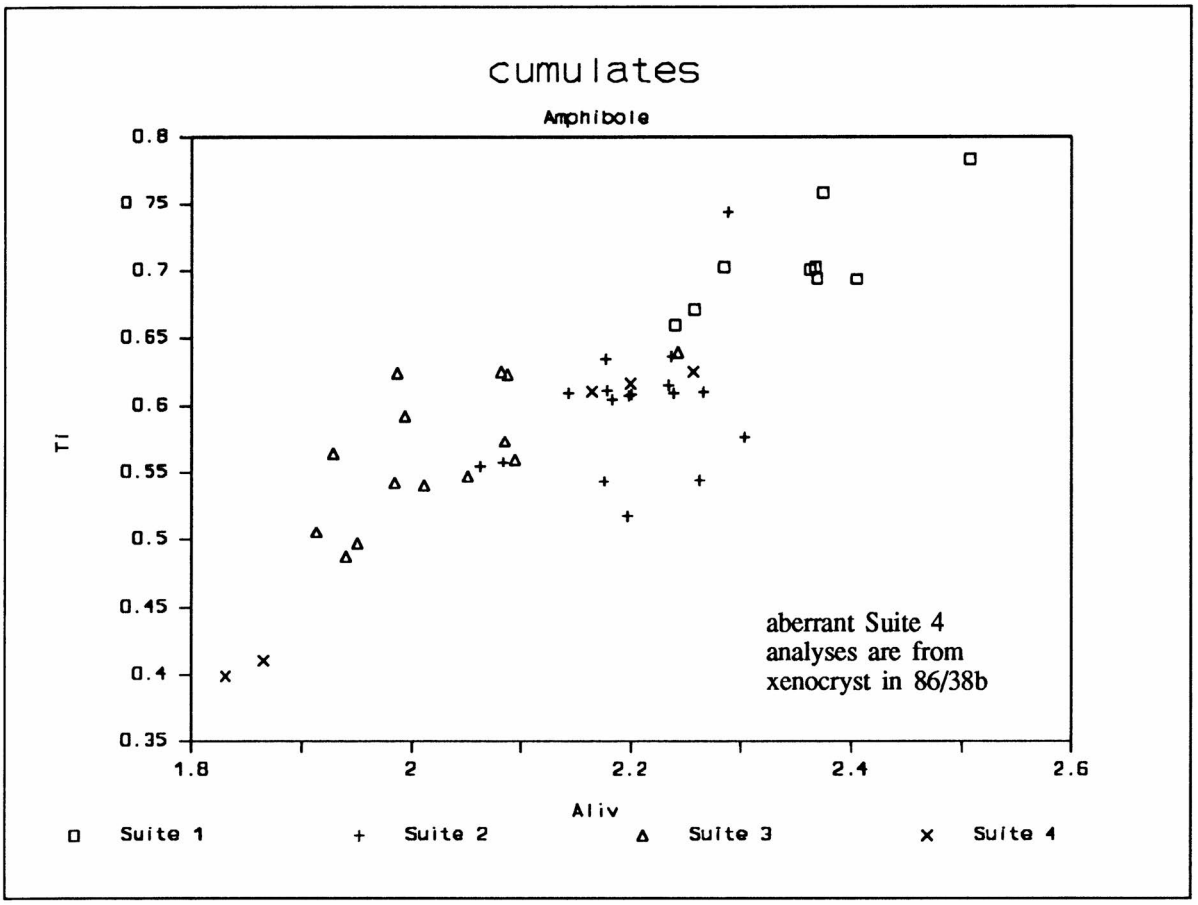


Figure 4.6.9

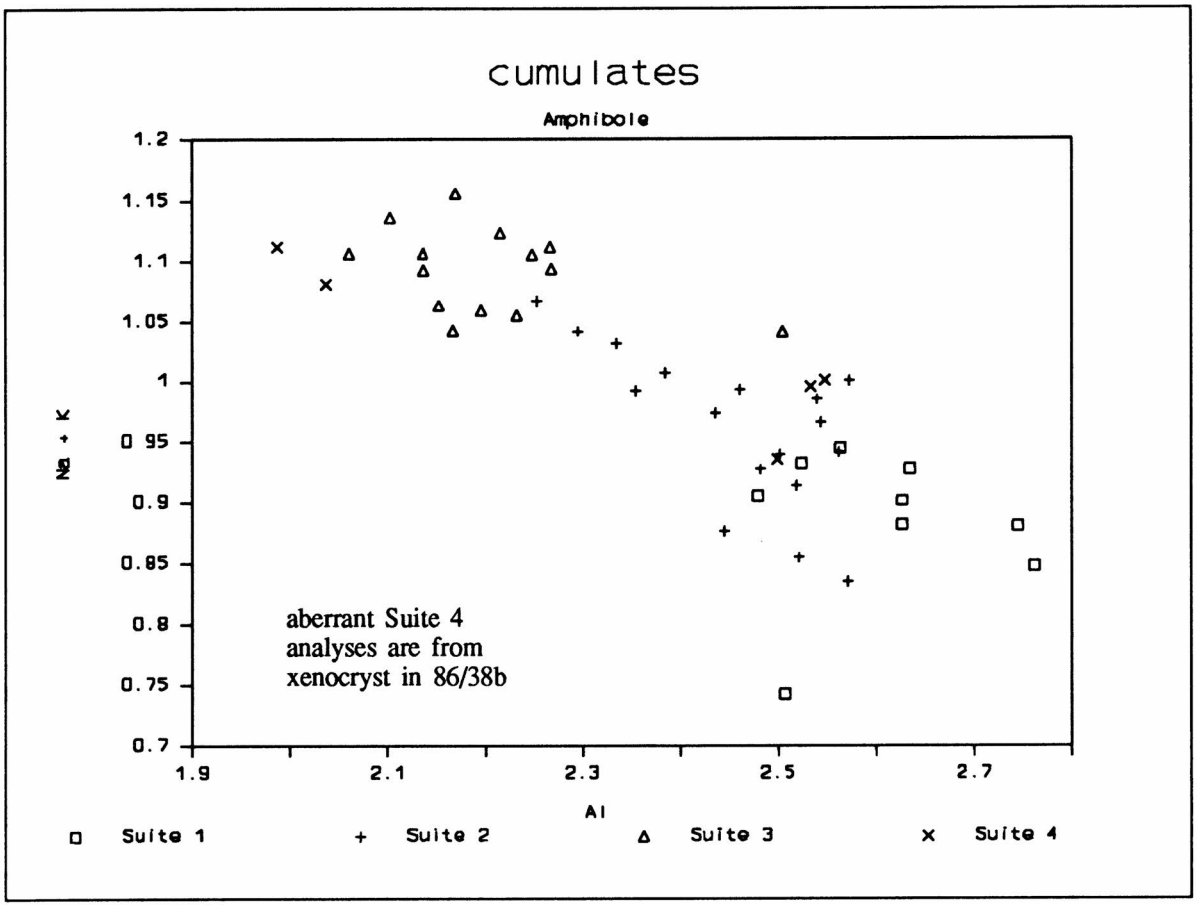

cumulates
Amphibole
1.2
1.15
1.1
1.05
1
0.95
0.9
0.85
0.8
0.75
0.7
1.9
2.1
2.3
2.5
2.7
Al
aberrant Suite 4
analyses are from
xenocryst in 86/38b
Suite 1
Suite 2
Suite 3
Suite 4

Figure 4.6.10

4.6.3 Feldspar

Plagioclase appears at the start of Suite 2 as interstitial or highly poikilitic crystals, reaching a maximum size of 6mm, with no sign of ever having had a euhedral form. These crystals must have grown by nucleation in the interstices between the early cumulate minerals. They are unzoned and have either very poorly developed or medium-wide twins, characteristic of Ca-rich plagioclase. Their composition ranges from An_{82} to An_{57} in four specimens, and reaches as low as An_{42} in 86/38g. The proportion varies from as little as 1% in 88/14j to 10% in 88/14n, with 86/38g at the end of the scale again with 30.5%.

Suite 3 is characterised by plagioclase with some evidence of an original euhedral shape. This is usually recorded by the zoning pattern since later overgrowth of more sodic plagioclase has resulted in a completely anhedral, intergrown mass, although some crystals still show sub-euhedral shape, up to 14mm long. Crystals typically have medium to narrow twins and a wide compositional range, from An_{62} to An_{17}. Plagioclase forms 30 - 66% of the rock.

Suite 4 has 66.5 - 76% feldspar, dominating the bulk composition of the blocks. Grains are generally subhedral, although the abundant glass sometimes outlines euhedral crystals. The composition ranges from An_{34} into the anorthoclase field, with a maximum value of Or_{26}. A low-quality analysis from 88/14a indicates that values of Or_{36} may be reached and an analysis from 88/14f gave An_{56}, indicating that some phenocrysts from earlier cumulates may be preserved. Plagioclase in Suite 4 has extremely narrow twins, giving way to the characteristic cross-hatching of anorthoclase (see Figure 4.5.9). Anorthoclase lies in the high albite-low sanidine series, and forms initially with a monoclinic structure with pericline twins. On cooling, the structure reverts to triclinic, with albite twins perpendicular to the earlier twins to give the cross-hatching effect (Deer *et al* 1966).

Feldspars are characterised by simple and limited solid solution. Albite and K-feldspar form a continuous series - $(Na,K)AlSi_3O_8$ - and albite has complete solid solution with anorthite ($CaAl_2Si_2O_8$), by the substitution $CaAl \Leftrightarrow NaSi$. Very little solution of other elements occurs in the cumulate feldspars, Fe_2O_3 being the most significant with up to 0.7% by weight, and none of these minor elements correlate with the Si, Al, Ca, Na or K.

Figure 4.6.11 shows the variation in feldspar compositions from Suite 2 to Suite 4. The large overlap between the suites is probably due to adcumulus overgrowth on the originally euhedral feldspar phenocrysts. The feldspar which mantles the early cumulate feldspars would have crystallised from an intercumulus melt in equilibrium with the main magma body, which would simultaneously have been precipitating feldspar phenocrysts. Thus the same feldspar composition appears both as phenocrysts (in evolved cumulates) and as overgrowths on more calcic feldspars (in earlier cumulates).

All zoning appears to be normal, that is, calcic cores are mantled by sodic rims, and sodic cores have potassic rims. There was apparently no simultaneous crystallisation of a plagioclase and a

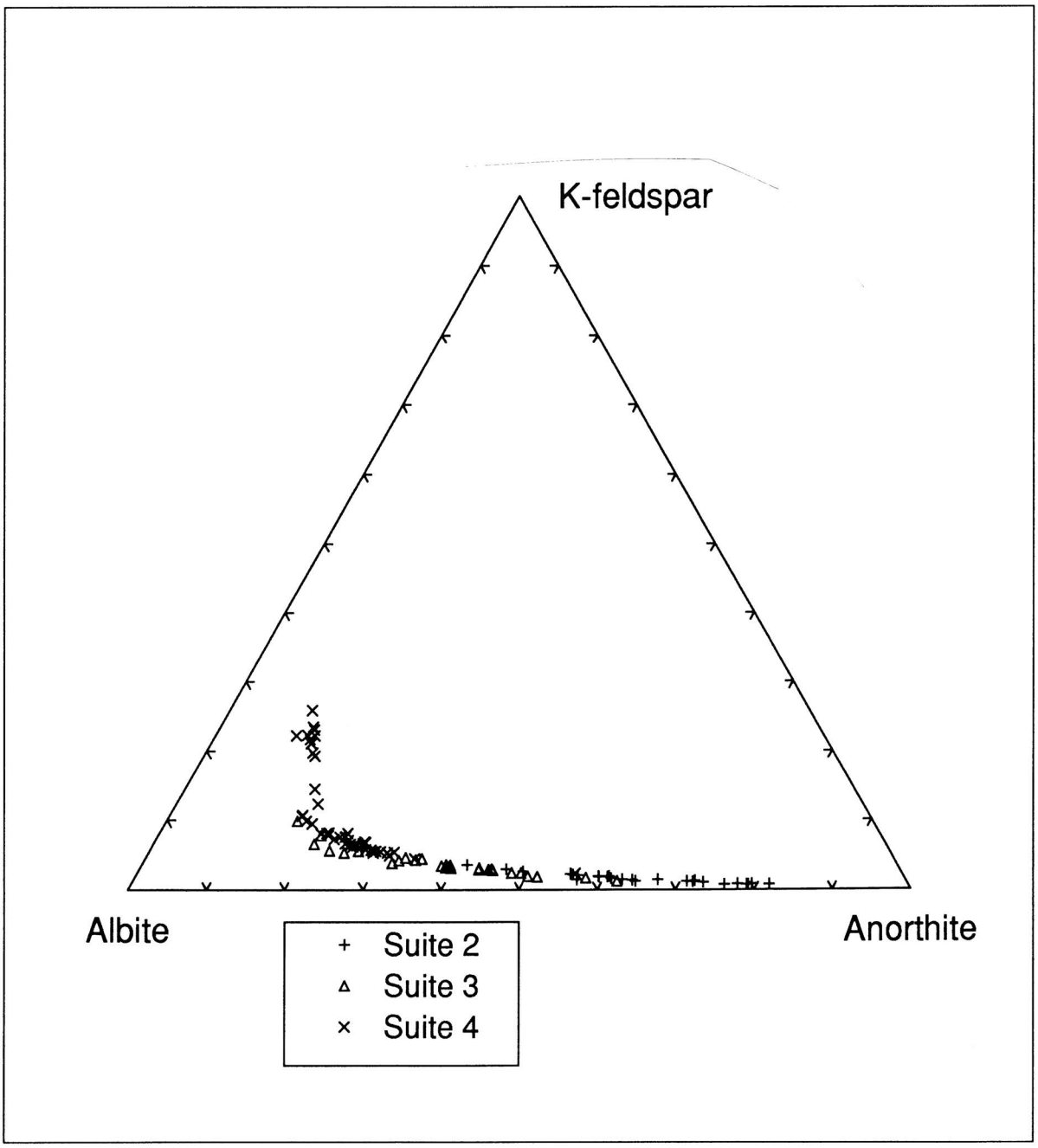


Figure 4.6.11. Triangle diagram summarising the change in feldspar composition, from its appearance in Suite 2, to the most evolved Suite 4 blocks. The large overlaps between each suite are due to the adcumulus overgrowth of the early calcic plagioclases by more sodic feldspar. The trend of these feldspars shows much less scatter than that of the Velay lavas, probably due to the monogenetic origin of the cumulates.

K-feldspar, although it would be very difficult to detect since there is so much zoning, and the two feldspars crystallising could be similar in composition.

4.6.4 Ti-magnetite

Ti-magnetite is present all of the twenty nine blocks studied. It is opaque and isotropic, white to light grey in reflected light. It is most abundant in Suite 1, with 9 - 27%, forming equant to non-equant grains up to 1.0 - 3.5mm diameter. Individual grains are difficult to distinguish, and polycrystalline patches up to 7mm are not uncommon. Figures 4.6.30 and 4.6.31 show the exceptional block 88/14m, with euhedral Ti-magnetite crystals in glass. Figures 4.5.5 and 4.5.6 show the normal appearance of Ti-magnetite in Suite 1.

Suite 2 has 7 - 14% Ti-magnetite forming grains of up to 0.2 - 1.2mm in diameter. In 86/38e there is an 11mm-long crystal intergrown with the single large amphibole. Occasionally subhedral crystals appear in this suite, and even a few with euhedral forms.

Suite 3 has 0.15 - 2.0% Ti-magnetite, individual grains reaching 0.2 - 0.6mm. Most are anhedral but a few are subhedral. Suite 4, with 0.15 - 1.5%, has the best formed crystals, especially within the glass, with individual grains reaching 0.2 - 1.0mm.

Many of the Ti-magnetites show some degree of alteration. The least altered are in Suite 1, the alteration appearing as a dendritic pattern around cracks, especially at the edges of crystals. Analyses of uniform areas are usually of the best quality, and are assumed to be unaltered. In Suites 3 and 4 alteration is much more severe, and has often caused pervasive chemical change, with a poor polish being obtained on these grains. Analyses of these crystals are characterised by a high Si-content and only four analyses from Suites 3 and 4 were used for this reason, since those with more than 1% SiO_2 were rejected.

The Ti-magnetites are characterised by a great deal of solid solution, with end-members including magnetite $Fe^{2+}Fe^{3+}{}_2O_4$, ulvöspinel $Fe^{2+}{}_2TiO_4$, spinel $MgAl_2O_4$, magnesioferrite $MgFe^{3+}{}_2O_4$, hercynite $Fe^{2+}Al_2O_4$ and jacobsite $MnFe^{3+}{}_2O_4$.

Figure 4.6.12 shows Fe^{2+} vs Ti, with the line of ulvöspinel solid solution added. There is only a poor correlation between these elements, and a surplus of Fe^{2+} above that needed for ulvöspinel. The single analysis from Suite 3 may be anomalous. The general trend is towards Ti-enrichment in the later suites, although Suite 2 contains those with the lowest Ti, similar to the situation in the ilmenites. The only other significant Ti-bearing phase present in these blocks is kaersutite (max 6.7% TiO_2), which decreases continuously in TiO_2-content from Suites 1 to 4. It is therefore unlikely that it affected a_{TiO_2} sufficiently to cause depletion in the Ti-content of the Suite 2 Ti-magnetites and ilmenites.

Figure 4.6.13 plots Al vs Mg, with the line of spinel solid solution added. The proportion of spinel is 3 - 34%, with the excess Mg probably forming magnesioferrite.

Fe^{2+}-2Ti represents the Fe^{2+} not in ulvöspinel and Figure 4.6.14 shows this plotted against

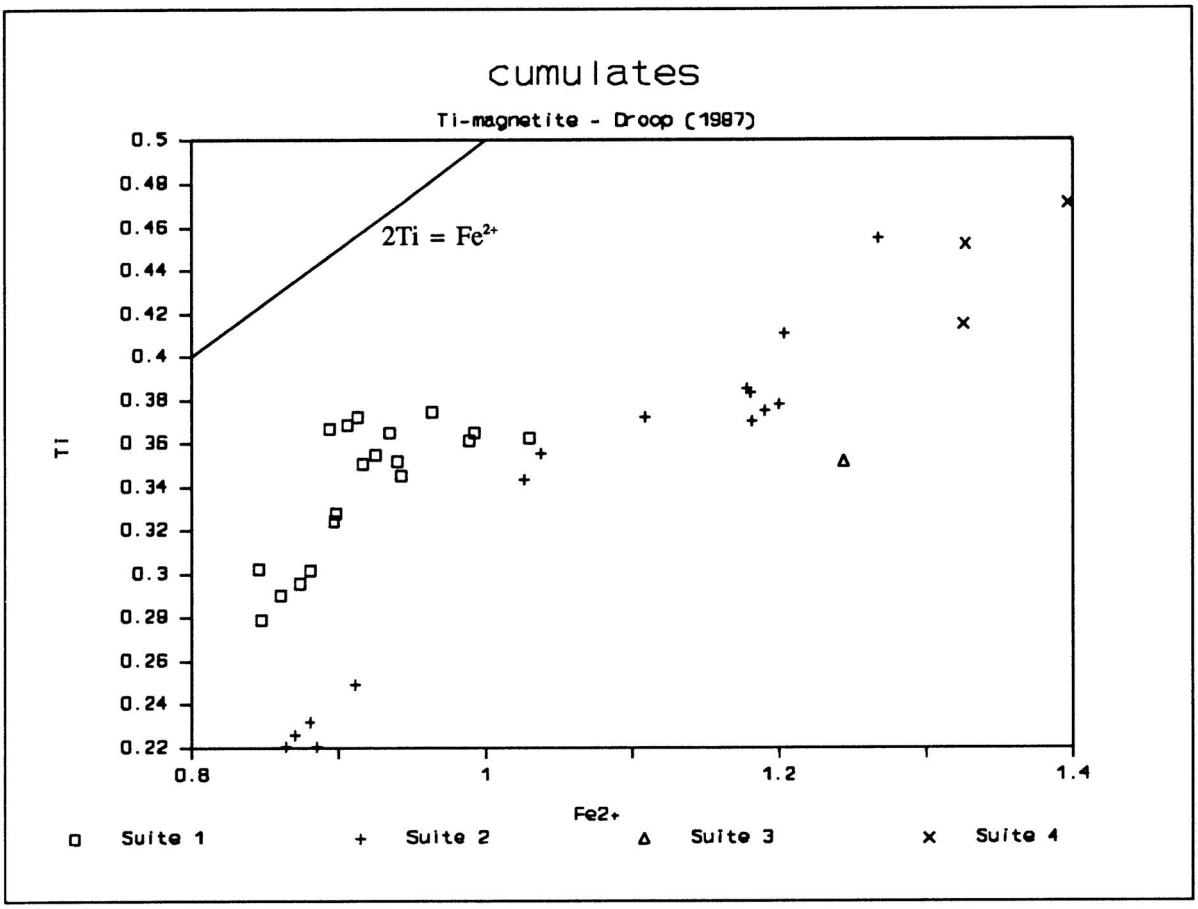


Figure 4.6.12

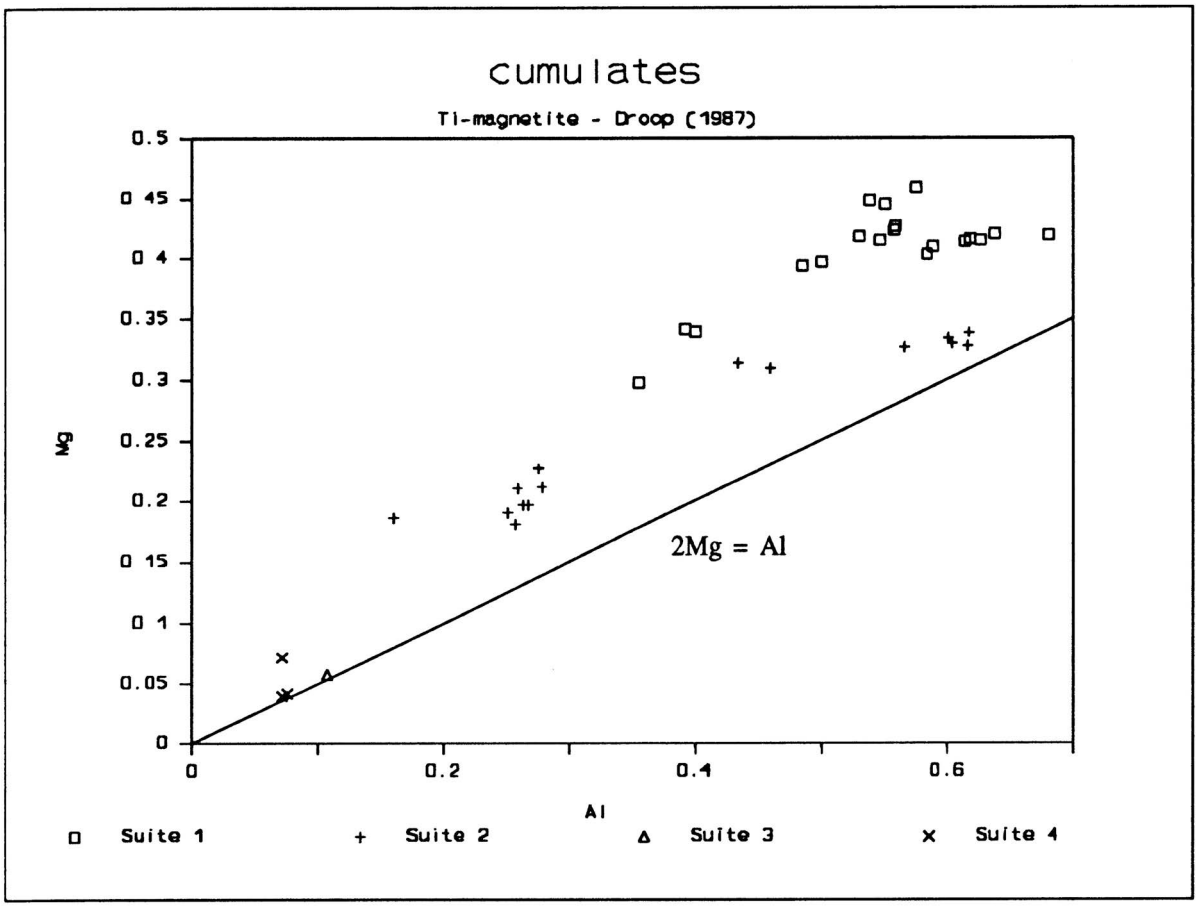


Figure 4.6.13

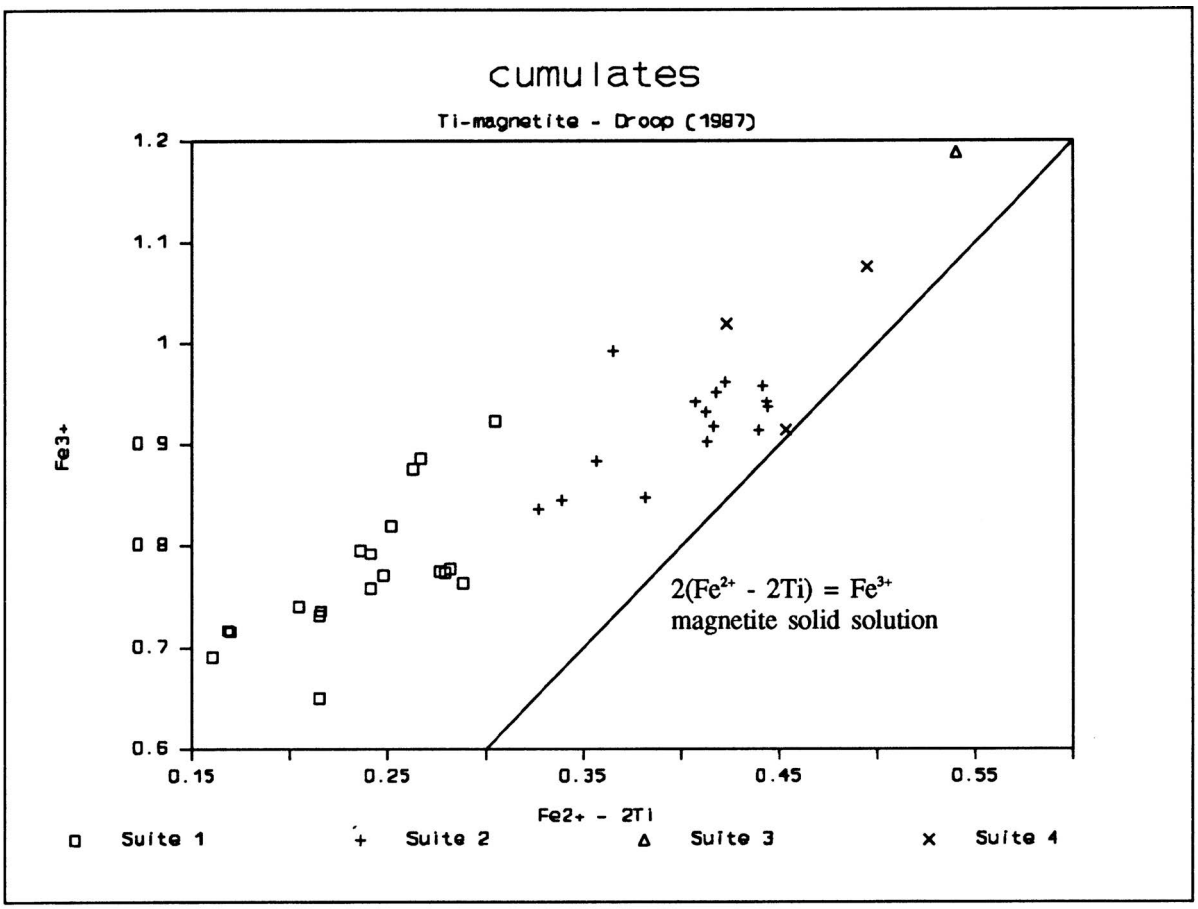


Figure 4.6.14

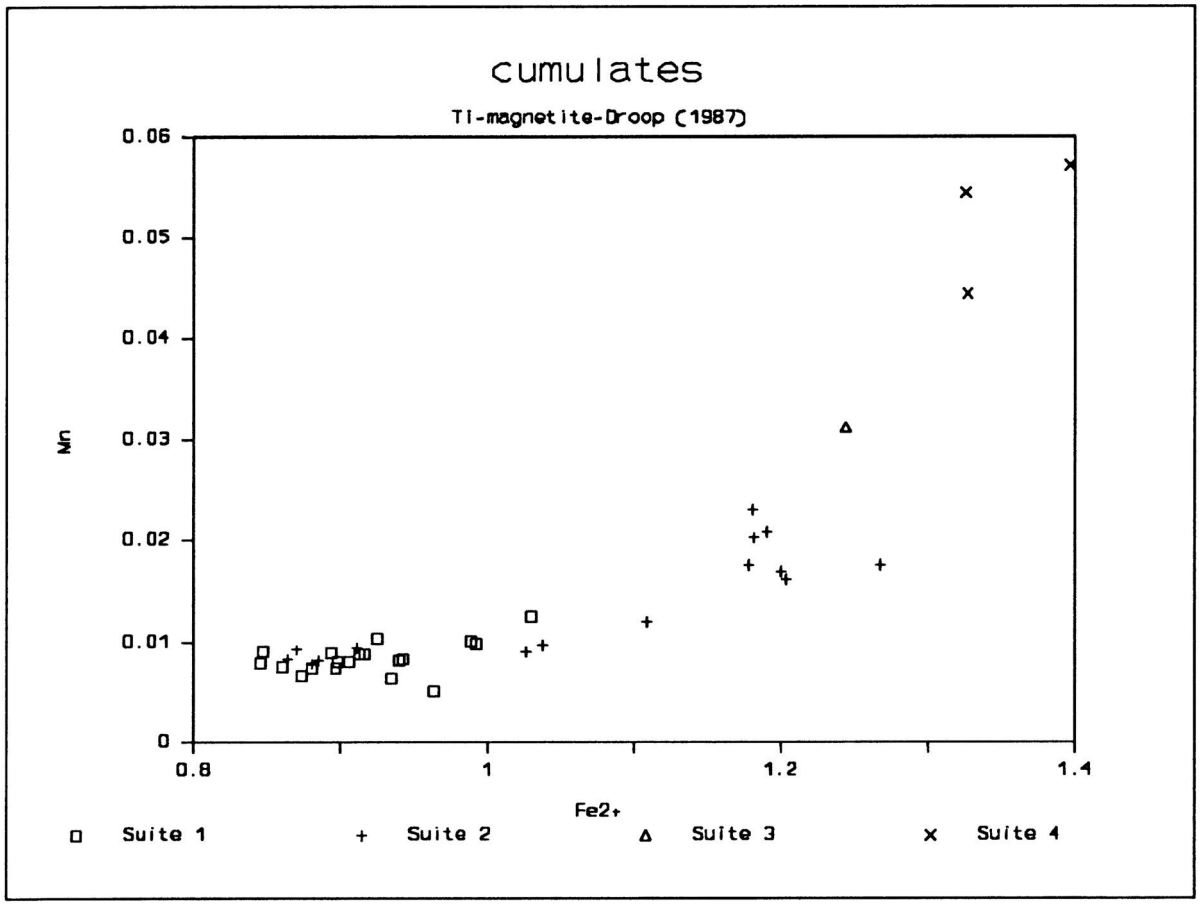


Figure 4.6.15

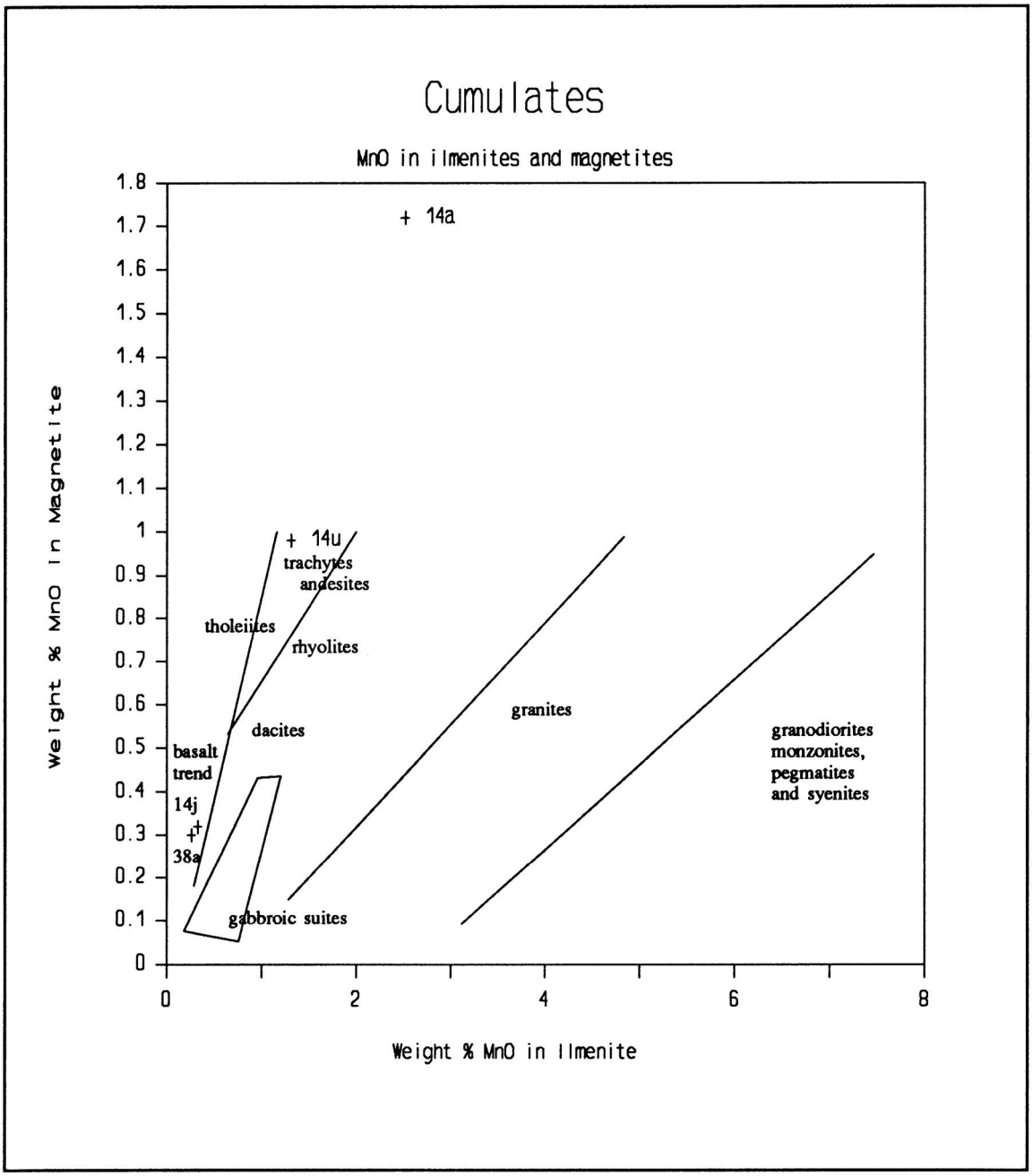


Figure 4.6.16. The Mn-contents of coexisting Ti-magnetites and ilmenites from the cumulate blocks 88/14a, 14j, 14u and 86/38a show that their parent liquids lay on the basalt to trachyte trend (after Haggerty 1976).

Fe^{3+}, with the line of magnetite solid solution added. The trend is fairly linear, the excess Fe^{3+} forming magnesioferrite in the Mg-rich Suite 1 Ti-magnetites and jacobsite in those of the Mn-rich Suite 4.

In Figure 4.6.15, Fe^{2+} is plotted against Mn showing a progressive increase in both from Suites 1 to 4. This pattern is seen in most of the cumulate minerals and is probably due to the increase in the Mn/Fe^{2+} of the differentiated magma.

Suite 1 Ti-magnetites contain roughly 30% magnetite, 30% ulvöspinel, 30% spinel and 10% magnesioferrite, whereas Suite 4 Ti-magnetites have 47% magnetite, 45% ulvöspinel, 3% spinel and 5% jacobsite, although cation distribution is partly a matter of choice and these figures are given only for comparison. Apart from the Si due to alteration, other elements such as Na, K and Ca are present in insignificant amounts.

Figure 4.6.16 shows a plot of the MnO-contents of coexisting Ti-magnetites and ilmenites in cumulate blocks 88/14a, 14j, 14u and 86/38a. The boundaries on the diagram were taken from Haggerty (1976) and show that the blocks lie on the basalt-trachyte trend, suggesting that they were derived from such magmas.

4.6.5 Ilmenite

Ilmenite is present through much of the series, with the highest proportions, up to 3.5%, appearing in Suite 1. It disappears at about the same time as pleonaste, then reappears in Suite 3, coexisting with Ti-magnetite until the end of the series. It is light grey in reflected light, and can be distinguished from Ti-magnetite by its lack of alteration and its bireflectance. In Suites 1 and 2, ilmenite grains are anhedral, and reach 5mm. When the mineral reappears in Suite 3 it forms up to 1.5% of the rock, with grains ≤ 1mm. Although usually anhedral, euhedral hexagonal ilmenite crystals are occasionally present, especially within areas of glass. Blocks 88/14q and 86/38e contain a deep red, high relief mineral, often overgrowing ilmenites. This is probably rutile (TiO_2), as a fibrous alteration product of the ilmenite.

Ilmenite forms a solid solution with haematite ($Fe^{2+}TiO_3$ - $Fe^{3+}{}_2O_3$), with Mg and Mn substituting for Fe^{2+}, and Al substituting for Fe^{3+}. Figure 4.6.17 shows Fe^{2+} vs Ti with the ilmenite solid solution line added. It shows only poor correlation, and other divalent elements are clearly needed to balance the Ti. Figure 4.6.18 plots Fe^{2+} vs Mg, showing that Mg accounts for most of the deficiency, with the highest Mg-content in the ilmenites of Suite 1. Figure 4.6.19 shows Fe^{2+} vs Mn, demonstrating the increase in Mn-content from Suites 1 to 4, probably due to increasing Mn/Fe^{2+} in the magma. Figure 4.6.20 shows that only a small amount of $Al \Leftrightarrow Fe^{3+}$ substitution takes place and that there is no correlation between these two elements. Since Ti is not replaced by other cations and Fe^{3+} shows little replacement they should show good correlation. Figure 4.6.21 shows this to be the case and that the proportion of ilmenite in the ilmenite-haematite solid solution varies from 78% to 97%. This variation is not progressive from Suite 1 to Suite 4 however. Suite 1 has 84-85% ilmenite,

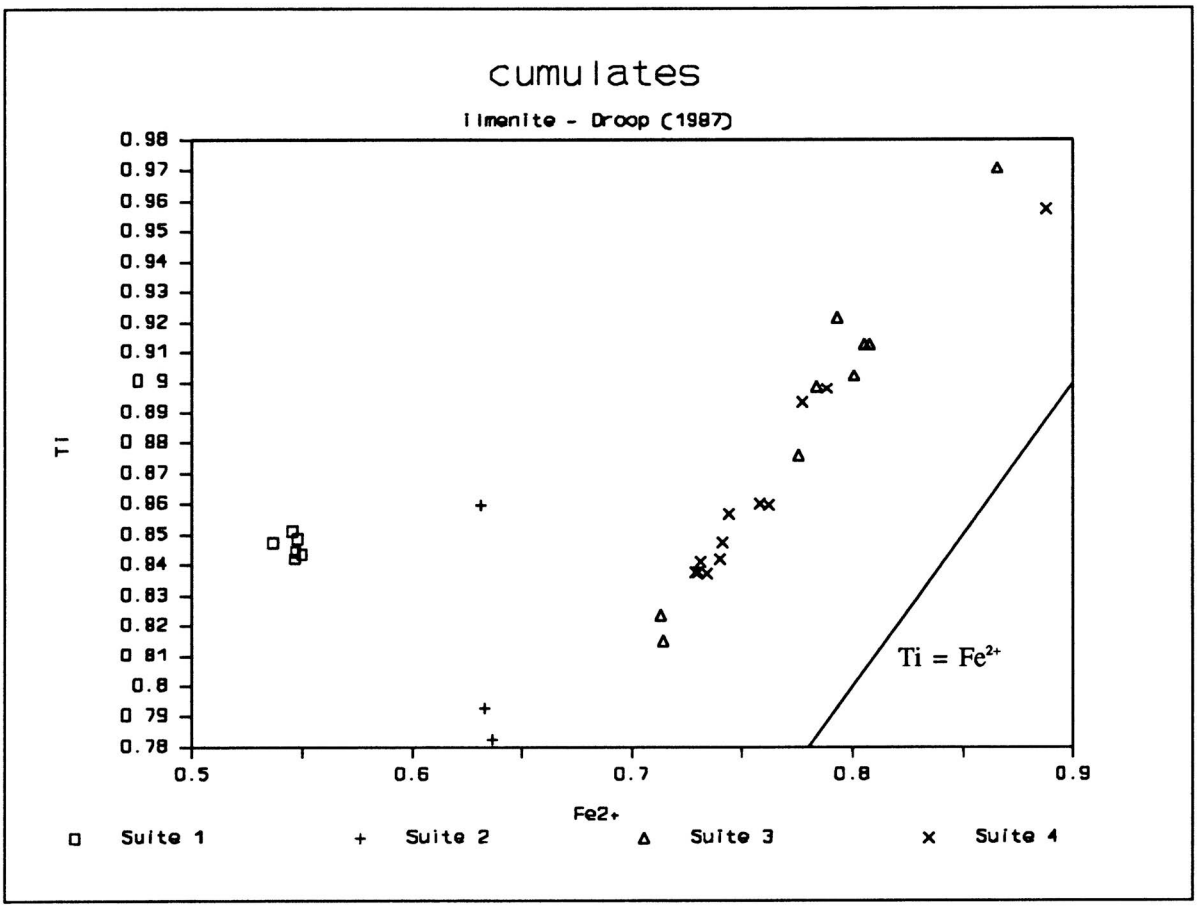


Figure 4.6.17

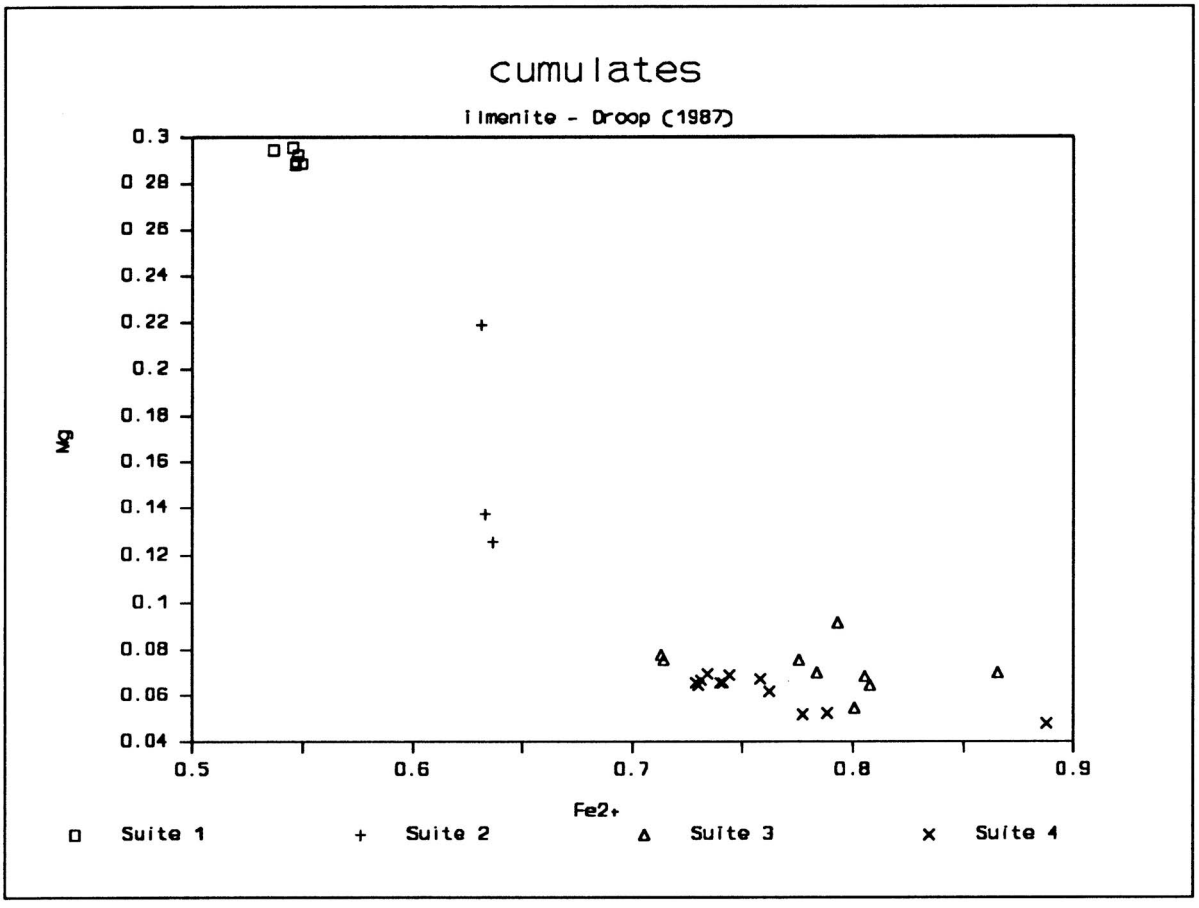


Figure 4.6.18

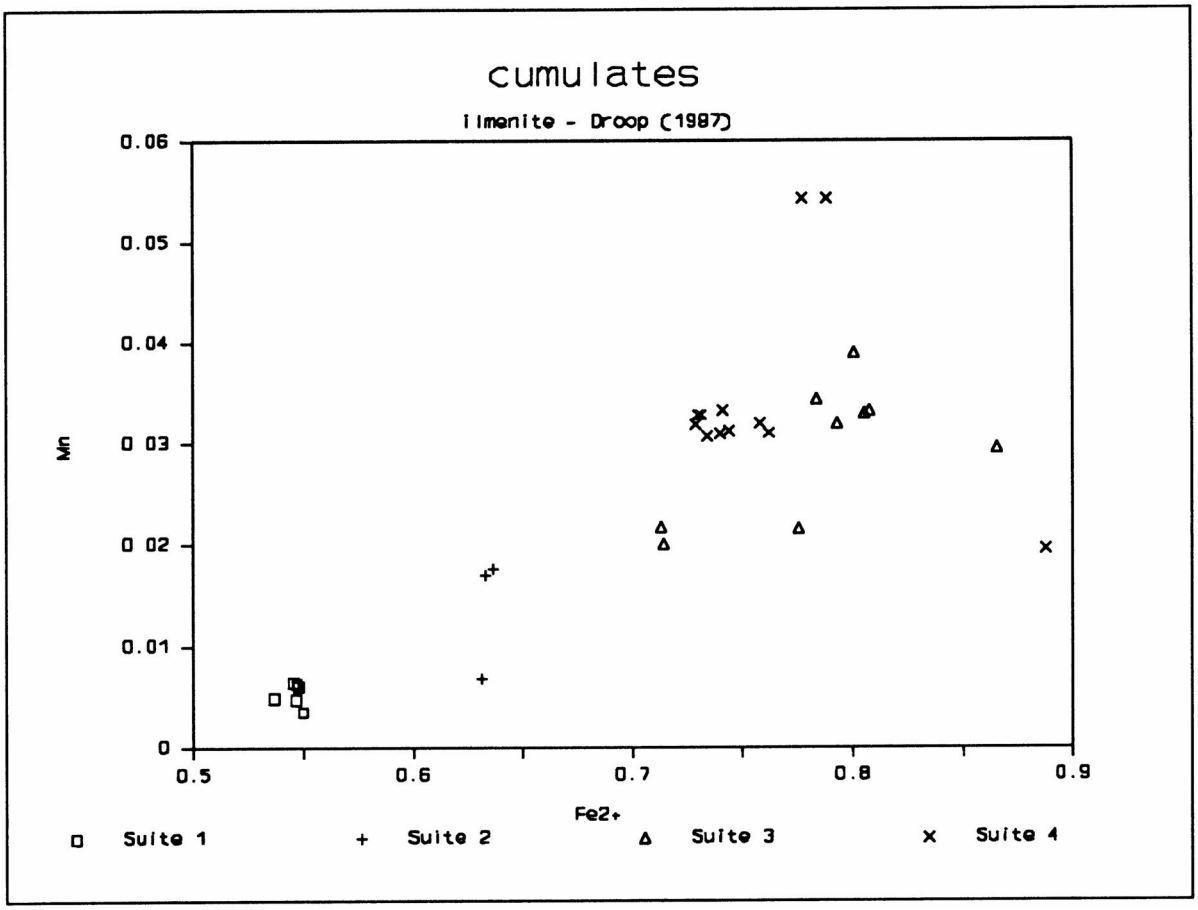


Figure 4.6.19

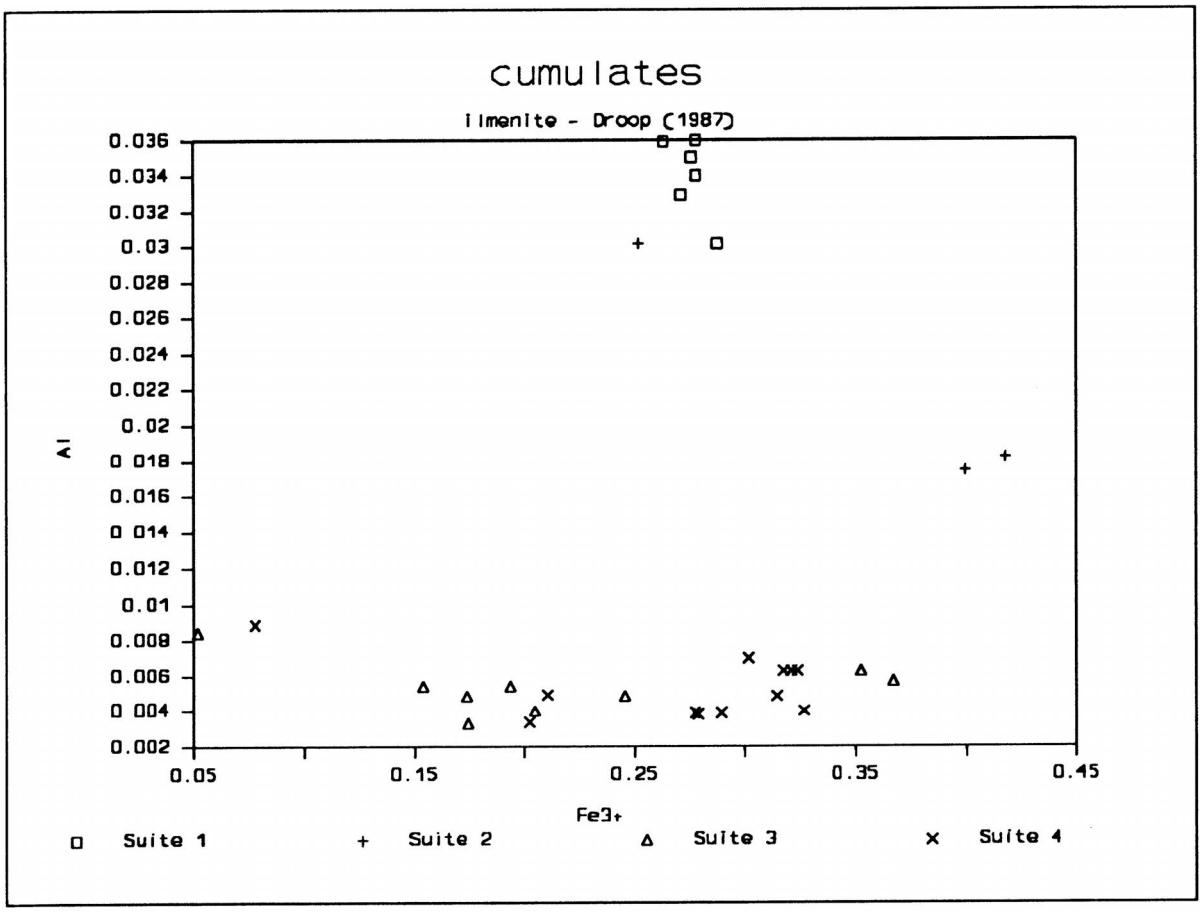


Figure 4.6.20

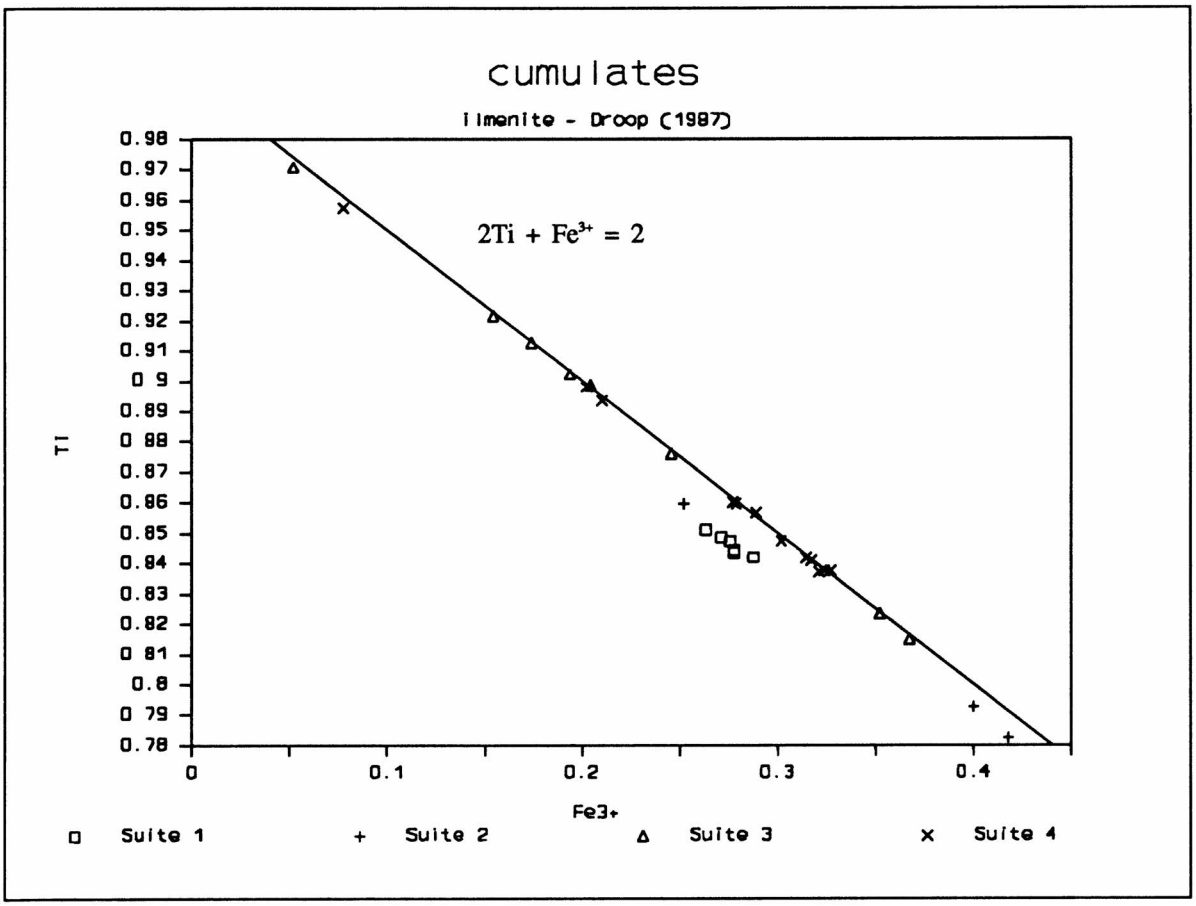

cumulates
Ilmenite - Droop (1987)
2Ti + Fe3+ = 2
Ti
0.98
0.97
0.96
0.95
0.94
0.93
0.92
0.91
0 9
0.89
0 88
0.87
0.86
0.85
0.84
0.83
0.82
0 81
0.8
0 79
0.78
0
0.1
0.2
0.3
0.4
Fe3+
Suite 1
Suite 2
Suite 3
Suite 4

Figure 4.6.21

Suite 2 has 78-85%, Suite 3 has 81-97% and Suite 4 has 83-95%. This apparently random variation may be due to the widely varying assemblage with which the ilmenite is in equilibrium, especially the other Ti-bearing phases such as Ti-magnetite.

Other elements such as Si, Ca, Na and K are present in only insignificant amounts.

4.6.6 Pleonaste (spinel-hercynite)

Pleonaste appears most commonly as anhedral, rounded patches in Suites 1 and 2. It is completely opaque, dull grey, isotropic, unaltered and shows no exsolution in reflected light. As Figure 4.5.4 shows, it is most abundant in Suite 1 (5 - 14%), before declining in proportion and finally disappearing in Suite 2. The rapid variation in proportion at the start of Suite 1 is probably due to Na_2O being rather unsuitable as an index at this point.

Its grain size is highly variable, from 0 - 6mm in Suite 1, the largest being quite elongate and angular, in contrast to the smaller, circular blobs. In Suite 2 the largest blobs are 0.6mm, the grain-size decreasing with the abundance. Pleonaste appears to have crystallised very early as it is often found as inclusions within the cpx and Ti-magnetite, and when adjacent to Ti-magnetite grains it is always more equant. Only pyrrhotite (section 4.6.10) appears to have formed earlier.

Pleonaste *sensu stricto* is a solid solution between spinel and hercynite with $Mg:Fe^{2+}$ between 3:1 and 1:1 (Deer *et al* 1966). The pleonastes in the cumulates have $Mg:Fe^{2+}$ of (1.6 - 1.1):1, but have significant magnetite substitution ($Fe^{3+} \Leftrightarrow Al$) and ulvöspinel substitution ($Fe^{2+}{}_2Ti \Leftrightarrow [Mg,Fe^{2+}]Al_2$).

Figure 4.6.22 shows Mg vs Fe^{2+} with the line $Mg + Fe^{2+} = 1$ plotted. The data consistently lie above this line due to ulvöspinel solid solution, in which the Ti accounts for some of the Fe^{2+}. Figure 4.6.23 shows Al vs Fe^{3+} in which the data plot below the line $Al + Fe^{3+} = 2$, again due to the Ti present in solid solution. Figure 4.6.24 shows the Ti-content of the pleonastes against Fe^{2+}. The Suite 2 data have significantly lower Ti, and lie well away from the Suite 1 trend.

The ranges of solid solution are: spinel 53 - 63%, hercynite 17 - 25%, magnetite 16 - 20% and ulvöspinel 3 - 6%, with most spinel and ulvöspinel in Suite 1 pleonastes and most hercynite and magnetite in those of Suite 2. In all samples probed Na, Si, K, Ca and Mn are insignificant.

Pleonaste appears in other alkali basalt provinces, both in the Group A megacrysts (Irving 1984) and the Type II nodules (Frey and Prinz 1978). In the megacryst suite it has $TiO_2 < 1\%$ (Binns *et al* 1970) whereas the Velay pleonastes have TiO_2 up to 2.7%. In the Type II nodules pleonaste is commonly Al-rich and Cr-poor, similar to those in the Velay. Several authors have suggested that pleonaste, in conjunction with the other minerals with which it is commonly associated, is the result of high pressure crystallisation of a basanite melt.

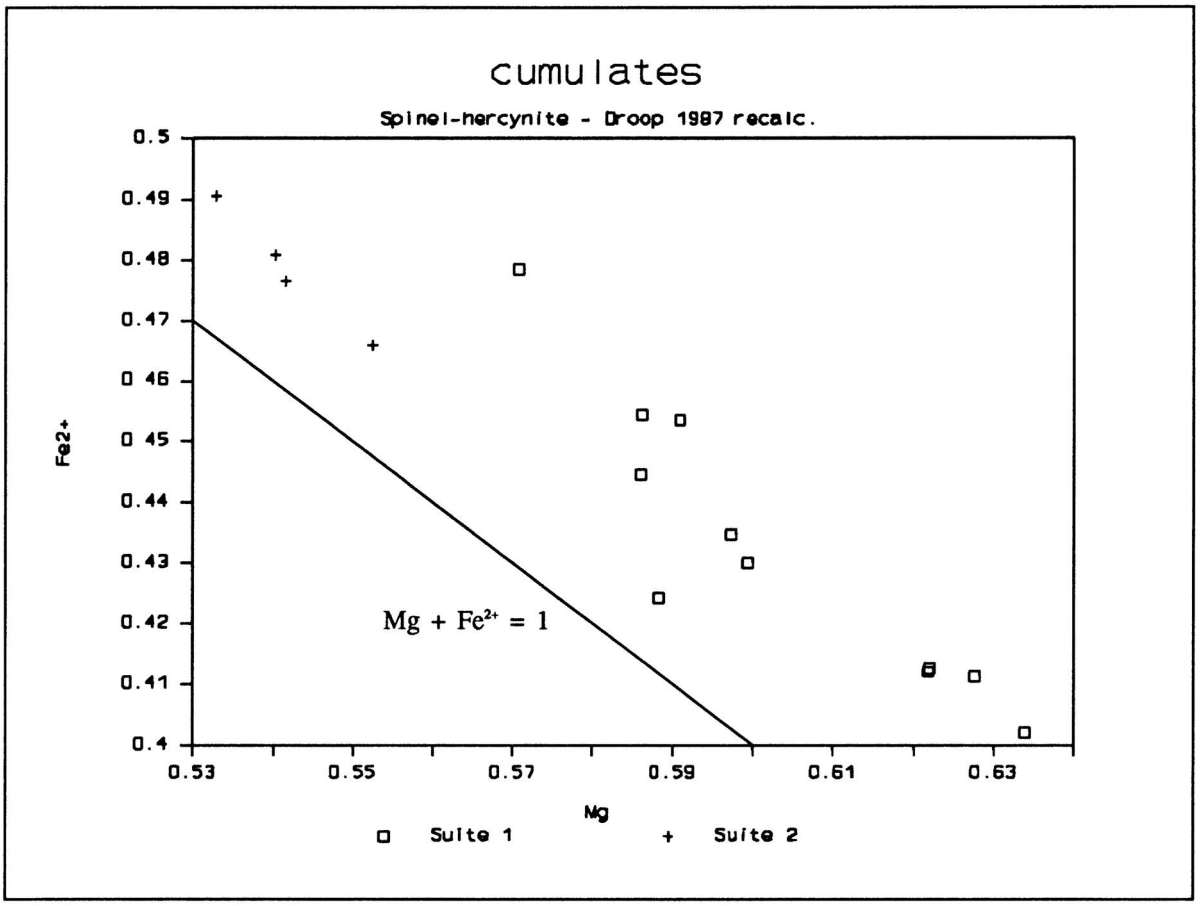


Figure 4.6.22

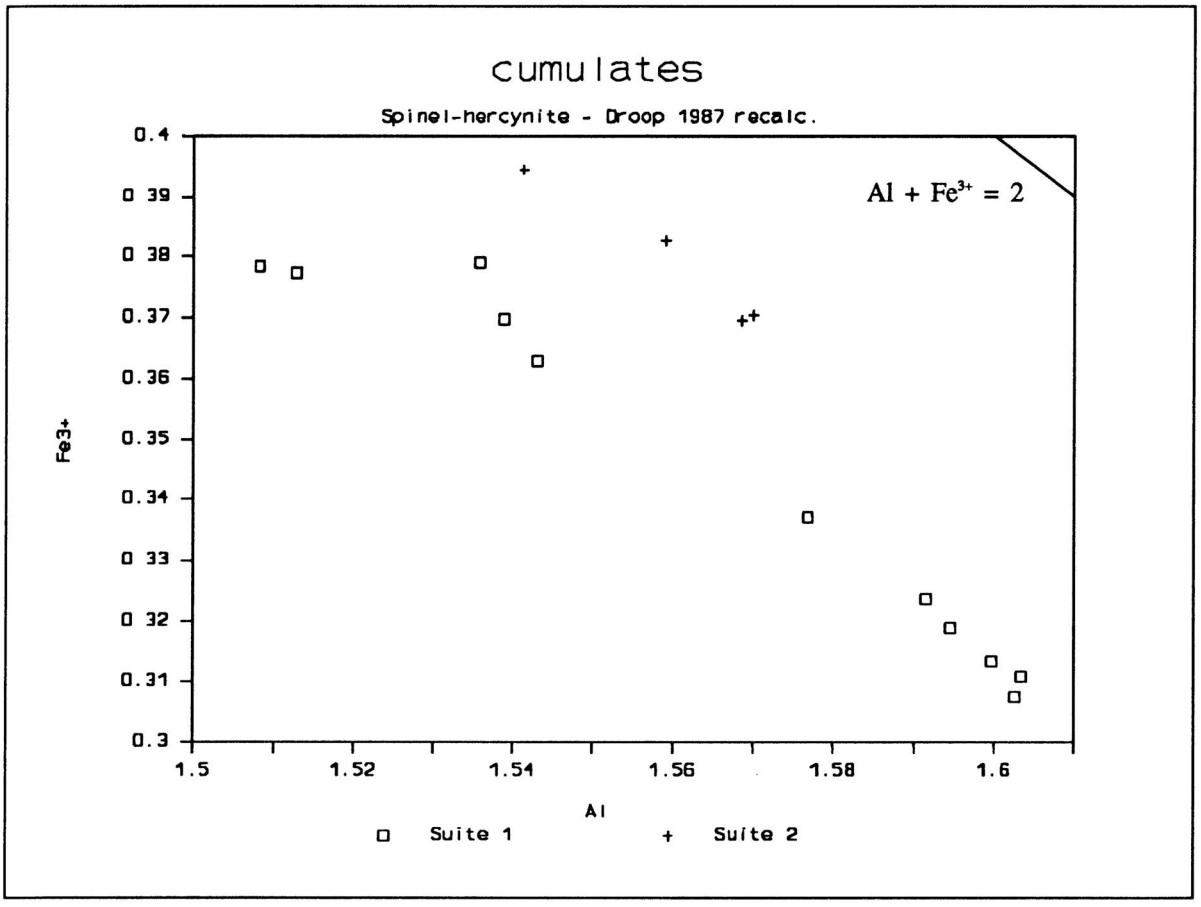


Figure 4.6.23

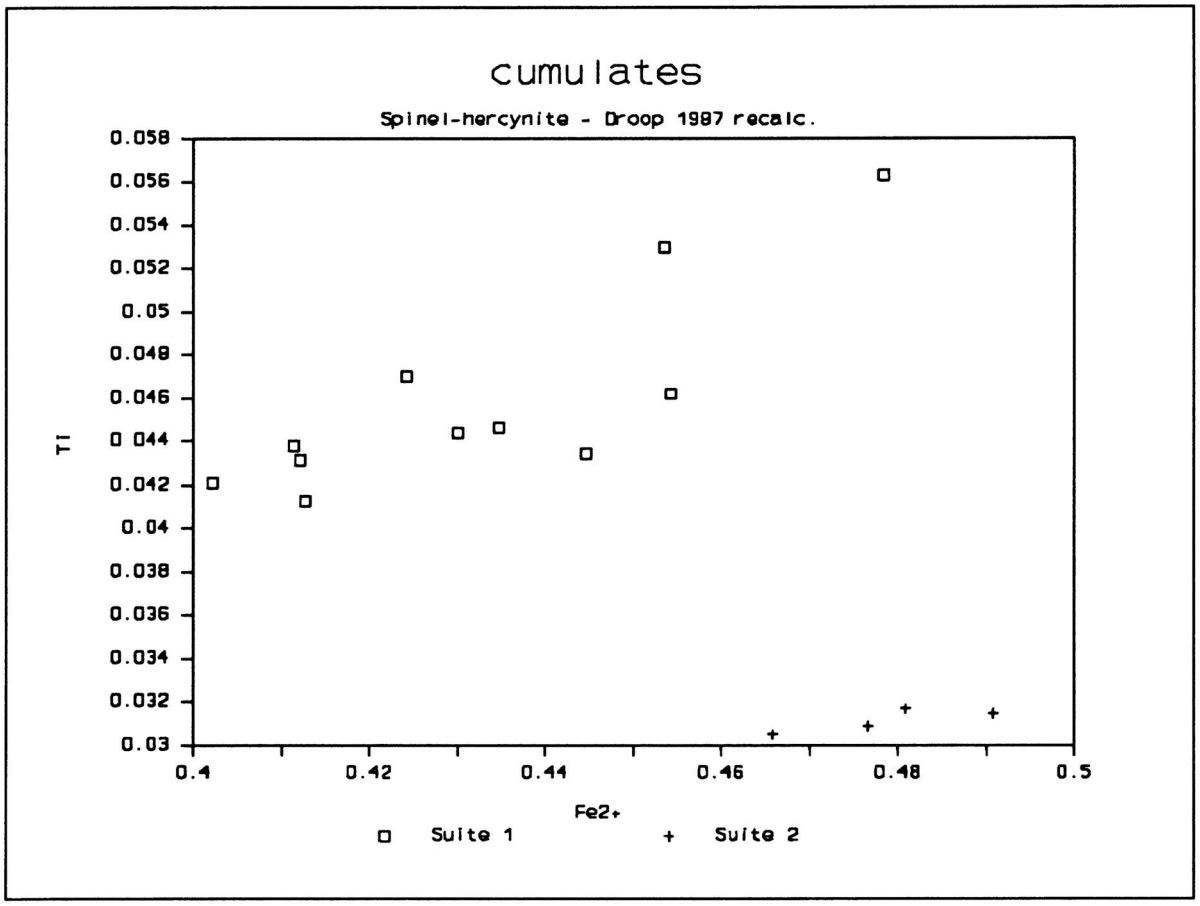

cumulates
Spinel-hercynite - Droop 1987 recalc.
0.058
0.056
0.054
0.052
0.05
0.048
0.046
0.044
0.042
0.04
0.038
0.036
0.034
0.032
0.03
TI
0.4
0.42
0.44
0.46
0.48
0.5
Fe2+
Suite 1
Suite 2

Figure 4.6.24

4.6.7 Biotite

Biotite first appears as small crystals in 88/14e, both within and overgrowing the abundant amphibole. The nature of this replacement is described in section 4.5.3 (*Suite 3*) and illustrated in Figure 4.6.25. The proportion of biotite is 2 - 9% in Suite 3, initially only replacing amphiboles, but later becoming more subhedral and showing signs of having settled from the melt. Maximum grain size reached is 4mm.

In Suite 4 the proportion rises to 8 - 17%, with two apparently anomalous blocks; 86/38b with 28%, and the biotite-rich layer in 88/14q with 38.5%. 88/14q shows that biotite can be concentrated on a small scale and 86/38b may represent part of such a layer. Crystals in Suite 4 are eu-subhedral and probably settled from the melt (see Figure 4.5.8). The partially resorbed clinopyroxene in this suite is often overgrown by small biotite crystals. Maximum grain size reached is 6mm.

No biotite in any cumulate block shows any pleochroic haloes, despite the occasional inclusion of zircons. This is probably due to their having formed recently.

The pleochroism of the biotites varies from yellow/red-brown/red-black to pale yellow/greeny-brown/dark red-brown, but shows no correlation with position in the series. Deer *et al* (1966) describe the $Ti:Fe^{3+}$ ratio as being the main control on colour, with high Ti giving reddish brown and high Fe^{3+} green, intermediate proportions giving yellow/greenish-brown. The cumulate biotites probably have high to intermediate $Ti:Fe^{3+}$ but the accuracy of the recalculation for Fe^{3+} leaves room for doubt.

Biotite has the formula:

$$K_2(Mg,Fe^{2+})_{6-4}(Fe^{3+},Al,Ti)_{0-2}[Si_{6-5}Al_{2-3}O_{20}](OH,F)_4$$

where K can be partially replaced by Na, and Fe^{2+} by Mn (rarely > 0.2 apfu). Biotite *sensu stricto* has Mg:Fe < 2:1, and all of those in the Velay blocks are true biotites. The calculation for Fe^{3+}, using Droop (1987) was made using 14 cations, excluding the K since these sites are often incompletely filled.

The only strong correlation is between Mg and Fe^{2+} as shown in Figure 4.6.26 ($Mg + Fe^{2+} = 4$ line added for reference), with the highest Fe^{2+} in Suite 4. Figure 4.6.27 shows that Mn correlates poorly with Fe^{2+}, with highest Mn in Suite 4. Fe^{3+} has a range of 0.8-1.4 apfu and shows no correlation with other elements. Other elements have relatively constant values: Al 2.4-2.7 apfu, Si 5.4-5.6 apfu, Ti 0.6-0.7 apfu, K 1.7-1.8 apfu, Na 0.18-0.30 apfu and Ca is absent from the biotite structure. The only trend is the slight Fe^{2+} enrichment relative to Mg in the biotites of the later cumulates.

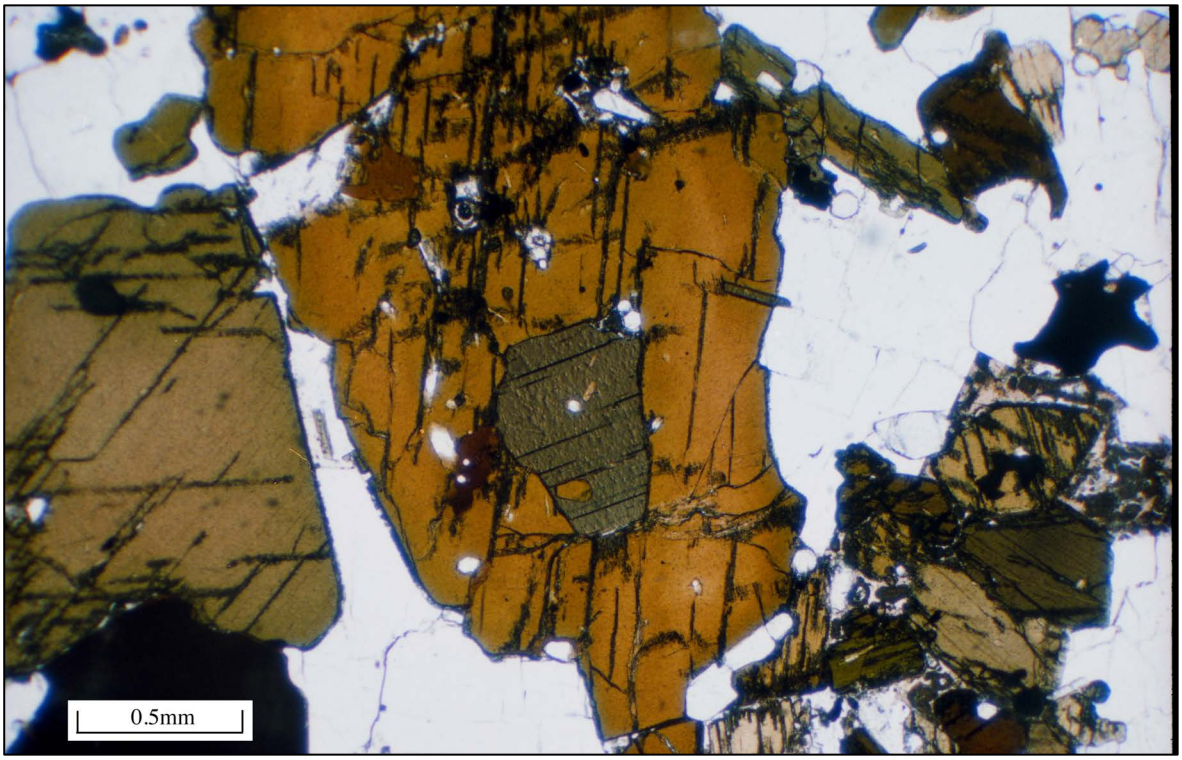


Figure 4.6.25. Biotite within a kaersutite amphibole in block 88/14u. This relationship is very common in Suite 3 blocks but does not imply that the biotite crystallised first. The biotite grew by reaction of the amphibole with intercumulus melt, although the connection with the melt is not usually in the plane of the section. (Plane polarised light).

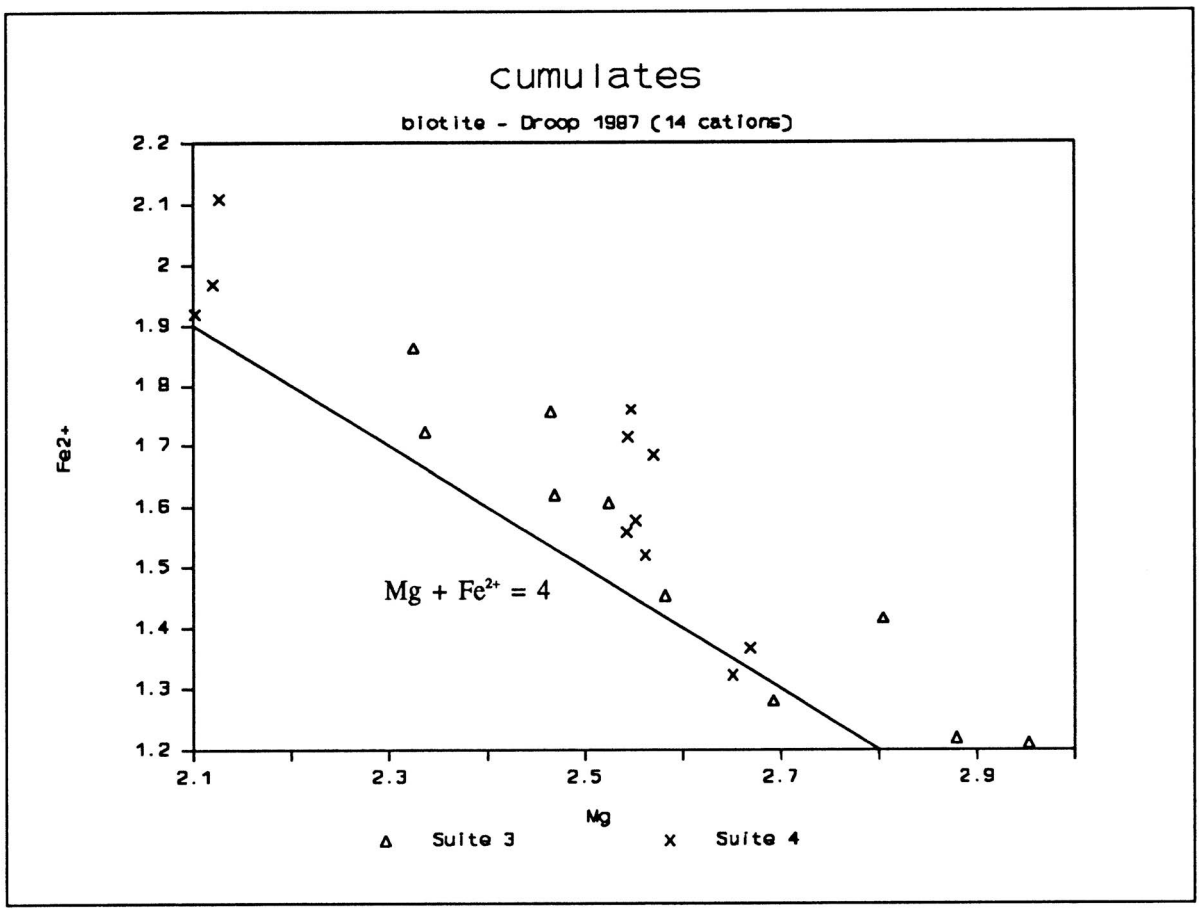


Figure 4.6.26

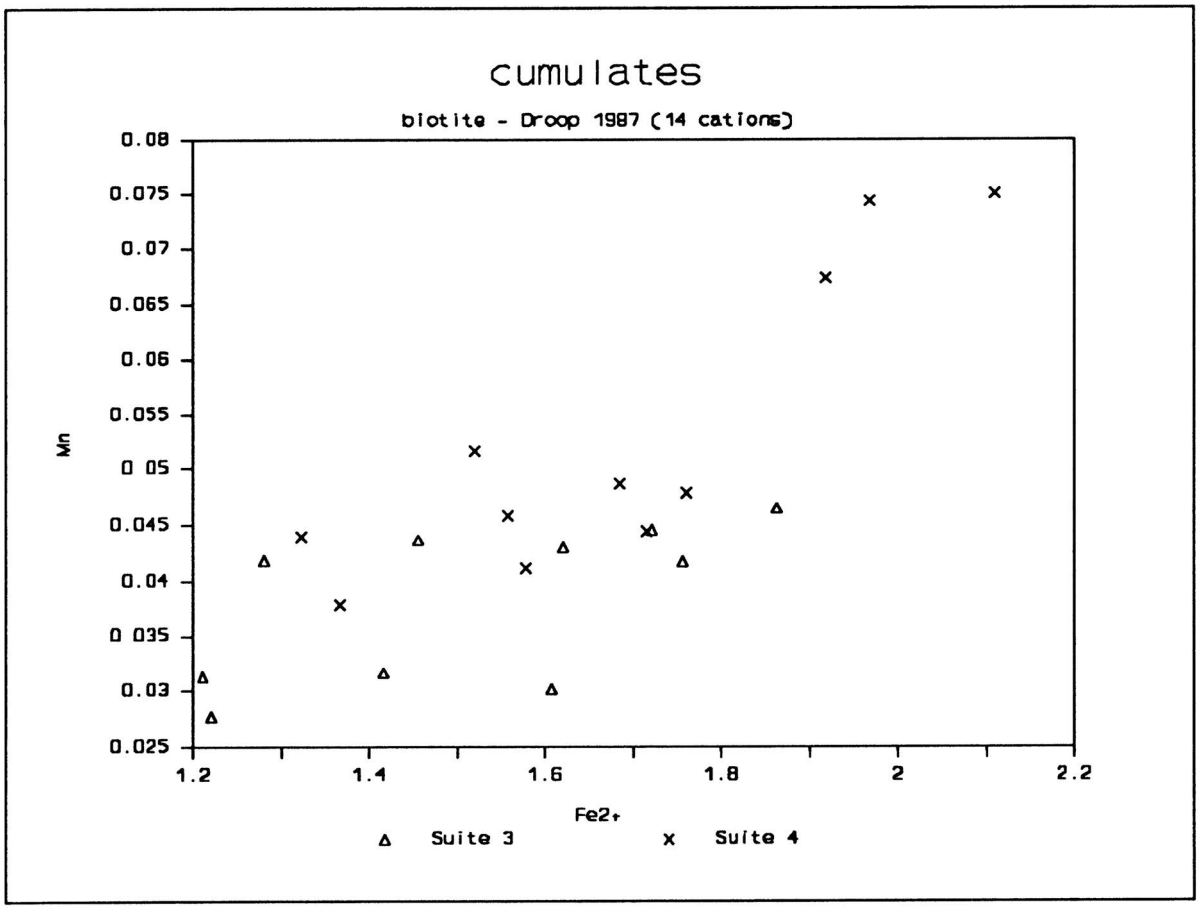


Figure 4.6.27

4.6.8 Apatite

Apatite is ubiquitous in the blocks of Suites 2, 3 and 4. It appears abruptly in 86/38g as fairly large 0.4 x 1.0mm crystals, forming 6% of the rock (see Figure 4.5.7). Both maximum grain size and proportion decrease towards the most evolved blocks. Occasional large crystals in the evolved blocks may be from disrupted early cumulates. Apatite is colourless throughout the series and occasionally contains fluid inclusions, either throughout the crystals, or restricted to their cores, especially at the Suite 3/Suite 4 boundary. It is always the earliest formed mineral.

The sudden appearance of large proportions of apatite, and its decline in importance with continued evolution of the blocks, parallels the trend seen in the Velay lavas. This is ascribed to the initial incompatible behaviour of P_2O_5, until $a_{P_2O_5}$ reaches the level at which apatite is able to nucleate. The rapid removal of P_2O_5 by apatite fractionation leaves little of this component in the liquid to form crystals later in the series, and so the proportion of apatite declines.

Test analyses showed that no element other than Ca^{2+} or P^{5+} appear in concentrations greater than about 1%.

4.6.9 Sphene and Zircon

As indicated at the top of Figure 4.5.4, sphene appears near the start of Suite 3 and makes its last appearance in 88/14k, half-way through the suite. It is colourless, has high relief and is usually present as an accessory phase. It is the last phase to crystallise, appearing either in the glass, or the outer parts of plagioclase and biotite crystals, and has a continuous size range of 0.1 - 4.0mm. The largest crystals appear in the glass of 88/14e, and are subhedral, enclosing opaques and apatite. They give 0.5% sphene in this section, which may not be representative of the rock as a whole.

Sphene usually appears as an-subhedral crystals, even when surrounded by glass. The few euhedral crystals are almost always in the glass, but their outline is not the classic elongate parallelogram of the lavas, but has more terminations, cutting off the sharp ends to give a more stubby crystal form, as shown in Figure 4.6.28. Sphene usually occurs in blocks with abundant carbonate, which can cause identification problems. The simplest distinguishing feature is the lack of variation in relief as the stage is rotated, whereas carbonate has strong variation.

Sphene appears at about the same point as biotite starts to replace the amphibole. Biotite rejects all Ca from the amphibole structure into the liquid, temporarily raising a_{CaO} and allowing sphene to crystallise at the expense of the Ti-bearing opaques. The overgrowth of sphene on opaques is quite common (see Figure 4.6.29), and the sphene-bearing blocks have a noticeably lower proportion of opaques. An increase in the oxygen fugacity of the melt is probably equally as important in causing such overgrowth (see section 3.2.9).

Block 88/14k witnesses not only the last appearance of the sphene but also the first appearance of zircon, with lower birefringence and a more equant form. It is intermittently present in the more evolved blocks, including the most evolved sample (88/14a). It has a smaller size range than that of

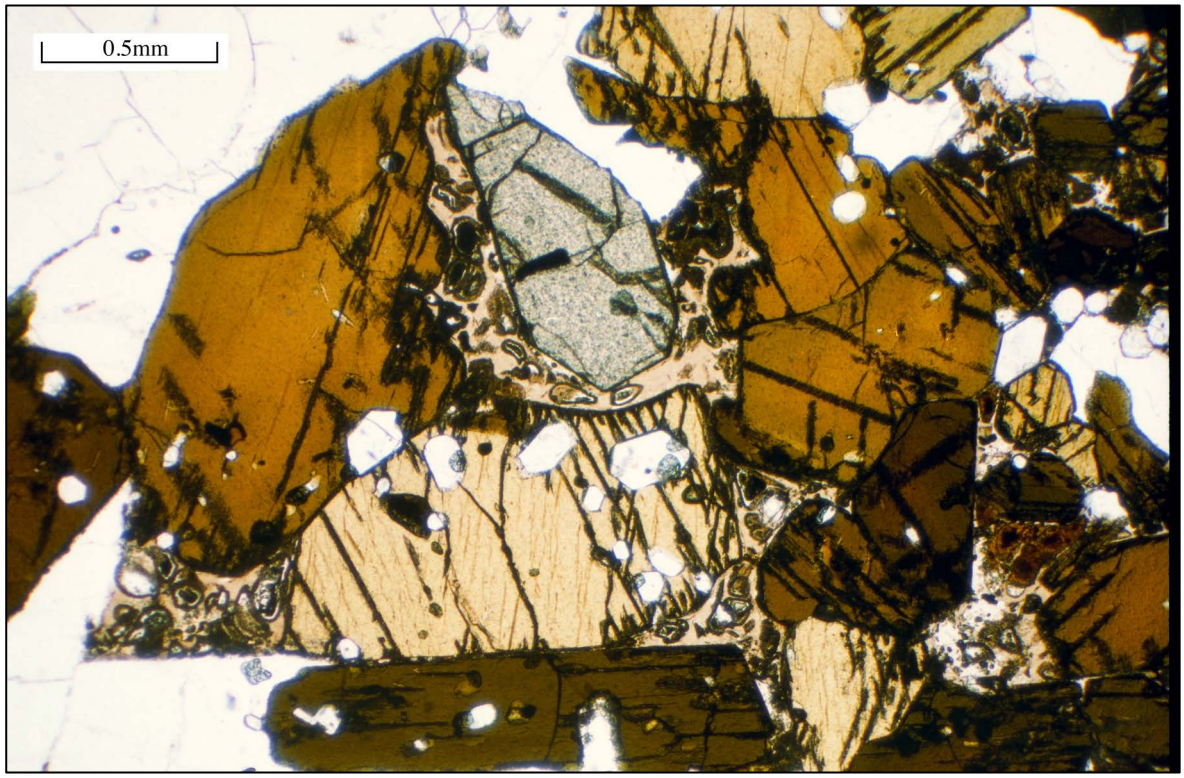


Figure 4.6.28. Euhedral sphene in a patch of pale brown glass in 88/14u (Suite 3). Due to its high relief it appears grey in this picture. It also lacks the characteristic wedge-shape of sphene. The colourless anhedral mineral is feldspar and the euhedral hexagons are apatite crystals. Kaersutite shows all shades from pale-yellow to olive-green and dark brown. (Plane polarised light).

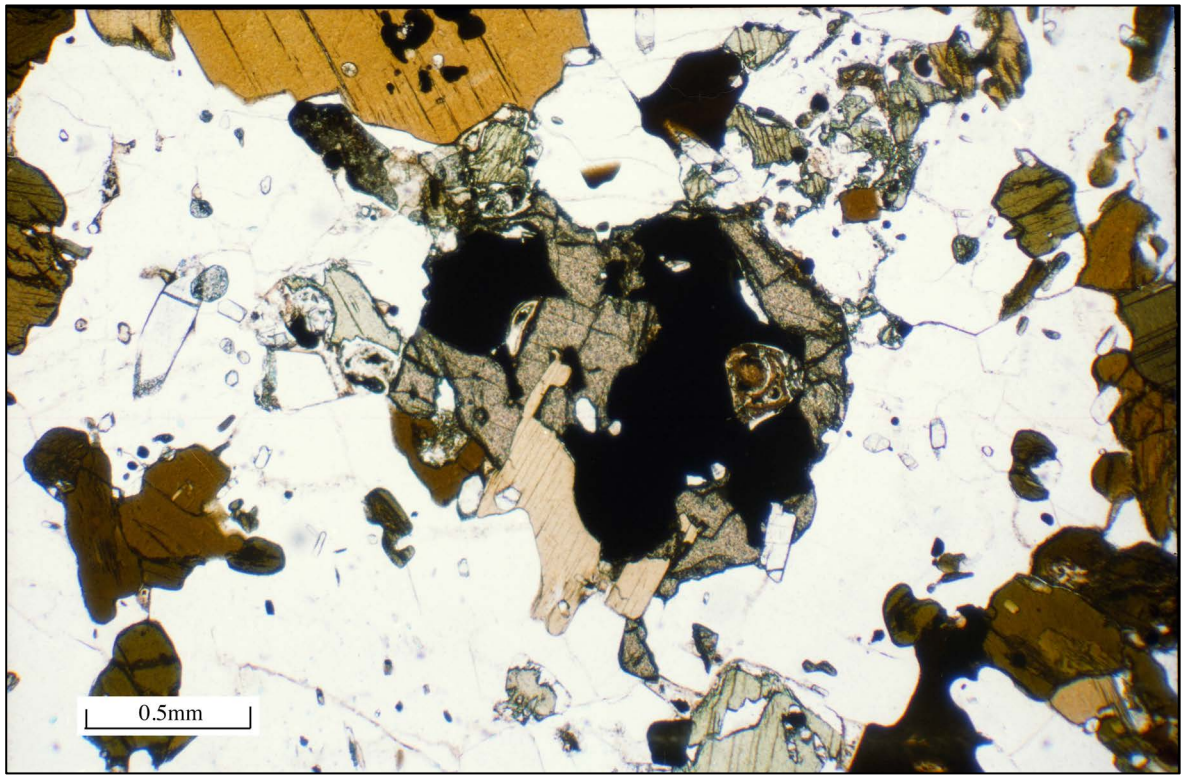


Figure 4.6.29. Block 88/14k (Suite 3) contains this opaque mineral (Ti-magnetite or ilmenite) overgrown by sphene. The reaction is caused, at least in part, by an increase in oxygen fugacity, which promotes the growth of Fe^{3+}-rich minerals and releases Ti to form sphene. Other minerals visible are feldspar (anhedral, colourless), biotite (subhedral, strong cleavage, orange to brown), apatite (euhedral, colourless), cpx (pale green, anhedral, reacting with liquid) and amphibole (olive green, anhedral). (Plane polarised light).

the sphene, from < 0.1mm to 0.4mm, and is colourless with high relief. Although often poorly formed, there are a few euhedral squares and diamonds within the glass. Zircon crystals are often found enclosed in the outer parts of plagioclase and biotite crystals, just like the sphene, and were clearly among the last phases to nucleate.

Both sphene and zircon were microprobed, but only sphene showed the presence of significant minor elements (1.75% Al_2O_3 and 1.85% FeO^T).

The presence in the blocks of both sphene and zircon demonstrates the miaskitic nature of the melt from which they were crystallising. In a peralkaline liquid the typical Zr/Ti-silicates include eudialyte, låvenite, mosandrite, aenigmatite and catapleite (see Table 3.1.6).

4.6.10 Pyrrhotite

Pyrrhotite is present throughout the series, but is far more common in Suites 1 and 2 than in the more evolved cumulates. It appears most commonly as circular blobs (≤ 0.15mm) within other minerals, especially clinopyroxene. It is pink in reflected light, shows strong bireflectance, and no exsolution was observed in any sample. In addition to the circular blobs, three blocks (88/14n, 88/14p and 88/14v) contain irregular fragments of the same material, although the total amount in any one block is always less than 0.5%. In Suites 3 and 4 the blobs are smaller, only 0.04mm diameter, and much less common. In Suite 4, only block 88/14s has a single blob of pyrrhotite, in an ilmenite crystal. Pyrrhotite is clearly most strongly associated with the crystallisation of the earliest minerals.

The general formula of pyrrhotite is Fe_nS, where $7/8 < n < 1$. The Fe-deficiency has been shown to be due to gaps in the structure, rather than the incorporation of excess S (Deer *et al* 1966). Two analyses of blobs in 86/38a gave $Fe_{0.92}S$, with trace amounts of Si, Al, Mg, Ca, Mn, Na, K and Ti. The detection of other elements, such as Ni, Co and Cu was not attempted.

The form of this sulphide shows that it was present as disseminated droplets of an immiscible liquid within the main body of silicate, which were incorporated into silicate crystals as they grew. The presence of subhedral pyrrhotite fragments in some blocks suggests that some crystallisation of this sulphide liquid took place. The sulphur present in the primary magma would have scavenged Fe to make a dense sulphide melt, which was rapidly removed into the cumulate pile, thus explaining the decrease in the amount of pyrrhotite from Suite 1 to Suite 4.

4.6.11 Glass and Carbonate

These two phases are dealt with in the same section because they are always intimately related in the blocks, and were probably coexisting immiscible liquids, as explained below.

Glass and carbonate are present in variable proportions, both relative and absolute, from the most primitive blocks to the most evolved, both increasing in amount towards the evolved end of the series. The total variation is from nearly 0% in some of the Suite 1 blocks, to 27% glass+carbonate in the most extreme case. In the most primitive blocks carbonate is often present alone, the only trace of

glass being a brown film on the crystal sutures. The carbonate fills interstices with very rounded outlines, occasionally showing signs of zoning as centripetal "dog-tooth" crystals grew. The more evolved blocks have a higher proportion of glass, as would be expected if they came from the top of a cumulate stack where adcumulus crystal growth had not yet filled in the interstices.

The carbonate usually appears in the glass either as diamond shapes, with rounded outlines due to the overgrowth of smaller crystals, or as irregular blobs making up as much as 50% of the glass+carbonate mix. A good example of such blobs is shown in Figure 4.5.3. These blobs are rounded and comprise several crystals, which is the classic texture for chilled immiscible liquids. 88/14m provides the best example of this relationship, with 18.5% glass+carbonate, as shown in Figures 4.6.30 and 4.6.31. The carbonate is present as cauliform blobs within the glass, forming over 50% of the mixture in some areas. The overall impression is of an emulsion in which finely divided blobs of unmixed carbonate liquid were quenched within a brown silicate melt. The melt is clearly intercumulus since adjoining crystals have sharp faces, often better than in the rest of the block. The melt also contains quenched crystals of amphibole and Ti-magnetite, identical to the minerals of the block.

The relationship of the melt to the block is almost always that of an intercumulus liquid, with sharp crystal faces on the adjoining minerals (section 4.5.2). Exceptions are the pale green cpx in the more evolved blocks, which has reacted with the liquid, and the margins of plagioclases adjacent to the glass in 86/38f, which show a sieve texture. Quench crystals in the glass of the Suite 1 blocks are always of minerals which appear in more evolved cumulates, e.g. amphibole quench crystals in clinopyroxene+Ti-magnetite blocks.

The glass is very often altered, with dissolution of the carbonate creating a cryptocrystalline mess. Unaltered glass varies in colour from dark brown in Suite 1 to pale brown in Suites 3 and 4, probably due to decreasing Fe-content, by analogy with the colour of fused XRF beads. The variation in the composition of the glass is examined with that of the bulk cumulates in section 5.7.2.

If the carbonate *did* form an immiscible liquid there should have been very little elemental exchange between it and the silicate melt, and therefore bulk chemical trends in the carbonates would be independent of those in the silicates. Figure 4.6.32 shows a correlation between Fe and Mg for 23 of the carbonate analyses, with a general tendency for Mg to increase as the compositions of the blocks evolve, contrary to the pattern in silicate minerals. This trend is weak, since Suite 4 has carbonates covering the whole range of compositions, and two of the analyses are not plotted: the carbonate of 88/14m is almost pure calcite, and block 88/14f produced one analysis of ankerite. All the other analyses were of Fe-rich magnesite, or Mg-rich siderite, with Ca always less than 15%. The only other correlation in the carbonates is between Mn and Fe, as shown in Figure 4.6.33, with more Mn and less Fe in the more evolved blocks. There is a good deal of scatter in Suite 4, but there is much less overlap between suites on this graph. The calcite and ankerite analyses have again been omitted. All other elements, including Na, Al, Si, K and Ti are present only in trace amounts.

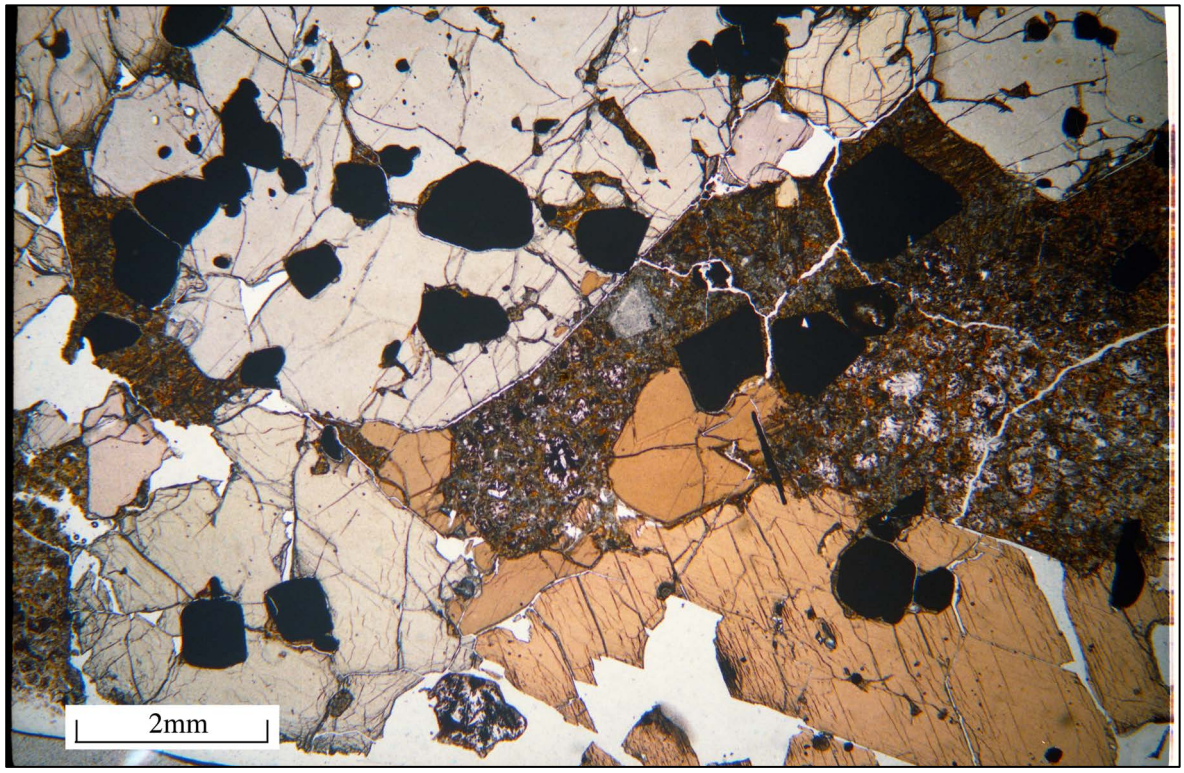


Figure 4.6.30. Block 88/14m (Suite 1) contains large areas of glass + carbonate, suggesting that it escaped adcumulus infilling of its interstices. It is unique in Suite 1 in that a few of the Ti-magnetites in the glass are euhedral (shown above), as are the clinopyroxene and amphibole, although on a larger scale than this photograph. (Plane polarised light).

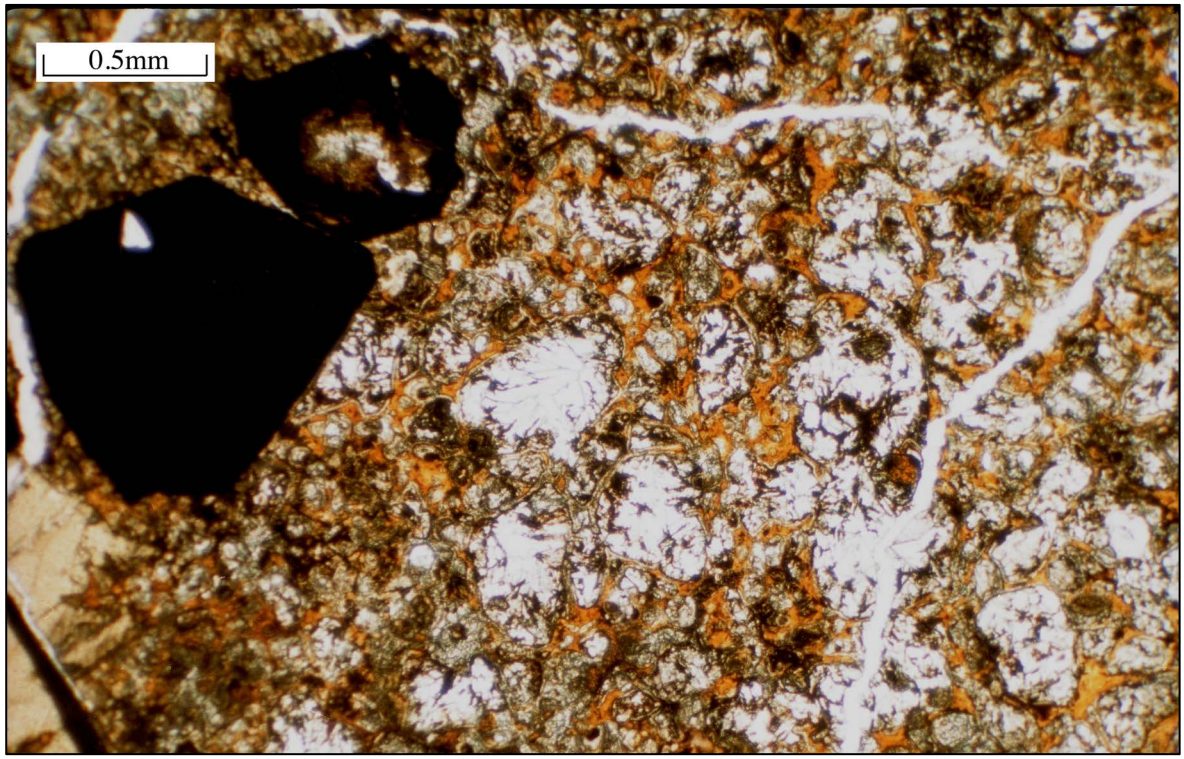


Figure 4.6.31. A close-up of an area to the centre right of Figure 4.6.30 (above). The picture shows the glass+carbonate mixture, with orange glass surrounding the rounded polycrystalline carbonate blobs. The same effect can be seen to a lesser extent in the glass of Figures 4.5.3 and 4.6.28. It is caused by the immiscibility of carbonate and silicate melts. (Plane polarised light).

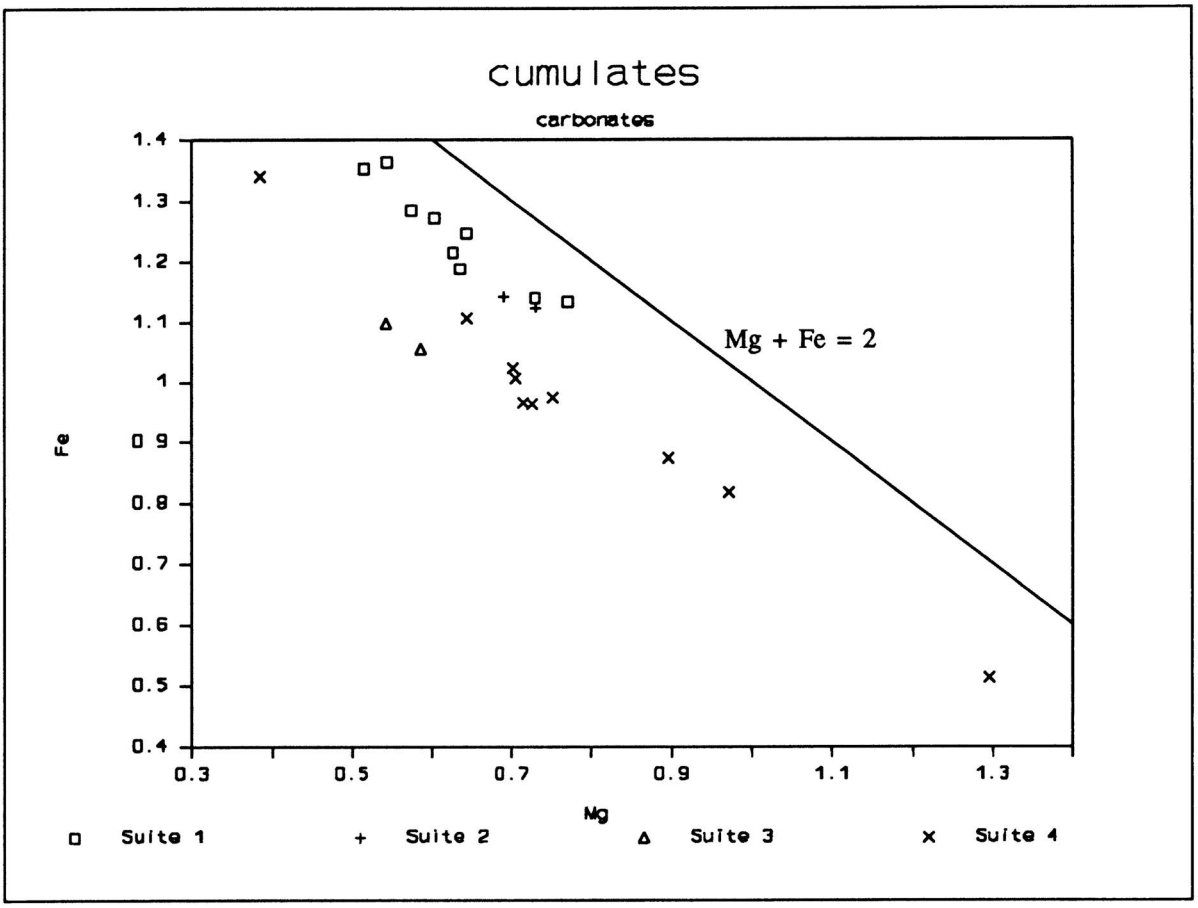


Figure 4.6.32

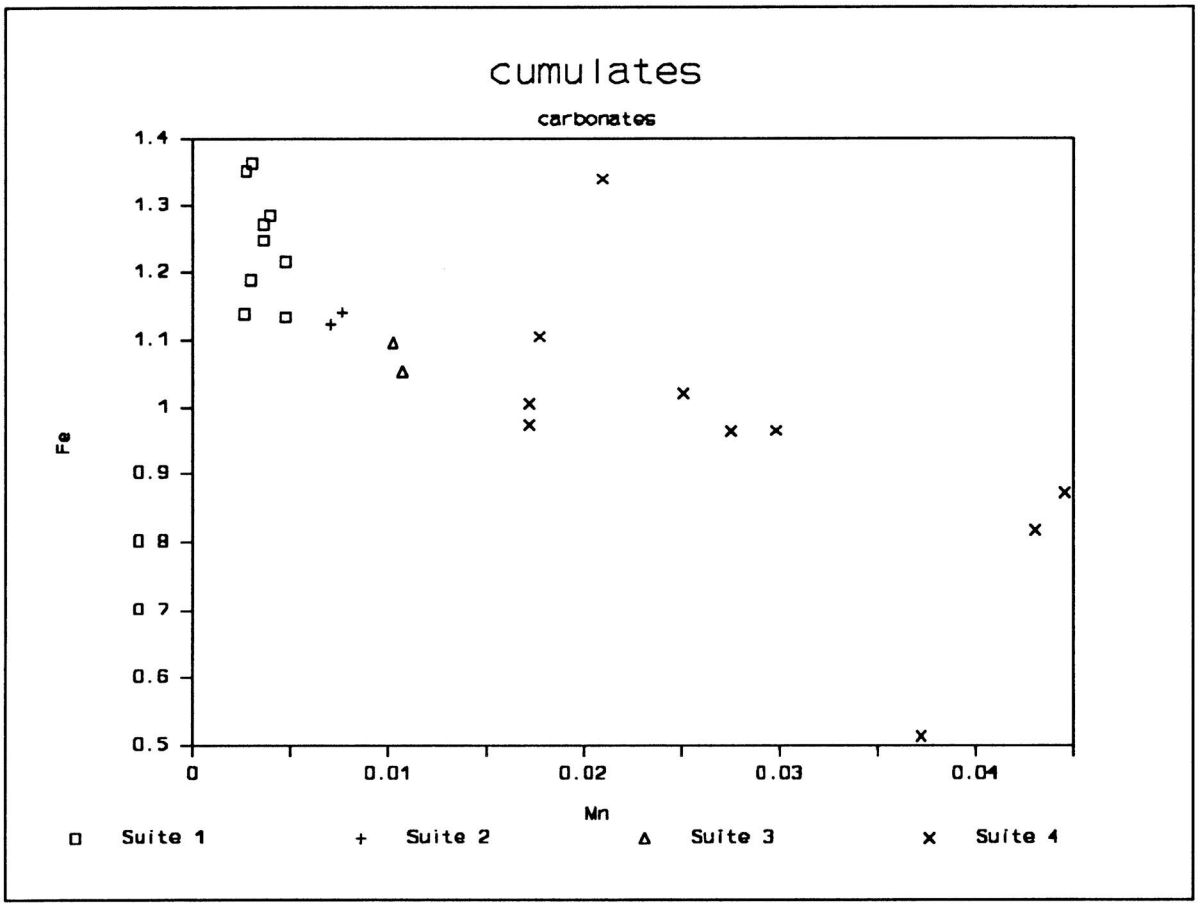


Figure 4.6.33

Studies of carbonatites have shown that the normal compositional trend is towards Fe-enrichment. Gittins (1989) gave a more detailed scheme:

1) Initial alkali enrichment, then depletion

2) Mg-depletion

3) Fe-enrichment, then either:

a) appearance of magnetite, and Fe-depletion (usually plutonic), or

b) continued Fe-enrichment to ferrocarbonatite (usually volcanic).

This is hard to reconcile with the Velay carbonates, since the observed Mg-enrichment is not included in the model. Fractionation of Fe-rich carbonate or magnetite seems to be required. Similarly it is hard to explain the presence of both the calcite-bearing 88/14m block, and the ankerite in 88/14f.

Gittins (1989) observed that calcite or dolomite are the first carbonates to crystallise from a carbonatite magma, depleting it in Ca + Mg. 88/14m and 88/14f may have retained samples of an early carbonate melt, before fractionation. Later removal of a sideritic carbonate or Fe-oxide would be needed to generate the Fe-rich⇒Mg-rich trend.

4.7 Other Occurrences of Cumulate Nodules

4.7.1 Introduction

The presence of xenoliths and megacrysts in lavas has been noted for hundreds of years, but they have been systematically studied only in the last few decades. Excluding crustal material, the common inclusions in alkali basalts have been found by many workers to fall into two groups, characterised by their clinopyroxene composition. These groups were designated the Cr-diopside type and the Al-augite type by Wilshire and Shervais (1975), who provided a broad review of the literature on the subject. Most authors at this time agreed that the Cr-diopside type represented samples of the mantle and that, on the basis of texture and composition, the Al-augite type represented high-pressure cumulates (Best 1975, Wilkinson 1975). Wilshire and Shervais (1975), however, produced an alternative model for the Al-augite inclusions of the western United States, on the basis of a small proportion which contained contacts between Cr-diopside and Al-augite material, and also by analogy with features seen in Alpine peridotite massifs. They proposed that the Al-augite material had a deep source, as a basaltic partial melt, which intruded the upper mantle as a network of narrow veins and dykes. These were subsequently disrupted and brought to the surface by a later generation of magma.

Later workers have tended to support the cumulate theory but both hypotheses have had supporters. In a paper about the San Carlos inclusions, Frey and Prinz (1978) reviewed the literature on both the Cr-diopside and Al-augite types. Table 4.7.1, from their paper, summarises the differences between the two types, which they renamed Group I and Group II to avoid some of the problems caused by classification by mineral composition alone. They also noted that Group I inclusions were ten times more abundant than those of Group II, and were never in equilibrium with

	Group I Cr-, Mg-rich	Group II Fe, Ti-rich
Mineralogy	* Olivine * Orthopyroxene * Clinopyroxene Spinel (mainly chromite-spinel) Phlogopite Pargasite	* Clinopyroxene * Olivine * Kaersutite (rarely includes phlogopite) * Spinel (mainly chromite-hercynite) Orthopyroxene (usually minor) Plagioclase Titanomagnetite Ilmenite Apatite
Modal proportions	Lherzolite and harzburgite are most abundant, i.e., ol ⩾ opx > cpx > sp, but some pyroxene-rich samples occur	Highly variable, but commonly cpx ⩾ opx and spinel is more abundant than in Group I
Mineral composition	Pyroxenes and spinels are Cr-rich and TiO_2-poor, silicates generally have Mg/Mg + ΣFe > 0.85	Pyroxenes are Al_2O_3-, and TiO_2-rich but Cr-poor, spinels are Al-rich and Cr-poor, silicates range widely in Mg/Mg + ΣFe, generally < 0.85
Textures	Xenomorphic-granular: metamorphic, recrystallized, triple point junctions; relict, large, exsolved clinopyroxene mainly in clinopyroxenites. Exsolution best developed in larger crystals. Deformation and kink bands are common in olivine and pyroxene. Evidence of minor partial melting along grain boundaries, and as veins (with plagioclase microlites); phlogopite, pargasite and clinopyroxene are most commonly involved	Often poikilitic, but many samples have recrystallized or annealed textures; thus, examples of igneous and metamorphic textures occur. Paragenesis: spinel, olivine, clinopyroxene (minor orthopyroxene), kaersutite and plagioclase. Olivines are always iddingsitized. Clinopyroxene is commonly intergrown with kaersutite, and often has exsolved orthopyroxene and spinel. In gabbros symplectite textures occur between olivine and plagioclase. Partial melting of all phases (especially kaersutite), as patches or veins, is present in most rocks
Structures	Orthopyroxenites and clinopyroxenites interlayered with lherzolite; contacts are usually plane-parallel. Sometimes inclusions are cut by kaersutite-rich veins	Pyroxene-rich units, as veins or layers cut olivine-rich units, and they sometimes completely surround olivine-rich lenses. In contrast to usual sharp contacts of Group I rock units, Group II contacts are often gradational
Rock types	Spinel lherzolite (most common) Spinel dunite Spinel harzburgite Spinel olivine orthopyroxenite Spinel orthopyroxenite Spinel olivine clinopyroxenite Spinel (olivine) websterite Spinel wehrlite	Spinel (olivine, kaersutite) clinopyroxenite (most common) Spinel (olivine, kaersutite) websterite Spinel (kaersutite) wehrlite Spinel kaersutite peridotite Spinel dunite Spinel (olivine, clinopyroxene) kaersutite Olivine spinelite (Olivine, kaersutite) gabbro

* May be major (>80% mineral in some samples).

Table 4.7.1. Characteristics of Group I and Group II inclusions at the San Carlos locality (Frey and Prinz 1978). Many of the Group II characteristics are the same as those of the Velay inclusions.

their host lavas, whereas Group II inclusions occasionally were. Rare earth element analyses and Sr-isotopes were also found to support a cumulate origin for the Group II inclusions.

The composition of minerals in the inclusions was thought to suggest high-pressure crystallisation, especially the Al-rich clinopyroxene, which has a composition similar to that produced experimentally at 13.5-22.5kb in basalt (Irving 1974). The occasional presence of garnet suggests pressures > 20kb, an absence of plagioclase suggests > 17kb and when present, olivine indicates < 20kb (Best 1975).

The smallest dimension of the parent bodies of the Group II inclusions is inferred to be at least a few metres, based on the rarity of wall contacts preserved in the cm-scale inclusions (Best 1975).

Nixon (1987) summarised much of what is known about world xenolith occurrences. The descriptions included in his book showed that the distinction between Group I and Group II inclusions was valid for virtually all localities. Menzies *et al* (1987) noted that Group II inclusions were 10,000 times more oxidised than the Group I mantle xenoliths, and equilibrated with a melt at 1300°C and with $\partial^{18}O = 5.7 \pm 0.3$. Such a low value of $\partial^{18}O$ is normal for the mantle or mantle-derived basalt, suggesting that the xenoliths have not been contaminated with crustal material.

O'Reilly and Griffin (1987) divided the Group II inclusions of eastern Australia into three sub-types:

1) Wehrlite series (cpx + olivine assemblages) + spinel, feldspar, opx, ilmenite, amphibole, mica, apatite and sulphides. Mainly cumulate structures. Formed at 28-58km depth, 950-1000°C (O'Reilly 1989).
2) Metapyroxenite series (subsolidus equilibrated wehrlite series). Mainly metamorphic textures.
3) Apatite/amphibole series (crystallised from an incompatible element and volatile enriched magma). Igneous to metamorphic microstructures, often with layering.

The apatite/amphibole inclusions were described in more detail by O'Reilly (1987). They are composed of amphibole, apatite, Al-augite, altered olivine, mica, Mg-ilmenite, spinel-rich Ti-magnetite, carbonate, rare rutile and sulphides, and have high TiO_2, K_2O, P_2O_5, REE (especially LREE), CO_2, Cl, F and H_2O. Their $^{87}Sr/^{86}Sr$ range is 0.70369-0.70398.

Megacrysts (crystals or crystal fragments > 5mm) are also commonly included in basalts and were classified by Irving (1984) into Groups A and B. Group A includes Al-augite, Al-bronzite, olivine, kaersutite, pyropic garnet, Fe-pleonaste and plagioclase, and is thought to be the product of fractional crystallisation of a basaltic liquid. Group B includes anorthoclase, Ti-mica, Fe-Na-salite, apatite, magnetite, ilmenite, zircon, corundum, rutile and sphene, and are almost never in equilibrium with basaltic liquids. They are presumed to have crystallised from relatively evolved liquids (nepheline benmoreite to phonolite) and were brought to the surface after mixing with more primitive magmas.

The consensus is therefore that the Group I inclusions are mantle samples and the Group II inclusions and all megacrysts are high pressure cumulates and phenocrysts of magmas, though not necessarily their host magma.

4.7.2 Comparison with the Velay Nodules

The cumulate inclusions of the Velay oriental clearly belong to Group II, on the basis of their Al-augites, Ti-rich kaersutites and pleonastes and their cumulate textures and variable modes. However, they differ from those described in most of the literature in many ways. The most primitive Velay blocks have cpx + spinel + Ti-magnetite, with no olivine. Olivine is absent from the entire Velay cumulate series, but is the most common mineral described in many Group II suites, for example at San Carlos (Frey and Prinz 1978). The closest analogy to the primitive Velay blocks in the suites described is in the Grand Canyon (Best 1975) where cpx + spinel + amphibole blocks are the second most abundant.

In an attempt to find a closer analogue for the Velay series a literature search was made for kaersutite-bearing nodule suites, which were then filtered to exclude those containing olivine or orthopyroxene. Surprisingly, of the four localities that remained -Mont Dore, Cantal, Laacher See and Tristan da Cunha - the first two are in the Massif Central and Laacher See is in the Eifel, only 600km to the NE of the Velay. These three are also the closest analogues to the Velay cumulates.

The Tristan da Cunha blocks were described by Le Maître (1969), with five bulk analyses. The blocks contain Al-augite (9% Al_2O_3, 3% TiO_2), kaersutite (6% TiO_2), plagioclase (An_{82-85}), Fe-oxides and biotite (in one block). Le Maître described the texture of these blocks as gabbroic and interpreted them as high pressure cumulates of Tristan magmas.

The blocks of the Mont Dore were first described by Lacroix (1917) with nine bulk analyses, but only limited hand-specimen descriptions of their constituent minerals, for example describing the K-feldspar as orthoclase, which is not usually seen in Group II inclusions. He described rocks ranging from holomelanocratic to 60%-leucocratic, containing augite, Ti-magnetite, hornblende, biotite, sphene, haüyne, andesine, labradorite, bytownite, orthoclase, nepheline and even olivine (in one block). He rejected a cumulate origin for the blocks, preferring *in situ* consolidation of magma as an explanation for their formation, by analogy with rocks he had observed in Réunion island.

Mervoyer *et al* (1973) also provided bulk analyses of three cumulate blocks from the Mont Dore. They contained plagioclase An_{75}, Al-augite (9% Al_2O_3) and amphibole (2.2% TiO_2) with biotite inclusions. No description of texture was given but the rocks were interpreted as being the fractionation products of a basic lava.

Cumulate nodules from the Cantal were studied by Maury (1968), who presented bulk analyses of two blocks from the Suc de Lac ankaramite neck. They contained plagioclase An_{70}, Ti-rich salite, Ti-magnetite, brown amphibole, haüyne, sphene and apatite, and were interpreted as cumulates, with intercumulus haüyne.

Jasmund and Seck (1964) investigated blocks from the Laacher See Tephra, in the Eifel. They

bulk-analysed 21 blocks and microprobed a few of their minerals. The blocks were composed of sanidine Or_{52-61}, plagioclase An_{31-42}, amphibole (2.7-5.1% TiO_2), salite/ferrosalite (1.1-2.1% TiO_2, Al_2O_3 not determined), haüyne, Ti-magnetite (1.1-2.6% MnO), sphene, apatite and glass.

The Laacher See blocks have also been studied more recently by Tait (1988). He gave four bulk analyses and described the petrography of 34 blocks in detail. Minerals in these samples were the same as those found by Jasmund and Seck (1964), with the addition of mica (maximum 12%). Feldspars ranged from plagioclase An_{62} to anorthoclase $An_{13}Or_{16}$ and from sanidine Or_{70} to Or_{44}, with coexisting plagioclase and sanidine both evolving towards the feldspar minimum at about Or_{33}. The amphibole in these blocks contained 1.9-5.5% TiO_2. The clinopyroxenes had 3.5-10.5% Al_2O_3, 0.6-4.1% TiO_2 and were divided into Types I and II. Type I was a green salite/ferrosalite with low Al_2O_3 and TiO_2, present in the felsic nodules. Type II was brown to grey-violet Mg-salite/diopside with high Al_2O_3 and TiO_2 and was only present in the mafic nodules. These two types of cpx were very similar, in appearance, composition and host blocks, to those of the Velay cumulates. Tait (1988) described the textures in the Laacher See blocks as being like those in layered cumulate blocks, but he interpreted most of them as forming part of the mass of crystals growing on the sides of a chamber.

Figure 5.7.4 (section 5.7.2) shows all the bulk analyses of the cumulate blocks of the Velay, Mont Dore, Cantal, Laacher See and Tristan da Cunha plotted on a silica vs. total alkalis diagram. In addition to their mineralogical similarities they follow a very similar evolutionary trend, which suggests they formed from similar parental magmas at similar P, T conditions.

None of the papers on these four areas mentions the presence of Group I xenoliths coexisting with the Group II inclusions, and Le Maître (1969) even notes their absence in Tristan. In both the Laacher See (Wörner *et al* 1982) and the Velay pyroclastics basement fragments are abundant, and in the former they have been used to estimate the depth of the magma chamber as 3-6 km (Wörner *et al* 1982). In the Velay there are no amphibolitic or granulitic fragments accompanying the granite blocks, which suggests the magma chamber was in the upper crust. Seismic sections through this part of the Massif Central (Sapin and Hirn 1974, Perrier and Ruegg 1973) show that there is a significant increase in P-wave velocity from 6.07 to 6.30 kms^{-1} at about 16km depth, probably at the base of the Velay anatectic granite (see Figure 2.2.3, section 2.2). This suggests that the maximum depth for the postulated magma chamber is 16km. Phase equilibria discussed in section 5.9.1.4 constrain the formation of the most primitive Velay cumulates to pressures of 4 - 20kb. Other evidence, presented in section 5.10, narrows this range to 5 - 7kbars, or 15 - 20km.

If fractional crystallisation in all five localities discussed in this section *did* take place in the upper crust, or at least within 20km of the surface, it might explain the unusual absence of olivine and orthopyroxene in their inclusions, compared to the "normal" Group II suites, as being due to lower pressure crystallisation. The suites of Group II nodules which coexist with Group I xenoliths appear to have formed at mantle pressures. Despite the large range of pressures over which the Group II

inclusions are then presumed to have formed, all the suites described contain Al-augite. It seems therefore that this mineral is a poor geobarometer, and that other factors such as temperature and Al_2O_3-activity have more effect on its composition.

Major differences between the Velay cumulates and those of the Laacher See, Mont Dore and Cantal include the absence of haüyne and sanidine and the abundance of biotite in the Velay. Haüyne can form up to 36% of a Cantal inclusion and 25% in the Laacher See, indicating a strongly SiO_2-undersaturated parent liquid. In the Laacher See the parent magma was deduced to be a basanite (Wörner and Schmincke 1984b) which differentiated to form first a mafic phonolite and then more evolved phonolitic compositions. In the Velay the parental magma was probably of a similarly undersaturated composition, as suggested by the Suite 3 blocks with 2 - 7% normative nepheline. The last formed blocks however, have mildly undersaturated to slightly oversaturated compositions (Suite 4 ranges from 1.2% normative nepheline to 0.4% quartz) and interstitial glasses can reach 20% normative quartz, as shown in Figure 5.7.4 (section 5.7.2). If the major recrystallisation of the granite blocks (section 4.2) and the elevated values of $(^{87}Sr/^{86}Sr)_{initial}$ in the more evolved cumulate blocks (section 5.8) are taken into account, it suggests that the parental magma suffered significant crustal contamination.

On the basis of Sr-isotopes Wörner *et al* (1984) proposed minor (0.2%) contamination of the Laacher See magma, which had little effect on its strongly undersaturated character. The evidence detailed above shows that the magma in the Velay chamber was probably contaminated by enough of a SiO_2-rich melt, from the granite walls of its chamber, to push the liquid from the undersaturated domain into the oversaturated. Isotopic modelling in section 5.8.4 suggests that up to 11% contamination may have taken place, simultaneous with fractionation.

The range of compositions and modes in the Velay, Laacher See and Mont Dore inclusion suites is unusually large compared with others from around the world. In eastern Australia, O'Reilly and Griffin (1987) found inclusions with similar mineralogy to the most evolved blocks of the Velay, and classified them as the apatite/amphibole series. They deduced that their parent magma was incompatible element and volatile enriched. If the primitive inclusions of the Velay *are* equivalent to the wehrlite series, and the evolved inclusions are equivalent to the apatite/amphibole series, the Velay suite demonstrates that both series are part of a continuum and should not be divided. In the same fashion, megacrysts may also form a continuous fractionation sequence, with Type A megacrysts resembling wehrlite series minerals and those of Type B resembling apatite/amphibole series minerals.

Chapter 5

Geochemistry of the lavas and cumulates

5.1 Previous work

One of the earliest studies of the geochemistry of the Velay oriental was that of Brousse (1971), as part of a larger study of the volcanism of the whole Massif Central. He divided the volcanic areas into three geochemical types: simple differentiated series (e.g. Chaîne-des-Puys), complex series (e.g. Mont Dore) and undifferentiated series (e.g. Aubrac), with the Velay as a simple differentiated series. He proposed a simple fractionating chamber as the source of the Chaîne-des-Puys lavas, on the basis of the progressive decrease in abundance of each rock type compared with its degree of evolution.

For the Velay oriental a lack of data precluded an equivalent conclusion, but Brousse noted that there was a paucity of intermediate composition lavas in the area, relative to the basic lavas and the evolved phonolites. Graphs of SiO_2, TiO_2, Al_2O_3, FeO^T, MgO, CaO, Na_2O and K_2O were presented for the Velay, each with about 50 analyses, although the data were not provided. These

graphs were not analysed, other than to note their strong trends in general, and the slight Fe-enrichment in the agpaiitic phonolites. The use of Thornton and Tuttle's (1960) Differentiation Index as the x-axis however, caused these trends to differ markedly from those using an incompatible trace element as fractionation index (see section 5.3).

Batard (1974) studied the feldspars in the Velay phonolites and trachytes in detail, with 18 lavas analysed for major elements, Rb, Sr and Li. FeO/Fe_2O_3 was found to be highly variable but always less than 0.8. H_2O+ was also variable, reaching 3% in the phonolites. From the mineralogical evidence Batard concluded that, in the trachytes, calcite cores in corroded plagioclase phenocrysts indicated CO_2 gas-transfer of Na. The phonolites were shown commonly to have early miaskitic affinities but to finish crystallising with agpaiitic characteristics.

Berger *et al* (1976) examined the lava sequence in a representative small area, centred on Boutières in the south of the Velay, which contained the whole range of lavas, from ankaramites to phonolites. They concluded that the lavas formed a sodic alkaline fractionation sequence, but noted the scarcity of intermediate (hawaiite, mugearite and benmoreite) lavas. Seven analyses of major elements were given.

The report by Olives *et al* (1976), on which the previous paper was based, was mainly concerned with the distribution and petrography of the lavas, although it also contained a section on their geochemistry. The curved trends shown by some variation diagrams were used as evidence that the lavas had evolved by fractional crystallisation.

In the same area, Berger (1977) identified two fractionation series in the Velay, one highly sodic leading from basalt to phonolite, the other sodic-potassic leading to quartz-trachyte. He noted that the sodi-potassic series was by far the smallest volumetrically and considered that it could have crossed the silica-saturation barrier by fractionation of pargasitic amphibole. Mechanisms proposed for the generation of the two series were a) two different parent magmas, or b) separation of the two series at the level of the hawaiites. Graphs with the trends of the two series plotted were presented, but only 10 major element analyses were given.

Batard *et al* (1977) summarised and expanded Batard's (1974) work on the Velay feldspars. The presence of porphyritic "sub-alkaline trachytes" as extrusion domes in the north of the Velay was noted, as well as their geochemical links with nearby phonolites. The postulated CO_2 gas-transfer model was refined, with sedimentary carbonate contamination eliminated on the basis of a very low Sr-content of only 40ppm in the calcite of the corroded plagioclase cores.

The rare quartz-trachyte of Roche Pointue (= Dents de Mézenc) was the subject of Berger *et al*'s (1978) paper. Following the theme of two fractionation series this trachyte was investigated as an end-product of the oversaturated trend. It exemplified the more potassic nature of this trend with K/Na = 0.95 as opposed to 0.58 for the phonolites. Detailed study of its mineral chemistry showed that the clinopyroxene ranged from augite in the phenocrysts to ferropigeonite in the groundmass. The presence of low-Ca cpx in the groundmass was ascribed to the silica oversaturation of the

magma and the relatively high (1085-1183˚C) temperatures calculated using plagioclase-liquid equilibria. Contamination or amphibole fractionation were suggested as the cause of the trachyte's excess silica, with the latter explanation preferred.

Berger and Lanöe (1978) enlarged the Boutières study area to the north and collected 30 samples for geothermometry and geobarometry. They tried a range of geothermometers and barometers including olivine-liquid, plagioclase-liquid, two feldspars, magnetite-ilmenite and amphibole stability. Combining these data they concluded that the Velay series had a temperature range of 1200-800˚C, oxygen fugacity $f(O_2) = 10^{-11}$ (at 1000˚C) and crystallised with $P_{H_2O} = 3.0 \pm 0.6$kb.

Mergoil (1980) summarised all previous work on the Velay oriental. His paper included an estimate of the mapped areas of lava types:

basalts, basanites, hawaiites	80%
mugearites, benmoreites, sub-alkaline trachytes	7%
trachytes, phonolites	13%

These demonstrated a prominent "Daly gap", assuming mapped area was proportional to lava volume. The geochemistry was described with the aid of a silica vs total alkalis graph with 113 analyses (data not given) which showed two clear trends in the evolved lavas. The phonolites of the sodic series were subdivided on the basis of their geochemistry, and the petrography of the sub-alkaline trachytes of the sodic-potassic series was described.

Another summary of Massif Central volcanism appeared in Maury and Varet (1980). They described the geochemical and mineralogical similarities of all the Massif Central basic lavas, and concluded that in the Velay the basanite to phonolite fractionation series had evolved in shallow magma reservoirs, whereas the basanite to quartz-trachyte series had been produced at depth, with P_{H_2O} = 1-3kbar, by analogy with the Chaîne-des-Puys. This oversaturated series was thought to have been generated by the fractionation of pargasitic amphibole rather than contamination with sialic crust.

The most recent and comprehensive study of the geochemistry of the Velay lavas was that by Villemant and Treuil (1983). They provided analyses of 17 trace elements for 37 specimens, and 10 major elements for 30 of these. Variation diagrams using these data showed strong trends with little scatter, which led the authors to conclude that a single primary liquid had undergone a single fractionation process, and to discard the earlier models of two independent series. The process of differentiation was deduced to be crystal fractionation from the variation diagrams and from a negative Eu-anomaly in the REE-diagrams, which became more intense in the most evolved rocks. The Velay lavas also had progressive LREE and HREE-enrichment, with corresponding MREE-depletion suggesting sphene fractionation.

Some analyses were discarded on the basis of excess Rb, which was thought to be due to hydrothermal alteration occurring immediately after emplacement. From changes in the bulk

distribution coefficient ($D_{element}$) for each element they inferred three separate stages of differentiation, with the removal of the following mineral assemblages:

1) basalt, basanite, hawaiite ⇒ *olivine + cpx*

2) mugearite, benmoreite, trachyte ⇒ *cpx + FeTi-oxides, then amphibole*

3) trachytes, phonolites ⇒ *K-feldspar + apatite + sphene*

Their graph of ln (Th) vs ln (K_2O) had a slope > 1, which would have implied a negative value for D_{K_2O} if Rayleigh fractionation had been the only process operating. To account for this the authors developed a model of selective exchange between the magma and a fluid phase, and deduced some of the properties of such a fluid.

The final part of the paper compared the Velay oriental lavas to those of the Chaîne-des-Puys. For both areas the calculated parental liquids and the most basic lavas were found to be similar, suggesting large scale homogeneity of both source material and magma generating process. Most of the differences between the series were found to be due to their having followed different fractionation paths, with that of the Chaîne-des-Puys leading to oversaturated end-products. The higher viscosity of SiO_2-rich Chaîne-des-Puys magmas probably accounted for their lower degree of maximum evolution, with F = 12% as opposed to 6% for the most evolved Velay phonolites. Different physical conditions in the magma chambers of each area were thought to be the cause of the difference in their fractionation paths.

5.2 Sampling for this study

Samples were collected to cover the maximum geographical and compositional range, from La Madeleine in the north to Mézilhac in the southeast, and from ankaramitic basalts to peralkaline phonolites (see sample location maps in back pocket). Unusual compositions tend to be over- rather than under-represented (compared to their volume), in the sample set.

Great care was taken to eliminate weathered samples before analysis, both in the field and by examination of thin sections. Most lavas are quite fresh, since their maximum age is 13Ma. For this reason the effect of weathering on the geochemistry of the samples has not been investigated.

Major (SiO_2, TiO_2, Al_2O_3, $Fe_2O_3^T$, MnO, MgO, CaO, Na_2O, K_2O, P_2O_5) and trace (Zn, Cu, Ni, Co, Cr, V, Ba, Ga, Rb, Sr, Y, Zr, Nb, Pb, Th, U) elements were measured for 124 samples from the Velay Miocene lavas. Full details are given in Appendix C. A representative 40 samples were chosen for $^{87}Sr/^{86}Sr$ analysis. Full details of these data are given in Appendix D.

5.3 Choice of Fractionation Index

5.3.1 Lavas

When plotting lava analyses on a graph to investigate evolutionary trends the choice of fractionation index is clearly important. The ideal index would be linearly related to the degree of

fractionation, for example it should be directly proportional to the degree of partial melting or percentage of a liquid that has crystallised. As Cox *et al* (1979) explain, none of the commonly used compound indices, such as those of Thornton & Tuttle (1960) or Kuno (1959), offers any great advantages over simple two-element diagrams. SiO_2 or MgO are the oxides commonly used as x-axes but in the Velay the suite has virtually zero MgO towards the end of the series, and SiO_2 increases in the basic members, but decreases at the end of the series. Hence neither element is suitable. Another problem with using the major elements as indices, especially SiO_2, is the "constant sum effect" (Chayes 1964), due to the fact that the oxides sum to 100%. As an example, if SiO_2 increases from 45% to 65% the sum of the remaining oxides reduces from 55% to 35% which can lead to spurious correlations appearing in graphs with SiO_2 as their index.

Cox *et al* (1979) pointed out that the ideal index would be a perfectly incompatible trace element, which would double in concentration when only half of the original liquid remained, independent of the minerals crystallising (or melting). It would also have the advantage that as a trace element it would be uninfluenced by the constant sum effect.

For the Velay Zr, Nb, Rb, Pb, U and Th are all suitably incompatible. Of these Zr is the best since it has one of the largest degrees of concentration, increasing by a factor of nearly 10, while its lowest value is >150ppm so that analytical accuracy is not a problem, as it is with Pb, U and Th. The main disadvantage of this type of index is that there may be considerable scatter in the most primitive lavas as a result of small variations in the degree of partial melting of the mantle. This is probably not too much of a problem in the Velay since Zr and Nb show strong coherence and therefore imply the same degree of partial melting for all the basic lavas.

Another type of graph to consider is that of Villemant *et al* (1980) in which the logarithm of an incompatible trace element is plotted against that of another oxide. This has the advantage that Rayleigh fractionation produces straight line segments, in which the slope is equal to (1 - D), where D is the bulk distribution coefficient of the y-axis element. It can also indicate circumstances in which the process of differentiation is not Rayleigh fractionation, when the slope of a line segment is greater than one. This type of graph is useful for quantifying distribution coefficients but may be unfamiliar to many readers. For this reason simple linear plots are given initially. Graphs of all elements are given in Figure 5.3.1.

Figure 5.3.1a-z

Graphs of whole rock analyses of Velay lavas

Throughout:

□ = alkali basalts, basanites and ankaramites
× = hawaiites
◇ = intermediate lavas (including mugearites and benmoreites)
+ = phonolites and nepheline trachytes
△ = quartz-trachytes

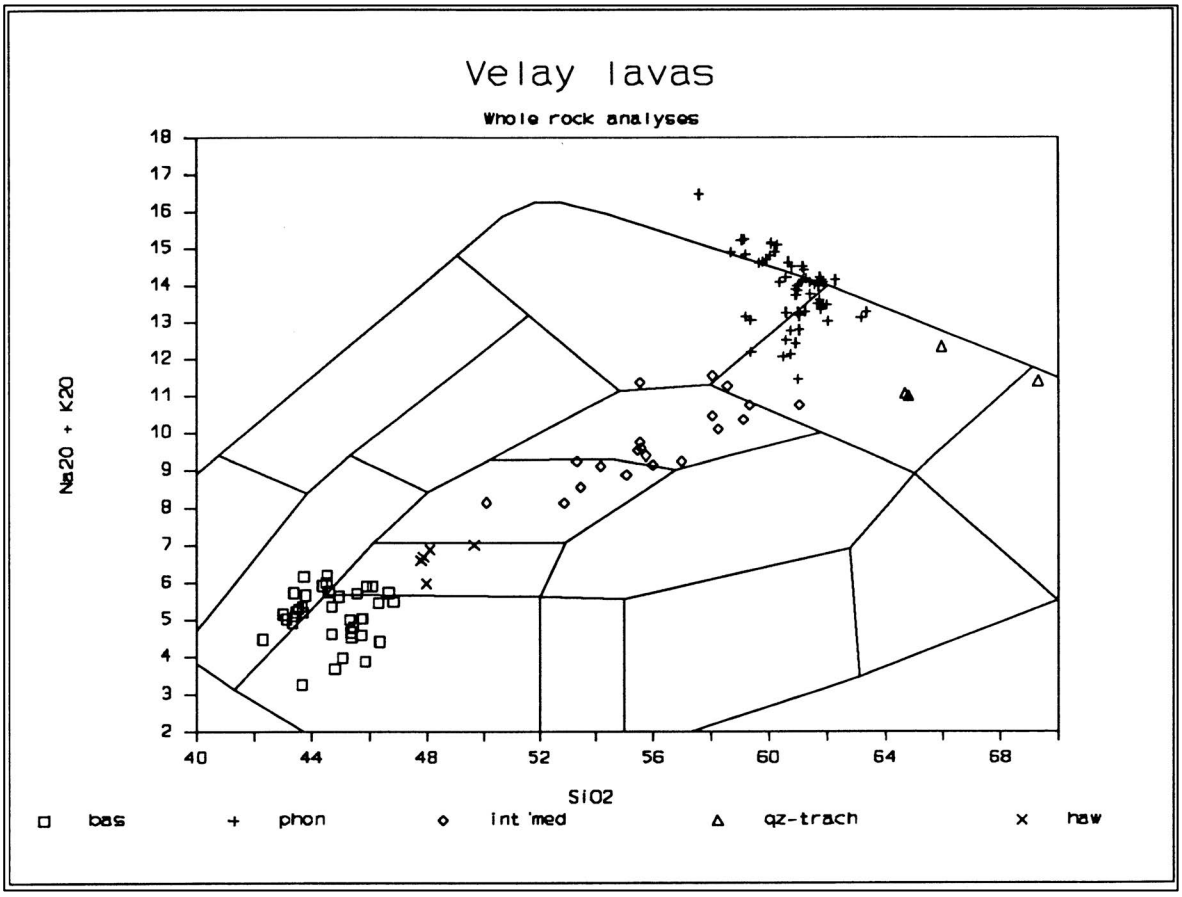


Figure 5.3.1a

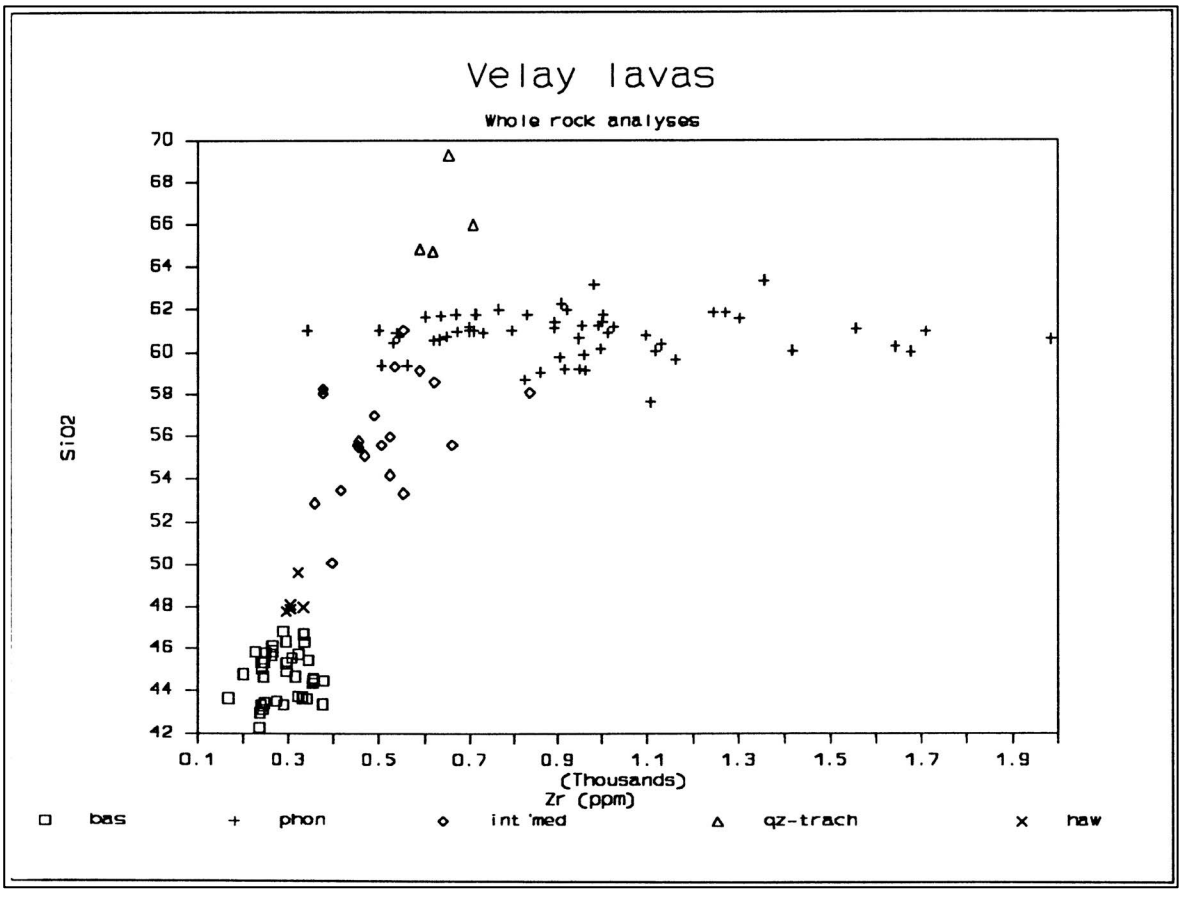


Figure 5.3.1b

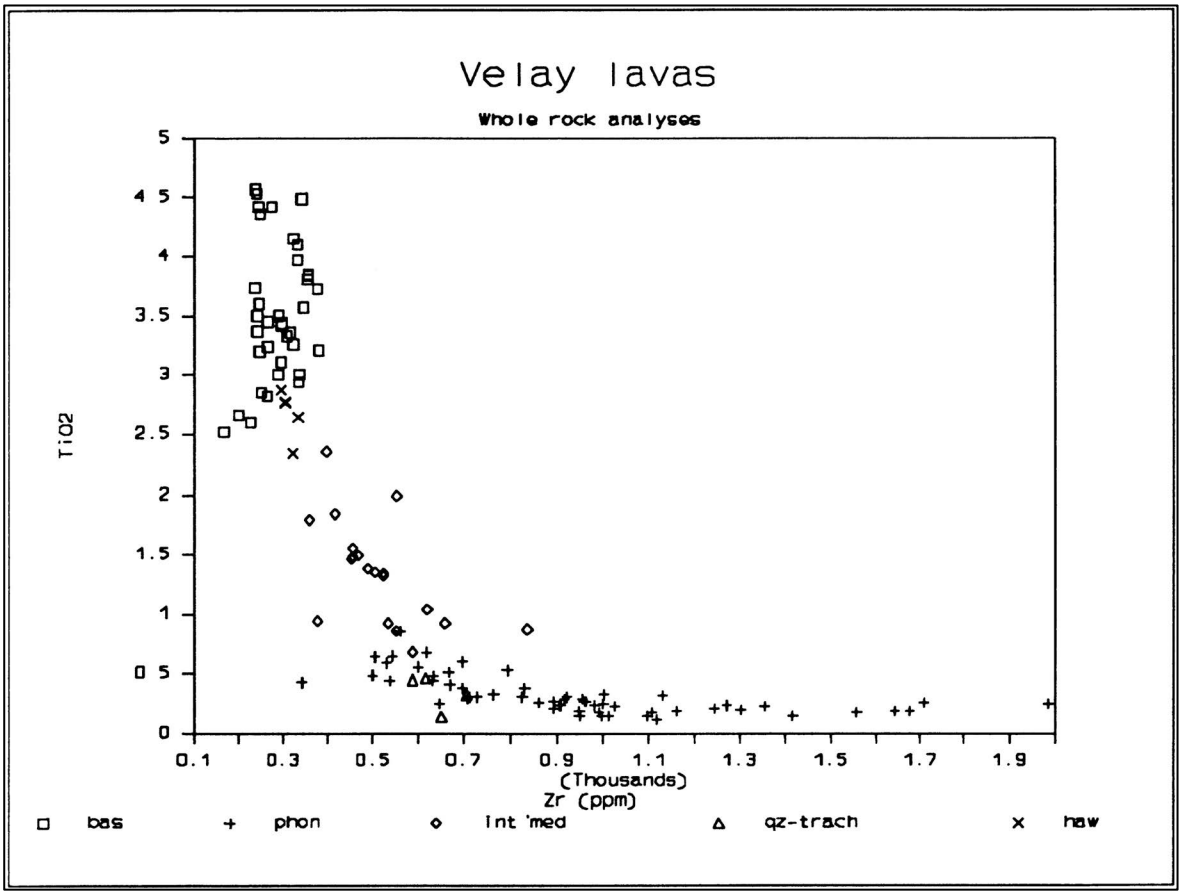


Figure 5.3.1c

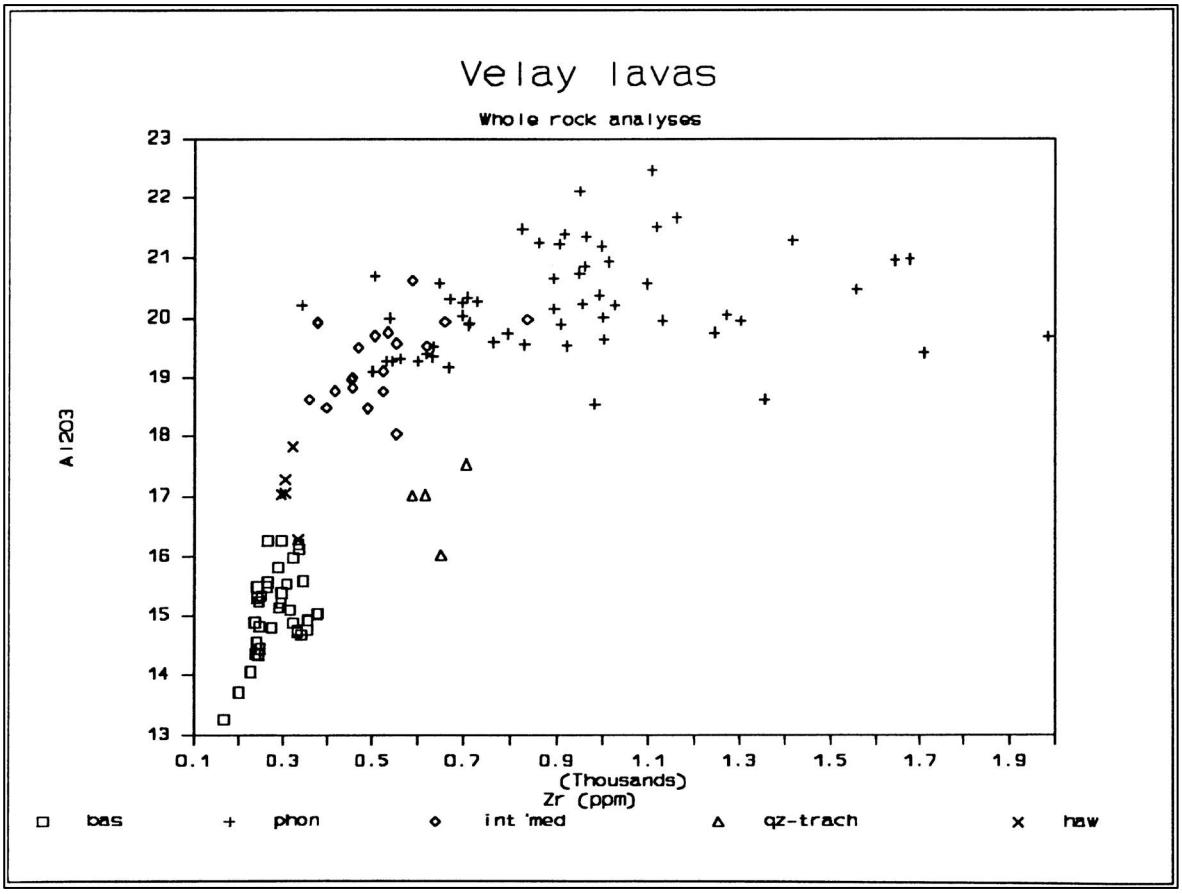


Figure 5.3.1d

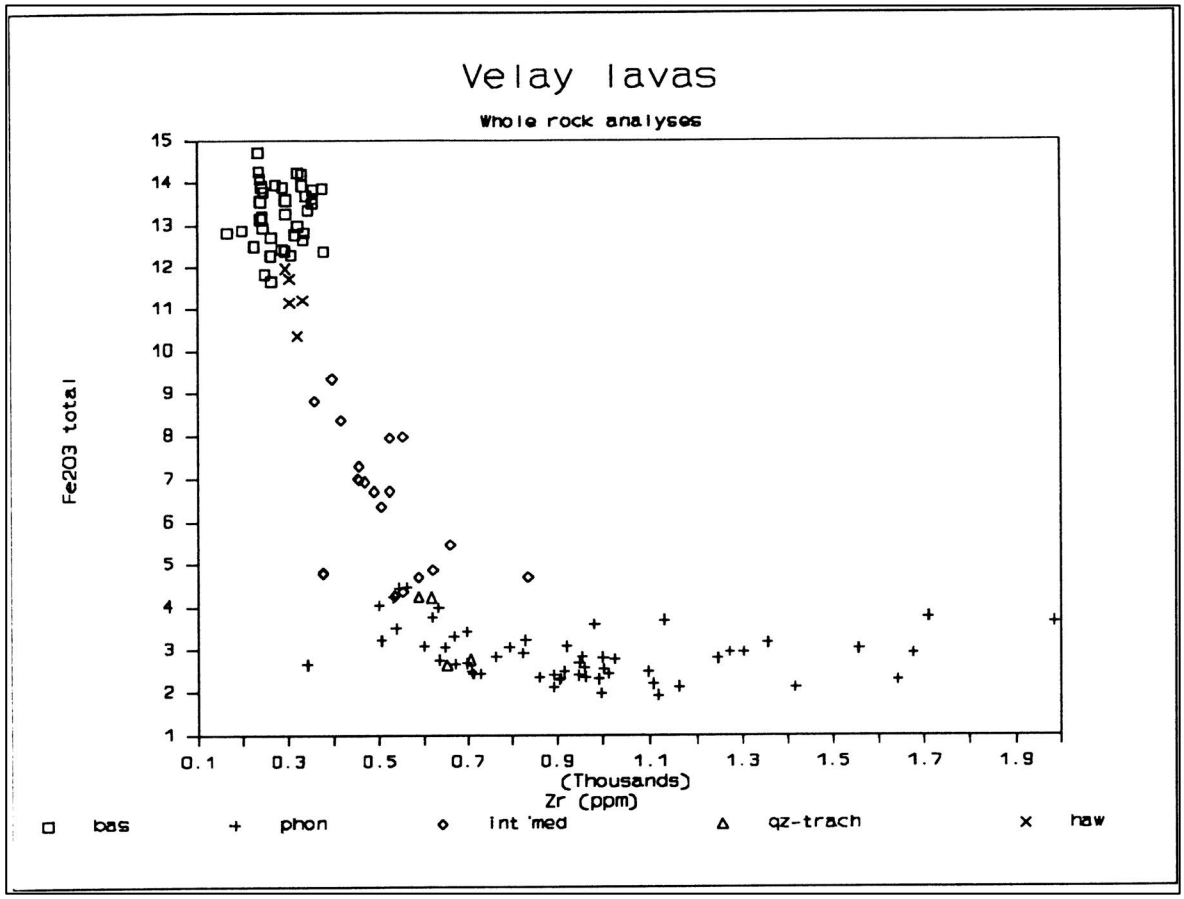


Figure 5.3.1e

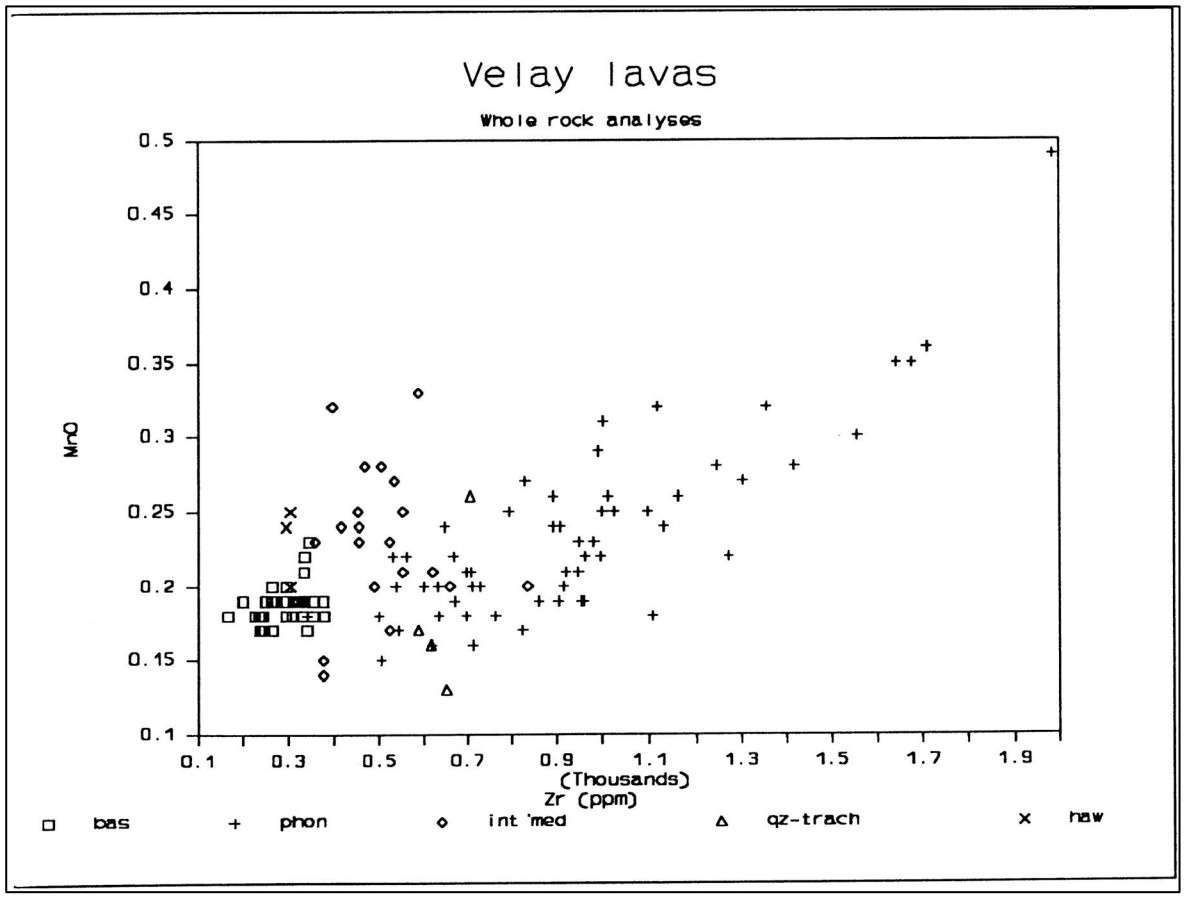


Figure 5.3.1f

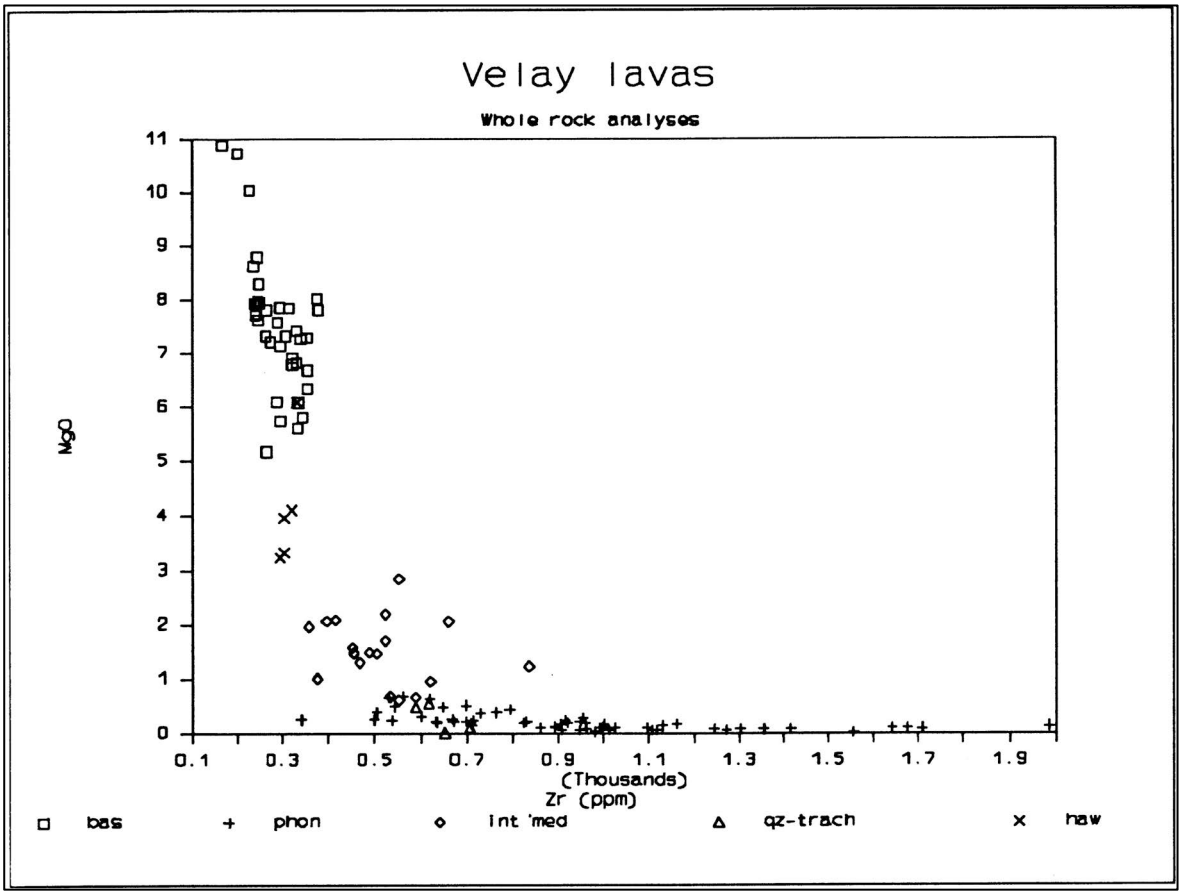


Figure 5.3.1g

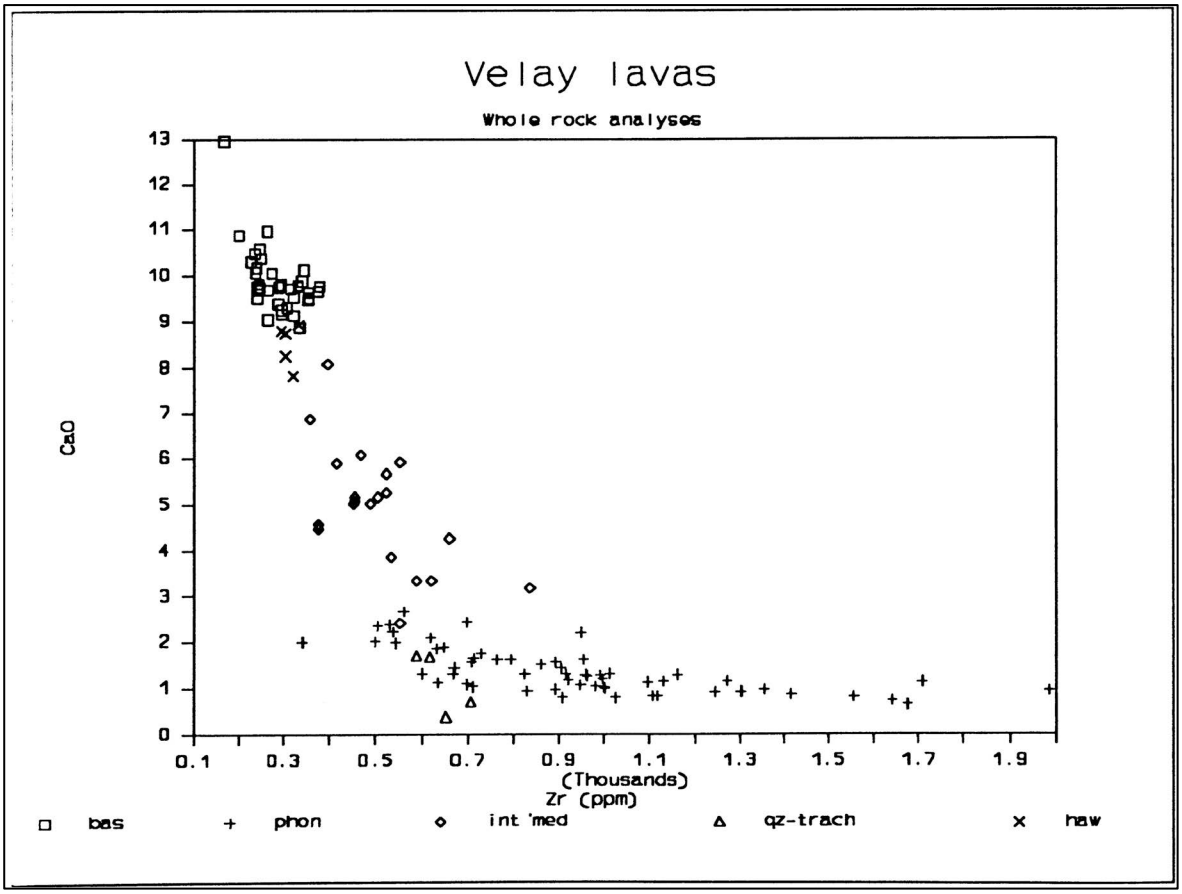


Figure 5.3.1h

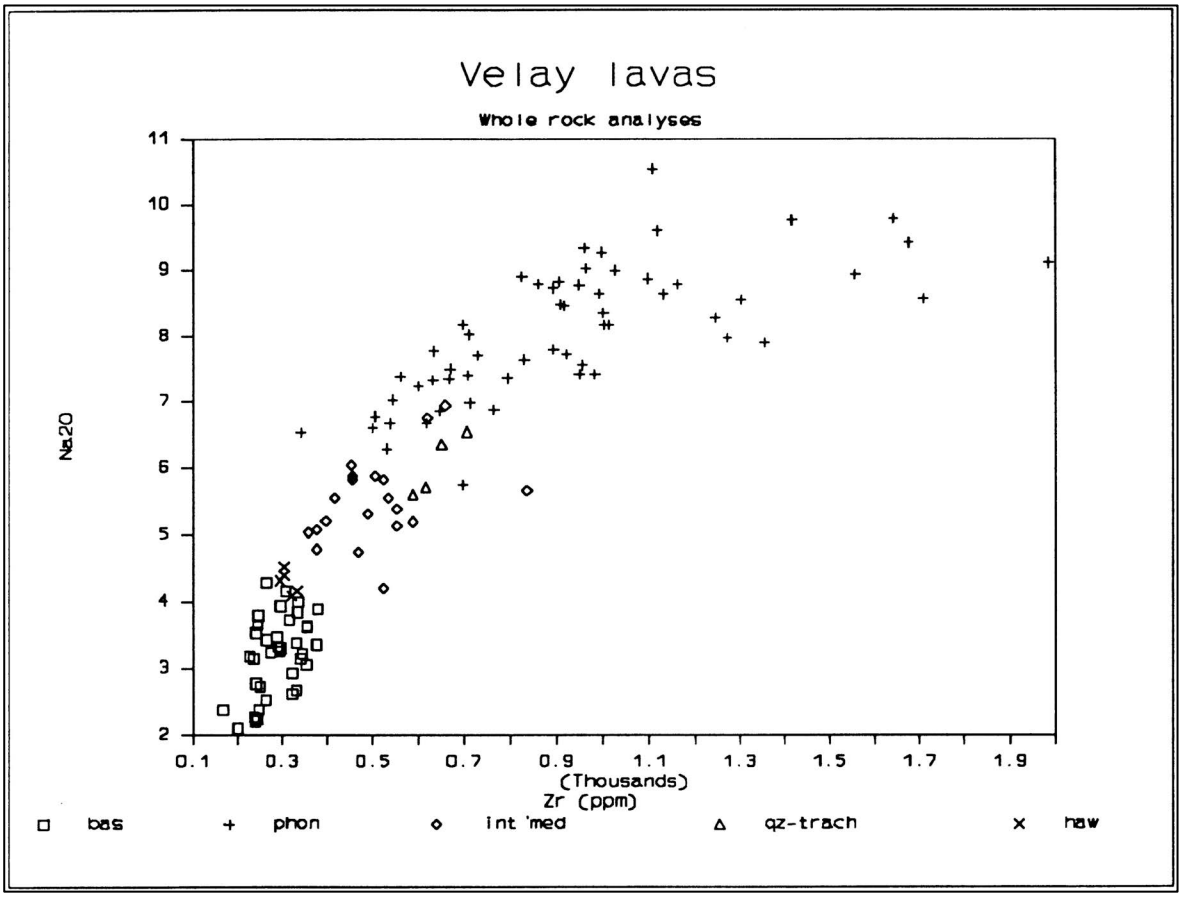


Figure 5.3.1i

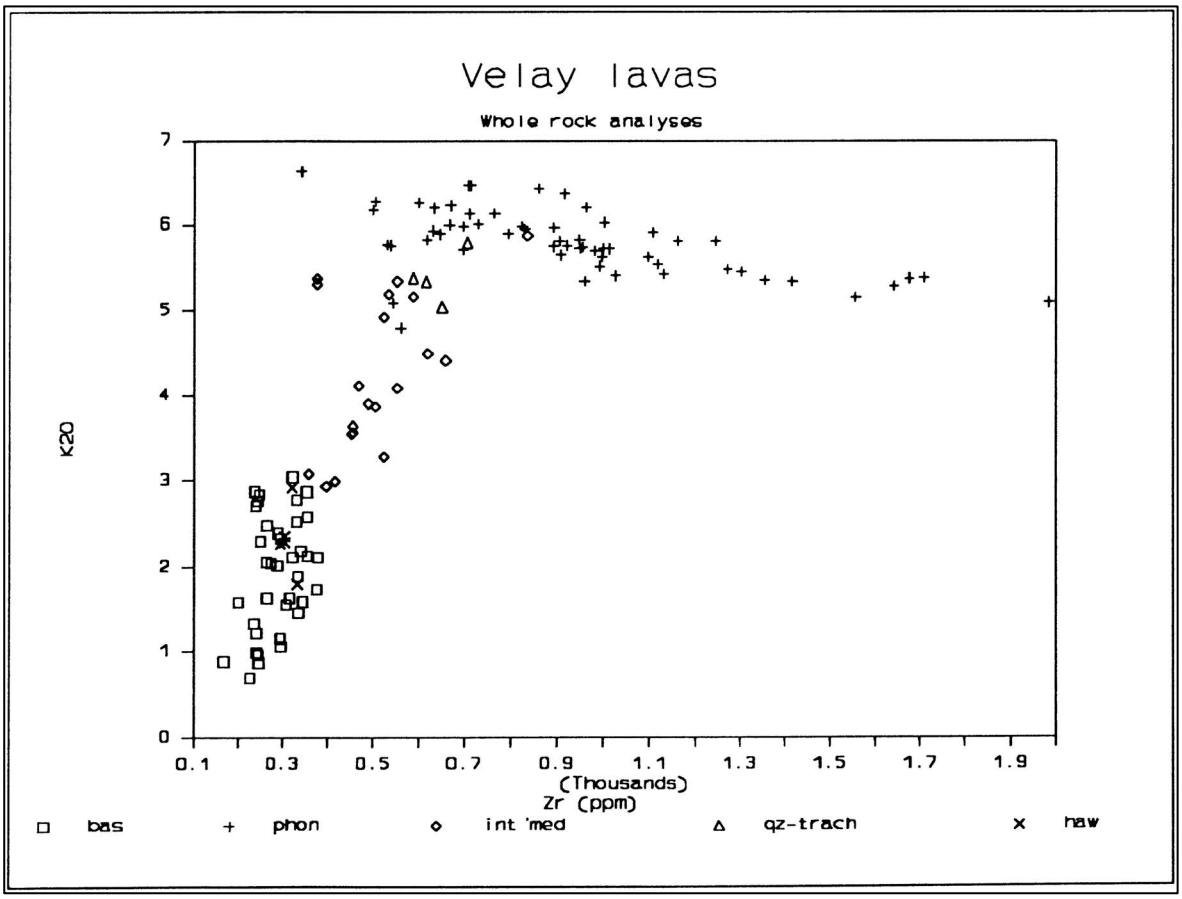


Figure 5.3.1j

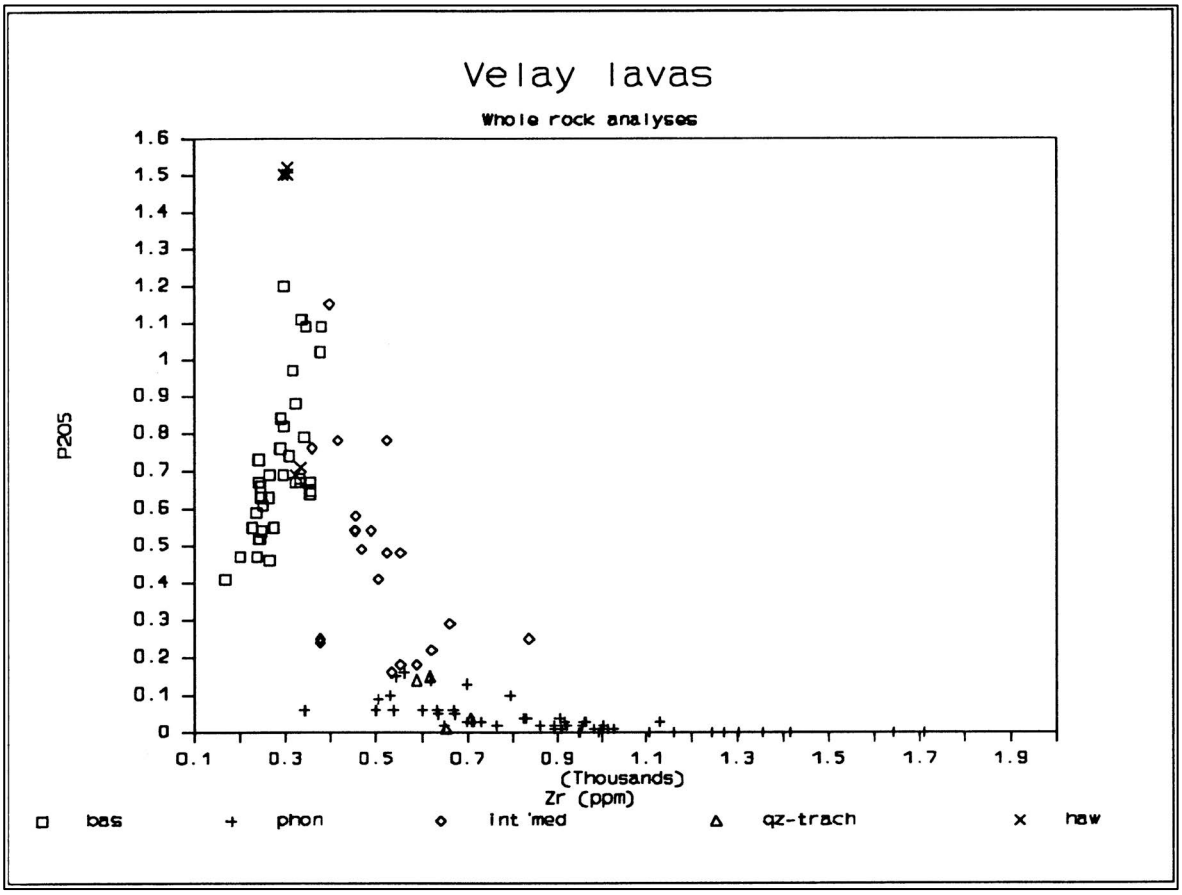


Figure 5.3.1k

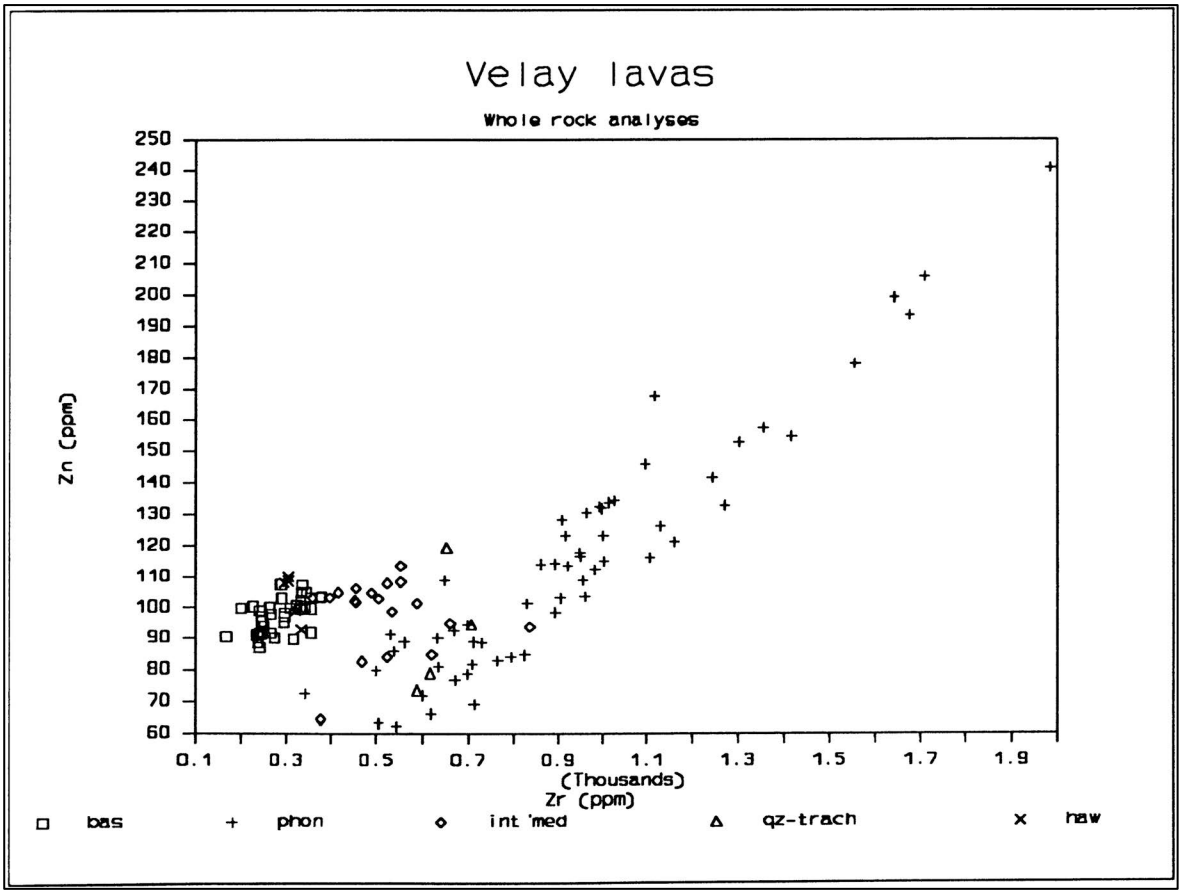


Figure 5.3.1l

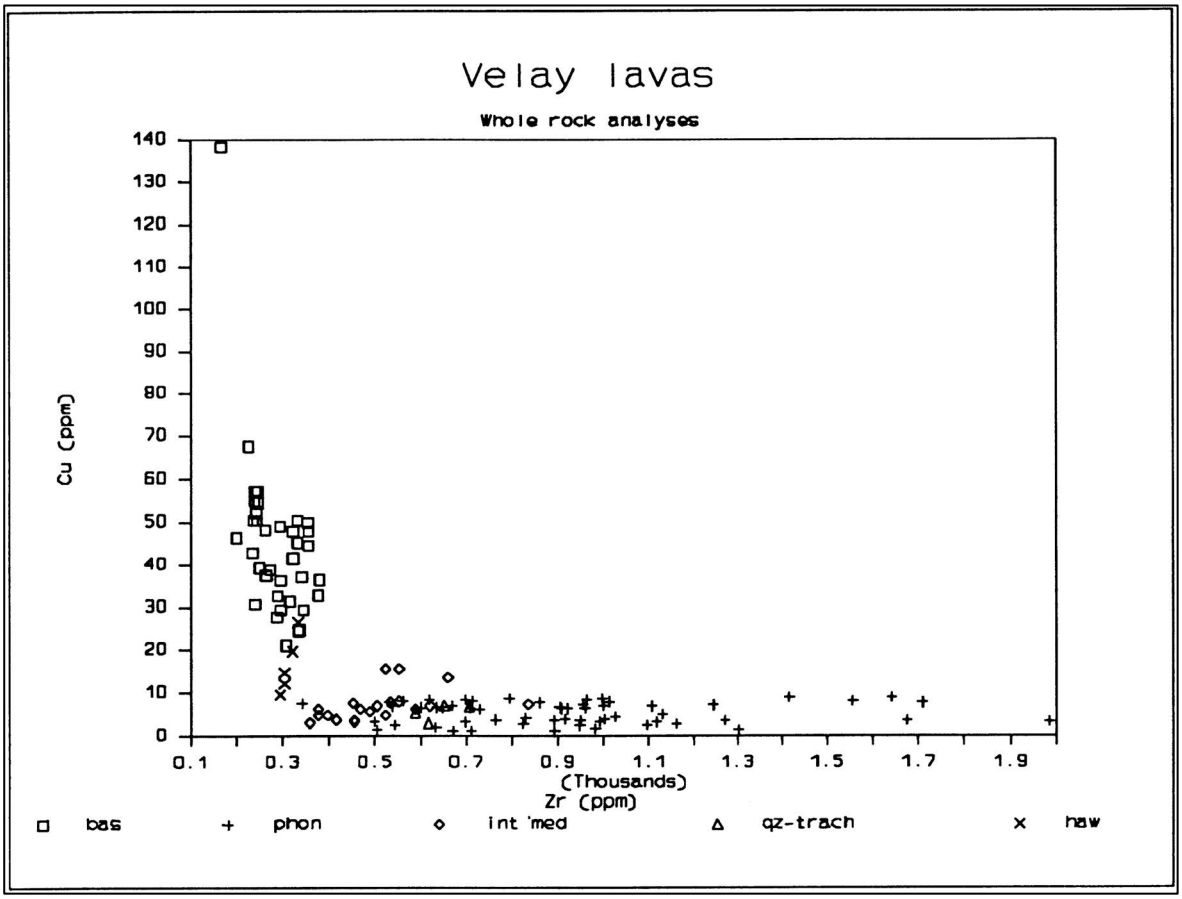


Figure 5.3.1m

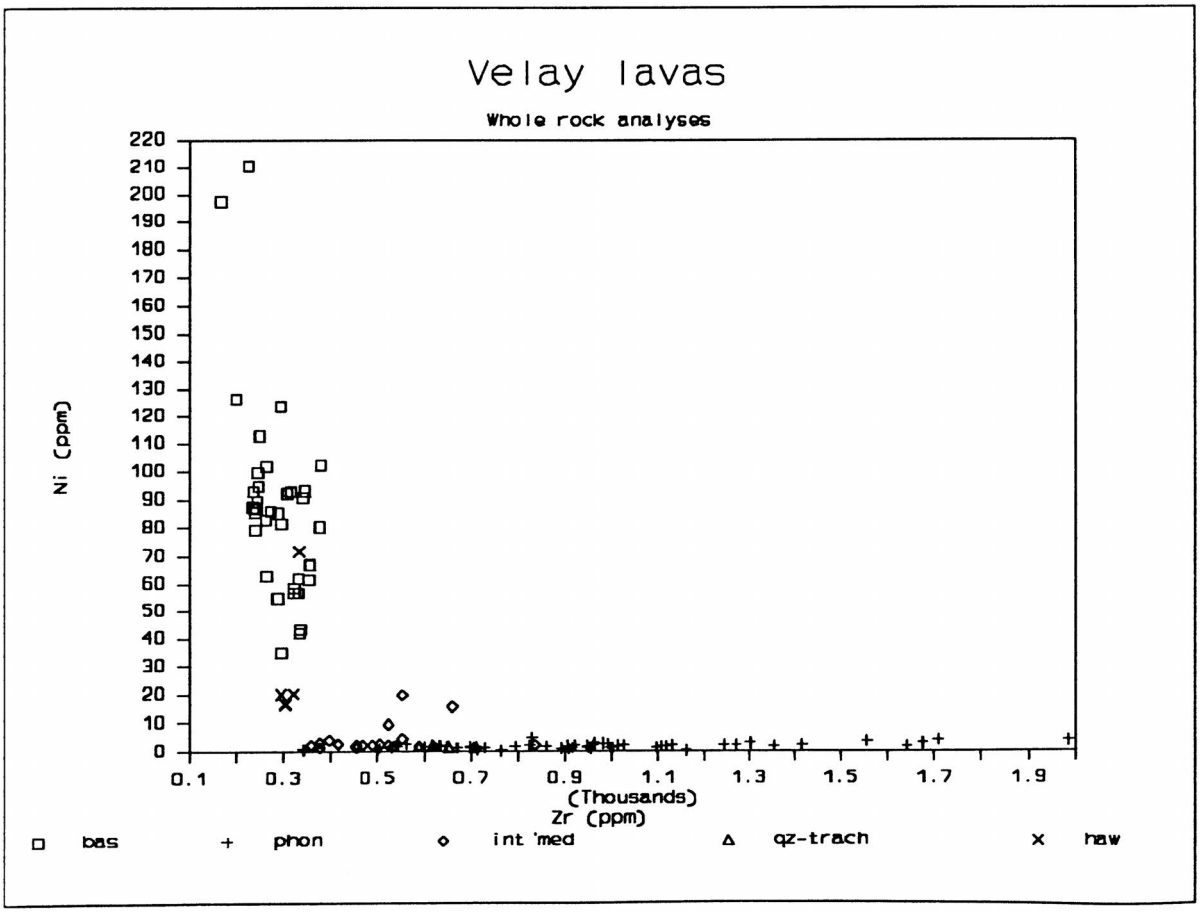


Figure 5.3.1n

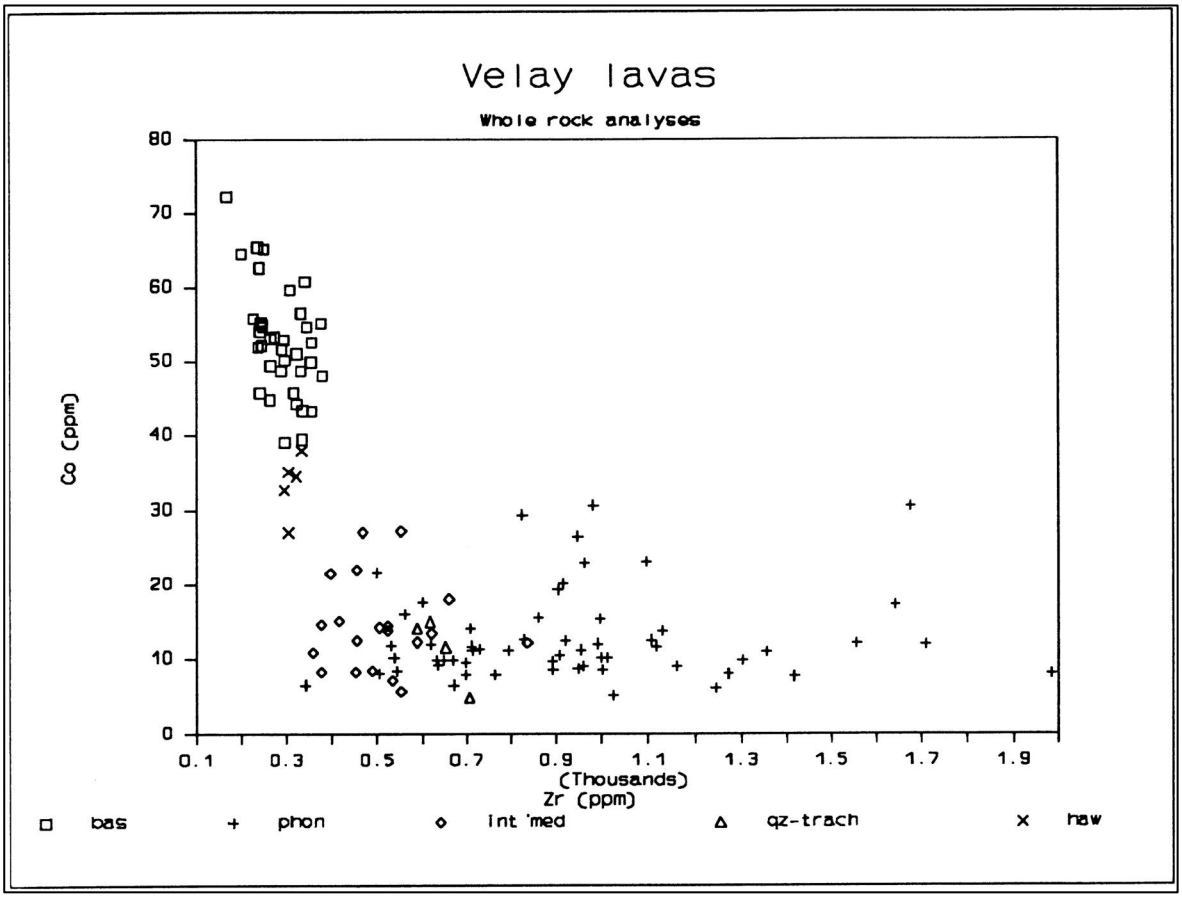


Figure 5.3.1o

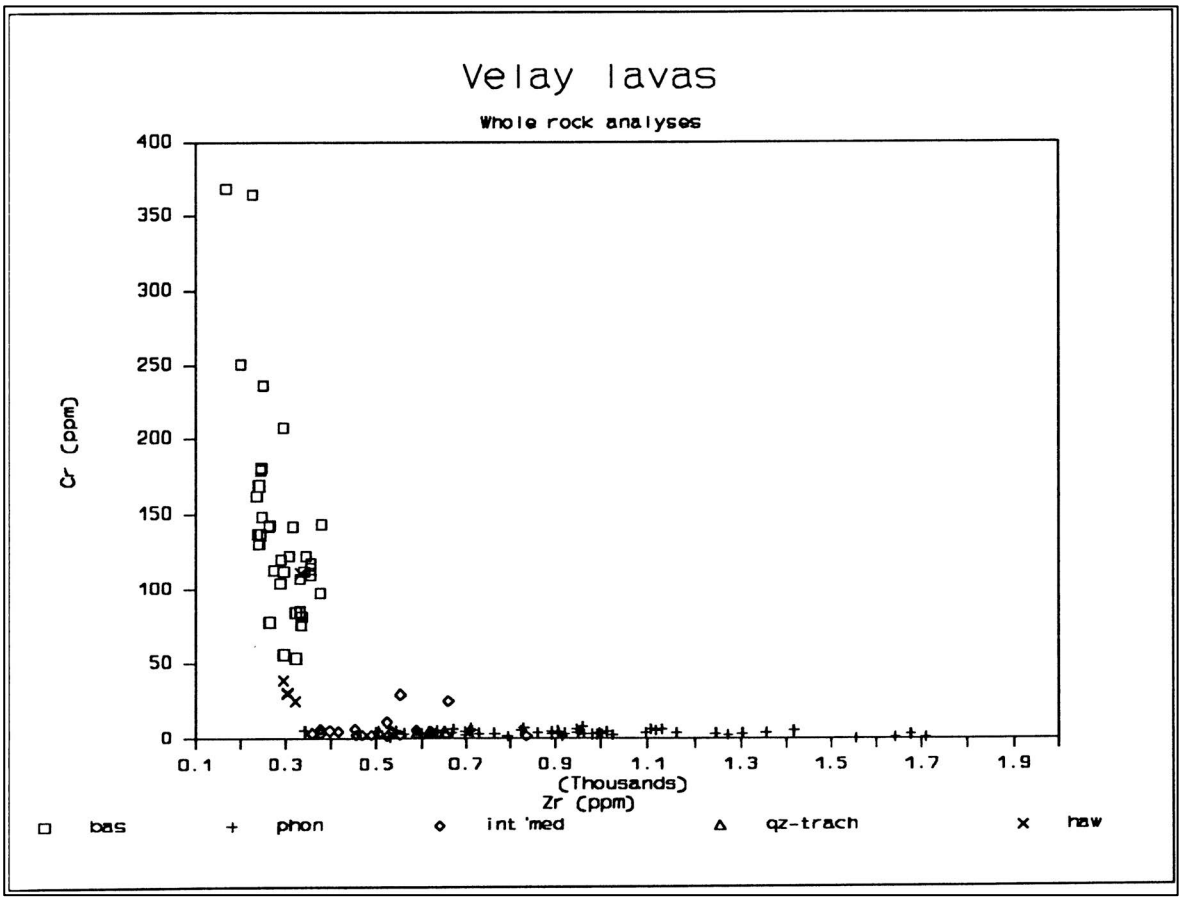


Figure 5.3.1p

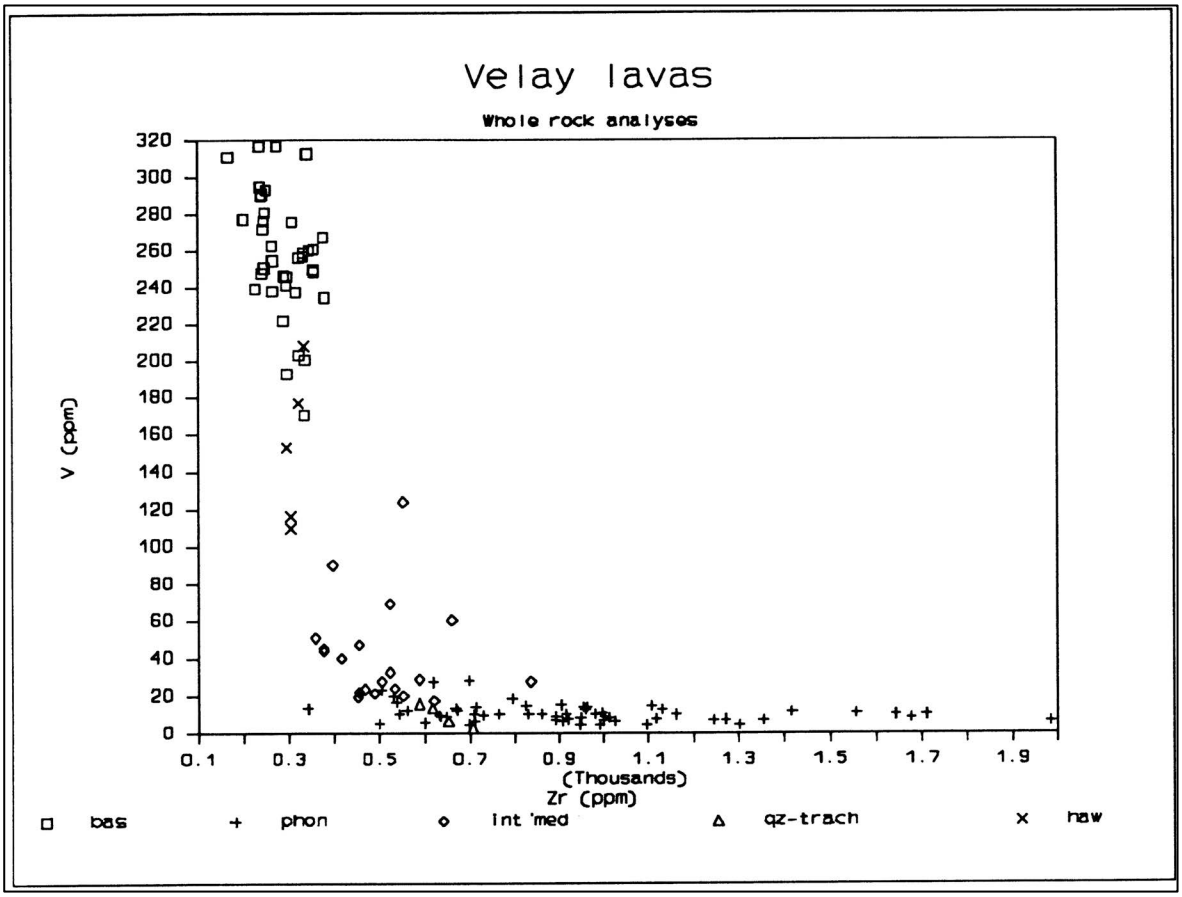


Figure 5.3.1q

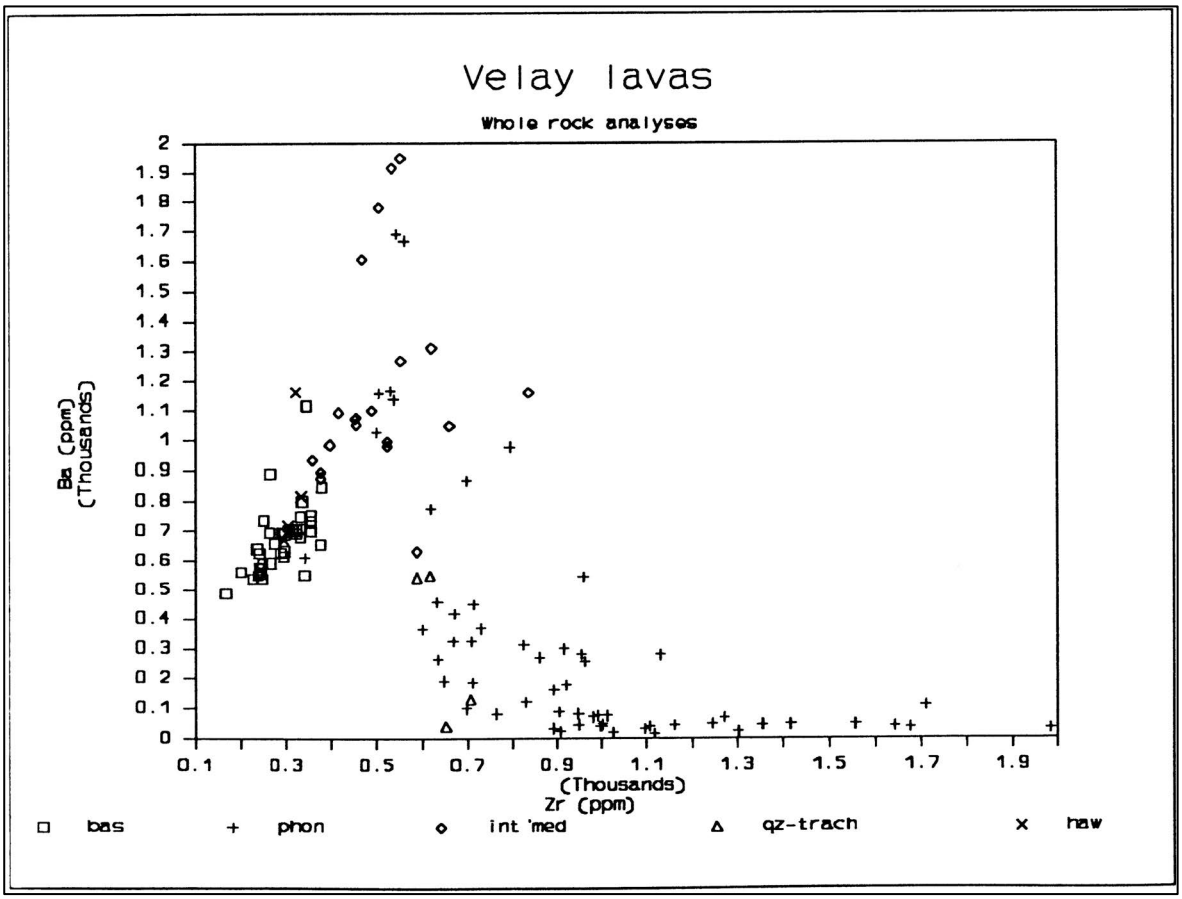


Figure 5.3.1r

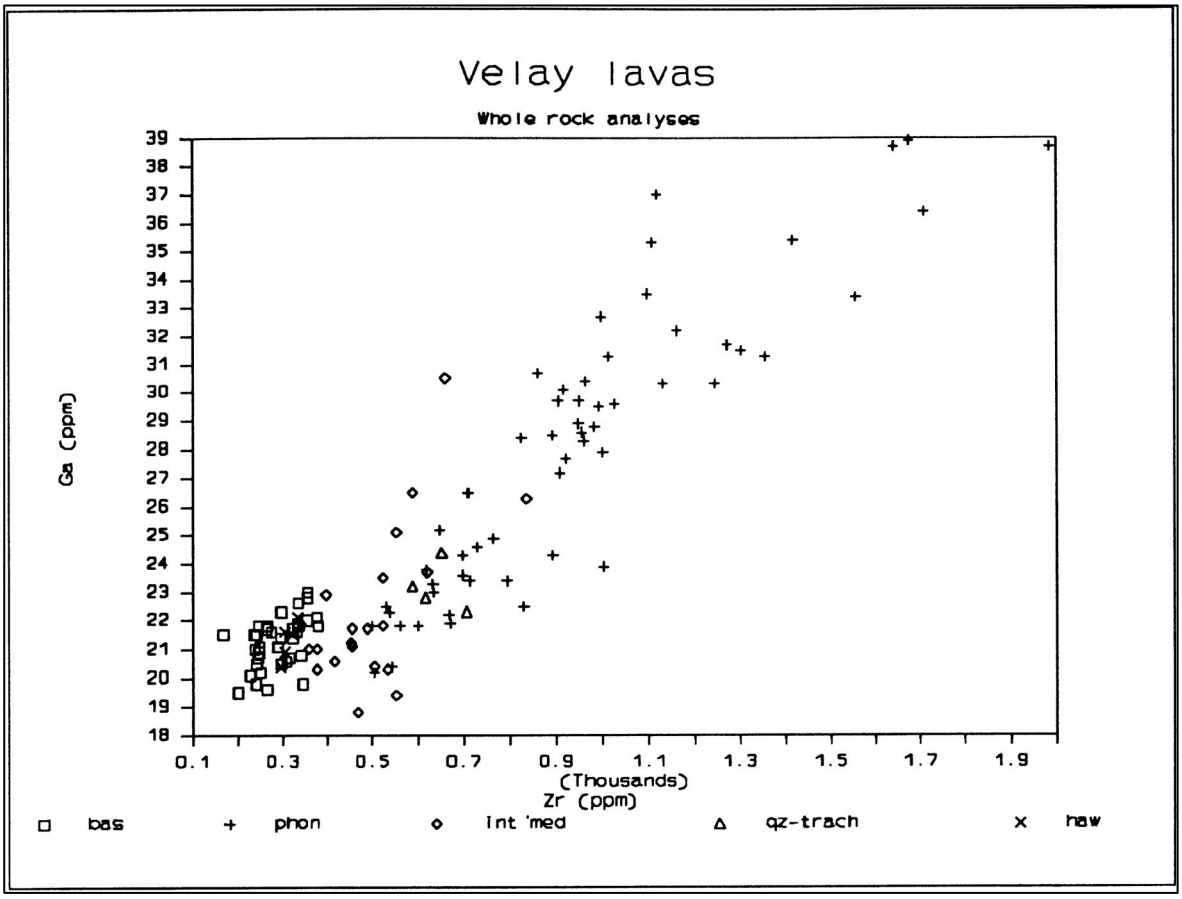


Figure 5.3.1s

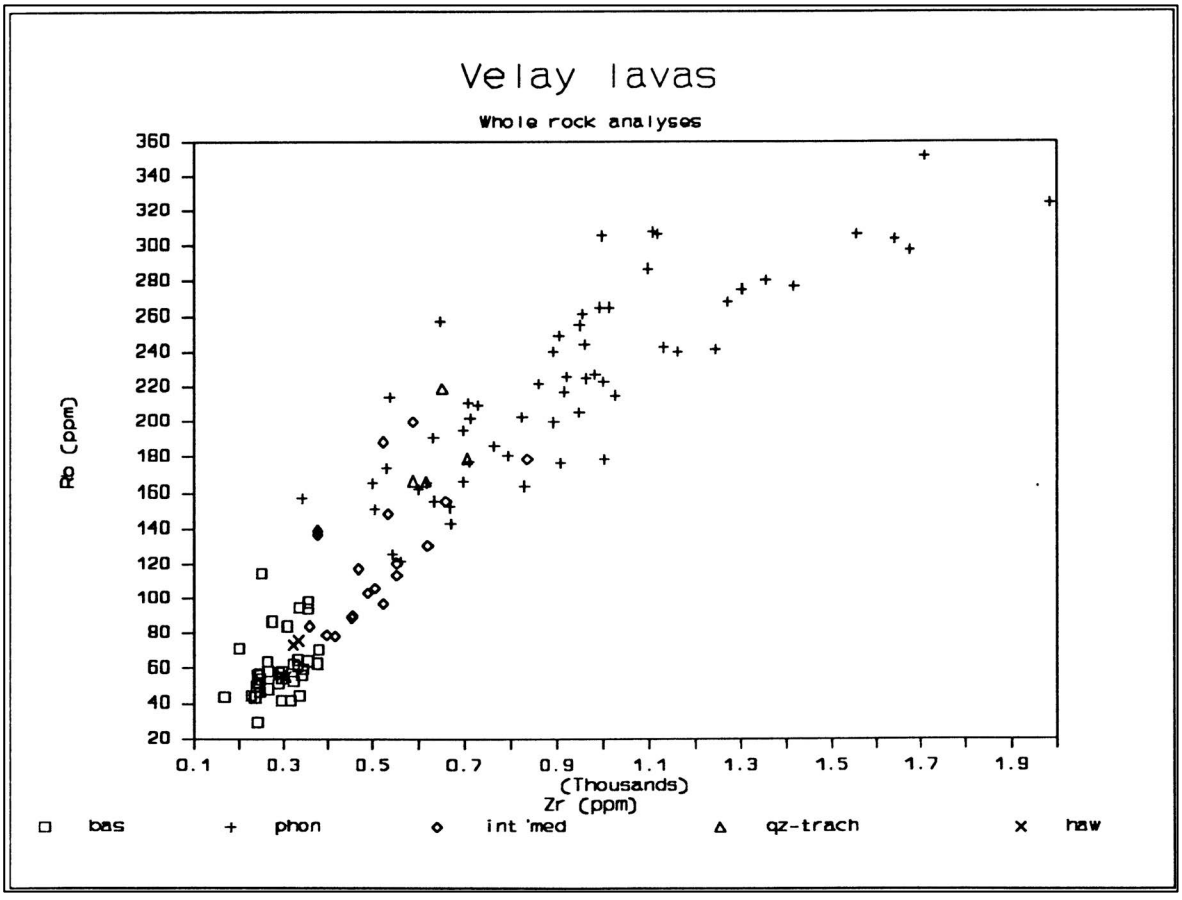


Figure 5.3.1t

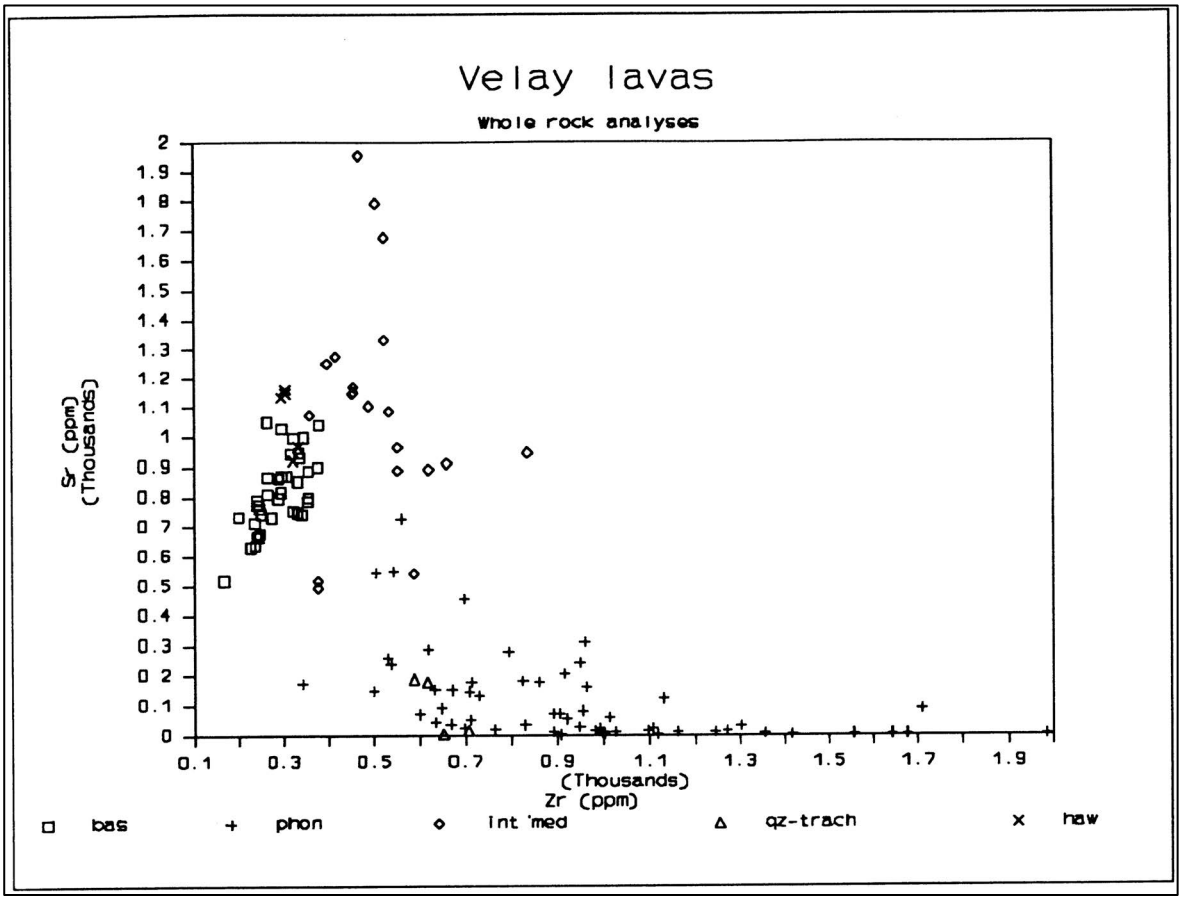


Figure 5.3.1u

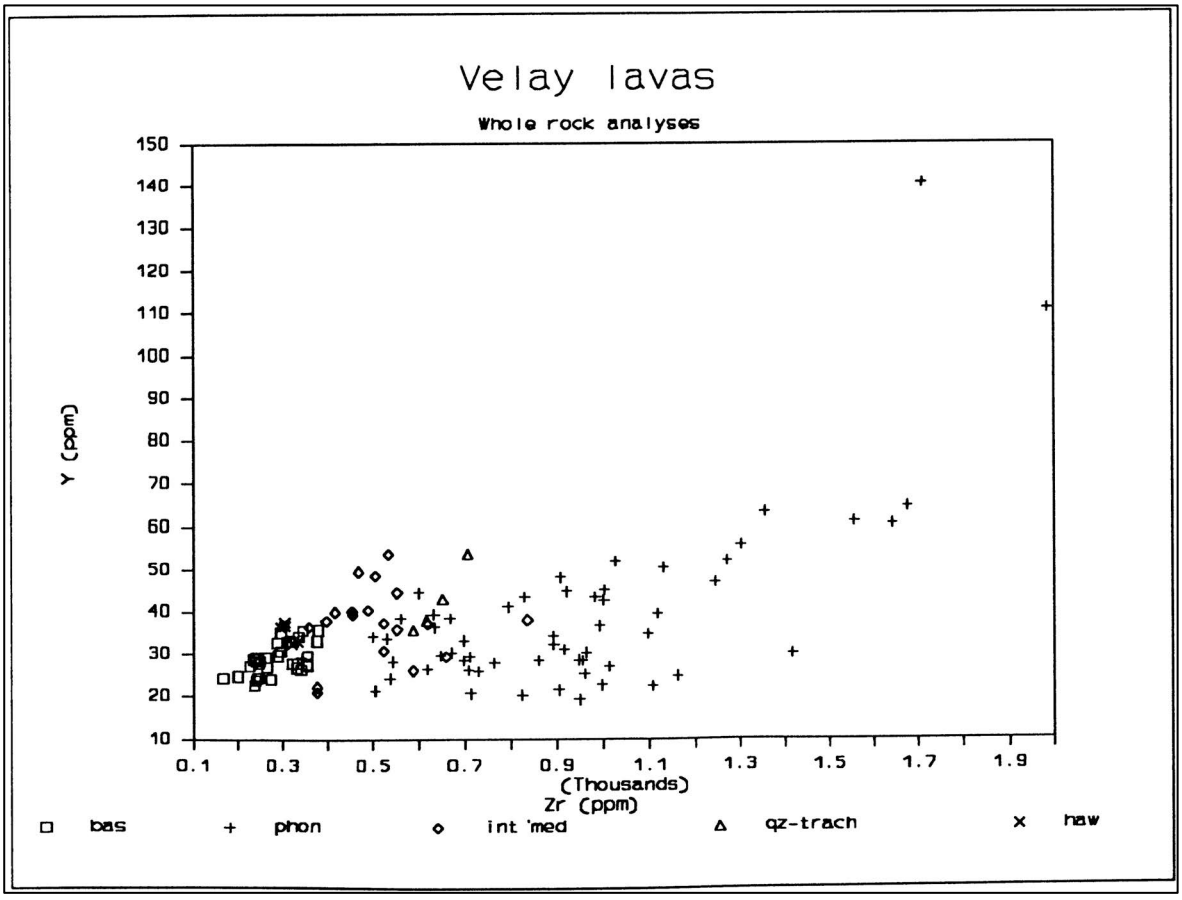


Figure 5.3.1v

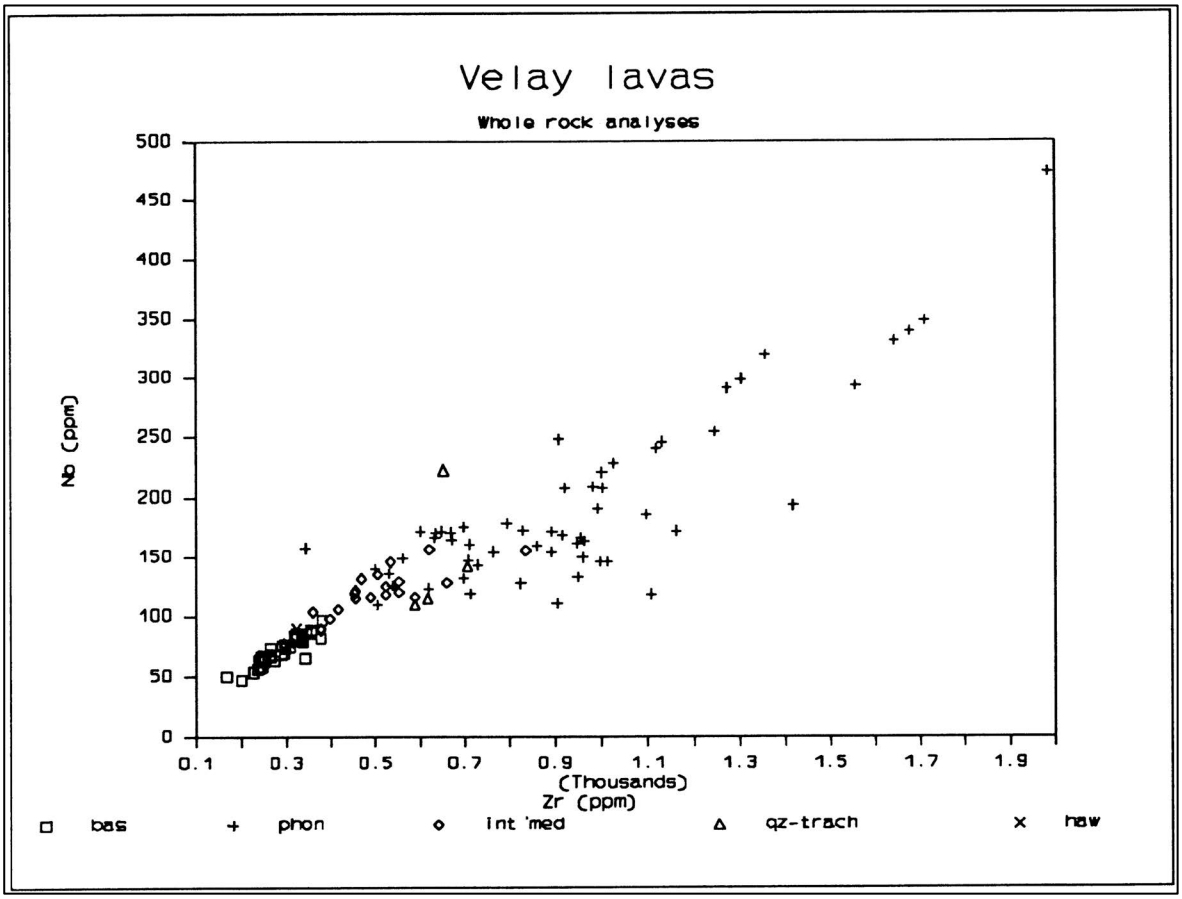


Figure 5.3.1w

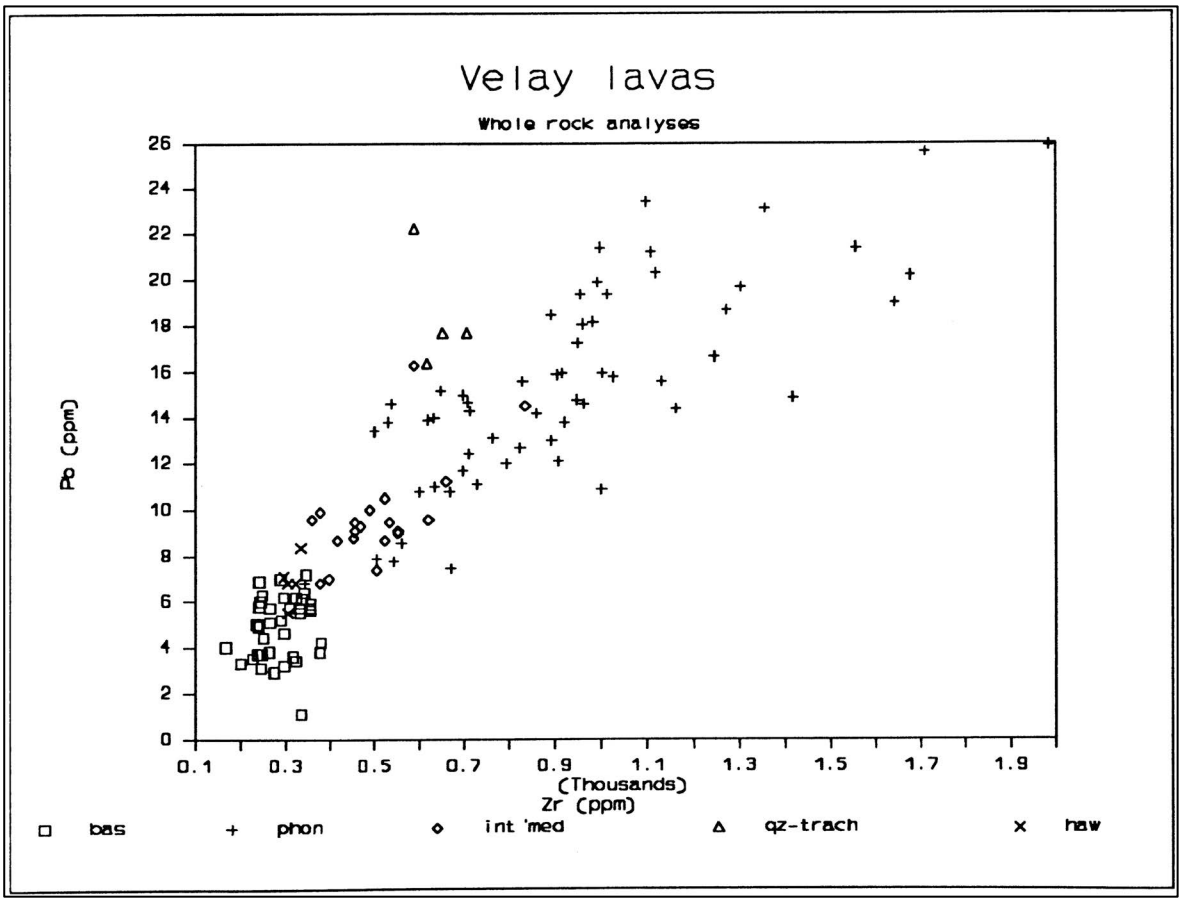


Figure 5.3.1x

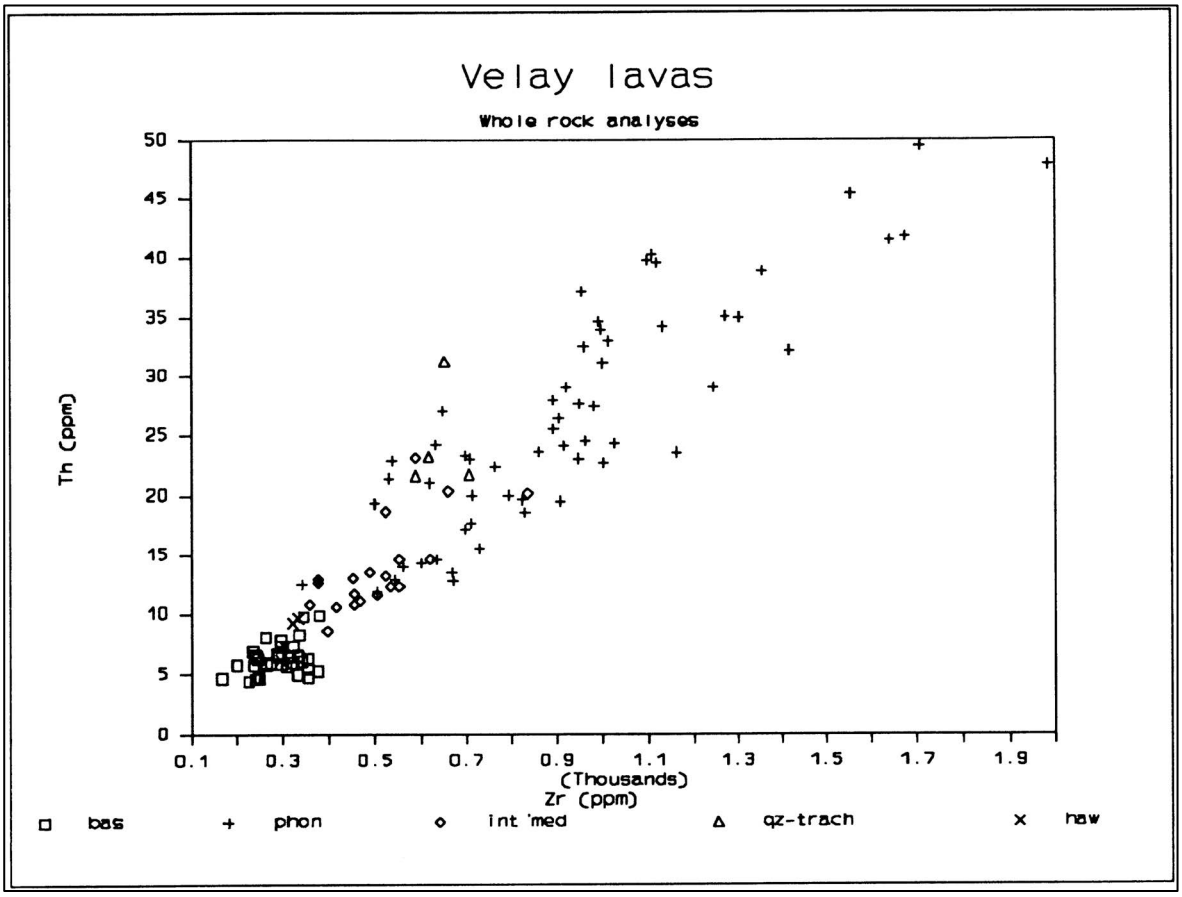


Figure 5.3.1y

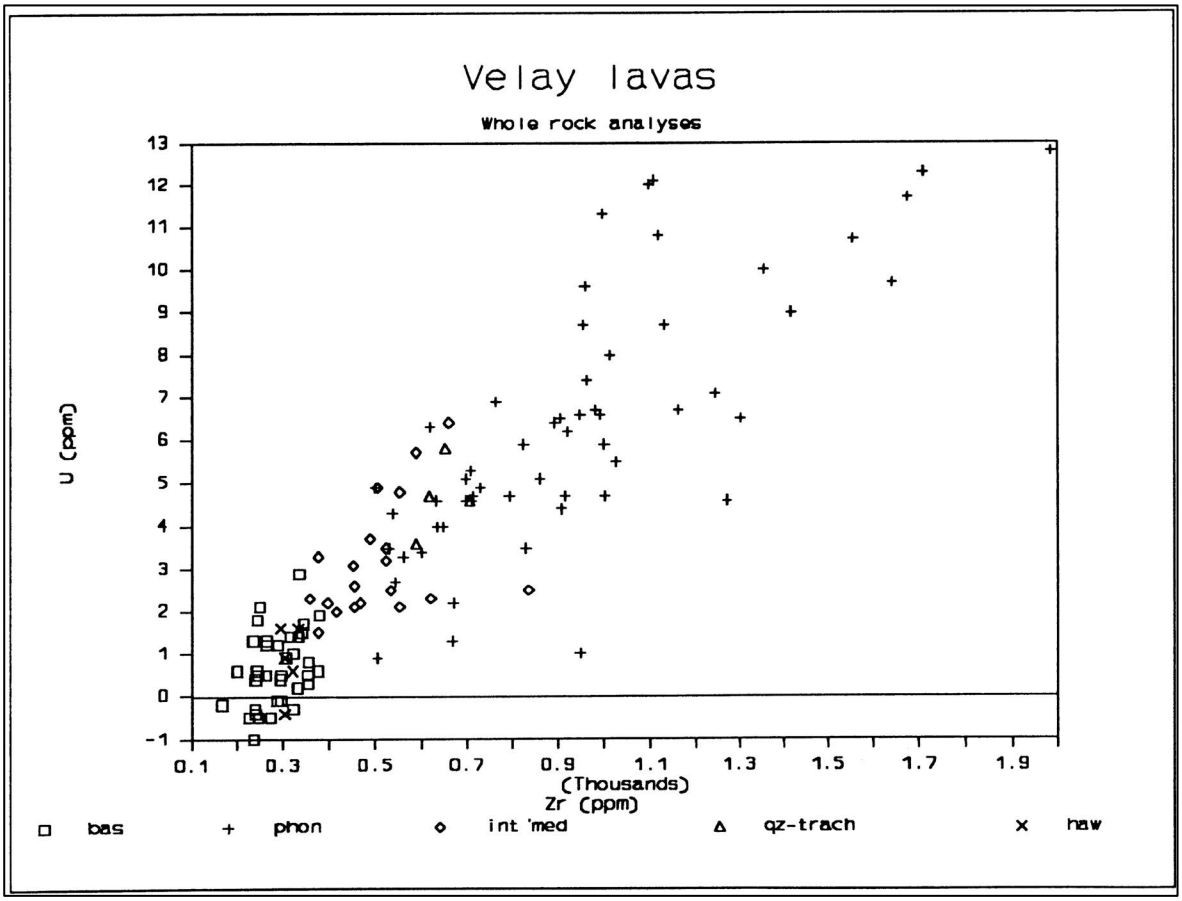


Figure 5.3.1z

5.3.2 Cumulates

Finding a suitable index for the cumulates poses a different problem. If an incompatible element were to be used, as for the lavas, the results would be meaningless, with the values being very nearly zero in every specimen. To obtain an index proportional to degree of fractionation we first need to obtain the equivalent expression to Rayleigh fractionation for the cumulate. For the liquid:

$$C_L = C_O F^{(D - 1)} \qquad (1)$$

where C_L is the concentration of a given element in the liquid, C_O is the concentration in the original (unfractionated) liquid, F is the weight fraction of the original liquid remaining and D is the bulk distribution coefficient of the element. D can also be expressed as:

$$D = C_S / C_L \qquad (2)$$

where C_S is the mean concentration of the element in the fractionating solids in equilibrium with the liquid. C_S can be thought of as representing the "instantaneous cumulate" forming from the liquid. Clearly, if the scale of a cumulate stack is large enough, a small cumulate nodule carried in a lava flow will have a composition which approximates that of the "instantaneous cumulate". Combining (1) and (2) gives:

$$C_S = C_O D F^{(D - 1)} \qquad (3)$$

which is the cumulate equivalent of the expression for Rayleigh fractionation. Figure 5.3.2 shows this relationship on a graph, with the Rayleigh fractionation of liquids (equation 1) for comparison. Examination of this graph shows that a linear relationship between C_S and F is obtained only when D = 2, so that equation (3) can be rearranged to give $F = C_S / 2C_O$. Unfortunately it is asking too much to find an element with D = 2 in every mineral assemblage throughout the fractionating series. Villemant *et al* (1980) derived D-values for the Chaîne-des-Puys series and the most suitable candidates were $Fe_2O_3^T$ (D = 1.5 to 2.9), Sc (D = 2.7), TiO_2 (D = 1.2 to 3.1), MgO (D = 1.8 to 3.1) and CaO (D = 1.3 to 2.6). None of these was sufficiently close to D = 2. However, if the value of D remains constant at any value, equation (3) can be rearranged to give F:

$$F = 10^{(\log C_S - \log D - \log C_O)/(D - 1)} \qquad (4)$$

Figure 5.3.3 shows F calculated from MgO using D = 3.86 and C_O = 8% from the Velay lava trend plotted against MgO. Over the range shown by the cumulates, MgO has a reasonably linear relationship with F and was therefore used as the x-axis for simplicity.

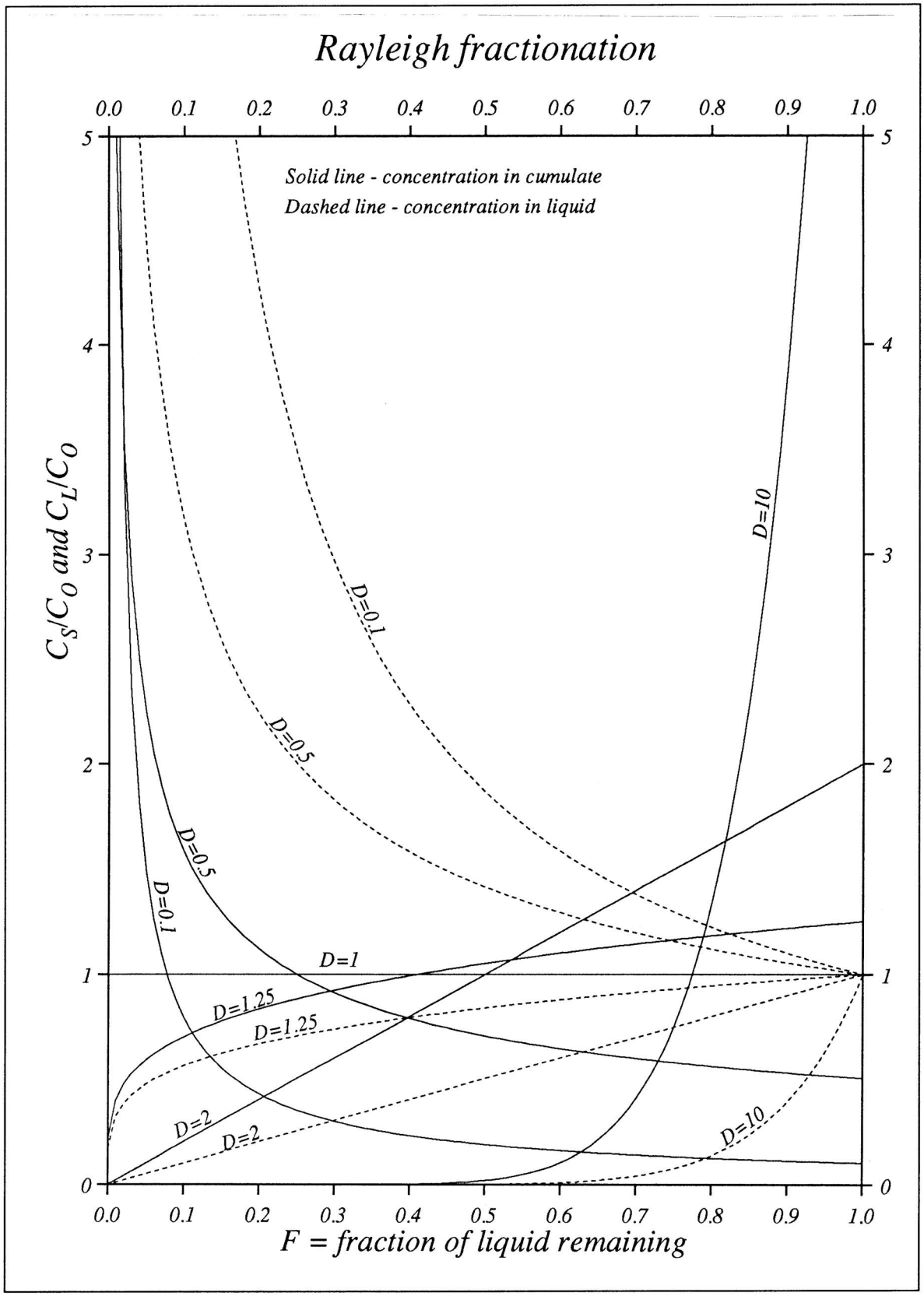


Figure 5.3.2. Concentration of elements of various bulk D in both lavas and cumulates during Rayleigh fractionation.

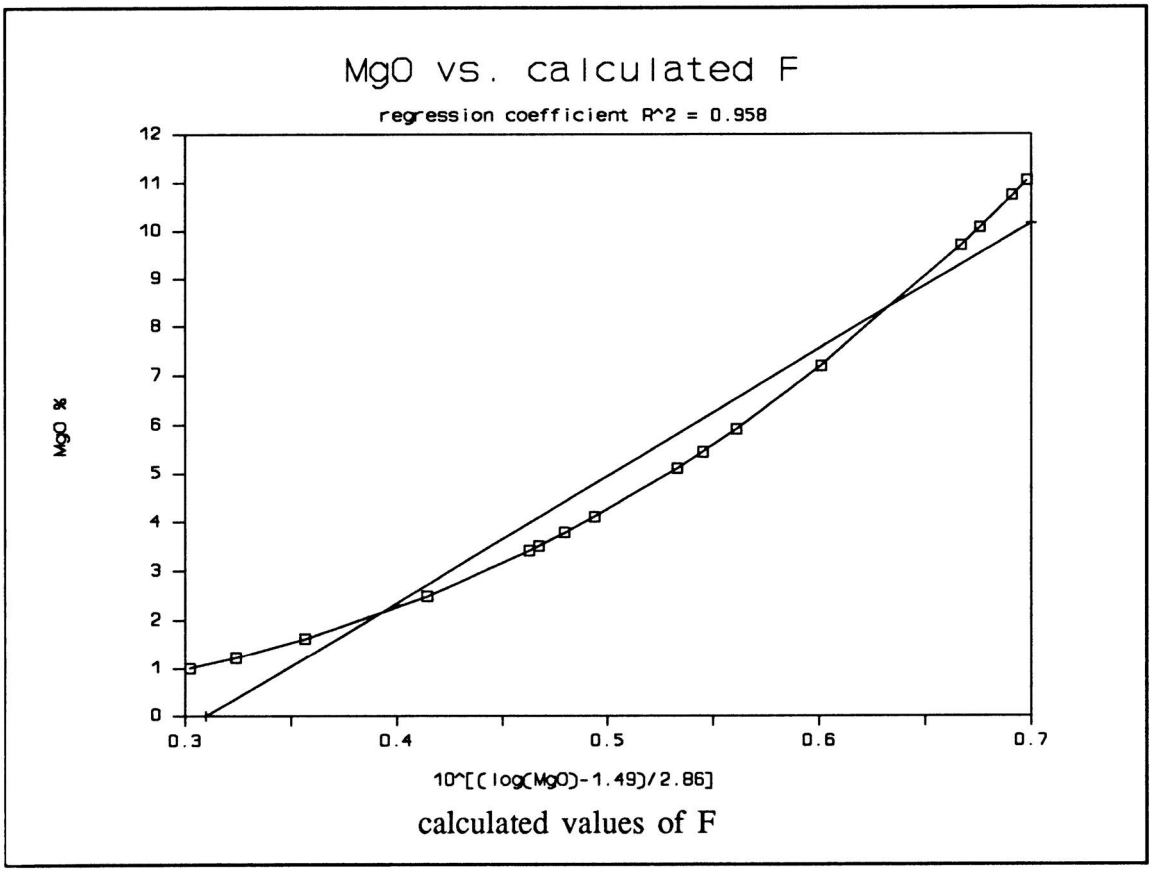


Figure 5.3.3. Regression line through MgO-F values, showing that MgO has a reasonably linear relationship with F over the range of cumulate data.

5.4 Petrogenesis of the evolved rocks

The process by which the evolved lavas (hawaiite to peralkaline phonolite) were formed can be deduced from the geochemistry, petrography, erupted proportions and sequence of eruption of all the Velay lavas. Additional information comes from mantle xenoliths.

Possible processes are partial melting of either mantle or crustal rocks, contamination, magma mixing, crystal-liquid fractionation and others such as gas transfer and liquid immiscibility. Villemant and Treuil (1983) concluded that the tight geochemical trends in their Velay analyses showed that they must have been formed by a single process operating on a fairly homogeneous parent magma. This is confirmed by the trends shown by the much larger number of analyses in the data set for this study.

5.4.1 Partial melting

The advantage of partial melting is that it provides a more plausible explanation than other mechanisms for the "Daly gap" in lava compositions (see section 1.4.1). The geochemical data do not however, support this mechanism. Figure 5.4.1 shows curves for batch melting for various values of distribution coefficient. Villemant *et al* (1980) point out that for the geologically reasonable range of F = 0-30%, elements with low D (< 0.5) can be quite strongly enriched, whereas elements with D > 1 show very little change in their concentration in the liquid. In the Velay lavas, by contrast, both incompatible *and* compatible elements show large changes in concentration through the series (see Figure 5.3.1).

Another difficulty for partial melting is the curved nature of many of the variation trends, for example 5.3.1c and e. This requires that the parent solid be composed of concentrically zoned minerals, whereas the minerals of most ultramafic nodules believed to represent mantle samples are remarkably homogeneous.

Finally, to derive highly incompatible-element enriched evolved lavas from mantle material would require exceptionally small degrees of partial melting, with consequent extraction difficulties, or exceptionally large amounts of mantle metasomatism, which is not observed in nodules brought to the surface.

Partial melting of crustal material is even less likely to be the source of the Velay lavas. The rarity of silica-undersaturated rocks poses the first problem and the primitive values (0.7033 - 0.7035) of $(^{87}Sr/^{86}Sr)_{initial}$ seen in the Velay lavas (see section 5.8) are hardly representative of a lithospheric source rock. The presence on oceanic islands of lava series identical to those of the Velay shows that crustal material is not necessary for their formation.

5.4.2 Contamination

The most obvious source of any contaminant is the crust. The Velay anatectic granite appears at the surface underlying all of the lavas, but it is impossible to produce a phonolite by contaminating an alkali basalt with a granitic melt. A possible contaminant could be silica-poor material from the

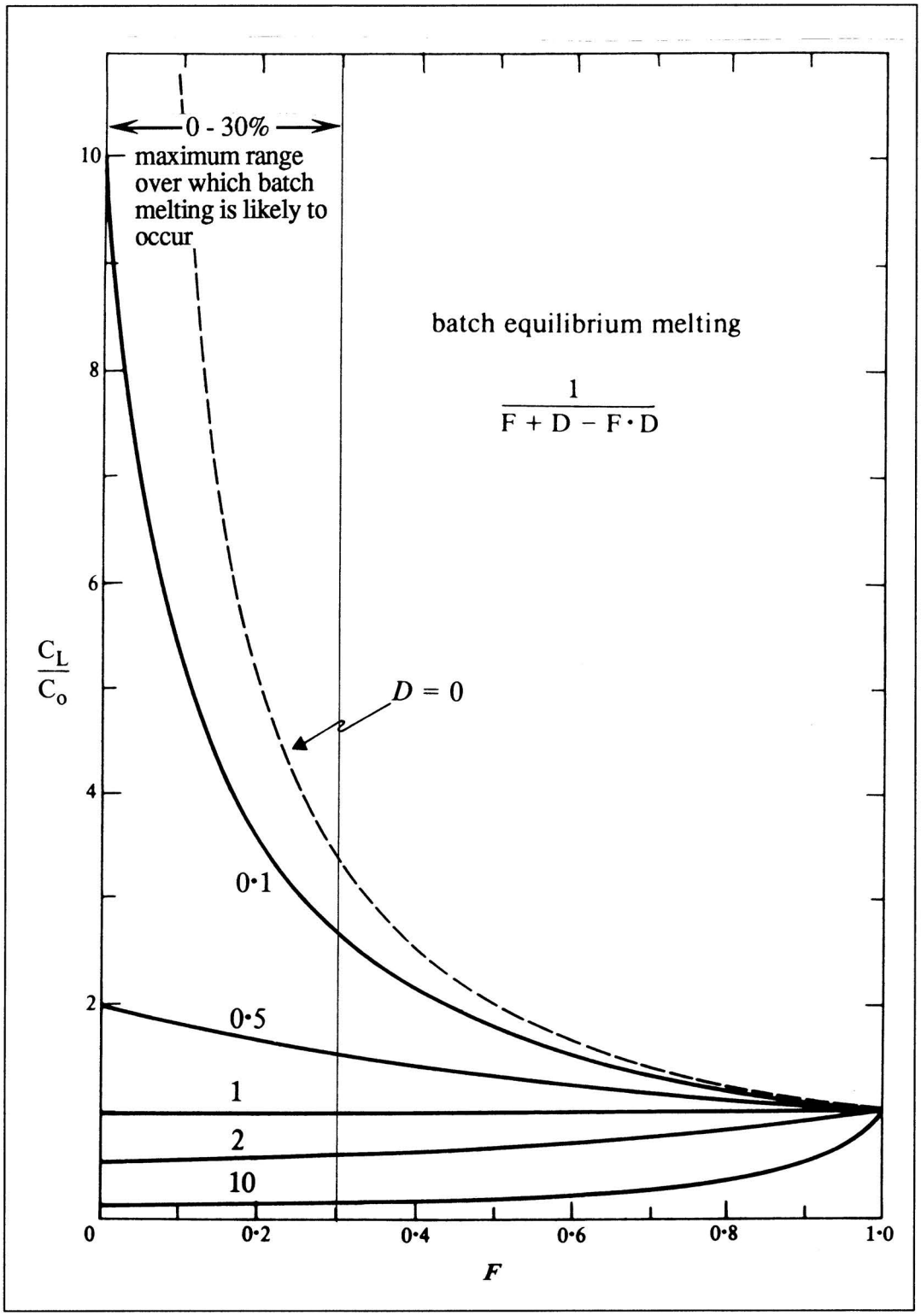


Figure 5.4.1. Concentration of elements of various bulk D during batch melting. The line at 30% melting indicates the upper end of the likely range over which this process operates. (Graph taken from Cox *et al* 1979).

lower crust, but this still has to overcome the problem that mixing an end-member contaminant with a parental basalt will produce straight lines on variation diagrams, contrary to the situation in the Velay. Villemant and Treuil (1983) proposed a mechanism of selective exchange of elements between the magma and a hydrothermal fluid. This would, however, lead to elevated values of $(^{87}Sr/^{86}Sr)_{initial}$ and $\partial^{18}O$. The first of these has been rejected for the Velay in this study (see section 5.8), and for the second Villemant and Treuil (1983) cite $\partial^{18}O$-values of +6 for the Velay basalts and +5 for the phonolites, neither of which indicates contamination.

A strong argument against crustal contamination is the same as for the previous section i.e. since identical lavas appear on oceanic islands, where there is no continental material, it cannot be necessary for the formation of such lavas.

5.4.3 Magma mixing

Like partial melting this model can explain the lack of intermediate lavas quite easily, with the end-members being the most abundant lavas and mixtures being less common. It is however impossible to produce curved or kinked trends on variation diagrams with mixing alone. Even if it were possible, the origin of the phonolitic end-member magma is unexplained. Also, in the Mont-Dore, where magma-mixing has been shown to have occurred, there is abundant petrographical evidence of mixing, from disequilibrium of phenocrysts to liquid-liquid chill relationships and intermingled lava types. Such evidence is not present in the Velay.

5.4.4 Crystal-liquid fractionation

Many workers in the Massif Central have supported the idea of fractional crystallisation as the dominant process leading to the evolved lavas, for example Varet (1969) preferred this mechanism for the genesis of the phonolites of the Cantal.

The supporting evidence is impressive. Whereas partial melting models give only small changes in the concentration of compatible elements Figure 5.3.2 shows that large changes can be produced by Rayleigh fractionation. Similarly, curved and kinked trends in variation diagrams can be accounted for either by constant high D-values, slowly changing D-values due to solid solution, or abruptly changing D-values due to the appearance or disappearance of phases from the liquidus. All of these are supported by corresponding changes in the mineral phases seen as phenocrysts in the lavas, with the exception of the aphyric evolved lavas of the Velay plateau (discussed at the end of this section). For example, Figure 5.3.1j shows K_2O becoming compatible at about Zr = 600ppm, while thin sections show that K-feldspar appears as a phenocryst in these specimens. The lavas also show linear trends through the origin for pairs of very incompatible elements. This is accounted for by Rayleigh fractionation.

Villemant and Treuil (1983) found a negative Eu-anomaly in REE patterns for the Velay evolved lavas, strongly suggesting that they have fractionated plagioclase.

The conclusion that crystal settling has occurred is hard to avoid given that observed phenocrysts have a greater density (from Deer *et al* (1966) than that calculated for the liquid represented by the groundmass. Coupled with the presence in some lavas of coarse-grained nodules with cumulate textures, composed of the same minerals as the phenocrysts, the process is clearly important in the Velay.

Several problems remain for Rayleigh fractionation. One is the observed lack of intermediate lavas, in contrast to a simple volumetric model where abundances of erupted lavas should decrease regularly with evolution. This does not mean that fractional crystallisation alone cannot have occurred, as explained in Chapter 1.

Another problem is that the lavas of which the Velay plateau is composed are largely aphyric, although their geochemical trends suggest an origin by crystal fractionation. If they had formed by process of crystal settling they would be expected to contain abundant phenocrysts. An alternative method of separating crystals from a melt is flow crystallisation (Irving 1978) where magma flowing through a conduit nucleates crystals onto the relatively cool walls. Thus crystals are left behind as the magma continues to flow towards the surface. Apart from variations in the mineral assemblage being removed, as a result of the range of pressures over which this process occurs, it is geochemically indistinguishable from crystal settling.

This mechanism can explain the absence of phenocrysts, while also allowing the eruption of all the plateau lavas through fissures at the surface. This is important since the density filter model, outlined in section 1.6.3, excludes the possibility of erupting evolved lavas (except phonolite) from a magma chamber, since there is no mechanism to bring them to the surface once formed. If however, they formed in the conduits on the way to the surface, the same mechanisms which allowed the dense basalt to rise could operate equally for the evolved magmas. The progression towards more evolved lavas at the top of the plateau could be due to a declining flow rate, allowing more crystallisation on the way to the surface.

Evidence for flow crystallisation would be provided by the presence of medium to coarse-grained dyke-like bodies in the basement beneath the plateau. However, if present, they would probably be too deep to be exposed at the surface today. The occasional coarse-grained nodules found in the lavas may be fragments of the crystal-lining of the conduit which were ripped off by the magma flow.

5.4.5 Other processes

This heading includes gas-transfer and liquid immiscibility. There is some evidence for both of these in the Velay. As mentioned in the introduction, Batard *et al* (1977) proposed gas-transfer as the means by which the Monac trachyte could have enriched its residual liquid in Na_2O, by CO_2-corrosion of plagioclase phenocrysts. Evidence for this is not, however, widespread in the Velay, and its effect on the liquid was probably small.

Liquid immiscibility is a potential mechanism for the differentiation of lavas, but compositions

giving silicate-silicate liquid immiscibility are unusual. Sulphide-silicate liquid immiscibility is known to operate in the formation of some ore-bodies, and carbonate-silicate liquid separation is also known to occur (Freestone and Hamilton 1980). Petrographic evidence for immiscible silicate liquids is absent in the Velay, but in the cumulates there are strong indications that small amounts of both sulphide and carbonate immiscible liquids were present in the magma chamber (see sections 4.6.10 and 4.6.11)

5.4.6 Conclusion

The dominant petrogenetic process for the Velay evolved lavas was crystal fractionation, either by crystal settling or by flow crystallisation. Other processes were either very subordinate or did not operate.

5.5 Calculation of parental liquid

The technique used by Villemant and Treuil (1983) to calculate the Velay parental liquid (Ve_0) was described in detail in Villemant *et al* (1980) for the Chaîne-des-Puys. They used a graph of ln(Th) vs ln(Ni), which as mentioned in section 5.3.1 renders suites of lavas with constant bulk distribution coefficient ($D_{element}$) as straight line segments. Villemant *et al* (1980) assumed that:

a) the primary magma evolved by fractional crystallisation alone, from a single composition parental magma,

b) D_{Ni} for the basic lavas could be extrapolated back to the primary liquid, i.e. there was no change in the fractionating assemblage before eruption,

c) the primary liquid was formed by 0-30% partial melting of peridotite mantle with 2500ppm Ni

d) D_{Ni} for peridotite was 5-10 during partial melting.

Of these assumptions, a),c) and d) are all quite reasonable. In the case of c) comparison can be made with the analyses of the lherzolite nodules 86/14 and 86/60 in this study, which have 2131ppm and 2485ppm Ni respectively. For b) it is not possible to tell if the fractionating assemblage was different to that deduced from the trend shown by the lavas, and must simply be assumed.

With these assumptions the batch melting equation, $C/C_0 = 1/(D + F - FD)$, is used with C_0 = 2500ppm, D = 5-10 and F = 0-30% to derive the concentration of Ni in the parental liquid. The calculated value, 350 ± 150ppm is then used to determine the concentration of Th in the initial liquid, which in turn is used to determine the concentrations of all other elements in the same magma by the same method. Figure 5.5.1 shows the ln(Th)-ln(Ni) graph with the construction lines used, with two other graphs as examples of the best and worst results from the data in this study. Even in Villemant and Treuil (1983) the trend on the ln(Th)-ln(Ni) graph is weak and the data used in this study do not improve the situation. In Figure 5.5.1a the trend line is drawn to the left of the data set to avoid the effect of included olivine phenocrysts giving elevated Ni-values (Villemant *et al* 1981). Villemant

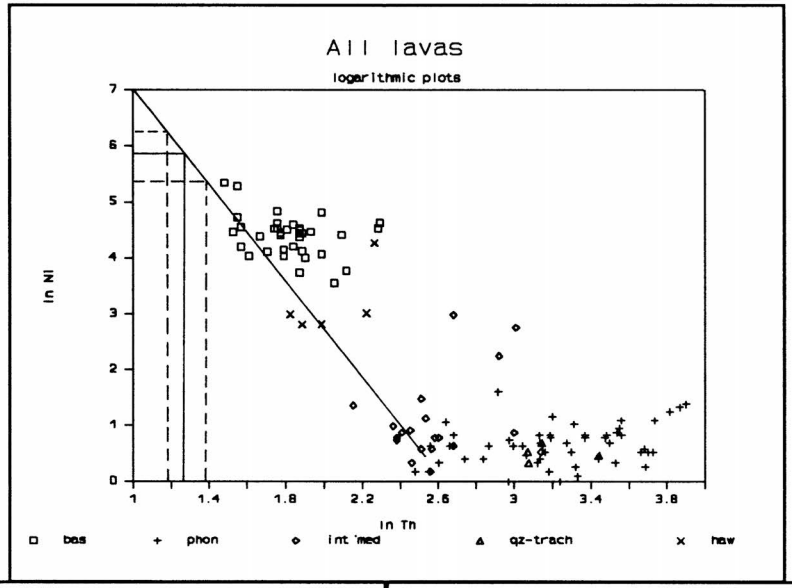


Figure 5.5.1a
Line fitted to left-hand side of data to avoid high Ni-values from olivine phenocrysts, as recommended by Villemant *et al* (1980). Expected Ni-content of 350 ± 150 ppm in primary basalt used to predict Th-content, in this case 3.5 ± 0.5 ppm

Figure 5.5.1b

Figure 5.5.1c

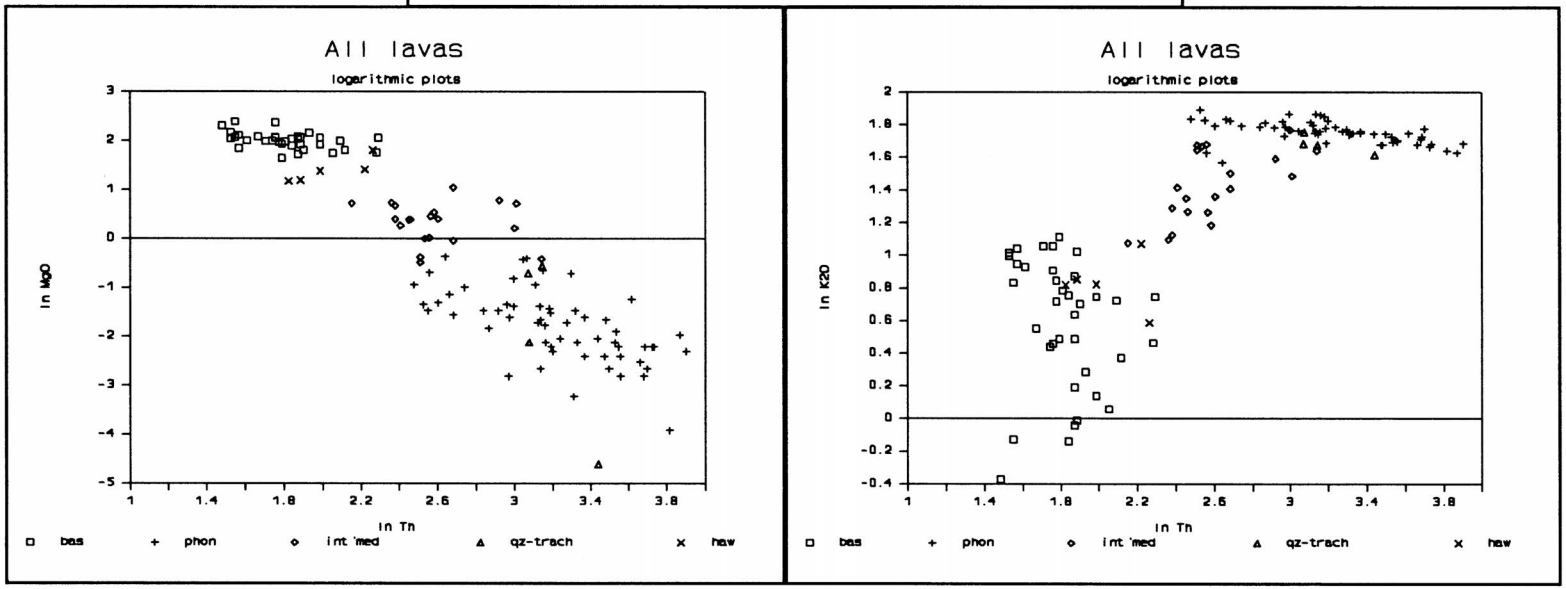


Figure 5.5.1. Method of Villemant *et al* (1980) for determining composition of primary magma.

and Treuil (1983) obtained 4ppm Th as the concentration in Ve_0 with about 20 data points. Data for this thesis total 124 analyses and give very poor trends for many elements, for example K_2O in Figure 5.5.1c. The removal of phenocryst-rich samples does not improve these trends. Nevertheless the same procedure as used by Villemant *et al* (1980) was attempted. Table 5.5.2 compares their results with those obtained in this study. It shows that the technique, although theoretically sound, is poor in practice. The error bars given are misleading in that they give no idea of error due to poor correlation lines, the values depending more on the slope of these correlation lines than on the initial Th concentration. Particular note should be taken of the very poor trend shown by the basic lavas on the ln(Th)-ln(K_2O) graph (Figure 5.5.1c). Villemant and Treuil (1983) obtained a value of D_{K_2O} less than zero from their graph, from which they deduced that a process other than crystal fractionation had caused enrichment of this element. The graph in this study shows a great deal of scatter and cannot be used to conclude that D_{K_2O} is less than zero.

The amount of fractionation that has taken place before the eruption of the most basic lavas can be calculated from the Th concentrations, in this case giving $F = 0.75 \pm 0.1$ for the most primitive basalts (4.7ppm) compared with 3.5 ± 0.5ppm in the parental liquid. All other graphs of elements against Th should give the same value of F since they are all dependent on the original Th values.

Finally it should be noted that neither of the calculated initial magmas would be in equilibrium with the olivine in mantle peridotite (Fo_{92}). Roeder and Emslie (1970) showed that a liquid in equilibrium with olivine with $Mg/Fe^{2+} = x$ would have $Mg/Fe^{2+} = 0.3x$. Both Villemant and Treuil's (1983) and this study's initial liquids would be in equilibrium with Fo_{84} olivine, only marginally more Mg-rich than olivine microphenocrysts in the most primitive basalts.

To calculate an equilibrium magma a programme was written, based on the procedure in Fitton and James (1986), to calculate the parent liquid by successive 0.1% incremental additions of equilibrium olivine, as $(Mg,Fe^{2+})_2SiO_4$. No improvement was found by reducing the increment size. $Fe_2O_3{}^T$ was divided in the ratio $Fe_2O_3/FeO = 0.15$ as recommended by Brooks (1976). Concentrations of elements incompatible in olivine can be calculated by "diluting" them by the amount of olivine added. Table 5.5.3 shows the result of this procedure on the estimated most primitive basalt, which was calculated using the trend lines of the Villemant and Treuil (1983) technique. The parental magma calculated in this way is picritic, not surprisingly after the addition of 50% forsteritic olivine.

The parental magmas calculated by these two techniques have very different compositions. To decide which is more likely to be correct it is necessary to examine some of the assumptions behind them. The postulated properties of mantle material, such as D_{Ni}, C_{Ni}, Fo-content of olivine, are probably reasonable since they are based on observation. However the assumption that initial liquids were in equilibrium with mantle olivines may not be valid. Some Massif Central basalts (though none in the Velay) contain abundant spinel-lherzolite nodules, showing that they have not undergone crystal settling. Their composition is not however, picritic. Indeed, true picrites are not found in the

Table 5.5.2
Compositions of parental liquids of the Velay basic lavas
Using the method of Villemant and Treuil (1983)

	Villemant and Treuil (1983)	This study	Comments on values obtained in this study (VT = Villemant and Treuil 1983)
Th initial value	4 ppm	3.5 ± 0.5 ppm	very poor
SiO_2	40.9 ± 0.9%	41.3 ± 0.9%	poor
TiO_2	3.2 ± 0.2%	5.55 ± 0.5%	OK, better than VT
Al_2O_3	15.7 ± 0.7%	13.3 ± 0.6%	OK
Fe_2O_3T	14.3 ± 1.6%	15.1 ± 0.7%	OK
MnO	not determined	0.17 ± 0.01%	poor
MgO	10 ± 2%	10.3 ± 1.2%	reasonable
CaO	10.3 ± 0.9%	10.8 ± 0.5%	good, better than VT
Na_2O	3.4 ± 0.3%	1.99 ± 0.24%	very poor
K_2O	0.9 ± 0.1%	1.33 ± 0.18%	extremely poor
P_2O_5	1 ± 0.1%	0.43 ± 0.08%	OK, much better than VT
Total	99.7%	100.3%	
Zn	not determined	93 ± 2 ppm	OK
Cu	" "	92 ± 20 ppm	OK
Co	ref. element	86 ± 14 ppm	OK
Cr	140 ± 40 ppm	400 ± 106 ppm	poor
V	not determined	337 ± 25 ppm	good
Ba	610 ± 30 ppm	480 ± 55 ppm	reasonable
Ga	not determined	21 ± 0.5 ppm	poor
Rb	36 ± 4 ppm	34 ± 4 ppm	poor
Sr	1140 ± 80 ppm	665 ± 65 ppm	OK, much better than VT
Y	not determined	21 ± 2 ppm	poor
Zr	250 ± 30 ppm	156 ± 25 ppm	OK, much better than VT
Nb	not determined	45 ± 5 ppm	OK
Pb	" "	3.5 ± 0.4 ppm	poor
U	1.0 ± 0.1 ppm	0.46 ± 0.1 ppm	poor

Table 5.5.3
Compositions of most primitive Velay basalt and parental magmas
Calculated by incremental addition of equilibrium olivine.

	Most primitive Velay basalt	Calc. parent magma in equilibrium with Fo_{92} olivine	Calc. parent magma with $Mg/Fe^{2+} = 2.1$ (Downes 1983)
SiO_2	43.0%	42.74%	43.28%
TiO_2	4.48%	3.04%	3.93%
Al_2O_3	14.50%	9.83%	12.70%
Fe_2O_3	14.26%	1.15%	1.49%
FeO	-	11.39%	11.90%
MnO	0.17%	0.12%	0.15%
MgO	8.70%	22.05%	14.03%
CaO	10.5%	7.12%	9.2%
Na_2O	2.26%	1.53%	1.98%
K_2O	1.00%	0.68%	0.88%
P_2O_5	0.53%	0.36%	0.46%
Total	99.40%	100.00%	99.99%
Ni	106 ppm	10 – 71 ppm	90 – 191 ppm
Zn	93 ppm	for D_{Ni} = 5-10	for D_{Ni} = 5-10
Cu	55 ppm		
Co	60 ppm		
Cr	180 ppm		
V	280 ppm	**50.3% olivine**	**16.3% olivine**
Ba	575 ppm	**added**	**added**
Ga	21 ppm		
Rb	45 ppm	30 ppm	39 ppm
Sr	650 ppm	432 ppm	559 ppm
Y	25 ppm	17 ppm	21 ppm
Zr	220 ppm	146 ppm	189 ppm
Nb	60 ppm	40 ppm	52 ppm
Th	4.7 ppm	3.1 ppm	4.0 ppm
Pb	3 ppm	2.0 ppm	2.6 ppm
U	0.5 ppm	0.33 ppm	0.43 ppm

Massif Central. If present at depth, their absence at the surface poses a problem, since although their high density would make their eruption less likely, some rare occurrences would be expected. In addition, some Massif Central basalts have Mg/Fe^{2+} ratios which show that they would be in equilibrium with mantle olivine. Disequilibrium partial melting of the mantle could provide an explanation for the Mg/Fe^{2+}-ratios of the Velay basalts, but Bédard (1989) has shown that equilibration of a melt with olivine is much too rapid for disequilibrium to be found in erupted lavas.

Jaques and Green (1980) showed that 0-20% partial melting of a pyrolite source at P = 10-17kb, T = 1200-1350˚C could give alkali basalt, possibly by adiabatic decompression. However, observed decoupling between some trace elements and their isotopic ratios in lavas cannot be reconciled with a simple partial melting model. For this reason various authors have proposed a process of mantle metasomatism to explain this decoupling. Downes (1983) confirmed this for the Massif Central, with primitive lavas showing incompatible trace element enrichment but isotopes suggesting a source depleted in these elements for a long time. Mantle metasomatism was also suggested by the presence of amphibole, phlogopite and apatite as accessory phases in mantle nodules carried to the surface by lavas. Downes (1983) concluded that due to metasomatism, lavas with $Mg/Fe^{2+} > 2.1$, Cr > 300ppm and Ni > 200ppm were probably parental. Chauvel and Jahn (1984) deduced that the source of the Massif Central basic lavas was a LREE, Rb-depleted mantle, metasomatised by a short-lived fluid phase immediately before 10-20% partial melting and eruption. Downes (1987a) further showed the source to be garnet lherzolite.

The consensus seems to be that the lavas with the highest Mg/Fe^{2+} in the Massif Central, often those bearing spinel lherzolite nodules, represent parental liquids, and that their trace element and isotopic compositions are due to metasomatism of a LIL,REE-depleted garnet lherzolite source. This metasomatism would permit the generation of alkali basalts with 10-20% partial melting, with equilibrium $Mg/Fe^{2+} \geq 2.1$.

On this basis the Velay most primitive basalt (Table 5.5.3) was calculated back to $Mg/Fe^{2+} = 2.1$, by the addition of 16.3% equilibrium olivine. This is a compromise, with Downes' (1983) value being based on observations of Massif Central lavas considered to be primary. The value of 16% olivine addition, equivalent to 14% fractionation, is essentially the *minimum* amount of fractionation that can have taken place before the eruption of the most basic Velay lavas. Its value as a true parental composition should be considered in this light.

5.6 Fractionation in the Velay lavas

5.6.1 Qualitative analysis

For the purpose of analysing the graphs of Figure 5.3.1 the fractionating series was divided into several sections, on the basis of inflections in the trends. They are:

a) basalts to hawaiites

b) hawaiites to intermediate lavas

c) intermediate lavas to miaskitic phonolites

d) miaskitic to agpaiitic phonolites

e) intermediate lavas to quartz-trachytes

The last of these was included to account for the branching-off of the quartz-trachytes from the main trend. The term "intermediate lavas" refers to mugearites and benmoreites as a group.

The following observations are based on Figure 5.3.1a-z, backed up by ln(Th)-ln(element) graphs.

5.6.1.1 Details of fractionation steps

Basalts to hawaiites

This step is characterised by decreasing TiO_2, $Fe_2O_3^T$, MgO, CaO, Cu, Ni, Co, Cr and V. The removal of forsteritic olivine is indicated by the coupled decrease in MgO and Ni, with Co, Cu Cr and V also compatible in this mineral. The decrease in CaO, while Al_2O_3 is increasing, shows that clinopyroxene (cpx) is being removed, but *not* plagioclase. Cr also has a strong affinity for cpx, which accounts for its decrease. $Fe_2O_3^T$ and TiO_2 concentrations in cpxs from the basalts are lower than in the whole rock so Ti-magnetite is required to cause the depletion in these elements, as well as V. The assemblage was therefore composed of olivine, cpx and Ti-magnetite.

The phenocryst-poor basalts contain olivine and Ti-magnetite microphenocrysts. The ankaramites, by contrast, have large euhedral olivine and cpx phenocrysts in roughly equal proportions. The olivine varies over the range Fo_{70-86}, mainly Fo_{80}, while the cpx is salite with 20% CaO, 1-4% TiO_2. Ti-magnetite (22% TiO_2) is also present. Rare spinel-hercynite (50% Al_2O_3) probably did not fractionate in significant proportions since Al_2O_3 for the lavas increases throughout the basalts.

Most of the hawaiites are nearly aphyric, with sporadic microphenocrysts of olivine Fo_{80}, cpx (22% CaO, 2.5% TiO_2) and Ti-magnetite (16-22% TiO_2). One specimen has phenocrysts of amphibole, cpx, plagioclase An_{48-52}, Ti-magnetite, olivine and trace apatite, with the amphibole, plagioclase and olivine showing signs of resorption. Olivine appears for the last time in the hawaiites.

In this first stage, evolution of the lavas seems to have been by removal of olivine, cpx and Ti-magnetite, with the latter two increasing in proportion through the sequence at the expense of the olivine.

Hawaiites to intermediate lavas

Figure 5.3.1 and especially ln(Th)-ln(element) graphs show a steeper decline in TiO_2, $Fe_2O_3^T$, MgO, CaO and V in this stage compared with the first. Cr, Ni, Cu and Co also continue to diminish, while P_2O_5 falls rapidly from a peak of 1.5% reached in the hawaiites.

The last observation is the easiest to explain, by the addition of apatite to the fractionating assemblage, and is confirmed by its abundance in thin section. Olivine however, is no longer present in the lavas and the rapid decrease in MgO is thus difficult to explain, since olivine contains up to 46% MgO compared with 14% for cpx. The fall in TiO_2, $Fe_2O_3^T$, CaO, Cr and V can be accounted for by the increased proportions of cpx and Ti-magnetite after the olivine disappears. Kaersutite amphibole is a common phenocryst in some of the intermediate lavas and its removal would cause a reduction in TiO_2, MgO, CaO, Cr, Co, V and Cu. Amphiboles also have a relatively strong affinity for Ba ($D_{Ba} = 7$) and Y ($D_Y = 1 - 7$) but Ba continues to increase, while Y starts by increasing then decreases, leaving it unclear whether significant amounts of amphibole have been extracted.

The intermediate lavas of the south of the Velay are almost aphyric, with apatite and Ti-magnetite (21-27% TiO_2) as the commonest microphenocrysts, accompanied by traces of kaersutite and plagioclase An_{36-44}. In the north of the Velay the intermediate lavas are exceptionally rich in phenocrysts, with apatite, Ti-magnetite (10-17% TiO_2), sphene, kaersutite (5% TiO_2), cpx, plagioclase An_{23-60} and alkali feldspar Or_{13-55} all appearing in various proportions, but dominated by kaersutite and feldspar. Cpx appears in most of these lavas but never exceeds 1.5% by volume.

Intermediate lavas to miaskitic phonolites

TiO_2 shows a gentle decline and $Fe_2O_3^T$, MgO, CaO, P_2O_5 and V continue to decrease, in most cases reaching quite low concentrations. SiO_2 and Al_2O_3 stay constant and Ba, Sr and, to a lesser extent, Y all show a dramatic fall after earlier incompatible behaviour.

As before $Fe_2O_3^T$, TiO_2 and V suggest Ti-magnetite removal, P_2O_5 demonstrates apatite extraction and, in the absence of olivine, MgO depletion indicates cpx and/or amphibole fractionation. The decline in CaO cannot be taken as evidence that cpx is being extracted since both SiO_2 and Al_2O_3 show a marked increase in compatibility, indicating that a significant amount of plagioclase is being removed. This is confirmed by the rapid decline in Sr, which is admitted into plagioclase in place of Ca.

Ba and Y are both compatible in amphibole and might be evidence that this is the dominant ferromagnesian mineral. However sphene has an even greater affinity for Y and alkali feldspar likewise for Ba *and* Sr. The high distribution coefficient of Y in sphene ($D_Y = 20\text{-}70+$, Pearce and Norry 1979) would appear to rule out its fractionation in significant quantities since Y falls by only ≈25% in this step, which would take only 0.4 - 1.3% sphene fractionation. Amphibole fractionation could account for MgO, Ba and Y depletion by itself. The question cannot easily be resolved without extra data.

Apatite and Ti-magnetite are still being removed. Plagioclase and/or alkali feldspar are being extracted and one or more of amphibole, sphene or cpx are also involved.

Phenocrysts are initially those of the phenocryst-rich intermediate lavas as described in the previous section, followed by those of the miaskitic phonolites, which have apatite, Ti-magnetite (10-16% TiO_2), sphene and occasional zircon, kaersutite (4-5% TiO_2), cpx, plagioclase An_{26-46} and alkali feldspar (sanidine and some anorthoclase). Apatite, Ti-magnetite and sphene are less abundant than in the intermediates and amphibole and cpx are both subordinate to alkali feldspar. Plagioclase is present only as relict cores to alkali feldspars. Thus plagioclase and amphibole seem to dominate the early stages, following on from the previous section, with alkali feldspar and some amphibole/cpx as the final assemblage.

Miaskitic to agpaiitic phonolites

This step records SiO_2, Al_2O_3 and $Fe_2O_3^T$ staying roughly constant, TiO_2, MgO and CaO gently decreasing in concentration and K_2O showing a significant decline from 6% to 5%. P_2O_5 reaches almost zero, Sr likewise, while Zn shows continuous enrichment in these lavas.

These data suggest that apatite and Ti-magnetite fractionation have almost ceased, with K-feldspar removal strongly affecting K_2O, SiO_2, Al_2O_3, Ba and Sr. A lack of Ti-magnetite seems to be suggested by the increase in Zn. Some amphibole/cpx must be fractionating to cause the reduction in MgO, TiO_2 and CaO.

Thin sections of the agpaiitic lavas contain apatite, Ti-magnetite (13% TiO_2), sphene, cpx and amphibole in trace amounts. K-feldspar dominates the assemblage volumetrically, appearing as sanidine or potassic anorthoclase in different specimens.

Intermediate lavas to quartz-trachytes

The quartz-trachytes are illustrated by only four analyses of three eruptive units, so trends are poorly defined. TiO_2, $Fe_2O_3^T$, MgO, CaO, P_2O_5 and V show a decrease from the values in the intermediate lavas, and continue trends shown by the intermediates themselves. Al_2O_3 shows a sharp decrease, from a previously incompatible trend - this points to the Al-rich mineral plagioclase being removed in large quantities, confirmed both by decreasing CaO and a marked depletion in Sr, almost to zero. Ba is also strongly depleted, and Zr shows signs of slight depletion, complicated by its use as the x-axis in Figures 5.3.1a-z.

Ti-magnetite removal is suggested by the decline in TiO_2, Fe_2O_3T and V, and apatite by that of P_2O_5. This leaves MgO, Ba and Zr to be explained. Ba and Zr are both strongly incorporated into biotite (D_{Ba} = 11, D_{Zr} = 4, Villemant *et al* 1980) which with 10-13% MgO could also account for the depletion of that element.

Biotite is present in thin section, reaching 1.1% by volume in the Dents de Mézenc specimens. This lava is used to indicate the phenocryst assemblage for the other quartz-trachytes, which are aphyric but for a few microphenocrysts of alkali feldspar. Dents de Mézenc also contains a trace of apatite, 0.4% Ti-magnetite, 0.3% kaersutite, 0.2% cpx, and nearly 20% plagioclase and anorthoclase.

The few grains of zircon present could have caused the reduction in Zr, but they may also be groundmass phases. In the Chaîne des Puys Villemant *et al* (1980) proved that the Zr depletion was not caused by zircon, using the Zr/Hf ratio, which differs for biotite and zircon.

5.6.1.2 Summary

Alkali basalts evolve to hawaiites by the fractionation of olivine, cpx and Ti-magnetite, with olivine and cpx dominant at the start and cpx and Ti-magnetite more important towards the end of this first stage.

From hawaiite to the intermediate lavas kaersutite amphibole appears on the liquidus with subordinate plagioclase. Cpx and Ti-magnetite continue to crystallise but in much reduced proportions, and apatite appears as a minor phase.

To reach miaskitic phonolite, plagioclase (and alkali feldspar) comes to dominate the assemblage, with amphibole and/or cpx as the ferromagnesian mineral(s). Apatite and Ti-magnetite continue to be removed. Sphene may also be involved, but only up to 1%.

Within the phonolites K-feldspar removal is the main influence on magma evolution, with the addition of a small amount of kaersutite or cpx.

To reach the composition of the rare quartz-trachytes the fractionating assemblage is dominated by plagioclase, anorthoclase and biotite, with small amounts of Ti-magnetite and apatite also involved.

5.6.2 Quantitative analysis

The principal method by which the types and amounts of minerals fractionating from lavas can be assessed is that of mixing calculations (Wright and Doherty 1970). The principle behind this is that for each oxide involved, for example SiO_2, $Fe_2O_3^T$, the following can be written:

$$X = \sum_{i=1}^{n} x_i y_i$$

where X is the weight percent of the oxide in the calculated mixture, x_i the weight percent of the oxide in mineral (or lava) i and y_i is the weight percent of mineral (or lava) i in the mixture. Then for each oxide j:

$$X_j - T_j = R_j$$

T_j is the weight percent of oxide j in the "target" composition and R_j is the residual difference between calculated and observed contents of oxide j. The aim is to minimise:

$$\sum_{j=1}^{n} \left(R_j\right)^2 = sum\ of\ squares\ of\ residuals$$

This should produce the closest analogue to a "target" lava using a mixture of minerals and an initial lava. In practice, the target is the primitive lava and the evolved lava is mixed with potential

fractionating minerals to keep all values positive. A programme based on Wright and Doherty (1970) was used, allowing the addition of weighting factors to oxides, the sign of results to be constrained to positive or negative, and the deletion of certain oxides to improve the fit.

The programme was used without oxide weighting, with no constraint on the sign of the result and with all major oxides included. This was to ensure that mixes were the best possible for the data and that there were always fewer phases in the mix than oxides. All lava and mineral analyses were normalised to 100%.

5.6.2.1 Problems encountered

The main problem was in the comparison of the sum of squares of residuals (SSR) for different mixing steps. For some steps it was very easy to get low residuals, for others much harder. This was usually due to the fact that the SSR is step-size dependent. This can be demonstrated by calculating the SSR for a mix with *only* the evolved lava and no minerals - theoretically the largest possible SSR for the step. The results vary from 14 to 156, showing that when attempting to minimise the SSR some steps have an order of magnitude advantage at the outset. Normally SSR<1 indicates a good mix.

5.6.2.2 Input Compositions

The compositions of the lavas used for each mixing step were obtained by taking average values from the graphs of Figure 5.3.1, using the overall trends. This avoids the problems of using single samples which may contain anomalous amounts of some oxides. To assess the trends for the basic lavas additional graphs with MgO as the x-axis were also examined.

Mineral analyses for each step were calculated as mean microprobe analyses of phenocrysts from the lavas in the step. Only euhedral phenocrysts clearly in equilibrium with the lava were used, with the rims of those from the start of a step and the cores of those at the end preferred.

To choose which minerals should be put into each mix the qualitative analysis (section 5.6.1) was the main source of information, combined with thorough petrographic descriptions of the lavas. All minerals observed in the lavas were used in initial mixes to avoid their premature exclusion.

5.6.2.3 Interpretation

This is the most subjective task involved in mixing. Assemblages matching the qualitative data were obviously preferred, especially when the relative proportions of minerals resemble those observed in thin sections i.e. a good mix with 20% sphene fractionation would probably be rejected.

All results are shown in Table 5.6.1.

Table 5.6.1 Results of mixing calculations

Primitive basalt to evolved basalt step

	Primitive basalt	Evolved basalt	Cpx	Olivine Fo80	Ti-mag-netite	Amphibole	Plagioclase An76	Spinel-hercynite	
SiO_2	43.0	46.5	46.24	39.32	0.17	38.94	52.59	0.08	SiO_2
TiO_2	3.6	3.0	2.35	0.04	20.24	5.85	0.14	1.12	TiO_2
Al_2O_3	14.5	16.0	8.05	0.08	6.09	13.70	29.43	54.00	Al_2O_3
Fe_2O_3	14.2	12.3	8.09	21.31	70.63	12.74	0.57	28.66	Fe_2O_3
MnO	0.18	0.19	0.12	0.27	0.57	0.08	0.01	0.09	MnO
MgO	8.5	6.0	12.51	41.78	5.19	11.79	0.10	16.98	MgO
CaO	10.5	9.1	20.82	0.21	0.04	11.24	12.44	0.00	CaO
Na_2O	2.5	3.7	0.69	0.03	0.03	2.65	4.05	0.01	Na_2O
K_2O	1.5	2.5	0.05	0.04	0.05	1.27	0.44	0.04	K_2O
P_2O_5	0.55	1.1	0.00	0.00	0.00	0.00	0.00	0.00	P_2O_5
Total	99.03	100.39	98.92	103.08	103.01	98.26	99.77	100.61	Total

(all norm-alised)	Prim. bas. target	Calculated mix	Residuals			
SiO_2	43.421	43.204	0.217			
TiO_2	3.635	3.381	0.254			
Al_2O_3	14.642	14.495	0.147	Sum of	Mix results	
Fe_2O_3	14.339	14.269	0.070	squares of		
MnO	0.182	0.189	-0.007	residuals	evolv. bas.	70.70%
MgO	8.583	8.526	0.057		olivine	2.81%
CaO	10.603	10.637	-0.035	0.308	cpx	20.06%
Na_2O	2.524	2.748	-0.223		Ti-mag.	3.88%
K_2O	1.515	1.775	-0.260		spin-herc.	2.55%
P_2O_5	0.555	0.775	-0.219			
Total	100.00	100.00				

Evolved basalt to hawaiite step

	Evolved basalt	Hawaiite	Cpx	Olivine Fo80	Ti-mag-netite	Amphibole	Plagioclase An65	
SiO_2	46.5	48.5	46.24	39.32	0.17	38.94	55.34	SiO_2
TiO_2	3.0	2.5	2.35	0.04	20.24	5.85	0.03	TiO_2
Al_2O_3	16.0	17.2	8.05	0.08	6.09	13.70	27.34	Al_2O_3
Fe_2O_3	12.3	11.0	8.09	21.31	70.63	12.74	0.31	Fe_2O_3
MnO	0.19	0.23	0.12	0.27	0.57	0.08	0.01	MnO
MgO	6.0	3.7	12.51	41.78	5.19	11.79	0.03	MgO
CaO	9.1	8.3	20.82	0.21	0.04	11.24	9.75	CaO
Na_2O	3.7	4.4	0.69	0.03	0.03	2.65	5.38	Na_2O
K_2O	2.5	2.9	0.05	0.04	0.05	1.27	0.75	K_2O
P_2O_5	1.1	1.5	0.00	0.00	0.00	0.00	0.00	P_2O_5
Total	100.39	100.23	98.92	103.08	103.01	98.26	98.92	Total

(all normalised)	Evol. bas. target	Calculated mix	Residuals			
SiO_2	46.319	46.299	0.020			
TiO_2	2.988	3.111	-0.122			
Al_2O_3	15.938	15.772	0.166	Sum of	Mix results	
Fe_2O_3	12.252	12.182	0.07	squares of		
MnO	0.189	0.212	-0.023	residuals	hawaiite	79.43%
MgO	5.977	5.933	0.044		olivine	2.13%
CaO	9.065	9.011	0.053	0.086	cpx	5.22%
Na_2O	3.686	3.838	-0.152		Ti-mag.	1.59%
K_2O	2.490	2.453	0.038		amphibole	11.64%
P_2O_5	1.096	1.189	-0.093			
Total	100.00	100.00				

Hawaiite to intermediate lava step

	Hawaiite	Intermed-iate lava	Cpx	Apatite	Ti-mag-netite	Amphibole	Plagioclase An56	Sphene	
SiO_2	48.5	55.0	48.81	0.92	0.13	39.00	57.73	28.45	SiO_2
TiO_2	2.5	1.4	1.65	0.02	13.56	4.76	0.06	33.27	TiO_2
Al_2O_3	17.2	19.0	5.89	1.10	2.69	13.13	25.84	1.61	Al_2O_3
Fe_2O_3	11.0	7.0	11.28	0.40	84.40	15.04	0.47	2.01	Fe_2O_3
MnO	0.23	0.25	0.39	0.10	1.44	0.25	0.02	0.09	MnO
MgO	3.7	1.4	10.97	0.07	1.80	11.16	0.04	0.06	MgO
CaO	8.3	5.0	21.25	51.84	0.01	11.46	7.96	26.79	CaO
Na_2O	4.4	5.5	1.09	0.00	0.02	2.56	6.43	0.11	Na_2O
K_2O	2.9	4.0	0.04	0.05	0.05	1.57	0.83	0.05	K_2O
P_2O_5	1.5	0.4	0.00	42.00	0.00	0.00	0.00	0.00	P_2O_5
Total	100.23	98.95	100.37	96.50	104.10	98.93	99.38	92.44	Total

(all normalised)	Hawaiite target	Calculated mix	Residuals			
SiO_2	48.389	48.360	0.028			
TiO_2	2.494	2.470	0.024			
Al_2O_3	17.161	17.119	0.042	Sum of	Mix results	
Fe_2O_3	10.975	10.959	0.016	squares of		
MnO	0.229	0.271	-0.042	residuals	interm.lava	59.70%
MgO	3.692	3.691	0.001		amphibole	23.16%
CaO	8.281	8.270	0.011	0.025	cpx	1.51%
Na_2O	4.390	4.523	-0.134		Ti-mag.	3.69%
K_2O	2.893	2.861	0.033		plagioclase	9.10%
P_2O_5	1.497	1.476	0.021		apatite	2.84%
Total	100.00	100.00				

Intermediate lava to miaskitic phonolite step

	Intermed-iate lava	Miaskitic phonolite	Cpx	Apatite	Ti-mag-netite	Amphibole	K-feldspar	Sphene	Plagioclase An56
SiO_2	55.0	61.5	48.81	0.92	0.13	39.00	65.23	28.45	57.73
TiO_2	1.4	0.7	1.65	0.02	13.56	4.76	0.05	33.27	0.06
Al_2O_3	19.0	19.5	5.89	1.10	2.69	13.13	19.28	1.61	25.84
Fe_2O_3	7.0	4.3	11.28	0.40	84.40	15.04	0.21	2.01	0.47
MnO	0.25	0.2	0.39	0.10	1.44	0.25	0.04	0.09	0.02
MgO	1.4	0.5	10.97	0.07	1.80	11.16	0.00	0.06	0.04
CaO	5.0	2.3	21.25	51.84	0.01	11.46	0.69	26.79	7.96
Na_2O	5.5	6.6	1.09	0.00	0.02	2.56	6.38	0.11	6.43
K_2O	4.0	6.2	0.04	0.05	0.05	1.57	7.24	0.05	0.83
P_2O_5	0.4	0.1	0.00	42.00	0.00	0.00	0.00	0.00	0.00
Total	98.95	101.9	100.37	96.50	104.10	98.93	99.12	92.44	99.38

(all normalised)	Intermed. target	Calculated mix	Residuals			
SiO_2	55.584	55.525	0.058			
TiO_2	1.415	1.371	0.043			
Al_2O_3	19.202	19.171	0.030	Sum of	Mix results	
Fe_2O_3	7.074	7.060	0.014	squares of		
MnO	0.253	0.209	0.044	residuals	miask phon	62.61%
MgO	1.415	1.393	0.022		amphibole	5.47%
CaO	5.053	5.098	-0.045	0.066	cpx	3.64%
Na_2O	5.558	5.766	-0.207		plagioclase	23.63%
K_2O	4.042	4.097	-0.055		Ti-mag.	3.78%
P_2O_5	0.404	0.309	0.095		apatite	0.57%
					sphene	0.31%
Total	100.00	100.00				

Miaskitic phonolite to agpaiitic phonolite step

	Miaskitic phonolite	Agpaiitic phonolite	Cpx	Apatite	Ti-mag-netite	Amphibole	K-feldspar	Sphene	
SiO_2	61.5	61.0	48.20	0.92	0.04	38.58	65.23	28.45	SiO_2
TiO_2	0.7	0.25	1.20	0.02	11.60	3.78	0.05	33.27	TiO_2
Al_2O_3	19.5	20.5	3.79	1.10	0.63	12.56	19.28	1.61	Al_2O_3
Fe_2O_3	4.3	3.0	15.28	0.40	86.44	20.12	0.21	2.01	Fe_2O_3
MnO	0.2	0.45	1.22	0.10	4.28	0.56	0.04	0.09	MnO
MgO	0.5	0.01	8.46	0.07	0.35	8.35	0.00	0.06	MgO
CaO	2.3	0.9	20.76	51.84	0.01	11.07	0.69	26.79	CaO
Na_2O	6.6	9.4	1.60	0.00	0.07	2.51	6.38	0.11	Na_2O
K_2O	6.2	5.0	0.06	0.05	0.05	2.09	7.24	0.05	K_2O
P_2O_5	0.1	0.0	0.00	42.00	0.00	0.00	0.00	0.00	P_2O_5
Total	101.9	100.51	100.57	96.50	103.47	99.62	99.12	92.44	Total

(all normalised)	Miask phon target	Calculated mix	Residuals			
SiO_2	60.353	60.395	-0.042			
TiO_2	0.687	0.706	-0.019			
Al_2O_3	19.136	18.640	0.497	Sum of	Mix results	
Fe_2O_3	4.220	4.165	0.054	squares of		
MnO	0.196	0.270	-0.074	residuals	agp phon	27.94%
MgO	0.491	0.752	-0.262		K-feldspar	60.67%
CaO	2.257	2.053	0.205	0.473	amphibole	8.87%
Na_2O	6.477	6.743	-0.266		Ti-mag.	1.68%
K_2O	6.084	6.009	0.075		apatite	0.61%
P_2O_5	0.098	0.267	-0.169		sphene	0.22%
Total	100.00	100.00				

Intermediate lava to quartz trachyte step

	Intermed-iate lava	Quartz trachyte	Cpx	Apatite	Ti-mag-netite	Amphibole	Plagioclase An56	Biotite	
SiO_2	55.0	66.0	48.81	0.92	0.13	39.00	57.73	35.56	SiO_2
TiO_2	1.4	0.3	1.65	0.02	13.56	4.76	0.06	6.59	TiO_2
Al_2O_3	19.0	16.7	5.89	1.10	2.69	13.13	25.84	13.67	Al_2O_3
Fe_2O_3	7.0	3.4	11.28	0.40	84.40	15.04	0.47	21.19	Fe_2O_3
MnO	0.25	0.2	0.39	0.10	1.44	0.25	0.02	0.39	MnO
MgO	1.4	0.3	10.97	0.07	1.80	11.16	0.04	11.30	MgO
CaO	5.0	1.0	21.25	51.84	0.01	11.46	7.96	0.00	CaO
Na_2O	5.5	6.0	1.09	0.00	0.02	2.56	6.43	0.77	Na_2O
K_2O	4.0	5.5	0.04	0.05	0.05	1.57	0.83	8.66	K_2O
P_2O_5	0.4	0.1	0.00	42.00	0.00	0.00	0.00	0.00	P_2O_5
Total	98.95	99.50	100.37	96.50	104.10	98.93	99.38	98.13	Total

(all normalised)	Intermed. target	Calculated mix	Residuals			
SiO_2	55.584	55.768	-0.184			
TiO_2	1.415	1.410	0.005			
Al_2O_3	19.202	19.310	-0.109	Sum of	Mix results	
Fe_2O_3	7.074	7.160	-0.086	squares of		
MnO	0.253	0.193	0.060	residuals	qz-trachyte	40.94%
MgO	1.415	1.661	-0.246		plagioclase	41.00%
CaO	5.053	4.882	0.171	0.578	biotite	11.40%
Na_2O	5.558	5.226	0.332		cpx	1.34%
K_2O	4.042	3.615	0.428		Ti-mag.	3.64%
P_2O_5	0.404	0.775	-0.371		apatite	1.69%
Total	100.00	100.00				

Primitive basalt - evolved basalt

This was one of the most difficult for which to obtain a good mix. Initially a mix of olivine, cpx and Ti-magnetite was tried, with very poor results. Amphibole, spinel-hercynite and plagioclaseAn_{76} were then added, the first two because of their occasional appearance in the Velay basalts, and plagioclase, despite a complete lack of petrographic or trace element evidence for its involvement in basalt evolution, because it is a common phenocryst phase in basalts from other localities.

The mix with olivine, cpx, Ti-magnetite and amphibole gave SSR=0.98, 18% amphibole, which is neither consistent with petrography nor a very good mix. Plagioclase gave SSR=0.07, 14% plagioclase, which is a good mix but is again unreasonable considering the other evidence. Spinel-hercynite gave SSR=0.31, 2.5% spinel-hercynite. This is the most consistent with petrography and is a reasonable mix.

Spinel-hercynite appears only in the ankaramites 86/63 (le Petit Champagnac) and 87/43 (near Bonnevialle), to the exclusion of Ti-magnetite. In 87/88 (la Besseyre-Basse) both spinels are present, as well as amphibole. This lava however is not part of the Velay Miocene plateau series. The reason for the near absence of phenocrysts in most of the plateau lavas is discussed in section 5.4.4.

From the petrographic evidence it is therefore surprising, but not unreasonable, that a small amount of spinel-hercynite removal should be required to give the observed trend of basalt evolution.

Evolved basalt - hawaiite

This step has the lowest SSR (=14.3) when no minerals are involved and was therefore the easiest for which to obtain low values. The same mineral compositions as for the previous step were used since the lavas of this step are largely aphyric, although a more sodic composition of plagioclase, with An_{65}, was used. The lowest SSR was obtained with olivine, cpx, Ti-magnetite, amphibole and plagioclase in the mix, but this was rejected on the basis of the continued lack of evidence for plagioclase fractionation. The best result which was consistent with petrographic evidence was amphibole 11.6%, cpx 5.2%, olivine 2.1% and Ti-magnetite 1.6%. This is again rather unexpected given the scarcity of amphibole (or indeed any phenocrysts) in these lavas.

Hawaiite - intermediate lavas

The abundance and variety of phenocrysts in the northern intermediate lavas made it relatively easy to obtain a good mix. By contrast the step-size, as shown by the mineral-free SSR, is relatively large at 91.8. The best mix, with SSR = 0.025, was obtained with nearly all the minerals included; amphibole 23%, plagioclase An_{56} 9%, Ti-magnetite 3.7%, apatite 3%, cpx 1.5%. When sphene was included it formed only 0.03% of the mix and was therefore excluded. A mix with amphibole omitted gave poor results so the large proportion in the mix is necessary.

The mineral compositions were taken from multiple microprobe analyses of phenocrysts in the intermediate lavas. Variation in the relative proportions of phenocrysts in these lavas makes comparison with the mixing results difficult, but they seem reasonable, with small amounts of

Ti-magnetite, cpx and apatite. In particular calculated P_2O_5 closely matches that in hawaiite, confirming that the proportion of apatite is correct. Plagioclase is not present in hawaiites, but appears in the intermediate lavas. Without it, SSR-values are much worse and so it seems genuinely to form a significant component of the fractionating assemblage. As described in section 5.6.1 Sr and Ba values fall dramatically at the start of the intermediates, almost certainly due to the extraction of large amounts of plagioclase.

Intermediate lavas - miaskitic phonolites

Compositions of amphibole, cpx, plagioclase, apatite, sphene and Ti-magnetite from the previous step were used, in addition to K-feldspar from the following phonolite step, since many feldspar phenocrysts in the miaskitic phonolites have quite potassic rims. Thus seven minerals were available for the initial mix. The SSR for the mineral-absent mix was 45.2, a reasonable sized step. The result for the mix with all the minerals was very good in terms of the low SSR (= 0.008), but the mineral and lava proportions were not reasonable, with 60% feldspar removal and only 22% miaskitic liquid remaining. Eliminating K-feldspar from the mix on the grounds that it is not significantly involved in the step from petrographical evidence gives a much improved result; plagioclase 23.6%, amphibole 5.5%, Ti-magnetite 3.8%, cpx 3.7%, apatite 0.6%, sphene 0.3%, and 63% liquid remaining, SSR=0.07. All other combinations of minerals tried gave lower SSR-values and negative values of K-feldspar (when included).

Qualitatively these results are reasonable, with plagioclase dominating the assemblage and amphibole, cpx and Ti-magnetite as the subordinate ferromagnesian phases, as in the lavas. Rare zircons are apparently not important in depleting the lavas in Zr since all incompatible elements show similar degrees of enrichment during fractionation.

Miaskitic phonolites - agpaiitic phonolites

This was another difficult step to model. The mineral-absent SSR=15.1 should have made it easy to obtain low values of SSR for mixes but it proved surprisingly difficult. Minerals input were K-feldspar, amphibole, cpx, Ti-magnetite, sphene and apatite, all from analyses of phenocrysts. Cpx produced a negative percentage in every mix in which it was included and so the best mix was K-feldspar 61%, amphibole 9%, Ti-magnetite 1.7%, apatite 0.6% and sphene 0.2%, with F (fraction of liquid remaining) = 28% and SSR=0.47. The apatite percentage is certainly too high (it should be 0.23%) since there is a lack of CaO in the calculated mix and the programme has used apatite (52% CaO) to elevate it. There is also a lack of Al_2O_3 and excess MgO and Na_2O. These excesses are probably due to an elevated percentage of amphibole caused by the programme trying to correct the CaO and Al_2O_3 deficits. To try to improve the results pure anorthite was added to the mix. This markedly improved the results (SSR=0.02, F=0.22) but since there is no calcic plagioclase in these lavas the problem cannot be regarded as resolved.

Apart from its poor residuals the mix gives quite reasonable mineral proportions compared with those predicted in the qualitative analysis.

Intermediate lavas - quartz trachytes

This step is inferred from the similarity between the phenocrysts of the quartz-trachyte of Dents de Mézenc (86/8, 87/58, 88/17) and those of the phyric intermediate lavas (see section 3.1.4.2). The large mineral-absent SSR=156.1 is mainly due to the 11% difference in SiO_2-content of the two lava end-members.

Initial mixes used the microprobed compositions of phenocrysts in the quartz-trachyte. These gave completely meaningless results, with zero quartz-trachyte in the mix, suggesting that the choice of minerals was incorrect. Switching to the minerals of the phyric intermediate lavas gave much more satisfactory results.

Minerals used were apatite, Ti-magnetite, plagioclase An_{56}, cpx and amphibole from the intermediate lavas and biotite from the quartz-trachyte. A mix with all these minerals gave negative amphibole. Eliminating it from the mix left the SSR unchanged at 0.56, with plagioclase 41%, biotite 11%, Ti-magnetite 3.6%, apatite 1.7%, cpx 1.3% and F = 0.41. Apatite has been overestimated by the programme due to insufficient CaO in the calculated mixture and should be 0.7%. K_2O is also too low in the mixture and the programme has added biotite to correct this, causing excess MgO in the process. Probably a plagioclase slightly richer in K_2O and Na_2O would greatly improve the result, by allowing a larger proportion of Ca-rich cpx to enter the mix. In general the minerals calculated in this mix match those deduced qualitatively from trace elements and observed in thin sections.

5.6.2.4 Comparison with cumulates

Figure 5.6.2 presents the results of the mixing calculations in a graphical form, with proportions of minerals in the fractionating assemblage plotted against Zr content of the lavas, as an indication of the fraction of liquid remaining. The diagram, although crude, shows a fair resemblance to that for the cumulates (Figure 4.5.4), with initially abundant cpx declining to low values, amphibole rising to dominate the assemblage and then being replaced by feldspar of a gradually evolving composition. Even the points at which apatite and sphene appear are comparable. Differences are due to many causes, not the least being that Na_2O, used as the x-axis for the cumulates, is a poor indicator of F. Other differences are caused by the highly imprecise nature of the mixing process with large, averaged steps, unlike the smooth, continuous variation in phenocryst compositions seen in reality (see Chapters 2 and 3). Even reducing step-size would not greatly improve the results due to the large degree of uncertainty in the compositions of the starting materials.

5.6.2.5 Constraint from incompatible elements

If incompatible elements such as Rb, Zr, Nb, Th, Pb and U are assumed to have D = 0 throughout the lava series, their degree of enrichment can be used to determine F, the fraction of liquid remaining. For each of the trace elements Rb, Zr, Nb, Th and Pb a similar figure is obtained;

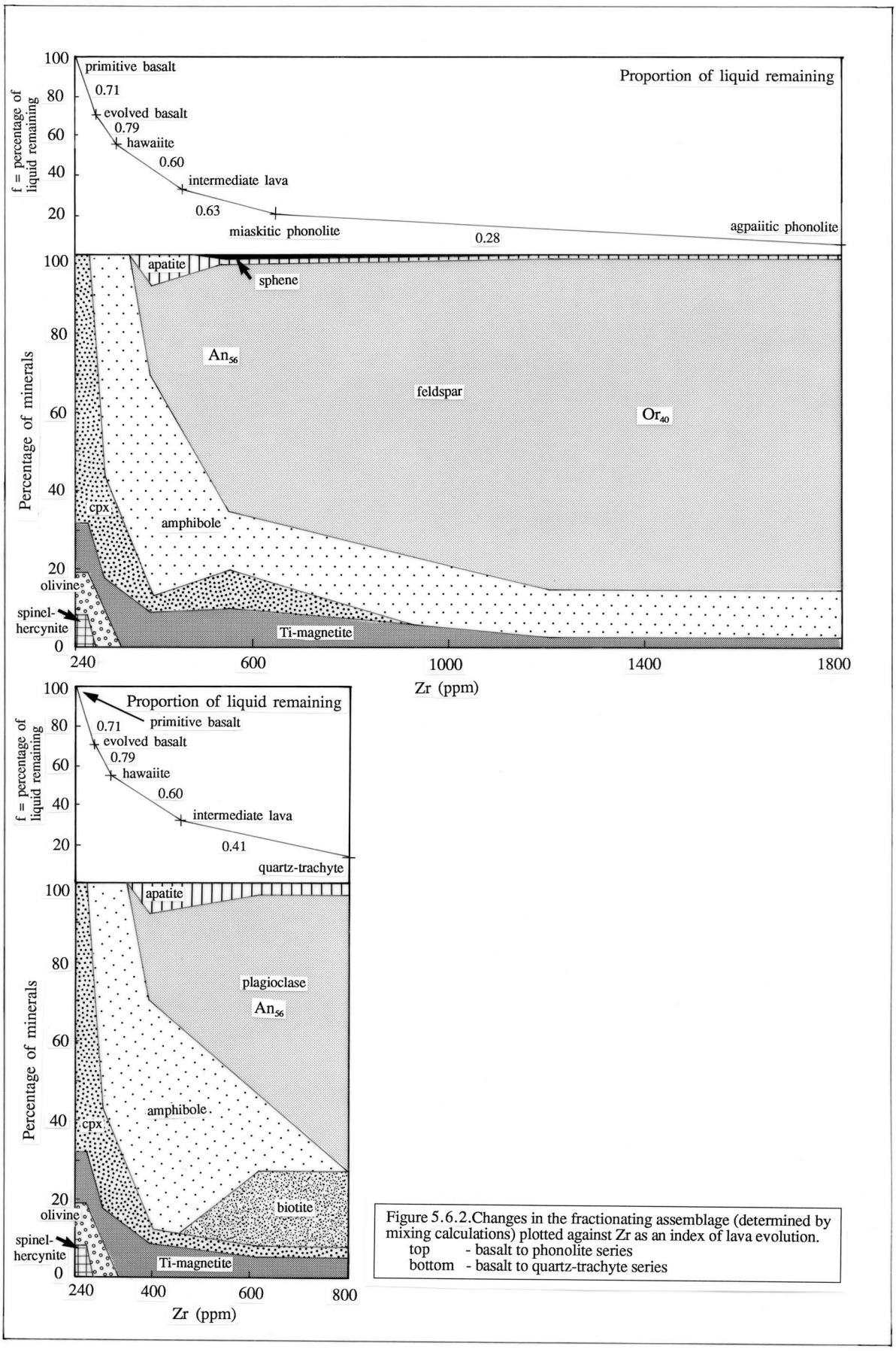


Figure 5.6.2.Changes in the fractionating assemblage (determined by mixing calculations) plotted against Zr as an index of lava evolution.
top - basalt to phonolite series
bottom - basalt to quartz-trachyte series

Rb 0.14, Zr 0.14, Nb 0.15, Th 0.12, Pb 0.13, average 0.13. Thus the most evolved phonolites were formed by 87% fractionation of the magma represented by the primitive basalts. Rb, Th and Pb also show the quartz-trachytes to represent 20% of the original basalt magma. To obtain equivalent figures for the mixing calculations the relative values of F for each step are simply multiplied together. This gives:

phonolites	0.71 x 0.79 x 0.60 x 0.63 x 0.28	= 0.059
quartz-trachytes	0.71 x 0.79 x 0.60 x 0.41	= 0.138

Both of these figures are lower than their respective values from incompatible elements. All of the individual steps in the mixing series can be shown to have smaller F-values than would be predicted from these trace elements. This is important because it means that only half the quantities of minerals calculated in the mixing programme should have been extracted.

The reason is probably the large proportions of amphibole sometimes calculated to be in the fractionating assemblages. Amphibole has a composition quite close to that of the lavas from which it crystallises and so relatively large amounts of the mineral can be extracted for only a small change in liquid composition. Small changes in amphibole composition can therefore lead to quite large variations in the percentage amphibole required.

5.6.2.6 Agpaiicity of the Velay phonolites

In section 3.1.5, the concept of agpaiicity is discussed in terms of its manifestation in the mineralogy of the phonolites. There are also compositional differences between miaskitic and agpaiitic phonolites, both in trace elements and ratios of major elements. Sørensen (1974) discussed the merits of the various agpaiicity indices proposed, preferring the expression α = (Na+K)/Al (molecular). This is based on the composition of the feldspars, in which $0 \leq \alpha \leq 1$.

In most phonolites fractionation is dominated by feldspar. This is shown by the mixing calculations of section 5.6.2.3 in which the intermediate lava to miaskitic phonolite step requires the removal of 24% plagioclase and 14% other minerals, and the miaskitic to agpaiitic phonolite step necessitates 61% alkali feldspar and 12% other minerals.

Most miaskitic phonolites have $\alpha < 1$ and distinctive petrography (described in section 3.1.5). The fractionation of plagioclase causes their agpaiicity to increase because anorthite has 15.4%(mol.) Al compared with the 8.5%(mol.) Al of a typical phonolite liquid. Thus its removal depletes the magma in Al and elevates the value of α. Bowen (1945) noted that pure albite never forms from a liquid containing CaO, the feldspar always containing some anorthite. This "plagioclase effect" is the main cause of increasing agpaiicity in Ca-bearing magmas.

Agpaiitic phonolites generally have $\alpha > 1$ and the removal of alkali feldspar, for which $\alpha = 1$, from such a magma will cause its agpaiicity to increase still further. This was called the "orthoclase effect" by Bailey and Schairer (1964), who also pointed out that alkali feldspars are more potassic than their host liquids, leading to increasing Na_2O/K_2O in the liquid.

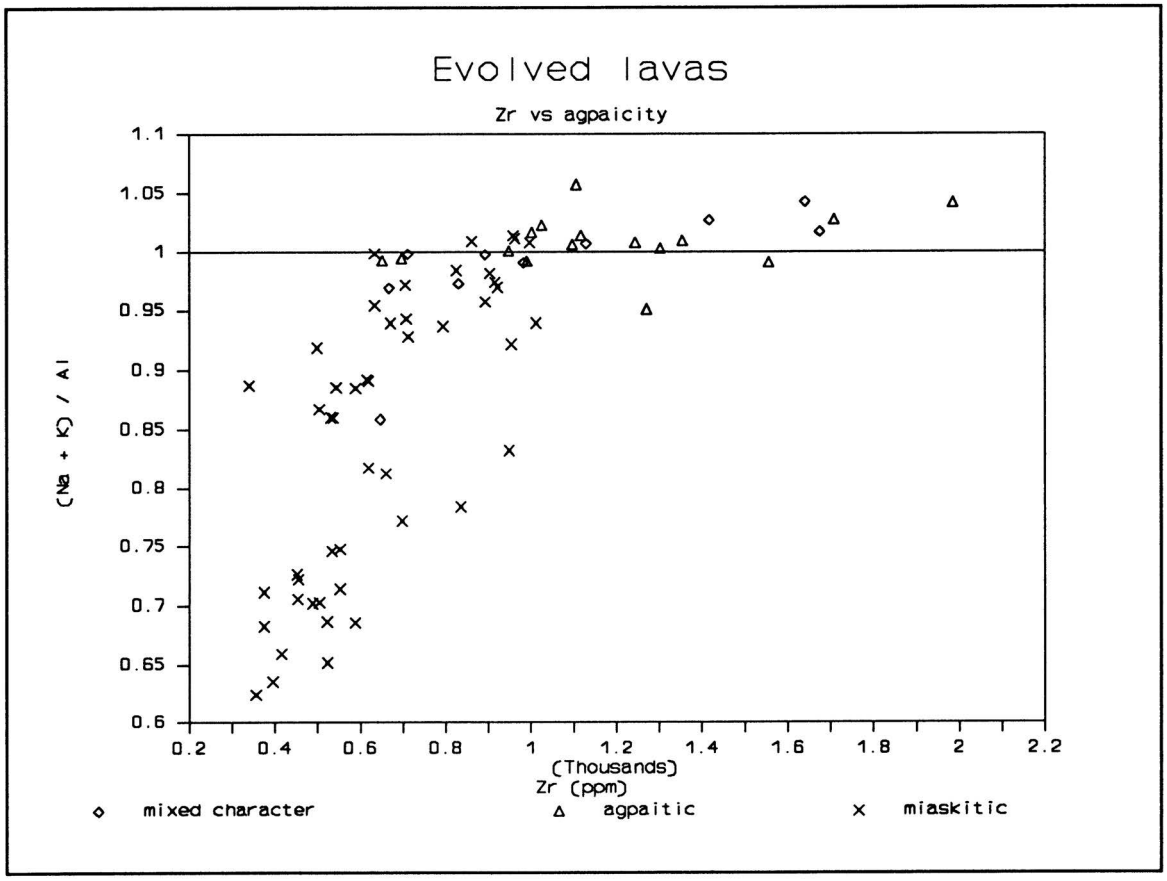


Figure 5.6.3. Evolved lavas of the Velay with symbols indicating categories of agpaiicity. Categories are defined using the minerals in the groundmass:

agpaiitic	=	poikilitic aenigmatite and euhedral nepheline present. Ti-magnetite absent or rare
miaskitic	=	Ti-magnetite present, aenigmatite and nepheline absent
mixed	=	any two agpaiitic indicators

Figure 5.6.3 shows Zr plotted against α to allow a test of their ability to predict agpaiitic mineralogy. The Velay lavas are shown as either agpaiitic, miaskitic or mixed character, based on their petrography. The graph shows that both Zr and α predict the petrography quite well.

5.6.2.7 Conclusions

The mixing technique of Wright and Doherty (1970), combined with constraints from incompatible trace elements, petrography and other trace elements, allows a reasonably quantitative assessment of the changing mineral phases and their proportions in the fractionating assemblage.

Two series can be followed, the first leading from the basalts to evolved phonolites by fractionation of calcic plagioclase and amphibole in the intermediate lavas, followed by K-feldspar and amphibole at the end of the series. The second series, leading from basalts to quartz-trachytes, departs from the first at the level of the intermediate lavas, by the fractionation of biotite and calcic plagioclase. Biotite has 9% K_2O and zero CaO, both of which would tend to prevent the K_2O content of the melt rising high enough, and the CaO falling low enough to allow the crystallisation of K-feldspar. Thus the appearance of biotite seems to control, or at least indicate, the divergence of the two series.

5.7 Bulk chemistry of the cumulates

5.7.1 Interpretation of major and trace element behaviour

In Chapter 4 the cumulates were subdivided into four suites:

Suite 1 - *no feldspar present*
Suite 2 - *feldspar and amphibole present, biotite absent*
Suite 3 - *feldspar, amphibole and biotite present*
Suite 4 - *feldspar and biotite present, amphibole absent or < 2%*

Figure 5.7.1 uses this classification in graphs of all measured elements plotted against MgO (see section 5.3.2 for reasons for this choice of index). Most of the major element graphs show a fairly linear relationship, with TiO_2, $Fe_2O_3^T$ and CaO decreasing as MgO increases and SiO_2, Al_2O_3, Na_2O and K_2O increasing as MgO decreases.

Major elements mainly indicate changing mineral proportions in the cumulates, whereas trace elements are more informative about the conditions in the magma chamber, since they can have a wide range of concentrations in a given mineral.

Five types of behaviour can be distinguished:

1) very compatible	(D > 3)
2) moderately compatible	(1 < D < 3)
3) moderately incompatible	(0.4 < D < 1)
4) very incompatible	(D < 0.4)
5) initially incompatible, later compatible	

Figure 5.7.1a-z

Graphs of whole rock analyses of Velay cumulates

Throughout:

□	=	Suite 1 cumulates
△	=	Suite 3 cumulates
×	=	Suite 4 cumulates
◇	=	lavas found as blocks in the same pyroclastics as the cumulates, plus glass compositions from welded pyroclastics (see Chapter 3 for full details)
+	=	interstitial glass from Suite 3 and Suite 4 cumulate blocks. Data given in Appendix C

Unfortunately no specimens of Suite 2 cumulates were suitable for whole rock analysis. The trends shown by the remaining data suggests that they would lie between those of Suites 1 and 3.

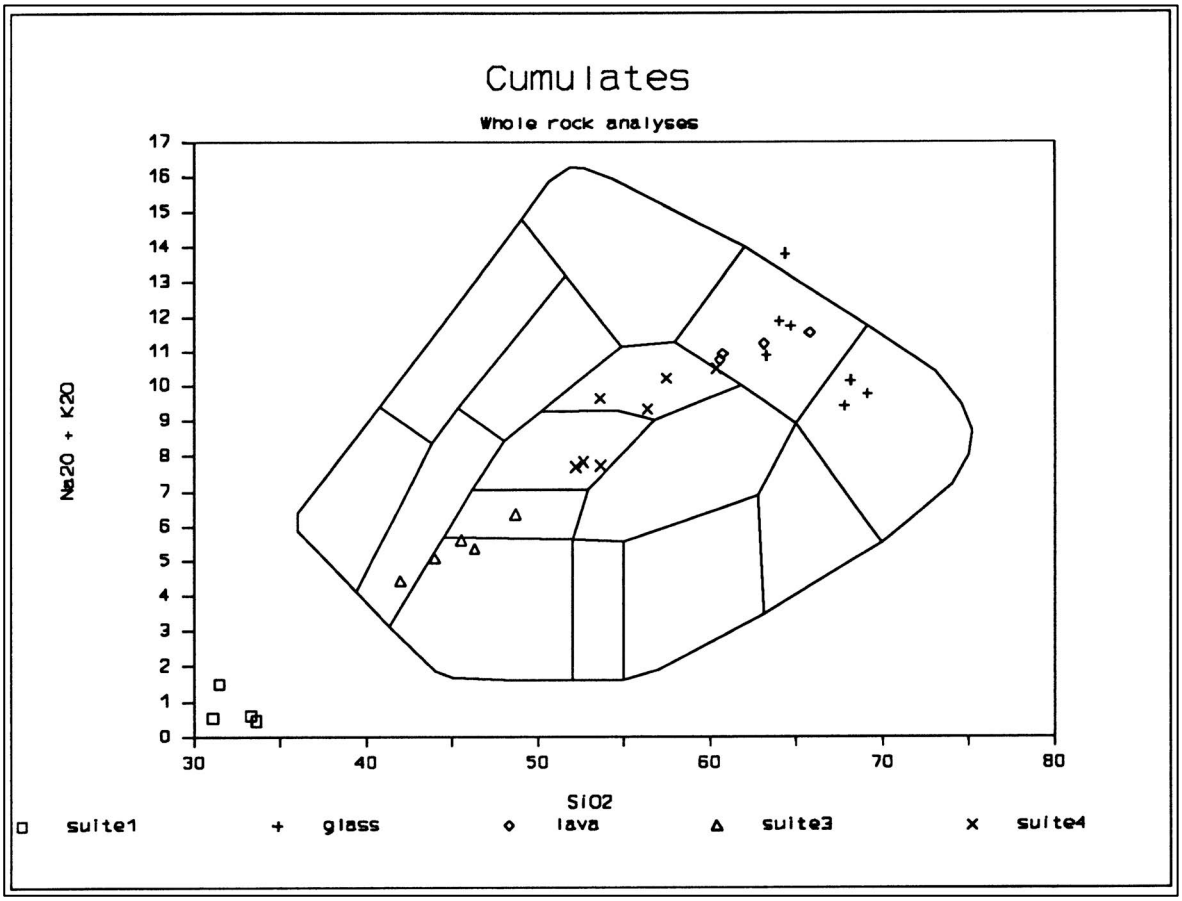


Figure 5.7.1a

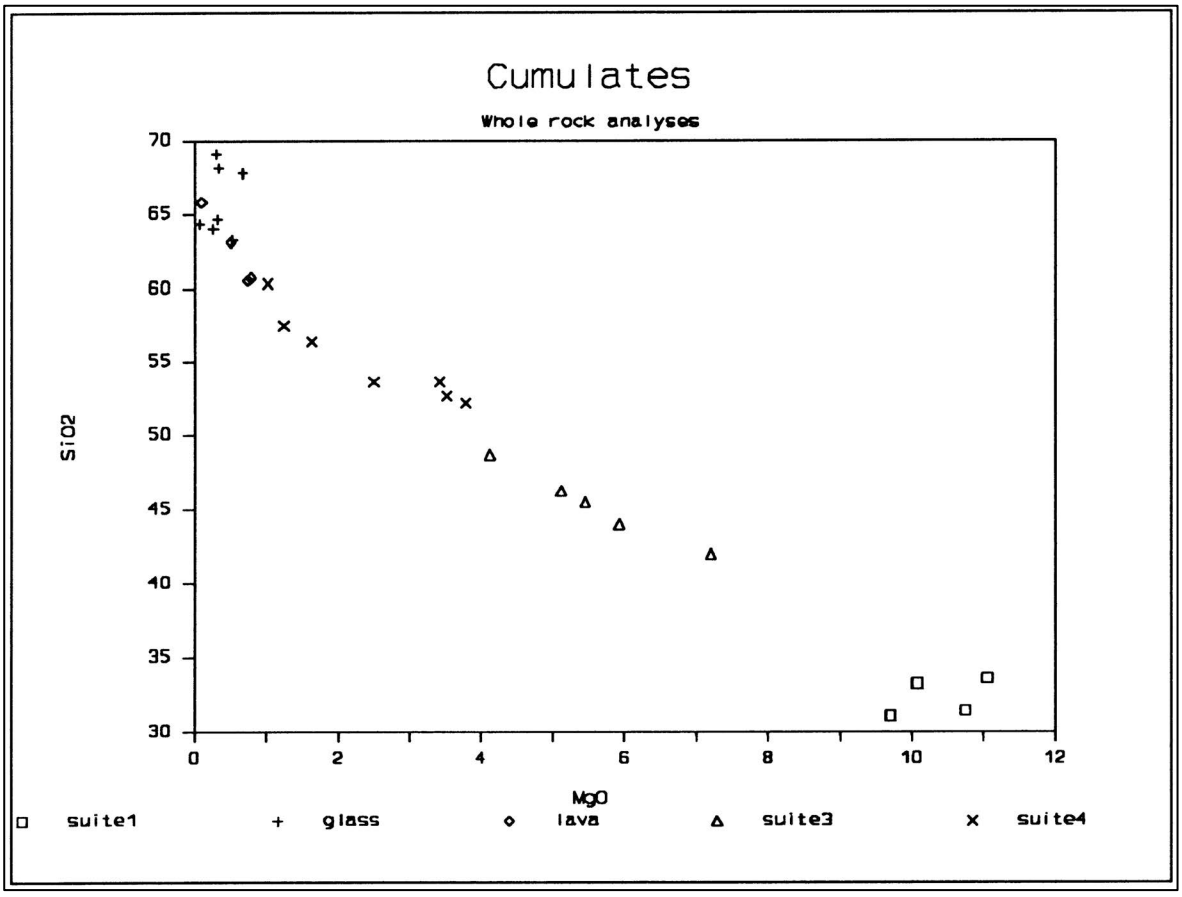


Figure 5.7.1b

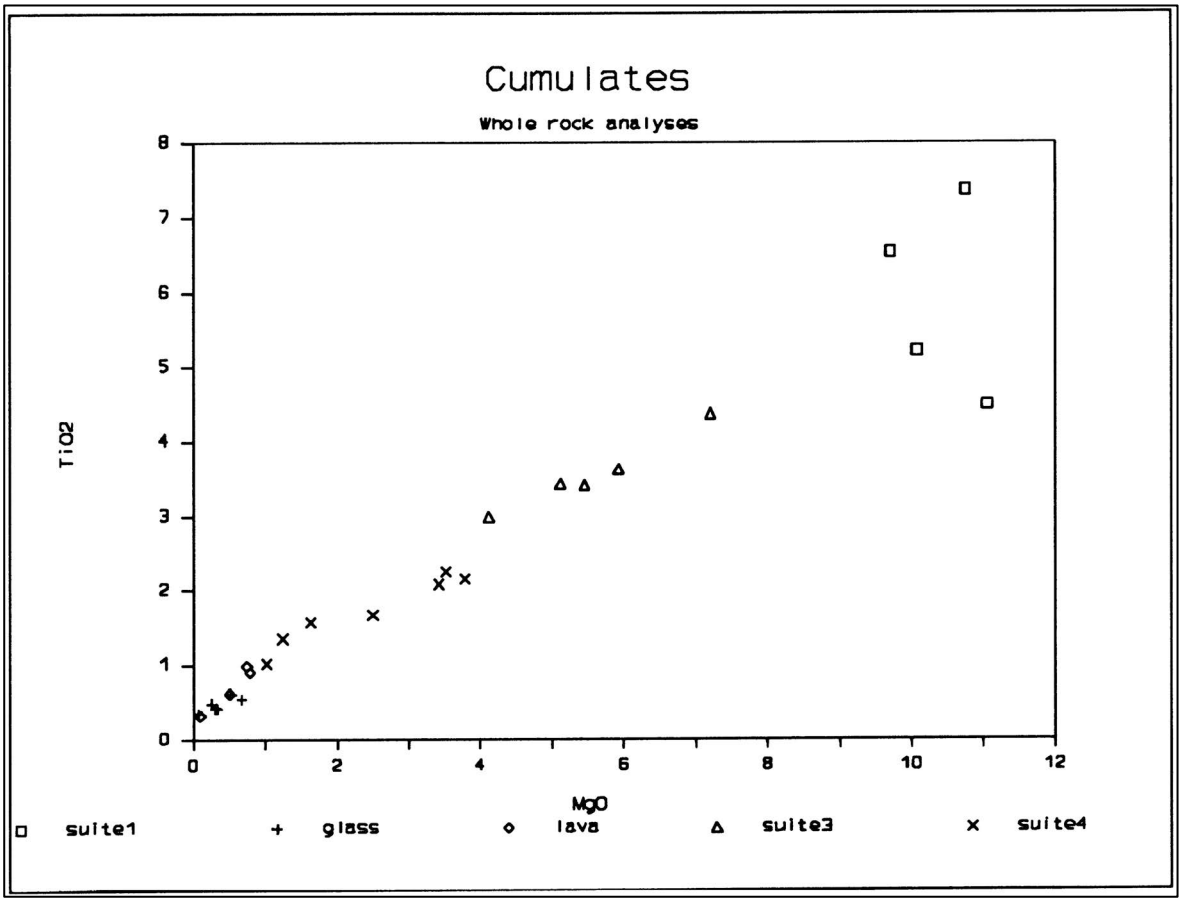


Figure 5.7.1c

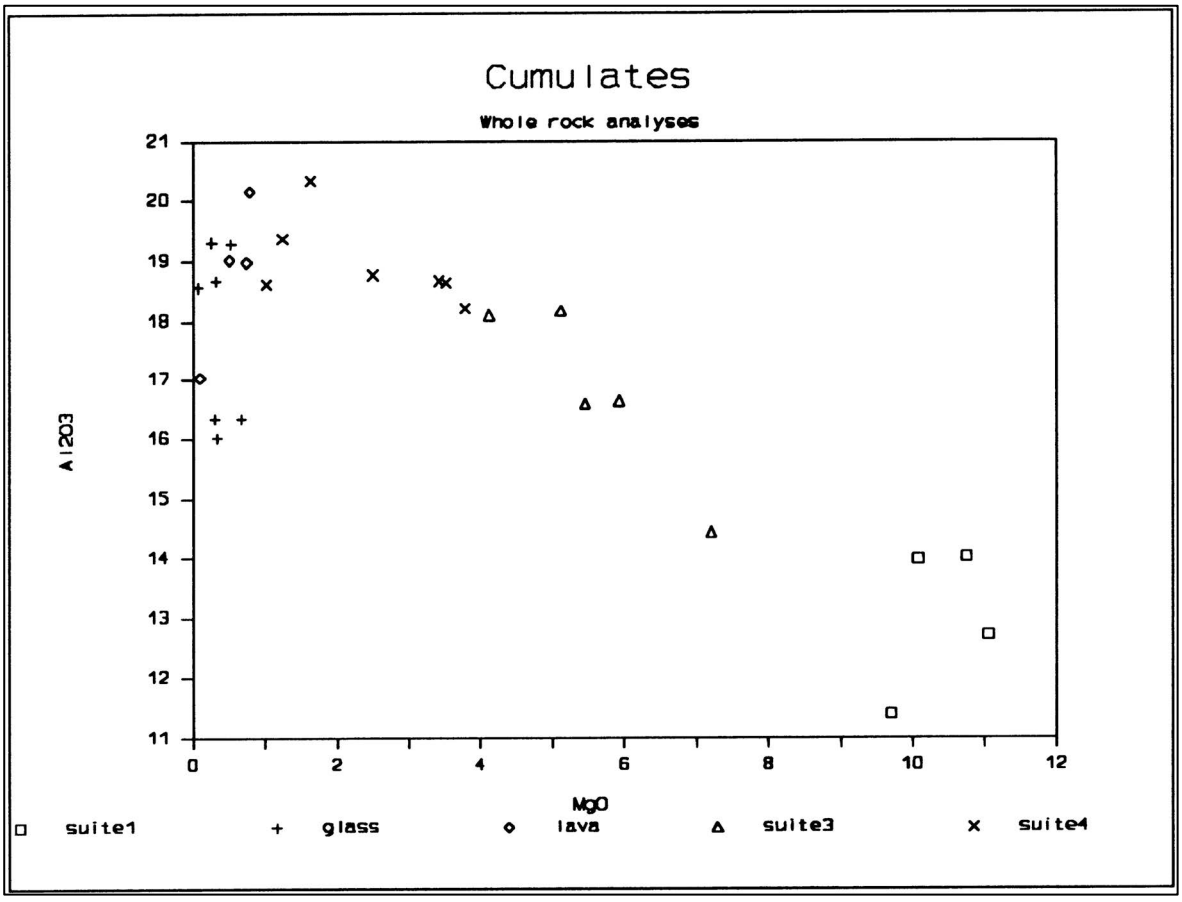


Figure 5.7.1d

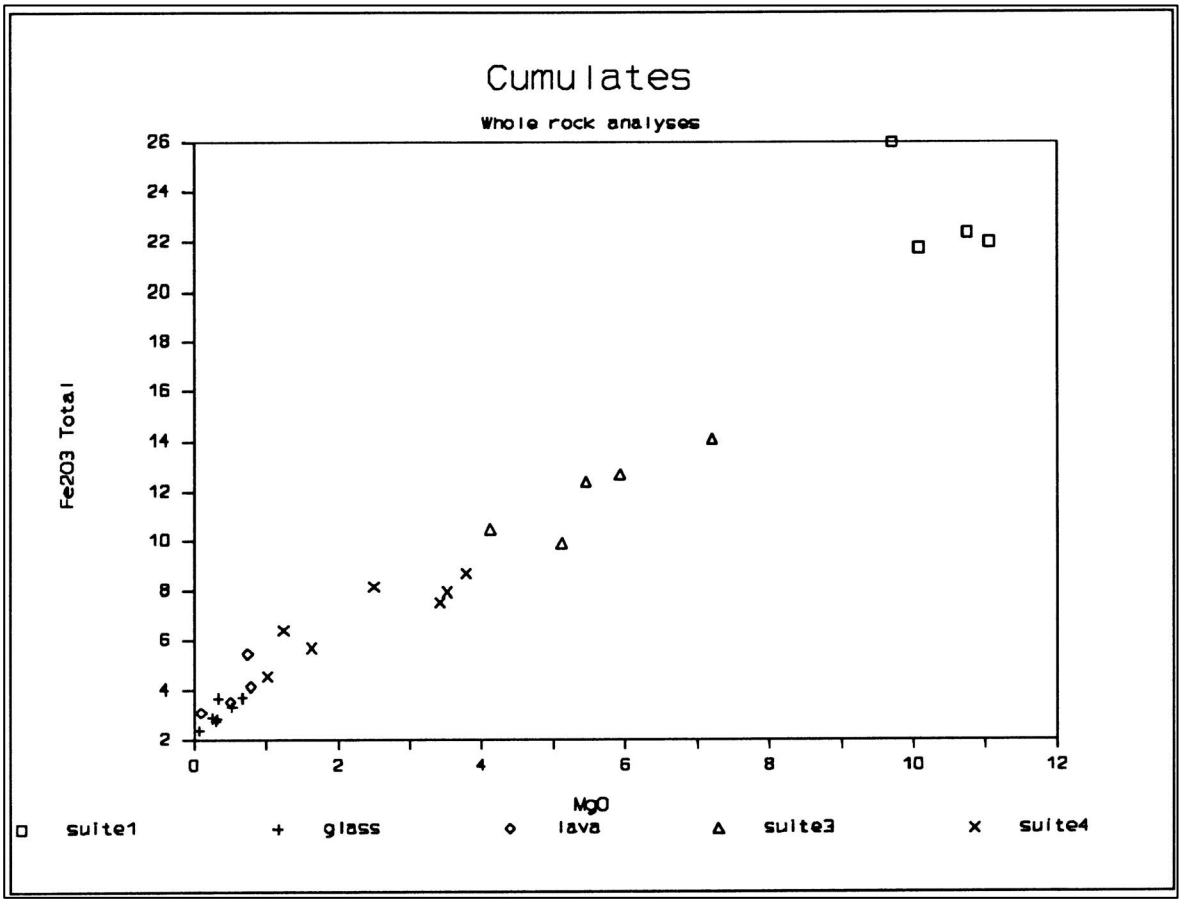


Figure 5.7.1e

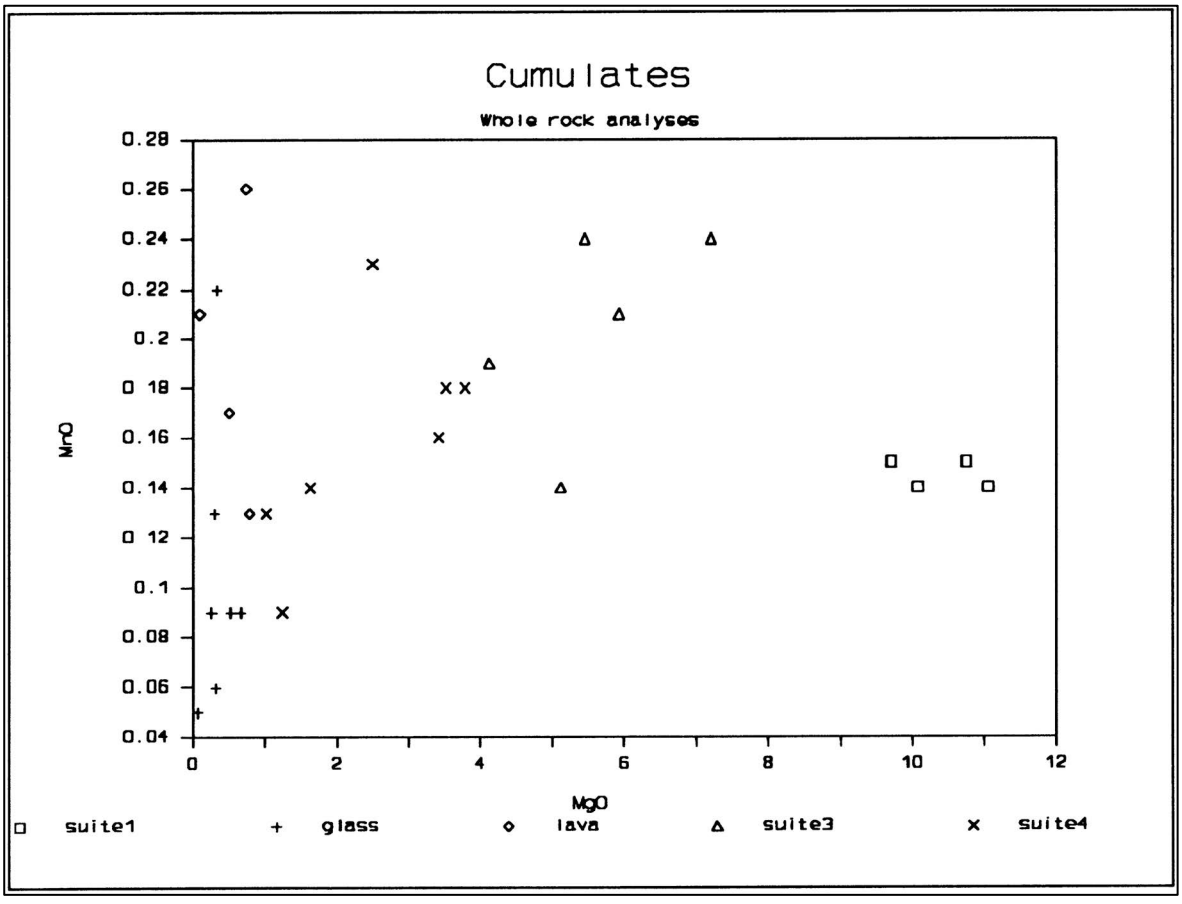


Figure 5.7.1f

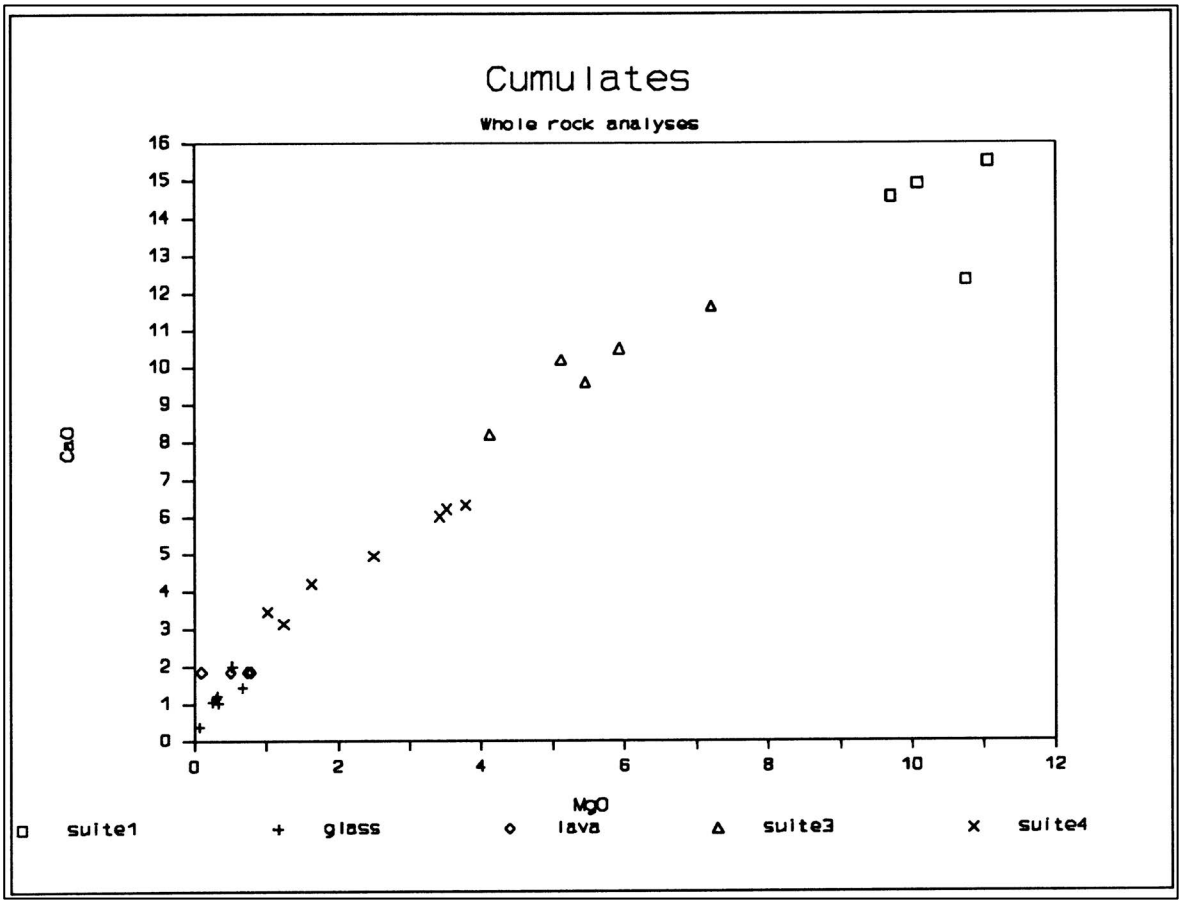


Figure 5.7.1g

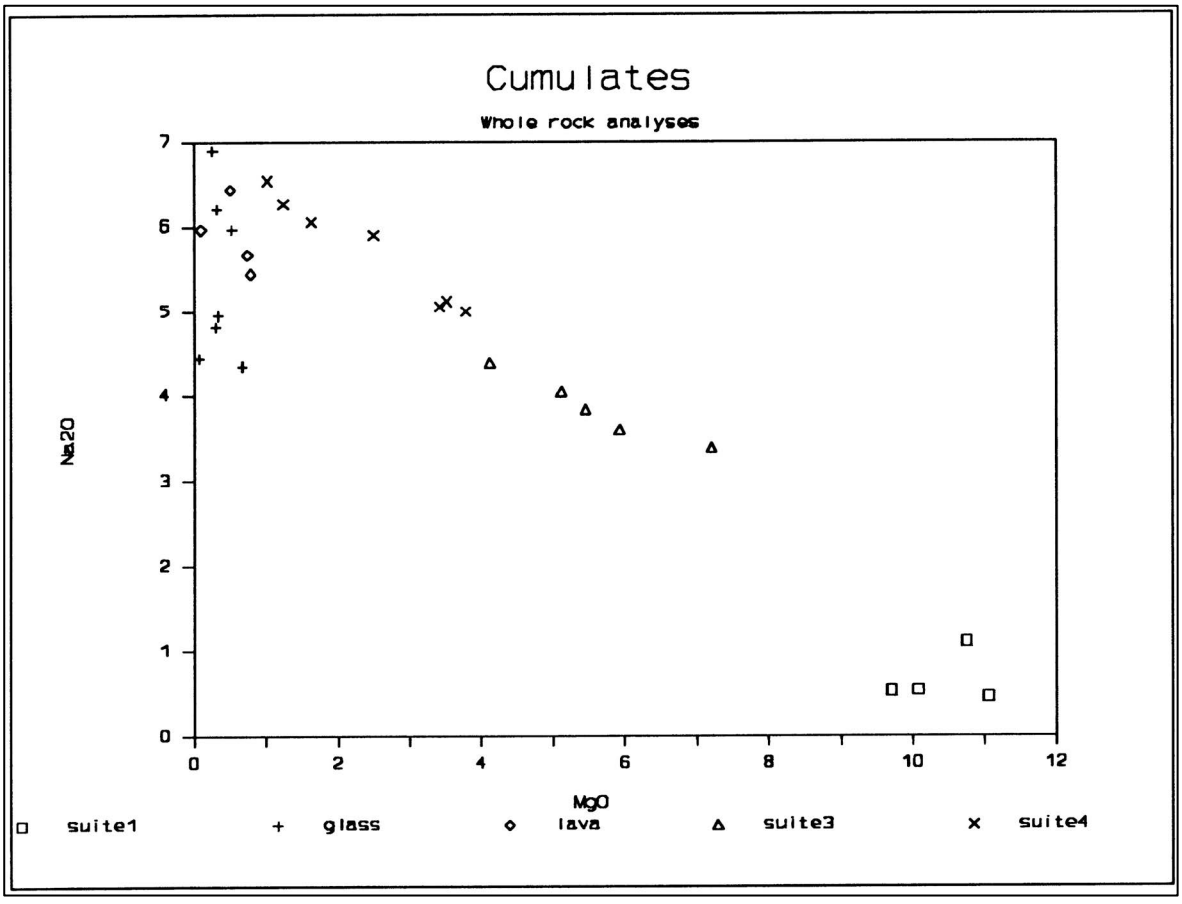


Figure 5.7.1h

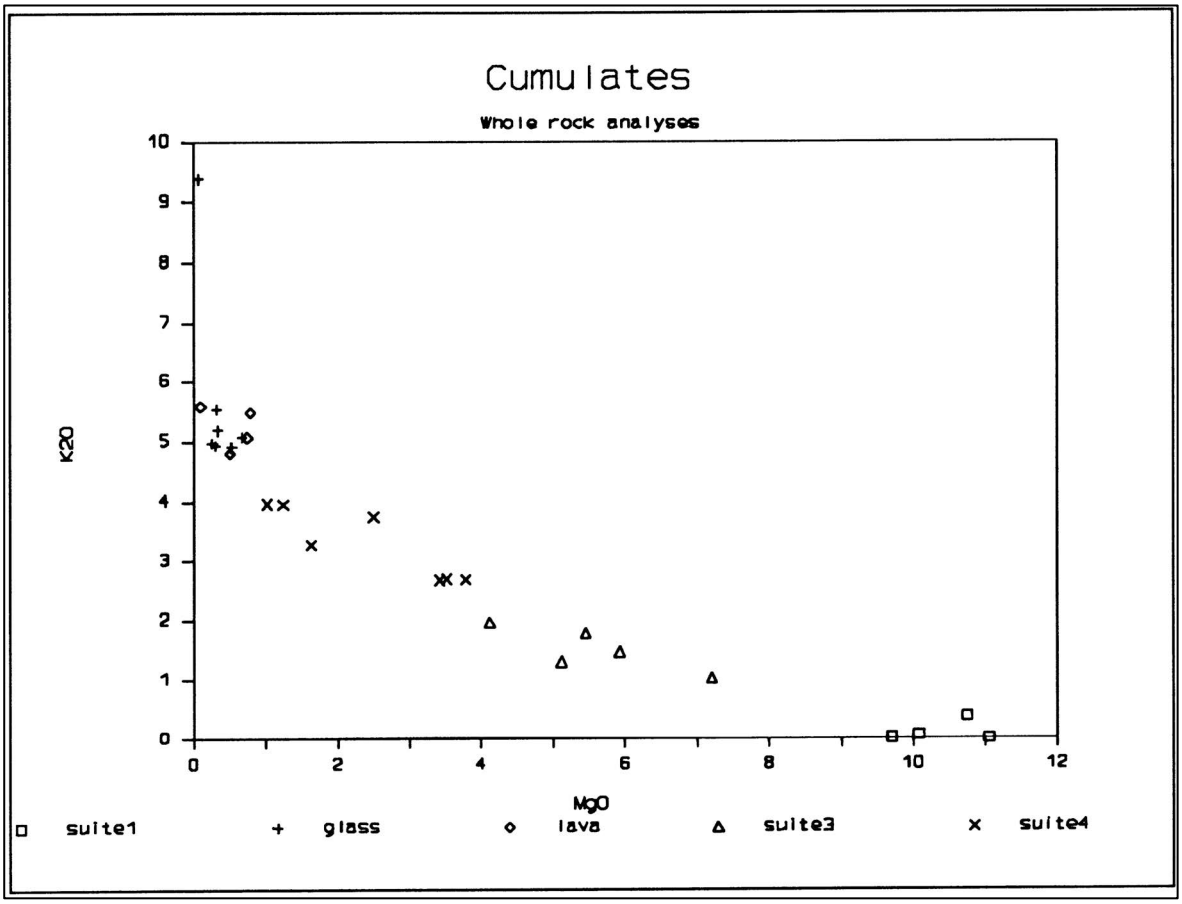


Figure 5.7.1i

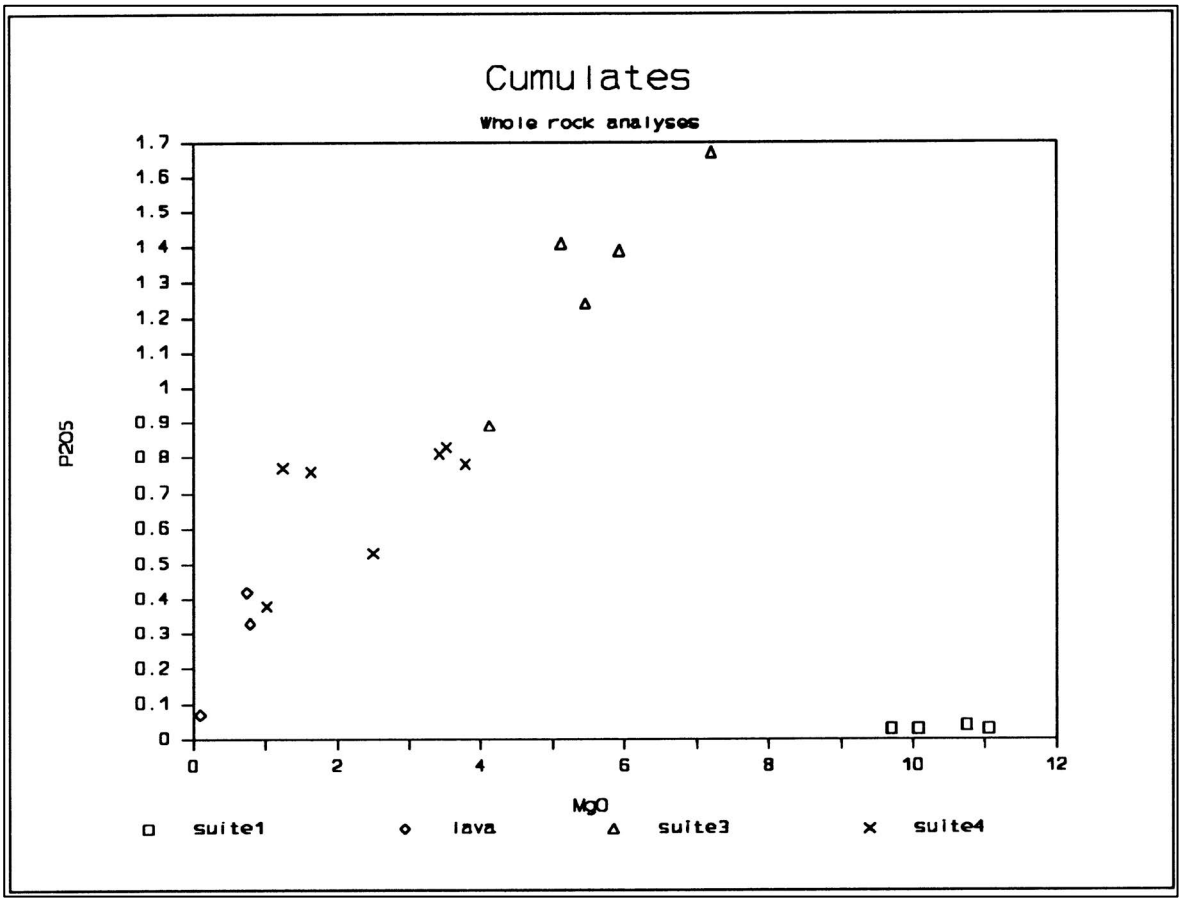


Figure 5.7.1j

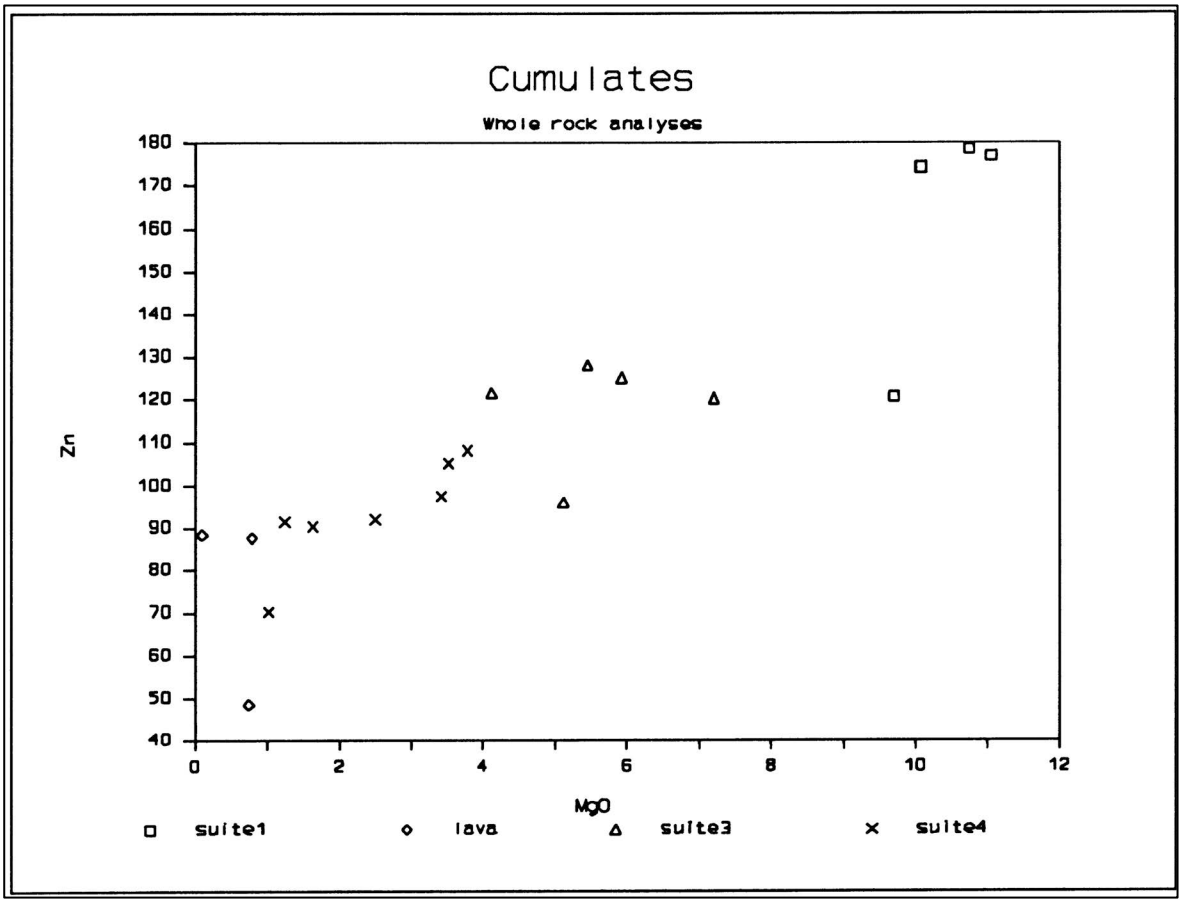


Figure 5.7.1k

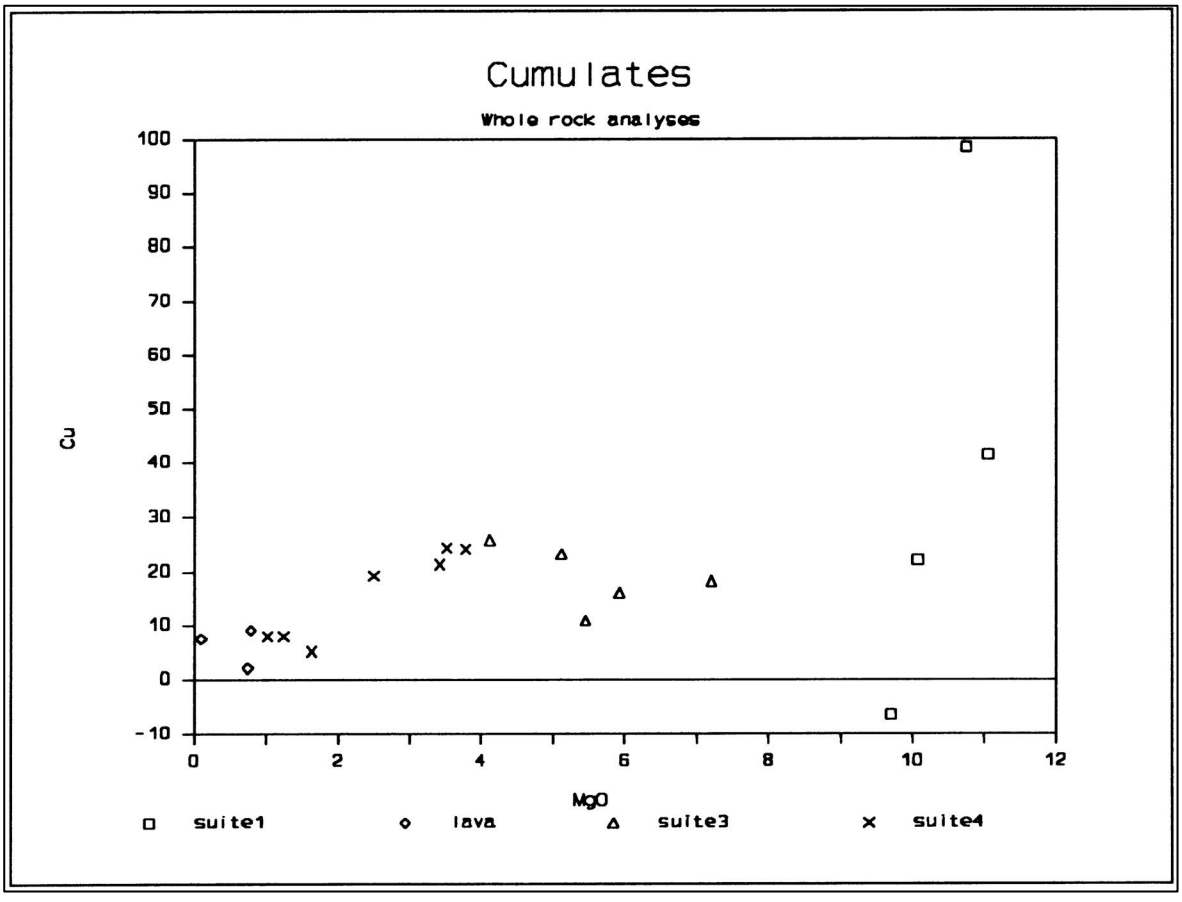


Figure 5.7.1l

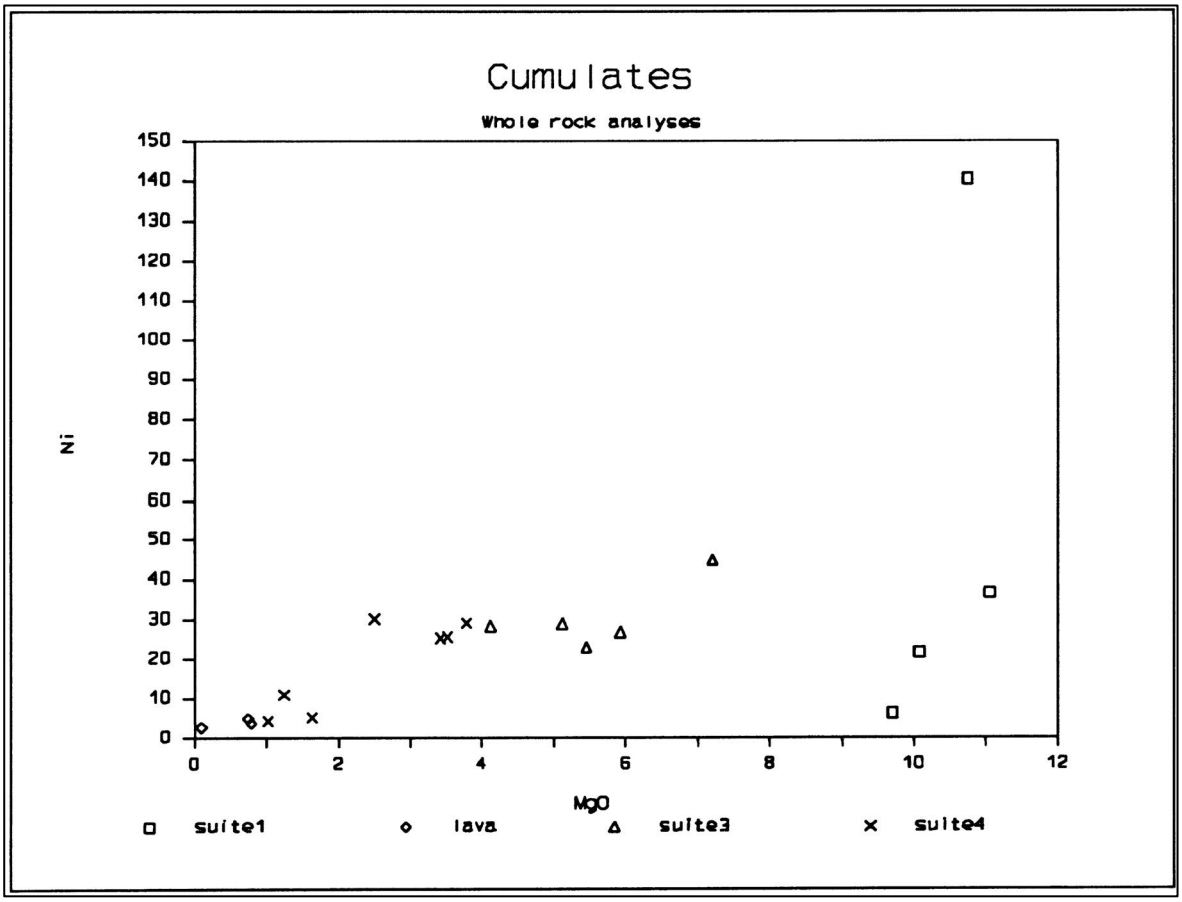


Figure 5.7.1m

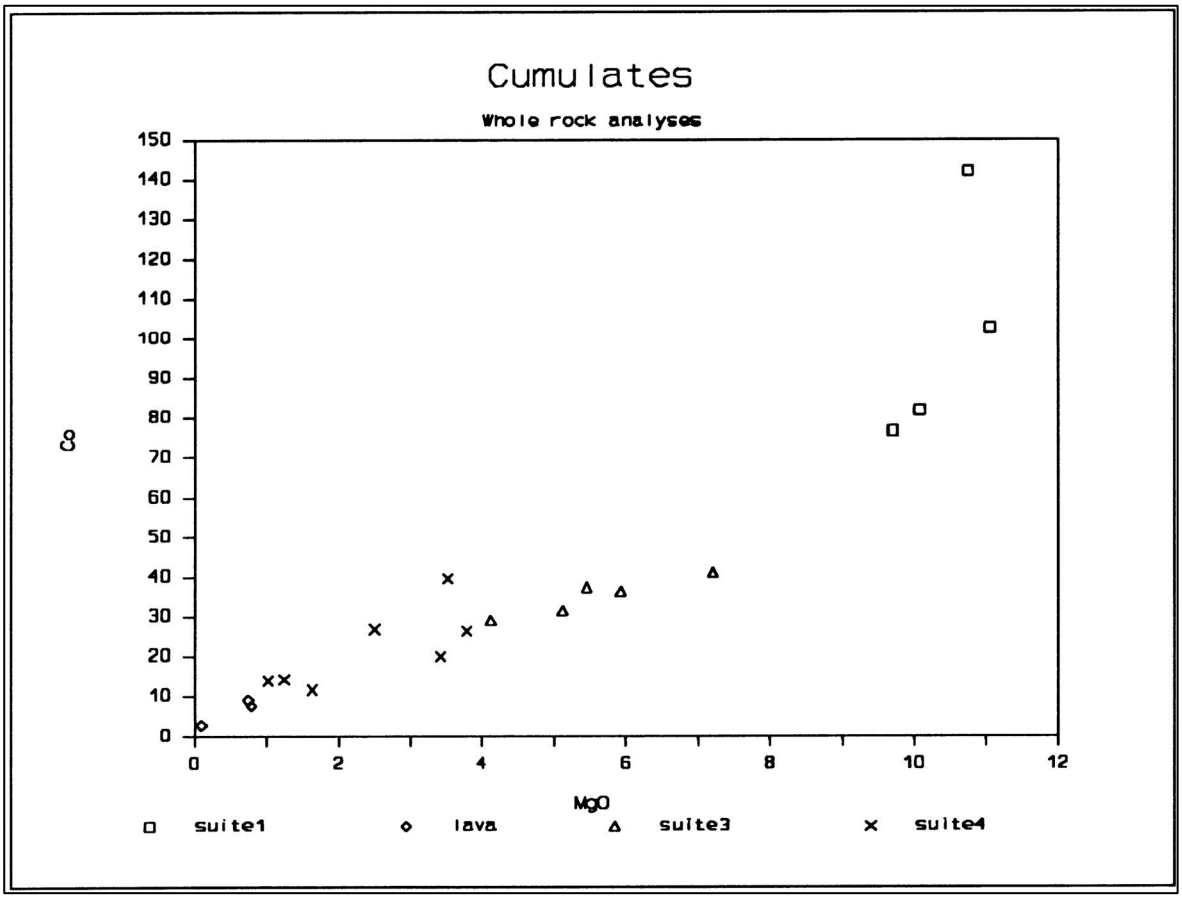


Figure 5.7.1n

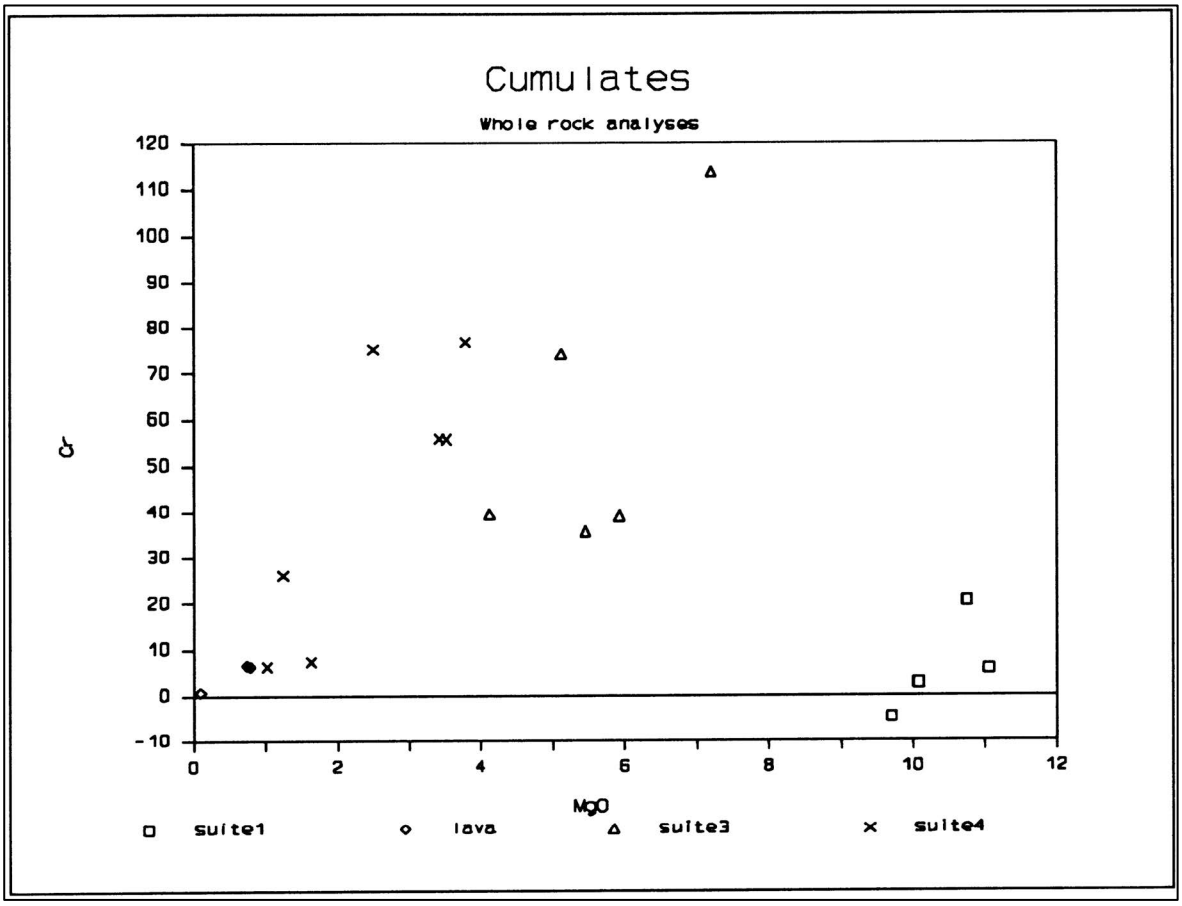


Figure 5.7.1o

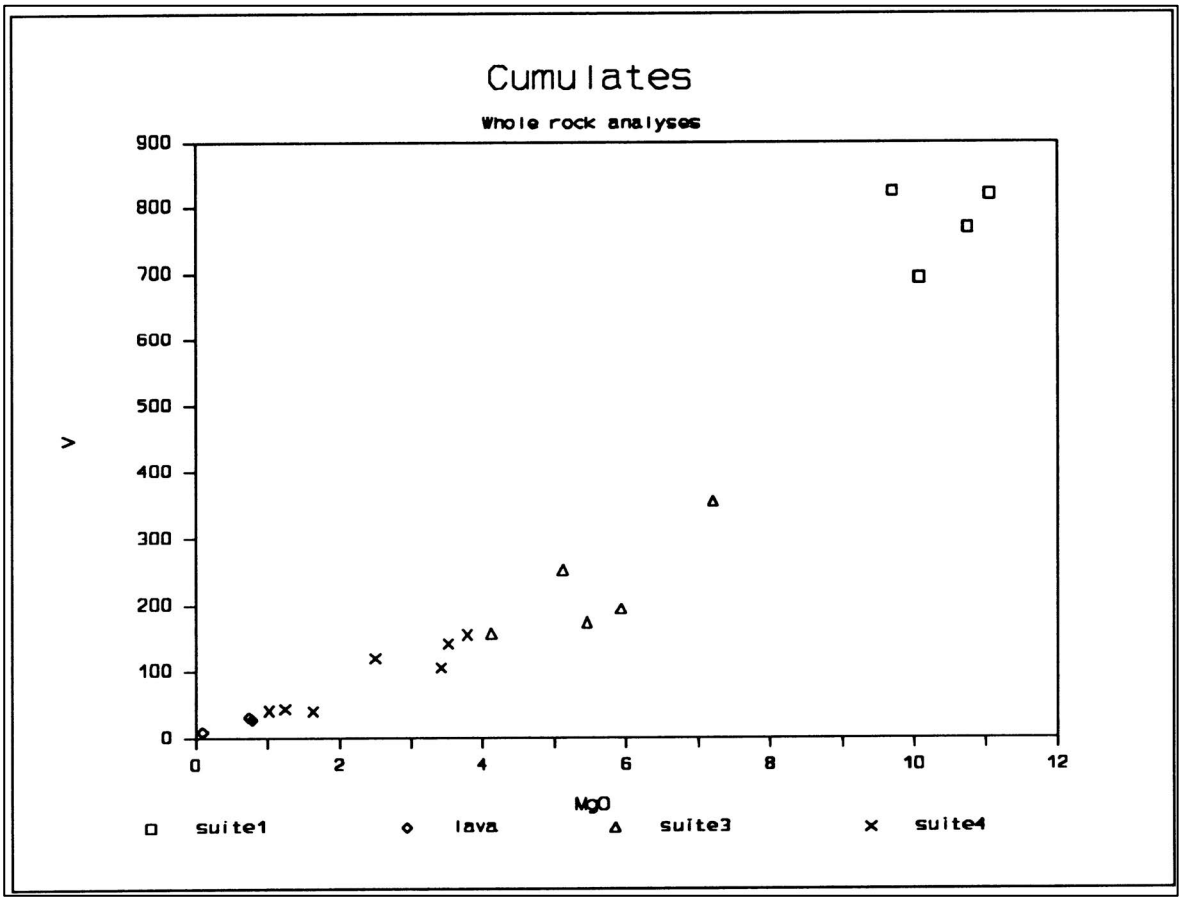


Figure 5.7.1p

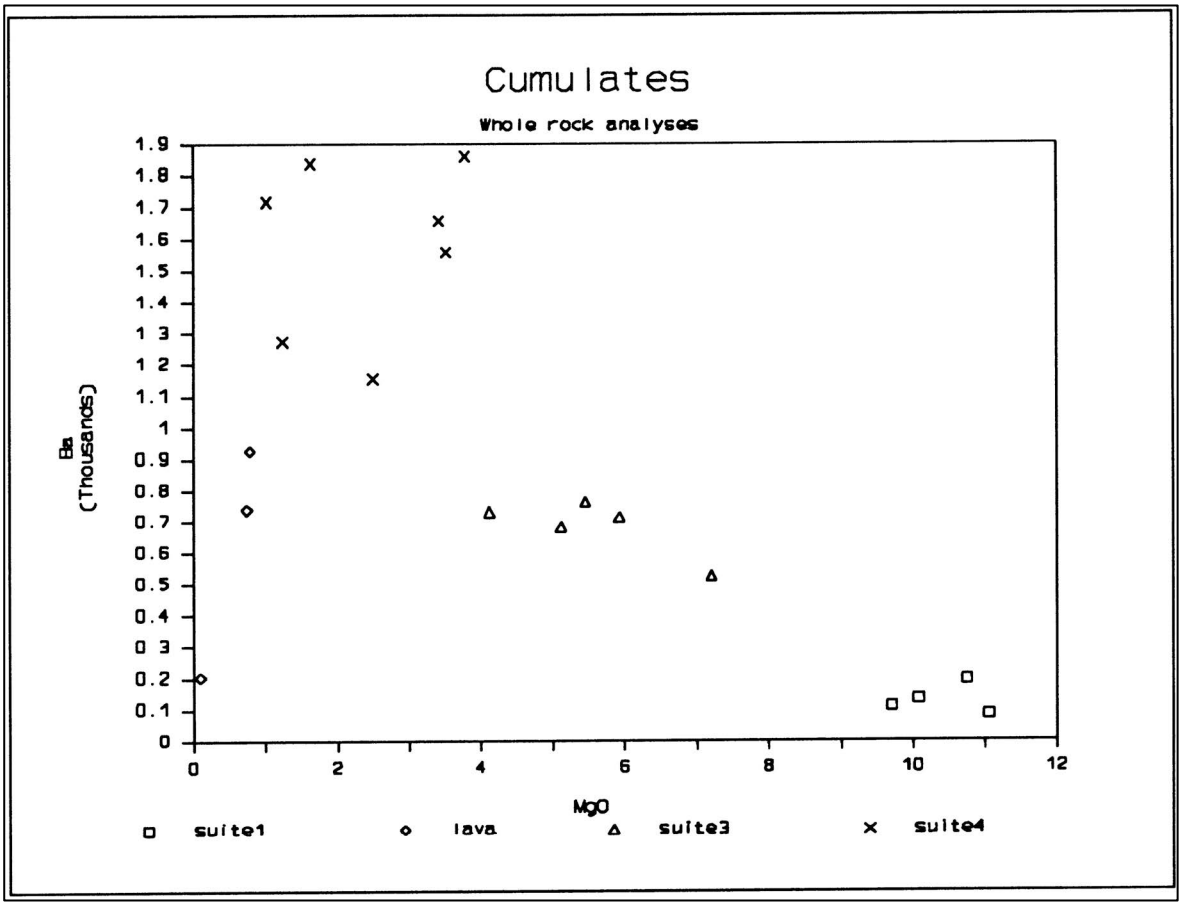


Figure 5.7.1q

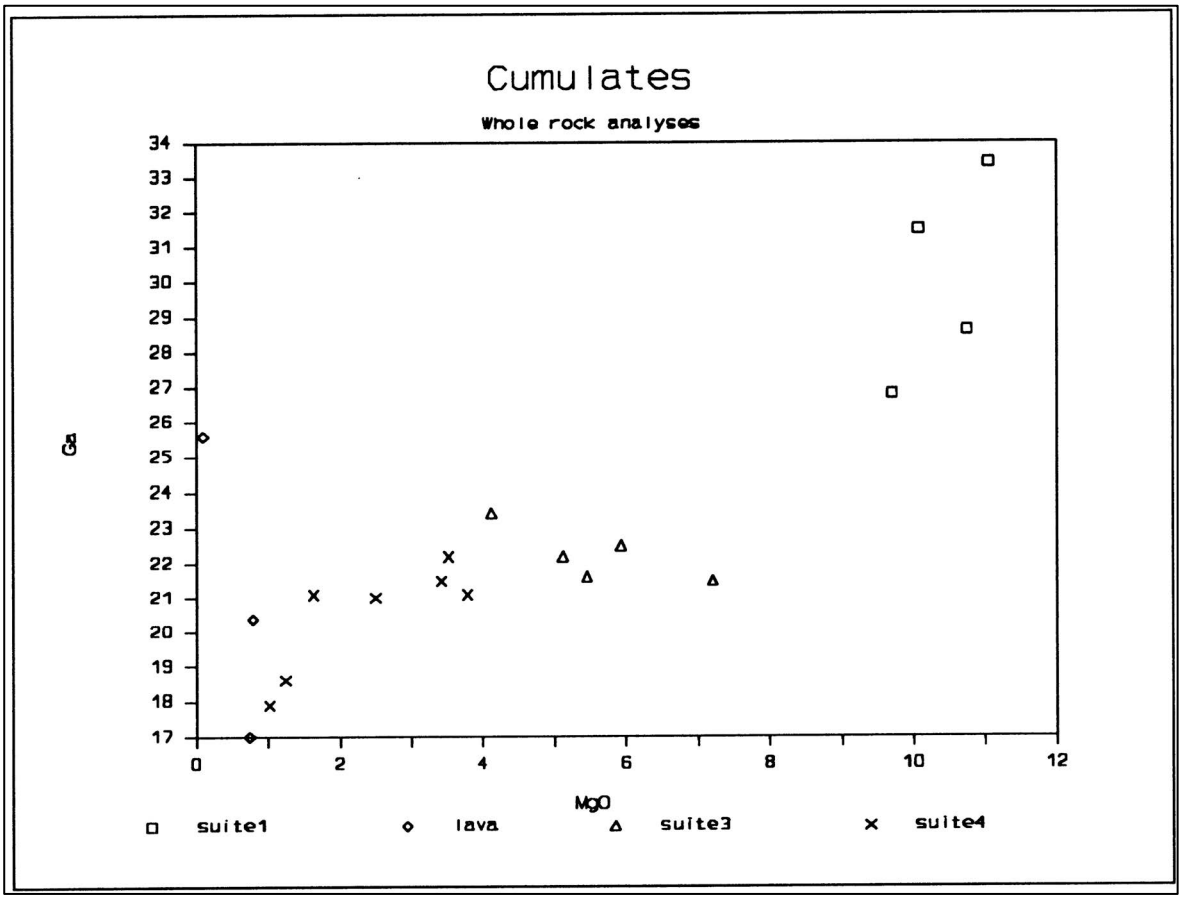


Figure 5.7.1r

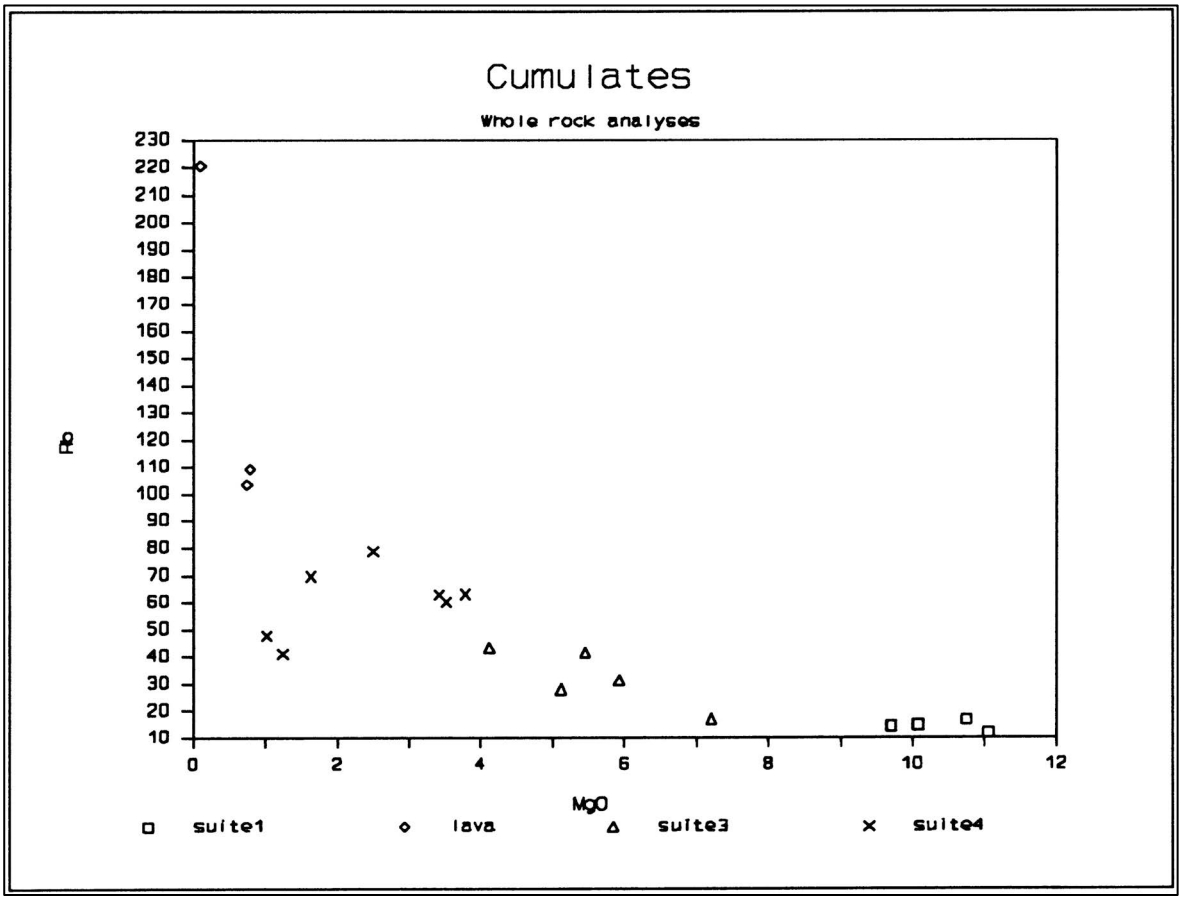


Figure 5.7.1s

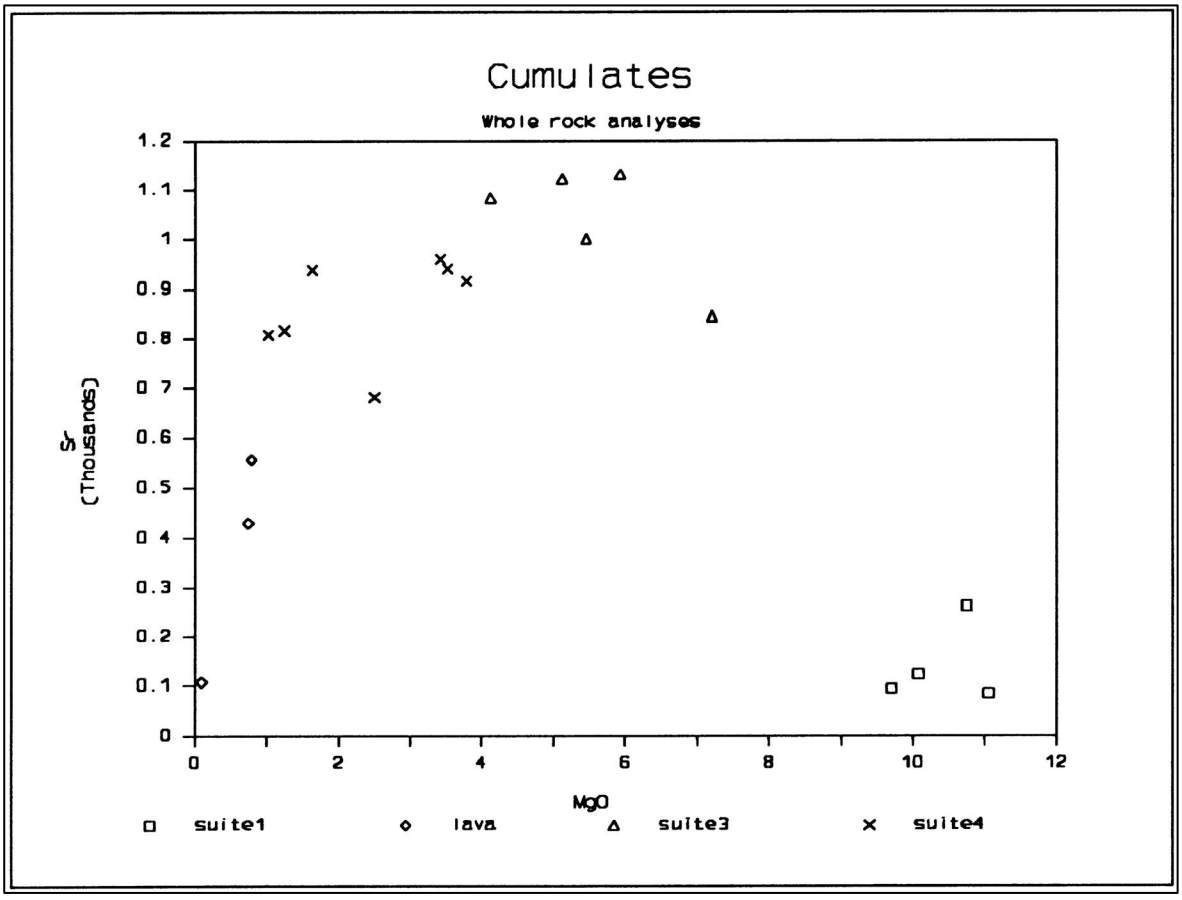


Figure 5.7.1t

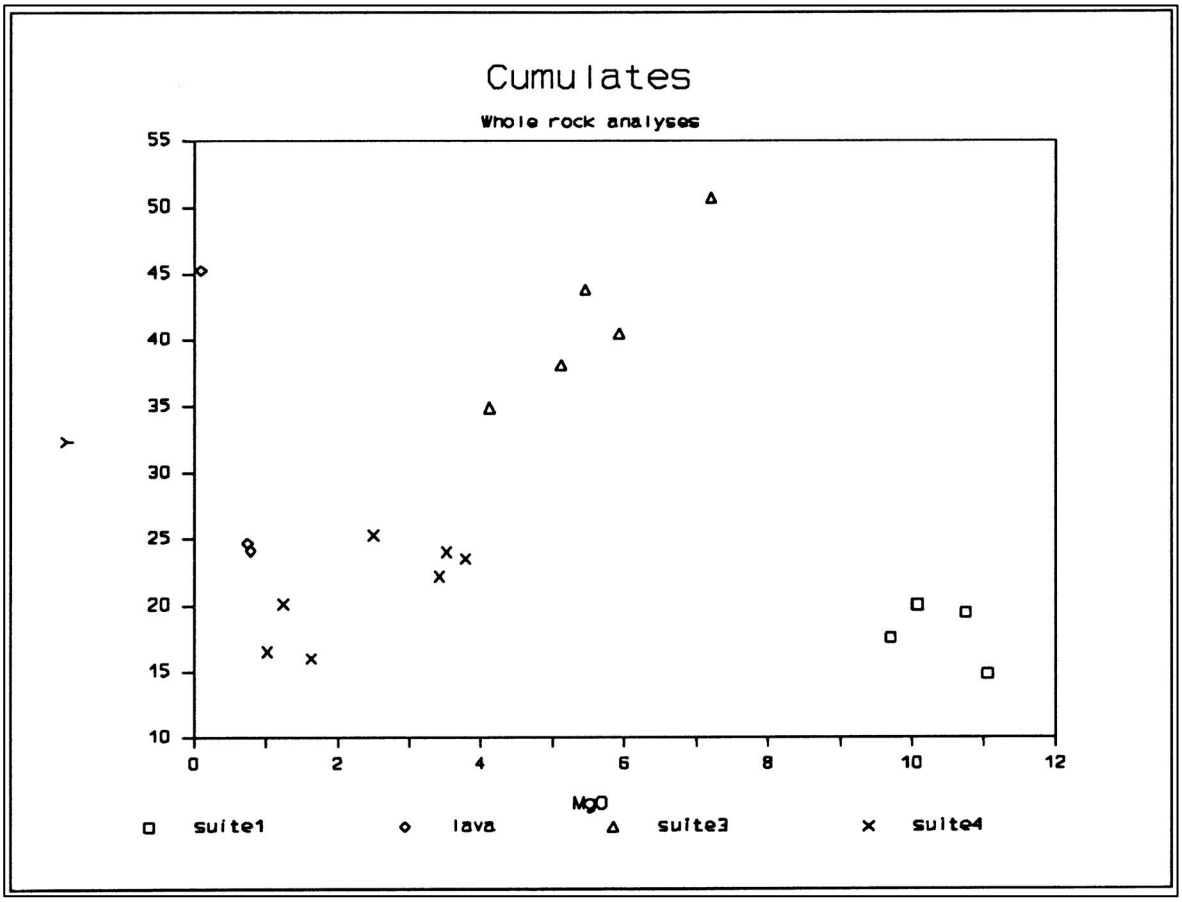


Figure 5.7.1u

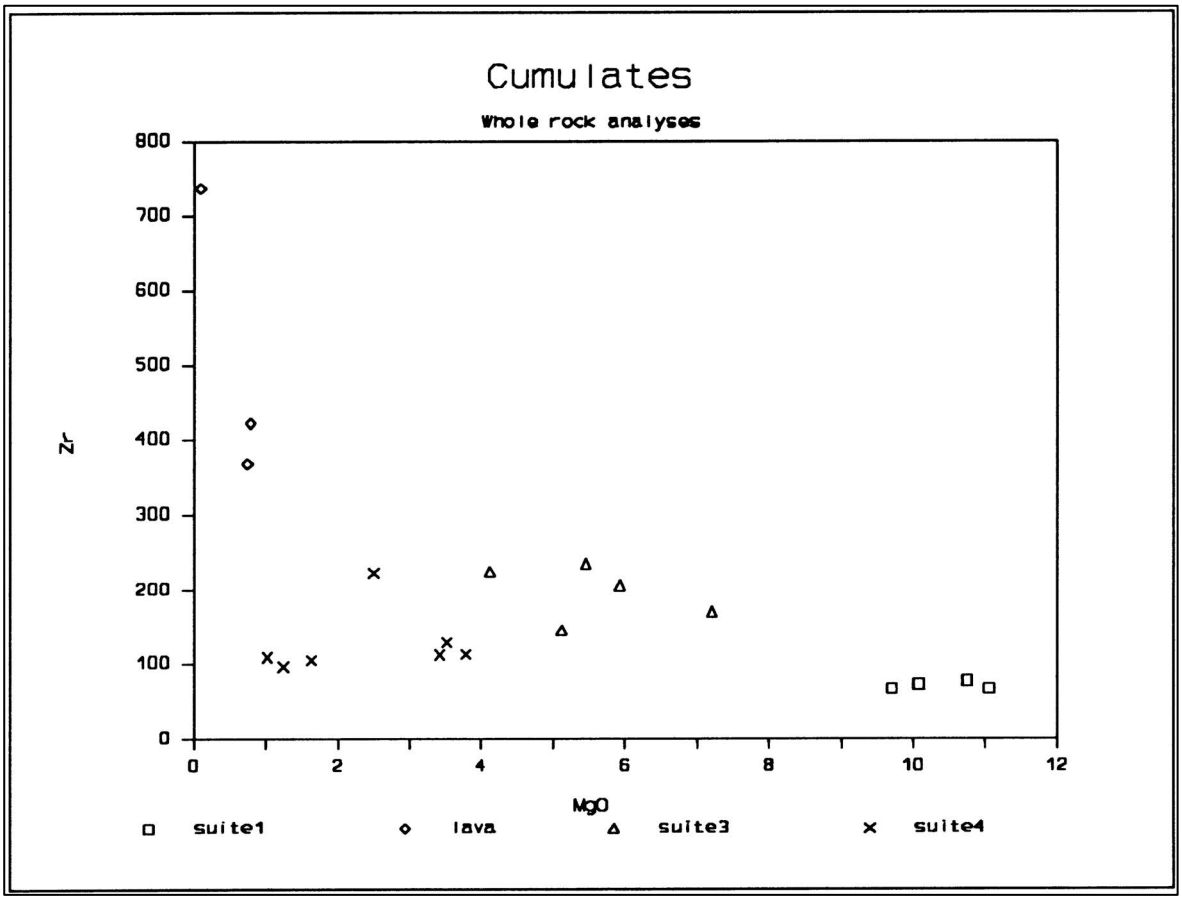


Figure 5.7.1v

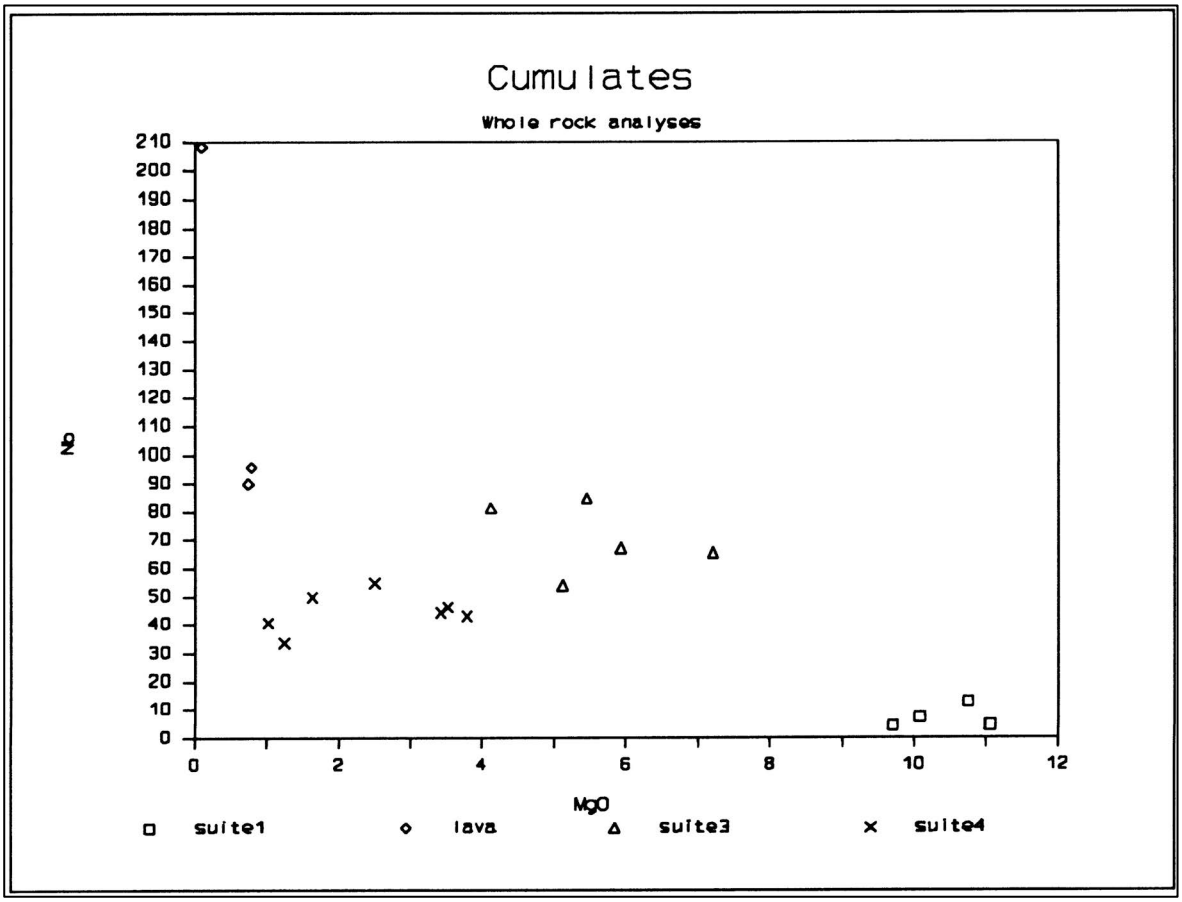


Figure 5.7.1w

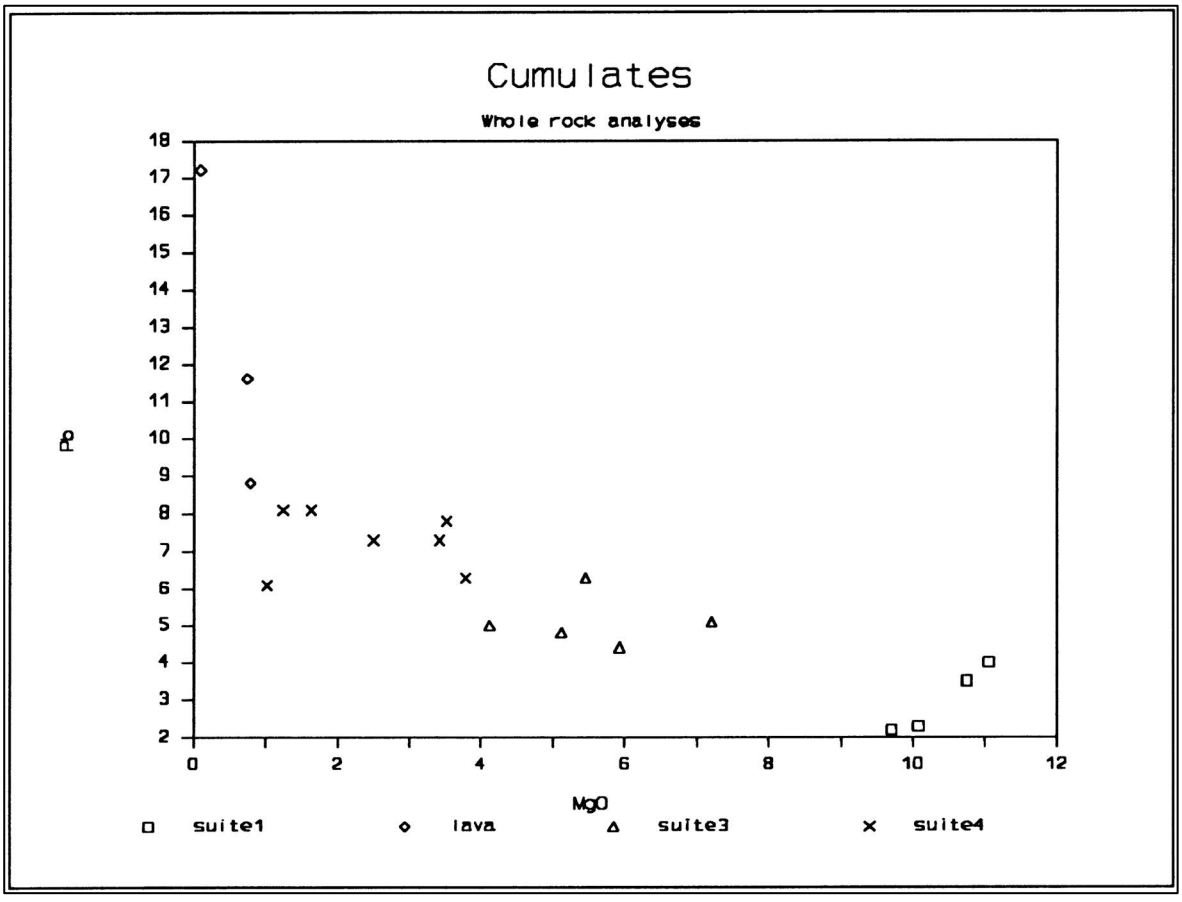


Figure 5.7.1x

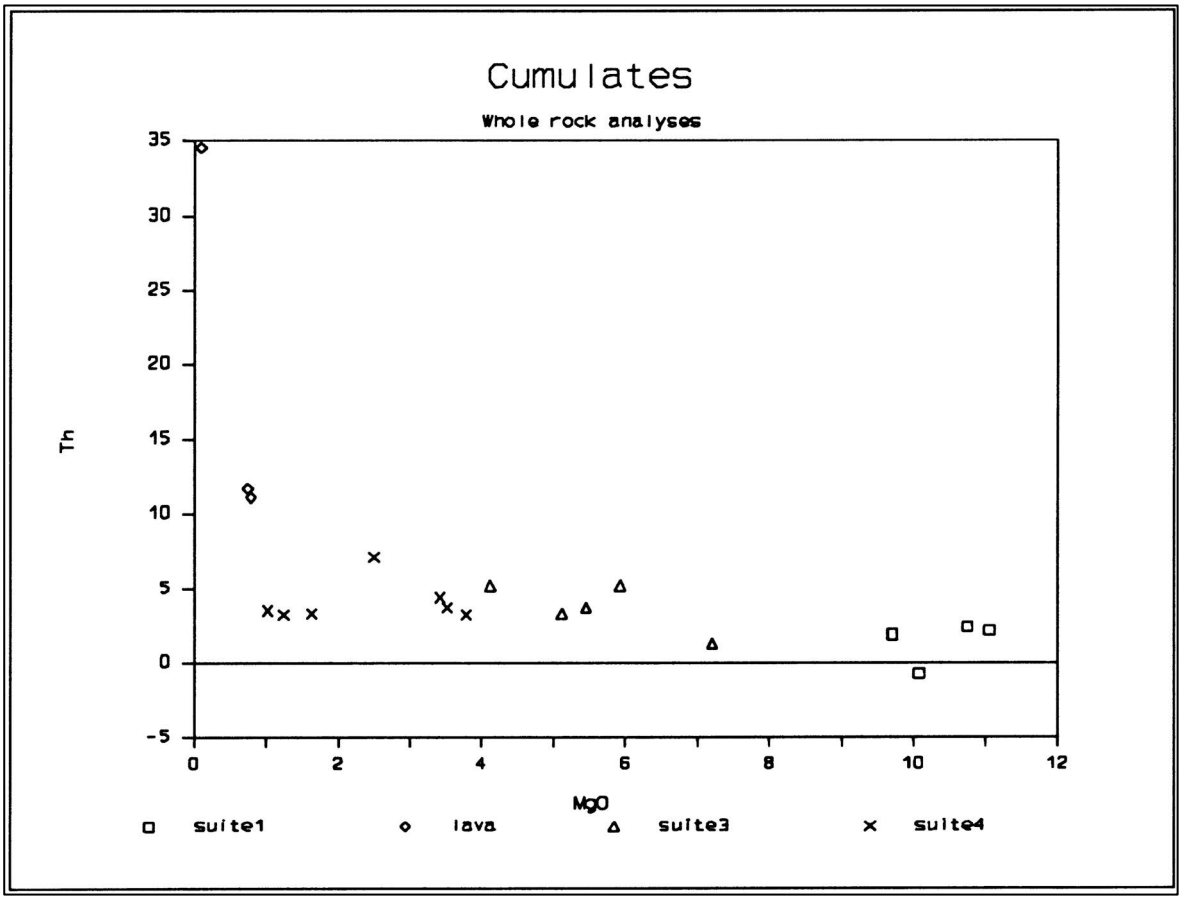


Figure 5.7.1y

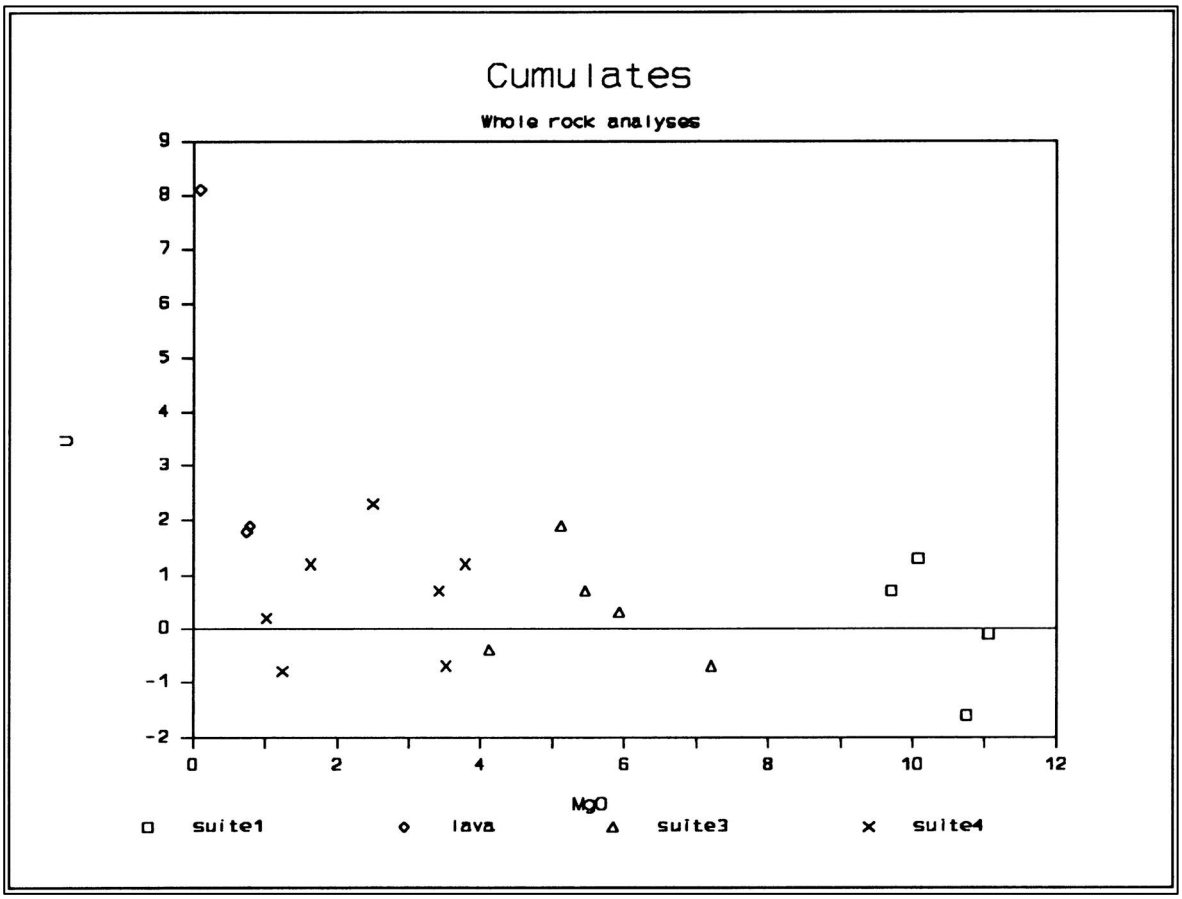


Figure 5.7.1z

The theoretical variations in abundance with evolution for elements with various D-values in the cumulates are shown in Figure 5.3.2.

1) Very compatible trace elements are Cu, Ni and to a lesser extent Co. They would ideally have high concentrations in the earliest formed nodules and very low concentrations in more evolved blocks, due to the early minerals removing all of the element from the melt.

   Cu and Ni show this extremely well with 100ppm Cu and 140ppm Ni in the most primitive blocks and less than 25ppm Cu and 30ppm Ni in the remaining cumulates. This behaviour implies bulk $D_{Cu,\ Ni} > 5$. Both of these elements are scavenged by sulphur, and pyrrhotite ($Fe_{0.92}S$) is present in the early cumulates.

   Co shows a less rapid depletion, probably with $D_{Co} = 2 - 5$. It is incorporated into Ti-magnetite in place of Fe^{2+}.

2) The major oxides TiO_2, $Fe_2O_3^T$, CaO and the trace elements Zn, V and Ga, are all moderately compatible elements. Zn and V probably substitute for Fe^{2+} and Fe^{3+} in magnetite. Ga is normally expected to proxy for Al in feldspar, but this is at odds with the absence of feldspar in the suite 1 blocks. Al_2O_3 in these rocks is in cpx (9%) and spinel-hercynite (47%) and it is possible that the latter may concentrate Ga. By contrast, Ga is slightly incompatible in the lavas.

3) Major elements showing moderate incompatibility are SiO_2, Al_2O_3, Na_2O and K_2O. The only trace element with this behaviour is Ba, which substitutes for K in biotite, K-feldspar and amphibole. The behaviour of these elements is identical to that in the Velay lavas, particularly for Ba. In the lavas Ba increases to a peak of 1900ppm in the intermediate lavas before falling rapidly almost to zero in the quartz-trachytes. In the cumulates Ba climbs slowly to 700ppm in the early (suites 1 and 3) cumulates before rising rapidly in the suite 4 nodules, exactly corresponding to a rapid extraction of Ba *from* the lavas *into* the cumulates.

4) The very incompatible trace elements in the cumulates are the same as those in the lavas; Rb, Zr, Nb, Pb, Th and U. Table 5.7.2 shows the highest and lowest values both in the basalt to quartz-trachyte series and in the cumulates, demonstrating that the cumulates have lower concentrations of these elements at every stage in their evolution, as predicted by section 5.3.2, equation (3) and shown in Figure 5.3.2.

   On the assumption that the highest and lowest values represent the maximum and minimum values of F, bulk D can be calculated as (conc. in cumulate)/(conc. in lava). These results are also given in Table 5.7.2.

5) P_2O_5, Sr, Y and Cr are all initially incompatible, with very low concentrations in the suite 1 cumulates, then relatively high values in suite 3, declining to lower values in the evolved suite 4 cumulates.

   The appearance of apatite controls P_2O_5, with zero in suite 1 blocks, then 1.7% P_2O_5 in suite 3 showing the onset of apatite fractionation. Sr substitutes for Ca in anorthitic

Table 5.7.2

Concentrations (in ppm) of incompatible trace elements in cumulate blocks and lavas

	Rb		**Zr**		**Nb**		**Pb**		**Th**		**U**	
	highest	lowest	highest	lowest	highest	lowest	highest	lowest	highest	lowest	highest	lowest
Cumulates	80	10	210	60	80	5	8	2	7	0	2.5	-1.5
Lavas	220	45	700	240	220	55	22	3	31	5	5.5	-0.5
Bulk D	0.36	0.22	0.30	0.25	0.36	0.09	0.36	0.67	0.23	-	0.45	-

plagioclase, which is absent from suite 1 blocks, highest in suite 3 and is less abundant in suite 4. Y is compatible in amphibole, sphene and apatite but since all of these are present in suite 3 and absent in suite 1 it is not possible to distinguish which has a controlling influence. The behaviour of these three elements is the same in the cumulates as in the lavas.

Cr is very compatible in the lavas, falling from 250ppm to 5ppm, presumably due to substitution of Cr^{3+} for Fe^{3+} in magnetite. In the cumulates however, the Cr-content of the primitive suite 1 nodules is very low, < 25ppm, rising to 110ppm in suite 3 blocks, before falling again to 10ppm in suite 4 blocks. The initial absence of Cr from the early blocks is difficult to explain, since Ti-magnetite is abundant in the rocks. Perhaps there are more primitive blocks, not analysed in this study, with high levels of Cr. The only mineral present in suites 3 and 4 which is absent from suite 1 blocks and also likely to contain high levels of Cr, is biotite, with $D_{Cr} = 5.4$ (Villemant *et al* 1981). Thus the trend in suites 3 and 4 is probably due to the removal of Cr from the liquid by biotite.

5.7.2 Interstitial glasses and lavas associated with the cumulates

As described in section 4.1, fragments of quartz-trachyte and some welded material were also found in the pyroclastics that hosted the cumulate blocks. After correction of their CaO-contents (see section 4.3 for explanation) analyses of three of these trachytes and the glass of the welded specimen (mean of 4 microprobe analyses) were plotted as diamonds in the graphs of Figure 5.7.1. For the major elements, excluding P_2O_5, they plot between the interstitial glasses and the most evolved cumulates, suggesting that they represent magma solidified before the final, most-evolved magma composition. On trace element graphs they plot on an extension of the trend given by the cumulates in most cases, with the exception of Ba, Rb, Y, Zr, Nb, Pb, Th and U. Concentrations of the highly incompatible elements Rb, Zr, Nb, Pb, Th and U are greatly elevated in the trachytes compared with the cumulates, exactly as would be predicted for lavas coexisting with cumulates. Ba is depleted in the lavas with respect to the cumulates since it becomes compatible in suite 4 blocks and is rapidly removed from the lavas. Y reaches higher levels in the lavas than in the suite 4 cumulates, which is much harder to explain, since the cumulates indicate that their host liquids should be depleted. Nevertheless the concentration of Y in the quartz-trachytes is similar to that in the Velay Miocene quartz-trachytes.

Throughout the cumulate series there is between 2% and 14% interstitial glass+carbonate, often showing signs of mutual immiscibility (see section 4.6.11 for details). It was shown on petrographic grounds that the glass is trapped intercumulus liquid, probably representing samples of the magmas that produced the cumulates. These glasses were microprobed using the technique described in Appendix C, in which the result given for each nodule is the mean of 2 - 4 analyses. The similarity of analyses from different areas of glass in a given thin section suggests that the glass is homogeneous on this scale.

The glass analyses are plotted as crosses on the major element graphs of Figure 5.7.1. On most

of these graphs they plot as expected, with lower TiO_2, $Fe_2O_3^T$ and CaO than the cumulates and higher SiO_2 and K_2O. Al_2O_3 and Na_2O are anomalous in that they show unexpectedly lower values than the most evolved cumulates. This depletion must have occurred either after the glass was incorporated into the cumulate, by loss of plagioclase components to the nearest feldspar crystals, or before its incorporation, by fractionation of plagioclase.

The graphs of lavas (Figure 5.3.1) show that for the quartz-trachytes the Al_2O_3-trend diverges from the main basalt-phonolite trend, towards lower values. Na_2O and CaO also show slightly lower values and SiO_2 distinctly higher values. These are the same trends shown by the intercumulus glasses, which suggests that plagioclase fractionation in the main body of melt was responsible for their composition. This ties in with section 5.6.2 in which it was concluded that the quartz-trachytes evolved by fractionation of calcic plagioclase due to the suppression of K-feldspar by biotite.

In Figure 5.7.3 the SiO_2-content of the cumulates and glasses is plotted against their normative quartz/nepheline. FeO/Fe_2O_3 was calculated using the formula of LeMaître (1976) and analyses giving zero quartz or nepheline were plotted at zero on the y-axis. Cumulate blocks are joined to their corresponding interstitial glasses by straight lines.

The graph shows two related trends, the first being that of the blocks, from 6.5% nepheline progressively towards 0.5% quartz in the most evolved cumulate. The same trend is reflected in the co-existing glasses, which range from 2% to 19% quartz, with the glasses poorest in normative-quartz occurring in the least evolved cumulates. This suggests a situation in which earlier, more deeply buried parts of the cumulate stack trapped slightly less evolved liquids than the most recent cumulates. The anomalous sample 88/14f is more altered than the other samples and had the highest pre-alteration proportion of glass+carbonate. This would account for its unusual position on the graph. Suite 1 samples are too far from conventional lava compositions to allow conventional norm calculation and were therefore omitted.

Section 4.6.2 describes suites of cumulates which show similarities with those of the Velay. Major element analyses are available for many of these and Figure 5.7.4 plots SiO_2 vs total alkalis for all of them, with the addition of the Velay cumulates, glasses and related lavas. Also shown on this graph are intercumulus glasses from the Laacher See nodules (Tait 1988). The trend shown by the set of all these cumulates is clearly the same as that for the Velay data alone, supporting the suggestion that they originated by similar means. The Velay glasses, with a trend towards rhyolitic compositions are, however, not matched by the four analyses of interstitial glasses in the Laacher See cumulates, which have a phonolitic composition. Cumulate nodules in the Laacher See are hosted by a phonolitic tephra which shows no signs of a trend towards silica-saturation.

Wörner *et al* (1984) and Wörner *et al* (1987), using $^{87}Sr/^{86}Sr$ and $\partial^{18}O$ respectively, showed that although there was some contamination of the magma by the wall-rocks it was at most only a few percent and not enough to affect major element concentrations significantly.

There is clearly the possibility of such wall-rock contamination having proceeded further in the

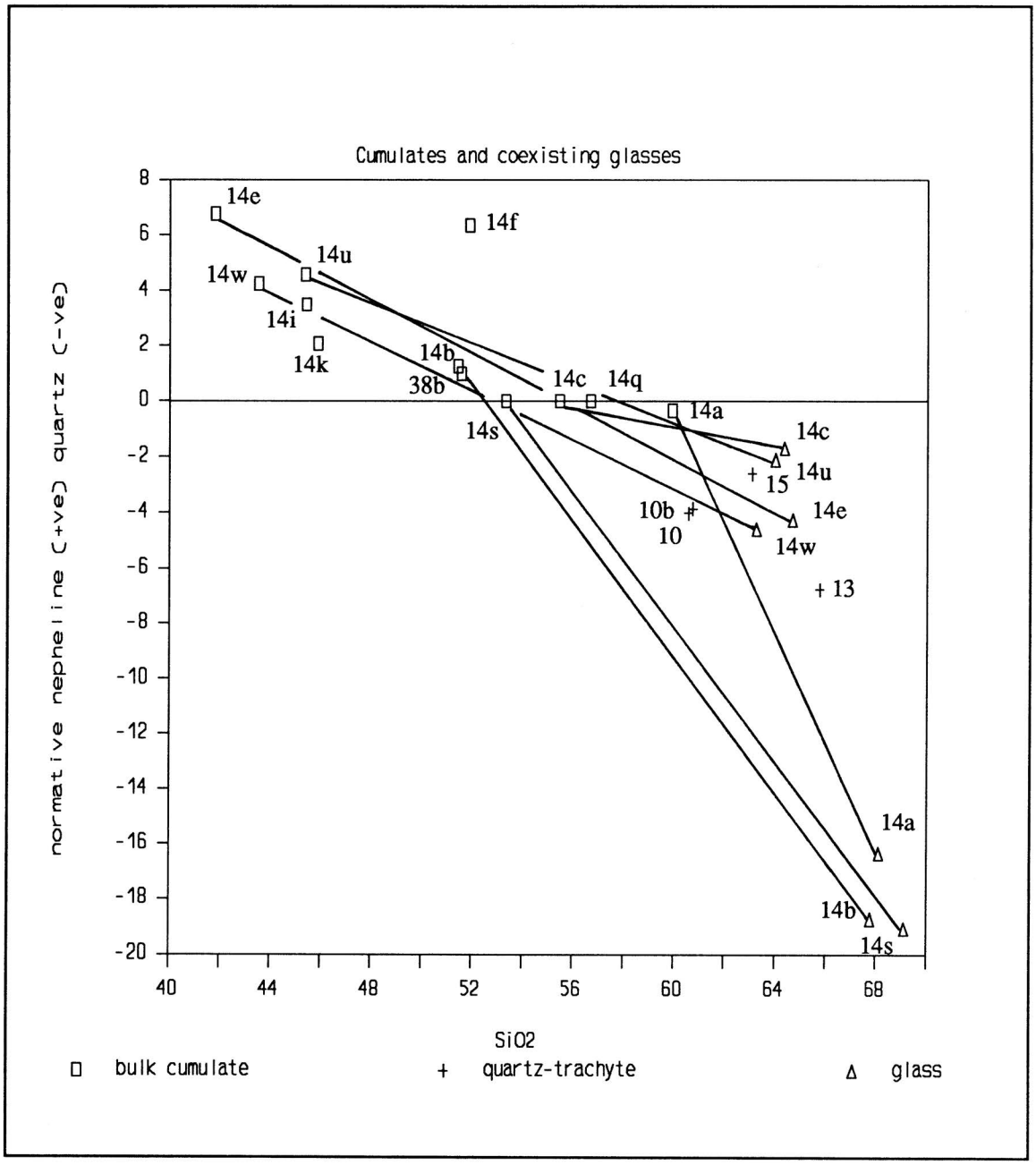


Figure 5.7.3. Silica saturation of bulk cumulates, their associated glasses and related lavas. Blocks and coexisting glasses are marked by their specimen number and joined by a line. Both axes are numbered in percent.

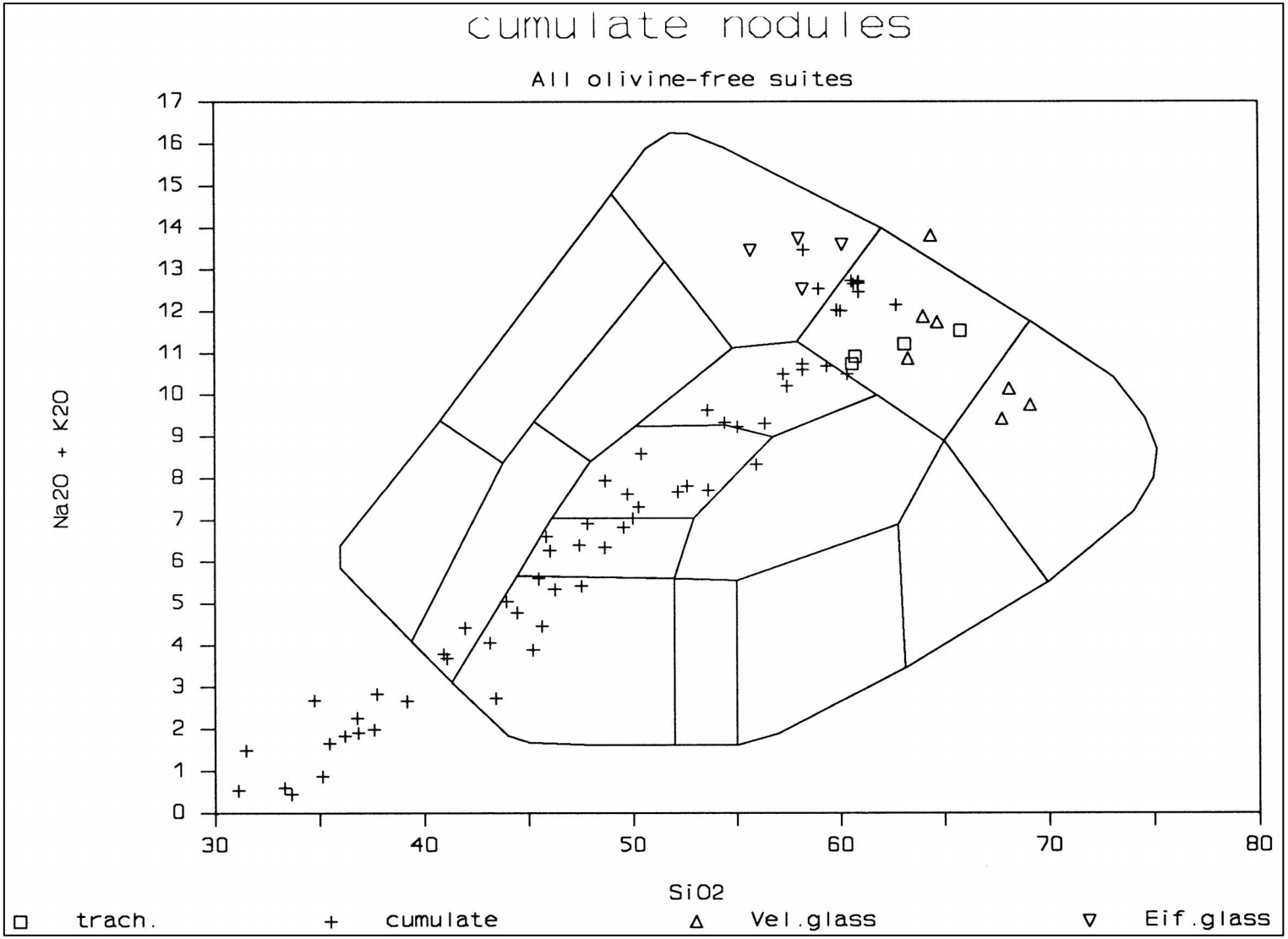


Figure 5.7.4. The olivine-free nodules of the Velay, Mont Dore, Cantal, Eifel and Tristan da Cunha plotted into Cox *et al's* (1979) grid. Coexisting glass is also shown for two of the suites, showing that in the Velay the liquid was evolving to an oversaturated composition, whereas in the Eifel the liquids were undersaturated and very similar to the host phonolite. The sources of the data are cited in the text (section 4.6.2). Key: trach. = Velay trachyte associated with cumulates, cumulate = bulk analyses of cumulate blocks, Vel.glass = glass in Velay cumulates, Eif.glass = glass in Eifel cumulates.

Velay and affecting the major elements to the extent that the magma crossed into the silica-saturated field. Fractionation would then tend to drive the residual liquid towards the rhyolite eutectic rather than phonolite. This possibility is tested with Sr-isotope data in section 5.8.

5.7.3 Conclusions

Evidence available from major and trace elements, added to that from petrography, shows that the cumulates were produced by fractionation of a nepheline-normative basaltic magma towards quartz-trachyte. However, at this stage it is not possible to distinguish between:

1) an origin by fractional crystallisation alone, as proposed for the Chaîne des Puys (Maury *et al* 1980), with the deviation from the basalt-phonolite trend caused by different T, P_{H_2O}, etc., or

2) an origin by crustal contamination combined with fractional crystallisation which caused a trend towards silica-saturated compositions. This process is called assimilation-fractional-crystallisation (AFC) and is discussed in section 5.8.4.

5.8 Sr-isotope data for the lavas and cumulates

5.8.1 Introduction

Forty lavas, four cumulates and six basement specimens were analysed for $^{87}Sr/^{86}Sr$. All of these data are given in Appendix D, together with details of the methods of analysis.

Figure 5.8.1 shows measured $^{87}Sr/^{86}Sr$ data for the lavas, without age correction. There is a wide range in phonolite (and quartz-trachyte) values, with the highest values in those with high $^{87}Rb/^{86}Sr$. The highest values of $^{87}Rb/^{86}Sr$ cover the range 13 - 203, which was able to affect the $^{87}Sr/^{86}Sr$ significantly in only 10Ma.

Figure 5.8.2 shows the same data after age correction. Ages were either directly measured by K/Ar or estimated from the known eruptive sequence in the area. Many of the phonolites produce values either much nearer to, or the same as, those of the less-evolved lavas after the age correction, although the Suc de Sara sample (87/55) overshoots the basalt range to the unlikely value of 0.695. This is lower than any recorded natural ratio, suggesting that the correction is in error, since the uncorrected $^{87}Sr/^{86}Sr$ is accurate. The age of this intrusion was measured by K/Ar and is probably reliable, whereas the Rb/Sr depends on a value of 5.6ppm Sr. Other phonolites that differ substantially from the basalt range, even after age correction, also have very high $^{87}Rb/^{86}Sr$, from 60 to 203, dependent on low Sr concentrations, from 4 - 12ppm.

The reliability of these Sr data was investigated by comparing the Sr-content of standard calibration samples, as determined by XRF, with their Sr-content determined chemically. Graphs of percentage error versus Sr-content show 50 - 30% errors for 3 - 10ppm Sr. Errors for these standards would tend to be smaller than those for the lavas since the calibration curve for the X-ray intensity is drawn as a regression line through the standards. Another factor to consider is the correlation of errors in Sr and Rb, due to their measurement by the same technique at the same time and on the

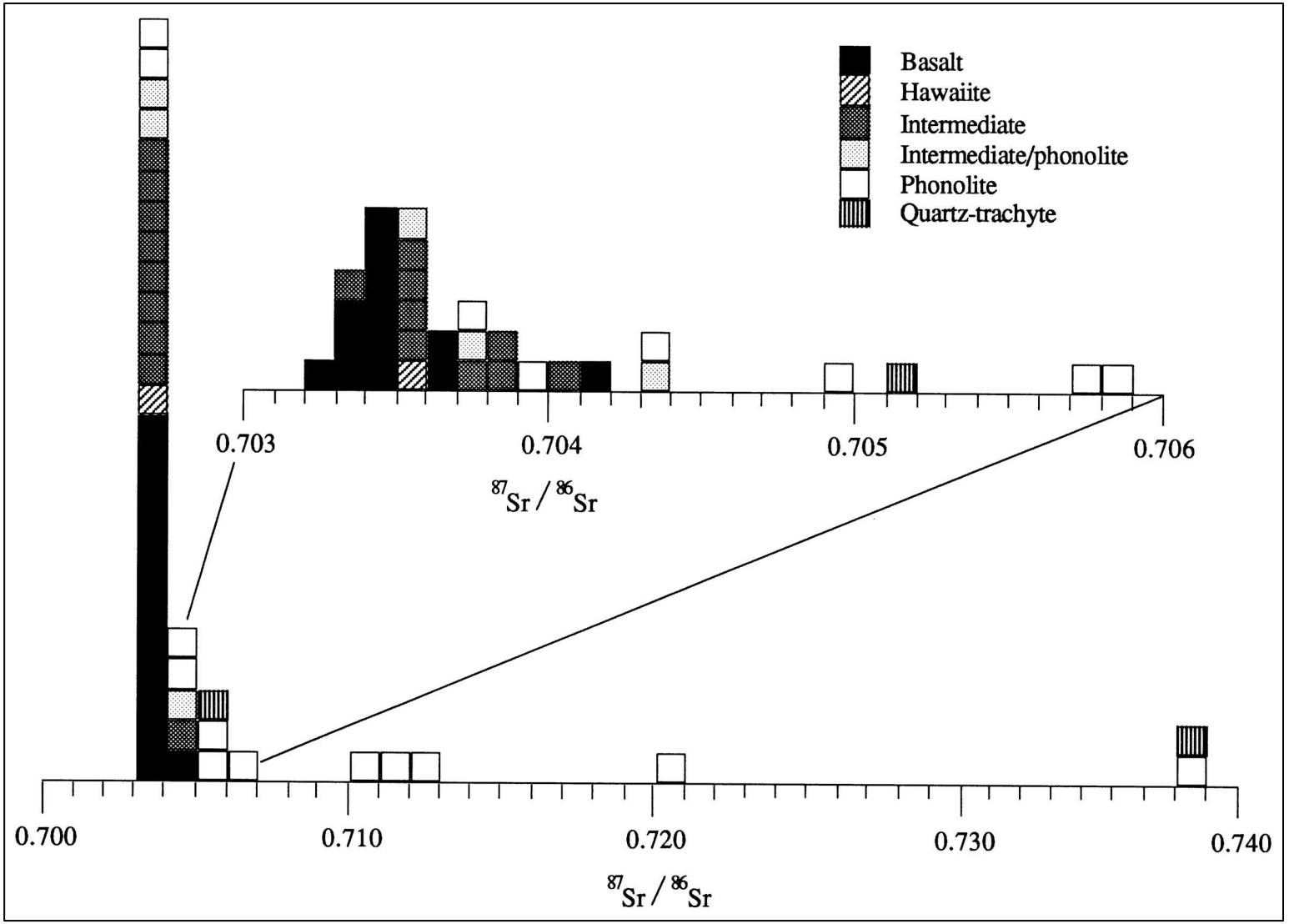


Figure 5.8.1. Sr-isotope data for Velay lavas before age-correction. Each square represents one analysis.

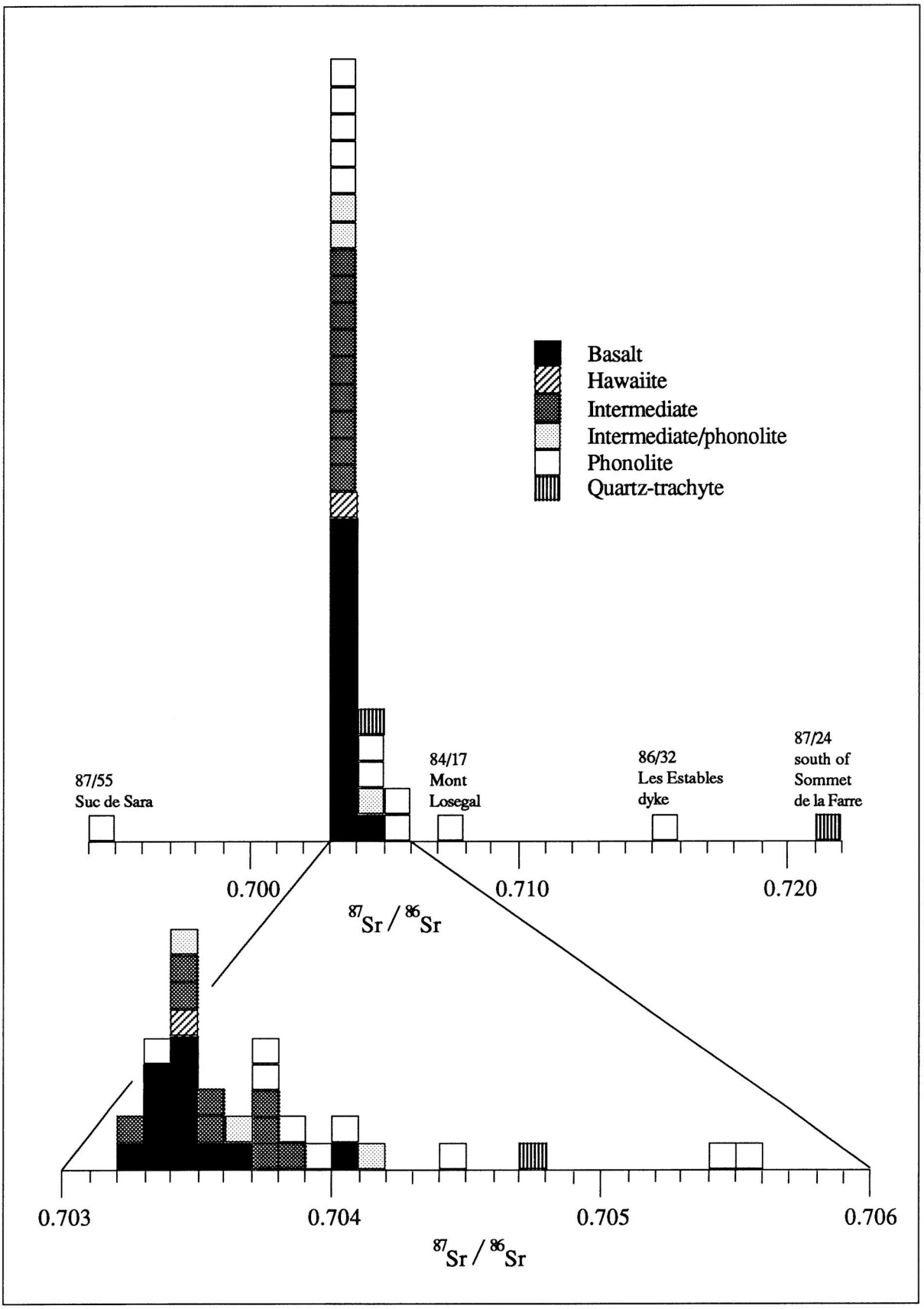


Figure 5.8.2. Sr-isotope data for Velay lavas, after age correction.
Each square represents one analysis.

same sample. This reduces the error on the ratio Rb/Sr. Errors in the data table of Appendix D were based on estimates from this correlation and reach a maximum of 10%. The result for sample 87/55 however, shows that the errors are clearly larger than this, probably due to the breakdown of Rb and Sr error correlation when Rb is large and Sr is very small.

For the reasons above it is therefore considered that the calculated initial values of the phonolites and other lavas with $^{87}Rb/^{86}Sr > 5$ are not valid. Better accuracy on Rb/Sr and more age data are needed to make them reliable. Only uncorrected $^{87}Sr/^{86}Sr$ values will be referred to.

5.8.2 Lavas

Basalts and hawaiite

Ten of the thirteen basalts analysed have $^{87}Sr/^{86}Sr$ in the range 0.703270 - 0.703492. These low values are discussed in section 5.8.5. Sample 84/40b from the base of the St Clément basalt plateau and 86/58 from the middle of the Gazeille sequence have slightly elevated values of 0.703690 and 0.703600. There seems to be little reason for this, since their age correction is small and they show no evidence of contamination. Sample 87/43 from a dyke near Bonnevialle shows an even higher ratio; 0.704101. This lava is an ankaramite and its abundant phenocrysts suggest that it resided in a magma chamber for some time before eruption. This may have allowed wall-rock contamination.

The only hawaiite sample analysed has $^{87}Sr/^{86}Sr = 0.703502$, slightly higher than the bulk of the basalts, due to its higher Rb/Sr ratio.

Intermediate lavas from the south of the Velay

Four samples were analysed, with 86/47, a mugearite flow north of Chaudeyrolles maar having a value in the main basalt range - 0.703300, whereas the remaining three, ranging from mugearite to trachyte, have values from 0.703514 to 0.703533, but with no correlation with composition.

Most of these lavas fall within the main basalt range after age correction.

Intermediate lavas from the north of the Velay

Three lavas falling in the trachyte or phonolite fields have been included in this category due to their petrographic similarity. Dents de Mézenc (88/17), a quartz-trachyte from the south of the Velay, was included for the same reason.

Nine lavas are thus included in this group. They are characterised by $^{87}Sr/^{86}Sr$-values elevated above those of the main basalt range, even after age-correction. Figure 5.8.3 shows graphs of SiO_2 and Pb in the lavas versus $^{87}Sr/^{86}Sr$. These elements were chosen because they are significantly higher in the basement granites than in the lavas. Both graphs show a weak correlation, albeit dependent on three points. Nevertheless the elevated values of these lavas do seem to be real. There are some possibly granite-derived K-feldspar and plagioclase xenocrysts in the samples with initial $^{87}Sr/^{86}Sr$ of 0.704128 and 0.703899 (87/31 and 87/33 respectively). The basement $^{87}Sr/^{86}Sr$-values marked on Figure 5.8.3 are listed in Appendix D and their bulk analyses in Appendix C. Figure 5.8.4 shows 1/Sr versus $^{87}Sr/^{86}Sr$ for the intermediate lavas of this section and five of the basement samples. On this type of graph the products of a single mixing process will plot on a straight line,

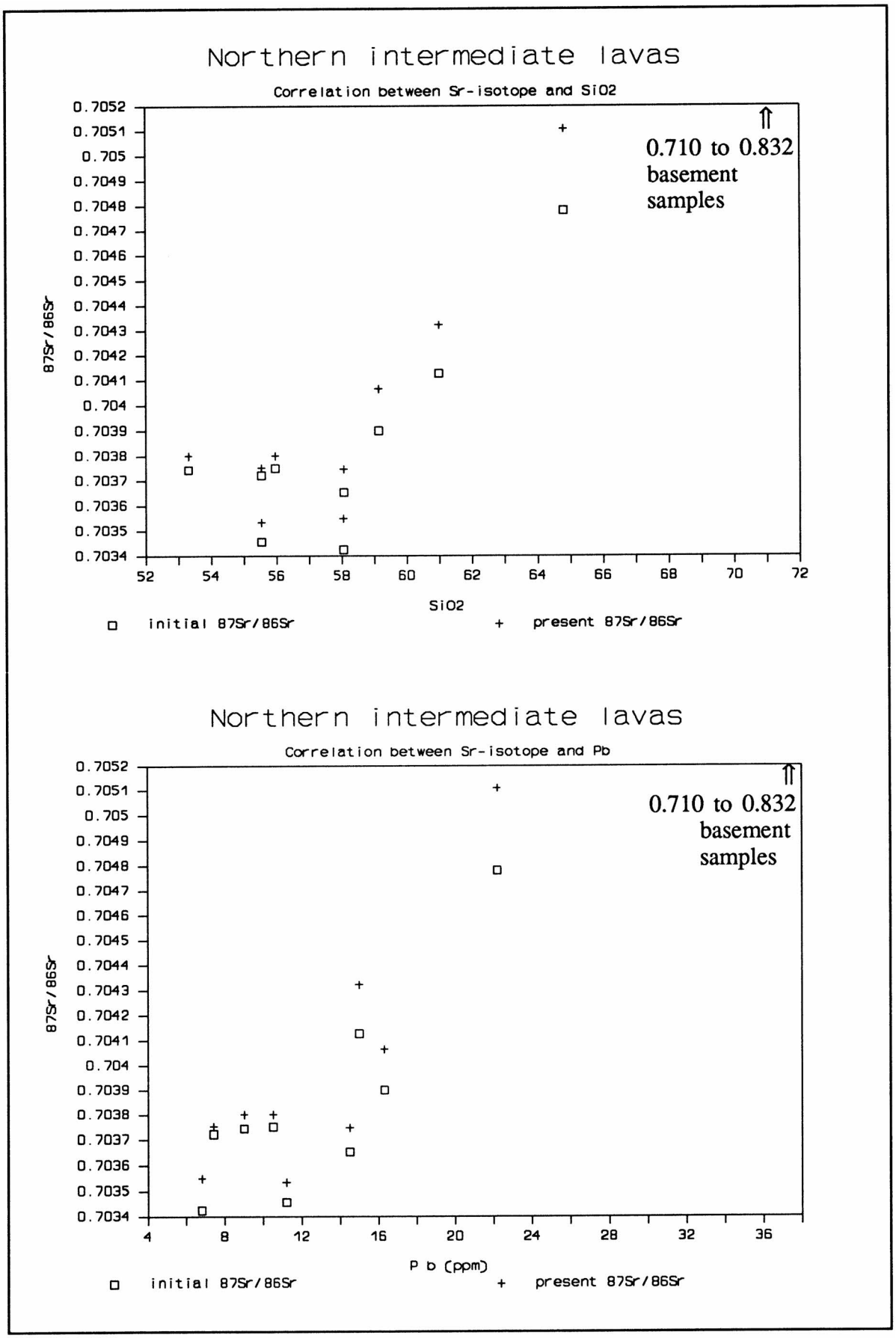


Figure 5.8.3. Graphs of SiO^2 (top) and Pb (bottom) against $^{87}Sr/^{86}Sr$, showing weak correlation in both cases.

with uncontaminated magma as one end-point and the contaminant as the other. The diagram shows that whereas the lavas do define a straight line, it does not go towards any analysed basement composition. Either the contaminant was substantially different to those analysed or some other process was involved. AFC (section 5.8.4) is a likely candidate.

The only other quartz-trachyte analysed, from south of Sommet de la Farre (87/24), has extremely high values of both $^{87}Sr/^{86}Sr$ and $^{87}Rb/^{86}Sr$ which renders any conclusion about its possible degree of contamination impossible.

Phonolites

As described in detail in the introduction, the high Rb/Sr of many of these lavas makes the calculation of initial $^{87}Sr/^{86}Sr$ unreliable. Nevertheless six of the twelve phonolites analysed have present day $0.703 < {}^{87}Sr/^{86}Sr < 0.706$, and nine fall in the same range after age correction. Contamination by the basement Hercynian granite seems unlikely in view of their extremely undersaturated compositions and the absence of petrographic evidence.

New K/Ar age determinations (section 1.3.3.2) show that the phonolites in the north of the Velay oriental are the oldest lavas in the whole of the Velay, with a mean age of about 13Ma. In an attempt to provide an independent confirmation of this the four northern phonolites for which $^{87}Sr/^{86}Sr$ has been measured (Loségal 84/17, Meygal 86/15, Miaune 87/13, Pot à Chard 87/65a) were used to calculate an isochron. For this they were assumed to have been erupted at the same time and with the same $(^{87}Sr/^{86}Sr)_{initial}$, which given the K/Ar evidence, the fact that they seem to be uncontaminated and to have had the same alkali basalt parent, is probably reasonable.

The four-point isochron gave an age of 14.1 ± 1.4 Ma (2σ error) and $(^{87}Sr/^{86}Sr)_{initial}$ of 0.703687 ± 0.000207. The agreement with the K/Ar ages is remarkable considering that the Rb/Sr system is usually insufficiently sensitive to give meaningful results with such young rocks. The $(^{87}Sr/^{86}Sr)_{initial}$ is within error of that of the alkali basalts considered to be parental to the Velay series, unlike the values obtained by using the K/Ar ages of these phonolites. The assumptions made for the isochron calculation however, mean that it is invalid to conclude from it that these phonolites can only have formed by fractional crystallisation of Velay alkali basalt. The coincidence of their $(^{87}Sr/^{86}Sr)_{initial}$ values may only *support* an argument based on other criteria.

5.8.3 Cumulates

Four cumulate samples were analysed for $^{87}Sr/^{86}Sr$. Figure 5.8.5 plots these values against SiO_2-content, showing that for these few data $^{87}Sr/^{86}Sr$ increases with SiO_2. Section 5.7 showed that SiO_2 increases with fractionation in the cumulates so $^{87}Sr/^{86}Sr$ was probably increasing with time. Section 5.7.3 concludes that the cumulates formed from lavas evolving to silica-saturated compositions, either by fractionation alone or by fractionation combined with contamination (AFC). The $^{87}Sr/^{86}Sr$ data support the AFC model, since fractionation alone cannot affect initial $^{87}Sr/^{86}Sr$ values.

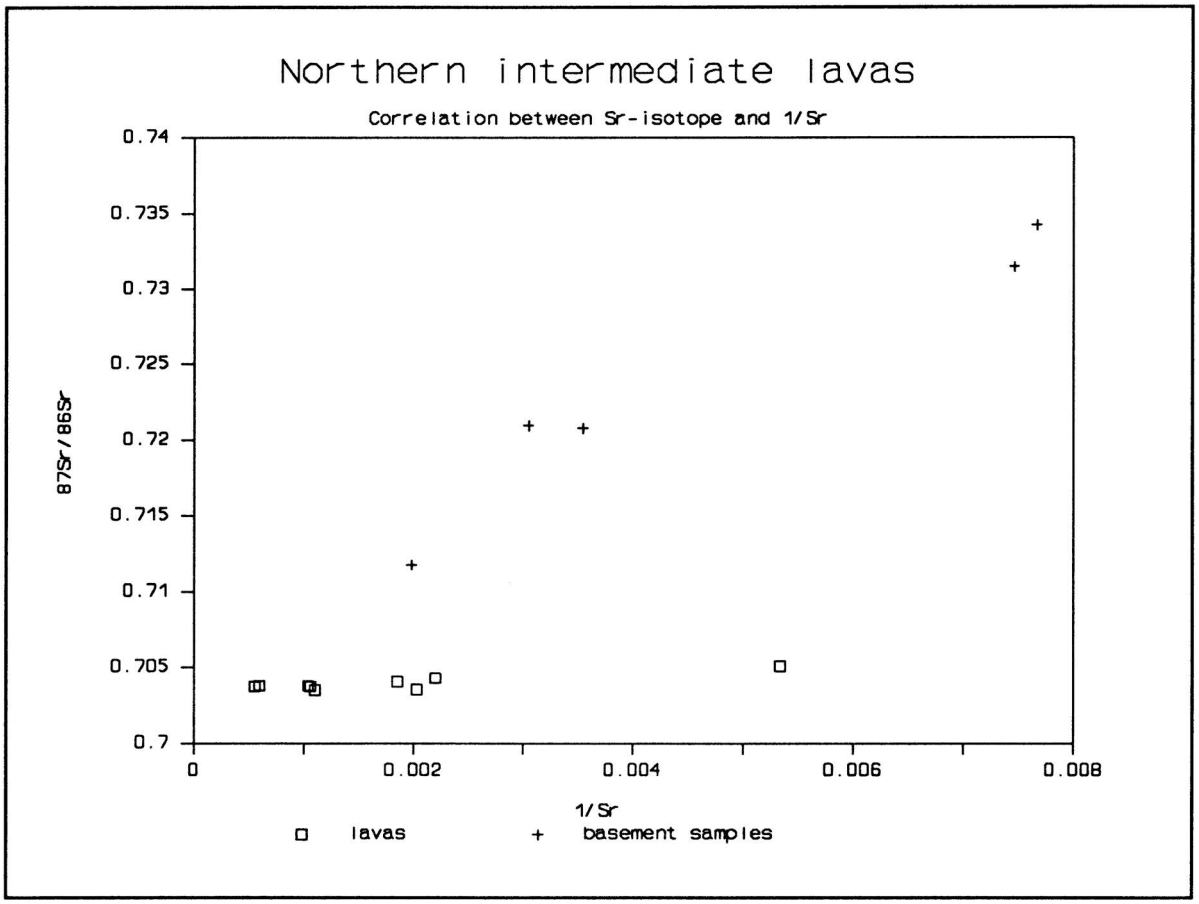


Figure 5.8.4. Correlation between $^{87}Sr/^{86}Sr$ (present day) and 1/Sr. If the lavas were the product of simple mixing between lavas with $^{87}Sr/^{86}Sr = 0.7035$ and granite basement they should lie on a line running towards the basement analyses. This is clearly not the case.

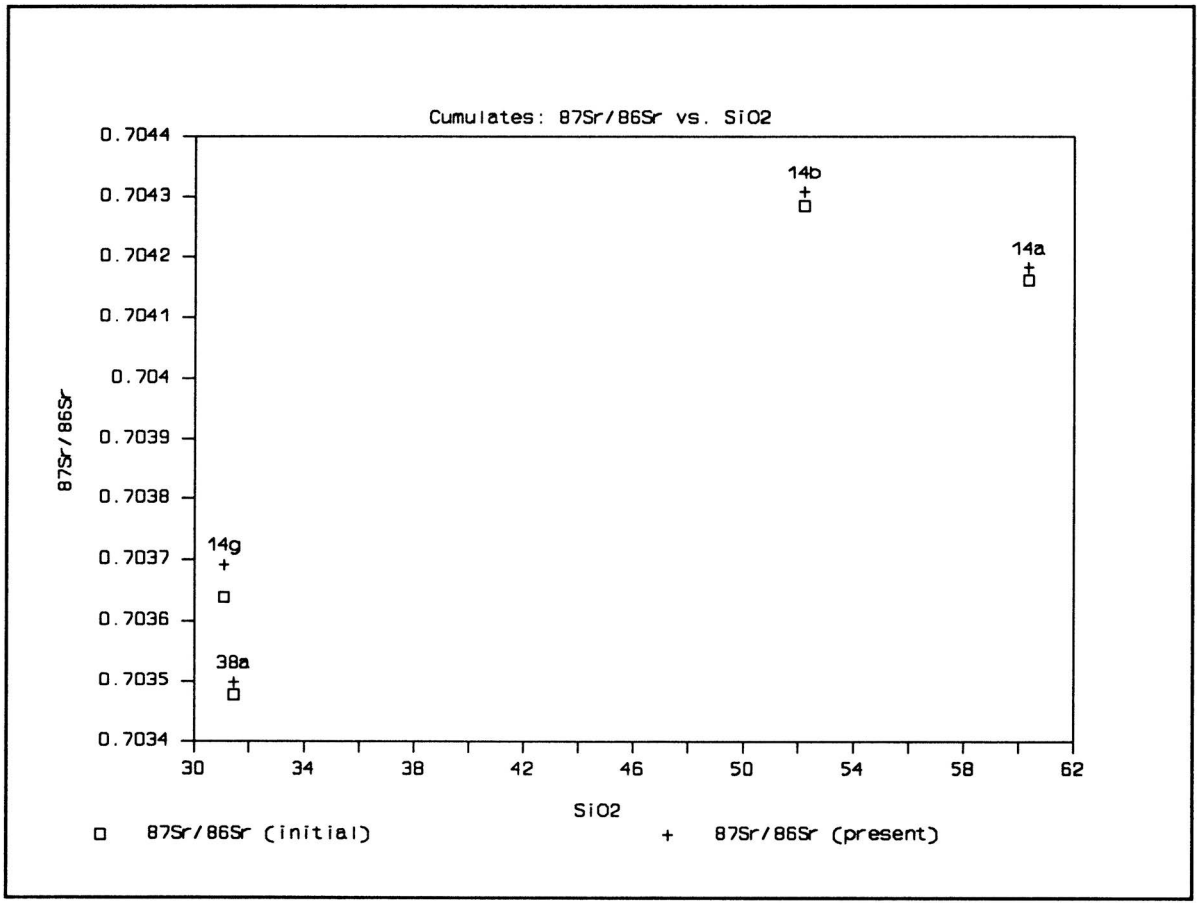


Figure 5.8.5. $^{87}Sr/^{86}Sr$ vs. SiO_2 for four cumulate blocks, showing that Sr is more radiogenic in more evolved samples.

Thus quartz-normative lavas and possibly related cumulates from the Velay all show signs of contamination. Figure 5.8.4 shows that the lavas are not the product of simple mixing, although AFC remains a possible mechanism, and the presence of variably contaminated cumulates in a single eruptive unit supports this.

5.8.4 Assimilation Fractional Crystallisation (AFC)

The details of the AFC model were presented by DePaolo (1981). The basic idea is that contamination of a magma, especially by melting of wall-rocks, is likely to be accompanied by simultaneous fractionation. Such fractionation will cause the trend of magma compositions to depart from simple mixing lines, sometimes to an extreme degree.

As pointed out in sections 5.8.2 and 5.8.3 AFC seems to be the most appropriate model for the evolution of the northern intermediate lavas and of the cumulates. The following represents an attempt to find suitable parameters for these rocks.

With a range of basement samples of varied composition it is necessary to choose a representative sample as the contaminant. Sample 86/62 was chosen because it is very fresh, has an igneous texture (as opposed to the metamorphic textures of some specimens) and has Sr and $^{87}Sr/^{86}Sr$ which are reasonably representative of the basement range. Its petrography is described briefly in Appendix B, and its bulk composition is given in Appendix C.

The first stage of magma evolution is shown by the line running from the bottom of Figure 5.8.6 to the right hand side. This is for an initial magma with 650ppm Sr and $^{87}Sr/^{86}Sr = 0.7034$, both of which are good estimates. The rate of contamination was set at 0.05 × the rate of crystallisation and the line is for $D_{Sr} = 0$, since Sr is initially incompatible. The line is stopped at 1800ppm Sr since this is the highest Sr concentration measured in the lavas (although these lavas themselves appear to be anomalous).

The second stage is shown by a new family of curves drawn from the final magma of the first stage, which had 1800ppm Sr and $^{87}Sr/^{86}Sr = 0.703568$. The change in parameters is necessary because at this point Sr becomes compatible in feldspar and starts to follow a very different path on the graph. The solid lines are of constant D_{Sr} where $D_{Sr} = 1$ is a simple mixing hyperbola between magma and contaminant. The dotted lines are for constant F (= mass of magma remaining/original mass of magma) which necessarily cut the solid lines.

The number of analyses which appear to have been affected by AFC is small and the fit is only moderate, for the first stage. Two basalts have elevated $^{87}Sr/^{86}Sr$, and as previously mentioned, the two intermediate lavas with highest Sr concentrations are also anomalous. Nevertheless, the four intermediate lavas with elevated $^{87}Sr/^{86}Sr$ fit moderately well, with $D_{Sr} \approx 2.2$ and F starting at 0.6, declining to 0.4 and reaching the quartz-trachyte with only 0.2 of the original lava remaining. Combining this with F = 0.36 (650/1800) for the first step gives 0.07 as the final proportion of parent

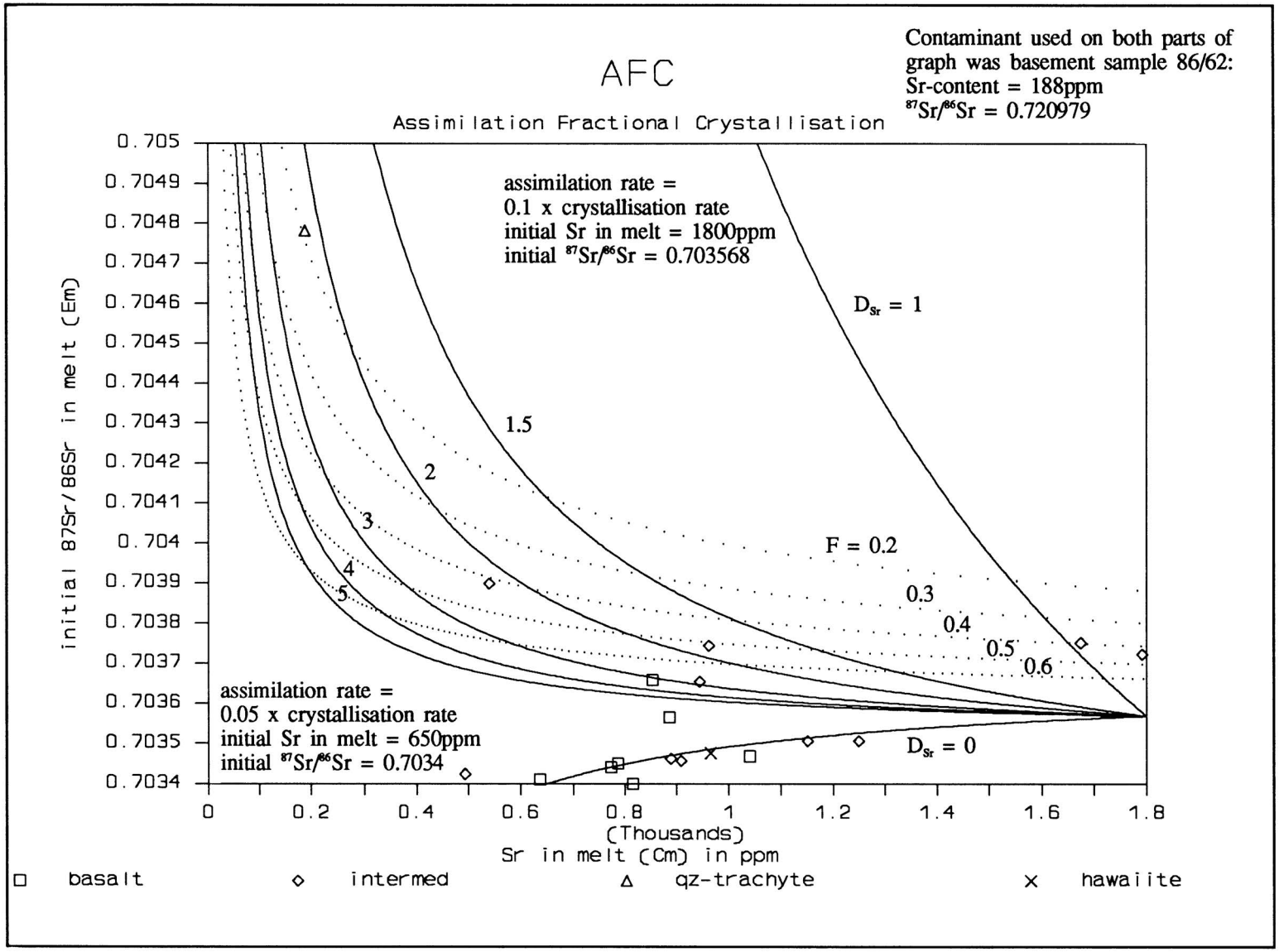


Figure 5.8.6. Sr-content of lavas versus their $^{87}Sr/^{86}Sr$-value. Solid lines show the evolution of magmas with constant D_{Sr} during AFC (DePaolo 1981). Dotted lines show constant F-values (F = fraction of original liquid remaining). All parameters are marked on the diagram.

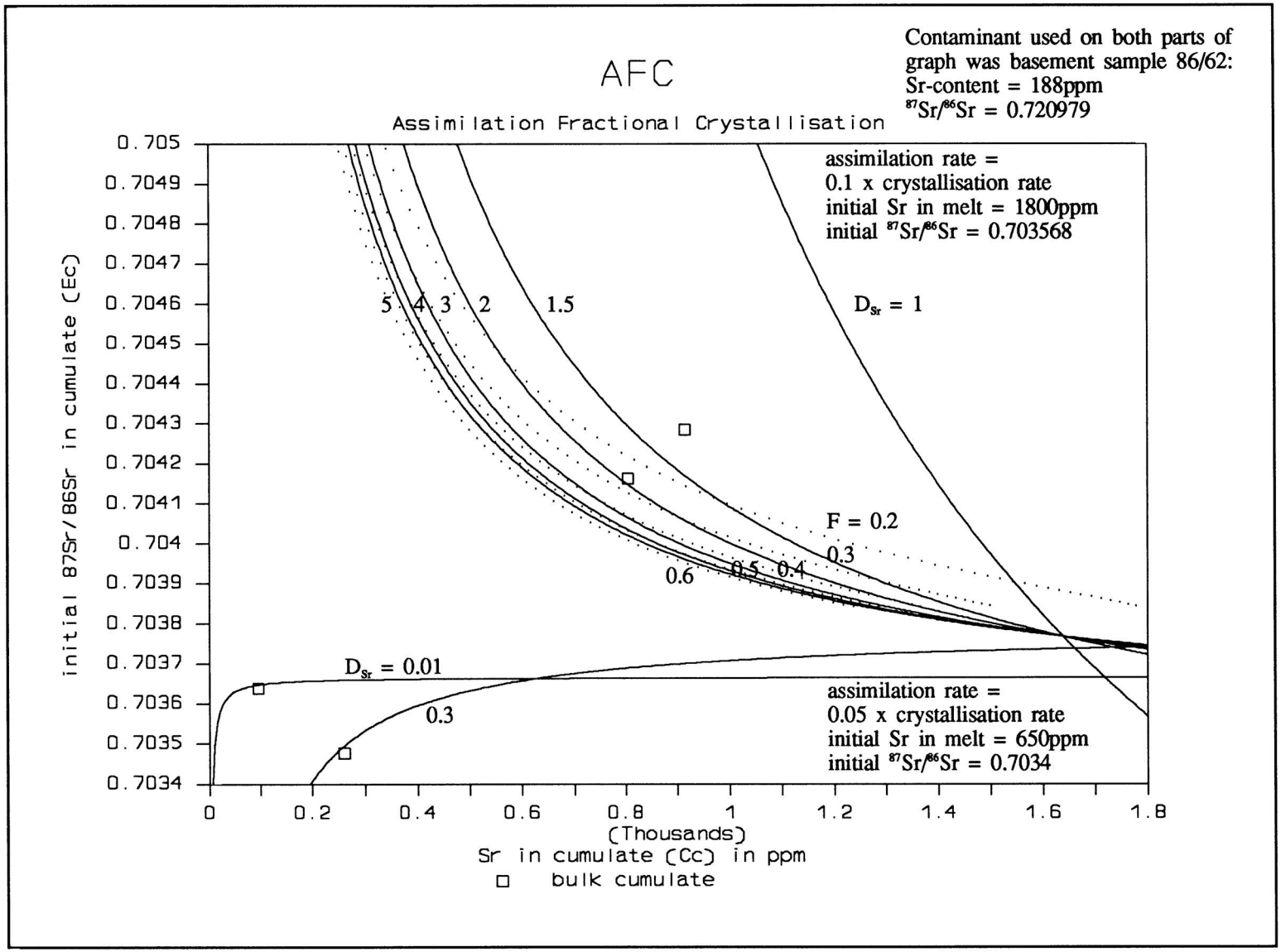


Figure 5.8.7. Sr-content of lavas versus their $^{87}Sr/^{86}Sr$-value. Solid lines show the evolution of cumulates with constant D_{Sr} during AFC (equations derived from those of DePaolo 1981). Dotted lines show constant F-values (F = fraction of original liquid remaining). Model parameters are shown.

basalt by the level of the quartz-trachyte, which is rather low compared to earlier estimates (section 5.6.2.5).

The maximum degree of contamination, reached in the Dents de Mézenc quartz-trachyte ($^{87}Sr/^{86}Sr_{initial}$ = 0.7048) is about 11%. This is calculated in two stages:

64% fractionation × 0.05 = 3% for the first stage, and

80% fractionation × 0.1 = 8% for the second stage.

Figure 5.8.7 is the corresponding graph for the evolution of the "instantaneous cumulate" being removed from the magma. The equations of the lines were derived from those for the magma using the assumption that the $^{87}Sr/^{86}Sr$ for such a cumulate is identical to the magma from which it was crystallising. The parameters that were used to draw this graph are essentially the same as for Figure 5.8.6, except for the first stage in which a cumulate with D_{Sr} = 0 would contain zero Sr. For this reason lines of D_{Sr} = 0.01 and 0.3 are given, to illustrate a good fit to the data points.

This graph is harder to read than that for the magmas. For the first stage the appropriate line for initial D_{Sr} should be followed until the target concentration is reached (target Sr = D_{Sr} × concentration in target magma [1800ppm]). At this point D_{Sr} changes and the value of $^{87}Sr/^{86}Sr$ reached should be traced across to where it intersects the line of the new D_{Sr} for stage 2.

Values of D_{Sr} for the second stage are represented by the upper family of curves on the graph. Parameters for this stage are exactly the same as in Figure 5.8.6, with 1800ppm initial Sr in the magma and $^{87}Sr/^{86}Sr$ = 0.703568. The upper two cumulate analyses shown are not a perfect fit to the model, but the left-hand one lies on the D_{Sr} = 2 line, at F ≈ 0.25 which is similar to the contaminated lavas in the previous diagram.

The value of such diagrams is clearly very limited with such tiny data sets, especially when these contain a number of anomalous points. The main purpose of this exercise is to illustrate the way in which they may be used.

AFC may also be used to explain unusual behaviour of some elements in lava trends. Villemant and Treuil (1983) concluded from their data for the Velay that K_2O increased too rapidly to be explained by Rayleigh fractionation alone, and went on to construct a complex model of selective enrichment by hydrothermal fluids. DePaolo (1981) points out that when the concentration of an incompatible element in an AFC contaminant is much greater than in the magma, it can increase more rapidly than could be achieved by Rayleigh fractionation alone, even for relatively low contamination rates. Such an explanation should be assessed for the Velay before recourse to more obscure processes.

5.8.5 Conclusions

The bulk of the Velay plateau lavas are characterised by $^{87}Sr/^{86}Sr$ in the range 0.7033 - 0.7035. This is similar to average values for ocean-island basalt (OIB), such as 0.7037 calculated by Faure

and Powell (1972). Similar values have been obtained in many continental alkali-basalt (CAB) provinces, such as the Ahaggar province with $^{87}Sr/^{86}Sr$ = 0.7031 - 0.7035 (6 analyses - Allègre *et al* 1981) and the Cameroon line with $^{87}Sr/^{86}Sr$ = 0.7029 - 0.7035 (63 analyses - Halliday *et al* 1988, Halliday *et al* 1990). In the Cameroon line province, which straddles the continent-ocean boundary, the authors noted that a lithospheric source was excluded since identical parent basalts had been erupted in both the continental and oceanic sectors and the lithosphere under oceans is thought to be extremely depleted due to the extraction of MORB. The Velay, and by implication the rest of the Massif Central, probably shares the same source for its parental alkali basalt magma as other CAB and OIB provinces around the world, and this source must lie beneath the lithosphere.

Allègre *et al* (1981) suggested that the lower mantle was the source of the Ahaggar lavas, by means of an enriched plume which traversed the asthenosphere and lithosphere. Halliday *et al* (1988, 1990) proposed a relationship between the Cameroon volcanism and the breakup of South America and Africa. They rejected a direct lower mantle plume source, since volcanism in the province shows no migration with time, and suggested instead a mechanism whereby plume-enriched asthenospheric mantle became incorporated into the thermally thinned lithospheric mantle as it cooled and thickened after rifting.

All these authors rejected the asthenosphere as a potential source as it was believed that its extreme depletion in incompatible elements (due to MORB extraction) and its homogeneity (due to convective stirring) would prevent it generating enriched OIB-type magma. The source of the Velay basalts is discussed further in Chapter 2.

5.9 Phase relations

The degree to which the phase relations of a suite of lavas such as those of the Velay can be determined is quite limited, due to the number of significant components involved. For example, in tholeiites and picrites the content of K_2O and TiO_2 is too small to be significant, whereas in alkali basalts and basanites this is not the case. As for the more evolved lavas, there may be thirteen significant components, including H_2O and CO_2, and up to nine phases present in the melt (although not necessarily in equilibrium), making it virtually impossible to determine completely its phase relations.

The following two sections aim to show that the crystallisation of the Velay basaltic lavas can be at least partially modelled.

5.9.1 The CMAS-system

O'Hara (1968) derived a hypothetical phase diagram based on the CMAS system by allocating all the oxides of natural lavas to C, M, A and S in such a way that all feldspars plot as anorthite, all magnetite and other spinels (s.l.) plot as spinel (s.s.), all olivines plot as forsterite and all clinopyroxenes plot on the diopside-CaTschermak join. Using published melting data on various natural lavas at different pressures he was able to deduce simple phase boundaries. These are

represented in two dimensions as projections onto various planes cutting through the CMAS-tetrahedron. The three planes used by O'Hara, and their projection points, are:

from M_2S (olivine) into MS - CS - A

from MS (enstatite) into M_2S - C_2S_3 - A_2S_3

from CMS_2 (diopside) into C_3A - M - S

5.9.1.1 MS - CS - A

This projection is illustrated in Figure 5.9.1 and shows the Velay basalts to lie on a linear trend aligned towards the MS vertex. The whole of this trend lies to the A and CS-enriched side of the projected univariant (four phases in equilibrium) points for the pressure range 1 atmosphere to 20 kbars.

The first task was to establish whether the linear trend is real, since the projection from M_2S is quite oblique and tends to elongate a set of data towards the MS vertex. To achieve this a second projection onto a plane at a steep angle to CS - MS - A was used. Figure 5.9.2 shows a sketch of the CMAS tetrahedron with the relevant planes marked. CA - M - S, shown in Figure 5.9.3, is collinear with the apparent trend in the data and at a steep angle to CS - MS - A. It shows clearly that the observed trend is an artifact of the projection.

Returning to the MS - CS - A projection, the data lie on an extension of one of the three-phase equilibria at 10, 15 or 20 kbars, with ol+cpx+plag+liquid, ol+cpx+spinel+liquid or ol+cpx+garnet+liquid respectively. Of these the 15 kbar equilibrium is the most likely since ultramafic nodules carried to the surface are spinel lherzolites and the rare ankaramitic basalts contain ol+cpx+spinel(+Ti-magnetite). The 1 atmosphere and 30 kbar phase relations are not appropriate. The fact that the lavas do not lie on a four-phase univariant point, despite almost certainly originating as a partial melt of either spinel- or garnet-lherzolite, is not very significant because of the inaccuracies involved in the construction of the diagram, combined with the oblique projection.

All of the data lie to the SiO_2-poor side of the olivine-gabbro plane, as would be expected for nepheline-normative alkali basalts and basanites.

5.9.1.2 M_2S - C_2S_3 - A_2S_3

This projection is shown in Figure 5.9.4. It is similar to MS - CS - A, but slightly less oblique, which is reflected in the small extent of data elongation towards M_2S.

The four-phase equilibria provided by O'Hara (1968) allow the exclusion of the 1 atmosphere, 10 and 30 kbar univariant points as lying too far from the data. In this projection the Velay basalts appear to lie on the 15kbar opx+cpx+ol+spinel+liquid or the 20 kbar opx+cpx+ol+spinel+garnet+liquid equilibria. This is consistent with the CS - MS - A projection.

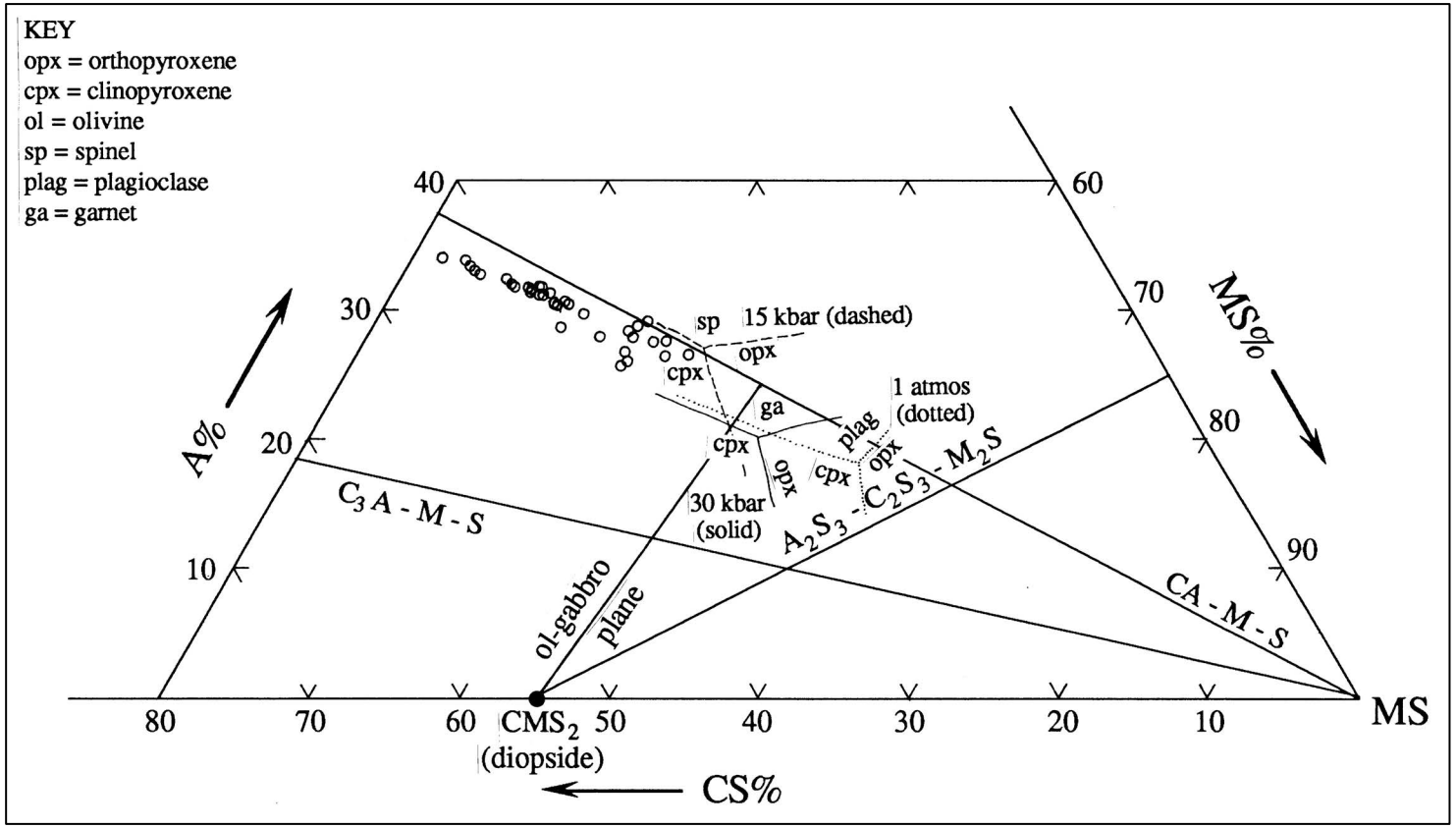


Figure 5.9.1. Projection from M_2S (olivine) into CS- MS-A, showing apparent elongated trend of data towards MS (enstatite).

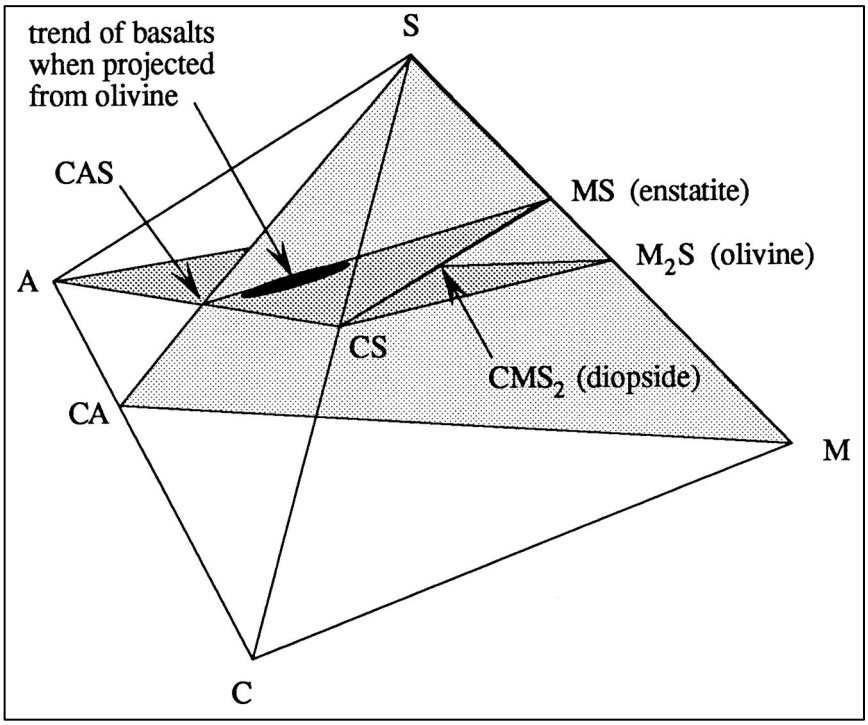


Figure 5.9.2. Sketch of CMAS system (O'Hara 1968) showing the trend produced when projecting from olivine into CS-MS-A. The plane CA-M-S is also shown, to demonstrate how it was used to examine whether the apparent trend was real, by projection from diopside.

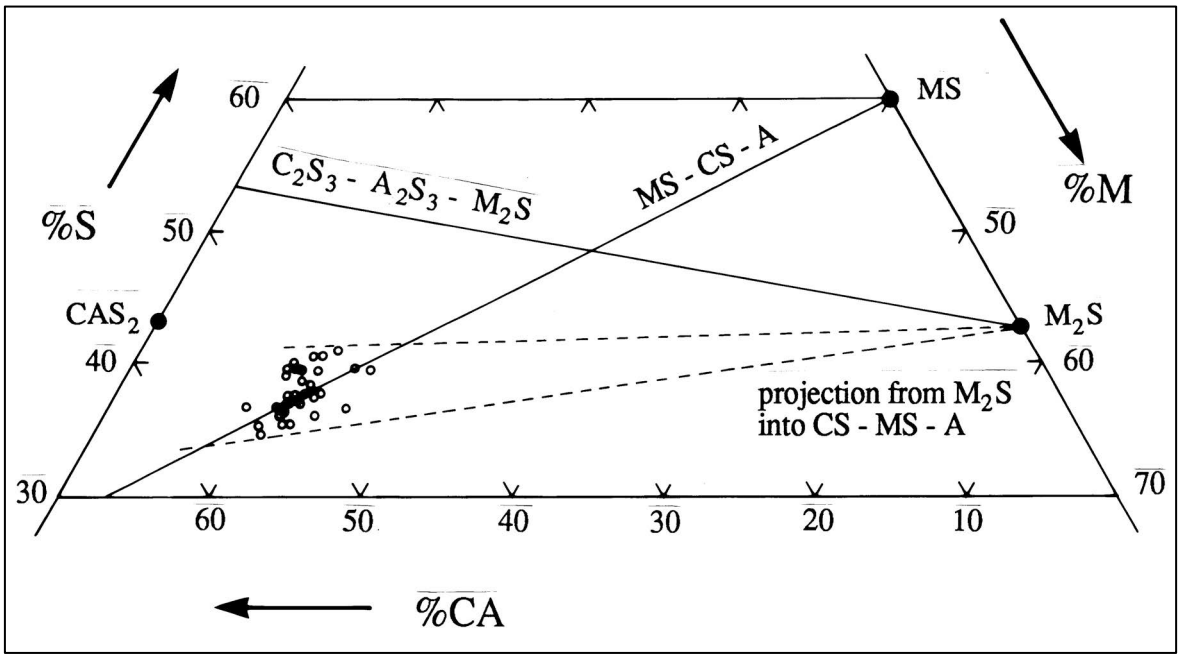


Figure 5.9.3. Projection from CMS_2 (diopside) into CA-M-S, showing that the apparent trend in Figure 5.9.1 is due to its oblique projection from M_2S.

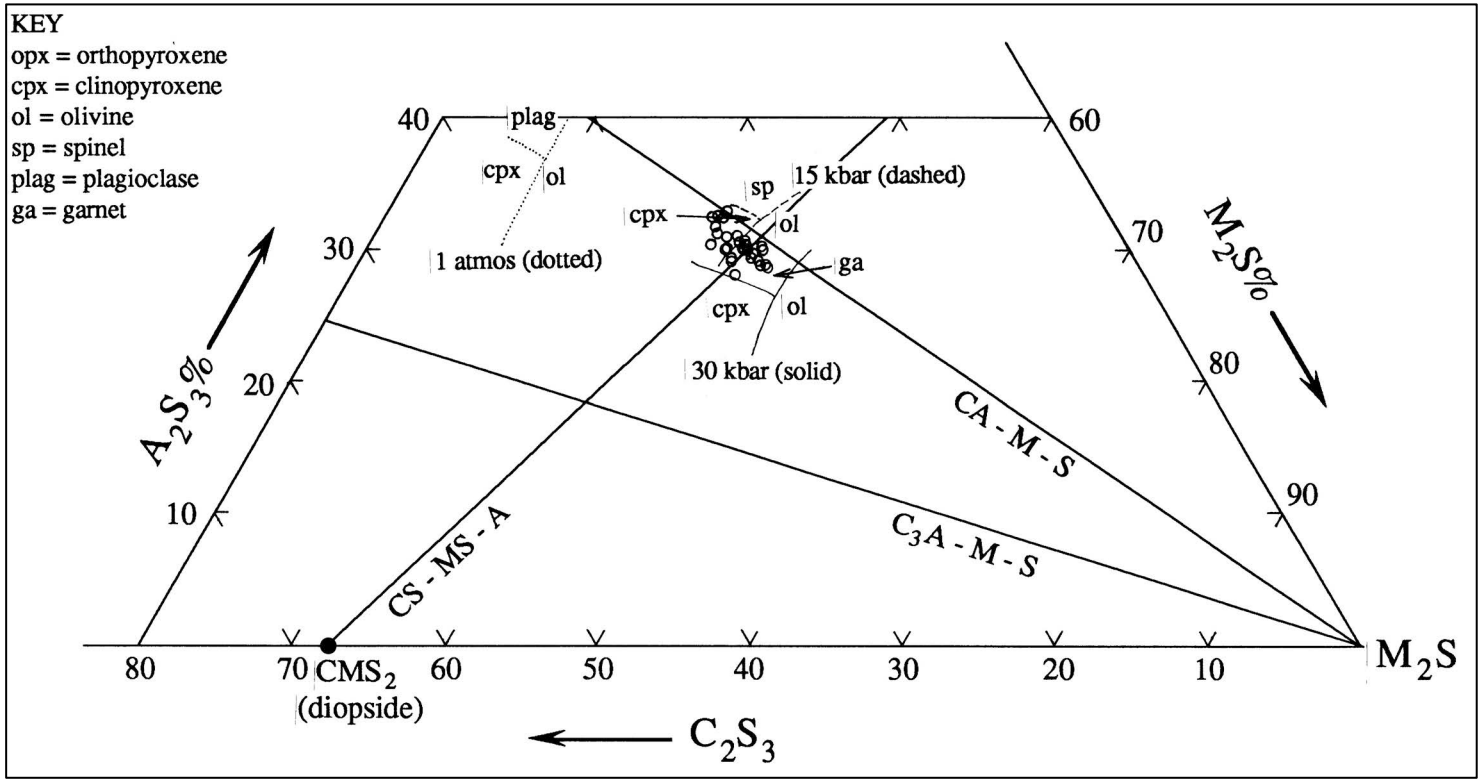


Figure 5.9.4. Projection from MS (enstatite) into C_2S_3-A_2S_3-M_2S, showing little apparent trend towards M_2S, due to the less oblique projection.

5.9.1.3 C_3A - M - S

This projection is shown in Figure 5.9.5. It resembles the plane CA - M - S, used to examine the trend in MS - CS - A, but has its C_3A vertex nearer to C on the CA-join. This brings the plane much closer to its projection point (CMS_2) than the Velay basalt data, with the result that the data appear to be tightly clustered. Again CA - M - S should be used as the best illustration of the true scatter in the data.

C_3A - M - S contains the trace of the olivine-gabbro plane which again shows that the Velay lavas lie to the SiO_2-poor side. The four-phase equilibria at 1 atmosphere, 5 and 10 kbar are all to the SiO_2-rich side of this line. The closest invariant point to the data is that of 15 kbar, for cpx+ol+opx+spinel+liquid.

5.9.1.4 CAS_2 - M_2S - CMS_2

This plane is the olivine gabbro join studied by Presnall *et al* (1978). The Velay basalts are shown projected into this plane from enstatite (MS) in Figure 5.9.6. The phase boundaries of Presnall *et al* (1978) would not be expected to coincide with those for natural lavas, since they were produced using only pure CMAS components, but they can be used to indicate the general relationships. To determine the equivalent position of the phase boundaries for natural lavas at 15 kbar in the O'Hara (1968) system, the original data at 13.5 kbar from Green and Ringwood (1967) were plotted. These loosely define phase boundaries with the pattern shown on the diagram, demonstrating that the cpx and spinel fields are in contact. Presnall *et al* (1978) found this to occur only at pressures greater than about 5 kbar for the pure CMAS system.

Mukhopadhyay (1990) conducted a detailed investigation of the di-$CaTs_{ss}$ + fo + sp + liquid univariant line in the CMAS system and found that the assemblage was only in equilibrium between 4 and 20 kbars. He noted that the temperature maximum on this line at 20kbar was well to the silica-undersaturated side of the CAS_2 - M_2S - CMS_2 join and would cause moderately silica-undersaturated liquids to migrate towards more silica-rich compositions. At the same time the assemblage would be subject to the reaction:

$$\text{fo} + \text{liquid} \Rightarrow \text{di-CaTs}_{ss} + \text{sp}$$

Thus the Velay ankaramites were alkali basalts which equilibrated at pressures of 4 to 20 kbars and fractionated ol + di-$CaTs_{ss}$ + sp (+ magnetite). The cumulate blocks contain no olivine and probably represent a later stage in which olivine has become unstable and only di-$CaTs_{ss}$ + sp are crystallising. The phase relations predict that the clinopyroxenes involved in this fractionation would be highly aluminous, becoming more so with evolution, at the same time as the liquid changes from silica-undersaturated to silica-saturated. This is exactly as seen in the Velay, with FaTs (= CaTs with some $Fe^{3+} \Leftrightarrow Al^{3+}$ substitution) of 15% in the cpxs of the ankaramites (section 3.2.3) and 23% FaTs in the cpxs of the most primitive cumulates (section 4.6.1). The change from silica-undersaturation to

saturation in the cumulates was described in section 5.7.2, but in section 5.8.4 it was shown that this change was mainly due to granite contamination.

5.9.1.5 Conclusions

The analysis attempted here is necessarily very crude, but the different projections do give fairly consistent results, suggesting that the Velay basalts are either partial melts of a spinel lherzolite at about 15 kbar (40-50 km depth), or equilibrated with cpx+opx+ol+spinel at that pressure.

As a source the mantle at 50km would not seem to be very promising since it would lie within the lithosphere for a normal continental section. There are two possible explanations, the first being that the asthenosphere rose to 50km due to thinning of the lithosphere. The decompression involved would account for the partial melting and volcanism. In favour of this is the presence of an anomalously low velocity zone beneath the crust of the Massif Central volcanic zone, to a depth of at least 50km (see section 2.2). This was interpreted by Perrier and Ruegg (1973) as being due to the presence of a partial melt in the mantle. However, this partial melt may have formed deeper in the mantle and migrated upwards into the lithospheric mantle.

In Chapter 2 it was concluded that the Velay basalts originated as partial melts at a depth of at least 100km, and migrated upwards and equilibrated with spinel-lherzolite before being erupted.

5.9.2 Other phase relations

In an attempt to determine its hydrous phase relations, Merrill and Wyllie (1975) conducted melting experiments on a kaersutite eclogite nodule, equivalent in composition to olivine basanite, with both H_2O-saturated conditions and 0.4wt% H_2O. The PT-graphs they produced are shown in Figure 5.9.7. No plagioclase, spinel or magnetite was reported in these experiments.

The first two diagrams in this figure are for equilibrium crystallisation and the liquidus diagram gives the most useful information for fractional crystallisation, showing that for any pressure at least 2 wt% H_2O is needed to give amphibole on the liquidus. Section 5.9.1 concludes that the Velay basalts apparently equilibrated at 15 kbar, but they show no more than a trace of amphibole, suggesting that their H_2O-content was less than 2wt%.

In the case of the Velay cumulate samples, assuming an olivine basanite parent magma, a pressure of 17 - 21 kbar is needed to give cpx on the liquidus without olivine, as observed in the nodules. The main limitation on this technique is the degree by which the Velay primary melt differs from the kaersutite eclogite used in the experiments. Nevertheless, a high pressure is suggested for the most primitive cumulate samples.

Cawthorn and O'Hara (1976) made an ambitious attempt to determine the hydrous phase relations in the system CaO-MgO-Al_2O_3-SiO_2-Na_2O-H_2O. To represent their results they used two of the CMAS projections from O'Hara (1968) (see section 5.9.1), at 5 kbar with H_2O-excess (8%wt) and 4% and 6% Na_2O. The authors found that amphibole was only able to nucleate with $Na_2O > 3\%$ and

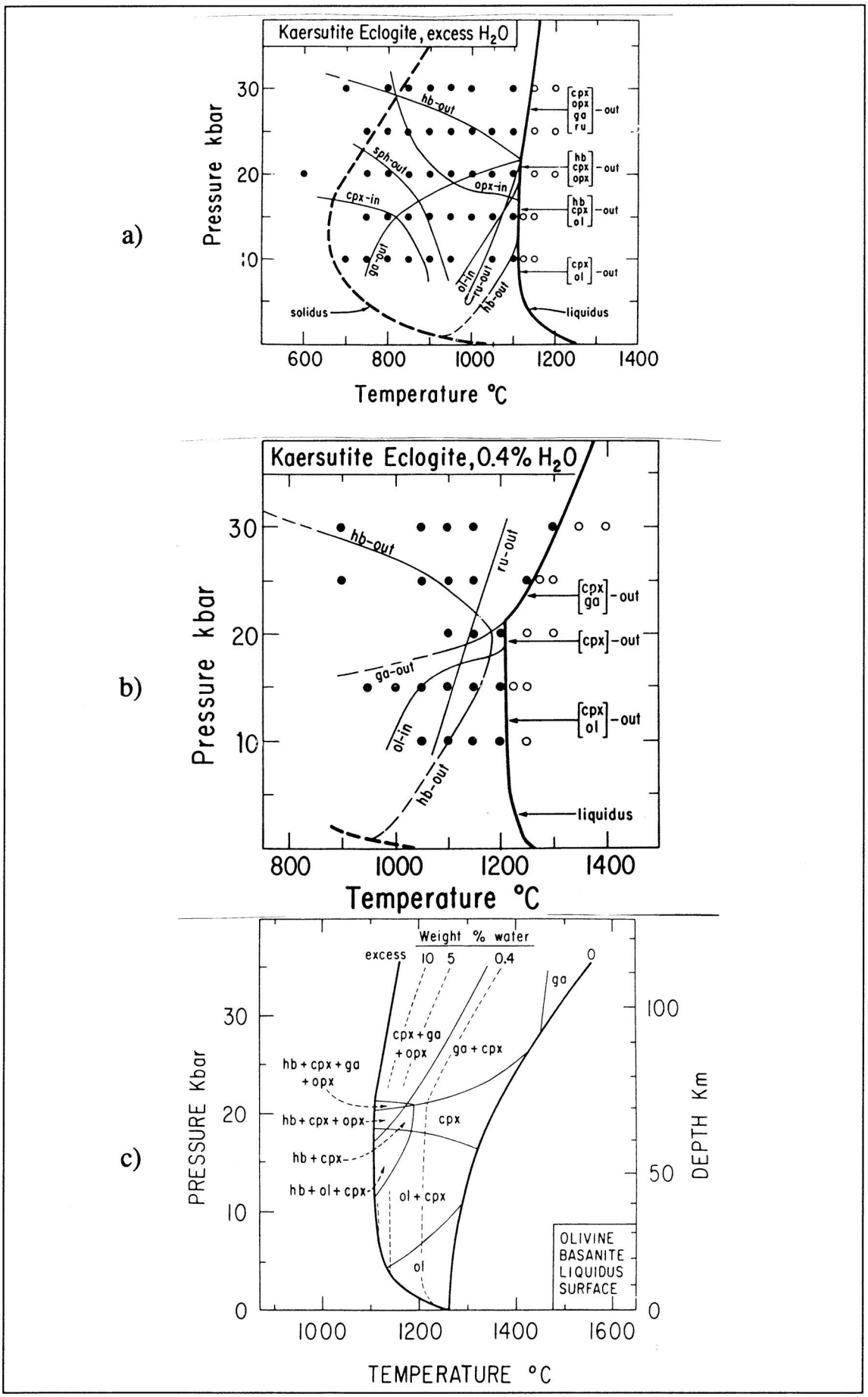


Figure 5.9.7. Experimental PT-diagrams for a kaersutite eclogite nodule, equivalent in composition to olivine basanite, from Merril and Wyllie (1975); a) with excess H_2O, b) with 0.4%(wt) H_2O, c) near-liquidus phase relations with H_2O% contours.

that it then tended to replace plagioclase/spinel as the aluminous phase. The degree of simplification severely limits the usefulness of the diagrams, but does allow a prediction of generalised liquid evolution. The sequence of *equilibrium* crystallisation for a typical basalt was:

$$\text{ol+cpx} \Rightarrow \text{ol+cpx+amph} \Rightarrow \text{amph} \Rightarrow \text{amph+opx}$$

and *fractional* crystallisation gave:

$$\text{ol+cpx} \Rightarrow \text{amph} \Rightarrow \text{amph+plag}$$

Due to the nature of the projections used the relative order of appearance of olivine and cpx could not be determined.

The sequence of fractional crystallisation bears some resemblance to that seen in the Velay lavas and especially to that in the cumulates. The non-appearance of olivine in the cumulates may be due to elevated pressure, but given the number of unquantified variables such as composition, P_{CO_2} (clearly important in the Velay), degree of low-pressure equilibration and so on, it would be unwise to come to any firm conclusions.

The results cited in this section suggest that the cumulates crystallised at a relatively high pressure to account for the absence of olivine. The simultaneous absence from these rocks of either orthopyroxene or garnet limits the pressure to less than about 20 kbar. The basalts are harder to assess, since only the ankaramites show significant phenocryst-content, with spinel and Ti-magnetite added to olivine and cpx. The information in Merrill and Wyllie (1975) suggests that they crystallised at less than 16 kbar.

5.10 Thermometry and barometry

Many geothermometers have been proposed and some of these are now well established and calibrated, for example the FeTi-oxide thermometer. Geobarometers are less common and usually have much lower resolution than needed, due to the overwhelming effect of temperature on most chemical equilibria. Of those that have been devised, many cannot be used in the Velay since the appropriate mineral assemblage does not occur. The following sections detail results from the few applicable systems.

Wherever possible microprobed mineral analyses were recalculated for Fe^{2+} and Fe^{3+} using the method described by Droop (1987), with both charge and cation balancing.

5.10.1 Coexisting Ti-magnetite and ilmenite thermometer

This was first proposed by Buddington and Lindsley (1964). They determined experimentally temperature and oxygen fugacity for various Ti-magnetite and ilmenite compositions, based on the reactions:

$$Fe_3O_4 + FeTiO_3 \Leftrightarrow Fe_2O_3 + Fe_2TiO_4$$

$$6Fe_2TiO_4 + O_2 \Leftrightarrow 2Fe_3O_4 + 6FeTiO_3$$

One problem with their system is that it took no account of the other components, such as

MgO, Al_2O_3 and MnO, which are often present in natural minerals. Several authors have tried to remedy this by suggesting *ad hoc* recalculation procedures for Ti-magnetite and ilmenite, for example Carmichael (1967), Anderson (1968), and others tried to assess the effects of the impurities, for example Speidel (1970) and Powell and Powell (1977). The most up-to-date scheme available is that of Anderson and Lindsley (1988) combined with the recalculation procedure of Stormer (1983). These are both based on equilibrium thermodynamics and take good account of other components present. They were both used for this study.

In the Velay lavas and cumulates Ti-magnetite is ubiquitous but ilmenite occurs only in the cumulates. In addition, alteration of Ti-magnetite reduces still further the number with both oxides measurable. Only Ti-magnetites with $SiO_2 \leq 1\%$ were used, although they may already be unacceptably altered. The Ti-magnetites in the most primitive cumulates contain up to 25% oxides other than FeO, Fe_2O_3 or TiO_2 and ilmenite can have up to 10%. The recalculation scheme provided by Stormer (1983) seems to give good results in spite of this.

The results obtained are given in Table 5.10.1 and Figure 5.10.2 plots temperature against oxygen fugacity (f_{O_2}). A fractionating body of magma remains at a fairly constant oxygen fugacity after it forms, with changes controlled mainly by silica activity. Since ultramafic xenoliths, and by implication the mantle, tend to have f_{O_2} near the quartz-fayalite-magnetite (QFM) buffer (Blundy *et al* 1991), basalts formed as partial melts of the mantle tend to have f_{O_2} within one or two log units of QFM. More evolved magmas may have higher f_{O_2}, largely due to SiO_2-increase. Figure 5.10.2 shows that the Velay cumulates plot about one log unit above QFM, slightly oxidised with respect to the mantle but well within the normal range for basalts.

Figure 5.10.3 attempts to relate the temperatures of the cumulates to their degree of evolution, as measured by Na_2O-content. A steady decrease in temperature from the primitive blocks to the evolved blocks would be expected, but block 88/14u does not fit this pattern. Its temperature was calculated from a only single oxide pair, as was that of 88/14s, and neither are therefore very reliable. The temperatures given by the other blocks seem to be reasonable.

5.10.2 Al^{IV} in amphibole thermobarometer

This is a relatively recent system, the parameters for which are still being refined. Nabelek and Lindsley (1985) proposed that Al^{IV} in amphibole could be used to derive temperatures with a pressure correction. Hammarstrom and Zen (1986) suggested that the relationship was particularly appropriate for calc-alkaline granitoids with nine equilibrium phases and fairly constant f_{O_2} and temperature, in which pressure would exert the main control on amphibole Al^{IV}-content. They calibrated their barometer using natural data with estimated pressures of crystallisation. Johnson and Rutherford (1989) attempted to eliminate uncertainties in the formulation by conducting melting experiments on a suitable natural rock, again with nine coexisting phases. Their data significantly

Table 5.10.1

Temperatures obtained for cumulate blocks using coexisting Ti-magnetite and ilmenite

Cumulate block	$X_{Fe_2TiO_4}$	X_{FeTiO_3}	Calculated temperature (ºC)		Oxygen fugacity ($logf_{O_2}$)	
			maximum	minimum	maximum	minimum
86/38a	0.597	0.825				
	0.548	0.831				
	0.548	0.830				
	0.534	0.834				
	0.535	0.838				
	0.561	0.830	1139	1043	-8.4	-9.6
86/14j	0.489	0.854				
	0.496		985	979	-10.4	
88/14u	0.376	0.908	820		-13.6	
88/14s	0.466	0.848	967		-10.6	
88/14a	0.510	0.888	942	879	-11.4	-12.4
	0.434	0.893				

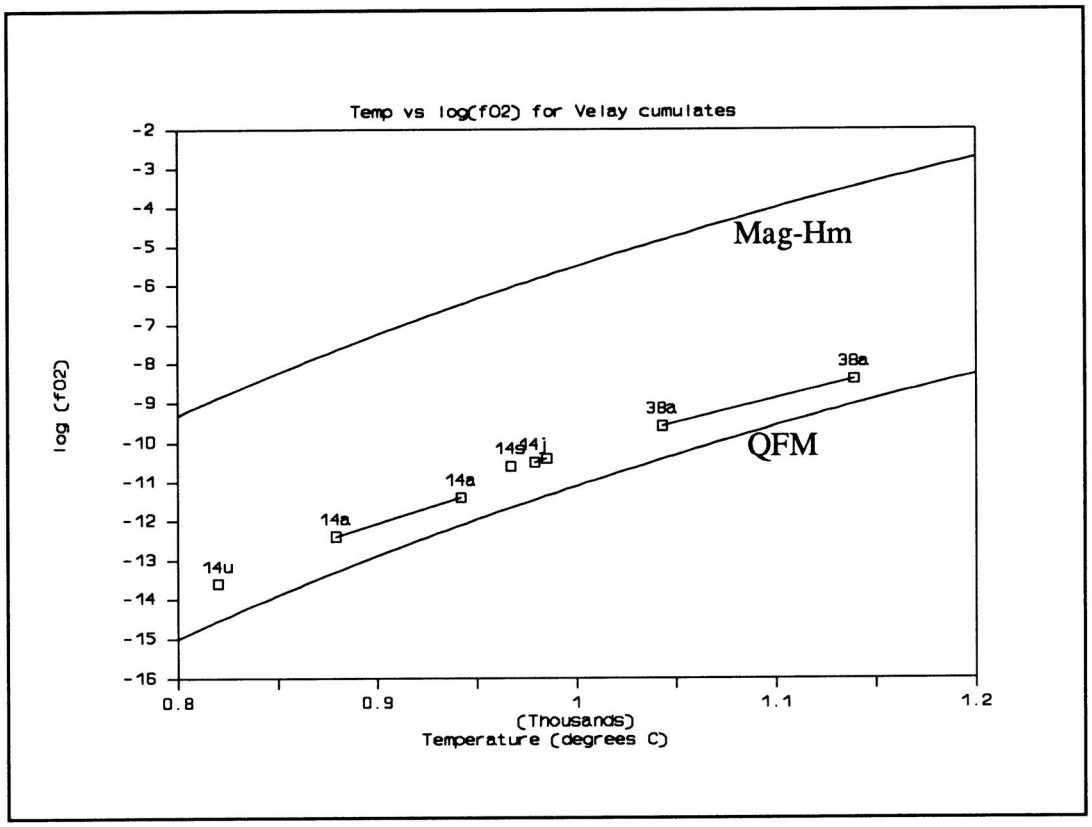


Figure 5.10.2. Oxygen fugacity versus temperature for some of the Velay cumulate blocks, calculated using coexisting Ti-magnetite and ilmenite. The quartz-magnetite-fayalite (QFM) and magnetite-hematite (Mag-Hm) buffers are shown for comparison.

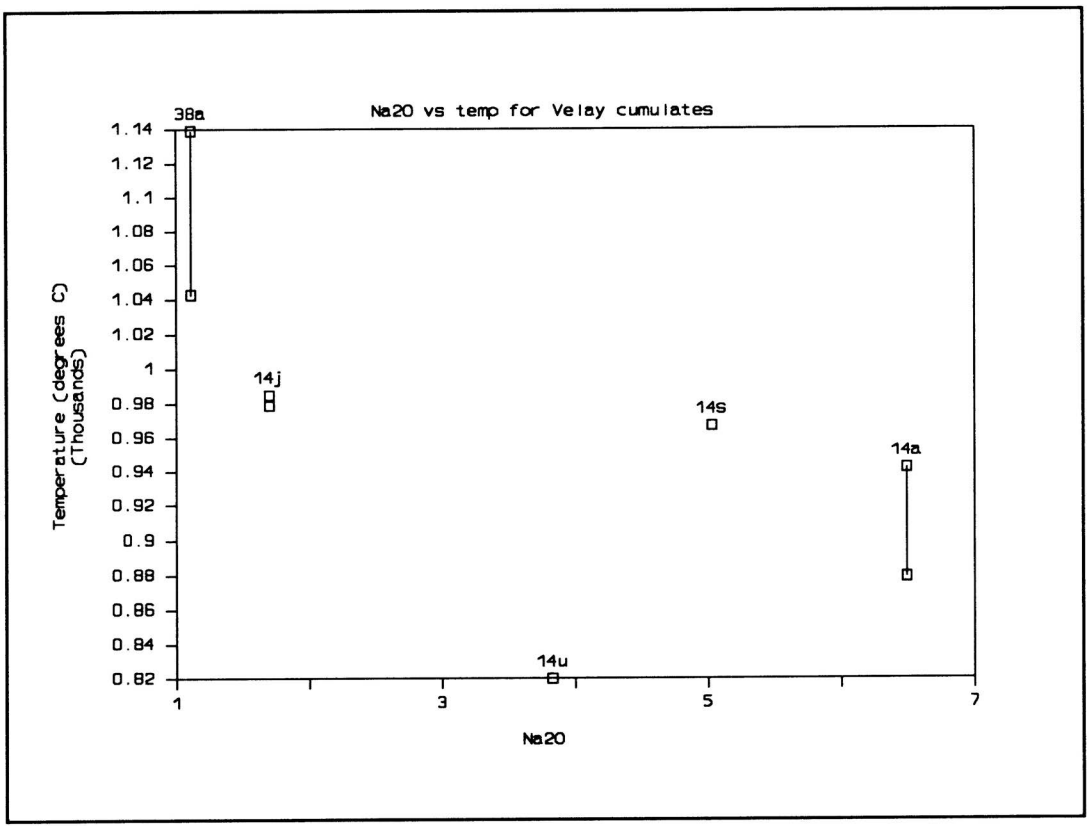


Figure 5.10.3. Temperature versus Na_2O-content for some of the Velay cumulates, where Na_2O serves as an index. Blocks with high Na_2O represent more evolved liquids and would be expected to have equilibrated at lower temperatures.

improved the precision of the barometer and also its accuracy. The narrow temperature range of their experiments limited the barometer to rocks that solidified at 720-780˚C.

Most recently, Blundy and Holland (1990) produced a new thermodynamically-based formulation from which they concluded that temperature had a stronger effect on amphibole composition than pressure, but that a large suite of coexisting phases was not necessary before the method could be applied - in particular the presence of quartz was not crucial. The correlation between Al^{IV} and pressure was found to be weak, although no attempt was made to use analyses equilibrated at a similar temperature.

Problems that may affect the Velay rocks include the silica-undersaturated nature of the magmas and high TiO_2-contents of their amphiboles. Both factors can increase amphibole Al^{IV}-content, hence the calculated pressures (at a given temperature) are a maximum.

Table 5.10.4 shows the data used, and Figure 5.10.5 is a pressure-temperature graph for the cumulates, summarising all the constraints on their crystallisation. The shaded box in the centre of the graph indicates the temperature range over which the magma probably cooled and the depth at which the chamber was emplaced. The vertical extent is the uncertainty and has no bearing on the size of the chamber. The constraints used include those from this section and the temperatures from section 5.10.1. In addition, Mukhopadhyay's (1990) pressure constraint, described in section 5.9.1.4, limits the magma chamber to ≥ 4 kbars. The absence of granulitic material associated with the cumulates and the abundance of granite fragments suggests the magma chamber was within the Velay granite, which is thought to extend to a depth of 16km from a seismic reflection data (section 4.6.2).

From the data available, the magma chamber of the cumulates was probably emplaced at 5 - 7 kbars, roughly equivalent to a depth of 15 - 20km, and cooled from its emplacement temperature of about 1200˚C to about 900˚C at the time of its eruption.

5.10.3 Ca in olivine and clinopyroxene thermobarometer

The Ca-content of olivine coexisting with clinopyroxene can be used to determine a pressure-temperature relationship in suitable rocks. This thermobarometer has been studied by several authors, in both synthetic and natural systems. Adams and Bishop (1986) produced a thermodynamically based thermobarometer in the CaO-FeO-MgO-SiO_2 system, and more recently Köhler and Brey (1990) calibrated their formula using experiments on a natural lherzolite.

The barometer of Adams and Bishop (1986) rejected the Velay clinopyroxenes as too aluminous. Köhler and Brey's (1990) model has no such test but clearly the results obtained using Al-rich clinopyroxenes are suspect. Similarly the lherzolites have olivines reaching Fo_{92}, whereas those of the Velay lavas reach only Fo_{86}. Another problem noted by the authors of these papers is the secondary fluorescence of Ca X-rays from clinopyroxenes adjacent to olivines, giving excessive apparent Ca-contents (phase boundary effect). This was avoided in this study by using analyses from

Table 5.10.4

Data used for AL^{IV}-in-amphibole thermobarometer

Specimen	**Si in amphibole** atoms p.f.u. (values are the mean of several analyses – number given in brackets)	**X_{ab} of plagioclase**	**Temperature at 1 atm. (ºC)**	**Temperature 10 kbars (ºC)**
Cumulates				
86/38e	5.7745 (6)	0.2531 (7)	1226	815
86/38f	5.9890 (6)	0.5933 (3)	1079	764
86/38g	5.8702 (5)	0.4286 (3)	1168	819
86/38h	5.7663 (3)	0.3898 (4)	1206	839
88/14e	6.0101 (2)	0.4823 (2)	1124	795
88/14i	6.0719 (1)	0.4856 (4)	1105	781
88/14j	5.7378 (2)	0.2215 (4)	1258	827
88/14n	5.8119 (2)	0.3750 (5)	1189	823
88/14u	5.9605 (3)	0.5546 (5)	1108	786
88/14w	5.8738 (2)	0.5294 (3)	1150	818
Lavas				
84/19a (Monac)	5.8037 (3)	0.4731 (2)	1192	845
86/56 (upper flow, St Clément)	6.0015 (1)	0.5820 (2)	1081	765
87/74 (Veyrines)	5.8495 (1)	0.6657 (2)	1087	769
87/70 (Chanis)	5.9447 (2)	0.6566 (4)	1063	751

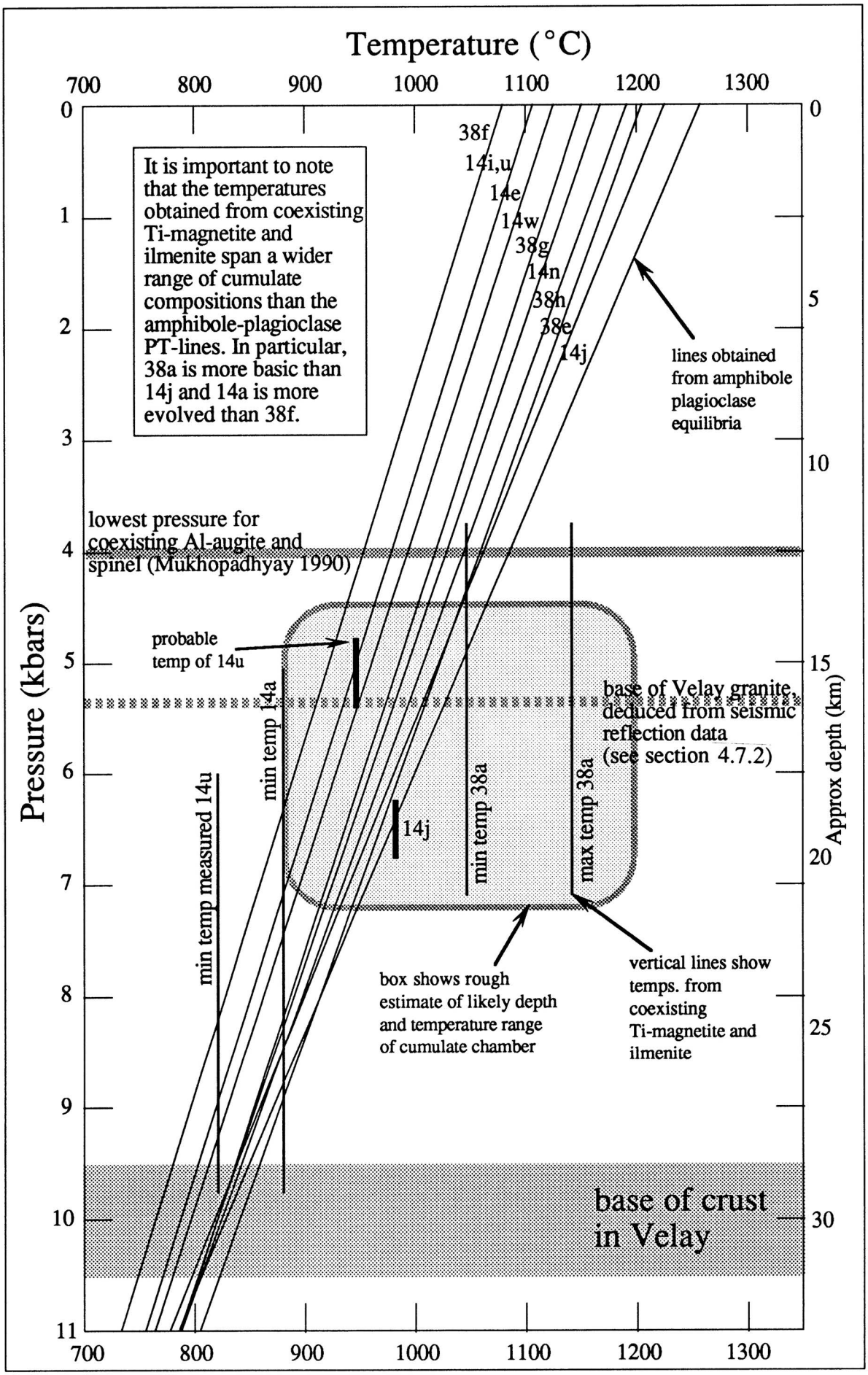


Figure 5.10.5. Pressure-temperature graph summarising all information relating to the depth of the cumulate magma chamber. The conclusion is that the cumulates crystallised towards the top of the lower crust, at a pressure of about 5 – 7 kbar.

the centre of the olivine phenocrysts, which show no zoning.

The Velay ankaramites, with coexisting clinopyroxene and olivine phenocrysts, are suitable for this thermobarometer, subject to the problems described above. After rejecting all unsuitable analyses the mean compositions of the olivine and clinopyroxenes were taken for each rock. These data are given in Table 5.10.6, and the results plotted on Figure 5.10.7. Also on this graph are the pressure-temperature lines for the northern Velay trachytes from the Al^{IV} in amphibole thermobarometer. These can be equated petrologically with the cumulates, and the lines they give on this graph are similar to those produced by the cumulates. By analogy alone, their depth of formation is presumed to be the same as that of the cumulates; 5 - 7 kbars.

The ankaramites range from around 1100˚C at P=0 to 1150-1200˚C at P=10 kbars. Mukhopadhyay's (1990) minimum limit of 4 kbars for the assemblage olivine + Al-rich augite + spinel is also marked. There is no way of directly measuring the temperature at which these lavas equilibrated, but in Green and Ringwood's (1967) anhydrous alkali basalt melting experiments, at various pressures, the third phase after olivine and cpx always formed above 1200˚C. Obviously this can be strongly affected by changes in the bulk composition of the starting material, fractional crystallisation and the addition of H_2O, but if we use 1200˚C ± 25˚C as a constraint it implies depths around the base of the crust or deeper, in line with the conclusion from the CMAS phase diagrams in section 5.9.1.

5.10.4 Conclusions

From the rather limited evidence available, the lavas of the Velay seem to be derived from a range of depths. The parental alkali basalts and related ankaramites show equilibration at pressures of about 10-15 kbars, at the base of the crust and deeper, from both phase relations and thermobarometry.

The cumulates and, by analogy, the phenocryst-rich trachytes from the northern Velay equilibrated at mid-crustal depths, at pressures around 5 - 7 kbars, which with the addition of crustal contamination caused them to follow a fractionation trend leading to quartz-trachytes. Their depth is well constrained by thermometry, thermobarometry, phase relations and coexisting wall-rock fragment composition.

Phonolites form the last group of lavas. No thermometers or barometers apply to their minerals, and their phase relations are not sufficiently well constrained to indicate their depth of equilibration. The surface uplift, noted in section 1.5, which occurred just prior to the eruption of the southern Velay phonolites, is sufficiently intense and localised to suggest that it was caused by near-surface injection of lavas to form large magma chambers. This conclusion is supported by the presence of the Suc de Sara and Rocher des Pradoux ring dykes (Mergoil 1968), which have a diameter of < 2km. The subsidence of an upward-tapering cylinder of rock into a magma chamber is needed for their formation, and with a ring-dyke diameter of 2km the depth of the chamber would be unlikely to exceed 5km. An independent calculation based on the eruptive pressure of the phonolite

Table 5.10.6

Data used for Ca-in-olivine and clinopyroxene thermobarometer

Specimen	**Ca in olivine** atoms p.f.u. (values are the mean of several analyses – number given in brackets)	**Ca in cpx** atoms p.f.u.	**Temperature at 1 atm. (ºC)**	**Temperature 10 kbars (ºC)**
84/43 ankaramite from St Clément section	0.00405 (2)	0.7552 (1)	1083	1146
86/53 ankaramite from near Machabert	0.0049 (3)	0.7888 (2)	1106	1170
86/63 ankaramite from Le Petit Champagnac	0.0059 (3)	0.8580 (8)	1122	1187
87/29 ankaramite from La Chaud de la Croix quarry	0.00515 (2)	0.8614 (9)	1100	1164
87/43 ankaramite from dyke on road near Hautevialle	0.0047 (3)	0.8197 (3)	1093	1157

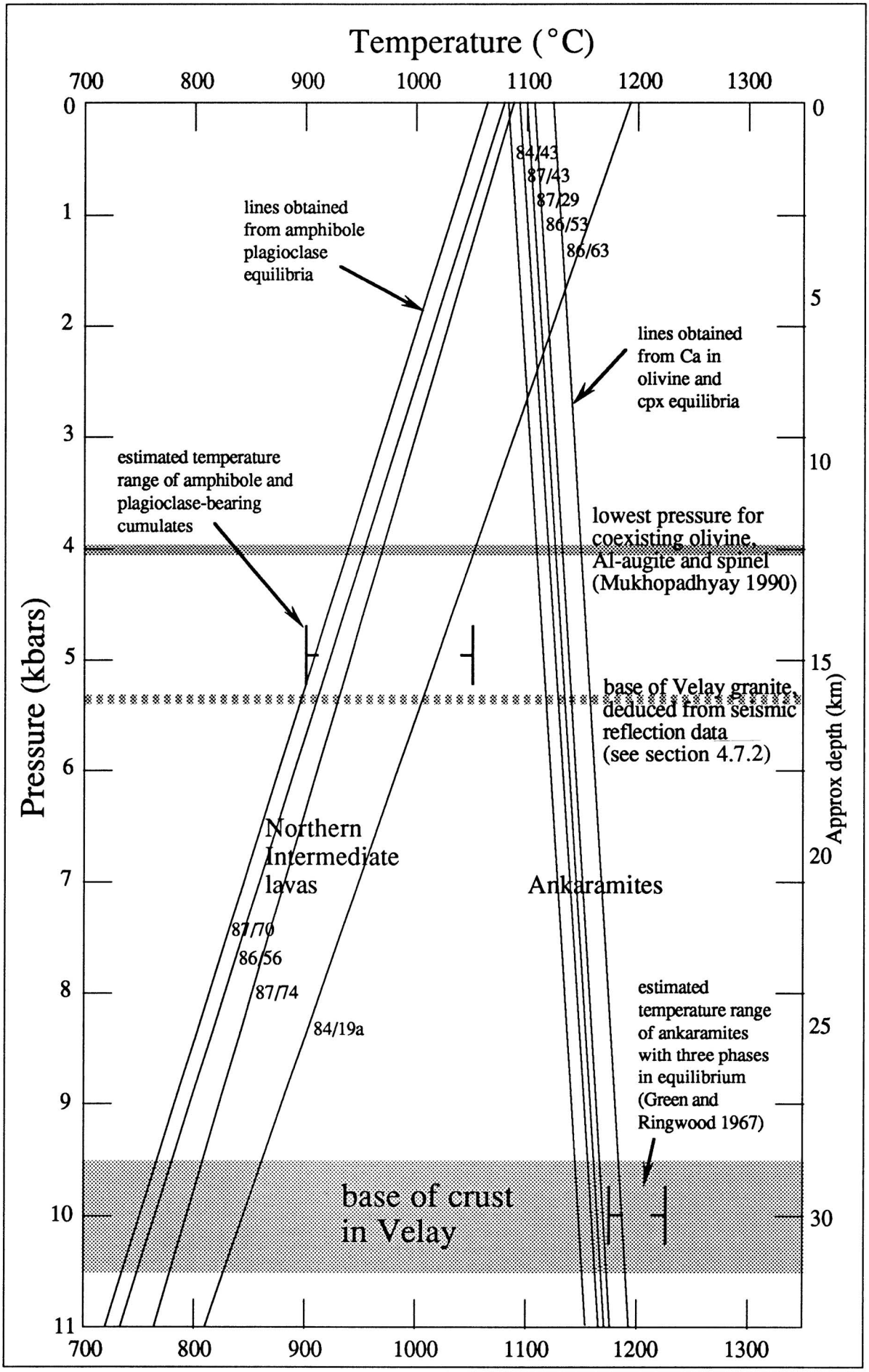


Figure 5.10.7. Pressure-temperature graph summarising all information relating to the depth of some of the Velay lavas. The conclusion is that the ankaramites crystallised at or below the base of the crust, whereas the trachytes from the northern Velay equilibrated at a similar depth to the cumulates.

domes (section 1.6.3) gives ~4km to the top of the magma chambers. Thus the fractionation of basalt to form phonolite took place in chambers within 5km of the surface.

In section 5.1 it was noted that Berger and Lanöe (1978) calculated a temperature range of 1200 - 800˚C for the Velay lavas, with $f_{O_2} = 10^{-11}$ (at 1000˚C) and $P_{H_2O} = 3.0 \pm 0.6$ kbars. Apart from the P_{H_2O}, which is rather high for the phonolites, these values are in reasonable agreement with those calculated in this study for the lavas and cumulates. Maury and Varet (1980) concluded that the phonolites formed in shallow magma reservoirs, whereas the quartz-trachytes formed at $P_{H_2O} = 1 - 3$ kbars. If $P_{Total} > P_{H_2O}$ then P_{Total} may have been similar to that estimated in this study (5 - 7 kbars).

5.11 Summary and conclusions

The hawaiite to phonolite evolved lavas of the Velay were formed from an alkali basalt parent by a process of crystal-liquid fractionation, either by crystal settling in a magma chamber or by flow crystallisation on conduit walls. No combination of partial melting, magma mixing, contamination or other established processes is able satisfactorily to account for the petrography, observed trends of compositional variation, REE-patterns and the existence of related cumulates. The remaining problems of bimodal distribution and the order of eruption are addressed in Chapter 1.

To calculate the parental magma a method of back-projection of compositional trends was used. This resulted in a fairly unusual composition for a primitive basalt, with 5.5% TiO_2 and MgO/FeO not in equilibrium with mantle olivine. Incremental addition of equilibrium olivine was tried as an alternative, and after 50% olivine addition the calculated composition was that of a picrite. This was also rejected as being unlikely due to the absence of such magnesian lavas in the Massif Central. The observation that similar basalts in the Massif carry lherzolite xenoliths and are therefore probably primary, indicates that equilibrium with mantle olivine is not a prerequisite for a parental magma. Accordingly, the Velay parent magma was calculated by olivine addition to reach the MgO/FeO of the lherzolite-bearing lavas. The lack of equilibrium with mantle olivine suggests modified mantle underlies the Massif Central, possibly altered by a process of mantle metasomatism.

The fractionation of the Velay lavas was investigated both qualitatively, using the variation of major and trace elements combined with petrography, and quantitatively, using mixing calculations with the major element contents of bulk lavas and their phenocrysts to confirm which minerals were being extracted and in what proportion. The results were, with minerals in decreasing order of importance:

primitive to evolved basalt	⇒	*cpx, ol, Ti-mag, spin-herc*
evolved basalt to hawaiite	⇒	*amph, cpx, ol, Ti-mag*
hawaiite to intermediate lava	⇒	*amph, plag* An_{56}*, Ti-mag, apat, cpx*
intermediate lava to miaskitic phonolite	⇒	*plag* An_{56}*, amph, Ti-mag, cpx, apat*
miaskitic to agpaiitic phonolite	⇒	*Kspar, amph, Ti-mag, apat, sphene*
intermediate lava to quartz trachyte	⇒	*plag* An_{56}*, biot, Ti-mag, apat, cpx*

The fractionation stages leading to quartz trachyte show many similarities with the cumulate series.

Constraints imposed by the degree of incompatible trace element enrichment show that the mixing calculations give too much fractionation, possibly due to excessive amphibole in the mixes.

All the data indicate that there were two fractionation series in the Velay, one leading from alkali basalt to phonolite, the other diverging at the mugearite/benmoreite level and leading to quartz trachyte. The point of divergence is marked by the appearance of biotite, which removes K_2O and leaves CaO, suppressing K-feldspar crystallisation and favouring plagioclase. It is not clear at this stage whether the biotite *causes* the increased silica-saturation or is a *consequence* of it, perhaps by granite contamination.

Examination of the bulk chemistry of the cumulate blocks shows that there is good correlation between predicted and observed variation in major and trace elements. This confirms the conclusion, reached on the basis of their petrography and mineral chemistry, that they formed by crystal settling from a melt. Even the compositions of their interstitial glasses are as would be expected. However, in contrast to equivalent glass from the Laacher See, which evolves towards phonolite, the Velay cumulate glasses evolve towards silica-saturated compositions, with up to 20% normative quartz. This is the same trend as shown by the cumulate blocks themselves.

The evidence shows that the cumulates were deposited by a body of magma evolving from alkali basalt to quartz-trachyte. Again, at this stage it is not possible to distinguish whether contamination or a change in the phase relations caused the deviation from the basalt-phonolite path.

The measurement of forty samples for $^{87}Sr/^{86}Sr$ allowed the investigation of possible granite contamination and the nature of the basalt source. Most lavas, especially the basalt, have initial $^{87}Sr/^{86}Sr$ in the range 0.7033 - 0.7035. The exceptions are the phenocryst-rich northern intermediate lavas and some of the cumulates, with values up to 0.705. The AFC-model is used to interpret these data since simple one-stage contamination can be ruled out. Although the data-set is extremely small it indicates rates of contamination 0.05 to 0.1 × the rate of fractionation. A total of 11% contamination affected the most silica-saturated lava, which seems to be the cause of the silica-saturation trend. This resolves the question raised by earlier data.

The uncontaminated basalt-phonolite series has low initial $^{87}Sr/^{86}Sr$ values, similar to those of OIB's and some CAB's. The lithosphere is unlikely to be the source for the Velay basalts since it would be expected to produce higher values than those of OIB's.

The phase relations of the Velay basalts are investigated using the CMAS-system, which attempts to account for the many significant components present in natural alkali basalts. In all projections of this system that were examined the basalts plotted near the 15 kbar univariant point, showing equilibrium with olivine, cpx, opx and spinel (i.e. spinel lherzolite). Some spinel-bearing ankaramites from the Velay indicate similar depths of equilibration. A recent study of the effect of Al solid-solution in cpxs at high pressure showed that the assemblage Al-rich cpx + olivine + spinel could only coexist between 4 and 20 kbars.

The equilibration of basalts at 15 kbars implies that it took place within the lithosphere. Other evidence reported in Chapter 2 shows that the Massif Central lavas were partial melts of garnet peridotite adiabatically uplifted from depths > 100km. These melts were equilibrated with spinel lherzolite before their eruption.

To complement the study of the phase relations, pressure and temperature were directly measured from equilibrium mineral compositions. Coexisting Ti-magnetite and ilmenite gave a temperature range of 1100 - 900°C for the primitive to evolved cumulates. When combined with the Al^{IV} in amphibole thermobarometer and other constraints a crystallisation pressure of 5 - 7 kbars was indicated. The Ca in olivine and cpx thermobarometer was used to give a pressure of 10 - 15 kbars for the Velay ankaramites. Phonolites offered no suitable mineral assemblages, but other evidence suggests shallow (< 5km) magma chambers.

These pressure and temperature estimates are in reasonable accord with previous work.

Chapter 6

Synthesis

6.1 The Massif Central

The Massif Central is a 300km-diameter area of elevated Hercynian crust in south central France, which suffered extension and graben formation in the Oligocene, and major alkaline volcanism from the mid-Miocene to the present. Geophysical work has shown that anomalously low density, low seismic velocity mantle, probably containing a small proportion of melt, underlies the volcanic areas, and mantle xenoliths show pervasive deformation, due either to asthenospheric diapirism or to extensional shear of the lithospheric mantle. Various lines of evidence suggest that the source material for the basic lavas was garnet-lherzolite, at depths of at least 100km.

The cause of the volcanism is harder to determine. A hotspot seems unlikely due to the small size of the volcanic area and the lack of a geographical age progression. Mantle metasomatism may

provide a more suitable explanation but it is difficult to assess, and most of the supposed metasomatised xenoliths are probably fragments of the lithospheric mantle.

The similarity of the Massif Central basic lavas to those of the ocean island basalts strongly suggests that continental lithosphere cannot have been a major source. Similarly the exclusion of the hotspot model rules out a lower mantle source. This leaves the convecting upper mantle (including the asthenosphere) as the only suitable source for the Massif lavas. However, the asthenosphere is thought to be strongly depleted in incompatible elements due to the extraction of mid-ocean ridge basalts, raising the problem of how it can produce the incompatible-element enriched alkali basalts. Possible explanations include the presence of trace-element enriched streaks (small scale heterogeneity) or the extraction of extremely small (< 0.5%) partial melts.

6.2 Velay oriental volcanism

The Velay oriental lies to the south-east of the Massif Central volcanic province and is one of the eight main volcanic districts. Like the Aubrac and Devès, the Velay oriental is a basalt plateau, but with the addition of abundant phonolite hills, with forms which show they were extruded as viscous lavas. The plateau reaches a maximum thickness of 200m, with the most basic alkali basalts at the base, followed by a fairly random sequence of more evolved lavas, up to and including hawaiite, and thin flows of mugearite and benmoreite at the top. The volume proportion of these intermediate lavas is small compared with that of the basaltic lavas and the phonolite, giving a classic "Daly gap" for this district.

The thickest and most complete plateau sections are found in the southern half of the Velay, while in the north the plateau often consists of only two basaltic flows, and intermediate compositions are represented by viscous, phenocryst-rich extrusions.

K-Ar dating shows that the plateau sequence was erupted between 11.7Ma and 7.6Ma, and the phonolites in the south of the Velay between 8.5Ma and 6.5Ma. New work for this thesis confirms these age ranges and establishes that the phonolites of the north were distinctly older than the other Velay lavas, with an age range of 13.3Ma to 10.5Ma.

A contour map of the basement-basalt contact demonstrates the degree of basement uplift, which is deduced to have occurred between about 10Ma and 8Ma. Comparison of the Velay basement uplift with that of Atakor, Mont Dore, Aïr and several in Eastern Australia strongly suggests that it was caused by the injection of basalt into the crust to form a magma chamber which elevated its roof hydrostatically.

Two chambers were formed, at different times in the north and south. The southern chamber had a volume in excess of 100km^3 and could easily have produced all the phonolite seen at the surface by fractional crystallisation alone. The distribution of trace elements in the phonolites and their varied petrography suggest that the chambers were zoned, with irregular roofs.

The scarcity of intermediate lavas, and the virtual absence of explosive volcanism, despite the highly viscous nature of the evolved phonolite magmas, are the two main features which need to be

explained in the Velay. Both are probably due to the contrast in the densities of the basement granite and primitive alkali basalt magma. Initial extension allowed the basalt to rise to the surface via fissures and to build the plateau. As extension weakened the later basalt magma became trapped in a crustal magma chamber as a consequence of its high density compared with the country rock, and proceeded to differentiate. Eventually the density of the evolved magma fell sufficiently below that of the basement granite to enable it to rise under hydrostatic (rather than gas-exsolution) pressure, and to extrude passively onto the surface as viscous domes.

Using the calculated hydrostatic pressure, combined with the maximum height reached by the phonolite domes, an estimate of the depth to the top of the magma chamber was made. The result suggests that the chambers were about 5km below the surface.

The hydrostatic pressure can also be combined with calculated magma viscosity to estimate eruption rates through conduits of various sizes, although the degree of uncertainty renders this rather inconclusive.

6.3 Petrography of the Velay lavas

The basalts and other lavas of the Velay oriental plateau are generally aphyric, with only a few microphenocrysts of olivine in the basalts, and Ti-magnetite, amphibole and apatite in the evolved lavas. The exceptions are the ankaramites, with olivine and clinopyroxene megacrysts and also Ti-magnetite and occasional pleonaste. None of these lavas show any sign of feldspar phenocrysts.

The intermediate extrusions of the northern Velay have abundant phenocrysts, including apatite, Ti-magnetite, sphene, amphibole, biotite, clinopyroxene, plagioclase and K-feldspar. These are similar in composition, appearance and crystallisation sequence in most cases. Some reaction relationships show decreasing oxygen fugacity during their crystallisation. These lavas are unique in the Velay in showing a weak trend towards silica saturation.

The phonolites can be divided into two groups, both mineralogically and chemically. The miaskitic phonolites are less evolved, have sphene and zircon as their Ti,Zr-silicates and nosean as their characteristic feldspathoid. Agpaiitic phonolites are more evolved, have exotic Ti,Zr-silicates such as aenigmatite and mosandrite, and are characterised by the feldspathoid nepheline. They are largely aphyric, with only a few phenocrysts of K-feldspar.

Agpaiitic phonolites are more common in the south than in the north, demonstrating that the division of the phonolites geographically and chronologically into northern and southern groups also extends to the petrography.

6.4 Geochemistry of the Velay lavas

Almost the entire suite of lavas in the Velay oriental can be shown to have formed by simple crystal-liquid fractionation. Evidence in favour of this includes the close match between phenocryst assemblages inferred from the whole-rock geochemical trends and those observed in thin section. The observed curved and kinked trends are also much easier to explain with crystal-liquid fractionation.

Partial melting models cannot explain the observed range in the concentrations of compatible elements, and contamination and melting models are excluded due to the absence of suitable contaminants or end-member magmas. Only crystal-liquid fractionation provides a suitable mechanism to produce the evolved lavas of the Velay, with the separation of crystals from the melt being achieved by flow crystallisation in the plateau lavas and by crystal settling in the phonolites.

Various attempts were made to calculate the parent liquid of the Velay volcanic series, with the conclusion that they were unlikely ever to have been in equilibrium with mantle olivine. This suggests some degree of mantle metasomatism, since the basalts have low $^{87}Sr/^{86}Sr$ and are unlikely to have been contaminated by lithospheric material. The most primitive Velay basalts are therefore probably primary, or have undergone only a small amount of olivine fractionation before eruption.

Fractionation of the lavas was assessed both qualitatively, by examination of major and trace element trends and phenocryst assemblages, and quantitatively, using a least-squares method with phenocryst and whole-rock compositions. It was found possible to model the entire Velay lava series as the result of phenocryst removal from a basalt melt. The steps were, with phenocrysts in order of decreasing proportion:

primitive to evolved basalt	*cpx, olivine, Ti-magnetite, pleonaste*
evolved basalt to hawaiite	*amphibole, cpx, olivine, Ti-magnetite*
hawaiite to intermediate lava	*amphibole, plagioclase, Ti-magnetite, apatite, cpx*
intermediate lava to miaskitic phonolite	*plagioclase, amphibole, Ti-magnetite, cpx, apatite, sphene*
miaskitic to agpaiitic phonolite	*K-feldspar, amphibole, Ti-magnetite, apatite, sphene*
(intermediate lava to quartz-trachyte	*plagioclase, biotite, Ti-magnetite, apatite, cpx)*

Phonolites were shown independently to be 6 - 20% of the parental alkali basaltic magma.

The Velay lavas form two series, the first, from basalt to agpaiitic phonolite, is overwhelmingly the most voluminous and seems to represent the normal low-pressure fractionation sequence. The second series diverges at the level of the benmoreites towards quartz-trachyte and rhyolite, and is marked by the appearance of biotite instead of K-feldspar. It is not clear at this stage whether the appearance of biotite is the cause, or a symptom of, the trend to silica-saturation.

Sr-isotopes show mantle values (0.7033 - 0.7035) for almost all the Velay basalt-phonolite series lavas, which are presumed to be uncontaminated, and to have a sub-lithospheric source. The lavas of the silica-saturated trend (the northern intermediate lavas and a quartz-trachyte from the south) have elevated $^{87}Sr/^{86}Sr$-values which show a slight correlation with SiO_2 and with Pb, both of which are more abundant in the basement granite than the lavas. Contamination by a process of simple mixing was rejected in favour of assimilation-fractional-crystallisation (AFC), which is discussed in section 6.5.

In an attempt to assess the depth at which the Velay basalt originated, they were projected into the CMAS system. The results suggest that they last equilibrated at 15 - 20kbar before eruption. Thermometry and barometry was attempted for the ankaramites and northern intermediate lavas. The ankaramites gave only poor results, which suggest that their phenocrysts formed at or below the base

of the crust (10-15kbar). The northern intermediate lavas are considered with the cumulates in the section 6.5.

6.5 Cumulate blocks

The cumulate blocks occur in a small pyroclastic unit in a valley just to the south-east of Mt Mézenc, in the southern Velay. The unit consists of unconsolidated pyroclastics, which are being eroded rapidly by a small stream, suggesting that they were erupted relatively recently. Fossil wood was dated using the carbon-14 technique, but the result showed that it was older than the 35,000 year maximum measurable by this method. One of the cumulate blocks yielded a K-Ar age of 8.5Ma, but this seems to be too high.

The blocks were deduced to be cumulates of the magma which produced the pyroclastics since its phenocrysts are the same as those in the most evolved cumulates. Evidence for the cumulus nature of the blocks includes the presence of intercumulus glass, modal and grain-size layering and adcumulus overgrowth on originally euhedral grains. The frequency distribution of the cumulate blocks shows that the least-evolved blocks are three times as abundant as the most-evolved.

Minerals in the blocks show continuous compositional variation over a wide range, and are used to divide the blocks into four suites, with Suite 1 the least evolved and Suite 4 the most evolved. The criteria are:

Suite 1 - *no feldspar present*
Suite 2 - *feldspar and amphibole present, biotite absent*
Suite 3 - *feldspar, amphibole and biotite all present*
Suite 4 - *feldspar and biotite present, amphibole absent or < 2%*

There is strong resemblance between the minerals of the cumulates and the phenocrysts of the intermediate lavas from the north of the Velay, both showing a trend towards silica-saturation and elevated values of $^{87}Sr/^{86}Sr$. The parental lava of the cumulates is deduced to be an alkali basalt, based on mineral compositions and assemblages in the most primitive blocks.

The geochemistry of the cumulates matches that which would be predicted for the cumulates of a body of magma evolving mainly by crystal-liquid fractionation, with no gap at intermediate compositions. The interstitial glasses of the blocks show strong silica-enrichment, possibly due to loss of other components to nearby minerals, but emphasising the trend of the blocks as a whole.

The evolved cumulates have elevated $^{87}Sr/^{86}Sr$, suggesting that they were formed from a liquid undergoing AFC, as previously concluded for the northern intermediate lavas. Modelling both lavas and cumulates is difficult since there are so few data, but results suggest that only small degrees of contamination, up to a maximum of 11%, are needed to account for the observed values of $^{87}Sr/^{86}Sr$.

An attempt was made to determine the depth at which the cumulate blocks formed, using thermobarometry and barometry. The coexisting FeTi-oxides thermometer, combined with the Al^{IV}-in-amphibole thermobarometer, shows that the cumulates probably equilibrated at 5 - 7kbars (15 - 20km). This is supported by the abundance of basement granite fragments and the absence of lower

crustal or mantle material in the pyroclastics. The northern intermediate lavas are presumed to have formed at a similar depth.

Comparison of the Velay cumulate nodule suite with others from around the world shows that those of the Velay belong to the established "Group II" type, with a continuous range from wehrlite to the rare apatite/amphibole type. This has not been reported previously in the literature.

6.6 Summary of events

Partial melting of garnet-lherzolite in the asthenosphere beneath the Velay produced an alkali basalt parent magma. Lithospheric extension, which probably caused the melting by decompression, allowed the melt to rise towards the surface, and to erupt from fissures to form the Velay plateau. Some of this magma was trapped at or below the base of the crust and crystallised olivine and cpx before subsequent eruption as ankaramite. The other plateau lavas are aphyric, and probably evolved by flow crystallisation, plating crystals onto the walls of their conduits on the way to the surface. If they had evolved in a magma chamber they would contain phenocrysts and would also have had no reason to rise towards the surface.

When the extensional force decreased, ascending dense basaltic magma became trapped within the lower density granite basement and formed a 100km^3 magma chamber which elevated its roof. Differentiation of this liquid by crystal settling produced successively more evolved liquids until the density of the remaining phonolite magma was low enough to cause it to rise to the surface under hydrostatic pressure alone. In the southern Velay this phonolite was extruded as viscous domes on top of the basaltic plateau.

Old, parental basalt has not been identified for the phonolites of the northern Velay. Possibly extension in this area was too weak to allow the primary basalt to reach the surface, or the Boutières graben may have affected its rise. Older basalts may yet be found.

The intermediate lavas of the north appear to have evolved by AFC at mid-crustal levels (by analogy with the cumulates) and are probably related to the phonolites only in having the same alkali basalt parent magma. The reason why the intermediate lavas were contaminated, whereas the phonolites were not, may have been due to the increased temperature of the crust at 15-20km depth, requiring a smaller input of heat to reach its solidus. At 1kbar the temperature of the crust must be raised by about 900˚C for anhydrous melting to occur, whereas at depth a rise of only 600˚C is required.

The cumulates are probably much more recent than the other Velay lavas. A small (< 1km^3) body of alkali basalt was emplaced at mid-crustal levels, and differentiated with simultaneous wallrock contamination (AFC) to give a biotite-trachyte. Build-up of CO_2 eventually caused an explosive eruption, which ripped up the roof, walls and cumulates of the chamber. This process, like that which formed the northern intermediate lavas, is insignificant when compared with that which formed the Velay phonolites.

References

ADAMS, G.E. & BISHOP, F.C. 1986. The olivine-clinopyroxene geobarometer: experimental results in the CaO-FeO-MgO-SiO_2 system. *Contrib. Mineral. Petrol.* **[94]**. p230-237

ALEPH & C.S.I.R.O. 1989. The Mineral Database. Published by: Aleph Enterprises, P.O. Box 213, Livermore, California

ALLÈGRE, C.J., DUPRÉ, B., LAMBRET, B. & RICHARD, P. 1981. The subcontinental versus suboceanic debate, I. Lead-neodymium-strontium isotopes in primary alkali basalts from a shield area: the Ahaggar volcanic suite. *Earth Planet. Sci. Lett.* **[52]**. p85-92

ANDERSON, A.T. 1968. The oxygen-fugacity of alkaline basalt and related magmas, Tristan da Cunha. *Am. J. Sci.* **[266]**. p704-727

ANDERSON, D.J. & LINDSLEY, D.H. 1988. Internally consistent solution models for Fe-Mg-Mn-Ti oxides: Fe-Ti oxides. *Amer. Mineral.* **[73]**. p714-726

AUTRAN, A. & AUBERT, M. (Eds.) 1980. Géologie des Pays Européens: France, Belgique, Luxembourg (C.N.F.G) 26e Congrès Géologique International; Éditions Dunod, Paris

AUTRAN, A. & DERCOURT, J. (Coordinateurs) 1980. Évolutions géologiques de la France. *Mémoire du B.R.G.M.* **[107]**. p138-159

AUTRAN, A. & PETERLONGO, J-M. (Eds.) 1980. Massif Central. *In:* AUTRAN, A. & AUBERT, M. (Eds.) 1980. Géologie des Pays Européens: France, Belgique, Luxembourg (C.N.F.G) 26e Congrès Géologique International; Éditions Dunod, Paris. p11-123

AZAMBRE, B. & GIROD, M. 1966. Phonolites agpaïtiques. *Bull. Soc. fr. Minéral. Cristallogr.* **[89]**. p514-520

BAILEY, D.K. & SCHAIRER, J.F. 1964. Feldspar-liquid equilibria in peralkaline liquids - the orthoclase effect. *Am. J. Sci.* **[262]**. p1198-1206

BAKER, I. 1968. Intermediate oceanic volcanic rocks and the 'Daly gap'. *Earth Planet. Sci. Lett.* **[4]**. p103-106

BATARD, F. 1974. Les feldspaths dans les roches volcaniques différenciées du Massif Central français. *Unpublished Ph.D. thesis*. Université de Clermont

BATARD, F., MERGOIL-DANIEL, J. & MERGOIL, J. 1977. Calcite et rôle possible du CO_2 dans la genèse des roches hyperalcalines et agpaïtiques du Velay oriental (Haute-Loire, Massif central français). *Bull. Soc. fr. Minéral. Cristallogr.* **[100]**. p343-347

BÉDARD, J.H. 1989. Disequilibrium mantle melting. *Earth Planet. Sci. Lett.* **[91]**. p359-366

BELL, K. (Ed.) 1989. Carbonatites. Unwin Hyman, London.

BERGER, E. 1977. Sur l'existence et l'origine de deux séries magmatiques alcalines dans le secteur des Boutières (Velay Oriental, France). *C. R. Acad. Sci. Sér. D* **[285]**. p127-130

BERGER, E., OLIVES, J. & RIVOIRARD, J. 1976. Contribution à l'étude des laves alcalines du Velay oriental (France): le secteur de la Croix de Boutières. *C. R. Acad. Sci. Sér. D* **[283]**. p451-454

BERGER, E., BROUSSE, R. & MAURY, R.C. 1978. Présence de ferropigeonite dans le trachyte quartzifère des Dents du Mézenc (Velay). *C. R. Acad. Sci. Sér. D* **[286]**. p811-814

BERGER, E. & LANOË, S. 1978. Une contribution à l'étude des séries magmatiques alcalines: Géochimie et conditions de cristallisation des laves du Velay oriental. *Unpublished report*. École Nationale Superieure des Mines, Paris. pp110

BEST, M.G. 1975. Amphibole-bearing cumulate inclusions, Grand Canyon, Arizona and their bearing on silica-undersaturated hydrous magmas in the upper mantle. *J. Petrol.* **[16]**. p212-236

BINNS, R.A., DUGGAN, M.B. & WILKINSON, J.F.G. 1970. High pressure megacrysts in alkaline lavas from northeastern New South Wales. *Am. J. Sci.* **[269]**. p132-168

BLACK, R. & GIROD, M. 1970. Late Palaeozoic to Recent igneous activity in West Africa and its relationship to basement structure. *In:* CLIFFORD, T.N. & GASS, I.G. (Eds.) 1970. African magmatism and tectonics. Oliver & Boyd (Longman), Edinburgh. p185-210

BLUNDY, J.D. & HOLLAND, T.J.B. 1990. Calcic amphibole equilibria and a new amphibole-plagioclase geothermometer. *Contrib. Mineral. Petrol.* **[104]**. p208-224

BLUNDY, J.D., BRODHOLT, J.P. & WOOD, B.J. 1991. Carbon-fluid equilibria and the oxidation state of the upper mantle. *Nature (London)* **[349]**. p321-324

BOBIER, C. & MACLE, M. 1967. Contribution des méthodes palaéomagnétiques à l'étude volcanologique du massif du Meygal (Velay). *C. R. Acad. Sci. Sér. D* **[265]**. p660-662

BOTTINGA, Y. & WEILL, D. 1970. Densities of liquid silicate systems calculated from partial molar volumes of oxide components. *Am. J. Sci.* **[269]**. p169-182

BOTTINGA, Y, WEILL, D. & RICHET, P. 1982. Density calculations for silicate liquids. I. Revised method for aluminosilicate compositions. *Geochim. Cosmochim. Acta* **[46]**. p909-919

BOULE, M. 1892. Description géologique du Velay. *Bull. Serv. Carte Géol. Fr.* **[28]**. p1-259

BOUT, P. 1966. Histoire et morphogénèse du système Velay SE - Boutières - Coiron. *Rev. Géogr. Phys. Géol. Dyn. (2)* **[8]**. p225-252

BOUT, P. 1968. Problèmes de volcanisme III. *Rev. d'Auvergne* **[82]**. p1-8

BOWEN, N.L. 1945. Phase equilibria bearing on the origin and differentiation of alkaline rocks. *Am. J. Sci.* **[243A]**. p75-89

B.R.G.M. geological maps: see CHIRON & KERRIAN (1979) and ROUIRE & CHIRON (1980)

BROOKS, C.K. 1976. The Fe_2O_3/FeO ratio of basalt analyses: an appeal for a standardised procedure. *Bull. Geol. Soc. Denmark* **[25]**. p117-120

BROUSSE, R. 1971. Magmatologie du volcanisme néogène et quaternaire du Massif Central. *In:* JUNG, J. (Symposium) 1971. Géologie, géomorphologie et structure profonde du Massif Central français; Plein Air Service Éd. Clermont-Ferrand. p377-478

BUDDINGTON, A.F. & LINDSLEY, D.H. 1964. Iron-titanium oxide minerals and synthetic equivalents. *J. Petrol.* **[5]**. p310-357

BURRUS, J. 1986. Thermal modelling in sedimentary basins; 1st I.F.P. Research conferences on exploration. Éd. Technip, Carcans, France

CANN, J.R. 1968. Bimodal distribution of rocks from volcanic islands. *Earth Planet. Sci. Lett.* **[4]**. p479-480

CANTAGREL, J-M. & MERGOIL, J. 1970. Mesure, par la méthode à l'argon, de l'âge de quelques roches volcaniques du Velay oriental (Massif Central français). *C. R. Acad. Sci. Sér. D* **[271]**. p760-763

CARMICHAEL, I.S.E. 1967. The iron-titanium oxides of salic volcanic rocks and their associated ferromagnesian silicates. *Contrib. Mineral. Petrol.* **[14]**. p36-64

CARMICHAEL, I.S.E. & NICHOLLS, I. 1967. Iron-titanium oxides and oxygen fugacities in volcanic rocks. *J. Geophys. Res.* **[72]**. p4665-4687

CATANZARO, E.J., MURPHY, T.J., GARNER, E.L. & SHIELDS, W.R. 1969. Absolute isotopic abundance ratio and atomic weight of terrestrial rubidium. *Journal of Research Natl. Bur. Standards - A. Physics and Chemistry* **[73A]**. p511-516

CAWTHORN, R.G. & O'HARA, M.J. 1976. Amphibole fractionation in calc-alkaline magma genesis. *Am. J. Sci.* **[276]**. p309-329

CHAUVEL, C. & JAHN, B-M. 1984. Nd-Sr isotope and REE geochemistry of alkali basalts from the Massif Central, France. *Geochim. Cosmochim. Acta* **[48]**. p93-110

CHAYES, F. 1963. Relative abundance of intermediate members of the oceanic basalt-trachyte association. *J. Geophys. Res.* **[68]**. p1519-1534

CHAYES, F. 1964. Variance-covariance relations in some published Harker diagrams of volcanic suites. *J. Petrol.* **[5]**. p219-237

CHIRON, J-C & KERRIAN, Y. 1979. Carte géologique de la France à 1:250,000 et notice explicative de la feuille - Lyon **[29]**. Bureau de Recherches Géologiques et Minières

CLAGUE, D.A. 1978. The oceanic basalt-trachyte association: an explanation of the 'Daly gap'. *J. Geol.* **[86]**. p739-743

CLIFFORD, T.N. & GASS, I.G. (Eds.) 1970. African magmatism and tectonics. Oliver & Boyd (Longman), Edinburgh

COISY, P. & NICOLAS, A. 1978a. Regional structure and geodynamics of the upper mantle beneath the Massif Central. *Nature (London)* **[274]**. p429-432

COISY, P. & NICOLAS, A. 1978b. Structure et géodynamique du manteau supérieur sous le Massif central (France) d'après l'étude des enclaves des basaltes. *Bull. Minéral.* **[101]**. p424-436

COX, K.G., BELL, J.D. & PANKHURST, R.J. 1979. The interpretation of igneous rocks. Allen & Unwin, London. pp450

COWARD, M.P., DIETRICH, D. & PARK, R.G. (Eds.) 1989. Alpine Tectonics. *Geol. Soc. Spec. Pub.* **[45]**. p265-283

DALRYMPLE, G.B. & LANPHERE, M.A. 1969. Potassium-argon dating. Freeman, San Francisco

DALY, R.A. 1925. The geology of Ascension island. *Proc. Am. Acad. Arts Sci.* **[60]**.p1-80

DALY, R.A. 1927. The geology of St. Helena island. *Proc. Am. Acad. Arts Sci.* **[62]**. p31-92

DEER, W.A., HOWIE, R.A. & ZUSSMAN, J. 1966. An introduction to the rock-forming minerals. Longman. pp528

DePAOLO, D.J. 1981. Trace elements and isotopic effects of combined wallrock assimilation and fractional crystallisation. *Earth Planet. Sci. Lett.* **[53]**. p189-202

DERRUAU, M. 1971. Sur le morphologie du Massif Central. *In:* JUNG, J. (Symposium) 1971. Géologie, géomorphologie et structure profonde du Massif Central français; Plein Air Service Éd. Clermont-Ferrand. p33-44

DEVEY, C. 1986. Stratigraphy and geochemistry of the Deccan Traps lavas, Western India. *Unpublished Ph.D. thesis*. Oxford University

DEWEY, J.F., HELMAN, M.L., TURCO, E., HUTTON, D.H.W. & KNOTT, S.D. 1989. Kinematics of the Western Mediterranean. *In:* COWARD, M.P., DIETRICH, D. & PARK, R.G. (Eds.) 1989. Alpine Tectonics. *Geol. Soc. Spec. Pub.* **[45]**. p265-283

DOWNES, H. 1983. The petrogenesis of coexisting saturated and undersaturated continental alkaline magma series. *Unpublished Ph.D. thesis*. Leeds University

DOWNES, H. 1987a. Tertiary and Quaternary volcanism in the Massif Central, France. *In:* FITTON, J.G. & UPTON, B.J.G. (Eds.) 1987. Alkaline igneous rocks. *Geol. Soc. Spec. Pub.* **[30]**. p517-530

DOWNES, H. 1987b. Relationship between geochemistry and textural type in spinel lherzolites, Massif Central and Languedoc, France. *In:* NIXON, P.H. (Ed.) 1987. Mantle xenoliths. Wiley, Chichester. p125-133

DOWNES, H. 1990. Shear zones in the upper mantle - Relation between geochemical enrichment and deformation in mantle peridotites. *Geology* **[18]**. p374-377

DROOP, G.T.R. 1987. A general equation for estimating Fe^{3+} concentrations in ferromagnesian silicates and oxides from microprobe analyses, using stoichiometric criteria. *Min. Mag.* **[51]**. p431-435

DUNCAN, R.A., PETERSON, N. & HARGRAVES, R.B. 1972. Mantle plumes, movement of the European plate, and polar wandering. *Nature (London)* **[239]**. p82-86

DUNCAN, R.A. & RICHARDS, M.A. 1991. Hotspots, mantle plumes, flood basalts, and true polar wander. *Rev. Geophys.* **[29]**. p31-50

DUNGAN, M.A., GROVE, T.L. & HILDRETH, W. (Eds.) 1984. Proceedings of the I.S.E.M. field conference on open magmatic systems, Dallas

DZURISIN, D. 1987. Mount St. Helens (84-34). Annual Report of the world volcanic eruptions in 1984, Volc. Soc. Japan. Supplement to: *Bull. Volc.* **[49]**. p40-41

EMILIANI, C. 1981. The Sea. Wiley Interscience, New York.

FAURE, G. 1986. Principles of isotope geology (2nd edn.). Wiley, New York

FAURE, G. & POWELL, J.L. 1972. Strontium isotope geology. Springer-Verlag, Berlin. pp188

FÉRAUD, G. 1981. Datation de reseaux de dykes et de roches volcaniques sous-marines par les méthodes K-Ar et ^{40}Ar-^{39}Ar. Utilisation des dykes comme marqueurs de paléocontraintes. *Unpublished Ph. D. thesis*. Université de Nice

FITTON, J.G. 1987. The Cameroon line, West Africa: a comparison between oceanic and continental alkaline volcanism. *In:* FITTON, J.G. & UPTON, B.J.G. (Eds.) 1987. Alkaline igneous rocks. *Geol. Soc. Spec. Pub.* **[30]**. p273-291

FITTON, J.G. & DUNLOP, H.M. 1985. The Cameroon line, West Africa, and its bearing on the origin of oceanic and continental alkali basalt. *Earth Planet. Sci. Lett.* **[72]**. p23-38

FITTON, J.G. & JAMES, D. 1986. Basic volcanism associated with intraplate linear features. *Phil. Trans. R. Soc. Lond.* **[317]**. p253-266

FITTON, J.G. & UPTON, B.J.G. (Eds.) 1987. Alkaline igneous rocks. *Geol. Soc. Spec. Pub.* **[30]**

FREESTONE, I.C. & HAMILTON, D.L. 1980. The role of liquid immiscibility in the genesis of carbonatites - an experimental study. *Contrib. Mineral. Petrol.* **[73]**. p105-117

FREY, F.A. & PRINZ, M. 1978. Ultramafic inclusions from San Carlos, Arizona: petrologic and geochemical data bearing on their petrogenesis. *Earth. Planet. Sci. Lett.* **[38]**. p129-176

FROIDEVAUX, C. 1974. Hot spot in France? *Nature (London)* **[248]**. p749-751

GARNER, E.L., MURPHY, T.J., GRAMLICH, J.W., PAULSEN, P.J. & BARNES, I.L. 1975. Absolute isotopic abundance ratios and the atomic weight of a reference sample of potassium. *Journal of Research Natl. Bur. Standards - A. Physics and Chemistry* **[79A]**. p713-725

GILL, R.C.O. 1973. Mechanism for the salic bias of continental alkaline provinces. *Nature Physical Sciences* **[242]**. p41-42

GIROD, M. 1968. Le massif volcanique de l'Atakor (Hoggar, Sahara algérien). Étude pétrographique, structurale et volcanologique. *Unpublished Doct. d'État thesis*. Université de Paris

GITTINS, J. 1989. The origin and evolution of carbonatite magmas. *In:* BELL, K. (Ed.) 1989. Carbonatites. Unwin Hyman, London. p580-600

GOËR de HERVÉ, A. & MERGOIL, J. 1971. Structure et dynamique des édifices volcaniques tertiaires et quaternaires. *In:* JUNG, J. (Symposium) 1971. Géologie, géomorphologie et structure profonde du Massif Central français; Plein Air Sérvice Éd. Clermont-Ferrand. p345-376

GOGUEL, J. 1967. Carte géologique de la France à 1:80,000 et notice explicative de la feuille - Le Puy **[186]**, 3e édition. Ministère de l'Industrie, Service de la Carte Géologique; Paris

GRANGEON, P. 1953. La flore Pontienne de Gourgouras (Ardèche). *Bull. Soc. Géol. Fr. 6e Sér.* **[3]**. p303-320

GREEN, D.H. & RINGWOOD, A.E. 1967. The genesis of basaltic magmas. *Contrib. Mineral. Petrol.* **[15]**. p103-190

HAGGERTY, S.E. 1976. Opaque mineral oxides in terrestrial igneous rocks. *In:* RUMBLE, D. (Ed.) 1976. Oxide minerals. *Min. Soc. Amer. Short Course Notes* **[3]**. p Hg101-169

HALLIDAY, A.N., DICKIN, A.P., FALLICK, A.E. & FITTON, J.G. 1988. Mantle dynamics: a Nd, Sr, Pb and O isotopic study of the Cameroon Line volcanic chain. *J. Petrol.* **[29]**. p181-211

HALLIDAY, A.N., DAVIDSON, J.P., HOLDEN, P., DeWOLF, C., LEE, D-C. & FITTON, J.G. 1990. Trace-element fractionation in plumes and the origin of HIMU mantle beneath the Cameroon line. *Nature (London)* **[347]**. p523-528

HAMMARSTROM J.M. & ZEN, E-A. 1986. Aluminium in hornblende: an empirical igneous geobarometer. *Amer. Mineral.* **[71]**. p1297-1313

HARRIS, C. 1982. Coarse-grained rocks of Ascension Island. *Unpublished Ph.D. thesis*. Oxford University

HILL, P.G. 1974. The petrology of the Aden volcano, People's Democratic Republic of Yemen. *Unpublished Ph.D. thesis*. Edinburgh University

HIRN, A. & PERRIER, G. 1974. Deep sounding in the Limagne graben. *In:* ILLIES, J.H. & FUCHS, K. (Eds.) 1974. Approaches to Taphrogenesis. (I.U.C.G. **[8]** Proc. Internat. Rift. Symposium). p329-340

ILLIES, J.H. & FUCHS, K. (Eds.) 1974. Approaches to Taphrogenesis. (I.U.C.G. **[8]** Proc. Internat. Rift. Symposium)

IRVING, A.J. 1974. Pyroxene-rich ultramafic xenoliths in the Newer Basalts of Victoria, Australia. *Neues Jahrb. Mineral. Abh.* **[120]**. p147-167

IRVING, A.J. 1978. Flow crystallisation: a mechanism for fractionation of primary magmas at mantle pressures. *EOS Trans. Am. Geophys. Union* **[59]**. p1214

IRVING, A.J. 1984. Polybaric mixing and fractionation of alkalic magmas: Evidence from megacryst suites. *EOS Trans. Am. Geophys. Union* **[65]**. p1153

JAQUES, A.L. & GREEN, D.H. 1980. Anhydrous melting of peridotite at 0-15 Kb pressure and the genesis of tholeiitic basalts. *Contrib. Mineral. Petrol.* **[73]**. p287-310

JASMUND, K. & SECK, H.A. 1964. Geochemische Untersuchungen an Auswürflingen (Gleesiten) des Laacher-See-Gebietes. *Beiträge zur Mineralogie und Petrographie* **[10]**. p275-295

JOHNSON, R.W. (Ed.) 1989. Intraplate volcanism in Eastern Australia and New Zealand. Cambridge University Press. pp408

JOHNSON, M.C. & RUTHERFORD, M.J. 1989. Experimental calibration of the aluminium-in-hornblende geobarometer with application to Long Valley caldera (California) volcanic rocks. *Geology* **[17]**. p837-841

JUNG, J. (Symposium) 1971. Géologie, géomorphologie et structure profonde du Massif Central français; Plein Air Service Éd. Clermont-Ferrand. pp610

KÖHLER, T.P. & BREY, G.P. 1990. Calcium exchange between olivine and clinopyroxene calibrated as a geothermobarometer for natural peridotites from 2 to 60 kb with applications. *Geochim. Cosmochim. Acta* **[54]**. p2375-2388

KUNO, H. 1959. Origin of Cenozoic petrographic provinces of Japan and surrounding areas. *Bull. Volc.* **[20]**. p37-76

LACROIX, A. 1917. Les laves à haüyne d'Auvergne et leurs enclaves homœogènes: importance théorique de ces dernières. *C. R. Acad. Sci. Sér. D* **[164]**. p581-588

LAPADU-HARGUES, P. 1971. Du Trias à l'Éocène dans la Massif Central. *In:* JUNG, J. (Symposium) 1971. Géologie, géomorphologie et structure profonde du Massif Central français; Plein Air Service Éd. Clermont-Ferrand. p291-294

Le BAS, M.J. 1980. Alkaline magmatism and uplift of continental crust. *Proc. Geol. Soc. Assoc. (1 & 2)* **[91]**. p33-38

Le MAÎTRE, R.W. 1969. Kaersutite-bearing plutonic xenoliths from Tristan da Cunha, South Atlantic. *Min. Mag.* **[37]**. p185-197

Le MAÎTRE, R.W. 1976. Some problems of the projection of chemical data into mineralogical classifications. *Contrib. Mineral. Petrol.* **[56]**. p181-189

Le ROEX, A.P., CLIFF, R.A. & ADAIR, B.J.I. 1990. Tristan da Cunha, South Atlantic: geochemistry and petrogenesis of a basanite-phonolite lava series. *J. Petrol.* **[31]**. p779-812

LIVERMORE, R.A., VINE, F.J. & SMITH, A.G. 1983. Plate motions and the geomagnetic field. I. Quaternary and late Tertiary. *Geophys. Journal* **[73]**. p153-171

LLOYD, F.E. & BAILEY, D.K. 1975. Light element metasomatism of the continental mantle: the evidence and the consequences. *Phys. Chem. Earth* **[9]**. p389-416

LUCAZEAU, F. 1986. The post-rift evolution of the Massif Central, France. *In:* BURRUS, J. 1986. Thermal modelling in sedimentary basins; 1st I.F.P. Research conferences on exploration. Éd. Technip, Carcans, France. p75-89

LUCAZEAU, F. & BAYER, R. 1982. Évolution géothermique et géodynamique du Massif Central français depuis l'Oligocène. *Ann. Géophys.* **[38]**. p405-429

LUCAZEAU, F., VASSEUR, G. & BAYER, R. 1984. Interpretation of heat flow data in the French Massif Central. *Tectonophysics* **[103]**. p99-119

MARSH, J.S. 1975. Aenigmatite stability in silica-undersaturated rocks. *Contrib. Mineral. Petrol.* **[50]**. p135-144

MAURY, R.C. 1968. 1. Contribution à la géologie du Cantal - les hautes vallées de la Petite Rhue et de la Veronne. 2. Fossilisation des bois dans les tephras volcaniques du Cantal. *Unpublished thesis*. Université d'Orsay

MAURY, R.C. & VARET, J. 1980. Le volcanisme tertiare et quaternaire en France. *In:* AUTRAN, A. & DERCOURT, J. (Coordinateurs) 1980. Évolutions géologiques de la France. *Mémoire du B.R.G.M.* **[107]**. p138-159

MAURY, R.C., BROUSSE, R., VILLEMANT, B., JORON, J-L., JAFFREZIC, H. & TREUIL, M. 1980. Cristallisation fractionée d'un magma basaltique alcalin: la série de la Chaîne des Puys (Massif Central, France). I. Pétrologie. *Bull. Minéral.* **[103]**. p250-266

MENZIES, M. & MURTHY, V.R. 1980. Mantle metasomatism as a precursor to the genesis of alkaline magmas - isotopic evidence. *Am. J. Sci.* **[280A]**. p622-638

MENZIES, M., ARCULUS, R.J., BEST, M.G., BERGMAN, S.C., EHRENBERG, S.N., IRVING, A.J., RODEN, M.F. & SCHULZE, D.J. 1987. A record of subduction processes and within-plate volcanism in lithospheric xenoliths of the southwestern USA. *In:* NIXON, P.H. (Ed.) 1987. Mantle xenoliths. Wiley, Chichester. p59-74

MERGOIL, J. 1968. Gisement en filons annulaires de phonolites du Velay (Massif Central français). *C. R. Acad. Sci. Sér. D* **[267]**. p1-3

MERGOIL, J. 1980. Le Velay oriental. *In:* AUTRAN, A & AUBERT, M. (Eds.) 1980. Géologie des Pays Européens: France, Belgique, Luxembourg (C.N.F.G) 26e Congrès Géologique International; Éditions Dunod, Paris. p89-94

MERGOIL, J., FRERICHMANN, U. & MERGOIL-DANIEL, J. 1979. Nouvelle interprétation des tufs phonolitiques de Saint-Pierre-Eynac (Haute-Loire, Massif Central français). *4e Colloque de Géomorphologie volcanique: Problèmes du volcanisme explosif*. p17-23

MERRILL, R.B. & WYLLIE, P.J. 1975. Kaersutite and kaersutite eclogite from Kakanui, New Zealand - water-excess and water deficient melting to 30 kilobars. *Geol. Soc. Am. Bull.* **[86]**. p555-570

MERVOYER, B., MAURY, R. & VARET, J. 1973. Un mécanisme possible d'évolution des trachyandesites du Massif Central par cristallisation fractionée sous pression d'eau. *C. R. Acad. Sci. Sér. D* **[277]**. p9-12

MINSTER, J.B. & JORDAN, T. 1978. Present day plate motions. *J. Geophys. Res.* **[83]**. p5331-5351

MORGAN, W.J. 1972. Plate motions and deep mantle convection. *Geol. Soc. Am. Mem.* **[132]**. p7-22

MORGAN, W.J. 1981. Hotspot tracks and the opening of the Atlantic and Indian oceans. *In:* EMILIANI, C. 1981. The Sea. Wiley Interscience, New York. p443-487

MUKHOPADHYAY, B. 1991. Forsterite-diopside-spinel-liquid equilibria in the system CaO-MgO-Al_2O_3-SiO_2 at 20 kbar and petrological applications. *Contrib. Mineral. Petrol.* **[106]**. p253-264

NABELEK, C.R. & LINDSLEY, D.H. 1985. Tetrahedral Al in amphibole: a potential thermometer for some mafic rocks. *Geol. Soc. Amer. Abstracts with Programs* **[17]**. p673

NICOLAS, A., LUCAZEAU, F. & BAYER, R. 1987. Peridotite xenoliths in Massif Central basalts, France: textural and geophysical evidence for asthenospheric diapirism. *In:* NIXON, P.H. (Ed.) 1987. Mantle xenoliths. Wiley, Chichester. p563-574

NIER, A.O. 1950. A redetermination of the relative abundances of the isotopes of carbon, nitrogen, oxygen, argon and potassium. *Phys. Rev.* **[77]**. p789-793
NIXON, P.H. (Ed.) 1987. Mantle xenoliths. Wiley, Chichester. pp844

O'HARA, M.J. 1968. The bearing of phase equilibria studies in synthetic and natural systems on the origin and evolution of basic and ultrabasic rocks. *Earth Planet. Sci. Rev.* **[4]**. p69-133
OLIVES, R., RIVOIRARD, J. & BERGER, E. 1976. Partie 1: Étude des laves alcalines du secteur des Boutières (Velay oriental). *Unpublished report*. École Nationale Superieure des Mines, Paris. pp100
O'REILLY, S.Y. 1987. Volatile-rich mantle beneath Eastern Australia. *In:* NIXON, P.H. (Ed.) 1987. Mantle xenoliths. Wiley, Chichester. p661-670
O'REILLY, S.Y. 1989. 6.2.4 Primary mineral assemblages and conditions of equilibration (part of Chapter 6; Xenoliths and Megacrysts of Eastern Australia). *In:* JOHNSON, R.W. (Ed.) 1989. Intraplate volcanism in Eastern Australia and New Zealand. Cambridge University Press. p263-265
O'REILLY, S.Y. & GRIFFIN, W.L. 1987. Eastern Australia - 4000km of mantle samples. *In:* NIXON, P.H. (Ed.) 1987. Mantle xenoliths. Wiley, Chichester. p267-280

PEARCE, J.A. & NORRY, M.J. 1979. Petrogenetic implications of Ti, Zr, Y, and Nb variations in volcanic rocks. *Contrib. Mineral. Petrol.* **[69]**. p33-47
PERRIER, G. & RUEGG, J.C. 1973. Structure profonde du Massif Central français. *Ann. Géophys.* **[29]**. p435-502
POWELL, R. & POWELL, M. 1977. Geothermometry and oxygen barometry using coexisting iron-titanium oxides: a reappraisal. *Min. Mag.* **[41]**. p257-263
PRESNALL, D.C., DIXON, S.A., DIXON, J.R., O'DONNELL, T.H., BRENNER, N.L., SCHROCK, R.L. & DYCUS, D.W. 1978. Liquidus relations on the join Diopside-Forsterite-Anorthite from 1 atm to 20 kbar: Their bearing on the generation and crystallisation of basaltic magma. *Contrib. Mineral. Petrol.* **[66]**. p203-220
PRÉVOT, M. & DALRYMPLE, G.B. 1971. Age potassium-argon et polarité magnétique de roches volcaniques mio-pliocènes du Velay (Massif Central, France): Essai de chronostratigraphique fine. *Ann. Géophys.* **[27]**. p423-427
PRÉVOT, M. & MERGOIL, J. 1973. Crystallization trend of titanomagnetites in an alkali basalt from Saint-Clément (Massif Central, France). *Min. Mag.* **[39]**. p474-481

RITTMANN, A. 1962. Volcanoes and their activity (translated into English by E.A. Vincent). Wiley, London
ROEDER, P.L. & EMSLIE, R.F. 1970. Olivine-liquid equilibrium. *Contrib. Mineral. Petrol.* **[29]**. p275-289
ROUIRE, J & CHIRON, J-C. 1980. Carte géologique de la France à 1:250,000 et notice explicative de la feuille - Valence **[34]**. Bureau de Recherches Géologiques et Minières
RUMBLE, D. (Ed.) 1976. Oxide minerals. *Min. Soc. Amer. Short Course Notes* **[3]**

SAPIN, M. & HIRN, A. 1974. Results of explosion seismology in the southern Rhône valley. *Ann. Géophys.* **[30]**. p181-202
SCROPE, G.P. 1858. The geology and extinct volcanoes of central France (2nd edition). J. Murray, London. pp258
SHAND, S.J. 1939. On the staining of feldspathoids, and on the zoned structure in nepheline. *Amer. Mineral.* **[24]**. p508-513
SHAW, H.R. 1972. Viscosities of magmatic silicate liquids: an empirical method of prediction. *Am. J. Sci.* **[272]**. p870-893
SØRENSEN, H. (Ed.) 1974. The alkaline rocks. Wiley, London
SØRENSEN, H. 1974. Alkali syenites, feldspathoidal syenites and related lavas. *In:* SØRENSEN, H. (Ed.) 1974. The alkaline rocks. Wiley, London. p22-52
SOURIAU, A., CORREIG, A.M. & SOURIAU, M. 1980. Attenuation of Rayleigh waves across the volcanic area of the Massif Central, France. *Phys. Earth Planet. Int.* **[23]**. p62-71
SPEIDEL, D.H. 1970. Effect of magnesium on the iron-titanium oxides. *Am. J. Sci.* **[268]**. p341-353

STEIGER, R.H. & JÄGER, E. 1977. Subcommision on geochronology: Convention on the use of decay constants in geo- and cosmochronology. *Earth Planet. Sci. Lett.* **[36]**. p359-362
STORMER, J.C. 1983. The effects of recalculation on estimates of temperature and oxygen fugacity from analyses of multicomponent iron-titanium oxides. *Amer. Mineral.* **[68]**. p586-594
SUN, S-S. & HANSON, G.N. 1975. Origin of Ross Island basanitoids and limitations upon the heterogeneity of mantle sources for alkali basalts and nephelinites. *Contrib. Mineral. Petrol.* **[52]**. p77-106
SUPPE, J. 1985. Principles of structural geology, Chapter 7: Intrusive and extrusive structures. Prentice-Hall, New Jersey. p209-253

TAIT, S.R. 1988. Samples from the crystallising boundary layer of a zoned magma chamber. *Contrib. Mineral. Petrol.* **[100]**. p470-483
THORNTON, C.P. & TUTTLE, O.F. 1960. Chemistry of igneous rocks I. Differentiation index. *Am. J. Sci.* **[258]**. p664-684

VARET, J. 1969. Les phonolites agpaïtiques et miaskitiques du Cantal septentrional (Auvergne, France). *Bull. Volc.* **[33]**. p621-656
VILLEMANT, B., JORON, J-L., JAFFREZIC, H., TREUIL, M., MAURY, R. & BROUSSE, R. 1980. Cristallisation fractionée d'un magma basaltique alcalin: la série de la Chaîne des Puys (Massif central, France). II. Géochimie. *Bull. Minéral.* **[103]**. p267-286
VILLEMANT, B., JAFFREZIC, H., JORON, J-L. & TREUIL, M. 1981. Distribution coefficients of major and trace elements; fractional crystallisation in the alkali basalt series of Chaîne des Puys (Massif Central, France). *Geochim. Cosmochim. Acta* **[45]**. p1997-2016
VILLEMANT, B. & TREUIL, M. 1983. Comportement des éléments traces et majeurs dans la série alcaline du Velay; comparaison avec la Chaîne des Puys (Massif Central, France). *Bull. Minéral.* **[106]**. p465-486
VINCENT, P. 1980. Le massif du Mont Dore. *In:* AUTRAN, A & AUBERT, M. Géologie des Pays Européens: France, Belgique, Luxembourg (C.N.F.G) 26e Congrès Géologique International; Éditions Dunod, Paris. p100-106

WAGER, L.R. BROWN, G.M. & WADSWORTH, W.J. 1960. Types of igneous cumulates. *J. Petrol.* **[1]**. p73-85
WELLMAN, P. 1989. Upper mantle, crust, and geophysical volcanology of Eastern Australia, section 1.4.9; Sub-volcanic intrusions. *In:* JOHNSON, R.W. (Ed.) 1989. Intraplate volcanism in Eastern Australia and New Zealand. Cambridge University Press. p33-36
WHITE, R.S. & McKENZIE, D.P. 1989. Magmatism at rift zones: the generation of volcanic continental margins and flood basalts. *J. Geophys. Res.* **[94]**. p7685-7730
WILKINSON, J.F.G. 1975. Ultramafic inclusions and high pressure megacrysts from a nephelinite sill, Nandewar Mountains, north-eastern New South Wales, and their bearing on the origin of certain ultramafic inclusions in alkaline rocks. *Contrib. Mineral. Petrol.* **[51]**. p235-262
WILSHIRE, H.G. & SHERVAIS, J.W. 1975. Al-augite and Cr-diopside ultramafic xenoliths in basaltic rocks from western United States. *Phys. Chem. Earth* **[9]**. p257-272
WILSON, J.T. 1963. A possible origin of the Hawaiian Islands. *Can. J. Phys.* **[41]**. p863-868
WILSON, J.T. 1965. Evidence from ocean islands suggesting movement in the earth. *Phil. Trans. R. Soc. London* **[258]**. p145-165
WILSON, M. & DOWNES, H. 1991. Tertiary-Quaternary extension related alkaline magmatism in western and central Europe. *J. Petrol.* **[in press]**
WIMMENAUER, W. 1974. The alkaline province of Central Europe and France. *In:* SØRENSEN, H. (Ed.) 1974. The alkaline rocks. Wiley, London. p238-271
WÖRNER, G., SCHMINCKE, H-U. & SCHREYER, W. 1982. Crustal xenoliths from the Quaternary Wehr volcano (East Eifel). *Neues Jb. Miner. Abh.* **[144]**. p29-55
WÖRNER, G. & SCHMINCKE, H-U. 1984a. Mineralogical and chemical zonation of the Laacher See Tephra Sequence (East Eifel, W. Germany). *J. Petrol.* **[25]**. p805-835
WÖRNER, G. & SCHMINCKE, H-U. 1984b. Petrogenesis of the zoned Laacher See Tephra. *J. Petrol.* **[25]**. p836-851

WÖRNER, G., ZINDLER, A. & STAUDIGEL, H. 1984. Isotopic constraints on the chemical evolution of the zoned Laacher See magma chamber by crystal fractionation, liquid state differentiation, magma mixing, and wall rock assimilation. *In:* DUNGAN, M.A., GROVE, T.L. & HILDRETH, W. (Eds.) 1984. Proceedings of the I.S.E.M. field conference on open magmatic systems, Dallas

WÖRNER, G., HARMON, R.S. & HOEFS, J. 1987. Stable isotope relations in an open magma system, Laacher See, Eifel (FRG). *Contrib. Mineral. Petrol.* **[95]**. p343-349

WRIGHT, T.L. & DOHERTY, P.C. 1970. A linear programming and least squares computer method for solving petrologic mixing problems. *Bull. Geol. Soc. Amer.* **[81]**. p1995-2008

Appendices

Appendix A - Specimen localities
Appendix B - Specimen petrography
Appendix C - Whole-rock and mineral analyses
Appendix D - Sr-isotope determination
Appendix E - K-Ar age determination

Appendix A

Specimen localities

All specimen localities are marked on the 1:50,000 geological maps in the pocket in the back cover, in addition to the descriptive locations and lat./long. given below.

Specimen number	longitude (east)	latitude (north)		1:50 000 map sheet
84/17	4° 2' 30.8"	45° 6' 3.0"	Mont Loségal	Yssingeaux
quarry on D35 from Le Pertuis to l'Herm				
84/18	4° 2' 39.8"	45° 6' 21.7"	" "	"
quarry 600m to N of 84/17, spotty facies				
84/19a	4° 3' 41.1"	45° 3' 8.4"	Suc de Monac	"
2km N of St Julien Chapteuil, quarry to S of Suc				
84/19b	4° 3' 41.1"	45° 3' 8.4"	" "	"
as above, sanidinite inclusion				
84/20	4° 9' 24.4"	45° 2' 18.0"	Montagne du Meygal	"
SE corner of Meygal, Lac Bleu quarry				
84/21	4° 17' 11.8"	44° 56' 44.3"	St Clément section	Monastier
D247 running SE from St Clément, road exposure, 2nd lowest flow				
84/22	4° 16' 23.7"	44° 56' 55.1"	" "	"
as above, cpx-phyric flow				
84/23	4° 15' 47.3"	44° 57' 8.2"	" "	"
as above, upper flow				
84/24a	4° 3' 51.8"	44° 55' 38.8"	Moulin Béraud	"
D631 1km S of Freycenet-la -Tour, road exposure				
84/24b	4° 3' 45.2"	44° 55' 57.8"	" "	"
as above, higher up slope at Reyrac				
84/25	4° 11' 58.1"	44° 53' 5.2"	South of Rocher de Cruzet	"
nr la Cayère, D378 3km S Mt Mézenc, road exposure in lowest flow				
84/26	4° 12' 49.4"	44° 52' 45.0"	Suc de Sara	"
end of small track running SW from Prévenchères (1km S of Borée). road cutting, inner contact 3m from granite				
84/27	4° 12' 40.4"	44° 52' 44.8"	" "	"
as above, near middle of intrusion				
84/28	4° 12' 34.4"	44° 52' 44.0"	" "	"
as above, 10m from outer contact				
84/29	4° 12' 32.6"	44° 52' 43.6"	" "	"
as above, near outer contact				
84/30	4° 12' 47.2"	44° 52' 46.2"	" "	"
as above, basalt dyke intruded along inner contact				
84/31	4° 12' 27.1"	44° 52' 45.0"	Rocher des Pradoux	"
4km S of Mt Mézenc, feldspar-phyric facies				
84/32	4° 12' 32.4"	44° 52' 43.5"	Suc de Sara	"
as 84/26, inner contact against granite				
84/33	4° 6' 15.2"	44° 55' 31.3"	Gazeille section	"
near la Vacheresse, in stream running WNW from Les Estables, lowest flow				
84/34	4° 6' 23.7"	44° 55' 30.7"	" "	"
as above, exposure beside D631. ?2nd lowest flow				
84/35	4° 6' 53.9"	44° 55' 5.7"	" "	"
as above, exposure at base of cliff in Vacheresse				
84/36	4° 7' 3.5"	44° 54' 50.3"	" "	"
as above, exposed beside D631				
84/37	4° 8' 37.2"	44° 54' 25.4"	" "	"
as above				
84/38	4° 4' 30.9"	44° 57' 33.8"	nr Laussonne	"
on D36 2km SE Laussonne				
84/39	4° 13' 3.6"	44° 58' 39.5"	nr Pont du Mont crossroads	"
1km SW Fay-sur-Lignon				
84/40	4° 17' 18.6"	44° 56' 38.3"	St Clément section	"
as 84/21, 1m above granite				
84/40a	4° 17' 19.7"	44° 56' 42.4"	" "	"
as 84/21, centre of flow				
84/40b	4° 17' 20.8"	44° 56' 46.3"	" "	"
as 84/21, high in flow				
84/41	4° 17' 11.8"	44° 56' 44.3"	" "	"
as 84/21, 2nd flow				
84/42	4° 16' 56.7"	44° 56' 50.6"	" "	"
as 84/21, 3rd flow				
84/43	4° 16' 23.7"	44° 56' 55.0"	" "	"
as 84/21, 4th flow				
84/44	4° 16' 24.2"	44° 56' 56.5"	" "	"
as 84/21, 5th flow				
84/45	4° 15' 51.3"	44° 57' 7.4"	" "	"
as 84/21, possibly same flow as 84/44				
84/46	4° 15' 47.3"	44° 57' 8.3"	" "	"
as 84/21, summit flow				

84/47 4° 15' 5.8" 44° 52' 49.9" nr St Martial "
D215 2.5km NW St Martial, near La Rouveyre
84/48 4° 15' 11.7" 44° 52' 48.0" " "
as above, basement
84/50 4° 16' 25.5" 44° 51' 44.0" " "
on D237 500m SW St Martial, roadside exposure of
porphyritic phonolite with inclusions
84/51 4° 10' 57.4" 44° 52' 32.2" nr Les Estables "
D377 junction with D378 3km SE Les Estables, roadside exposure

85/ 1 4° 21' 25.3" 44° 58' 26.4" St Julien Boutières Lamastre
basalt neck on opposite side of valley to town
85/ 2 4° 21' 0.0" 44° 57' 49.2" nr Tabuant "
1.5km S of St Julien Boutières
85/ 3 4° 19' 6.0" 44° 55' 58.5" Chanéac "
D378 W of town, roadside exposure
85/ 4 4° 19' 28.1" 44° 53' 10.4" Cornuscle "
D282 2km S of Arcens, flow emerging from Sommet de la Farre
85/ 5 4° 21' 17.6" 44° 52' 49.3" Ribefaite "
D282 2km SW of Mariac, roadside exposure
85/ 6 4° 19' 35.9" 44° 51' 56.4" Sommet de la Farre "
3km NW of Dornas, sample from peak
85/ 7 4° 19' 29.2" 44° 51' 49.8" " " "
as above, basalt flow below peak
85/ 8 4° 19' 24.2" 44° 51' 37.6" " " "
as above, roadside exposure of weathered quartz trachyte
85/ 9 4° 19' 4.3" 44° 51' 8.8" Col de Joux Monastier
3.5km SE St Martial
85/10 4° 22' 51.8" 44° 49' 41.9" Don peak Lamastre
3.5km SE Dornas
85/12 4° 16' 48.7" 44° 55' 42.8" Serres Monastier
3km SE St Clément, outcrop on path
85/13 4° 16' 43.8" 44° 55' 49.5" " "
as above
85/14 4° 17' 0.6" 44° 55' 36.8" " "
as above
85/15 4° 15' 37.3" 44° 54' 28.7" nr Borée "
250m N of Echamps, 2km NE Borée, roadside exposure by 3km post
85/16 4° 15' 51.7" 44° 54' 41.8" " "
as above, across small valley
85/17 4° 15' 32.6" 44° 54' 39.1" " "
as above, at head of small valley, downhill of 85/15
85/18 4° 14' 57.4" 44° 55' 0.6" Reynaud-Tempoyrac "
2km NNE of Borée, at junction of Reynaud and Tempoyrac roads
85/19 4° 15' 26.2" 44° 55' 13.6" " " "
as above, roadside exposure 500m S of Reynaud

86/ 1 4° 13' 22.5" 44° 52' 29.0" Suc de Sara "
3km SW of Borée, at peak
86/ 2 4° 16' 7.9" 44° 47' 35.6" Ray Pic Burzet
waterfall 2.5km SW of Lachamp-Raphaël
86/ 3 4° 11' 55.3" 44° 54' 46.7" Mont Mézenc Monastier
east peak
86/ 4 4° 0' 47.8" 44° 56' 1.4" nr Le Monastier "
1.5km SE Monastier on D535, roadside exposure
86/ 5 4° 4' 34.0" 44° 54' 50.7" La Roche Basse "
1.5km W Freycenet-la-Tour
86/ 6 4° 5' 35.5" 44° 55' 1.3" Roche du Bachat "
3.5km SE of Freycenet-la -Tour
86/ 7 4° 3' 51.9" 44° 55' 39.0" Moulin Béraud "
as 84/24
86/ 8 4° 11' 31.5" 44° 55' 38.7" La Roche Pointue "
1.5km N of Mt Mézenc, roadside exposure. (Also known as Dents de Mézenc)
86/ 9 4° 12' 36.0" 44° 57' 25.7" Mont Signon "
500m NE of Chaudeyrolles
86/14 4° 1' 4.4" 45° 2' 5.0" Mont Peylenc Yssingeaux
3.5km W of St Julien Chapteuil, quarry in basalt
lava lake with abundant xenoliths
86/15 4° 9' 24.4" 45° 2' 18.0" Meygal "
as 84/20
86/17 4° 16' 25.4" 44° 51' 43.7" nr St Martial Monastier
as 84/50
86/18 4° 8' 3.7" 45° 3' 25.4" Meygal Yssingeaux
Le Testaouaire, north peak of Montagne du Meygal
86/19 4° 11' 16.4" 45° 3' 18.4" Pic du Lisieux "
1km SE of peak, quarry
86/20 4° 11' 49.5" 45° 3' 44.6" " " "
at peak
86/21 4° 10' 0.8" 45° 6' 31.7" Suc d'Achon "
5km SE of Yssingeaux

86/22 4° 2' 31.0" 45° 6' 2.9" Mont Loségal "
as 84/17
86/23 4° 0' 31.3" 45° 12' 15.0" nr Retournac Monistrol
N103 2km W of Retournac, excavation beside road
86/24 3° 58' 14.5" 45° 13' 28.8" Miaune "
5.5km NW of Retournac, at peak
86/25 3° 57' 57.8" 45° 13' 35.5" " "
as above, lower down to N
86/26 4° 0' 2.7" 45° 11' 23.3" Mt Gerbizon "
1.5km SE of Chamalières-sur-Loire, at peak
86/27 4° 0' 3.7" 45° 11' 32.0" " "
as above, lower on same peak
86/29 4° 11' 12.0" 44° 52' 44.9" nr Les Estables Monastier
at hairpin bend on D378, 3.5km SE of Les Estables, roadside exposure
86/30 4° 12' 8.8" 44° 53' 6.9" " " "
at Goudet, nr 84/25, roadside exposure
86/31 4° 13' 37.8" 44° 55' 58.7" nr Chaudeyrolles Monastier
7km NE of Mézenc on D410, road exposure at hairpin bend
86/32 4° 9' 47.0" 44° 53' 32.2" nr Les Estables "
D36 1.5km SE Les Estables, dyke SW of road, bearing 300°
86/33 4° 13' 23.1" 44° 53' 28.8" Suc de Touron "
1.5km ESE Borée, new road cutting from main road
86/34 4° 13' 28.1" 44° 53' 39.0" nr Suc de Touron "
1290m peak 500m NE of 86/33, sample from scree
86/35 4° 15' 15.3" 44° 53' 13.3" nr Molines "
1.5km SE of Borée on minor road, road exposure
86/36 4° 13' 1.7" 44° 54' 0.6" Suc de Chabrières "
2km W of Borée, centre of phonolite exposure at top of landslip
86/37 4° 13' 1.7" 44° 54' 0.6" " " "
as above, 10cm from edge of phonolite exposure
86/38 4° 13' 2.4" 44° 53' 59.1" nr Suc de Chabrières "
as above, cumulate nodules from pyroclastics
86/39 4° 10' 33.1" 44° 52' 47.0" Serre de Grésier "
3km SE Les Estables, at peak
86/40 4° 12' 0.8" 44° 52' 27.1" Rocher de Pradoux "
as 84/31, but at the top of the hill near the main road
86/41 4° 18' 11.6" 44° 48' 18.4" Suc de Montivernoux Burzet
1km SE of Lachamp-Raphaël, at peak
86/42 4° 11' 22.9" 44° 50' 55.4" nr Suc de Séponet Monastier
1km E of Suc, in boulder flow
86/43 4° 13' 53.0" 44° 50' 44.6" nr Gerbier de Jonc "
500m E of Gerbier de Jonc, at Bourges, road exposure
86/44 4° 3' 46.8" 45° 5' 36.6" Suc de Pertuis Yssingeaux
500m SE of Le Pertuis, on hillside
86/45 4° 5' 50.6" 45° 3' 4.6" Peyre de Bard "
2.5km S of Queyrières
86/46 4° 7' 9.2" 45° 1' 15.2" Mont de la Tortue "
4.5km ESE St Julien Chapteuil
86/47 4° 12' 2.3" 44° 57' 49.0" nr Chaudeyrolles Monastier
at Fayard, 1.5km N of Chaudeyrolles, road exposure
86/48 4° 6' 18.9" 44° 55' 27.1" Gazeille section "
as 84/33, further upstream
86/49 4° 6' 22.0" 44° 55' 22.6" " " "
as 84/33, further upstream
86/50 4° 6' 26.6" 44° 55' 19.6" " " "
as 84/33, further upstream
86/51 4° 6' 32.3" 44° 55' 15.0" " " "
as 84/33, further upstream
86/52 4° 6' 45.9" 44° 55' 8.1" " " "
as 84/33, further upstream at la Vacheresse
86/53 4° 6' 31.3" 44° 58' 41.5" nr Machabert "
3km W of St Front, on D39, road exposure
86/54 4° 11' 20.4" 44° 59' 16.3" Les Roches "
nr Roffiac, 4km E of St Front
86/55 4° 15' 59.9" 44° 57' 5.9" St Clément section "
as 84/21, at hairpin bend just S of village
86/56 4° 16' 13.7" 44° 57' 6.5" " " "
as 84/21, 400m E of village, highest flow
86/57 4° 7' 0.4" 44° 54' 46.6" Gazeille section "
as 84/33, further upstream than 86/52
86/58 4° 7' 10.9" 44° 54' 43.0" " " "
as 84/33, further upstream than 86/57
86/59 4° 7' 25.4" 44° 54' 34.7" " " "
as 84/33, beside bridge at Beauregard, upstream of 86/58
86/60 4° 15' 5.8" 44° 53' 21.2" nr Molines "
as 86/35, on hillside to NW, olivine nodules in pyroclastics
86/61 4° 15' 7.5" 44° 53' 24.0" " "
as 86/60, at top of slope
86/62 4° 20' 58.4" 44° 58' 16.7" nr St Julien Boutières Lamastre
500m S of town, at junction of D101 and D120, road exposure
86/63 4° 12' 28.8" 45° 0' 2.7" Le Petit Champagnac Monastier
2km NW of Fay-sur-Lignon, 1280m peak NW of village

86/64 4° 16' 41.0" 44° 53' 29.0" nr Molines "
3km ESE Borée, nr Hennes, small outcrop to W of 1161m spot height
86/65 4° 15' 5.2" 44° 54' 15.0" Rocher de Pialoux "
1km NE of Borée, at peak
86/66 4° 5' 56.7" 44° 56' 17.7" nr Freycenet-la-Tour "
2.5km E of Freycenet, road exposure
86/67 4° 14' 10.8" 44° 53' 46.8" Roche de Borée "
at Borée, beside track running along S edge
86/68 4° 12' 39.9" 44° 52' 46.0" Suc de Sara "
as 84/26, loose boulder in stream
86/69 4° 13' 3.8" 44° 53' 58.1" nr Suc de Chabrières "
as 86/36, welded tuff fragment
86/70 4° 14' 10.6" 44° 53' 46.8" Roche de Borée "
as 86/67, inclusions in phonolite

87/ 1 4° 10' 40.1" 44° 52' 29.3" nr Serre de Grésier "
on D378a, 3.5km SSE Les Estables, road exposure
87/ 2 4° 13' 14.5" 44° 54' 49.4" nr Mt Mézenc "
on road to S of Vialeret, 2km E of Mézenc, road exposure
87/ 3 4° 13' 38.1" 44° 55' 58.8" nr Chaudeyrolles Monastier
as 86/31, but different facies
87/ 4 4° 1' 4.4" 45° 2' 4.9" Mt Peylenc Yssingeaux
as 86/14, ultramafic nodules
87/ 5 4° 1' 4.5" 45° 2' 4.9" " "
as 86/14, other nodules
87/ 6 4° 1' 4.3" 45° 2' 4.8" " "
as 86/14, basalt specimen
87/ 7a 4° 9' 59.7" 45° 3' 5.7" La Chau de Carle "
3km E of Meygal, nr D42, top of small phonolite hill
87/ 7b 4° 9' 59.7" 45° 3' 5.7" " " "
as above, tiny basalt intrusion into 87/7a phonolite
87/ 8 4° 13' 23.9" 44° 58' 59.9" Fay-sur-Lignon Monastier
500m SW village, on D26. Road exposure
87/ 9 4° 13' 30.4" 44° 59' 15.1" " "
on hillside to E of village, very poor weathered exposure
87/10 4° 3' 3.3" 45° 14' 3.8" Mont de la Madeleine Monistrol
3.5km NNE Retournac, southern end of ridge
87/11 4° 4' 0.5" 45° 15' 8.0" La Dent "
6km NNE Retournac, road exposure at top of hill
87/12 3° 56' 30.8" 45° 13' 21.6" Roche-en-Régnier Craponne
5km NE Vorey, small peak in centre of village
87/13 3° 57' 41.5" 45° 13' 23.5" Miaune Monistrol
quarry on ridge running SW from peak
87/14 3° 59' 3.7" 45° 13' 14.5" Suc de Chaumont "
1km SE Miaune, at peak
87/15 4° 8' 50.4" 44° 58' 39.1" St Front Monastier
D263 in St Front, roadside exposure
87/16 4° 8' 45.6" 44° 56' 42.0" Rocher d'Aiglet "
4km S of St Front, from boulder on N slope
87/17 4° 6' 57.8" 44° 53' 45.2" Rocher Tourte "
3km WSW Les Estables, on NW side
87/18 4° 8' 22.7" 44° 53' 58.6" Rechausseyre "
1.5km WSW Les Estables, near peak
87/19 4° 16' 15.9" 44° 58' 35.5" Rimande section "
2.5km NNE St Clément, roadside exposure 50m E of Beaudac
87/20 4° 15' 59.0" 44° 58' 37.8" " " "
as above, 250m W of Beaudac
87/21 4° 15' 53.3" 44° 58' 40.6" " " "
as above, 500m W of Beaudac
87/22 4° 18' 17.9" 44° 56' 39.7" nr St Clément "
nr Orselas Bas, 3km ESE St Clément, road exposure
87/23 4° 18' 5.9" 44° 57' 32.5" " "
3km ENE St Clément, exposed beside track
87/24 4° 19' 27.8" 44° 51' 39.7" Sommet de la Farre Lamastre
as 85/8
87/25 4° 19' 28.8" 44° 51' 47.7" " " "
as 85/7
87/26 4° 19' 36.0" 44° 51' 56.4" " " "
as 85/6
87/27 4° 18' 14.3" 44° 51' 15.1" nr St Martial Monastier
at Combe Fege, 2.5km SE St Martial, road exposure
87/28 4° 17' 47.4" 44° 51' 24.6" " "
at La Faye, 2km SE St Martial, road exposure
87/29 4° 10' 48.1" 45° 2' 10.1" La Chaud de la Croix Yssingeaux
3km SW Pic du Lisieux, quarry
87/30 4° 3' 39.2" 45° 3' 11.1" Suc de Monac "
as 84/19
87/31 4° 6' 38.7" 45° 3' 32.2" Mt Chabrier "
2km SE of Queyrières, small quarry
87/32 4° 5' 56.0" 45° 4' 24.6" Queyrières "
centre of village, small volcanic neck

87/33 4° 5' 43.7" 45° 4' 13.5" nr Queyrières "
400m SW of village on D18. Nr La Varenne, roadside exposure
87/34 4° 5' 4.5" 45° 4' 48.2" Le Rand "
Near Sénéol, 1km NW Queyrières. Exposed on track
87/35 4° 6' 22.1" 45° 6' 25.8" Suc de Champblanc "
4km SSW Yssingeaux, exposed on W side of hill
87/36 4° 6' 23.4" 45° 7' 0.9" Suc de Saussac "
3km SSW Yssingeaux, exposed on S side of hill
87/37 4° 3' 55.6" 45° 8' 7.4" nr Pérignac "
4.5km W Yssingeaux, roadside exposure of basalt overlying maar deposit
87/38 4° 2' 59.0" 45° 9' 18.1" nr St Julien du Pinet "
963m hill 500m E of village, NE side
87/39 4° 3' 20.5" 45° 9' 3.9" Suc d'Eyme "
NW corner of Suc, exposed on path
87/40 4° 3' 33.3" 45° 8' 54.1" " "
as above, nearer summit
87/41 4° 2' 27.8" 45° 5' 56.5" nr Mt Loségal "
quarry beside D35, SW corner of Mt Loségal, upper of two flows
87/42 4° 2' 2.7" 45° 7' 13.6" nr Bonnevialle "
on D43 between Hautevialle and Bonnevialle, 4km ESE Rosières, road exposure
87/43 4° 2' 2.7" 45° 7' 13.6" " "
as above, cpx-phyric dyke cutting 87/42
87/44 4° 2' 28.2" 45° 6' 47.8" Riou Frait "
2.5km NW Le Pertuis, exposed on small track N of Riou Frait. Very weathered
87/45 3° 58' 6.8" 45° 8' 33.0" La Plaine Yssingeaux
2km NW Rosières, S edge of plateau top
87/46 4° 0' 19.0" 45° 9' 20.2" Suc de Jalore "
2.5km NNE Rosières, exposed nr peak on N side
87/47 4° 8' 42.4" 44° 54' 18.3" Gazeille section Monastier
as 84/33, 750m W of Les Estables
87/48 4° 11' 36.8" 44° 54' 41.3" Mont Mézenc "
southern peak
87/49 4° 6' 13.5" 44° 58' 45.4" nr Machabert "
3km W of St Front, quarry on hillside, medium-grained basalt
87/50 4° 10' 54.7" 44° 53' 38.8" Cirque de Boutières "
2km SSW Mézenc, 1621m peak
87/51 4° 11' 36.7" 44° 53' 22.6" " " "
2.5km S of Mézenc, 1558m peak at N end of ridge
87/52 4° 12' 31.7" 44° 52' 42.7" Suc de Sara "
as 84/26, in stream. Gneissic rock outside contact
87/53 4° 12' 33.4" 44° 52' 43.6" " "
as 84/26, veined phonolite facies near outer contact
87/54 4° 12' 34.6" 44° 52' 43.8" " "
as 84/26, veined tinguaite near outer contact
87/55 4° 12' 39.0" 44° 52' 44.4" " "
as 84/26, porous tinguaite near centre of intrusion
87/56 4° 12' 49.3" 44° 52' 44.5" " "
as 84/26, phonolite near inner contact
87/57 4° 11' 1.9" 44° 56' 26.5" nr Chaudeyrolles "
2km SW Chaudeyrolles, peak on opposite side of maar
87/58 4° 11' 28.0" 44° 55' 43.8" La Roche Pointue "
as 86/8, quarry just to N. (Also known as Dents de Mézenc)
87/59 4° 5' 25.3" 44° 59' 9.6" Bournac "
4km WNW St Front, hillside on W side of village, granulite nodules in tuff
87/60 4° 13' 12.1" 44° 49' 3.3" Le Coux Burzet
3km S of Gerbier de Jonc, sample from S slope
87/61 4° 21' 46.6" 44° 47' 43.5" nr Mézilhac Privas
D122 1.5km SSE Mézilhac, small quarry beside road
87/62 4° 21' 4.0" 44° 50' 39.7" nr Grand Dornas Lamastre
1km S of Dornas, exposed on small track from Chauchaï towards W
87/63 4° 21' 25.8" 44° 52' 52.1" Ribefaite "
as 85/5
87/64 4° 1' 49.6" 45° 9' 2.0" Suc de Fiallet Yssingeaux
3.5km NE Rosières, small quarry near D7
87/65 4° 0' 33.6" 45° 5' 22.7" Pot à Chard "
Le Gascou 4km W of Le Pertuis, stream section and cliff
87/66 4° 2' 51.1" 45° 2' 39.0" nr St Pierre Eynac "
on D26 1.5km NW St Julien Chapteuil, just after
road crosses stream, diatreme debris in small cliff
87/67 4° 2' 50.2" 45° 2' 43.4" " "
as above, 150m to N, phonolite dyke
87/68 4° 2' 5.3" 45° 2' 55.6" St Pierre Eynac "
2.5km NW of St Julien Chapteuil, N of St Pierre Eynac, under la Vierge
87/69 4° 2' 17.0" 45° 3' 8.0" Mont Plaux "
as above, quarry 500m N of village
87/70 4° 4' 57.6" 45° 3' 18.1" Mont Chanis "
3km NE St Julien Chapteuil, rubble slope on S side
87/71 4° 3' 52.5" 45° 7' 55.5" Suc de Charbonnière "
5km WSW Yssingeaux, W side of Suc
87/72 4° 3' 16.0" 45° 8' 2.9" Glavenas "
5.5km W of Yssingeaux, under Glavenas church

87/73 4° 3' 17.4" 45° 8' 8.4" Pied de Glavenas "
as above, hill to N
87/74 4° 2' 47.1" 45° 9' 58.9" Veyrines "
1.5km NNE of St Julien du Pinet, hill 300m SW Veyrines village, track on S side
87/75 4° 7' 50.3" 45° 8' 41.2" Yssingeaux "
500m E of town centre, quarry in Colline de St Roche
87/76 4° 13' 18.3" 44° 50' 38.1" Gerbier de Jonc Monastier
south side
87/77 4° 9' 44.2" 44° 50' 45.2" Suc de Montfol "
5km W Gerbier de Jonc, E side
87/78 4° 10' 38.0" 44° 51' 10.6" Suc de la Lauzière "
3.5km WNW Gerbier de Jonc, SE side
87/79 4° 10' 36.9" 44° 50' 53.7" Suc de Séponet "
3.5km W of Gerbier de Jonc, NW side
87/80 4° 16' 38.0" 44° 54' 11.8" nr Echamps "
3km ENE Borée, nr 1181m peak, 100m N of les Baumes
87/81 4° 17' 41.6" 44° 54' 11.3" Rocher de Soutron "
4km E of Borée, at peak
87/88 4° 2' 21.5" 44° 55' 53.5" La Besseyre-basse "
3.5km ESE Le Monastier on D535, road exposure

88/ 1 4° 6' 56.0" 44° 56' 21.3" La Freydeyre "
4km E of Freycenet-la-Tour, small quarry near 1256m spot height
88/ 2a 4° 9' 46.8" 44° 53' 47.6" nr Les Estables "
1km SSE Les Estables, granite from quarry
88/ 2b 4° 9' 44.6" 44° 53' 49.8" " "
as above, siltstone at S corner of quarry, above granite
88/ 3a 4° 9' 26.0" 44° 51' 53.8" nr Suc de Taupernas "
5.5km WNW Gerbier de Jonc on D377, road exposure of basalt
88/ 3b 4° 9' 26.0" 44° 51' 53.8" nr Suc de Taupernas Monastier
as above, xenolith in basalt
88/ 3c 4° 9' 22.2" 44° 51' 51.8" " "
as above, in gulley just to W, granite basement
88/ 4 4° 8' 29.7" 44° 52' 3.5" nr Touzières "
4.5km SSE Les Estables, 1450m peak
88/ 5 4° 8' 30.0" 44° 51' 38.6" " "
as above, 750m to S, 1468m peak
88/ 6 4° 8' 16.2" 44° 51' 31.7" " "
as above, 500m to SE, 1457m peak
88/ 7 4° 9' 23.0" 44° 46' 58.3" nr Usclades-et-Rieutord Burzet
8km SE Lac d'Issarlès, 750m N of village, small quarry
88/ 8 4° 5' 37.6" 44° 47' 7.9" nr La Palisse "
4km SE of Lac d'Issarlès, on D116 near dam, quarry
88/ 9 4° 13' 41.4" 44° 54' 9.9" nr Suc de Chabrières Monastier
as 86/36, down stream near bridge, pyroclastics exposed in stream
88/10 4° 13' 41.4" 44° 54' 9.9" " " "
as above, trachyte clast
88/11 4° 13' 41.4" 44° 54' 9.9" " " "
as above, trachyte clast
88/12 4° 13' 36.5" 44° 54' 7.7" " " "
as above, trachyte vein/dyke
88/13 4° 13' 36.5" 44° 54' 7.7" " " "
as above, spheroid weathering out of pyroclastics
88/13b 4° 13' 14.4" 44° 53' 58.0" " " "
as 86/36, slightly downstream of landslip, trachyte dyke in stream
88/14 4° 13' 2.0" 44° 53' 58.8" " " "
as 86/36, cumulate nodules in pyroclastics
88/15 4° 13' 2.3" 44° 53' 58.6" " " "
as 86/36, welded nodule in pyroclastics
88/16 4° 7' 35.8" 45° 0' 59.1" Montusclat Yssingeaux
5.5km SE St Julien Chapteuil, small exposures 300m NNE of village
88/17 4° 11' 12.3" 44° 55' 41.0" La Roche Pointue Monastier
as 86/8, 500m W, nr Chastelas. (Also known as Dents de Mézenc)
88/18 4° 0' 32.3" 44° 55' 57.7" nr Le Monastier "
1.5km SE of Le Monastier, railway cutting just N of D535
88/19 3° 59' 37.5" 44° 55' 36.5" " "
1.5km S of Le Monastier, quarry beside D500
88/20 4° 3' 38.1" 45° 5' 34.1" Suc de Pertuis Yssingeaux
as 86/44, new road cutting
88/21 4° 2' 34.1" 45° 2' 51.4" nr St Pierre Eynac "
500m to NNW of 87/66, N of D261, silicified sediments
88/22 4° 13' 22.5" 44° 53' 27.4" Suc de Touron Monastier
as 86/33, D378 roadside exposure, medium-grained facies
88/23 4° 14' 0.2" 44° 53' 39.5" nr Borée "
750m SW of Borée, on D215. Road exposure by small track. Dyke bearing 300°
88/24 4° 13' 43.1" 44° 53' 26.8" Prévenchères "
1.5km SW Borée on D215. Road exposure 200m W of village, phonolite
88/24b 4° 13' 43.1" 44° 53' 26.8" " "
as above, xenolith in phonolite
88/25 4° 13' 2.4" 44° 53' 58.8" Suc de Chabrières "
as 86/36, cumulate nodule

88/26	4° 3' 38.0"	45° 5' 34.1"	Suc de Pertuis	Yssingeaux
as 88/20				
88/27	4° 2' 30.8"	45° 6' 3.1"	Mont Loségal	"
as 84/17				
88/28	3° 57' 21.0"	45° 13' 19.1"	Miaune	Monistrol
as 87/13				
88/29	4° 10' 48.0"	45° 2' 9.9"	La Chaud de la Croix	Yssingeaux
as 87/29				
88/30	4° 0' 32.4"	44° 55' 57.7"	nr Le Monastier	Monastier
as 88/18				
88/31	4° 6' 13.5"	44° 58' 45.3"	nr Machabert	"
as 87/49				
88/32	4° 13' 23.9"	44° 58' 59.7"	Fay-sur-Lignon	"
as 87/8				
88/33	4° 13' 15.3"	44° 53' 26.3"	Suc de Touron	"
as 86/33				
88/34	4° 13' 1.4"	44° 53' 59.8"	Suc de Chabrières	"
as 86/36				
88/35	4° 21' 46.6"	44° 47' 43.5"	nr Mézilhac	Privas
as 87/61				
88/36	4° 14' 42.1"	44° 55' 9.9"	nr La Rochette	Monastier
2.5km N of La Rochette, exposure near D278, in stream. Dyke bearing 320°				

Appendix B

Specimen petrography

Key

Minerals are listed in order of decreasing proportion in the section(s).
Rock names are based mainly on the SiO_2 vs (Na_2O + K_2O) diagram in Cox *et al* (1979), but simplified so that the term "basalt" refers to the area around the boundary between the fields of basalt and basanite, and "phonolite" includes the phonolite field and the part of the trachyte field which lies near the boundary with phonolite. Other names are self-explanatory.
Numbers missing from the numerical sequence refer to specimens from areas other than the Velay oriental.
Anorthite content of plagioclase and orthoclase content of K-feldspar (where given) were determined mainly optically, but sometimes by microprobe.
Feldspathoids in groundmass are sometimes prefixed by "?", to denote the tentative nature of their identification. Criteria used were:

nepheline = anisotropic, uniaxial negative, clear, hexagonal and square sections
sodalite = isotropic, clear, hexagonal sections
nosean = isotropic, inclusion-rich, hexagonal sections
analcite = isotropic, clear, anhedral

Nepheline was stained in some sections, using the method of Shand (1939), to aid identification. The method is: smear phosphoric acid over an uncovered section, wait 3 minutes then rinse it clean. Immerse section in 0.25% methylene blue solution for 1 minute, then dip in water a few times to remove excess. Cover with glass slip.

Minerals:

aug = augite
aeg-aug = aegirine-augite
aeg = aegirine
diopside
aenig = aenigmatite
enstatite
olivine
quartz
Kspar = K-feldspar (undifferentiated)
orthoclase
san = sanidine
anorth = anorthoclase
plag = plagioclase
neph = nepheline
sodalite
nosean
analcite
zeol = zeolites (undifferentiated)
opaques = opaques (undifferentiated)
Ti-mag = Ti-rich magnetite
pleonaste
chromian spinel
pyrrhotite
amph = amphibole (mainly kaersutite)
arfvedsonite
mosandrite
eudialyte
biot = biotite
musc = muscovite
sphene
zircon
allanite
apat = apatite
glass

* = microphenocrysts + = partially resorbed or relict mineral ( ) = trace amount

Specimens

Specimen number and rock type	Phenocrysts	Groundmass
84/17 Phonolite = 86/22, 88/27	aphyric	san,aeg-aug,neph,Ti-mag,aenig
84/18 Phonolite	(sphene*)	san,aeg-aug,neph,Ti-mag,aenig
84/19a Benmoreite = 87/30	plag An47-57,amph+,san,Ti-mag*, (aug*),(sphene*),(biot*),(apat*)	san,aug,Ti-mag
84/19b Sanidinite	Coarse-grained rock: san,aug,Ti-mag,apat,sphene,zircon	
84/20 Phonolite = 86/15	aphyric	san,aeg-aug,neph,Ti-mag, aenig,(sphene)
84/21 Basalt	(olivine*)	glass,aug,plag An67,Ti-mag,olivine
84/22 Basalt	aug+,(olivine*)	plag An67,aug,Ti-mag
84/23 Benmoreite/mugearite	(amph*+),(Ti-mag*),(apat*),(plag An43*+)	plag An45,apat,Ti-mag,aug
84/24a Mugearite = 86/7	Ti-mag*,(apat*)	plag An45,aug,Ti-mag,olivine,apat

84/24b	(Ti-mag*),(apat*)	plag An45,aug,Ti-mag,olivine,apat
Mugearite		
84/25	olivine*	plag An65,aug,Ti-mag,olivine
Basalt		
84/26	(san)	san,neph,aeg
Phonolite		
= 87/56		
84/27	aphyric	san,neph,aenig,aeg,zeol,Ti-mag
Tinguaite		
= 87/55		
84/28	aphyric	san,neph,aeg,aenig,Ti-mag,
Tinguaite		zeol,eudialyte
= 87/55		
84/29	aphyric	san,neph,zeol,aeg,aenig,eudialyte
Phonolite		
= 87/53		
84/30	No section	
Basalt		
84/31	san,(aeg-aug*),(Ti-mag*),(amph*),(sphene*)	san,aeg-aug,Ti-mag
Phonolite		
= 86/40		
84/32	aphyric	san,neph,aeg,aenig
Phonolite		
84/33	olivine*	glass,aug,Ti-mag,olivine,plag An70
Basalt		
84/34	olivine*	glass,aug,Ti-mag,olivine,plag An66
Basalt		
84/35	olivine*	plag An60,aug,Ti-mag,olivine
Basalt		
84/36	olivine*	plag An66,aug,Ti-mag,olivine
Basalt		
84/37	aug,olivine	plag An66,aug,Ti-mag,olivine
Basalt		
84/38	olivine*	glass,aug,plag An64,Ti-mag,olivine
Basalt		
84/39	aug,olivine	plag An70,aug,olivine,Ti-mag
Basalt		
84/40	No section	
Basalt		
84/40a	(olivine*)	glass,aug,Ti-mag,plag An70,olivine
Basalt		
84/40b	(olivine*)	glass,aug,Ti-mag,plag An70,olivine
Basalt		
84/41	aphyric	glass,plag An63,aug,Ti-mag,olivine
Basalt		
84/42	(olivine*)	plag An64,aug,Ti-mag,olivine
Basalt		
84/43	aug,olivine,(Ti-mag)	plag An66,aug,Ti-mag,olivine
Basalt		
84/44	(Ti-mag*),(aug*)	plag An64,aug,Ti-mag,(olivine)
Hawaiite		
84/45	(Ti-mag*),(aug*)	plag An64,aug,Ti-mag,(olivine)
Hawaiite		
84/46	(amph*+),(Ti-mag*),(apat*),(plag*+)	plag An59,aug,Ti-mag
Benmoreite/hawaiite		
84/47	No section	
Basalt		
84/48	No section	
Basement gneiss		
84/50	No section	
Phonolite		
= 86/17		
84/51	No section	
Phonolite		

85/ 1	olivine,aug*	aug,olivine,plag An52,Ti-mag
Basalt		
85/ 2	Coarse-grained: orthoclase,plag An16,quartz,biot,musc,zircon	
Basement gneiss		
85/ 3	olivine	aug,olivine,Ti-mag,plag An57
Basalt		
85/ 4	olivine*	aug,plag An54,Ti-mag,olivine
Basalt		
85/ 5	san*	san,aeg,neph,Ti-mag,aenig
Phonolite		
= 87/63		
85/ 6	(san)	san,aeg,neph,(sphene)
Phonolite		
= 87/26		

85/ 7	olivine*	plag An65,glass,aug,Ti-mag,olivine
Basalt		
= 87/25		
85/ 8	(san)	san,aeg,arfvedsonite,aenig,Ti-mag
Quartz-trachyte		
= 87/24		
85/ 9	san,(amph*+),(Ti-mag*),(aeg*),(sphene*)	san,aeg,aenig,Ti-mag,(apat),(sphene)
Phonolite		
85/10	aug,olivine,Ti-mag	plag An71,aug,olivine,Ti-mag
Basalt		
85/12	olivine*	plag An55,Ti-mag,aug,olivine
Basalt		
85/13	olivine*	plag An58,aug,Ti-mag,olivine
Basalt		
85/14	aphyric	plag An59,aug,Ti-mag,olivine
Basalt		
85/15	aphyric	san,aeg,aenig,Ti-mag
Phonolite		
85/16	aphyric	san,aeg,aenig,Ti-mag
Phonolite		
85/17	(Ti-mag*)	plag An61,Ti-mag,aug,(olivine)
Hawaiite		
85/18	san Or47-53,amph*+,aug*,Ti-mag*,	san,aeg,Ti-mag,(sphene)
Phonolite	sphene*,(plag An42*),(apat*)	
85/19	olivine*	plag An65,aug,Ti-mag,olivine
Basalt		

86/ 1	No section	
Phonolite		
86/ 2	No section	
Basalt with lherzolite xenoliths		
86/ 3	No section	
Phonolite		
= 87/48		
86/ 4	No section	
Basement granite		
86/ 5	No section	
Basalt		
86/ 6	san,anorth Or17,aeg-aug*,Ti-mag*,(sphene*)	san,aeg,aenig,(sphene)
Phonolite		
86/ 7	No section	
Mugearite		
= 84/24a		
86/ 8	anorth+ Or13-42,biot+,aeg-aug*,amph*+,	san,aug,Ti-mag
Quartz-trachyte	(Ti-mag*),(plag An71-15),(apat*),(zircon*)	
= 87/58, 88/17		
86/ 9	(san),(sphene*)	san,aeg,neph,aenig,Ti-mag
Phonolite		
86/14	Coarse-grained: olivine,diopside,enstatite,chromian spinel	
Lherzolite nodule		
86/15	see 84/20	
Phonolite		
= 84/20		
86/17	No section	
Phonolite		
= 84/50		
86/18	san,aeg-aug,Ti-mag*,(sphene*)	san,aeg,neph,(Ti-mag)
Phonolite		
86/19	No section	
Phonolite		
86/20	san Or41-43,(amph*+),(aeg-aug*),	san,neph,aeg,Ti-mag
Phonolite	(Ti-mag*),(sphene*),(neph)	
86/21	san,plag An20	san,aeg,neph
Phonolite		
86/22	No section	
Phonolite		
= 84/17, 88/27		
86/23	Coarse-grained: quartz,orthoclase,plag,biot,musc,(allanite),(opaques),(zircon)	
Basement gneiss		
86/24	No section	
Phonolite		
= 86/25, 87/13, 88/28		
86/25	san Or 45-51,amph*+,Ti-mag*,(sphene*),	san,nosean,aeg,Ti-mag,sphene,apat
Phonolite	(aug*),(zircon*),(apat*)	
= 86/24, 87/13, 88/28		
86/26	No section	
Phonolite/benmoreite		
= 86/27		

86/27	amph+,(aug),(Ti-mag*),(sphene*),	san,aeg-aug,Ti-mag,zeol,sphene
Phonolite/ benmoreite	(anorth Or40-55),(apat*),(zircon*)	
= 86/26		
86/29	olivine*	aug,plag An60,Ti-mag,olivine
Basalt		
86/30	No section	
Basement gneiss		
86/31	anorth+,san,amph+,(Ti-mag*)	san,aug,Ti-mag,apat
Phonolite		
86/32	aphyric	san,neph,aeg,aenig,Ti-mag
Phonolite		
86/33	san,nosean,amph+,Ti-mag*,sphene*,	san,aeg-aug,sphene,
Phonolite	apat*,(aug*)	nosean,Ti-mag,apat
= 88/33		
86/34	No section	
Phonolite		
86/35	No section	
Phonolite		
86/36	No section	
Phonolite		
= 86/37		
86/37	san,(amph*+),(Ti-mag*),(sphene*)	san,aeg,nosean
Phonolite		
= 86/36		
86/38a to h	Cumulate nodules - petrography described in detail elsewhere	
86/39	No section	
Phonolite		
86/40	plag An35,san Or51-57,amph+,aug,sphene*,	san,aeg-aug,Ti-mag,zeol,
Phonolite	nosean*,Ti-mag*,(biot*),(apat*)	sphene,apat
86/41	san,plag An30,(amph*+)	san,aeg-aug,Ti-mag
Phonolite		
86/42	(san)	san,aeg,zeol,neph,aenig
Phonolite		
86/43	plag An26,san,(amph*+),(aug*),(Ti-mag*)	san,aeg-aug,Ti-mag,zeol
Phonolite		
86/44	(amph*+)	san,neph,aeg,aenig,(Ti-mag)
Phonolite		
= 88/20, 88/26		
86/45	san,plag An43,aeg-aug*,sphene*	san,neph,aeg,Ti-mag
Phonolite		
86/46	anorth Or29-38,plag An17-19,(aeg*)	anorth,neph,aeg,aenig,Ti-mag
Phonolite		
86/47	(Ti-mag*),(apat*)	plag An45-55,Ti-mag,aug,apat
Mugearite/benmoreite		
86/48	olivine*	glass,Ti-mag,olivine,aug,plag An71
Basalt		
86/49	olivine*	glass,aug,Ti-mag,olivine,plag An68
Basalt		
86/50	olivine*	aug,glass,Ti-mag,olivine,plag An69
Basalt		
86/51	(olivine*)	glass,aug,Ti-mag,olivine,plag An64
Basalt		
86/52	olivine*	aug,glass,plag An67,Ti-mag,olivine
Basalt		
86/53	aug,olivine,(Ti-mag*),(amph*+)	plag An64,aug,Ti-mag,olivine
Basalt		
86/54	san Or20-30,(Ti-mag*),(aeg-aug*),	san,aeg,Ti-mag,aenig,(sphene)
Phonolite	(sphene*),mosandrite	
86/55	(Ti-mag*)	plag An64,aug,Ti-mag,(olivine)
Hawaiite		
86/56	(amph*+),(plag An42*),(Ti-mag*),(apat*)	plag An55,aug,Ti-mag,(amph+)
Benmoreite/mugearite		
86/57	olivine*	plag An65,aug,Ti-mag,olivine
Basalt		
86/58	olivine*	plag An64,aug,Ti-mag,olivine
Basalt		
86/59	No section	
Basalt		
86/60	No section	
Lherzolite nodules		
86/61	No section	
Basalt		
86/62	Coarse-grained: orthoclase,quartz,plag,biot,(musc),(opaques),(zircon)	
Basement granite		
86/63	aug,olivine,pleonaste	aug,olivine,Ti-mag,plag An70,biot
Basalt		
86/64	san*	san,?sodalite,aeg,aenig,Ti-mag
Phonolite		
86/65	No section	
Phonolite		

86/66	olivine*,aug,(Ti-mag*)	plag An68,Ti-mag,aug,olivine
Basalt		
86/67	san,aeg-aug,(amph),(Ti-mag*),	san,neph,aeg-aug,Ti-mag,aenig
Phonolite	(sphene*),(apat*)	
86/68	No section	
Tinguaite		
86/69	Welded tuff. Clasts include: granite minerals,88/14 minerals,basalt	
= 88/15		
86/70	san,amph,aug,Ti-mag*,sphene*,apat*	san,aeg,?sodalite,neph,
Coarser-grained enclave in 86/67		Ti-mag,sphene,apat
87/ 1	No section	
Basalt		
87/ 2	No section	
Phonolite		
87/ 3	No section	
Phonolite		
87/ 4	No section	
Lherzolite nodules		
= 86/14		
87/ 5	No section	
Scoriaceous nodules		
87/ 6	No section	
Basalt		
87/ 7a	plag An46,amph*+,san,aug,(Ti-mag*),(apat*)	san,aeg-aug,Ti-mag,(apat)
Phonolite		
87/ 7b	(olivine*)	aug,plag An64,Ti-mag,olivine
Basalt		
87/ 8	plag An36+,Ti-mag*,(apat*),(amph*+)	plag An64,Ti-mag,aug,(apat)
Mugearite		
= 88/32		
87/ 9	No section	
Phonolite		
87/10	No section	
Mugearite		
87/11	plag An59,aug*,Ti-mag*	plag An59,Ti-mag,aug,(apat)
Benmoreite		
87/12	san,amph*+,Ti-mag*,(sphene*),	san,aeg-aug,Ti-mag,zeol
Phonolite	(zircon*),(apat*)	
87/13	see 86/25	
Phonolite		
= 86/24, 86/25, 88/28		
87/14	No section	
Phonolite		
87/15	aug,olivine	plag An70,aug,Ti-mag,olivine
Basalt		
87/16	No section	
Phonolite		
87/17	No section	
Phonolite		
87/18	No section	
Phonolite		
87/19	No section	
Basalt		
87/20	No section	
Basalt		
87/21	aug,olivine,Ti-mag*	plag An64,aug,olivine,Ti-mag
Basalt		
87/22	san*	san,aeg-aug,Ti-mag
Phonolite		
87/23	(Ti-mag*),(apat*),(amph*+)	san,plag An56,aug,Ti-mag
Mugearite		
87/24	see 85/8	
Quartz-trachyte		
= 85/8		
87/25	olivine*	plag An65,glass,aug,Ti-mag,olivine
Basalt		
= 85/7		
87/26	see 85/6	
Phonolite		
= 85/6		
87/27	san,(amph*+),(aeg*),(Ti-mag*),	san,aeg,neph,Ti-mag,aenig
Phonolite	(sphene*),(apat*)	
87/28	No section	
Phonolite		
87/29	aug,amph+,olivine,Ti-mag	glass,aug,plag An67,
Basalt		olivine,Ti-mag
= 88/29		
87/30	see 84/19a	
Benmoreite		
= 84/19a		

87/31	san,plag,amph+,Ti-mag*,aug*,	san,aug,Ti-mag,(apat)
Phonolite	(apat*),(sphene*)	
87/32	amph+,aug,plag An48-52+,Ti-mag*,	plag An56-59,aug,Ti-mag,
Hawaiite	(olivine*+),(apat*)	olivine,(apat)
87/33	plag An60,amph+,san,aug*,(Ti-mag*),	san,aeg-aug,Ti-mag,(sphene)
Benmoreite	(sphene*),(apat*)	
87/34	san,(plag An37),(amph*+),(aug*),	san,nosean,aeg-aug,Ti-mag,
Phonolite	(sphene*),(Ti-mag*)	sphene,(apat)
87/35	No section	
Phonolite		
87/36	san,(sphene*),(Ti-mag*),(aeg-aug*)	san,aeg,nosean
Phonolite		
87/37	No section	
Basalt		
87/38	olivine,aug	aug,olivine,plag An70,Ti-mag
Basalt		
87/39	see 87/40	
Phonolite		
= 87/40		
87/40	san,amph*+,(aug*),(sphene*),	san,neph,aeg,Ti-mag,sphene
Phonolite	(apat*),(zircon*)	
= 87/39		
87/41	No section	
Basalt		
87/42	(olivine*)	aug,plag An70,olivine,
Basalt		glass,Ti-mag
87/43	aug,olivine,(pleonaste*),(pyrrhotite*)	aug,glass,plag An72,Ti-mag,olivine
Basalt		
87/44	san*	san,aeg-aug,Ti-mag
Quartz-trachyte		
87/45	olivine,(aug*)	plag An60,aug,Ti-mag,glass,olivine
Basalt		
87/46	san,plag An36,aug,(amph*+),(sphene*),	san,nosean,aeg,Ti-mag,(sphene)
Phonolite	(Ti-mag*),(apat*)	
87/47	olivine*	aug,Ti-mag,plag An66,olivine,biotite
Basalt		
87/48	san,aeg*,(Ti-mag*),(biot*+),(apat*)	san,neph,aeg,aenig,Ti-mag
Phonolite		
= 86/3		
87/49	aug,olivine,(plag+),(Ti-mag*)	plag An70,aug,olivine,Ti-mag,
Basalt		glass,(biot)
= 88/31		
87/50	No section	
Phonolite		
87/51	(Ti-mag*),(apat)	san,aug,Ti-mag,(apat)
Benmoreite		
87/52	Coarse grained: plag,orthoclase,quartz,biot,musc,(opaques),(zircon)	
Basement gneiss		
87/53	No section	
Phonolite		
= 84/29		
87/54	No section	
Tinguaite		
87/55	see 84/27, 84/28	
Tinguaite		
= 84/27, 84/28		
87/56	No section	
Phonolite		
= 84/26		
87/57	No section	
Phonolite		
87/58	see 86/8	
Quartz-trachyte		
= 86/8, 88/17		
87/59	Various coarse-grained granulite nodules	
87/60	aphyric	san,aeg,Ti-mag,aenig
Phonolite		
87/61	No section	
Phonolite		
= 88/35		
87/62	san,aeg*,(amph*+),(Ti-mag*),(apat*)	san,aeg,Ti-mag,analcite,(sphene)
Phonolite		
87/63	No section	
Phonolite		
= 85/5		
87/64	olivine*,Ti-mag*,(amph+),(aug+)	aug,plag An69,Ti-mag,olivine
Basalt		
87/65	amph*+,(neph*),(san),(sphene*)	san,aeg,nosean,neph
Phonolite		
87/66	Diatreme infill, with clasts of: quartz, K-spar, biot and igneous and sedimentary lithics	

87/67	(san*),(sphene*)	san,aeg,?analcite
Phonolite		
87/68	Kspar+,plag ?An30,(Ti-mag*),(apat*)	san,aeg-aug,Ti-mag,(apat)
Benmoreite/trachyte		
87/69	No section	
Phonolite		
87/70	anorth,amph+,plag An27-44,Ti-mag*, (aug),(apat*),(biot*)	san,aeg-aug,Ti-mag,apat
Benmoreite/phonolite		
87/71	No section	
Basalt		
87/72	plag,san,aug*,(sphene*),(Ti-mag*),(apat*)	san,aeg-aug,Ti-mag,(apat)
Benmoreite		
87/73	No section	
Phonolite		
87/74	amph+,aug*,Ti-mag*,plag An23-34,(apat*)	plag An53,aeg-aug,Ti-mag,(apat)
Mugearite/benmoreite		
87/75	(olivine*),(apat*)	plag An60,aug,Ti-mag,olivine
Hawaiite		
87/76	san	san,aeg,neph,aenig,Ti-mag
Phonolite		
87/77	No section	
Phonolite		
87/78	No section	
Phonolite		
87/79	No section	
Phonolite		
87/80	(san),(amph*+),(sphene*)	san,neph,aeg
Phonolite		
87/81	san,aeg-aug*,Ti-mag*,(amph*+),(sphene*)	san,aeg,Ti-mag,nosean
Phonolite		
87/88	aug,amph+,Ti-mag+,olivine+,pleonaste+,	aug,plag An65,Ti-mag,olivine
Basalt	apat+,(plag An54+)	
88/ 1	(Ti-mag*),(apat*)	plag An55,san,Ti-mag,glass,aug
Mugearite		
88/ 2a	Coarse-grained: orthoclase,quartz,plag An30,biot,opaques,apat,(allanite),(zircon)	
Basement granite		
88/ 2b	No section	
Siltstone		
88/ 3a	No section	
Basalt with basement xenoliths		
88/ 3b	No section	
Basement xenolith		
88/ 3c	Coarse-grained: orthoclase,quartz,biot,musc,plag An32,(allanite),(apat),(zircon)	
Basement granite		
88/ 4	No section	
Phonolite		
88/ 5	No section	
Phonolite		
88/ 6	(san),(Ti-mag*),(sphene*)	san,aeg-aug,Ti-mag,sphene
Phonolite		
88/ 7	No section	
Basalt		
88/ 8	Coarse-grained: orthoclase,quartz,plag An27,biot,apat,(zircon)	
Basement granite		
88/ 9	No section	
Pyroclastics		
88/10a	plag An44,biot+,anorth+,aug+,amph+,	carbonate,san,plag An38,Ti-mag,apat
Mugearite	Ti-mag*,apat*	
88/10b	plag An55,biot,amph+,Ti-mag*,(apat*)	san,carbonate,plag,Ti-mag,biot,apat
Benmoreite		
88/11	No section	
Similar material to 88/10a,b (not analysed)		
88/12	No section	
Finer-grained vein of similar material to 88/10a,b (not analysed)		
88/13a	No section	
Spheroid in pyroclastics		
88/13b	anorth,biot,plag ?An40,(Ti-mag*),(apat*)	san,carbonate,Ti-mag
Trachyte		
88/14a to w	Large suite of cumulate nodules described in detail elsewhere	
88/15	see 86/69	
Welded pyroclastics		
= 86/69		
88/16	amph,plag An44,anorth,Ti-mag*,aug, sphene*,apat*	san,aug,Ti-mag,plag An38,apat
Mugearite/benmoreite		
88/17	see 86/8	
Quartz-trachyte		
= 86/8, 87/58		

88/18 No section
Basalt
= 88/30
88/19 No section
Basalt
88/20 No section
Phonolite
= 86/44, 88/26
88/21 No section
Silicified sediments
88/22 san,neph,(apat),(sphene*) san,neph,aeg
Phonolite
88/23 Ti-mag* plag An60,aug,Ti-mag,biot,(apat)
Mugearite
88/24a san,Ti-mag*,(aeg*),(zircon*) san,neph,aeg,Ti-mag
Phonolite with basement xenoliths
88/24b Coarse-grained: orthoclase,quartz,plag,biot,(zircon),(opaques)
Basement xenolith
88/25 Described with 88/14a to w elsewhere

88/26 see 86/44
Phonolite
= 86/44, 88/20
88/27 see 84/17
Phonolite
= 84/17, 86/22
88/28 see 86/25
Phonolite
= 86/24, 86/25, 87/13
88/29 see 87/29
Basalt
= 87/29
88/30 aug*,olivine* aug,plag An55,Ti-mag,olivine
Basalt
= 88/18
88/31 see 87/49
Basalt
= 87/49
88/32 see 87/8
Mugearite
= 87/8
88/33 see 86/33
Phonolite
= 86/33
88/34 No section
Phonolite
= 86/36, 86/37
88/35 san,amph+,(aug*),(Ti-mag*),(apat*),(biot*) san,aeg,Ti-mag,(biot)
Phonolite
= 87/61
88/36 san,amph+,aug,Ti-mag*,sphene*,(apat*) san,aeg,Ti-mag,(sphene),(apat)
Phonolite

Appendix C

Whole-rock and mineral analyses

C.1 Whole-rock analysis

C.1.1 Details of XRF spectrometer

The machine used was a Phillips PW1400 X-ray fluorescence (XRF) spectrometer, with data processing using the X14 package on a PDP11 minicomputer. A Rh-tube was used to generate the X-rays for both the major and trace element analyses. Analysing crystals used were; LiF 220, LiF 200, PE and PX1. At least 25 U.S.G.S. standards were used to calibrate the machine on a regular basis, bracketing the specimen unknowns in composition.

Majors - Fused glass beads were used for major element determination. Since no heavy absorber was added to the flux the X14 package makes a correction using α-values (absorbance factors) for mass absorption, using De Jongh's formula.

Traces - Trace elements were analysed in two groups. The first group includes Nb, Zr, Y, Sr, Rb, Pb, U, Th, Zn, Cu, Ni and Ga, with mass absorption determined using the Rh Compton scatter peak. The second group includes Co, Cr, V and Ba, and in addition to the Compton scatter peak these have mass absorption corrected for the Fe, Mn and Ti absorption edges and line overlaps.

C.1.2 Sample Preparation

Sawing - Samples were sawn into 5-10mm thick slabs using a diamond saw, removing all weathered material. All metal traces from the saw were ground off. Slabs were washed in individual beakers of deionised water in an ultrasonic bath and dried in an oven. Dried slabs were stored in sealed, labelled plastic bags.

Crushing - At first samples were passed through a jaw-crusher and reduced to 5mm chips. This stage was later found to be unnecessary, and was omitted to reduce contamination. A "Tema" swing-mill was used to reduce the slabs/chips to a powder. A tungsten-carbide container was used with the mill. Fineness of powder was assessed qualitatively by the "grittiness" on the fingers. Most rocks were fine-grained lavas and amounts ≈100g were sufficient to ensure homogeneity. For less homogeneous rocks, such as ankaramites, the results of several runs were added together.

In all the processes involving powdered rock the equipment was cleaned thoroughly with acetone between samples, to avoid contamination. All powders were stored in airtight jars.

C.1.3 Bead and pellet manufacture

Beads - Rock powder was weighed into crucibles and heated overnight at 110˚C. The resulting weight loss is H_2O-. The crucibles were then placed in a furnace at 1000˚C and left overnight. Weight loss is H_2O+, with structurally bound volatiles giving positive values, offset by FeO conversion to Fe_2O_3. Powders were allowed to cool in desiccators. Some peralkaline phonolites had such low melting points that their powders sintered at 1000˚C and had to be reground with a mortar and pestle.

The flux used was Spectroflux 100 lithium tetraborate ($Li_2B_4O_7$), which was dried for at least one hour at 600˚C, and allowed to cool in a desiccator. 5.0000g ± 0.0001g flux and 1.0000g ± 0.0001g rock powder were weighed into a $Pt^{95\%}Au^{5\%}$ crucible (cleaned in boiling 50% HCl between samples) and thoroughly stirred. This crucible was put in a furnace at 1225-30˚C, and swirled every 5 minutes to ensure thorough dissolution. After 15-20 minutes the melt was poured into a Pt/Au mould, removed from the furnace and quenched over a jet of compressed air. If the bead showed an even colour and a smooth base it was labelled and sealed in a plastic bag ready for analysis.

Pellets - approximately 10g of rock powder was weighed out and put in a mortar. $1cm^3$ "Moviol" organic binding agent was then thoroughly mixed with this powder. The mixture was put into a polished piston mould and tamped down, before inserting the piston and applying about 10^5 Pa for a few minutes. If the pellet was of good enough quality after removal from the mould it was placed

in an oven to dry overnight. Finally loose powder was removed and the pellet sealed in a plastic bag ready for analysis.

C.1.4 Precision and accuracy

Devey (1986) investigated analytical variation due to both bead-making and machine analysis by making multiple beads of the same sample, and by reanalysing one bead 67 times. He showed that the maximum variation in both cases was about 1% for SiO_2 and 8% for P_2O_5. These two elements were respectively the best and worst for precision, due to their concentration in the average rock, with SiO_2 usually >45% and P_2O_5 <1%. Normalisation of totals was recommended for the best results.

Accuracy can be assessed by comparison with standards. Devey (1986) found errors were no more than 5% for most major and trace elements. Investigation of Sr analysis for this thesis demonstrated that errors increase dramatically below about 10ppm Sr. This limit probably applies to most of the trace elements.

In addition, K_2O was measured by atomic absorption spectrophotometry, and the results are compared with those from XRF in Figure C.2. The similarity between the results from these very different techniques suggests that they are accurate.

C.1.5 Problems encountered

Most beads produced low totals, varying from 93% to 100%. Standards gave good totals (99 - 101%) so machine calibration was eliminated, especially since the SiO_2 calibration line was re-run several times and beads with low totals remained low. The beads themselves were therefore implicated. Two factors affect the quality of a bead;

a) rock powder (and flux)
b) manufacturing process.

a) rock powder (and flux)

No correlation was found between analysis totals and:

Rock type - over the range ankaramite to peralkaline phonolite.
Trace element content - maximum content 0.5% traces.
Measured H_2O+ - powders appear to be anhydrous after 12 hours at 1000˚C.

Weighing inaccuracy for the powder+flux gives a maximum error on the total of ±0.05%. The flux might have been damp even after the 600˚C oven, but there was no correlation between poor totals and particular pots of flux. A new flux was tried by some workers in the department, but after initially good results the same problems with poor totals reappeared.

b) manufacturing process

The main variable in the process was the length of time the melt spent in the furnace, assuming the crucible was swirled sufficiently to give complete dissolution of the rock powder. To gauge the effect of "cooking time" on totals several beads were made of the alkali-rich phonolite 86/64, with 5, 10, 15, 20, 25 and 30 minutes cooking time. The results are presented in Table C.1. The 30-minute bead shows some loss of alkalis, but only about 0.06% in all. The low totals of the 5 and 10 minute beads are harder to explain. Possibly some grains of powder were left undissolved in the glass, which would lower the apparent proportion of rock present. The conclusion from this experiment is that 15-20 minutes was the ideal time to leave the melt in the furnace.

Confirmation that K_2O loss was insignificant was provided by the 16 K_2O analyses of the K-Ar dated specimens (see section 1.3.3.2). These analyses were made by atomic absorption spectrophotometry (AAS). Figure C.2 compares K_2O by XRF analysis with K_2O by AAS, showing that the results are closely similar, despite the fact that none of the analyses are on a split of the same powdered sample.

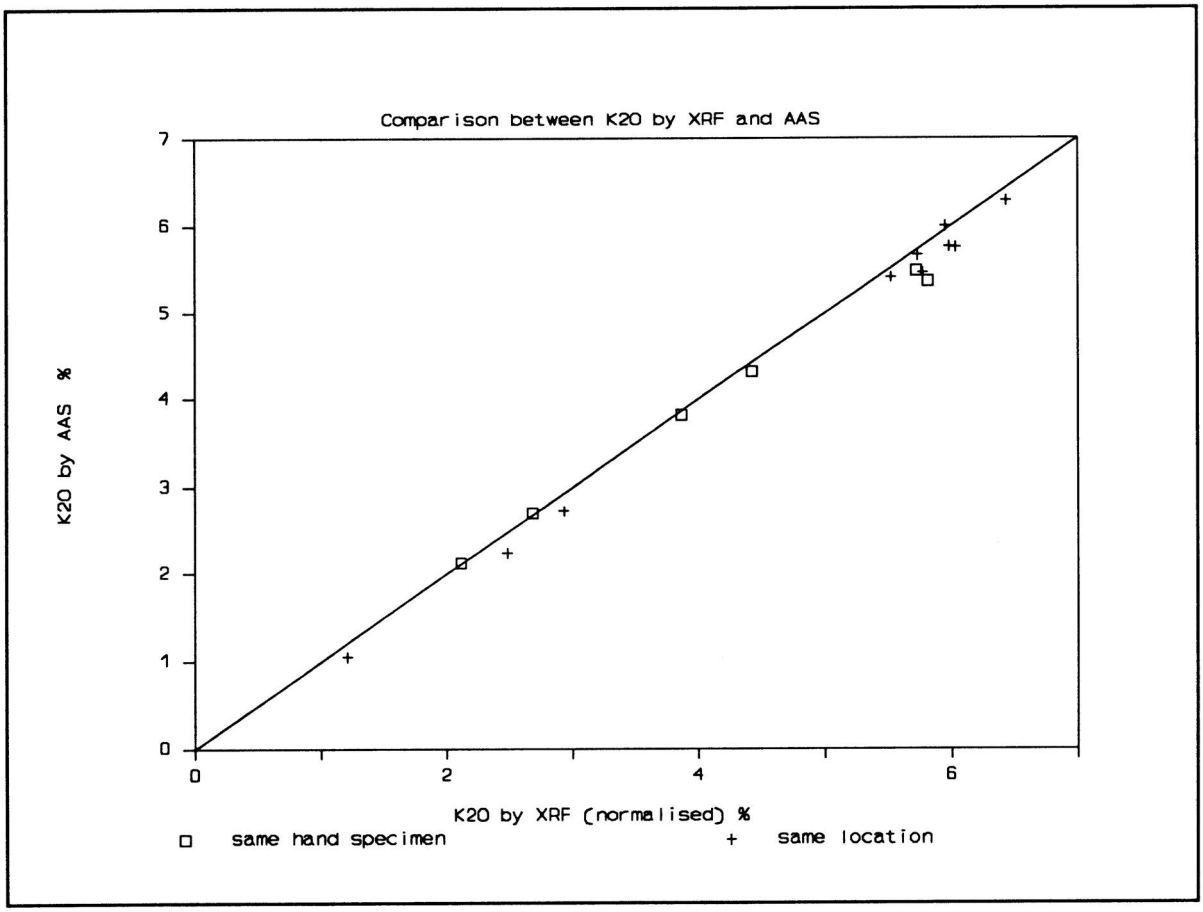
Conclusion

The main source of error on the major element totals remains a mystery. However, normalisation produces consistent results whatever the total. The second part of the 86/64 experiment (Table C.1) involved making beads with varied flux to rock ratios. Beads were made with this as 4:1 and 6:1, and after normalisation these gave results very similar to those from the 5:1 beads. All the

Table C.1
Experimental beads of 86/64

86/64 phonolite	5 mins	10 mins	15 mins	20 mins	25 mins	30 mins	4:1	6:1
SiO2	59.79	62.08	62.89	62.94	63.18	62.78	78.54	51.79
TiO2	0.22	0.23	0.23	0.23	0.23	0.23	0.28	0.19
Al2O3	17.66	18.28	18.51	18.52	18.58	18.49	23.05	15.25
Fe2O3	3.03	3.11	3.12	3.13	3.15	3.12	3.87	2.60
MnO	0.31	0.32	0.32	0.32	0.32	0.32	0.39	0.27
MgO	0.08	0.08	0.07	0.09	0.08	0.07	0.08	0.07
CaO	0.95	0.97	0.97	0.97	0.97	0.96	1.20	0.81
Na2O	7.85	7.84	7.82	7.88	7.89	7.79	9.73	6.62
K2O	5.42	5.45	5.41	5.40	5.35	5.29	6.72	4.52
P2O5	0.00	0.00	0.00	0.00	0.00	0.00	0.00	0.00
Total	95.31	98.36	99.34	99.48	99.75	99.05	123.86	82.12
(normalised)								
SiO2	62.73	63.12	63.31	63.27	63.34	63.38	63.41	63.07
TiO2	0.23	0.23	0.23	0.23	0.23	0.23	0.23	0.23
Al2O3	18.53	18.58	18.63	18.62	18.63	18.67	18.61	18.57
Fe2O3	3.18	3.16	3.14	3.15	3.16	3.15	3.12	3.17
MnO	0.33	0.33	0.32	0.32	0.32	0.32	0.31	0.33
MgO	0.08	0.08	0.07	0.09	0.08	0.07	0.06	0.09
CaO	1.00	0.99	0.98	0.98	0.97	0.97	0.97	0.99
Na2O	8.24	7.97	7.87	7.92	7.91	7.86	7.86	8.06
K2O	5.69	5.54	5.45	5.43	5.36	5.34	5.43	5.50
P2O5	0.00	0.00	0.00	0.00	0.00	0.00	0.00	0.00
Total	100.01	100.00	100.00	100.01	100.00	99.99	100.00	100.01

Figure C.2
Comparison between XRF and AAS analyses of K_2O



analyses in this thesis were therefore normalised, and those with the worst totals (< 96%) were remade from scratch. The vast majority of analyses in this thesis have totals above 97%.

C.2 Mineral analyses

C.2.1 Details of microprobe

The machine used was a Cambridge Instruments Microscan 9 electron microprobe with two wavelength dispersive spectrometers. Its specimen stage could be programmed to record locations so that batches of analyses can be left to run automatically. The microprobe was variously controlled by a DECwriter terminal, a BBC micro and an Opus IBM-compatible p.c. These applied the ZAF correction (Z = atomic number, A = absorption, F = secondary fluorescence) to convert apparent percentage element to true percentage. Standards were used to calibrate for all elements before each run.

C.2.2 Sample preparation

Samples were prepared as standard thin sections, with a thickness of 30μm on 25mm x 48mm glass slides. These were polished to a tolerance of 0.05μm, and a 200Å thick layer of carbon was applied to prevent charge buildup on the specimen. Reflected light petrography was carried out before the application of this coating.

C.2.3 Operating conditions

Spot analyses on minerals

Beam size was 0.5 - 1.0μm. Accelerating potential 20kV. Beam current 4×10^{-8}A. Most of the error was in counting statistics, with $2\sigma = 1\%$ for the major (>5%) elements.

Raster analyses on glasses

Glasses are much more delicate than minerals and suffer particularly from loss of Na_2O due to the intense heat of the beam causing boiling and increased mobilisation of volatile components.

Two analytical methods were tried, the first being to defocus the beam to reduce its intensity. This vastly increased the Na_2O content, but gave low totals, either due to dissolved water in the glass, or lost counts at the defocussed edges of the beam. Since this technique was so unquantifiable it was not used.

The second technique was to raster the beam across a known area of the sample, also reducing the effective intensity of the beam. Reducing the beam current from 4.0×10^{-8}A to 3.4×10^{-8}A (the maximum range) made no significant difference to the results. The main variables were the area of the raster and the scan rate.

If the area was too small, the beam intensity remained too high and Na_2O was lost. If the area was too large, the beam defocussed at the edges of the scan and counts were lost, giving low totals. The best compromise was found to be a 30μm square.

The scan rate had to be at a high enough rate to reduce the beam intensity, but if the rate was too high the scanning coils generated too much electronic noise and gave a poor signal/noise ratio. The best compromise was 4 seconds per scan.

No clear criteria could be used to assess the final analyses, but totals > 95% usually indicated loss of volatiles, and totals < 90% usually indicated loss of counts. The best analyses were those with the highest values of Na_2O and totals between 90% and 95%.

A specialised program for glass analysis which measures Na_2O content at timed intervals and extrapolates back to time = 0, is now available. This was not available when this study was made.

Appendix C
1) Whole rock analyses

Key:

Phon'ite	= phonolite
phon	= phonolite
benm'ite	= benmoreite
mug'ite	= mugearite
mug	= mugearite
haw'ite	= hawaiite
haw	= hawaiite
qz-trach	= quartz-trachyte
lherz	= lherzolite

125	F84/17	F84/19A	F84/21	F84/23	F84/25	F84/33	F84/34	F84/36	F84/37	F84/39	F84/40B	F84/41	F84/42	F84/43	F84/44	F84/45	F84/46	F84/50	F85/5	F85/6	F85/7	F85/15	F85/16	F85/18	SH86/6
analyses	phon'ite	benm'ite	basalt	ben/mug	basalt	basalt	basalt	basalt	basalt	basalt	basalt	basalt	basalt	basalt	haw'ite	haw'ite	ben/haw	phon'ite	phon'ite	phon'ite	basalt	phon'ite	phon'ite	phon'ite	phon'ite
SiO2	61.25	57.52	43.34	54.61	42.65	42.65	43.48	46.53	43.84	44.71	43.07	45.04	45.04	44.62	47.27	47.35	54.57	59.67	62.67	59.81	44.61	60.66	61.73	60.46	60.10
TiO2	0.33	0.93	3.94	1.44	3.67	4.37	4.47	3.12	3.53	3.32	4.04	3.21	3.39	3.15	2.84	2.73	1.53	0.27	0.24	0.19	3.42	0.20	0.24	0.41	0.19
Al2O3	19.49	19.68	14.58	18.65	14.76	14.18	14.61	15.29	14.95	15.08	14.56	15.74	15.98	14.57	16.86	16.87	18.54	20.78	18.41	20.89	15.28	19.65	20.01	20.15	20.56
Cr2O3	0.00	0.00	0.02	0.00	0.02	0.02	0.02	0.03	0.03	0.03	0.02	0.01	0.01	0.03	0.01	0.01	0.00	0.00	0.00	0.00	0.02	0.00	0.00	0.00	0.00
Fe2O3T	2.53	4.74	13.82	6.90	13.62	13.76	13.65	12.44	12.95	12.95	14.00	12.79	12.48	12.72	11.84	11.61	7.18	2.57	3.56	2.90	13.18	2.90	2.94	2.64	2.38
MnO	0.31	0.15	0.19	0.25	0.19	0.17	0.17	0.18	0.18	0.17	0.18	0.19	0.20	0.17	0.24	0.20	0.23	0.19	0.23	0.35	0.19	0.27	0.22	0.19	0.21
MgO	0.18	0.99	6.76	1.54	7.89	8.69	7.24	7.90	7.83	7.81	7.32	6.69	5.09	7.51	3.21	3.92	1.46	0.19	0.04	0.11	7.08	0.09	0.06	0.23	0.07
CaO	1.00	4.51	9.71	4.95	9.49	9.59	9.85	9.86	9.63	9.38	9.64	9.00	9.53	10.41	8.71	8.18	5.00	1.29	1.04	0.64	9.10	0.92	1.16	1.44	1.07
Na2O	8.11	4.72	3.35	5.95	3.29	2.23	3.14	3.26	3.58	3.48	2.63	2.89	4.20	3.73	4.27	4.34	5.79	9.30	7.36	9.40	3.28	8.44	7.96	7.44	8.71
K2O	5.98	5.24	2.76	3.48	1.71	2.73	2.18	1.16	0.94	0.98	2.50	2.08	1.60	0.86	2.25	2.26	3.57	5.33	5.66	5.36	2.31	5.38	5.48	6.18	5.78
P2O5	0.02	0.25	0.66	0.53	1.00	0.51	0.79	0.69	0.65	0.66	0.67	0.87	0.68	0.62	1.48	1.48	0.57	0.03	0.01	-0.01	0.81	0.00	0.00	0.05	0.00
Total	99.21	98.73	99.13	98.31	98.29	98.90	99.60	100.46	98.11	98.56	98.62	98.49	98.21	98.40	98.98	98.94	98.44	99.62	99.22	99.65	99.28	98.52	99.81	99.20	99.08
Zn ppm	115.1	64.5	102.5	102.3	103.3	91.4	100.3	95.3	95.4	87.1	99.6	100.7	97.9	97.1	108.1	110.2	101.8	103.5	112.4	193.5	98.2	152.7	132.7	76.9	117.9
Cu ppm	3.9	4.7	45.3	7.6	32.9	52.3	37.2	49.1	50.4	57.2	50.5	41.6	37.7	57.1	9.7	14.7	3.3	6.5	1.7	3.6	36.3	1.3	3.7	1.1	2.4
Ni ppm	1.4	3.1	62.2	1.8	80.5	87.0	90.8	123.7	89.6	85.5	56.8	58.6	63.0	99.6	20.1	16.8	2.1	2.3	2.8	3.0	81.7	3.0	2.3	1.2	2.0
Co ppm	8.6	8.2	56.5	8.2	55.1	55.2	60.8	52.9	52.2	45.7	48.7	44.2	49.4	55.0	32.7	27.0	12.4	9.1	30.7	30.6	50.1	9.8	8.0	6.5	26.5
Cr ppm	3.1	6.5	107.1	6.5	97.8	136.6	112.1	206.9	179.0	169.1	84.9	53.6	77.8	180.5	38.9	30.8	2.4	8.3	3.0	2.9	111.8	3.7	2.5	6.4	6.2
V ppm	9.1	45.0	256.6	19.6	267.0	271.4	312.4	241.1	276.1	247.7	258.6	203.3	237.8	250.6	152.9	116.4	47.1	13.2	10.4	8.5	245.6	4.7	7.4	12.2	4.9
Ba ppm	46.8	890.4	677.7	1068.1	653.2	570.1	547.8	612.7	560.8	552.2	745.1	689.3	590.2	534.7	670.1	715.3	1071.8	539.6	70.3	36.8	630.9	22.9	67.0	414.9	81.8
Ga ppm	23.9	21.0	21.9	21.2	22.1	20.7	20.8	21.4	21.8	20.5	21.6	21.4	21.8	20.9	20.4	20.9	21.7	28.3	28.8	38.9	20.5	31.5	31.7	21.9	28.9
Rb ppm	178.4	136.3	64.9	88.9	62.7	51.7	56.2	42.1	56.9	56.2	61.1	52.8	48.5	46.5	56.2	55.4	89.6	244.3	226.8	297.4	54.5	275.1	268.2	142.7	205.1
Sr ppm	5.7	515.9	747.8	1144.6	897.6	667.3	742.3	815.4	774.4	773.4	853.3	996.3	811.6	760.7	1132.7	1147.0	1168.0	309.6	15.2	5.2	870.8	31.5	15.8	151.4	29.3
Y ppm	45.0	22.3	26.8	39.8	33.0	24.4	26.3	30.6	29.2	29.2	27.7	32.8	29.3	27.8	36.3	37.4	39.1	25.2	43.3	64.4	30.6	55.6	52.0	30.1	28.5
Zr ppm	1001.4	375.1	331.1	451.2	375.7	243.3	340.4	294.0	244.2	240.5	330.7	322.3	263.5	245.7	293.8	303.6	454.7	958.4	982.2	1675.1	295.6	1302.1	1271.1	670.6	947.8
Nb ppm	207.5	88.1	82.6	119.3	81.7	66.3	65.4	69.7	58.8	58.0	83.8	85.1	66.2	58.6	72.8	77.5	114.8	149.7	208.8	339.4	76.3	298.7	290.8	164.7	161.2
Pb ppm	16.0	9.9	5.7	8.8	3.8	6.0	6.4	6.2	3.1	6.9	5.5	3.4	5.7	3.7	7.1	6.8	9.5	18.1	18.2	20.2	3.2	19.7	18.7	7.5	14.8
Th ppm	22.7	12.6	6.6	13.0	5.3	4.6	6.1	7.3	6.5	6.6	5.0	7.3	6.0	6.3	6.2	7.3	10.8	32.5	27.4	41.8	5.9	35.0	35.1	12.8	23.0
U ppm	4.7	1.5	0.2	3.1	0.6	0.6	1.5	0.4	1.8	0.4	1.4	1.0	1.3	0.5	1.6	-0.4	2.1	9.6	6.7	11.7	0.5	6.5	4.6	2.2	6.6
total traces(%)	0.17	0.22	0.26	0.31	0.28	0.23	0.25	0.27	0.25	0.24	0.27	0.27	0.24	0.24	0.27	0.27	0.32	0.25	0.18	0.28	0.26	0.23	0.22	0.17	0.17

125	SH86/8	SH86/9	SH86/15	SH86/18	SH86/20	SH86/21	SH86/25	SH86/27	SH86/29	SH86/31	SH86/32	SH86/33	SH86/35	SH86/37	SH86/40	SH86/41	SH86/42	SH86/43	SH86/44	SH86/45	SH86/46	SH86/47	SH86/48	SH86/49	SH86/50
analyses	qz-trach	phon'ite	phon'ite	phon'ite	phon'ite	phon'ite	phon'ite	phon/ben	basalt	phon'ite	phon'ite	phon'ite	phon'ite	phon'ite	phon'ite	phon'ite	phon'ite	phon'ite	phon'ite	phon'ite	phon'ite	mug/ben	basalt	basalt	basalt
SiO2	64.36	60.39	61.80	60.81	60.51	59.34	58.66	57.34	45.85	59.94	60.20	58.53	59.59	58.11	58.65	60.54	60.52	59.93	60.23	60.35	59.91	53.63	42.97	42.57	42.70
TiO2	0.46	0.38	0.38	0.21	0.29	0.12	0.29	0.86	3.60	0.64	0.25	0.31	0.19	0.15	0.63	0.49	0.23	0.44	0.18	0.27	0.15	1.31	4.31	4.53	4.47
Al2O3	16.94	19.79	19.58	20.54	20.18	21.24	21.18	19.73	15.73	19.03	19.56	21.41	21.63	21.70	20.44	18.96	19.99	19.15	20.04	19.80	20.27	18.92	14.29	14.22	14.33
Cr2O3	0.00	0.00	0.00	0.00	0.00	0.00	0.00	0.00	0.02	0.00	0.00	0.00	0.00	0.00	0.00	0.00	0.00	0.00	0.00	0.00	0.00	0.00	0.03	0.02	0.02
Fe2O3T	4.21	2.65	3.22	2.12	2.48	1.92	2.47	4.63	13.48	4.39	3.65	2.91	2.14	2.64	3.18	4.02	2.75	3.95	2.27	2.37	2.45	7.86	13.63	14.12	13.89
MnO	0.16	0.21	0.27	0.26	0.21	0.32	0.20	0.20	0.23	0.17	0.49	0.17	0.26	0.23	0.15	0.18	0.25	0.20	0.29	0.24	0.25	0.23	0.17	0.17	0.17
MgO	0.57	0.23	0.23	0.12	0.19	0.06	0.24	1.21	5.85	0.49	0.14	0.20	0.17	0.23	0.39	0.26	0.11	0.22	0.11	0.13	0.11	1.68	8.21	7.86	7.60
CaO	1.67	1.08	0.95	0.97	1.56	0.83	1.30	3.15	10.21	1.95	0.94	1.31	1.29	2.17	2.33	2.00	0.79	1.84	1.26	1.54	1.12	5.61	9.64	9.97	10.04
Na2O	5.69	8.08	7.66	8.69	7.34	9.49	8.39	5.59	3.25	6.94	9.06	8.89	8.79	7.28	6.70	6.56	8.91	7.25	8.51	7.66	8.75	5.77	2.35	2.26	2.18
K2O	5.31	5.90	5.96	5.72	6.42	5.47	6.31	5.80	1.60	5.02	5.07	5.96	5.80	5.62	6.20	6.13	5.35	5.87	5.43	5.87	5.55	3.24	2.80	2.84	2.67
P2O5	0.15	0.03	0.04	0.01	0.03	-0.01	0.03	0.25	1.10	0.15	-0.01	0.04	0.00	0.00	0.09	0.06	0.01	0.06	0.00	0.02	-0.01	0.77	0.53	0.47	0.51
Total	99.52	98.74	100.09	99.46	99.20	98.78	99.08	98.77	100.92	98.74	99.36	99.71	99.88	98.14	98.77	99.21	98.92	98.92	98.32	98.26	98.56	99.02	98.92	99.03	98.60
Zn ppm	78.9	94.6	101.4	114.2	81.9	167.6	123.3	93.6	105.2	62.4	240.7	84.8	121.3	116.6	63.3	79.9	134.2	90.3	132.5	98.4	145.7	108.0	92.3	88.8	91.8
Cu ppm	3.0	3.3	4.3	3.7	6.5	3.3	3.9	7.4	29.4	2.5	3.5	2.8	2.9	3.6	1.4	3.5	4.5	2.0	3.5	1.0	2.6	4.9	54.6	50.5	55.1
Ni ppm	2.0	1.5	5.0	1.1	1.5	1.8	1.2	2.4	93.3	1.9	3.8	2.1	0.2	1.3	1.2	0.7	2.2	2.3	2.6	1.0	1.3	2.2	94.8	93.1	87.1
Co ppm	14.9	9.5	12.6	9.6	14.0	11.7	20.1	12.1	54.7	8.4	8.1	29.4	9.1	8.7	8.1	21.6	5.2	9.8	12.0	8.6	23.0	13.7	54.6	51.9	62.6
Cr ppm	4.7	2.2	7.3	3.0	5.1	5.8	1.9	1.5	122.5	5.8	-2.3	5.4	4.2	3.9	5.9	4.4	2.8	3.9	3.0	4.9	4.1	1.9	148.6	137.1	130.3
V ppm	13.7	4.9	10.5	7.3	10.1	7.7	10.2	27.5	259.8	10.3	6.3	15.0	10.0	8.1	23.4	5.3	6.3	9.7	4.5	8.9	4.7	32.6	280.4	294.5	289.8
Ba ppm	543.9	99.4	120.5	33.7	323.5	16.2	297.0	1157.1	1115.0	1687.7	32.0	309.7	43.6	46.0	1157.1	1022.4	21.1	456.4	75.0	161.7	31.8	973.6	588.8	547.9	576.0
Ga ppm	22.8	23.6	22.5	28.5	26.5	37.0	30.1	26.3	19.8	20.4	38.7	28.4	32.2	29.7	20.2	21.8	29.6	23.3	29.5	24.3	33.5	23.5	21.1	21.0	19.8
Rb ppm	166.0	165.9	163.4	239.8	210.6	306.3	216.9	178.3	60.0	125.4	324.2	202.5	240.0	254.8	150.9	165.2	214.9	190.5	264.8	199.2	286.9	96.8	54.0	50.3	52.0
Sr ppm	176.0	23.7	35.3	13.1	147.7	4.6	204.7	945.0	998.2	548.4	3.8	181.2	12.7	242.5	544.7	148.2	14.0	154.4	24.0	71.6	17.3	1329.6	676.3	636.4	666.4
Y ppm	37.8	33.0	43.3	34.1	26.1	39.4	30.9	37.8	35.3	28.2	110.7	20.3	24.8	19.2	21.4	34.1	51.8	39.2	36.4	32.0	34.5	37.1	24.4	22.7	23.8
Zr ppm	615.7	696.7	830.3	892.2	707.8	1116.7	915.3	835.0	344.1	543.2	1984.9	825.1	1160.8	948.6	503.7	498.3	1025.3	633.5	990.5	893.1	1096.9	522.2	247.7	236.6	238.5
Nb ppm	115.2	175.6	172.2	154.0	147.4	239.8	168.2	155.2	85.7	124.2	473.6	127.5	171.7	133.1	109.6	140.0	227.9	166.3	190.6	171.2	185.4	124.7	66.9	63.1	64.7
Pb ppm	16.4	11.7	15.6	18.5	14.7	20.3	16.0	14.5	7.2	7.8	25.9	12.7	14.4	17.3	7.9	13.4	15.8	14.0	19.9	13.0	23.4	8.7	6.3	3.7	4.9
Th ppm	23.2	17.1	18.5	27.9	23.0	39.6	24.1	20.1	9.8	12.9	47.8	19.6	23.5	27.6	11.9	19.3	24.3	24.2	34.7	25.5	39.8	13.2	4.8	5.8	4.6
U ppm	4.7	4.6	3.5	6.4	5.3	10.8	4.7	2.5	1.7	2.7	12.8	5.9	6.7	1.0	0.9	4.9	5.5	4.6	6.6	6.4	12.0	3.5	-0.5	-1.0	-0.3
total traces(%)	0.18	0.14	0.16	0.16	0.18	0.2	0.21	0.35	0.33	0.32	0.33	0.19	0.19	0.19	0.26	0.22	0.18	0.18	0.18	0.17	0.19	0.33	0.24	0.23	0.24

Whole rock analyses - lavas

125	SH86/51	SH86/52	SH86/53	SH86/54	SH86/55	SH86/56	SH86/57	SH86/58	SH86/59	SH86/63	SH86/64	SH86/65	SH86/66	SH86/67	SH87/1	SH87/7a	SH87/8	SH87/10	SH87/11	SH87/12	SH87/13	SH87/15	SH87/17	SH87/19	SH87/21
analyses	basalt	basalt	basalt	phon'ite	haw'ite	ben/mug	basalt	basalt	basalt	basalt	phon'ite	phon'ite	basalt	phon'ite	basalt	phon'ite	mug'ite	mug'ite	benm'ite	phon'ite	phon'ite	basalt	phon'ite	basalt	basalt
SiO2	43.31	44.10	46.56	61.01	47.40	54.91	43.74	44.09	43.14	43.35	63.18	61.36	44.96	60.36	44.79	58.83	49.07	54.00	54.56	58.89	57.95	41.15	60.89	47.24	45.19
TiO2	4.11	3.79	2.98	0.31	2.73	1.46	3.78	3.80	4.38	2.50	0.23	0.33	3.39	0.32	3.37	0.66	2.30	1.46	1.33	0.27	0.26	3.64	0.55	2.98	2.93
Al2O3	14.72	14.66	15.74	19.63	17.03	18.72	14.64	14.77	14.67	13.17	18.58	19.40	16.15	19.96	15.13	18.85	18.12	19.14	19.36	21.24	20.84	14.48	19.05	16.41	15.74
Cr2O3	0.02	0.02	0.02	0.00	0.01	0.00	0.02	0.02	0.02	0.06	0.00	0.00	0.01	0.00	0.02	0.00	0.00	0.00	0.00	0.00	0.00	0.03	0.00	0.01	0.02
Fe2O3T	14.08	13.45	12.35	2.40	11.00	6.88	13.56	13.52	13.83	12.73	3.15	2.80	13.50	3.69	12.81	3.65	9.16	6.81	6.25	2.36	2.32	14.33	3.05	12.81	12.50
MnO	0.19	0.18	0.19	0.20	0.25	0.24	0.19	0.19	0.19	0.18	0.32	0.18	0.20	0.24	0.19	0.16	0.31	0.27	0.28	0.22	0.19	0.18	0.20	0.21	0.21
MgO	6.85	7.26	6.07	0.16	3.27	1.45	6.55	6.28	7.15	10.81	0.08	0.39	5.70	0.15	7.87	0.63	2.02	1.28	1.43	0.10	0.12	8.39	0.32	5.68	5.94
CaO	9.43	9.43	9.34	1.03	8.64	5.09	9.34	9.56	9.97	12.86	0.97	1.60	9.19	1.16	9.74	2.04	7.94	5.96	5.08	1.26	1.48	10.20	1.30	9.00	8.68
Na2O	2.59	3.03	3.45	7.93	4.46	5.73	3.56	3.59	3.20	2.36	7.89	6.81	3.90	8.65	3.73	6.49	5.11	4.65	5.78	9.00	8.63	3.06	7.15	3.89	3.89
K2O	3.01	2.85	2.01	6.05	2.32	3.50	2.09	2.56	2.03	0.87	5.35	6.08	1.05	5.43	1.63	5.66	2.87	4.04	3.79	6.18	6.31	1.29	6.18	1.91	1.42
P2O5	0.66	0.64	0.76	0.03	1.50	0.53	0.64	0.66	0.55	0.41	0.00	0.02	1.19	0.03	0.97	0.14	1.13	0.48	0.40	0.03	0.02	0.57	0.06	1.12	1.08
Total	98.97	99.41	99.46	98.73	98.62	98.50	98.12	99.03	99.13	99.30	99.77	98.97	99.25	99.99	100.25	97.13	98.03	98.09	98.25	99.54	98.12	97.32	98.76	101.26	97.59
Zn ppm	101.0	103.3	107.6	88.9	108.8	106.2	99.6	92.0	90.2	90.6	157.1	83.0	97.2	126.3	89.8	66.3	103.2	82.7	102.8	130.5	114.1	91.2	72.1	104.9	107.5
Cu ppm	48.0	50.0	27.7	1.1	12.2	3.7	44.6	47.9	39.0	138.2	-6.4	3.8	29.4	5.1	31.5	8.5	4.8	6.3	6.9	8.5	7.8	42.9	6.6	24.4	24.7
Ni ppm	56.7	61.5	54.7	1.9	16.7	1.4	67.2	67.0	85.9	197.5	1.7	0.3	35.1	2.4	93.1	1.9	3.9	2.4	2.5	3.2	1.7	87.5	1.9	42.2	43.5
Co ppm	51.0	49.9	48.7	11.7	35.1	22.0	52.6	43.2	53.3	72.2	10.9	7.9	39.0	13.7	45.7	11.9	21.5	27.0	14.1	22.9	15.5	65.4	17.6	39.4	43.3
Cr ppm	84.3	109.5	103.8	6.8	30.0	2.6	117.6	114.2	113.0	368.6	4.1	3.7	56.2	6.3	141.7	4.1	5.3	2.8	3.7	3.2	3.8	162.0	3.8	76.2	81.6
V ppm	256.1	249.4	222.0	6.5	110.1	22.0	260.6	248.5	316.6	310.8	7.1	10.4	192.7	12.9	237.2	27.5	90.1	23.5	27.5	14.1	10.3	316.5	5.5	170.5	200.7
Ba ppm	698.8	699.5	624.0	185.9	699.4	1049.0	727.3	749.4	657.4	486.1	45.9	81.7	686.9	276.1	703.7	769.1	980.5	1603.8	1776.4	252.6	267.3	638.2	364.2	704.7	796.5
Ga ppm	21.7	22.0	21.1	26.5	21.6	21.1	22.8	23.0	21.6	21.5	31.3	24.9	22.3	30.3	20.7	23.8	22.9	18.8	20.4	30.4	30.7	21.5	21.8	22.6	21.8
Rb ppm	62.4	64.1	51.4	177.0	55.6	89.7	97.8	94.0	86.8	43.8	280.1	185.8	58.0	242.4	42.0	165.3	78.9	117.0	105.6	224.6	221.3	43.7	161.7	94.7	44.7
Sr ppm	753.8	786.5	795.6	52.3	1160.0	1150.9	799.3	886.0	732.0	517.6	8.3	19.2	1027.9	123.5	942.5	286.2	1249.9	1952.5	1791.4	162.0	179.0	712.6	70.9	948.4	931.8
Y ppm	27.8	27.6	32.6	29.1	36.6	39.9	27.4	29.4	24.1	24.4	63.4	27.8	35.0	50.3	33.0	26.4	37.6	49.3	48.3	30.1	28.3	28.8	44.3	34.0	34.1
Zr ppm	321.1	353.8	287.7	711.2	303.9	453.9	354.8	354.7	274.0	167.4	1354.9	764.1	295.1	1129.6	314.9	619.9	395.3	466.7	503.7	962.1	860.7	234.9	600.9	332.9	334.6
Nb ppm	81.2	88.5	68.2	160.6	77.7	121.4	86.4	86.1	63.2	50.2	319.0	154.4	73.6	245.2	83.3	123.4	97.4	131.4	135.0	163.5	159.3	56.2	171.7	80.6	78.4
Pb ppm	6.2	5.7	7.0	12.4	5.5	9.1	5.9	5.6	2.9	4.0	23.1	13.1	4.6	15.6	3.6	13.9	7.0	9.3	7.4	14.6	14.2	5.0	10.8	1.1	6.1
Th ppm	6.0	5.5	6.7	17.6	6.6	11.7	6.3	4.8	5.9	4.7	38.9	22.4	7.8	34.2	6.5	21.0	8.6	11.1	11.6	24.5	23.6	6.9	14.3	6.5	8.3
U ppm	-0.3	0.5	-0.1	4.6	0.9	2.6	0.8	0.3	-0.5	-0.2	10.0	6.9	-0.1	8.7	1.4	6.3	2.2	2.2	4.9	7.4	5.1	1.3	3.4	1.4	2.9
total traces(%)	0.26	0.27	0.25	0.15	0.27	0.31	0.28	0.28	0.26	0.25	0.23	0.14	0.27	0.23	0.28	0.22	0.31	0.45	0.46	0.21	0.19	0.25	0.16	0.27	0.28

125	SH87/22	SH87/23	SH87/24	SH87/25	SH87/26	SH87/27	SH87/29	SH87/30	SH87/31	SH87/32	SH87/33	SH87/34	SH87/36	SH87/38	SH87/40	SH87/41	SH87/42	SH87/43	SH87/44	SH87/46	SH87/47	SH87/48	SH87/49	SH87/50	SH87/51
analyses	phon'ite	mug'ite	qz-trach	basalt	phon'ite	phon'ite	basalt	benm'ite	phon'ite	haw'ite	benm'ite	phon'ite	phon'ite	basalt	phon'ite	basalt	basalt	basalt	qz-trach	phon'ite	basalt	phon'ite	basalt	phon'ite	benm'ite
SiO2	60.92	53.24	68.13	42.53	59.98	61.43	45.49	57.10	59.82	49.41	57.62	60.57	59.33	45.69	59.95	44.71	45.07	44.68	66.04	60.06	44.68	59.75	45.01	59.24	58.57
TiO2	0.29	1.83	0.14	3.43	0.19	0.25	3.20	0.92	0.59	2.33	0.66	0.24	0.15	2.59	0.52	2.76	2.81	2.65	0.33	0.30	3.27	0.25	3.50	0.86	1.04
Al2O3	20.13	18.69	15.75	14.85	20.85	20.82	15.37	19.59	19.87	17.75	20.08	21.50	20.89	14.02	19.40	15.16	15.11	13.69	17.55	19.37	15.25	19.04	15.48	19.28	19.53
Cr2O3	0.00	0.00	0.00	0.02	0.00	0.00	0.02	0.00	0.00	0.00	0.00	0.00	0.00	0.05	0.00	0.02	0.04	0.04	0.00	0.00	0.02	0.00	0.02	0.00	0.00
Fe2O3T	2.82	8.33	2.60	13.64	2.29	3.09	11.51	4.70	3.36	10.33	4.57	2.32	1.96	12.46	3.01	12.01	11.66	12.84	2.76	2.37	12.06	3.71	13.56	4.47	4.87
MnO	0.19	0.24	0.13	0.19	0.35	0.24	0.17	0.14	0.18	0.19	0.32	0.19	0.22	0.18	0.25	0.19	0.19	0.19	0.26	0.16	0.18	0.35	0.18	0.22	0.21
MgO	0.29	2.07	0.01	7.44	0.11	0.50	7.72	0.99	0.51	4.09	0.64	0.18	0.12	10.01	0.43	7.17	7.83	10.69	0.12	0.24	7.19	0.10	7.72	0.69	0.96
CaO	1.61	5.87	0.37	9.57	0.74	1.91	8.93	4.42	2.39	7.81	3.27	1.45	1.19	10.28	1.59	10.73	10.21	10.84	0.70	1.61	9.13	1.12	9.75	2.67	3.35
Na2O	7.52	5.54	6.24	3.27	9.75	6.95	3.38	5.00	5.64	4.07	5.07	8.96	9.15	3.17	7.23	2.47	2.69	2.09	6.55	6.79	4.08	8.42	2.77	7.37	6.75
K2O	5.71	2.98	4.96	2.34	5.26	5.96	2.45	5.28	5.60	2.91	5.03	5.89	5.55	0.69	5.80	2.02	2.26	1.58	5.80	6.29	1.52	5.28	1.21	4.79	4.50
P2O5	0.02	0.78	0.01	0.82	0.00	0.02	0.45	0.24	0.13	0.69	0.18	0.04	0.01	0.55	0.10	0.62	0.60	0.47	0.04	0.03	0.73	0.00	0.73	0.16	0.22
Total	99.50	99.56	98.34	98.10	99.52	101.17	98.69	98.38	98.09	99.58	97.44	101.34	98.57	99.69	98.28	97.85	98.46	99.77	100.15	97.23	98.10	98.02	99.93	99.75	100.00
Zn ppm	109.1	104.9	119.2	103.1	199.2	109.0	91.8	64.7	78.7	99.0	101.4	103.1	131.8	100.3	84.1	100.0	93.9	99.9	94.6	69.2	99.8	205.8	99.1	88.9	85.0
Cu ppm	7.5	3.8	7.1	32.7	9.0	6.7	37.5	6.1	8.5	19.6	6.2	6.7	8.8	67.6	8.7	48.2	39.3	46.4	6.8	8.2	21.0	7.8	30.8	8.1	6.9
Ni ppm	0.9	2.7	1.6	85.4	1.7	1.7	101.8	1.2	1.9	20.4	1.7	2.0	1.4	210.5	1.9	82.8	112.8	126.3	1.4	0.7	92.5	4.0	79.4	2.9	1.9
Co ppm	11.2	15.0	11.5	51.7	17.3	9.9	53.1	14.5	7.9	34.6	12.2	19.3	15.3	55.8	11.1	44.7	65.1	64.5	4.8	11.1	59.7	11.9	54.1	16.0	13.3
Cr ppm	5.7	5.0	4.5	119.9	0.9	3.8	142.4	3.6	4.6	25.2	5.8	5.2	4.3	364.2	1.8	142.1	236.2	250.8	3.7	5.6	122.6	0.6	130.5	3.6	4.7
V ppm	14.4	40.0	6.6	245.9	10.0	9.2	254.3	44.0	28.4	176.8	28.7	15.2	11.1	239.2	18.9	262.3	292.7	277.0	2.9	14.2	275.3	10.0	290.6	12.2	17.7
Ba ppm	278.9	1090.4	40.7	692.6	38.9	190.9	887.6	871.8	861.9	1160.2	627.2	88.6	41.1	535.9	973.1	693.6	733.9	559.5	128.3	447.9	702.9	109.1	623.3	1666.5	1308.1
Ga ppm	28.6	20.6	24.4	21.1	38.7	25.2	19.6	20.3	24.3	21.5	26.5	29.7	32.7	20.1	23.4	21.7	20.2	19.5	22.3	23.4	20.6	36.4	21.5	21.8	23.7
Rb ppm	261.2	78.2	218.9	57.7	303.4	256.8	58.2	138.9	194.7	73.4	199.3	249.1	305.3	44.9	180.3	64.0	114.4	71.5	178.8	201.7	84.2	351.4	29.6	121.6	130.3
Sr ppm	81.8	1273.4	4.1	861.3	5.9	91.2	866.1	493.5	454.6	919.8	540.2	72.2	7.5	630.2	279.0	1049.7	744.3	733.1	15.3	177.5	870.6	89.2	791.1	726.7	888.9
Y ppm	28.3	39.7	42.7	29.7	60.6	29.4	27.0	21.0	28.4	32.3	26.0	21.5	22.6	27.3	40.9	29.1	28.3	24.9	53.5	20.6	32.8	140.3	28.4	38.2	36.8
Zr ppm	954.2	415.1	651.7	288.9	1641.1	647.3	263.5	374.7	697.4	320.6	587.6	904.0	996.6	226.3	793.7	263.3	250.0	199.8	705.0	712.6	307.4	1708.5	240.1	560.6	620.2
Nb ppm	166.2	105.8	222.3	75.3	331.6	171.7	74.0	89.5	131.8	89.3	116.1	111.0	146.4	53.8	178.4	68.7	62.9	47.3	141.9	118.8	74.7	348.6	57.4	149.3	155.9
Pb ppm	19.4	8.7	17.7	5.2	19.0	15.2	5.1	6.8	15.0	6.8	16.3	15.9	21.4	3.5	12.0	3.8	4.4	3.3	17.7	14.3	5.7	25.6	5.8	8.6	9.6
Th ppm	37.2	10.6	31.2	6.5	41.5	27.0	5.8	12.9	23.3	9.2	23.1	26.4	34.0	4.4	20.0	8.1	4.7	5.8	21.7	20.0	5.7	49.5	6.5	14.0	14.6
U ppm	8.7	2.0	5.8	1.2	9.7	4.0	1.2	3.3	5.1	0.6	5.7	6.5	11.3	-0.5	4.7	0.5	2.1	0.6	4.6	4.7	0.9	12.3	-0.4	3.3	2.3
total traces(%)	0.2	0.32	0.14	0.27	0.27	0.16	0.29	0.22	0.26	0.3	0.23	0.17	0.18	0.26	0.26	0.29	0.28	0.25	0.14	0.19	0.28	0.31	0.25	0.34	0.33

Whole rock analyses - lavas

125	SH87/55	SH87/57	SH87/60	SH87/61	SH87/62	SH87/65a	SH87/67	SH87/68	SH87/70	SH87/72	SH87/74	SH87/75	SH87/76	SH87/77	SH87/79	SH87/80	SH87/81	SH87/88	SH88/1	SH88/6	SH88/16	SH88/17	SH88/23	SH88/30	SH88/36
analyses	phon'ite	phon'ite	phon'ite	phon'ite	phon'ite	phon'ite	phon'ite	ben/trach	ben/phon	benm'ite	mug/ben	haw'ite	phon'ite	phon'ite	phon'ite	phon'ite	phon'ite	basalt	mug'ite	phon'ite	mug/ben	qz-trach	mug'ite	basalt	phon'ite
SiO2	60.90	60.21	61.35	58.88	59.94	57.18	60.35	59.96	55.54	58.76	52.48	48.08	61.80	61.37	60.65	59.73	60.80	42.79	56.42	61.40	55.06	64.00	52.16	43.84	59.82
TiO2	0.18	0.31	0.51	0.57	0.43	0.18	0.15	0.85	0.92	0.91	1.96	2.65	0.21	0.24	0.25	0.15	0.30	3.38	1.37	0.48	1.32	0.44	1.77	3.16	0.42
Al2O3	20.41	20.04	19.05	18.77	19.68	22.30	20.74	19.24	19.93	19.57	17.75	16.33	19.74	19.61	19.76	21.16	19.17	15.04	18.30	19.44	18.46	16.80	18.38	14.82	19.81
Cr2O3	0.00	0.00	0.00	0.00	0.00	0.00	0.00	0.00	0.00	0.00	0.00	0.02	0.00	0.00	0.00	0.00	0.00	0.03	0.00	0.00	0.00	0.00	0.00	0.02	0.00
Fe2O3T	3.01	2.40	3.29	4.12	3.44	2.18	2.41	4.27	5.45	4.22	7.86	11.25	2.79	2.30	2.79	2.12	3.02	13.13	6.65	2.75	6.61	4.20	8.70	12.19	2.60
MnO	0.30	0.20	0.22	0.21	0.20	0.18	0.26	0.25	0.20	0.27	0.21	0.19	0.28	0.24	0.25	0.28	0.21	0.18	0.20	0.18	0.17	0.17	0.23	0.18	0.18
MgO	0.02	0.37	0.27	0.65	0.25	0.07	0.07	0.60	2.05	0.67	2.80	6.11	0.09	0.06	0.13	0.09	0.20	7.30	1.48	0.21	2.15	0.48	1.93	7.71	0.25
CaO	0.82	1.73	1.31	2.33	2.18	0.84	1.31	2.37	4.28	3.84	5.83	8.96	0.92	0.79	1.02	0.87	1.17	11.05	4.98	1.12	5.18	1.68	6.77	9.64	1.96
Na2O	8.91	7.63	7.30	6.12	6.56	10.47	8.11	5.30	6.94	5.50	5.06	4.17	8.28	8.37	8.26	9.71	7.58	3.16	5.27	7.74	4.13	5.54	4.97	3.83	6.40
K2O	5.14	5.94	5.96	5.62	5.67	5.87	5.67	5.25	4.42	5.14	4.03	1.81	5.80	5.57	5.65	5.32	5.65	1.48	3.86	6.17	4.84	5.31	3.04	2.08	6.51
P2O5	-0.01	0.03	0.06	0.10	0.06	0.00	0.01	0.18	0.29	0.16	0.47	0.71	0.00	0.01	0.01	0.00	0.02	1.19	0.53	0.05	0.47	0.14	0.75	1.07	0.06
Total	99.69	98.86	99.31	97.37	98.41	99.27	99.08	98.27	100.02	99.05	98.46	100.28	99.91	98.57	98.77	99.44	98.11	98.74	99.06	99.54	98.38	98.76	98.70	98.53	98.01
Zn ppm	178.3	88.8	92.6	91.5	85.9	116.3	133.7	108.5	94.9	98.8	113.7	93.0	141.6	128.2	123.1	154.5	113.6	98.6	104.8	81.0	84.2	73.6	103.2	103.5	72.7
Cu ppm	8.1	6.1	7.0	7.9	6.9	6.9	8.0	8.0	13.5	7.8	15.5	26.4	7.2	6.4	7.1	9.0	6.4	38.8	5.7	6.7	15.5	5.5	3.0	36.6	7.6
Ni ppm	3.5	1.5	1.4	1.6	2.3	1.7	2.0	4.4	15.8	1.8	19.9	71.9	2.3	1.0	1.5	2.2	2.2	104.7	2.2	2.3	9.5	1.7	2.2	102.5	0.7
Co ppm	12.1	11.3	9.9	11.8	10.1	12.5	10.2	5.6	18.0	7.1	27.2	37.9	6.1	10.5	10.1	7.7	12.4	47.3	8.4	9.2	14.4	14.0	10.8	48.0	6.5
Cr ppm	-0.1	3.6	4.1	1.4	4.1	6.5	4.9	2.2	24.9	4.5	29.5	110.7	3.6	4.3	0.0	5.5	3.5	160.2	2.4	5.4	11.1	4.1	3.5	143.5	5.3
V ppm	11.2	9.7	13.6	19.8	17.0	14.7	8.2	20.1	60.3	23.8	124.0	208.0	7.2	6.6	6.9	11.6	7.6	211.7	21.2	9.1	68.8	15.9	50.7	234.5	13.3
Ba ppm	46.7	364.9	322.0	1165.6	1135.3	39.8	75.2	1947.4	1043.5	1912.8	1265.8	811.9	47.9	24.9	40.7	47.0	176.3	567.3	1097.0	262.2	991.0	537.7	931.5	841.8	607.4
Ga ppm	33.4	24.6	22.2	22.5	22.3	35.3	31.3	19.4	30.5	20.3	25.1	22.1	30.3	27.2	27.9	35.4	27.7	19.7	21.7	23.0	21.8	23.2	21.0	21.8	21.9
Rb ppm	306.5	208.9	152.0	173.6	213.9	307.4	264.9	113.1	155.0	147.9	120.3	75.9	241.4	176.3	222.9	277.0	225.4	44.2	102.9	155.3	188.0	166.4	84.0	70.7	157.1
Sr ppm	5.8	133.9	38.7	256.5	239.2	22.4	61.1	886.4	908.9	1085.7	962.6	965.5	12.3	2.3	11.1	3.0	55.3	1076.1	1101.8	44.7	1674.1	187.4	1072.5	1040.1	173.5
Y ppm	61.1	25.7	38.2	33.5	24.2	22.5	27.0	44.3	29.3	53.4	35.6	32.8	46.9	48.0	42.6	30.0	44.6	31.4	40.1	36.1	30.6	35.5	36.3	35.6	29.2
Zr ppm	1555.8	728.1	667.6	529.9	537.0	1106.2	1012.2	552.3	660.1	533.6	552.2	332.5	1244.2	907.4	1000.4	1417.2	921.2	211.4	488.7	634.1	522.7	588.2	356.3	377.8	340.1
Nb ppm	292.9	143.6	170.7	136.0	126.0	118.3	146.2	129.0	127.7	145.8	119.7	79.8	253.7	247.6	220.2	193.1	207.4	61.7	115.6	170.0	117.9	109.5	103.3	96.8	157.7
Pb ppm	21.4	11.1	10.8	13.8	14.6	21.2	19.4	9.1	11.2	9.5	9.0	8.4	16.7	12.1	10.9	14.9	13.8	3.6	10.0	11.0	10.5	22.2	9.6	4.2	6.8
Th ppm	45.4	15.5	13.5	21.4	22.9	40.3	33.0	12.3	20.3	12.3	14.6	9.6	29.0	19.5	31.1	32.2	29.0	4.0	13.5	14.6	18.6	21.6	10.8	9.9	12.5
U ppm	10.7	4.9	1.3	3.5	4.3	12.1	8.0	2.1	6.4	2.5	4.8	1.6	7.1	4.4	5.9	9.0	6.2	-1.4	3.7	4.0	3.2	3.6	2.3	1.9	1.6
total traces(%)	0.26	0.18	0.16	0.25	0.25	0.19	0.18	0.39	0.32	0.41	0.34	0.29	0.21	0.16	0.18	0.22	0.19	0.27	0.31	0.15	0.38	0.18	0.28	0.32	0.16

Whole rock analyses - lava

16	SH86/38a	SH86/38b	SH88/14a	SH88/14b	SH88/14c	SH88/14e	SH88/14f	SH88/14g	SH88/14h	SH88/14i	SH88/14k	SH88/14l	SH88/14q	SH88/14s	SH88/14u	SH88/14w
analyses	suite 1	suite 4	suite 4	suite 4	suite 4	suite 3	suite 4	suite 1	suite 1	suite 3	suite 3	suite 1	suite 4	suite 4	suite 3	suite 3
SiO2	31.57	51.57	59.92	51.43	55.45	41.80	51.89	30.73	33.22	45.41	48.06	33.39	56.70	53.33	45.36	43.09
TiO2	7.39	2.20	1.01	2.11	1.53	4.34	1.61	6.47	5.21	3.38	2.95	4.45	1.33	2.06	3.41	3.56
Al2O3	14.08	18.27	18.48	17.96	20.00	14.37	18.17	11.27	13.96	17.85	17.87	12.64	19.11	18.57	16.53	16.30
Cr2O3	0.01	0.01	0.00	0.01	0.00	0.01	0.01	0.00	0.00	0.01	0.01	0.00	0.00	0.01	0.01	0.01
Fe2O3T	22.46	7.77	4.54	8.56	5.60	14.02	7.88	25.71	21.70	9.72	10.37	21.85	6.32	7.46	12.36	12.43
MnO	0.15	0.18	0.13	0.18	0.14	0.24	0.22	0.15	0.14	0.14	0.19	0.14	0.09	0.16	0.24	0.21
MgO	10.78	3.44	1.00	3.73	1.59	7.17	2.41	9.59	10.05	5.02	4.06	10.98	1.21	3.39	5.43	5.80
CaO	12.39	6.09	3.43	6.22	4.12	11.58	4.77	14.40	14.87	9.99	8.08	15.39	3.08	5.98	9.54	10.28
Na2O	1.11	5.03	6.49	4.94	5.95	3.38	5.71	0.52	0.54	3.98	4.34	0.46	6.18	5.03	3.83	3.53
K2O	0.39	2.64	3.93	2.64	3.22	1.03	3.62	0.01	0.07	1.28	1.94	0.00	3.90	2.66	1.76	1.43
P2O5	0.04	0.81	0.38	0.77	0.75	1.66	0.51	0.03	0.03	1.38	0.88	0.03	0.76	0.81	1.24	1.36
Total	100.35	98.01	99.32	98.55	98.37	99.59	96.81	98.90	99.79	98.16	98.75	99.34	98.69	99.44	99.70	98.00
Zn ppm	178.6	105.1	70.2	108.1	90.3	120.2	92.1	120.6	174.1	96.1	121.5	176.8	91.4	97.6	128.0	125.1
Cu ppm	98.4	24.3	7.9	24.1	5.2	18.3	19.2	-6.5	22.2	23.2	25.8	41.5	7.9	21.4	10.8	16.1
Ni ppm	140.4	25.5	4.2	29.0	5.1	44.7	30.1	6.2	21.6	28.8	28.2	36.6	10.9	25.3	23.0	26.8
Co ppm	142.0	39.7	13.8	26.2	11.6	41.0	26.8	76.6	81.8	31.4	29.0	102.8	14.2	19.9	37.3	36.2
Cr ppm	20.5	55.6	6.2	76.8	7.3	113.6	75.1	-4.8	2.7	74.1	39.5	5.8	26.2	55.7	35.7	39.1
V ppm	768.2	141.7	40.8	155.1	39.2	355.2	119.3	823.0	693.7	253.2	156.6	819.3	43.9	105.6	173.1	194.8
Ba ppm	194.8	1558.4	1717.4	1859.4	1836.3	523.6	1153.8	110.8	134.7	680.7	729.1	83.5	1272.2	1658.9	761.6	713.4
Ga ppm	28.6	22.2	17.9	21.1	21.1	21.5	21.0	26.8	31.5	22.2	23.4	33.4	18.6	21.5	21.6	22.5
Rb ppm	16.8	60.2	47.7	63.0	69.7	16.9	78.6	14.2	14.7	27.9	43.1	11.8	41.2	62.7	41.5	31.2
Sr ppm	262.2	941.0	807.4	916.5	938.1	844.8	682.4	94.1	124.0	1122.1	1082.9	84.3	815.5	959.3	1000.6	1131.6
Y ppm	19.4	24.0	16.5	23.5	16.0	50.7	25.3	17.5	20.0	38.1	34.9	14.8	20.1	22.2	43.8	40.5
Zr ppm	76.3	129.5	108.6	112.9	105.3	170.1	222.8	66.2	71.9	145.8	224.0	66.1	96.1	111.7	234.7	205.3
Nb ppm	12.8	46.0	40.6	43.0	49.7	65.4	54.7	4.3	7.1	53.9	81.2	4.5	33.6	44.2	84.6	67.1
Pb ppm	3.5	7.8	6.1	6.3	8.1	5.1	7.3	2.2	2.3	4.8	5.0	4.0	8.1	7.3	6.3	4.4
Th ppm	2.4	3.7	3.5	3.2	3.3	1.3	7.1	1.9	-0.7	3.3	5.2	2.2	3.2	4.4	3.7	5.2
U ppm	-1.6	-0.7	0.2	1.2	1.2	-0.7	2.3	0.7	1.3	1.9	-0.4	-0.1	-0.8	0.7	0.7	0.3
total traces(%)	0.20	0.32	0.29	0.35	0.32	0.24	0.26	0.14	0.14	0.26	0.26	0.15	0.25	0.32	0.26	0.27

Whole rock analyses - cumulates

9	F85/2	SH86/14	SH86/23	SH86/30	SH86/60	SH86/62	SH87/52	SH88/2a	SH88/8
analyses	gneiss	lherz	gneiss	gneiss	lherz	granite	gneiss	granite	granite
SiO2	69.49	43.76	72.60	73.94	42.67	69.65	67.50	70.35	69.87
TiO2	0.55	0.13	0.08	0.17	0.05	0.42	0.39	0.47	0.17
Al2O3	16.00	3.10	14.60	14.11	1.60	16.03	15.63	14.60	15.30
Cr2O3	0.00	0.31	0.00	0.00	0.41	0.00	0.00	0.00	0.00
Fe2O3T	2.74	9.66	0.79	1.28	9.40	2.15	2.33	2.85	3.51
MnO	0.03	0.14	0.05	0.02	0.12	0.02	0.04	0.03	0.09
MgO	1.01	39.28	0.18	0.41	44.42	0.77	0.96	0.88	1.97
CaO	2.28	3.16	0.40	0.82	1.57	1.93	0.80	1.02	0.98
Na2O	4.35	0.14	3.69	3.21	0.09	4.21	4.47	2.92	2.37
K2O	3.17	0.01	4.67	5.57	0.01	3.83	4.57	5.19	3.95
P2O5	0.10	0.02	0.31	0.11	0.01	0.08	0.08	0.33	0.38
Total	99.72	99.69	97.37	99.64	100.34	99.12	96.77	98.64	98.60
Zn ppm	57.3	52.5	38.4	28.0	53.5	62.5	46.1	49.8	58.7
Cu ppm	2.7	19.3	-2.0	1.7	11.0	-0.7	7.4	10.7	13.4
Ni ppm	4.4	2130.5	2.4	4.2	2484.6	4.3	4.5	8.3	15.4
Co ppm	34.2	118.4	33.1	41.2	131.9	28.1	21.3	17.2	21.5
Cr ppm	16.9	1951.7	10.2	11.6	2691.5	16.5	13.9	24.1	35.9
V ppm	39.3	68.6	10.2	13.4	28.7	35.2	35.4	32.6	25.5
Ba ppm	732.6	6.8	159.1	428.0	38.0	627.7	554.8	579.2	462.3
Ga ppm	23.7	2.9	22.6	17.0	1.7	27.2	22.8	20.8	20.1
Rb ppm	131.4	3.6	395.9	176.3	1.0	188.4	167.7	247.0	217.2
Sr ppm	504.0	47.3	42.8	136.9	7.0	327.9	282.1	130.4	134.0
Y ppm	11.4	3.2	14.0	9.9	2.2	7.8	9.5	27.8	31.1
Zr ppm	230.5	14.0	36.8	86.3	12.0	153.4	125.1	176.8	115.1
Nb ppm	9.1	1.8	16.9	9.6	2.6	8.2	11.6	17.8	5.8
Pb ppm	38.5	-0.1	23.8	30.2	2.8	52.1	64.2	27.2	23.4
Th ppm	20.8	0.0	4.2	8.9	1.0	15.3	13.0	21.3	9.2
U ppm	3.2	0.4	3.5	3.9	0.8	1.9	3.8	4.1	7.4
total traces(%)	0.19	0.44	0.08	0.10	0.55	0.16	0.14	0.14	0.12

Whole rock analyses - basement samples and lherzolite nodules

2) Microprobe analyses

Ti-magnetite, spinel-hercynite, biotite, clinopyroxene and aenigmatite have Fe^{3+} calculated using the method of Droop (1987).
Lines after specimen numbers contain information about analyses.
All analyses with same letter of alphabet were made on the same mineral grain e.g. centre a, edge a.

Key:	centre	= centre of grain	(1.17V)	= 1.17% Vanadium in analysis
	edge	= edge of grain		
	hwce	= half-way between centre and edge of grain		
	next	= next point in traverse, consecutive from 1st analysis	res.	= resorbing
	ph.	= phenocryst	big,euhed,	
	gmass	= groundmass grain	w.ovrgrth	= description of grain
	glom	= glomerocryst	greencore	= cpx phenocryst with green core
	xeno	= xenocryst	in amph	= grain enclosed in amphibole

olivine	86/53	86/53	86/53	87/29 gmass	87/29 big centre	87/29 big centre	86/63 euhed centre	86/63 centre	86/63 centre	86/63 centre	86/63	86/57 big centre	86/58	86/58 big centre a	86/58 big edge a	84/43 ?gmass group	84/43 euhedsmall centre	84/43 hwce	86/66 corebrown mess	84/40b	84/40b	84/40b	84/33	84/33 big centre	84/21
Na2O	0.02	0.02	0.07	0.07	0.99	0.02	0.34	0	0.02	0.02	0	0	0	0	0.04	0.02	0.03	0.02	0.07	0.02	0	0	0.05	0.05	0
MgO	43.79	44.05	42.82	44.03	45.84	46.52	41.04	42.62	41.66	42.55	43.29	41.46	40.54	41.14	35.79	41.79	39.31	39.81	42.33	40.31	39.02	38.83	44.56	42.82	39.15
Al2O3	0.08	0.08	0.22	0.17	0	0.08	0.05	0.03	0.03	0.08	0.08	0.03	0.03	0.03	0.03	0.08	0.41	0.08	0.08	0.05	0.08	0.03	0.06	0.05	0.05
SiO2	39.66	38.99	39.19	40.24	40.43	40.67	38.79	39.64	38.65	38.88	39.06	39.7	39.59	39.73	38.19	39.82	39.06	39.25	39.06	39.14	38.99	38.68	39.91	39.86	38.79
K2O	0.04	0.04	0.04	0.04	0.04	0.04	0.04	0.04	0.08	0.02	0.04	0.04	0.04	0.05	0.02	0.02	0.04	0.04	0.04	0.04	0.05	0.04	0.02	0.04	0.02
CaO	0.17	0.17	0.21	0.24	0.2	0.19	0.24	0.23	0.27	0.18	0.27	0.1	0.18	0.25	0.38	0.2	0.17	0.13	0.27	0.2	0.25	0.27	0.19	0.17	0.23
TiO2	0.04	0.04	0.02	0.02	0.04	0.02	0.02	0.07	0.04	0.04	0	0.02	0.02	0.05	0.12	0.05	0.04	0.02	0.05	0.02	0.07	0.04	0.04	0.04	0.05
MnO	0.16	0.22	0.19	0.24	0.16	0.15	0.28	0.3	0.07	0.04	0.2	0.32	0.39	0.36	0.59	0.26	0	0.32	0.26	0.36	0.47	0.4	0.18	0.23	0.39
FeO	18.46	18.26	18.33	16.98	14.14	13.23	19.77	16.89	15.2	16.61	14.6	19.61	21.32	20.49	26.76	19.74	22.44	22.24	19.04	21.36	22.65	23.08	16.31	18.14	22.2
Total	102.42	101.87	101.09	102.03	101.84	100.92	100.57	99.82	96.02	98.42	97.54	101.28	102.11	102.1	101.92	101.98	101.5	101.91	101.2	101.5	101.58	101.37	101.32	101.4	100.88
Na+	0.0009	0.0009	0.0033	0.0033	0.0474	0.0009	0.0169	0	0.0009	0.0009	0	0	0	0	0.0019	0.0009	0.0015	0.0009	0.0033	0.0009	0	0	0.0024	0.0024	0
Mg2+	1.6257	1.6462	1.6112	1.6283	1.6827	1.7089	1.5658	1.6119	1.6271	1.631	1.6599	1.5635	1.5291	1.5459	1.3918	1.5657	1.4976	1.511	1.5977	1.5314	1.4909	1.4905	1.6556	1.6025	1.5034
Al3+	0.0024	0.0024	0.0067	0.0051	0	0.0024	0.0015	0.0009	0.0009	0.0025	0.0025	0.0009	0.0009	0.0009	0.0009	0.0024	0.0123	0.0024	0.0024	0.0015	0.0025	0.0009	0.0018	0.0015	0.0015
Si4+	0.9879	0.9778	0.9895	0.9986	0.9958	1.0024	0.993	1.006	1.0129	0.9999	1.0049	1.0046	1.0018	1.0018	0.9965	1.0011	0.9984	0.9996	0.9892	0.9977	0.9996	0.9963	0.995	1.0009	0.9994
K+	0.0012	0.0012	0.0012	0.0012	0.0012	0.0012	0.0012	0.0012	0.0025	0.0006	0.0012	0.0012	0.0012	0.0015	0.0006	0.0006	0.0012	0.0012	0.0012	0.0012	0.0015	0.0012	0.0006	0.0012	0.0006
Ca2+	0.0045	0.0045	0.0056	0.0064	0.0053	0.005	0.0066	0.0063	0.0076	0.0049	0.0074	0.0027	0.0049	0.0068	0.0107	0.0054	0.0046	0.0035	0.0073	0.0055	0.0069	0.0074	0.0051	0.0045	0.0063
Ti4+	0.0007	0.0008	0.0005	0.0004	0.0007	0.0004	0.0005	0.0014	0.0008	0.0008	0	0.0005	0.0005	0.0009	0.0024	0.0009	0.0008	0.0005	0.0009	0.0005	0.0014	0.0008	0.0007	0.0008	0.0009
Mn2+	0.0034	0.0047	0.0041	0.0051	0.0034	0.0031	0.006	0.0064	0.0016	0.0009	0.0043	0.0068	0.0084	0.0077	0.013	0.0056	0	0.0069	0.0056	0.0078	0.0102	0.0087	0.0037	0.0048	0.0085
Fe2+	0.3845	0.3829	0.387	0.3523	0.2913	0.2727	0.4233	0.3585	0.3332	0.3573	0.3141	0.4149	0.4512	0.4321	0.584	0.415	0.4797	0.4736	0.4033	0.4554	0.4856	0.4972	0.34	0.381	0.4784
Total	3.0112	3.0214	3.0091	3.0007	3.0278	2.997	3.0148	2.9926	2.9875	2.9988	2.9943	2.9951	2.998	2.9976	3.0018	2.9976	2.9961	2.9996	3.0109	3.0019	2.9986	3.003	3.0049	2.9996	2.999

olivine	87/43 centre	87/43 centre	87/43 edge	87/43 centre	87/43 gmass	87/32 centre c	87/32 edge c	87/32 centre	86/55	86/14 mantle nodule	86/14 mantle nodule	86/14 mantle nodule
Na2O	0	0	0.03	0.02	0.05	0.02	0	0.02	0.03	0.02	0.03	0.02
MgO	41.68	43.59	42.47	41.9	42.75	40.93	36.27	43.99	42.7	47.2	48.28	48.29
Al2O3	0.06	0.05	0.03	0.08	0.03	0.05	0.03	0.05	0.05	0.05	0.03	0.03
SiO2	38.95	39.93	39.03	39.5	39.23	39.32	38.04	39.32	40.08	40.22	40.42	40.28
K2O	0.04	0.04	0.04	0.05	0.04	0.04	0.05	0.02	0.04	0.02	0.04	0.04
CaO	0.17	0.18	0.23	0.17	0.21	0.21	0.25	0.19	0.23	0.06	0.06	0.07
TiO2	0.04	0.04	0.04	0.04	0.04	0.02	0.04	0.02	0.05	0	0	0.02
MnO	0.28	0.24	0.27	0.3	0.24	0.38	0.87	0.32	0.3	0.14	0.15	0.12
FeO	19.72	17.16	18.09	19.47	18	19.94	26.19	16.07	18.62	10.43	10.47	10.63
Total	100.94	101.23	100.23	101.53	100.59	100.91	101.74	100	102.1	98.14	99.48	99.5
Na+	0	0	0.0015	0.0009	0.0024	0.0009	0	0.0009	0.0015	0.0009	0.0015	0.0009
Mg2+	1.5814	1.6267	1.6113	1.5768	1.6146	1.5537	1.4114	1.6568	1.59	1.7606	1.7783	1.7801
Al3+	0.0018	0.0015	0.0009	0.0024	0.0009	0.0015	0.0009	0.0015	0.0015	0.0015	0.0009	0.0009
Si4+	0.9916	0.9999	0.9936	0.9973	0.9942	1.0016	0.9933	0.9938	1.0014	1.0066	0.999	0.9963
K+	0.0012	0.0012	0.0012	0.0015	0.0012	0.0012	0.0016	0.0006	0.0012	0.0006	0.0012	0.0012
Ca2+	0.0046	0.0048	0.0063	0.0046	0.0056	0.0057	0.0071	0.0052	0.0062	0.0017	0.0016	0.0018
Ti4+	0.0008	0.0008	0.0008	0.0008	0.0008	0.0005	0.0008	0.0005	0.0009	0	0	0.0004
Mn2+	0.006	0.0051	0.0058	0.0064	0.0052	0.0083	0.0193	0.0068	0.0063	0.003	0.0031	0.0025
Fe2+	0.4199	0.3593	0.3852	0.4112	0.3815	0.4247	0.5719	0.3397	0.3892	0.2184	0.2164	0.2198
Total	3.0073	2.9993	3.0066	3.0019	3.0064	2.9981	3.0063	3.0058	2.9982	2.9933	3.002	3.0039

Lavas - olivine analyses

carbonate	87/88b spherule centre	87/88b enclosed	87/88b brown	87/88b infill centre	87/88b	87/88a sheaf	87/43 in olivine	87/43 in gmass spherule	86/25 in glom
Na2O	0.25	0.07	0.21	0.3	0	0.04	0.05	0.02	0.17
MgO	24.86	19.06	24	27.71	23.06	1.33	10.13	15.04	2.1
Al2O3	0	0	0.03	0	0.03	0.02	0	0.03	0.34
SiO2	0.03	0.08	0.03	0.03	0.16	0.02	0.1	0.03	0.02
K2O	0.03	0.03	0.06	0.05	0.06	0.04	0.04	0.03	0.07
CaO	1.86	1.91	1.41	2.76	1.95	39.86	11.36	8.26	59.83
TiO2	0.03	0.05	0.05	0.05	0.17	0.02	0.02	0.02	0.1
MnO	0.5	0.53	0.5	0.55	0.52	0.95	0.71	0.61	1.7
FeO	26.05	34.51	26.7	22.22	27.02	12.7	34.01	31.67	0.04
CO2	46.39	43.76	47.01	46.33	47.03	45.02	43.58	44.29	35.63
Total-CO2	53.61	56.24	52.99	53.67	52.97	54.98	56.42	55.71	64.37
Na+	0.0154	0.0045	0.0129	0.0183	0	0.0026	0.0033	0.0013	0.0118
Mg2+	1.1806	0.9491	1.1365	1.3022	1.0934	0.0664	0.5158	0.7497	0.1124
Al3+	0	0	0.0011	0	0.0011	0.0008	0	0.0012	0.0144
Si4+	0.001	0.0027	0.001	0.0009	0.0051	0.0007	0.0034	0.001	0.0007
K+	0.0012	0.0013	0.0024	0.002	0.0024	0.0017	0.0017	0.0013	0.0032
Ca2+	0.0635	0.0684	0.048	0.0933	0.0665	1.4298	0.4159	0.296	2.3032
Ti4+	0.0007	0.0013	0.0012	0.0012	0.0041	0.0005	0.0005	0.0005	0.0027
Mn2+	0.0135	0.015	0.0135	0.0147	0.014	0.0269	0.0205	0.0173	0.0517
Fe2+	0.6942	0.9643	0.7095	0.586	0.7189	0.3556	0.9717	0.8859	0.0012
C4+	2.0183	1.9963	2.0394	1.9947	2.043	2.0578	2.0329	2.0225	1.7477
Total-C4+	1.9701	2.0066	1.9261	2.0186	1.9055	1.885	1.9328	1.9542	2.5013

Lavas - carbonate analyses

sphene	86/27	86/27	85/18	86/20
Na2O	0.09	0	0.36	0
MgO	0.09	0.06	0	0.07
Al2O3	1.73	1.75	1.38	1.58
SiO2	28.91	29.26	29.32	26.29
K2O	0.04	0.04	0.04	0.07
CaO	25.64	26.18	26.47	28.85
TiO2	34.46	35.47	31.95	31.18
MnO	0.04	0.11	0.03	0.19
FeO	1.93	1.85	1.86	1.59
Total	92.93	94.72	91.41	89.82
Na+	0.0063	0	0.025	0
Mg2+	0.0047	0.0031	0	0.0038
Al3+	0.0719	0.0714	0.0582	0.0691
Si4+	1.0173	1.0105	1.0512	0.9751
K+	0.0017	0.0017	0.0017	0.0031
Ca2+	0.9667	0.9688	1.017	1.1464
Ti4+	0.912	0.9213	0.8616	0.8696
Mn2+	0.0013	0.0033	0.0009	0.006
Fe2+	0.0569	0.0533	0.0558	0.0493
Total	3.0388	3.0334	3.0714	3.1224

Lavas - sphene analyses

Ti-mag	86/53	84/45 blobby centre c	84/45 blobby edge c	84/45	84/45	84/45	87/29 gmass	87/29 gmass	87/29 assoc w cpx	87/29 big gmass	87/29 big centre	87/29	84/43	84/43	84/43	86/66	84/40b big gmass	84/40b big gmass	84/40b small gmass	84/40b big gmass	84/33 rim of pheno	84/33 core of pheno	84/33 gmass	84/21	84/21
Na2O	0.03	0	0	0.05	0	0.05	0.05	0.03	0	0.82	0	0.03	0.11	0.03	0.03	0.05	0.03	0	0.05	0	0	0.03	0	0.03	0.08
MgO	3.71	4.31	4.62	5.07	5.69	4.31	5.61	5.38	6.5	6.15	6.88	6.32	5.8	6.81	3.82	4.78	5.31	5.37	5.34	5.21	6.31	6.04	4.6	5.13	4.99
Al2O3	5.84	6.33	5.87	6.81	6.03	4.86	4.54	4.46	6.06	4.72	9.8	5.77	10.63	10.76	3.97	6.66	4.2	4.76	4.35	4.3	6.13	11.29	5.11	4.25	4.25
SiO2	0.55	0.03	0.03	0.03	0.03	0	0	0.1	0.58	0.29	0.05	0.03	0.13	0.08	0.05	0.03	0	0.1	0.52	0.08	0.26	0.85	0.13	0.16	0.05
K2O	0.06	0.05	0.05	0.04	0.04	0.06	0.06	0.06	0.06	0.05	0.04	0.04	0.05	0.04	0.04	0.04	0.05	0.05	0.08	0.06	0.05	0.05	0.11	0.11	0.07
CaO	0.09	0.03	0.01	0	0	0	0.05	0.06	0.09	0.04	0	0.04	0	0	0.04	0	0.02	0.15	0.15	0.05	0.1	0.13	0.14	0.05	0.06
TiO2	21.95	14.64	15.82	15.75	15.29	18.39	22.72	23.06	21.14	22.5	15.04	19.83	10.88	12.45	22.46	18.76	23.31	22.5	23.18	23.47	23.01	17.15	25.19	23.3	23.09
MnO	0.68	0.49	0.53	0.63	0.41	0.73	0.6	0.63	0.63	0.6	0.39	0.54	0.35	0.35	0.65	0.56	0.65	0.68	0.69	0.6	0.44	0.4	0.59	0.74	0.67
FeO	63.66	67.47	67.33	67.16	67.6	66.97	63.97	64.04	62.94	63.55	64.03	61.45	66.43	64.3	63.49	67.44	62.78	61.47	61.37	62.12	59.91	60.93	59.44	62.3	62.17
Total	96.57	93.35	94.26	95.54	95.09	95.37	97.6	97.82	98	98.72	96.23	94.05	94.38	94.82	94.55	98.32	96.35	95.08	95.73	95.89	96.21	96.87	95.31	96.07	95.43
recalc	98.54	96.69	97.5	98.81	98.54	98.29	99.91	100.04	100.36	101.36	99.4	96.56	98.13	98.31	96.63	101.17	98.46	97.16	97.69	97.88	98.11	99.23	96.77	98.12	97.5
Na+	0.0023	0	0	0.0038	0	0.0039	0.0037	0.0023	0	0.0596	0	0.0024	0.0086	0.0024	0.0024	0.0037	0.0023	0	0.0037	0	0	0.0022	0	0.0023	0.0061
Mg2+	0.2127	0.266	0.2813	0.3018	0.3422	0.2585	0.3193	0.3053	0.3632	0.3443	0.3935	0.3712	0.3454	0.3973	0.2269	0.2738	0.3057	0.3119	0.3068	0.3004	0.3549	0.3335	0.2625	0.2956	0.2902
Al3+	0.265	0.309	0.2827	0.3207	0.2871	0.2307	0.2043	0.2005	0.2677	0.2091	0.4434	0.2682	0.5011	0.4968	0.1864	0.3015	0.1913	0.2187	0.1979	0.1962	0.2726	0.4934	0.2305	0.1938	0.1955
Si4+	0.0213	0.0012	0.0012	0.0012	0.0012	0	0	0.0039	0.0219	0.0108	0.0018	0.0012	0.0053	0.0031	0.0019	0.0012	0	0.004	0.0202	0.003	0.0098	0.0314	0.0051	0.0063	0.0019
K+	0.0028	0.0025	0.0025	0.0019	0.0019	0.0029	0.0028	0.0027	0.0027	0.0023	0.0018	0.0019	0.0024	0.0019	0.0019	0.0018	0.0023	0.0023	0.0037	0.0028	0.0023	0.0022	0.0055	0.0056	0.0033
Ca2+	0.0037	0.0012	0.0005	0	0	0	0.0021	0.0025	0.0036	0.0016	0	0.0017	0	0	0.0017	0	0.0009	0.0063	0.0063	0.0021	0.0041	0.0051	0.0058	0.0021	0.0026
Ti4+	0.6351	0.4559	0.486	0.4732	0.4641	0.5566	0.6529	0.6605	0.5962	0.6358	0.4341	0.588	0.3272	0.3665	0.6735	0.542	0.6772	0.6594	0.6722	0.6829	0.6532	0.4778	0.7254	0.6777	0.6775
Mn2+	0.0222	0.0172	0.0184	0.0214	0.0141	0.0249	0.0195	0.0204	0.0201	0.0192	0.0127	0.018	0.0118	0.0115	0.022	0.0182	0.0214	0.0225	0.0225	0.0198	0.0141	0.0125	0.0191	0.0242	0.022
Fe2+	2.0485	2.3365	2.3	2.244	2.2814	2.2539	2.0438	2.0398	1.974	1.997	2.0558	2.0263	2.2209	2.1049	2.1169	2.1667	2.0284	2.0032	1.9791	2.0102	1.8911	1.8882	1.9033	2.0153	2.0285
Total	3.2136	3.3895	3.3726	3.368	3.392	3.3314	3.2484	3.2379	3.2494	3.2797	3.3431	3.2789	3.4227	3.3844	3.2336	3.3089	3.2295	3.2283	3.2124	3.2174	3.2021	3.2463	3.1572	3.2229	3.2276
Na+	0.0021	0	0	0.0034	0	0.0035	0.0034	0.0021	0	0.0545	0	0.0022	0.0075	0.0021	0.0022	0.0034	0.0021	0	0.0035	0	0	0.002	0	0.0021	0.0057
Mg2+	0.1986	0.2354	0.2502	0.2688	0.3027	0.2328	0.2949	0.2829	0.3353	0.3149	0.3531	0.3396	0.3027	0.3522	0.2105	0.2482	0.284	0.2898	0.2865	0.2801	0.3325	0.3082	0.2494	0.2752	0.2697
Al3+	0.2474	0.2735	0.2515	0.2857	0.2539	0.2078	0.1887	0.1858	0.2472	0.1913	0.3979	0.2454	0.4392	0.4404	0.1729	0.2734	0.1777	0.2032	0.1848	0.1829	0.2554	0.456	0.219	0.1804	0.1817
Si4+	0.0199	0.0011	0.0011	0.0011	0.0011	0	0	0.0036	0.0202	0.0099	0.0016	0.0011	0.0046	0.0027	0.0018	0.0011	0	0.0037	0.0189	0.0028	0.0092	0.029	0.0048	0.0059	0.0018
K+	0.0026	0.0022	0.0022	0.0017	0.0017	0.0026	0.0026	0.0025	0.0025	0.0021	0.0016	0.0017	0.0021	0.0017	0.0018	0.0016	0.0021	0.0021	0.0035	0.0026	0.0022	0.002	0.0052	0.0052	0.0031
Ca2+	0.0035	0.0011	0.0004	0	0	0	0.0019	0.0023	0.0033	0.0015	0	0.0016	0	0	0.0016	0	0.0008	0.0059	0.0059	0.002	0.0038	0.0047	0.0055	0.002	0.0024
Ti4+	0.5929	0.4035	0.4323	0.4215	0.4105	0.5012	0.603	0.612	0.5504	0.5816	0.3895	0.538	0.2868	0.3249	0.6248	0.4914	0.6291	0.6128	0.6278	0.6368	0.612	0.4415	0.6893	0.6308	0.6297
Mn2+	0.0207	0.0152	0.0164	0.0191	0.0125	0.0224	0.018	0.0189	0.0186	0.0176	0.0114	0.0165	0.0103	0.0102	0.0204	0.0165	0.0199	0.0209	0.021	0.0185	0.0132	0.0116	0.0181	0.0225	0.0204
Fe2+	1.3806	1.1487	1.1621	1.1247	1.0932	1.2339	1.2758	1.3021	1.2085	1.1444	1.0238	1.1734	0.9586	0.9572	1.3861	1.2176	1.3158	1.2958	1.3192	1.3338	1.2668	1.1379	1.4102	1.3226	1.3214
Fe3+	0.5317	0.9193	0.8838	0.8741	0.9245	0.7958	0.6117	0.5878	0.614	0.6823	0.821	0.6805	0.988	0.9086	0.5779	0.7468	0.5685	0.5657	0.529	0.5406	0.5049	0.607	0.3983	0.5533	0.5641
Total	3	3	3	3.0001	3.0001	3	3	3	3	3.0001	2.9999	3	2.9998	3	3	3	3	2.9999	3.0001	3.0001	3	2.9999	2.9998	3	3

Ti-mag	86/57 centre b	86/57 edge b	86/57 gmass	86/58 centre d	86/58 edge d	86/58 blobby ovrgrth d	87/43 gmass	86/55 w holes hwce	86/55 centre	86/55 big gmass centre	86/55 blobby	86/8 subhed in cluster	86/8 big + 'splat'	86/8 big centre	86/8 anhed	86/8 in kspar centre	86/8 gmass	86/19a pheno	86/19a centre	86/19a big centre	86/19a in amph	86/47 uniform centre a	86/47 edge a	86/47 centre	86/27
Na2O	0.03	0.03	0.19	0.03	0.03	0.05	0.05	0.03	0	0.05	0.08	0	0.09	0	0.03	0.06	0	0	0.14	0	0	0	0	0	0.06
MgO	4.33	3.96	3.26	4.41	4.36	4.09	4.83	4.06	4.74	3.43	3.4	0.21	0.27	0.18	0.21	0.03	0.4	1.45	1.17	0.99	1.78	1.81	1.46	2	0.46
Al2O3	3.78	2.47	1.66	4.61	4.14	3.15	5.27	3.75	6.48	2.71	2.32	0.93	4.33	0.68	2.03	1.32	0.45	2.05	2.04	1.71	3.48	2.1	2.79	3.11	0.76
SiO2	0	0	0.13	0	0.05	0	0.13	0	0.03	0.16	0.49	0.1	0.05	0.1	0.08	0.03	0	0.03	0.7	0.05	0.08	0	0.21	0.08	0
K2O	0.05	0.05	0.09	0.05	0.05	0.06	0.06	0.05	0.05	0.06	0.06	0.04	0.04	0.04	0.05	0.05	0.13	0.06	0.06	0.05	0.04	0.04	0.05	0.05	0.05
CaO	0	0	0.14	0	0	0.01	0.2	0.01	0	0.09	0.19	0	0	0	0.01	0	0	0	0.01	0.01	0.07	0	0	0	0
TiO2	23.42	23.55	24.22	22.16	22.66	23.3	21.3	19.59	16.42	21.82	22.42	16.61	14.93	16.12	11.46	15	14.14	16.74	16.94	17.24	14.14	9	11.33	10.27	14.25
MnO	0.68	0.71	0.75	0.63	0.63	0.7	0.59	0.79	0.65	0.78	0.89	1.65	1.65	1.66	1.5	1.5	1.54	1.99	2.13	2.06	1.25	0.89	0.9	0.89	2.95
FeO	63.86	65.51	64.19	63.98	63.66	64.62	63.53	67.29	67.47	64.13	64.18	78.27	76.79	78.74	79.58	77.54	78.04	74.71	73.15	74.52	75.82	80.51	77.95	78.22	77.35
Total	96.15	96.28	94.63	95.87	95.58	95.98	95.96	95.57	95.84	93.23	94.03	97.81	98.15	97.52	94.95	95.53	94.7	97.03	96.34	96.63	96.66	94.35	94.69	94.62	95.88
recalc	98.21	98.47	96.66	98.08	97.71	98.13	98.27	98.38	99	95.46	96.18	101.5	101.83	101.32	99.37	99.36	98.79	100.59	99.67	100.06	100.55	99.33	99.05	99.22	100
Na+	0.0023	0.0024	0.015	0.0024	0.0024	0.0038	0.0037	0.0024	0	0.0039	0.0063	0	0.0075	0	0.0027	0.0053	0	0	0.0116	0	0	0	0	0	0.0053
Mg2+	0.2521	0.2334	0.196	0.2574	0.2552	0.2403	0.2802	0.2441	0.2818	0.2097	0.2054	0.0133	0.0167	0.0116	0.014	0.0018	0.0266	0.0909	0.0731	0.0625	0.1118	0.1226	0.0961	0.1321	0.0302
Al3+	0.1741	0.115	0.079	0.2127	0.1917	0.1464	0.2419	0.1784	0.3048	0.1311	0.1111	0.0465	0.212	0.0346	0.1073	0.068	0.0237	0.1015	0.1008	0.0853	0.1729	0.1125	0.1454	0.1624	0.0397
Si4+	0	0	0.0053	0	0.0019	0	0.0051	0	0.0012	0.0067	0.02	0.0043	0.002	0.0044	0.0035	0.0013	0	0.0013	0.0292	0.002	0.0033	0	0.0093	0.0035	0
K+	0.0023	0.0024	0.0048	0.0024	0.0024	0.0028	0.0028	0.0024	0.0024	0.003	0.0029	0.002	0.002	0.0021	0.0027	0.0026	0.0075	0.003	0.003	0.0025	0.002	0.0022	0.0027	0.0027	0.0026
Ca2+	0	0	0.0061	0	0	0.0005	0.0084	0.0005	0	0.0039	0.0083	0	0	0	0.0005	0	0	0	0.0005	0.0005	0.003	0	0	0	0
Ti4+	0.6879	0.7004	0.7344	0.6525	0.6694	0.6909	0.6236	0.5943	0.4925	0.673	0.6839	0.5314	0.4662	0.5203	0.3865	0.4947	0.4763	0.5288	0.5342	0.548	0.4488	0.3074	0.3764	0.3421	0.4723
Mn2+	0.0225	0.0238	0.0257	0.0209	0.021	0.0235	0.0194	0.0269	0.022	0.0271	0.0305	0.0596	0.0581	0.0603	0.0569	0.0556	0.0584	0.0709	0.0756	0.0736	0.0446	0.0341	0.0337	0.0333	0.1102
Fe2+	2.086	2.1671	2.1645	2.0953	2.0913	2.131	2.0683	2.2699	2.2503	2.1997	2.1768	2.7847	2.666	2.8258	2.9851	2.8444	2.9231	2.6245	2.5654	2.634	2.6759	3.0587	2.8794	2.8986	2.8514
Total	3.2272	3.2445	3.2308	3.2436	3.2353	3.2392	3.2534	3.3189	3.355	3.2581	3.2452	3.4418	3.4305	3.4591	3.5592	3.4737	3.5156	3.4209	3.3934	3.4084	3.4623	3.6375	3.543	3.5747	3.5117
Na+	0.0021	0.0022	0.0139	0.0022	0.0022	0.0035	0.0034	0.0022	0	0.0036	0.0058	0	0.0066	0	0.0023	0.0046	0	0	0.0103	0	0	0	0	0	0.0045
Mg2+	0.2344	0.2158	0.182	0.2381	0.2366	0.2226	0.2584	0.2206	0.252	0.1931	0.1899	0.0116	0.0146	0.0101	0.0118	0.0016	0.0227	0.0797	0.0646	0.055	0.0969	0.1011	0.0814	0.1109	0.0258
Al3+	0.1618	0.1063	0.0734	0.1967	0.1778	0.1356	0.2231	0.1613	0.2725	0.1207	0.1027	0.0405	0.1854	0.03	0.0904	0.0587	0.0202	0.089	0.0891	0.0751	0.1498	0.0928	0.1231	0.1363	0.0339
Si4+	0	0	0.0049	0	0.0018	0	0.0047	0	0.0011	0.0062	0.0185	0.0037	0.0017	0.0038	0.003	0.0011	0	0.0011	0.0258	0.0018	0.0029	0	0.0079	0.0029	0
K+	0.0021	0.0022	0.0045	0.0022	0.0022	0.0026	0.0026	0.0022	0.0021	0.0028	0.0027	0.0017	0.0017	0.0018	0.0023	0.0022	0.0064	0.0026	0.0027	0.0022	0.0017	0.0018	0.0023	0.0023	0.0022
Ca2+	0	0	0.0057	0	0	0.0005	0.0077	0.0005	0	0.0036	0.0077	0	0	0	0.0004	0	0	0	0.0004	0.0004	0.0026	0	0	0	0
Ti4+	0.6395	0.6476	0.6819	0.6035	0.6207	0.6399	0.575	0.5372	0.4404	0.6197	0.6322	0.4632	0.4077	0.4512	0.3258	0.4272	0.4064	0.4637	0.4723	0.4823	0.3889	0.2535	0.3187	0.2871	0.4035
Mn2+	0.0209	0.022	0.0239	0.0193	0.0195	0.0218	0.0179	0.0243	0.0197	0.025	0.0282	0.0519	0.0508	0.0523	0.048	0.048	0.0498	0.0622	0.0668	0.0648	0.0386	0.0281	0.0285	0.0279	0.0941
Fe2+	1.3759	1.4009	1.4384	1.3371	1.3574	1.3828	1.2841	1.2831	1.1657	1.3917	1.4078	1.4003	1.3275	1.389	1.2592	1.3656	1.3211	1.3173	1.3406	1.3598	1.2504	1.1205	1.212	1.1465	1.2702
Fe3+	0.5632	0.6029	0.5715	0.6008	0.5818	0.5908	0.6231	0.7687	0.8465	0.6337	0.6045	1.0269	1.0039	1.0618	1.2569	1.0909	1.1733	0.9843	0.9274	0.9586	1.0682	1.4021	1.2261	1.2861	1.1657
Total	2.9999	2.9999	3.0001	2.9999	3	3.0001	3	3.0001	3	3.0001	3	2.9998	2.9999	3	3.0001	2.9999	2.9999	2.9999	3	3	3	2.9999	3	3	2.9999

Lavas - Ti-magnetite analyses

Ti-mag	86/27	84/23	84/23	87/70 in amph centre	87/70 in cpx centre	86/40 centre	86/40 big centre	86/20	86/20 v. big centre	85/18	85/18	86/54 in glom	86/54
Na2O	0.03	0.08	0	0	0.06	0	0.03	0.03	0	0	0.29	0.03	0.14
MgO	0.73	0.95	0.83	4.84	0.73	0.77	1.01	0.06	0.06	0.15	0.65	0.06	0.03
Al2O3	0.85	1.55	1.47	6.07	0.84	1.19	2.07	0.14	0.34	0.51	0.57	0.17	0.08
SiO2	0.03	0	0	0	0	0.05	0	0.08	0.13	0	0	0	0.03
K2O	0.06	0.04	0.05	0.05	0.05	0.05	0.05	0.05	0.05	0.06	0.05	0.05	0.06
CaO	0	0	0.01	0.04	0	0	0	0	0	0	0.11	0	0
TiO2	13.94	22.4	22.86	11.58	14.82	9.7	9.12	15.57	12.7	10.25	10.03	12.46	12.95
MnO	2.52	1.45	1.54	0.55	2.33	2.43	2.3	4.7	5.89	5.26	4.53	4.38	4.71
FeO	77.84	69.79	69.44	72.38	76.42	79.38	80.24	74.51	73.7	79.1	80.05	77.47	77.98
Total	96	96.26	96.2	95.51	95.25	93.57	94.82	95.14	92.87	95.33	96.28	94.62	95.98
recalc	100.18	98.65	98.47	99.72	99.21	98.39	99.78	98.96	97.07	100.24	101.43	99.06	100.46
Na+	0.0026	0.0064	0	0	0.0053	0	0.0027	0.0027	0	0	0.0256	0.0027	0.0124
Mg2+	0.0479	0.0582	0.0507	0.2991	0.0479	0.0531	0.0683	0.004	0.0042	0.0102	0.0438	0.0041	0.0019
Al3+	0.0439	0.0749	0.0709	0.2966	0.0434	0.0651	0.1109	0.0075	0.0183	0.0276	0.0305	0.0093	0.0043
Si4+	0.0013	0	0	0	0	0.0022	0	0.0035	0.0061	0	0	0	0.0013
K+	0.0032	0.002	0.0025	0.0025	0.0026	0.0028	0.0027	0.0027	0.0028	0.0033	0.0027	0.0027	0.0032
Ca2+	0	0	0.0005	0.0017	0	0	0	0	0	0	0.0054	0	0
Ti4+	0.4613	0.6909	0.7043	0.3612	0.4909	0.3376	0.3117	0.5189	0.4405	0.3537	0.3417	0.4273	0.4372
Mn2+	0.0939	0.0503	0.0534	0.0194	0.0868	0.0954	0.0885	0.1765	0.2301	0.2043	0.174	0.1691	0.1791
Fe2+	2.8643	2.3933	2.3792	2.5111	2.8145	3.0728	3.0508	2.7609	2.8437	3.0351	3.0335	2.9553	2.9275
Total	3.5184	3.276	3.2615	3.4916	3.4914	3.629	3.6356	3.4767	3.5457	3.6342	3.6572	3.5705	3.5669
Na+	0.0022	0.0059	0	0	0.0046	0	0.0022	0.0023	0	0	0.021	0.0023	0.0104
Mg2+	0.0408	0.0533	0.0466	0.257	0.0412	0.0439	0.0564	0.0035	0.0036	0.0084	0.0359	0.0034	0.0016
Al3+	0.0374	0.0686	0.0652	0.2548	0.0373	0.0538	0.0915	0.0065	0.0155	0.0228	0.025	0.0078	0.0036
Si4+	0.0011	0	0	0	0	0.0018	0	0.003	0.0052	0	0	0	0.0011
K+	0.0027	0.0018	0.0023	0.0021	0.0022	0.0023	0.0022	0.0023	0.0024	0.0027	0.0022	0.0023	0.0027
Ca2+	0	0	0.0005	0.0015	0	0	0	0	0	0	0.0044	0	0
Ti4+	0.3933	0.6327	0.6478	0.3103	0.4218	0.2791	0.2572	0.4478	0.3727	0.292	0.2803	0.359	0.3677
Mn2+	0.0801	0.0461	0.0491	0.0167	0.0746	0.0789	0.073	0.1523	0.1947	0.1686	0.1427	0.1421	0.1506
Fe2+	1.2636	1.5177	1.547	1.0311	1.2924	1.1536	1.1188	1.2854	1.1748	1.1093	1.0508	1.2048	1.1907
Fe3+	1.1787	0.674	0.6414	1.1264	1.126	1.3866	1.3986	1.0969	1.2312	1.3961	1.4376	1.2783	1.2715
Total	2.9999	3.0001	2.9999	2.9999	3.0001	3	2.9999	3	3.0001	2.9999	2.9999	3	2.9999

Lavas - Ti-magnetite analyses (continued)

spin-herc	86/63	86/63 centre	86/63 centre a	86/63 inclusion in ol	87/43 inclusion in ol	87/88b centre	87/88b	87/88b centre	87/88a centre
Na2O	0	0	0	0.04	0.02	0.02	0	0.13	0
MgO	17.15	16.92	16.77	17.82	16.24	14.91	15	15.53	15.38
Al2O3	55.62	53.87	54.24	54.47	51.82	48.13	48.57	50.1	48.96
SiO2	0.06	0.06	0.06	0.12	0.09	0.09	0.09	0.09	0.12
K2O	0.04	0.05	0.04	0.04	0.02	0.03	0.03	0.03	0.05
CaO	0	0	0	0	0	0	0	0	0
TiO2	0.94	0.92	0.99	1.43	1.31	1.99	2	1.79	1.74
MnO	0.11	0.03	0.12	0.03	0.18	0.12	0.2	0.13	0.17
FeO	25.84	25.19	26.43	23.45	28.06	32.26	32.08	31.21	30.49
Total	99.76	97.04	98.65	97.4	97.74	97.55	97.97	99.01	96.91
recalc	100.92	98.21	99.87	98.46	99.09	99.14	99.53	100.58	98.42
Na+	0	0	0	0.002	0.001	0.001	0	0.0072	0
Mg2+	0.6946	0.7048	0.6906	0.7328	0.6836	0.6459	0.6458	0.6568	0.6641
Al3+	1.782	1.7752	1.7671	1.7717	1.7253	1.6491	1.6544	1.676	1.6727
Si4+	0.0016	0.0017	0.0017	0.0033	0.0025	0.0026	0.0026	0.0026	0.0035
K+	0.0013	0.0017	0.0013	0.0013	0.0007	0.001	0.001	0.001	0.0017
Ca2+	0	0	0	0	0	0	0	0	0
Ti4+	0.0193	0.0193	0.0206	0.0297	0.0278	0.0435	0.0434	0.0382	0.038
Mn2+	0.0026	0.0007	0.0028	0.0007	0.0042	0.003	0.0049	0.0031	0.0042
Fe2+	0.5873	0.5889	0.6107	0.5412	0.6627	0.7842	0.7751	0.7407	0.739
Total	3.0887	3.0923	3.0948	3.0827	3.1078	3.1303	3.1272	3.1256	3.1232
Na+	0	0	0	0.0019	0.001	0.001	0	0.0069	0
Mg2+	0.6747	0.6838	0.6694	0.7131	0.6599	0.619	0.6195	0.6304	0.6379
Al3+	1.7308	1.7222	1.713	1.7242	1.6655	1.5805	1.5871	1.6087	1.6067
Si4+	0.0016	0.0016	0.0016	0.0032	0.0024	0.0025	0.0025	0.0025	0.0034
K+	0.0013	0.0016	0.0013	0.0013	0.0007	0.001	0.001	0.001	0.0016
Ca2+	0	0	0	0	0	0	0	0	0
Ti4+	0.0187	0.0187	0.02	0.0289	0.0268	0.0417	0.0416	0.0367	0.0365
Mn2+	0.0025	0.0007	0.0027	0.0007	0.0041	0.0029	0.0047	0.003	0.004
Fe2+	0.3407	0.3325	0.3469	0.3121	0.3622	0.4186	0.4182	0.3894	0.3942
Fe3+	0.2297	0.2388	0.2451	0.2146	0.2775	0.333	0.3254	0.3215	0.3156
Total	3	2.9999	3	3	3.0001	3.0002	3	3.0001	2.9999

Lavas - spinel-hercynite (pleonaste) analyses

biotite	84/19a near plag	86/8	86/8 big subhed	86/8	86/8	86/8 ovrgrth on amph	86/63 tiny
Na2O	0.88	0.72	0.68	0.87	0.8	1.15	0.65
MgO	13.58	9.78	11.36	11.55	12.49	13.47	14.42
Al2O3	13.28	13.53	14.12	13.52	13.52	13.6	12.73
SiO2	35.84	35.22	35.32	35.85	35.86	36.3	36.83
K2O	8.67	8.5	8.76	8.63	8.73	8.45	9.23
CaO	0.01	0.01	0	0	0	0.01	0.03
TiO2	8.3	6.72	7.13	6.17	6.33	6.07	9.45
MnO	0.36	0.47	0.27	0.39	0.43	0.31	0.09
FeO	13.85	21.47	18.2	18.96	17.66	15.46	11.21
Total	94.77	96.42	95.84	95.94	95.82	94.82	94.64
recalc	95.16	97.2	96.48	96.72	96.65	95.5	94.58
Na+	0.2685	0.2234	0.2098	0.2676	0.2455	0.3532	0.1963
Mg2+	3.1844	2.3361	2.6859	2.7378	2.9479	3.1719	3.3421
Al3+	2.4639	2.5557	2.6411	2.5342	2.5235	2.533	2.3346
Si4+	5.6389	5.6438	5.6044	5.701	5.6789	5.7353	5.728
K+	1.7397	1.7372	1.7734	1.7506	1.7642	1.7032	1.8318
Ca2+	0.0019	0.0019	0	0	0	0.0019	0.0047
Ti4+	0.9824	0.8098	0.8505	0.7377	0.7536	0.7215	1.1056
Mn2+	0.0482	0.0636	0.0362	0.0526	0.058	0.0418	0.0121
Fe2+	1.8229	2.8773	2.4151	2.5218	2.3389	2.0431	1.4579
Total	16.1508	16.2488	16.2164	16.3033	16.3105	16.3049	16.0131
sub-tot	14.1407	14.2863	14.2332	14.2851	14.3008	14.2466	13.9803
Na+	0.2658	0.2189	0.2064	0.2623	0.2403	0.3471	0.1966
Mg2+	3.1527	2.2893	2.6419	2.6832	2.8859	3.117	3.3468
Al3+	2.4394	2.5045	2.5978	2.4836	2.4704	2.4892	2.3379
Si4+	5.5828	5.5307	5.5126	5.5872	5.5595	5.636	5.7361
K+	1.7224	1.7024	1.7443	1.7157	1.7271	1.6737	1.8344
Ca2+	0.0019	0.0019	0	0	0	0.0019	0.0047
Ti4+	0.9726	0.7936	0.8366	0.723	0.7377	0.709	1.1072
Mn2+	0.0477	0.0623	0.0356	0.0516	0.0568	0.0411	0.0121
Fe2+	1.3471	1.8978	1.6218	1.5534	1.3221	1.2115	1.46
Fe3+	0.4577	0.9218	0.7537	0.9181	0.9676	0.7962	0
tot	15.9901	15.9232	15.9507	15.9781	15.9674	16.0227	16.0358
sub-tot	14	14	14	14.0001	14	14	14.0001

Lavas - biotite analyses

cpx	86/63	86/63 v. big centre a	86/63 v. big edge a	86/63 v. big edge a	86/63 embayed centre b	86/63 embayed edge b	86/63 gmass	86/63 embayed edge	86/63	86/66	86/66	86/66	87/29 gmass	87/29	87/29 greencore centre q	87/29 edge q	87/29 centre i	87/29 edge i	87/29 green centre j	87/29 edge j	87/29 centre k	87/29 edge k	84/43	84/43	86/53
	hwce																								
Na2O	0.68	0.69	0.4	0.47	0.69	0.85	1.12	0.73	0.62	0.77	0.87	0.95	1.46	0.77	0.98	1.36	0.76	0.84	2.02	0.6	1.04	0.49	0	0.9	0.93
MgO	11.35	13.22	12.67	10.52	13.84	9.28	10.01	14.16	12.54	11.66	12.06	12.43	13.22	12.29	9.18	13.38	12.3	12.87	7.94	11.38	10.93	13.09	12.89	13.19	12.93
Al2O3	9.39	8.02	7.8	10.5	7.52	9.98	10.31	7.06	8.88	9.14	8.34	8.73	7.07	8	6.84	5.61	7.89	7.52	6.16	9.3	7.87	4.71	7.79	6.72	9.15
SiO2	43.57	46.64	45.79	42.12	48.2	41.92	43.56	48.73	45.99	44.84	45.02	46.27	48.02	46.67	47.26	48.76	46.6	46.11	46.84	43.26	45.54	47.84	47.62	48.96	46.08
K2O	0.08	0.01	0.03	0.06	0.02	0.33	0.15	0.06	0.03	0.03	0.05	0.03	0.03	0.02	0.05	0.03	0.03	0.03	0.03	0.05	0.05	0.05	0.02	0.05	0.03
CaO	22.38	20.48	20.32	21.75	20.86	19.2	18.17	21.66	20.78	19.87	20.15	20.24	20.96	20.84	21.66	22.16	21.59	20.56	20.29	21.92	21.28	22.19	19.34	18.88	19.93
TiO2	3.16	1.71	1.59	3.57	1.19	4.04	3.3	1.26	1.71	2.26	2.26	2.45	2.02	2.52	1.64	2.39	2.42	2.28	1.51	4.19	2.52	2.63	1.94	1.47	2.71
MnO	0	0.08	0.01	0.08	0.1	0.18	0.19	0.04	0.12	0.15	0.15	0.12	0.14	0.18	0.48	0.14	0.1	0.15	0.7	0.12	0.2	0.21	0.14	0.19	0.11
FeO	7.83	6.28	3.08	7.57	5.77	7.84	10.62	5.4	6.55	7.59	7.69	8.11	7.35	8.06	11.81	6.88	7.67	7.54	13.89	8.04	9.24	7.13	8.17	8.75	7.78
Total	98.44	97.13	91.69	96.64	98.19	93.62	97.43	99.1	97.22	96.31	96.59	99.33	100.27	99.35	99.9	100.71	99.36	97.9	99.38	98.86	98.67	98.34	97.91	99.11	99.65
recalc	99.0182	97.3597	91.4082	96.9792	98.3923	93.6599	97.7123	99.3879	97.4501	96.5301	96.9743	99.6933	100.8879	99.6164	100.2473	101.2873	99.7036	98.3201	100.1425	99.3014	99.1634	98.5598	97.6245	99.2316	100.0217
Na+	0.0506	0.0508	0.031	0.0356	0.05	0.066	0.0842	0.0527	0.0458	0.0576	0.0651	0.0691	0.1054	0.056	0.0725	0.0975	0.0556	0.0623	0.1521	0.0445	0.0772	0.0361	0	0.0652	0.0674
Mg2+	0.6479	0.7497	0.7482	0.6106	0.7733	0.5544	0.5778	0.7842	0.7123	0.672	0.6949	0.696	0.7322	0.6887	0.5221	0.7389	0.6896	0.7311	0.4592	0.6475	0.6233	0.7415	0.7257	0.7358	0.7201
Al3+	0.424	0.3599	0.3643	0.4821	0.3325	0.4715	0.4706	0.3095	0.399	0.4169	0.3801	0.3865	0.31	0.3547	0.3077	0.2449	0.3499	0.338	0.2817	0.4185	0.355	0.211	0.3468	0.2965	0.4033
Si4+	1.6689	1.7748	1.8146	1.6405	1.8067	1.68	1.687	1.8109	1.7531	1.734	1.7407	1.7384	1.7845	1.7549	1.8034	1.8068	1.7527	1.7573	1.8179	1.6517	1.7425	1.8179	1.7989	1.8328	1.7218
K+	0.0037	0.0005	0.0014	0.0028	0.0009	0.0169	0.0074	0.0027	0.0014	0.0014	0.0023	0.0014	0.0013	0.0009	0.0023	0.0013	0.0014	0.0014	0.0014	0.0023	0.0023	0.0023	0.0009	0.0022	0.0013
Ca2+	0.9186	0.835	0.8627	0.9076	0.8379	0.8246	0.754	0.8623	0.8486	0.8233	0.8348	0.8148	0.8347	0.8396	0.8856	0.8798	0.8701	0.8396	0.8438	0.8969	0.8725	0.9036	0.7829	0.7574	0.798
Ti4+	0.0909	0.0489	0.0474	0.1046	0.0336	0.1219	0.0961	0.0353	0.049	0.0658	0.0658	0.0693	0.0565	0.0712	0.047	0.0666	0.0685	0.0653	0.0441	0.1202	0.0724	0.0751	0.0552	0.0414	0.0761
Mn2+	0	0.0025	0.0002	0.0026	0.0032	0.006	0.0063	0.0013	0.0039	0.0049	0.0049	0.0038	0.0045	0.0056	0.0156	0.0045	0.0032	0.0048	0.0231	0.0039	0.0064	0.0069	0.0045	0.0061	0.0036
Fe2+	0.2509	0.1998	0.1022	0.2467	0.1809	0.2627	0.344	0.1679	0.2089	0.2454	0.2486	0.2549	0.2284	0.2535	0.377	0.2133	0.2414	0.2403	0.4508	0.2567	0.2957	0.2265	0.2581	0.274	0.2432
	4.0555	4.0219	3.972	4.0331	4.019	4.004	4.0274	4.0268	4.022	4.0213	4.0372	4.0342	4.0575	4.0251	4.0332	4.0536	4.0324	4.0401	4.0741	4.0422	4.0473	4.0209	3.973	4.0114	4.0348
Na+	0.0499	0.0505	0.0312	0.0353	0.0498	0.0659	0.0836	0.0523	0.0455	0.0573	0.0645	0.0685	0.1039	0.0557	0.0719	0.0962	0.0552	0.0617	0.1493	0.044	0.0763	0.0359	0	0.065	0.0668
Mg2+	0.639	0.7456	0.7535	0.6056	0.7696	0.5538	0.5739	0.779	0.7084	0.6684	0.6885	0.6901	0.7218	0.6844	0.5178	0.7291	0.6841	0.7238	0.4508	0.6407	0.616	0.7376	0.7306	0.7337	0.7139
Al3+	0.4182	0.3579	0.3669	0.4781	0.3309	0.471	0.4674	0.3074	0.3968	0.4147	0.3766	0.3832	0.3056	0.3525	0.3052	0.2417	0.3471	0.3346	0.2766	0.4141	0.3509	0.2099	0.3492	0.2957	0.3998
Si4+	1.6461	1.7651	1.8274	1.627	1.7982	1.6783	1.6755	1.7988	1.7435	1.7248	1.7247	1.7237	1.7592	1.744	1.7886	1.7829	1.7386	1.7399	1.7848	1.6345	1.7221	1.8085	1.8111	1.8276	1.7069
K+	0.0036	0.0005	0.0014	0.0028	0.0009	0.0169	0.0073	0.0027	0.0014	0.0014	0.0023	0.0014	0.0013	0.0009	0.0023	0.0013	0.0014	0.0014	0.0014	0.0023	0.0023	0.0023	0.0009	0.0022	0.0013
Ca2+	0.906	0.8305	0.8688	0.9002	0.8339	0.8238	0.7489	0.8566	0.844	0.8189	0.8271	0.8079	0.8229	0.8344	0.8783	0.8682	0.8631	0.8313	0.8285	0.8875	0.8623	0.8989	0.7882	0.7552	0.7911
Ti4+	0.0897	0.0486	0.0477	0.1037	0.0334	0.1218	0.0954	0.0351	0.0487	0.0655	0.0652	0.0687	0.0557	0.0708	0.0466	0.0657	0.0679	0.0647	0.0433	0.1189	0.0716	0.0747	0.0556	0.0413	0.0754
Mn2+	0	0.0025	0.0002	0.0026	0.0032	0.006	0.0063	0.0013	0.0039	0.0049	0.0049	0.0038	0.0044	0.0056	0.0155	0.0044	0.0032	0.0048	0.0227	0.0039	0.0063	0.0069	0.0045	0.0061	0.0036
Fe2+	0.0833	0.1334	0.1029	0.1462	0.1233	0.2504	0.2601	0.0869	0.1422	0.1805	0.1357	0.151	0.0551	0.1771	0.2751	0.0518	0.1431	0.1188	0.2243	0.1287	0.152	0.1629	0.2599	0.2391	0.1376
Fe3+	0.1642	0.0653	0	0.0985	0.0567	0.012	0.0816	0.0799	0.0656	0.0636	0.1106	0.1017	0.1701	0.0748	0.0988	0.1587	0.0964	0.1191	0.2183	0.1253	0.1402	0.0624	0	0.0341	0.1035
sum	4	3.9999	4	4	3.9999	3.9999	4	4	4	4	4.0001	4	4	4.0002	4.0001	4	4.0001	4.0001	4	3.9999	4	4	4	4	3.9999

cpx	86/53	87/88b centre	87/88b pheno	87/88b centre	87/88b amph product	87/88a	87/88a	87/88a	87/43 centre d	87/43 hwce d	87/43 edge d	87/43 giant centre e	87/43 giant edge e	87/43 gmass	87/32 centre	87/32 edge	87/32 centre	86/55	86/55	86/27	86/27	86/27	86/27	87/74 centre	87/74 edge
Na2O	0.88	0.74	0.75	0	0.44	0.63	0.8	1.12	0.7	0.76	0.4	0.73	0.35	0.51	0.64	0.94	0.66	0.35	0.26	1.26	1.2	1.86	1.28	0.79	0.74
MgO	13.13	12.53	12.39	12.03	12.91	12.01	11.97	13.67	13.49	13.35	13	12.88	13.64	11.53	12.51	11.57	11.91	13.44	13.79	9.88	9.19	7.72	8.32	10.76	12.49
Al2O3	8.47	8.99	8.98	10.09	6.96	9.34	9.48	6.47	7.42	8.25	5.31	8.78	5.25	9.01	8.36	4.32	8.46	5.54	5.79	7.91	2.03	4.94	2.9	8.95	8.08
SiO2	46.62	44.43	45.87	44.87	47.71	45.36	45.2	48.56	48.47	47.47	47.75	47.04	48.15	44.23	45.96	49.2	45.51	48.64	48.64	45.83	49.67	48.01	47.72	44.59	45.52
K2O	0.03	0.03	0.03	0.05	0.08	0.05	0.05	0.03	0.03	0.03	0.03	0.03	0.03	0.29	0.03	0.05	0.03	0.05	0.03	0.03	0.03	0.05	0.06	0.05	0.03
CaO	19.65	20.96	20.93	20.94	22.05	20.69	20.8	20.36	20.54	20.67	21.94	20.55	21.97	21.59	21.87	21.31	21.78	21.55	21.5	20.76	21.39	20.25	21.34	21.34	20.63
TiO2	2.23	2.4	2.6	2.75	3.08	2.51	3.14	1.43	1.61	1.78	2.51	2.01	2.23	3.1	2.55	1.04	2.75	2.64	2.38	2.3	1.15	1.07	1.4	2.86	2.71
MnO	0.11	0.11	0.12	0.12	0.14	0.16	0.08	0.12	0.12	0.12	0.19	0.12	0.16	0.1	0.07	0.46	0.14	0.15	0.1	0.26	1.02	0.92	1.1	0.15	0.15
FeO	7.57	7.06	7.46	7.52	6.18	7.93	7.42	7.01	6.84	6.73	7.85	6.8	7.54	8.03	7.14	10.01	7.92	7.94	7.71	11.22	13.6	14.67	14.28	8.81	7.75
Total	98.69	97.25	99.13	98.37	99.55	98.68	98.94	98.77	99.22	99.16	98.98	98.94	99.32	98.39	99.13	98.9	99.16	100.3	100.2	99.45	99.28	99.49	98.4	98.3	98.1
recalc	98.9902	97.7604	99.4473	98.3626	99.5554	98.9667	99.2141	99.1615	99.3573	99.4261	99.1922	99.1215	99.575	98.8272	99.501	99.2511	99.5432	100.3965	100.3009	99.9782	99.6864	100.1231	98.996	98.6759	98.4603
Na+	0.0642	0.0549	0.0547	0	0.0318	0.0464	0.0585	0.0816	0.0506	0.0552	0.0295	0.0531	0.0253	0.0377	0.0466	0.0696	0.0482	0.025	0.0188	0.0933	0.0904	0.14	0.0982	0.0585	0.0545
Mg2+	0.7361	0.7172	0.6946	0.6787	0.7171	0.6777	0.6728	0.764	0.7487	0.7427	0.7325	0.7182	0.7642	0.6573	0.7023	0.6574	0.6715	0.745	0.7635	0.5629	0.5311	0.447	0.4891	0.6149	0.7093
Al3+	0.3757	0.4071	0.3983	0.4504	0.3059	0.4167	0.4215	0.2862	0.3258	0.3629	0.2368	0.3872	0.2327	0.4064	0.3712	0.1943	0.3774	0.2428	0.2536	0.3566	0.0928	0.2264	0.1347	0.4045	0.3631
Si4+	1.7538	1.7062	1.7255	1.6984	1.7782	1.7172	1.7046	1.8212	1.8048	1.772	1.8054	1.7601	1.8101	1.6919	1.7313	1.8756	1.7217	1.8095	1.8072	1.7523	1.9265	1.8649	1.8827	1.7096	1.7344
K+	0.0014	0.0014	0.0014	0.0023	0.0036	0.0023	0.0023	0.0014	0.0013	0.0013	0.0014	0.0013	0.0014	0.0143	0.0014	0.0023	0.0014	0.0022	0.0013	0.0014	0.0014	0.0023	0.0028	0.0023	0.0014
Ca2+	0.7921	0.8626	0.8435	0.8493	0.8806	0.8392	0.8405	0.8183	0.8196	0.8268	0.8888	0.8239	0.8851	0.8849	0.8827	0.8705	0.8829	0.859	0.8559	0.8505	0.8889	0.8428	0.9021	0.8766	0.8423
Ti4+	0.0631	0.0692	0.0735	0.0782	0.0862	0.0714	0.0891	0.0403	0.0452	0.05	0.0713	0.0567	0.063	0.0892	0.0722	0.0298	0.0782	0.0738	0.0665	0.0662	0.0336	0.0313	0.0415	0.0825	0.0776
Mn2+	0.0036	0.0037	0.0038	0.0039	0.0045	0.0052	0.0025	0.0038	0.0038	0.0038	0.0061	0.0038	0.0052	0.0032	0.0023	0.0149	0.0045	0.0047	0.0031	0.0085	0.0336	0.0303	0.0367	0.0048	0.0048
Fe2+	0.2383	0.2268	0.2346	0.2381	0.1926	0.2511	0.2341	0.22	0.213	0.2102	0.2483	0.2127	0.237	0.257	0.225	0.3191	0.2505	0.247	0.2395	0.3589	0.4412	0.4766	0.4711	0.2824	0.247
	4.0283	4.0491	4.0299	3.9993	4.0005	4.0272	4.0259	4.0368	4.0128	4.0249	4.0201	4.017	4.024	4.0419	4.035	4.0335	4.0363	4.009	4.0094	4.0506	4.0395	4.0616	4.0589	4.0361	4.0344
Na+	0.0637	0.0542	0.0543	0	0.0318	0.0461	0.0581	0.0809	0.0504	0.0549	0.0294	0.0529	0.0251	0.0373	0.0462	0.069	0.0478	0.0249	0.0188	0.0921	0.0895	0.1379	0.0968	0.058	0.054
Mg2+	0.7309	0.7085	0.6894	0.6788	0.717	0.6731	0.6685	0.757	0.7463	0.7381	0.7288	0.7152	0.7596	0.6505	0.6962	0.6519	0.6655	0.7433	0.7617	0.5559	0.5259	0.4402	0.482	0.6094	0.7033
Al3+	0.3731	0.4022	0.3953	0.4505	0.3059	0.4139	0.4188	0.2836	0.3248	0.3607	0.2356	0.3856	0.2313	0.4022	0.368	0.1927	0.374	0.2423	0.253	0.3521	0.0919	0.223	0.1327	0.4009	0.36
Si4+	1.7415	1.6855	1.7127	1.6987	1.778	1.7056	1.6936	1.8046	1.799	1.761	1.7964	1.7527	1.7993	1.6744	1.7163	1.86	1.7062	1.8054	1.803	1.7304	1.9077	1.8366	1.8554	1.6943	1.7196
K+	0.0014	0.0014	0.0014	0.0023	0.0036	0.0023	0.0023	0.0014	0.0013	0.0013	0.0014	0.0013	0.0014	0.0142	0.0014	0.0023	0.0014	0.0022	0.0013	0.0014	0.0014	0.0023	0.0028	0.0023	0.0014
Ca2+	0.7865	0.8521	0.8372	0.8494	0.8805	0.8335	0.8351	0.8108	0.817	0.8217	0.8844	0.8204	0.8798	0.8757	0.875	0.8633	0.875	0.8571	0.8539	0.8399	0.8802	0.83	0.889	0.8688	0.8351
Ti4+	0.0627	0.0684	0.073	0.0782	0.0862	0.0709	0.0885	0.0399	0.0451	0.0497	0.0709	0.0565	0.0626	0.0883	0.0716	0.0296	0.0775	0.0736	0.0663	0.0654	0.0333	0.0308	0.0409	0.0818	0.0769
Mn2+	0.0036	0.0037	0.0038	0.0039	0.0045	0.0052	0.0025	0.0038	0.0038	0.0038	0.0061	0.0038	0.0052	0.0032	0.0023	0.0148	0.0045	0.0047	0.0031	0.0084	0.0333	0.0298	0.0362	0.0048	0.0048
Fe2+	0.1523	0.0785	0.1439	0.2381	0.1911	0.1684	0.1554	0.1086	0.174	0.1347	0.1871	0.161	0.164	0.1299	0.1189	0.2167	0.1403	0.2195	0.2108	0.2045	0.3196	0.2874	0.2902	0.1726	0.1426
Fe3+	0.0843	0.1455	0.089	0	0.0015	0.081	0.0772	0.1094	0.0383	0.0742	0.06	0.0508	0.0716	0.1244	0.1041	0.0997	0.1079	0.0269	0.0281	0.1499	0.1173	0.182	0.1741	0.1073	0.1023
sum	4	4	4	3.9999	4.0001	4	4	4	4	4.0001	4.0001	4.0002	3.9999	4.0001	4	4	4.0001	3.9999	4	4	4.0001	4	4.0001	4.0002	4

cpx	87/74 green core c	87/74 non-green edge c	87/74 green centre	87/70 fragment	87/70 centre g	87/70 green rim g	87/70 in amph	86/8 small	86/8 medium subhed	86/8 medium edge	86/8 bigsubhed centre	86/8 subhed	86/8 gmass centre	86/8 gmass centre	84/19a big green	84/19a gmass	84/19a big green hwce	86/20 deepgreen centre	86/20 deep brown	86/20 grn/brn end sect.	85/18 green centre r	85/18 diffgreen edge r	85/18 centre	86/46	86/46
Na2O	1.51	0.64	1.61	1.13	0.69	1.75	0.71	0.6	0.68	0.41	0.7	0.65	0.93	0.11	1.31	0.76	1.1	2.12	2.12	1.52	1.33	0.95	2.07	5.08	9.35
MgO	8.77	11.43	8.92	9.88	15.12	9.85	13.45	11.45	9.45	8.78	11.32	11.23	9.63	9.1	9.98	13.37	9.99	4.73	4.12	7.5	10.13	9.94	8.5	0.69	0.07
Al2O3	6.06	6.64	4.27	5.75	4.98	4.55	6.05	1.95	2.57	1.21	7.83	2.09	1.36	2.98	4.67	1.96	4.75	3.85	2.43	3.91	3.23	3	3.1	1.25	0.6
SiO2	46.82	47.38	49.02	47.54	50.88	49.68	48.46	51.4	49.39	47.79	45.36	50.16	50.56	49.84	47.73	51.49	48.28	45.78	46.79	47.63	49.44	49.91	48.17	48.56	50.63
K2O	0.03	0.03	0.05	0.03	0.03	0.05	0.03	0.03	0.05	0.08	0.03	0.06	0.07	0.44	0.03	0.07	0.03	0.16	0.1	0.05	0.05	0.03	0.06	0.11	0.07
CaO	20.7	21.41	20.98	21.83	20.23	21.19	21.61	19.46	17.9	18.82	21.65	19.09	18.04	18.79	21.61	22.88	22.19	20.16	19.79	21.23	20.96	21.13	19.42	14.6	7
TiO2	1.57	2.07	0.96	1.45	0.85	1.1	1.63	0.44	0.55	0.35	2.54	0.41	0.27	0.24	1.47	0.85	1.43	1.49	1.05	1.01	0.78	0.72	2.15	0.55	1.29
MnO	0.58	0.29	0.79	0.5	0.12	0.63	0.12	1.23	1.5	1.75	0.16	1	1.5	1.38	0.52	0.57	0.48	2.3	2.7	1.37	0.95	0.99	1.71	3.03	2.25
FeO	12.83	9.51	13.32	11.34	6.5	11.9	6.78	14.89	18.02	17.51	9.37	13.98	17.38	13.96	11.52	7.23	11.38	18.88	19.22	15	11.65	11.65	13.82	24.66	24.95
Total	98.87	99.4	99.92	99.45	99.4	100.7	98.84	101.45	100.11	96.7	98.96	98.67	99.74	96.84	98.84	99.18	99.63	99.47	98.32	99.22	98.52	98.32	99	98.53	96.21
recalc	99.4565	99.6381	100.4783	99.9615	99.5295	101.2672	99.1227	101.7282	100.4512	97.1129	99.436	98.9277	100.0706	96.5867	99.424	99.441	100.1038	100.5489	99.2012	99.9194	98.9682	98.4967	99.6478	99.9786	98.2354
Na+	0.1138	0.0469	0.12	0.0838	0.0493	0.1282	0.0519	0.044	0.0514	0.0321	0.0519	0.0488	0.0701	0.0085	0.098	0.0556	0.0814	0.1653	0.1674	0.1156	0.0999	0.0711	0.1568	0.4077	0.757
Mg2+	0.507	0.6452	0.5105	0.5643	0.8331	0.5551	0.7529	0.6443	0.5472	0.5303	0.6443	0.6477	0.5578	0.5345	0.5745	0.7497	0.5698	0.2835	0.2502	0.4388	0.5836	0.5727	0.4949	0.0425	0.0043
Al3+	0.2769	0.2963	0.1934	0.2598	0.2173	0.2027	0.2677	0.0867	0.1177	0.0579	0.3524	0.0954	0.0621	0.1383	0.2126	0.0868	0.2143	0.1827	0.1165	0.1812	0.1473	0.1366	0.1427	0.0612	0.0296
Si4+	1.8164	1.7944	1.8829	1.822	1.8811	1.8788	1.8202	1.9407	1.9186	1.9364	1.7321	1.9413	1.9653	1.9643	1.8439	1.9374	1.8476	1.8416	1.9063	1.8698	1.9114	1.9298	1.8819	2.009	2.1134
K+	0.0014	0.0014	0.0023	0.0014	0.0013	0.0023	0.0014	0.0014	0.0023	0.0039	0.0014	0.0028	0.0033	0.0223	0.0014	0.0032	0.0014	0.0082	0.0054	0.0024	0.0023	0.0014	0.0028	0.006	0.0035
Ca2+	0.8604	0.8689	0.8634	0.8966	0.8014	0.8587	0.8696	0.7873	0.7451	0.8171	0.8859	0.7917	0.7514	0.7936	0.8944	0.9224	0.9099	0.8689	0.8639	0.8932	0.8684	0.8755	0.813	0.6471	0.313
Ti4+	0.0457	0.0589	0.0277	0.0417	0.0236	0.0314	0.046	0.0125	0.0161	0.0107	0.073	0.0119	0.0079	0.0071	0.0427	0.024	0.0412	0.045	0.0321	0.0297	0.0228	0.0209	0.0632	0.0172	0.0404
Mn2+	0.0191	0.0093	0.0256	0.0161	0.0038	0.0202	0.0038	0.0393	0.0493	0.0601	0.0053	0.0328	0.0493	0.0462	0.0169	0.0181	0.0156	0.0783	0.0933	0.0455	0.0311	0.0325	0.0566	0.1062	0.0795
Fe2+	0.4163	0.3013	0.4279	0.3634	0.2011	0.3763	0.2131	0.4701	0.5855	0.5934	0.2992	0.4526	0.565	0.4602	0.3721	0.2274	0.3642	0.6352	0.6548	0.4926	0.3766	0.3766	0.4515	0.8532	0.8711
	4.057	4.0226	4.0537	4.0491	4.012	4.0537	4.0266	4.0263	4.0332	4.0419	4.0455	4.025	4.0322	3.975	4.0565	4.0246	4.0454	4.1087	4.0899	4.0688	4.0434	4.0171	4.0634	4.1501	4.2118
Na+	0.1122	0.0466	0.1184	0.0828	0.0492	0.1265	0.0516	0.0437	0.051	0.0318	0.0513	0.0485	0.0695	0.0086	0.0966	0.0553	0.0805	0.1609	0.1637	0.1136	0.0988	0.0708	0.1544	0.393	0.7189
Mg2+	0.4999	0.6416	0.5037	0.5575	0.8306	0.5477	0.7479	0.6401	0.5427	0.5248	0.6371	0.6437	0.5533	0.5379	0.5665	0.7451	0.5634	0.276	0.2447	0.4314	0.5773	0.5703	0.4872	0.041	0.0041
Al3+	0.273	0.2946	0.1908	0.2566	0.2167	0.2	0.2659	0.0861	0.1167	0.0573	0.3484	0.0948	0.0616	0.1392	0.2096	0.0863	0.2119	0.1779	0.1139	0.1781	0.1457	0.136	0.1405	0.059	0.0281
Si4+	1.7909	1.7843	1.858	1.7999	1.8755	1.8539	1.8082	1.928	1.9028	1.9163	1.7126	1.9292	1.9496	1.9767	1.8182	1.9256	1.8269	1.7929	1.8644	1.8382	1.8909	1.9216	1.8525	1.9363	2.0071
K+	0.0014	0.0014	0.0023	0.0014	0.0013	0.0023	0.0014	0.0014	0.0023	0.0039	0.0014	0.0028	0.0033	0.0224	0.0014	0.0032	0.0014	0.008	0.0053	0.0024	0.0023	0.0014	0.0028	0.0058	0.0033
Ca2+	0.8483	0.864	0.852	0.8857	0.799	0.8473	0.8639	0.7822	0.739	0.8086	0.8759	0.7868	0.7454	0.7986	0.8819	0.9168	0.8997	0.8459	0.8449	0.8781	0.8591	0.8718	0.8003	0.6237	0.2973
Ti4+	0.0451	0.0586	0.0273	0.0412	0.0235	0.031	0.0457	0.0124	0.016	0.0106	0.0722	0.0118	0.0078	0.0071	0.0421	0.0239	0.0407	0.0438	0.0314	0.0292	0.0226	0.0208	0.0622	0.0166	0.0384
Mn2+	0.0188	0.0092	0.0253	0.0159	0.0038	0.0199	0.0038	0.039	0.0489	0.0595	0.0052	0.0326	0.0489	0.0465	0.0167	0.018	0.0154	0.0762	0.0912	0.0447	0.0308	0.0324	0.0557	0.1024	0.0755
Fe2+	0.2419	0.2322	0.2632	0.2135	0.1646	0.2123	0.1324	0.3886	0.4819	0.4628	0.1608	0.3753	0.4647	0.4631	0.1998	0.1527	0.2254	0.3009	0.3766	0.2814	0.2438	0.3239	0.2573	0.3883	0.2239
Fe3+	0.1686	0.0674	0.159	0.1455	0.0359	0.159	0.0793	0.0784	0.0988	0.1244	0.135	0.0745	0.0958	0	0.1671	0.0733	0.1347	0.3175	0.2638	0.2029	0.1288	0.0511	0.1872	0.434	0.6034
sum	4.0001	3.9999	4	4	4.0001	3.9999	4.0001	3.9999	4.0001	4	3.9999	4	3.9999	4.0001	3.9999	4.0002	4	4	3.9999	4	4.0001	4.0001	4.0001	4.0001	4

cpx	86/46	86/46	86/46	86/54 in glom	86/54 in glom	86/54 pheno centre f	86/54 pheno edge f	86/54 in glom centre	86/54 gmass	86/25	86/25	86/25	86/40 small centre	86/40 green centre h	86/40 green edge h	86/14 mantle nodule	86/14 mantle nodule
Na2O	8.3	4.93	4.25	3	7.35	1.67	1.8	10.64	1.84	4.03	3.44	3.58	1.47	1.93	1.48	1.55	1.5
MgO	0.34	0.97	1.14	3.52	1.5	9.68	9.19	0.4	9.09	2.56	2.69	2.87	10.09	8.15	9.8	14.83	15.1
Al2O3	0.72	1.03	1.13	0.84	0.71	2.74	2.8	0.65	3.01	1.22	1.38	1.61	4.78	3.73	5.43	6.3	6.13
SiO2	48.89	49.08	48.36	49.91	50.19	50.65	50.21	51.76	50.13	49.49	48.63	47.24	48.09	49.09	45.98	51.06	51.2
K2O	0.07	0.15	0.05	0.05	0.05	0.03	0.06	0.05	0.06	0.08	0.1	0.2	0.05	0.05	0.07	0.03	0.05
CaO	11.63	14.98	15.76	17.98	11.04	20.98	20.7	5.79	20.41	16.2	16.87	18.78	21.26	20.59	21.43	20.59	20.25
TiO2	0.66	0.68	0.63	0.74	1.28	0.65	0.7	0.19	0.76	0.97	1.17	1.1	1.21	0.66	1.6	0.66	0.6
MnO	2.64	2.93	3.25	3.27	2.48	1.22	1.36	1.62	1.29	3.14	3.18	2.92	0.63	1.18	0.64	0.07	0.1
FeO	25.91	24.54	24.53	20.97	23.28	12.67	12.81	27.74	13.36	21.96	21.51	21.16	10.9	14.35	11.49	3.17	3.3
Total	99.16	99.29	99.1	100.28	97.88	100.29	99.63	98.84	99.95	99.65	98.97	99.46	98.48	99.73	97.92	98.26	98.23
recalc	101.7994	100.6755	100.3805	101.0932	99.6259	100.8144	100.1778	101.6149	100.5166	100.6885	99.8835	100.9102	99.0499	100.4238	98.7783	98.4451	98.4055
Na+	0.6658	0.3916	0.3396	0.2324	0.5843	0.1233	0.1341	0.8441	0.1371	0.3151	0.2711	0.2832	0.11	0.1448	0.1125	0.1108	0.1073
Mg2+	0.0209	0.0594	0.07	0.2096	0.0916	0.5504	0.5269	0.0243	0.5202	0.1539	0.1629	0.1744	0.5806	0.4705	0.5722	0.8153	0.83
Al3+	0.0353	0.0498	0.0549	0.0394	0.0345	0.1233	0.1271	0.0315	0.1362	0.0582	0.0659	0.0774	0.2177	0.1704	0.2509	0.274	0.2664
Si4+	2.0228	2.0119	1.9918	1.9941	2.0575	1.9321	1.9317	2.1173	1.9253	1.9962	1.9766	1.9261	1.8571	1.9017	1.8012	1.8834	1.8886
K+	0.0035	0.0079	0.0025	0.0024	0.0025	0.0014	0.0028	0.0025	0.0028	0.0039	0.0054	0.0103	0.0023	0.0023	0.0033	0.0013	0.0022
Ca2+	0.5156	0.6579	0.6954	0.7697	0.4851	0.8575	0.8533	0.2537	0.8399	0.7002	0.7347	0.8205	0.8797	0.8548	0.8994	0.8139	0.8003
Ti4+	0.0206	0.0209	0.0196	0.0223	0.0394	0.0186	0.0203	0.0059	0.0219	0.0293	0.0357	0.0338	0.035	0.0193	0.0471	0.0184	0.0166
Mn2+	0.0925	0.1017	0.1134	0.1107	0.0862	0.0394	0.0444	0.056	0.042	0.1074	0.1094	0.1009	0.0207	0.0386	0.0212	0.0022	0.0031
Fe2+	0.8965	0.8411	0.8449	0.7008	0.7982	0.4041	0.4122	0.949	0.4291	0.7407	0.7313	0.7215	0.352	0.4649	0.3764	0.0978	0.1017
	4.2735	4.1422	4.1321	4.0814	4.1793	4.0501	4.0528	4.2843	4.0545	4.1049	4.093	4.1481	4.0551	4.0673	4.0842	4.0171	4.0162
Na+	0.6232	0.3782	0.3287	0.2278	0.5592	0.1218	0.1324	0.7881	0.1353	0.307	0.2649	0.2731	0.1085	0.1424	0.1102	0.1103	0.1069
Mg2+	0.0196	0.0574	0.0678	0.2054	0.0877	0.5436	0.52	0.0227	0.5132	0.15	0.1592	0.1682	0.5727	0.4627	0.5604	0.8118	0.8267
Al3+	0.033	0.0481	0.0531	0.0386	0.033	0.1218	0.1254	0.0294	0.1344	0.0567	0.0644	0.0746	0.2147	0.1676	0.2457	0.2728	0.2653
Si4+	1.8933	1.9428	1.9281	1.9543	1.9692	1.9082	1.9065	1.9768	1.8994	1.9452	1.9317	1.8573	1.8319	1.8702	1.7641	1.8754	1.881
K+	0.0033	0.0076	0.0024	0.0024	0.0024	0.0014	0.0028	0.0023	0.0028	0.0038	0.0053	0.0099	0.0023	0.0023	0.0032	0.0013	0.0022
Ca2+	0.4826	0.6353	0.6732	0.7543	0.4643	0.8469	0.8422	0.2369	0.8286	0.6823	0.718	0.7912	0.8677	0.8407	0.8809	0.8104	0.7971
Ti4+	0.0193	0.0202	0.019	0.0219	0.0377	0.0184	0.02	0.0055	0.0216	0.0286	0.0349	0.0326	0.0345	0.019	0.0461	0.0183	0.0165
Mn2+	0.0866	0.0982	0.1098	0.1085	0.0825	0.0389	0.0438	0.0523	0.0414	0.1047	0.1069	0.0973	0.0204	0.038	0.0208	0.0022	0.0031
Fe2+	0.0711	0.4002	0.4343	0.4475	0.2492	0.2507	0.2505	0.0897	0.262	0.4151	0.442	0.2673	0.1841	0.2586	0.1212	0.0463	0.0529
Fe3+	0.768	0.412	0.3836	0.2393	0.5148	0.1484	0.1563	0.7963	0.1613	0.3067	0.2727	0.4284	0.1631	0.1986	0.2474	0.0511	0.0484
sum	4	4	4	4	4	4.0001	3.9999	4	4	4.0001	4	3.9999	3.9999	4.0001	4	3.9999	4.0001

feldspar	F84/33 big xeno edge	F84/33 gmass	F84/33 big xeno core a	F84/33 big xeno rim a	86/57 gmass	87/43 gmass	87/43 gmass	87/29 gmass	87/29 gmass	86/32 pheno centre	86/32 pheno centre	86/32 gmass	86/32 gmass	86/55 gmass	F84/23 res phenohwce c	F84/23 res phenocentre c	F84/23 res phenoedge c	86/56 pheno centre d	86/56 pheno edge d	86/19a big frag centre	86/19a pheno	86/19a pheno	87/74 pheno centre h	87/74 pheno edge h	87/74 pheno centre
Na2O	3.07	2.95	7.56	3.06	4.75	3.11	2.97	3.73	4.82	5.13	5.63	4.78	4.53	4.41	5.84	5.94	6.14	6.27	6.25	5.01	5.7	4.75	7.29	7.31	7.18
MgO	0.11	0.17	0.04	0.11	0.02	0.15	0.15	0.11	0.21	0.04	0.02	0.08	0.08	0.11	0.06	0.08	0.06	0.02	0.04	0.06	0.02	0.04	0	0	0.14
Al2O3	30.77	30.85	24.65	30.76	28.81	30.82	30.46	29.03	28.25	27.16	27.51	28.27	29.01	28.91	26.76	26.63	26.42	26.16	26.37	27.91	26.64	27.88	20.36	24.65	24.53
SiO2	50.57	50.37	61.61	51.34	54.22	49.81	49.5	52.61	54.08	54.65	56.02	53.13	53.01	53.86	57.75	57.96	58.52	58.27	58.13	52.97	54.96	53.65	63.49	59.62	59.67
K2O	0.39	0.45	0.7	0.44	0.27	0.33	0.3	0.51	0.58	0.74	0.75	0.46	0.36	0.27	0.58	0.59	0.61	0.71	0.5	0.49	0.63	0.46	4.69	1.24	1.27
CaO	14.03	14.04	6.02	13.79	11.08	14.46	14.61	12.37	11.13	9.9	9.6	11.22	12.02	11.45	8.64	8.45	8.32	7.86	8.42	10.54	9.38	11.24	2.07	6.47	6.7
TiO2	0.21	0.21	0.02	0.19	0.19	0.17	0.13	0.23	0.21	0.06	0	0.15	0.11	0.13	0.08	0.06	0.06	0.06	0.08	0.08	0.08	0.06	0.15	0.06	0.04
MnO	0.01	0.01	0.01	0.01	0.04	0.01	0.03	0	0.03	0.01	0.01	0.03	0.03	0.01	0	0.01	0	0.03	0.01	0	0.03	0.01	0.01	0.01	0.01
FeO	0.64	0.67	0.09	0.58	0.62	0.81	0.84	0.74	0.69	0.42	0.13	0.72	0.64	0.64	0.33	0.35	0.39	0.35	0.54	0.36	0.39	0.49	0.3	0.32	0.35
Total	99.8	99.72	100.7	100.28	100	99.67	98.99	99.33	100	98.11	99.67	98.84	99.79	99.79	100.04	100.07	100.52	99.73	100.34	97.42	97.83	98.58	98.36	99.68	99.89
Na+	0.2724	0.262	0.6471	0.2696	0.4165	0.2772	0.2667	0.3308	0.424	0.4576	0.4932	0.4257	0.4	0.3876	0.5072	0.5156	0.5305	0.5458	0.5418	0.4511	0.5096	0.4232	0.6434	0.637	0.6249
Mg2+	0.0075	0.0116	0.0026	0.0074	0.0013	0.0103	0.0104	0.0075	0.0142	0.0027	0.0013	0.0055	0.0054	0.0074	0.004	0.0053	0.004	0.0013	0.0027	0.0042	0.0014	0.0027	0	0	0.0094
Al3+	1.6599	1.6662	1.283	1.648	1.536	1.6705	1.6631	1.5656	1.5111	1.4731	1.4654	1.5308	1.5575	1.5451	1.4132	1.4054	1.388	1.3846	1.3899	1.528	1.4481	1.5102	1.0926	1.306	1.298
Si4+	2.3139	2.3076	2.7199	2.3331	2.4519	2.29	2.2925	2.4067	2.4538	2.5142	2.5311	2.4403	2.4141	2.4417	2.5868	2.5946	2.6078	2.616	2.599	2.4599	2.534	2.4651	2.8901	2.6794	2.6782
K+	0.0228	0.0263	0.0394	0.0255	0.0156	0.0194	0.0177	0.0298	0.0336	0.0434	0.0432	0.027	0.0209	0.0156	0.0331	0.0337	0.0347	0.0407	0.0285	0.029	0.0371	0.027	0.2724	0.0711	0.0727
Ca2+	0.6879	0.6892	0.2848	0.6715	0.5369	0.7123	0.725	0.6063	0.5411	0.488	0.4648	0.5522	0.5865	0.5562	0.4147	0.4053	0.3973	0.3781	0.4034	0.5245	0.4634	0.5534	0.101	0.3116	0.3222
Ti4+	0.0072	0.0072	0.0007	0.0065	0.0065	0.0059	0.0045	0.0079	0.0072	0.0021	0	0.0052	0.0038	0.0044	0.0027	0.002	0.002	0.002	0.0027	0.0028	0.0028	0.0021	0.0051	0.002	0.0014
Mn2+	0.0004	0.0004	0.0004	0.0004	0.0015	0.0004	0.0012	0	0.0012	0.0004	0.0004	0.0012	0.0012	0.0004	0	0.0004	0	0.0011	0.0004	0	0.0012	0.0004	0.0004	0.0004	0.0004
Fe2+	0.0245	0.0257	0.0033	0.022	0.0234	0.0311	0.0325	0.0283	0.0262	0.0162	0.0049	0.0277	0.0244	0.0243	0.0124	0.0131	0.0145	0.0131	0.0202	0.014	0.015	0.0188	0.0114	0.012	0.0131
Total	4.9965	4.9962	4.9812	4.984	4.9896	5.0171	5.0136	4.9829	5.0124	4.9977	5.0043	5.0156	5.0138	4.9827	4.9741	4.9754	4.9788	4.9827	4.9886	5.0135	5.0126	5.0029	5.0164	5.0195	5.0203

feldspar	87/74 pheno centre	87/70 pheno centre k	87/70 pheno edge k	87/70 pheno centre l	87/70 pheno edge l	86/27 pheno	86/27 pheno	86/47 pheno centre b	86/47 pheno edge b	86/8 big phenocentre	86/8 big phenohwce	86/8 phenocore	86/8 pheno centre e	86/8 pheno edge e	86/8 pheno rim e	86/8 centre gmass	86/8 centre gmass	86/8 centre pheno centre	86/8 pheno centre	86/8 pheno centre	86/6 pheno	85/18 pheno centre	85/18 pheno edge	85/18 pheno centre	86/45 pheno tatty
Na2O	8.08	6.84	7.8	7.83	6.25	7.1	4.96	4.81	5.89	7.65	8.15	7.41	7.91	7.69	6.76	7.06	8.16	7.64	8.83	6.66	8.58	6.03	5.39	5.27	8.03
MgO	0	0.04	0	0.02	0.04	0.08	0.02	0.06	0.06	0.02	0.02	0.04	0	0	0.04	0	0	0	0	0	0.02	0	0.02	0	0.02
Al2O3	22.81	25.56	23.41	23.79	26.89	22.37	18.81	28.49	26.61	20.57	20.9	22.23	23.87	23.7	19.32	18.67	19.42	20.65	20.97	16.9	20.9	19.08	18.97	18.6	23.9
SiO2	62.36	57.99	61.16	61	56.27	62.92	65.77	54.7	57.46	65.45	63.15	62.64	61.03	60.48	66.43	65.59	66.76	63.58	64.3	67.6	68.37	65.74	65.87	65.9	62.2
K2O	1.83	0.73	1.21	1.09	0.52	7.25	9.07	0.37	0.56	3.99	2.93	2.41	1.06	0.97	5.32	5.98	4.36	2.71	1.94	7.43	2.91	8.24	8.52	9.08	0.8
CaO	4.27	7.5	5.33	5.49	8.99	0.44	0.24	10.59	8.67	2.04	2.44	4.07	5.88	5.86	0.82	0.66	1.26	2.71	2.8	0.27	1.37	0.54	0.47	0.35	5.22
TiO2	0.04	0.04	0.07	0.04	0.06	0.06	0.06	0.08	0.09	0.02	0.02	0.06	0.02	0.06	0.06	0.07	0.11	0.04	0.02	0.02	0	0.06	0.04	0.04	0.02
MnO	0	0.05	0	0	0.01	0.01	0.01	0.03	0.03	0	0.03	0	0.01	0.01	0	0	0	0.01	0.01	0	0.01	0.38	0.01	0	0
FeO	0.29	0.39	0.32	0.3	0.36	0.39	0.35	0.68	0.75	0.19	0.17	0.35	0.23	0.3	0.29	0.32	0.42	0.2	0.17	0.59	0.14	0.19	0.16	0.19	0.03
Total	99.68	99.14	99.3	99.56	99.39	100.62	99.29	99.81	100.12	99.93	97.81	99.21	100.01	99.07	99.04	98.35	100.49	97.54	99.04	99.47	102.3	100.26	99.45	99.43	100.22
Na+	0.7004	0.6001	0.6792	0.6801	0.549	0.619	0.437	0.4219	0.5127	0.6606	0.7188	0.6453	0.6849	0.6717	0.5883	0.6225	0.7016	0.6735	0.7666	0.5833	0.7175	0.527	0.4732	0.464	0.6895
Mg2+	0	0.0027	0	0.0013	0.0027	0.0054	0.0014	0.004	0.004	0.0013	0.0014	0.0027	0	0	0.0027	0	0	0	0	0	0.0013	0	0.0013	0	0.0013
Al3+	1.2023	1.3635	1.2394	1.2564	1.4363	1.1858	1.0075	1.5195	1.4083	1.0799	1.1208	1.1771	1.2567	1.2588	1.0223	1.0009	1.0152	1.1069	1.107	0.9	1.0626	1.014	1.0126	0.9957	1.2479
Si4+	2.788	2.624	2.7467	2.7327	2.5494	2.8291	2.9883	2.4747	2.5794	2.9147	2.8725	2.8134	2.7254	2.7247	2.9815	2.9825	2.9602	2.8908	2.8792	3.0537	2.9486	2.9634	2.9825	2.9923	2.7547
K+	0.1044	0.0421	0.0693	0.0623	0.0301	0.4159	0.5257	0.0214	0.0321	0.2267	0.17	0.1381	0.0604	0.0558	0.3046	0.3469	0.2466	0.1572	0.1108	0.4282	0.1601	0.4739	0.4922	0.526	0.0452
Ca2+	0.2046	0.3636	0.2565	0.2635	0.4364	0.0212	0.0117	0.5134	0.417	0.0973	0.1189	0.1959	0.2814	0.2829	0.0394	0.0322	0.0599	0.132	0.1343	0.0131	0.0633	0.0261	0.0228	0.017	0.2477
Ti4+	0.0013	0.0014	0.0024	0.0013	0.002	0.002	0.0021	0.0027	0.003	0.0007	0.0007	0.002	0.0007	0.002	0.002	0.0024	0.0037	0.0014	0.0007	0.0007	0	0.002	0.0014	0.0014	0.0007
Mn2+	0	0.0019	0	0	0.0004	0.0004	0.0004	0.0011	0.0011	0	0.0012	0	0.0004	0.0004	0	0	0	0.0004	0.0004	0	0.0004	0.0145	0.0004	0	0
Fe2+	0.0108	0.0148	0.012	0.0112	0.0136	0.0147	0.0133	0.0257	0.0282	0.0071	0.0065	0.0131	0.0086	0.0113	0.0109	0.0122	0.0156	0.0076	0.0064	0.0223	0.005	0.0072	0.0061	0.0072	0.0011
Total	5.0118	5.0141	5.0055	5.0088	5.0199	5.0935	4.9874	4.9844	4.9858	4.9883	5.0108	4.9876	5.0185	5.0076	4.9517	4.9996	5.0028	4.9698	5.0054	5.0013	4.9588	5.0281	4.9925	5.0036	4.9881

feldspar	86/20 pheno centre	86/20 big phenocentre	86/46 zoned ph.centre f	86/46 zoned ph.next f	86/46 zoned ph.next f	86/46 zoned ph.rim f	86/54 pheno centre i	86/54 pheno edge i	86/25 pheno centre j	86/25 pheno edge j	86/40 pheno centre m	86/40 pheno edge m
Na2O	6.37	6.57	9.69	9.07	7	8.32	8.34	7.67	5.64	6.56	4.78	5.01
MgO	0	0	0.02	0.02	0	0	0	0.02	0	0	0	0
Al2O3	18.84	19.08	22.5	22.85	19.15	19.11	20.25	19.75	19.07	19.58	19.06	20.07
SiO2	65.21	65.51	62.65	62.95	65.8	65.78	62.98	67.3	66.26	64.44	65.24	61.97
K2O	7.24	6.91	0.39	0.42	6.41	5.1	3.11	5	8.89	8.17	9.57	7.87
CaO	0.4	0.47	3.7	3.96	0.57	0.37	2.28	0.93	0.39	0.78	0.55	0.81
TiO2	0.02	0.02	0.04	0.06	0.04	0.02	0.09	0.08	0.02	0.06	0.06	0.15
MnO	0	0	0.01	0.04	0.01	0.03	0.01	0	0.01	0	0.01	0
FeO	0.17	0.13	0.25	0.27	0.13	0.22	0.22	0.2	0.1	0.35	0.17	0.23
Total	98.25	98.69	99.25	99.64	99.11	98.95	97.28	100.95	100.38	99.94	99.44	96.11
Na+	0.5642	0.5784	0.8397	0.7816	0.613	0.7279	0.7409	0.6556	0.4917	0.5772	0.4219	0.4555
Mg2+	0	0	0.0013	0.0013	0	0	0	0.0013	0	0	0	0
Al3+	1.0146	1.0214	1.1855	1.1973	1.0197	1.0165	1.0938	1.0265	1.0109	1.0475	1.0228	1.1096
Si4+	2.9788	2.9747	2.7999	2.7979	2.9719	2.9679	2.8855	2.967	2.9793	2.9242	2.9696	2.9061
K+	0.4219	0.4003	0.0222	0.0238	0.3694	0.2936	0.1818	0.2812	0.51	0.473	0.5557	0.4708
Ca2+	0.0196	0.0229	0.1772	0.1886	0.0276	0.0179	0.1119	0.0439	0.0188	0.0379	0.0268	0.0407
Ti4+	0.0007	0.0007	0.0013	0.002	0.0014	0.0007	0.0031	0.0027	0.0007	0.002	0.0021	0.0053
Mn2+	0	0	0.0004	0.0015	0.0004	0.0011	0.0004	0	0.0004	0	0.0004	0
Fe2+	0.0065	0.0049	0.0093	0.01	0.0049	0.0083	0.0084	0.0074	0.0038	0.0133	0.0065	0.009
Total	5.0063	5.0033	5.0368	5.004	5.0083	5.0339	5.0258	4.9856	5.0156	5.0751	5.0058	4.997

Lavas - feldspar analyses

amphibole	87/88b	87/88a	87/88a	87/88a	kaersutitmount	kaersutitmount	87/74	87/70	87/70	86/8	86/8	86/8	86/8	84/19a	84/19a	84/19a	86/27	86/27	86/56	86/40
	centre		centre	centre	centre	edge	centre	centre		resorbinghwce	subhedcentre	edge	small,recentre	slargecentre		centre				centre
Na2O	2.75	2.82	3.02	2.73	2.3	2.26	2.37	2.52	2.61	2.7	2.68	2.53	2.58	2.61	2.57	2.34	3.12	2.72	2.92	2.51
MgO	11.4	13.02	11.6	12.17	11.26	11.26	10.5	13.64	13.71	11.5	11.2	11.89	8.87	10.75	9.85	12.15	11.28	11.53	10.3	8.35
Al2O3	13.34	14.06	14.02	12.77	14.02	13.96	13.69	12.98	13.07	12.13	14.18	14.27	10.45	12.94	12.99	14.09	13.38	13.22	12.74	12.56
SiO2	39.58	39.01	38.83	39.43	38.23	38.57	38.84	39.94	39.88	40.64	38.16	38.66	37.76	38.29	37.92	38.3	39.1	38.73	40.23	38.58
K2O	1.13	1.43	1.17	1.61	1.15	1.15	1.77	1.51	1.45	1.2	1.26	1.29	1.22	1.55	1.53	1.39	1.7	1.81	1.26	2.09
CaO	11.06	11.52	11.25	11.19	11.27	11.15	11.3	11.64	11.57	11.24	11.88	12.04	9.69	11.42	11.74	11.95	11.12	11.37	10.96	11.07
TiO2	5.72	6	5.83	5.86	5.92	5.77	5.33	4.3	4.53	4.95	5.74	5.95	5.01	4.75	4.82	5.68	4.78	5.61	4.89	3.78
MnO	0.14	0.04	0.11	0.16	0.05	0	0.22	0.11	0.11	0.32	0.2	0.12	1.03	0.24	0.3	0.12	0.43	0.24	0.35	0.56
FeO	12.08	9.5	12.18	11.12	12.04	11.91	13.69	10.4	10.13	14.58	12.69	11.7	21.1	14.43	15.09	11.15	14.02	12.62	15.31	18.11
Total	97.2	97.4	98.01	97.04	96.24	96.03	97.71	97.04	97.06	99.26	97.99	98.45	97.71	96.98	96.81	97.17	98.93	97.85	98.96	97.61
Na+	0.7979	0.81	0.8712	0.7924	0.6743	0.6632	0.6914	0.7291	0.753	0.7765	0.7773	0.7262	0.7826	0.7725	0.7665	0.6804	0.9029	0.7921	0.8444	0.7526
Mg2+	2.5402	2.874	2.5733	2.7174	2.5381	2.5376	2.3565	3.0302	3.0407	2.5396	2.4993	2.6245	2.0693	2.446	2.2561	2.7118	2.5114	2.5803	2.2903	1.9242
Al3+	2.3524	2.4548	2.4597	2.2564	2.499	2.4876	2.4307	2.2805	2.293	2.1193	2.5029	2.4919	1.9282	2.3285	2.3531	2.4877	2.357	2.3403	2.241	2.2894
Si4+	5.9187	5.7783	5.7799	5.9085	5.7813	5.832	5.8495	5.9538	5.9356	6.0222	5.7129	5.726	5.9106	5.8461	5.8283	5.7367	5.8404	5.8147	6.0015	5.9651
K+	0.2156	0.2706	0.2218	0.3079	0.2217	0.2217	0.3403	0.2866	0.2755	0.2262	0.2411	0.2438	0.2446	0.3028	0.2992	0.2664	0.3231	0.3464	0.2402	0.4125
Ca2+	1.7719	1.8282	1.7943	1.7963	1.8265	1.8062	1.8235	1.8595	1.845	1.7845	1.9055	1.9107	1.6253	1.868	1.9329	1.9179	1.7799	1.8288	1.7516	1.8341
Ti4+	0.6434	0.6684	0.6529	0.66	0.6734	0.656	0.6036	0.4819	0.5071	0.5521	0.646	0.663	0.5897	0.545	0.5569	0.6399	0.5367	0.6334	0.5486	0.4395
Mn2+	0.018	0.0053	0.0143	0.0207	0.0064	0	0.0281	0.0143	0.0143	0.0401	0.0252	0.0151	0.1364	0.0312	0.0388	0.0153	0.0548	0.0307	0.0439	0.0734
Fe2+	1.5104	1.1767	1.5161	1.3938	1.523	1.5064	1.7239	1.2961	1.261	1.8068	1.5888	1.4489	2.7625	1.8423	1.9394	1.3968	1.7511	1.5843	1.9102	2.3424
Total	15.7685	15.8663	15.8835	15.8534	15.7437	15.7107	15.8475	15.932	15.9252	15.8673	15.899	15.8501	16.0492	15.9824	15.9712	15.8529	16.0573	15.951	15.8717	16.0332
Alvi	0.2711	0.2331	0.2396	0.1649	0.2803	0.3196	0.2802	0.2343	0.2286	0.1415	0.2158	0.2179	-0.1612	0.1746	0.1814	0.2244	0.1974	0.155	0.2425	0.2545
Aliv	2.0813	2.2217	2.2201	2.0915	2.2187	2.168	2.1505	2.0462	2.0644	1.9778	2.2871	2.274	2.0894	2.1539	2.1717	2.2633	2.1596	2.1853	1.9985	2.0349

Lavas - amphibole analyses

aenig-matite	86/46	86/46	86/46	86/54
Na2O	8.05	8.79	8.4	7.09
MgO	0	0	0.16	0.13
Al2O3	1.06	0.18	0.76	3.19
SiO2	40.13	42.7	41.11	41.01
K2O	0.12	0.08	0.15	0.58
CaO	0.28	0.92	0.26	0.24
TiO2	7.88	4.26	7.23	6.73
MnO	4.72	5.64	4.94	4.7
FeO	37.38	35.19	37.59	34.13
Total	99.62	97.76	100.6	97.8
recalc	99.8976	98.1393	100.9295	97.8795
Na+	2.272	2.5081	2.3461	1.9924
Mg2+	0	0	0.0346	0.0279
Al3+	0.1819	0.0318	0.1299	0.5451
Si4+	5.84	6.2843	5.9225	5.9433
K+	0.0227	0.0141	0.0277	0.108
Ca2+	0.0437	0.145	0.0398	0.0374
Ti4+	0.8623	0.4714	0.7835	0.7332
Mn2+	0.5815	0.7031	0.6025	0.5773
Fe2+	4.5501	4.3316	4.5295	4.1363
	14.3542	14.4894	14.4161	14.1009
Na+	2.2159	2.4234	2.2784	1.9781
Mg2+	0	0	0.0336	0.0277
Al3+	0.1774	0.0307	0.1262	0.5412
Si4+	5.6959	6.072	5.7516	5.9008
K+	0.0221	0.0136	0.0269	0.1072
Ca2+	0.0426	0.1401	0.0387	0.0371
Ti4+	0.841	0.4555	0.7609	0.728
Mn2+	0.5672	0.6794	0.5851	0.5732
Fe2+	4.1417	3.78	4.0524	4.0208
Fe3+	0.2961	0.4053	0.3464	0.0859
sum	13.9999	14	14.0002	14

Lavas - aenigmatite analyses

Mosandr-ite (30 Ox)	86/54	86/54	86/54	86/54	86/54	86/54	86/54	86/54	86/54
Na2O	7.11	7.13	7.46	7.57	7.23	7.21	7.31	7.09	6.99
MgO	0.09	0.09	0.16	0.11	0.07	0	0.11	0.13	0.09
Al2O3	0.09	0.09	0.07	0.16	0.09	0	0.09	0.16	0.07
SiO2	31.05	30.75	31.43	31.23	31.03	30.76	31.25	30.99	31.2
K2O	0.04	0.05	0	0.05	0.04	0	0.06	0.04	0.04
CaO	33.08	32.35	31.7	31.76	32.5	32.66	31.94	31.51	32.71
TiO2	7.91	8.34	7.43	7.58	8	7.91	7.49	7.92	7.94
MnO	1.47	1.72	1.55	1.47	1.35	1.48	1.54	1.66	1.51
FeO	1.54	1.37	1.89	1.74	1.49	1.49	1.7	1.63	1.53
ZrO2							6.36	5.03	4.92
Ce2O3							2.02	3.11	2.62
Total	82.38	81.89	81.69	81.67	81.8	81.51	89.87	89.27	89.62
Na+	3.2385	3.2644	3.4192	3.47	3.3085	3.3193	3.1618	3.0941	3.0305
Mg2+	0.0311	0.0312	0.0568	0.0384	0.0241	0	0.0362	0.0433	0.0296
Al3+	0.0254	0.0255	0.0199	0.0455	0.0255	0	0.0241	0.0433	0.0188
Si4+	7.2944	7.2626	7.4263	7.3847	7.3263	7.305	6.9739	6.974	6.9745
K+	0.0113	0.0142	0	0.0142	0.0113	0	0.0161	0.0108	0.0107
Ca2+	8.3277	8.1879	8.027	8.0469	8.2215	8.3111	7.6363	7.5987	7.8355
Ti4+	1.3976	1.4817	1.3206	1.3485	1.4201	1.4128	1.2564	1.3402	1.3353
Mn2+	0.2922	0.3435	0.3095	0.2941	0.2696	0.2983	0.291	0.3164	0.2861
Fe2+	0.3021	0.2711	0.3734	0.3439	0.2937	0.2954	0.3178	0.307	0.2861
Zr4+	0	0	0	0	0	0	0.6919	0.5518	0.536
Ce3+	0	0	0	0	0	0	0.1663	0.2569	0.2149
Total	20.9203	20.8821	20.9527	20.9862	20.9006	20.9419	20.5718	20.5365	20.558

Lavas - mosandrite analyses

cpx	14a centre	14a centre	14a centre	14a centre	14a centre	14b	14b	14c	14c	14s centre	14s centre	14s centre	38b	38b	38b	14e	14e	14i in amph	14i in amph	14u	14w	14w	14j centre d	14j edge d	14j centre e
Na2O	0.8	0.82	0.81	0.82	0.85	0.8	0.77	0.62	0.71	0.82	0.83	0.82	0.68	0.79	0.74	1.03	1.33	1.1	0.99	1.06	0.74	0.79	0.66	0.28	0.54
MgO	10.01	11.34	10.25	9.99	9.97	12.1	11.71	11.72	11.53	12.37	12.52	11.51	12	11.93	11.74	12.42	12.31	12.07	12.2	12.07	14	13.48	11.94	11.78	12.85
Al2O3	1.36	1.3	1.89	1.39	1.39	1.96	1.43	1.5	1.87	1.61	1.73	1.81	1.66	1.54	1.43	2.58	3.72	3.56	4.64	2.68	0.98	1.1	9.38	9.48	8.04
SiO2	50.88	51.66	50.52	50.45	50.41	51.19	51.76	52.05	51.4	52.01	52.2	48.57	51.68	51.04	48.26	51.11	50.59	50.52	49.72	51.52	53.41	53.25	44.75	44.95	46.64
K2O	0.03	0.03	0.05	0.03	0.03	0.03	0.03	0.03	0.03	0.03	0.03	0.05	0.06	0.03	0.05	0.03	0.17	0.11	0.06	0.14	0.05	0.05	0.03	0.03	0.03
CaO	22.19	21.22	21.72	22.16	22.1	20.63	21.23	20.15	20.06	20.73	20.01	19.6	20.74	20.33	20.39	22.06	21.25	21.58	22.04	21.36	22.14	22.25	21	21.21	21.44
TiO2	0.37	0.35	0.33	0.39	0.33	0.6	0.34	0.33	0.44	0.43	0.41	1.07	0.41	0.37	0.37	0.77	1.07	1.2	1.56	0.56	0.24	0.23	2.82	2.67	2.18
MnO	1.26	1.34	1.4	1.38	1.34	0.9	0.72	1.05	0.95	0.93	0.91	0.76	0	0.88	0.82	0.4	0.34	0.33	0.33	0.46	0.45	0.46	0.16	0.12	0.08
FeO	14.11	13.67	13.88	14.27	13.88	10.95	11.52	12.47	12.88	11.06	11.02	16.22	9.03	11.24	11.47	8.88	8.75	9.24	8.11	10	7.95	8.57	7.83	8.06	6.97
Total	101.01	101.73	100.85	100.88	100.3	99.16	99.51	99.92	99.87	99.99	99.66	100.41	96.26	98.15	95.27	99.28	99.53	99.71	99.65	99.85	99.96	100.18	98.57	98.58	98.77
recalc	101.4878	102.2	101.3619	101.4453	100.833	99.3708	99.7073	99.9938	100.0517	100.2027	99.7763	101.2465	96.0555	98.3522	95.8129	99.5834	99.9195	100.008	99.9136	100.1382	100.0932	100.3428	98.9346	98.7578	99.0235
Na+	0.0592	0.0598	0.0602	0.0608	0.0634	0.059	0.0567	0.0456	0.0526	0.0599	0.0608	0.0614	0.0511	0.0588	0.0572	0.0753	0.0972	0.0801	0.0722	0.0774	0.0532	0.0569	0.0484	0.0205	0.0394
Mg2+	0.5699	0.6371	0.5837	0.5709	0.572	0.6865	0.6637	0.6623	0.6537	0.6956	0.7041	0.6635	0.6911	0.6846	0.7	0.699	0.6902	0.6772	0.6825	0.6773	0.7762	0.7482	0.6758	0.6664	0.7211
Al3+	0.0611	0.058	0.085	0.0627	0.0629	0.0878	0.064	0.067	0.0837	0.0716	0.0771	0.0827	0.0757	0.0699	0.0673	0.1148	0.165	0.1579	0.2053	0.119	0.0429	0.0483	0.42	0.4242	0.357
Si4+	1.9435	1.9472	1.9303	1.9344	1.9402	1.9489	1.9686	1.9736	1.9553	1.9624	1.97	1.8784	1.9971	1.9651	1.9307	1.9304	1.9032	1.9017	1.8663	1.9396	1.9871	1.9835	1.6997	1.7059	1.7562
K+	0.0014	0.0014	0.0023	0.0014	0.0014	0.0014	0.0014	0.0014	0.0014	0.0014	0.0014	0.0023	0.0028	0.0014	0.0024	0.0014	0.0081	0.0054	0.0027	0.0068	0.0022	0.0022	0.0014	0.0014	0.0014
Ca2+	0.9083	0.8571	0.8893	0.9103	0.9115	0.8416	0.8652	0.8186	0.8176	0.8383	0.8091	0.8122	0.8587	0.8386	0.8741	0.8928	0.8565	0.8704	0.8865	0.8617	0.8827	0.8881	0.8548	0.8625	0.865
Ti4+	0.0106	0.01	0.0094	0.0113	0.0095	0.0172	0.0098	0.0093	0.0126	0.0122	0.0116	0.0311	0.0118	0.0106	0.0111	0.0218	0.0303	0.0339	0.044	0.0158	0.0067	0.0065	0.0806	0.0762	0.0618
Mn2+	0.0409	0.0428	0.0452	0.0449	0.0437	0.0291	0.0231	0.0337	0.0306	0.0297	0.029	0.0249	0	0.0287	0.0279	0.0127	0.0109	0.0106	0.0106	0.0147	0.0141	0.0145	0.0052	0.0039	0.0025
Fe2+	0.4508	0.431	0.4436	0.4576	0.4468	0.3486	0.3663	0.3955	0.4098	0.349	0.3479	0.5245	0.2919	0.3618	0.3837	0.2805	0.2753	0.2909	0.2547	0.3149	0.2473	0.267	0.2488	0.2559	0.2195
	4.0457	4.0444	4.049	4.0543	4.0514	4.0201	4.0188	4.007	4.0173	4.0201	4.011	4.081	3.9802	4.0195	4.0544	4.0287	4.0367	4.0281	4.0248	4.0272	4.0124	4.0152	4.0347	4.0169	4.0239
Na+	0.0585	0.0591	0.0595	0.06	0.0626	0.0587	0.0564	0.0455	0.0524	0.0596	0.0606	0.0602	0.0514	0.0585	0.0564	0.0748	0.0963	0.0795	0.0718	0.0769	0.053	0.0567	0.048	0.0204	0.0392
Mg2+	0.5635	0.6301	0.5766	0.5633	0.5647	0.6831	0.6606	0.6611	0.6509	0.6921	0.7022	0.6503	0.6945	0.6813	0.6906	0.694	0.6839	0.6725	0.6783	0.6727	0.7738	0.7454	0.67	0.6636	0.7168
Al3+	0.0604	0.0574	0.084	0.0619	0.0621	0.0874	0.0637	0.0669	0.0833	0.0712	0.0769	0.0811	0.0761	0.0696	0.0664	0.114	0.1635	0.1568	0.204	0.1182	0.0428	0.0481	0.4164	0.4224	0.3549
Si4+	1.9215	1.9258	1.9069	1.9085	1.9156	1.9392	1.9594	1.9702	1.9469	1.9526	1.9646	1.8411	2.007	1.9556	1.9048	1.9166	1.8859	1.8884	1.8548	1.9265	1.981	1.976	1.6851	1.6987	1.7458
K+	0.0014	0.0014	0.0023	0.0014	0.0014	0.0014	0.0014	0.0014	0.0014	0.0014	0.0014	0.0023	0.0028	0.0014	0.0024	0.0014	0.008	0.0054	0.0027	0.0068	0.0022	0.0022	0.0014	0.0014	0.0014
Ca2+	0.898	0.8477	0.8785	0.8981	0.8999	0.8374	0.8612	0.8172	0.8141	0.8341	0.8069	0.7961	0.863	0.8345	0.8624	0.8864	0.8487	0.8643	0.881	0.8559	0.88	0.8847	0.8474	0.8589	0.8599
Ti4+	0.0105	0.0099	0.0093	0.0111	0.0094	0.0171	0.0098	0.0093	0.0125	0.0121	0.0116	0.0305	0.0119	0.0105	0.011	0.0216	0.03	0.0337	0.0437	0.0157	0.0067	0.0065	0.0799	0.0759	0.0614
Mn2+	0.0404	0.0423	0.0447	0.0443	0.0431	0.029	0.023	0.0336	0.0305	0.0296	0.0289	0.0244	0	0.0286	0.0275	0.0126	0.0108	0.0105	0.0105	0.0146	0.0141	0.0144	0.0052	0.0039	0.0025
Fe2+	0.3101	0.2946	0.293	0.2908	0.2889	0.2869	0.3085	0.3738	0.3563	0.2873	0.314	0.2759	0.2934	0.3018	0.2176	0.193	0.1637	0.2052	0.1792	0.2318	0.2094	0.2206	0.1435	0.2043	0.1469
Fe3+	0.1356	0.1317	0.1452	0.1607	0.1522	0.06	0.0561	0.021	0.0517	0.06	0.0329	0.2382	0	0.0582	0.161	0.0855	0.1091	0.0837	0.0739	0.081	0.0371	0.0454	0.1032	0.0505	0.0713
sum	3.9999	4	4	4.0001	3.9999	4.0002	4.0001	4	4	4	4	4.0001	4.0001	4	4.0001	3.9999	3.9999	4	3.9999	4.0001	4.0001	4	4.0001	4	4.0001

cpx	14j edge e	14n centre f	14n edge f	14n centre g	14n edge g	38e	38e	38e	38e	38e	38h	38h	38h	14d centre a	14d edge a	14d centre	14h centre b	14h edge b	14h centre c	14h edge c	14l centre	14l centre	14m centre	14p centre	14p centre
Na2O	0.68	0.78	0	1.55	0.63	0.54	0.76	0.68	0.58	0.7	0.82	0.8	0.86	0.64	0.79	0.69	0.84	0.76	0.83	0.71	0	0.74	0.5	0.74	0.78
MgO	11.73	11.78	11.37	11.94	11.42	12.44	12.31	12.13	12.2	12.26	10.74	11.2	10.64	12.14	11.95	11.76	11.45	11.23	11.04	10.89	11.83	11.99	11.39	11.79	11.77
Al2O3	9.57	7.88	7.89	7.37	7.91	8.7	8.87	8.89	8.51	8.81	8.97	8.33	8.76	9.33	9.35	9.45	10.11	10.92	10.86	10.85	9.87	9.29	8.62	9.35	9.27
SiO2	45.04	46.2	46.14	47.57	46.41	46.13	45.67	44.97	44.77	44.5	44.04	44.85	43.77	45.81	45.73	45.39	44.41	44.09	43.55	43.25	44.39	45.34	46.72	45.16	41.99
K2O	0.05	0.05	0.05	0.03	0.03	0.03	0.03	0.03	0.03	0.02	0.03	0.03	0.03	0.03	0.03	0.03	0.03	0.03	0.03	0.03	0.03	0.03	0.03	0.02	0.03
CaO	21.22	21.22	21.35	21.5	21.68	20.56	20.68	20.26	20.57	20.53	21.29	21.46	21.29	21.27	21.5	21.39	20.99	21.25	21.08	21.31	21	21.22	21.31	21.31	20.81
TiO2	2.71	2.3	2.3	1.97	2.3	1.98	1.96	2.02	1.83	2.34	2.52	2.32	2.46	2.45	2.53	2.58	3.1	3.35	3.36	3.2	2.79	2.47	2.52	2.47	2.58
MnO	0.11	0.22	0.18	0.15	0.16	0.16	0.18	0.15	0.16	0.19	0.26	0.18	0.19	0.15	0.08	0.08	0.15	0.07	0.14	0.11	0.1	0.11	0.18	0.14	0.1
FeO	7.8	8.38	8.62	8.43	8.73	8.36	8.45	8.33	8.35	8.18	9.35	8.74	9.1	7.72	7.78	7.73	7.9	7.82	7.94	7.8	7.79	7.81	8.72	7.81	8.07
Total	98.91	98.81	97.9	100.51	99.27	98.9	98.91	97.46	97	97.53	98.02	97.91	97.1	99.54	99.74	99.1	98.98	99.52	98.83	98.15	97.8	99	99.99	98.79	95.4
recalc	99.2485	99.1718	97.8239	101.1796	99.5455	99.1979	99.3909	97.8717	97.4713	98.0318	98.5756	98.4058	97.6625	99.8532	100.1286	99.4173	99.3648	99.8572	99.2326	98.5319	97.8429	99.3953	100.0804	99.1853	96.1771
Na+	0.05	0.0575	0	0.1122	0.0464	0.0395	0.056	0.0508	0.0437	0.0522	0.0613	0.0597	0.0651	0.0464	0.0572	0.0503	0.0619	0.0557	0.0612	0.0529	0	0.054	0.0365	0.0542	0.0599
Mg2+	0.6613	0.6665	0.648	0.6645	0.6439	0.7001	0.6947	0.694	0.7027	0.7025	0.6181	0.6426	0.6177	0.6789	0.6679	0.6613	0.646	0.63	0.6249	0.6207	0.673	0.6753	0.6357	0.6658	0.6938
Al3+	0.4269	0.3526	0.3557	0.3245	0.3528	0.3872	0.3959	0.4024	0.3878	0.3992	0.4083	0.378	0.4021	0.4126	0.4133	0.4203	0.4513	0.4846	0.4861	0.489	0.4441	0.4137	0.3807	0.4176	0.4321
Si4+	1.7038	1.7536	1.7643	1.7764	1.7558	1.7423	1.7294	1.7268	1.73	1.7109	1.7004	1.7266	1.705	1.7189	1.7148	1.7125	1.6812	1.6598	1.6539	1.654	1.6945	1.7132	1.7495	1.7112	1.6608
K+	0.0023	0.0023	0.0023	0.0013	0.0014	0.0014	0.0014	0.0014	0.0014	0.0009	0.0014	0.0014	0.0014	0.0014	0.0014	0.0014	0.0014	0.0014	0.0014	0.0014	0.0014	0.0014	0.0014	0.0009	0.0014
Ca2+	0.8602	0.8631	0.8748	0.8604	0.8789	0.832	0.8392	0.8336	0.8517	0.8458	0.8807	0.8853	0.8886	0.8552	0.864	0.8646	0.8514	0.8571	0.8579	0.8732	0.8591	0.8592	0.855	0.8653	0.882
Ti4+	0.0771	0.0657	0.0662	0.0554	0.0655	0.0563	0.0557	0.0584	0.0532	0.0677	0.0731	0.0671	0.0721	0.0692	0.0714	0.0732	0.0883	0.0948	0.0961	0.0921	0.0801	0.0702	0.0709	0.0704	0.0768
Mn2+	0.0036	0.0071	0.0057	0.0047	0.0052	0.0052	0.0057	0.0048	0.0053	0.0062	0.0086	0.0058	0.0063	0.0047	0.0025	0.0025	0.0048	0.0023	0.0046	0.0037	0.0032	0.0036	0.0056	0.0046	0.0033
Fe2+	0.2469	0.266	0.2757	0.2632	0.2762	0.2642	0.2676	0.2674	0.2698	0.2629	0.3018	0.2813	0.2966	0.2421	0.244	0.2439	0.2502	0.2461	0.2522	0.2496	0.2487	0.2468	0.2732	0.2475	0.2669
	4.0321	4.0344	3.9927	4.0626	4.0261	4.0282	4.0456	4.0396	4.0456	4.0483	4.0537	4.0478	4.0549	4.0294	4.0365	4.03	4.0365	4.0318	4.0383	4.0366	4.0041	4.0374	4.0085	4.0375	4.077
Na+	0.0496	0.057	0	0.1105	0.0461	0.0392	0.0554	0.0503	0.0432	0.0516	0.0605	0.059	0.0642	0.0461	0.0567	0.0499	0.0613	0.0553	0.0606	0.0524	0	0.0535	0.0364	0.0537	0.0588
Mg2+	0.656	0.6608	0.6492	0.6543	0.6397	0.6952	0.6869	0.6872	0.6948	0.6941	0.6099	0.635	0.6093	0.6739	0.6619	0.6564	0.6402	0.625	0.619	0.6151	0.6723	0.669	0.6344	0.6596	0.6807
Al3+	0.4235	0.3496	0.3564	0.3195	0.3505	0.3845	0.3914	0.3985	0.3834	0.3944	0.4029	0.3735	0.3967	0.4096	0.4096	0.4172	0.4472	0.4808	0.4815	0.4846	0.4436	0.4099	0.3799	0.4137	0.4239
Si4+	1.6902	1.7386	1.7675	1.749	1.7444	1.7301	1.7099	1.7099	1.7105	1.6905	1.6779	1.7062	1.6819	1.7064	1.6993	1.6998	1.666	1.6467	1.6382	1.639	1.6928	1.6973	1.7458	1.6953	1.6294
K+	0.0023	0.0023	0.0023	0.0013	0.0014	0.0014	0.0014	0.0014	0.0014	0.0009	0.0014	0.0014	0.0014	0.0014	0.0014	0.0014	0.0014	0.0014	0.0014	0.0014	0.0014	0.0014	0.0014	0.0009	0.0014
Ca2+	0.8534	0.8557	0.8764	0.8471	0.8732	0.8262	0.8297	0.8254	0.8421	0.8357	0.869	0.8748	0.8766	0.849	0.8562	0.8582	0.8437	0.8503	0.8498	0.8653	0.8582	0.8512	0.8532	0.8573	0.8653
Ti4+	0.0765	0.0651	0.0663	0.0545	0.0651	0.0559	0.0551	0.0578	0.0526	0.0669	0.0721	0.0663	0.0711	0.0687	0.0708	0.0727	0.0875	0.0941	0.0952	0.0913	0.08	0.0695	0.0707	0.0697	0.0753
Mn2+	0.0036	0.007	0.0057	0.0046	0.0052	0.0052	0.0056	0.0048	0.0052	0.0061	0.0085	0.0057	0.0062	0.0047	0.0025	0.0025	0.0048	0.0023	0.0046	0.0037	0.0032	0.0036	0.0056	0.0046	0.0032
Fe2+	0.1494	0.1614	0.2762	0.0742	0.1966	0.1784	0.1293	0.1472	0.1315	0.1166	0.1388	0.1363	0.1301	0.1527	0.1333	0.1528	0.1394	0.1496	0.136	0.1385	0.2361	0.1333	0.2472	0.1337	0.0353
Fe3+	0.0955	0.1023	0	0.1849	0.0778	0.084	0.1353	0.1176	0.1353	0.1432	0.159	0.1417	0.1625	0.0876	0.1085	0.0893	0.1085	0.0946	0.1138	0.1088	0.0123	0.1112	0.0254	0.1115	0.2266
sum	4	3.9998	4	3.9999	4	4.0001	4	4.0001	4	4	4	3.9999	4	4.0001	4.0002	4.0002	4	4.0001	4.0001	4.0001	3.9999	3.9999	4	4	3.9999

cpx	14p centre	14v centre h	14v edge h	14v centre	14v centre	38a	38a centre	38a	38a	38a	38a	14r megacryst	14r megacryst	14r megacryst
Na2O	0.73	0.64	0.59	0.77	0.61	0.5	0.88	0.69	0.91	0.74	0.79	1.71	0.02	0.62
MgO	11.79	11.8	11.97	12.11	11.86	10.32	10.93	10.93	11.03	11.47	11.41	12.49	11.49	11.6
Al2O3	9.48	9.38	9.59	9.31	9.54	11.1	11.5	10.98	10.33	10.25	10.34	8.6	10.11	10.11
SiO2	44.7	45.51	45.34	45.39	45.34	41.66	41.84	43.48	44.31	43.48	43.28	46.79	44.77	45.23
K2O	0.03	0.02	0.05	0.03	0.03	0.06	0.21	0.06	0.06	0.03	0.05	0.03	0.03	0.02
CaO	20.91	21.19	21.3	21.34	21.38	20.67	19.75	21.52	21.02	21.05	21.01	21.1	21.26	21.36
TiO2	2.54	2.49	2.6	2.57	2.72	3.43	3.79	3.5	3.12	2.97	3.05	2.17	2.6	2.77
MnO	0.11	0.08	0.1	0.08	0.08	0.11	0.19	0.11	0.05	0.19	0.12	0.1	0.11	0.1
FeO	8.03	7.66	7.56	7.66	7.58	8.7	7.63	7.37	7.79	7.65	7.59	7.64	7.75	7.69
Total	98.32	98.77	99.1	99.26	99.14	96.55	96.72	98.64	98.62	97.83	97.64	100.63	98.14	99.5
recalc	98.732	99.0247	99.3913	99.6734	99.4111	96.9148	97.1524	98.948	98.9576	98.2861	98.113	101.4252	98.1295	99.7446
Na+	0.054	0.0468	0.043	0.0561	0.0444	0.038	0.0662	0.0507	0.0671	0.0548	0.0586	0.1233	0.0014	0.0451
Mg2+	0.6693	0.6647	0.6723	0.6798	0.6659	0.6011	0.6318	0.6188	0.6243	0.6554	0.6532	0.6919	0.651	0.6491
Al3+	0.4258	0.4179	0.4262	0.4134	0.4239	0.5114	0.5258	0.4917	0.4623	0.4631	0.4681	0.377	0.4532	0.4476
Si4+	1.7028	1.7201	1.7086	1.7102	1.7084	1.628	1.6228	1.6517	1.6826	1.667	1.6627	1.7391	1.7017	1.6981
K+	0.0014	0.0009	0.0023	0.0014	0.0014	0.0028	0.0103	0.0027	0.0027	0.0014	0.0023	0.0013	0.0014	0.0009
Ca2+	0.8536	0.8582	0.8601	0.8614	0.8632	0.8655	0.8208	0.8758	0.8552	0.8648	0.8647	0.8402	0.8659	0.8593
Ti4+	0.0728	0.0709	0.0736	0.0729	0.077	0.1007	0.1105	0.1	0.089	0.0857	0.0882	0.0607	0.0742	0.0783
Mn2+	0.0037	0.0025	0.0032	0.0025	0.0025	0.0038	0.0063	0.0037	0.0016	0.0062	0.0039	0.0031	0.0037	0.0032
Fe2+	0.2559	0.2421	0.2382	0.2413	0.2389	0.2844	0.2475	0.2342	0.2473	0.2454	0.2438	0.2374	0.2465	0.2414
	4.0393	4.0241	4.0275	4.039	4.0256	4.0357	4.042	4.0293	4.0321	4.0438	4.0455	4.074	3.999	4.023
Na+	0.0535	0.0465	0.0427	0.0556	0.0441	0.0377	0.0655	0.0503	0.0666	0.0542	0.0579	0.1211	0.0014	0.0448
Mg2+	0.6628	0.6607	0.6677	0.6732	0.6617	0.5958	0.6252	0.6143	0.6193	0.6483	0.6459	0.6793	0.6512	0.6454
Al3+	0.4217	0.4154	0.4233	0.4094	0.4212	0.5069	0.5203	0.4881	0.4586	0.4581	0.4628	0.3702	0.4533	0.445
Si4+	1.6862	1.7098	1.6969	1.6937	1.6975	1.6136	1.6059	1.6397	1.6692	1.6489	1.644	1.7075	1.7021	1.6884
K+	0.0014	0.0009	0.0023	0.0014	0.0014	0.0028	0.0102	0.0027	0.0027	0.0014	0.0023	0.0013	0.0014	0.0009
Ca2+	0.8453	0.8531	0.8542	0.8531	0.8577	0.8578	0.8123	0.8694	0.8484	0.8554	0.855	0.8249	0.8661	0.8544
Ti4+	0.0721	0.0705	0.0731	0.0722	0.0765	0.0998	0.1094	0.0993	0.0883	0.0848	0.0872	0.0596	0.0742	0.0779
Mn2+	0.0037	0.0025	0.0032	0.0025	0.0025	0.0038	0.0062	0.0037	0.0016	0.0061	0.0039	0.003	0.0037	0.0032
Fe2+	0.1366	0.1688	0.1547	0.1231	0.1611	0.1757	0.1202	0.1452	0.1498	0.1127	0.1061	0.0151	0.2466	0.1714
Fe3+	0.1168	0.0719	0.0819	0.1159	0.0763	0.1062	0.1247	0.0873	0.0955	0.13	0.135	0.218	0	0.0686
sum	4.0001	4.0001	4	4.0001	4	4.0001	3.9999	4	4	3.9999	4.0001	4	4	4

Cumulates - clinopyroxene analyses (continued)

biotite	14a centre	14b	14c centre	14c	14f centre	14s centre	14s centre	38b	38b	38b	38b	14e centre	14i	14u centre	14w	14w centre	38f	38f	38f	38f	38f
Na2O	0.6	0.67	0.64	0.62	0.97	0.64	0.58	0.67	0.47	0.66	0.66	0.87	0.69	0.69	0.84	0.71	0.63	0.59	0.73	0.67	0.68
MgO	8.9	11.01	8.56	8.96	10.93	10.95	10.99	10.85	10.85	10.93	11.05	12.96	10.83	10.71	12.16	12.57	9.89	9.92	10.72	11.38	10.41
Al2O3	12.87	14.1	14.13	14.2	13.45	14.02	13.82	13.68	13.58	13.48	13.36	14.1	14.39	14.36	14.33	14.79	13.81	13.8	13.66	13.93	13.86
SiO2	35.1	35.42	32.97	35.02	36.02	35.61	35.68	35.28	35.55	33.01	33.37	36.61	35.46	35.82	35.83	36.47	35.31	34.72	33.63	34.43	34.36
K2O	8.63	8.61	8.34	8.52	8.74	8.46	8.74	9.18	9.09	8.42	8.54	8.82	8.49	9.12	8.91	8.77	8.69	8.45	8.49	8.77	8.62
CaO	0	0	0	0.01	0	0	0.01	0.04	0.01	0	0	0	0	0	0	0	0	0.01	0	0	0
TiO2	6.07	5.86	5.65	5.74	5.84	6.18	5.93	5.84	5.53	5.64	5.7	5.39	6.08	6.27	5.99	5.11	6.09	6.12	5.5	4.74	5.9
MnO	0.55	0.39	0.48	0.55	0.36	0.35	0.31	0.33	0.36	0.32	0.28	0.24	0.23	0.32	0.24	0.21	0.35	0.33	0.32	0.31	0.32
FeO	22.44	19.75	21.47	21.91	19.95	19.68	20.06	20.01	19.01	19.54	19.5	17.66	19.38	20.28	17.87	17.27	21.01	21.45	19.78	19.81	20.42
Total	95.16	95.81	92.24	95.53	96.26	95.89	96.12	95.88	94.45	92	92.46	96.65	95.55	97.57	96.17	95.9	95.78	95.39	92.83	94.04	94.57
recalc	95.91	96.71	93.08	96.32	96.98	96.75	97	96.66	95.16	93.09	93.51	97.56	96.34	98.31	96.94	96.77	96.55	96.33	93.83	95.17	95.49
Na+	0.1906	0.2073	0.2086	0.1947	0.2986	0.1972	0.1801	0.2084	0.1479	0.2135	0.2123	0.2632	0.2129	0.2099	0.2578	0.2171	0.1972	0.1849	0.2353	0.2123	0.2154
Mg2+	2.1682	2.6216	2.1498	2.1631	2.5948	2.5998	2.6109	2.5958	2.6178	2.73	2.7443	3.0213	2.5755	2.5116	2.859	2.9428	2.3713	2.3938	2.6514	2.773	2.5286
Al3+	2.4815	2.6552	2.807	2.7122	2.5249	2.6324	2.5975	2.5891	2.5915	2.6625	2.6252	2.6002	2.7078	2.6648	2.6656	2.739	2.6198	2.6351	2.6723	2.6846	2.6637
Si4+	5.7382	5.6578	5.5564	5.6736	5.7371	5.6725	5.6872	5.6634	5.7551	5.5315	5.5598	5.7277	5.6582	5.637	5.6526	5.728	5.6804	5.6225	5.581	5.6306	5.5997
K+	1.7998	1.7548	1.7924	1.7601	1.7765	1.7192	1.7776	1.881	1.8775	1.8005	1.8162	1.7598	1.7278	1.8308	1.7935	1.7574	1.7845	1.7457	1.7968	1.8297	1.7921
Ca2+	0	0	0	0.0019	0	0	0.0019	0.0068	0.0019	0	0	0	0	0	0	0	0	0.0019	0	0	0
Ti4+	0.7466	0.7036	0.7159	0.699	0.6997	0.7399	0.7107	0.7052	0.6732	0.7109	0.7139	0.6345	0.7297	0.7423	0.711	0.604	0.7366	0.7454	0.686	0.5827	0.7227
Mn2+	0.0766	0.0528	0.0689	0.0759	0.0488	0.0469	0.0421	0.0453	0.0496	0.0453	0.039	0.032	0.0307	0.0426	0.0322	0.0283	0.0474	0.0457	0.0449	0.0432	0.0441
Fe2+	3.068	2.6388	3.0258	2.9682	2.658	2.6218	2.6741	2.6865	2.574	2.7391	2.7173	2.3106	2.586	2.6696	2.3576	2.2689	2.8267	2.9047	2.7451	2.7092	2.7832
Total	16.2695	16.2919	16.3248	16.2487	16.3384	16.2297	16.2821	16.3815	16.2885	16.4333	16.428	16.3493	16.2286	16.3086	16.3293	16.2855	16.2639	16.2797	16.4128	16.4653	16.3495
sub-tot	14.2791	14.3298	14.3238	14.292	14.2633	14.3133	14.3225	14.2853	14.2612	14.4193	14.3995	14.3263	14.2879	14.2679	14.278	14.311	14.2822	14.3472	14.3807	14.4233	14.342
Na+	0.1869	0.2025	0.2039	0.1907	0.2931	0.1929	0.176	0.2042	0.1452	0.2073	0.2064	0.2572	0.2086	0.206	0.2528	0.2124	0.1933	0.1804	0.2291	0.2061	0.2103
Mg2+	2.1258	2.5613	2.1012	2.1189	2.5469	2.5429	2.5521	2.544	2.5699	2.6506	2.6682	2.9525	2.5236	2.4644	2.8033	2.8788	2.3244	2.3359	2.5812	2.6916	2.4683
Al3+	2.433	2.5941	2.7435	2.6568	2.4783	2.5748	2.539	2.5374	2.544	2.5851	2.5524	2.541	2.6532	2.6148	2.6137	2.6795	2.568	2.5713	2.6016	2.6058	2.6002
Si4+	5.626	5.5276	5.4308	5.5577	5.6312	5.5483	5.5591	5.5503	5.6497	5.3706	5.4055	5.5972	5.5442	5.5312	5.5425	5.6035	5.5682	5.4864	5.4333	5.4654	5.4662
K+	1.7646	1.7144	1.7519	1.7241	1.7437	1.6816	1.7376	1.8434	1.8431	1.7481	1.7658	1.7197	1.693	1.7964	1.7586	1.7192	1.7492	1.7035	1.7492	1.776	1.7494
Ca2+	0	0	0	0.0019	0	0	0.0019	0.0067	0.0019	0	0	0	0	0	0	0	0	0.0019	0	0	0
Ti4+	0.732	0.6874	0.6997	0.6847	0.6868	0.7237	0.6947	0.6911	0.6609	0.6902	0.6941	0.62	0.715	0.7284	0.6972	0.5909	0.722	0.7274	0.6678	0.5656	0.7055
Mn2+	0.0751	0.0516	0.0673	0.0743	0.0479	0.0459	0.0412	0.0444	0.0487	0.044	0.0379	0.0313	0.0301	0.0418	0.0316	0.0277	0.0465	0.0446	0.0437	0.0419	0.043
Fe2+	2.1089	1.5194	1.9175	1.9678	1.7597	1.5575	1.5781	1.7141	1.6844	1.3218	1.3657	1.2103	1.607	1.7558	1.4161	1.2199	1.8619	1.7212	1.4546	1.2797	1.6199
Fe3+	0.8991	1.0587	1.0399	0.9398	0.8492	1.0069	1.0358	0.9187	0.8425	1.3376	1.2762	1.0477	0.9269	0.8637	0.8956	0.9997	0.9089	1.1132	1.2178	1.35	1.0969
tot	15.9514	15.917	15.9557	15.9167	16.0368	15.8745	15.9155	16.0543	15.9903	15.9553	15.9722	15.9769	15.9016	16.0025	16.0114	15.9316	15.9424	15.8858	15.9783	15.9821	15.9597
sub-tot	13.9999	14.0001	13.9999	14	14	14	14	14	14.0001	13.9999	14	14	14	14.0001	14	14	13.9999	14	14	14	14

Cumulates - biotite analyses

Ti-mag	14a	14a	14s	14u	14j	14j	14n	14n	38e	38e	38e	38e	38e	38h	38h	38h	38h	38h	38h	14d	14h	14h	14l	14l	14m
Na2O	0	0	0.06	0.14	0	0	0	0.14	0	0.08	0.13	0.03	0	0.03	0	0	0	0	0	0	0.08	0.13	0.03	0	0.18
MgO	0.69	0.72	1.26	1.03	6.04	6.16	3.82	4.28	6.61	6.76	6.61	6.78	6.52	3.32	3.25	3.49	3.39	3.74	3.5	8.67	8.42	8.24	8.75	8.51	6.65
Al2O3	1.57	1.67	1.57	2.42	11.35	10.78	6.35	6.56	15.7	15.34	15.27	15.59	14.27	3.61	5.85	5.92	5.66	5.81	6.02	17.77	15.26	15.06	16.75	16.22	9.93
SiO2	0.34	0.93	0.16	0.16	0.13	0.3	0.74	0	0.11	0.05	0.05	0.08	0.08	0.68	0.61	0.98	0.69	0.97	0.29	0	0.05	0.08	0.16	0.08	0.11
K2O	0.06	0.1	0.06	0.04	0.04	0.05	0.07	0.05	0.04	0.05	0.04	0.04	0.05	0.05	0.04	0.04	0.04	0.05	0.05	0.05	0.05	0.04	0.04	0.04	0.04
CaO	0.09	0.07	0.01	0.02	0	0	0.03	0	0	0	0	0	0	0.03	0.01	0.04	0	0.04	0	0	0	0	0	0	0
TiO2	14.34	16.34	15.64	12.44	13.31	13.82	14.71	13.91	8.8	9.05	8.75	9.18	9.85	16.11	13.49	13.23	13.08	13.51	13.6	11.44	13.34	13.13	11.96	12.01	14.17
MnO	1.67	1.76	1.36	0.98	0.31	0.33	0.51	0.4	0.29	0.33	0.3	0.28	0.33	0.55	0.53	0.65	0.63	0.72	0.55	0.33	0.29	0.27	0.28	0.24	0.34
FeO	74.58	72.02	73	77.28	65.19	65.54	66.06	70.68	65.45	65.58	65.14	64.09	65.5	68.43	68.66	66.74	67.97	66	67.27	59.3	60.56	60.67	60.52	60.28	65.25
Total	93.34	93.61	93.12	94.51	96.37	96.98	92.29	96.02	97	97.24	96.29	96.07	96.6	92.81	92.44	91.09	91.46	90.84	91.28	97.56	98.05	97.62	98.49	97.38	96.67
recalc	97.06	96.78	96.65	98.71	99.65	100.23	95.33	99.74	100.75	101.05	100.11	99.71	100.29	95.94	95.8	94.32	94.85	94.02	94.61	100.69	101.14	100.74	101.68	100.54	100.07
Na+	0	0	0.0053	0.0122	0	0	0	0.0112	0	0.0059	0.0096	0.0023	0	0.0025	0	0	0	0	0	0	0.0056	0.0092	0.0021	0	0.0134
Mg2+	0.0457	0.0466	0.0828	0.0677	0.3457	0.3506	0.2364	0.2591	0.3714	0.3797	0.3752	0.3831	0.3701	0.2089	0.2048	0.2215	0.2162	0.2373	0.2227	0.4637	0.4533	0.4469	0.4662	0.4603	0.3809
Al3+	0.0823	0.0854	0.0815	0.1259	0.5137	0.4851	0.3111	0.3142	0.698	0.6815	0.6859	0.6966	0.6408	0.1797	0.2916	0.2972	0.2853	0.2915	0.3033	0.7518	0.6501	0.6459	0.706	0.6938	0.45
Si4+	0.0152	0.0403	0.0071	0.0072	0.0051	0.0115	0.0307	0	0.0041	0.0018	0.0018	0.003	0.003	0.0287	0.0259	0.0417	0.0296	0.0412	0.0123	0	0.0017	0.0028	0.0058	0.0028	0.0042
K+	0.0032	0.0057	0.0032	0.0021	0.0018	0.0023	0.0035	0.0024	0.0018	0.0023	0.0018	0.0018	0.0023	0.0025	0.002	0.002	0.0021	0.0026	0.0026	0.0022	0.0022	0.0017	0.0017	0.0017	0.0018
Ca2+	0.0043	0.0031	0.0005	0.0011	0	0	0.0012	0	0	0	0	0	0	0.0013	0.0005	0.0018	0	0.0018	0	0	0	0	0	0	0
Ti4+	0.4795	0.5323	0.518	0.4136	0.3844	0.3969	0.4596	0.4247	0.2495	0.2565	0.2507	0.2617	0.2822	0.5117	0.4288	0.4236	0.4207	0.4325	0.4368	0.3088	0.3626	0.3592	0.3216	0.3277	0.4096
Mn2+	0.0628	0.0646	0.0508	0.0367	0.0102	0.0108	0.018	0.0137	0.0093	0.0106	0.0096	0.0089	0.0108	0.0198	0.0191	0.0235	0.0229	0.0258	0.02	0.0101	0.0089	0.0083	0.0084	0.0074	0.0111
Fe2+	2.7728	2.6093	2.689	2.857	2.0937	2.093	2.2954	2.3997	2.0643	2.0665	2.0756	2.0318	2.0864	2.4173	2.4277	2.3758	2.4314	2.3492	2.4027	1.7798	1.8301	1.8463	1.8097	1.8294	2.0978
Total	3.4658	3.3873	3.4382	3.5235	3.3546	3.3502	3.3559	3.425	3.3984	3.4048	3.4102	3.3892	3.3956	3.3724	3.4004	3.3871	3.4082	3.3819	3.4004	3.3164	3.3145	3.3203	3.3215	3.3231	3.3688
Na+	0	0	0.0046	0.0104	0	0	0	0.0098	0	0.0052	0.0084	0.002	0	0.0022	0	0	0	0	0	0	0.0051	0.0083	0.0019	0	0.0119
Mg2+	0.0396	0.0413	0.0722	0.0576	0.3092	0.314	0.2113	0.2269	0.3279	0.3346	0.3301	0.3391	0.327	0.1858	0.1807	0.1962	0.1903	0.2105	0.1965	0.4195	0.4103	0.4038	0.4211	0.4155	0.3392
Al3+	0.0712	0.0756	0.0711	0.1072	0.4594	0.4344	0.2781	0.2752	0.6162	0.6005	0.6034	0.6166	0.5661	0.1599	0.2573	0.2632	0.2511	0.2586	0.2676	0.6801	0.5884	0.5836	0.6377	0.6263	0.4007
Si4+	0.0132	0.0357	0.0062	0.0061	0.0046	0.0103	0.0274	0	0.0036	0.0016	0.0016	0.0027	0.0027	0.0255	0.0229	0.0369	0.0261	0.0365	0.0109	0	0.0015	0.0025	0.0052	0.0025	0.0037
K+	0.0028	0.005	0.0028	0.0018	0.0016	0.0021	0.0031	0.0021	0.0016	0.002	0.0016	0.0016	0.002	0.0022	0.0018	0.0018	0.0018	0.0023	0.0023	0.002	0.002	0.0015	0.0015	0.0015	0.0016
Ca2+	0.0037	0.0027	0.0004	0.0009	0	0	0.0011	0	0	0	0	0	0	0.0012	0.0004	0.0016	0	0.0016	0	0	0	0	0	0	0
Ti4+	0.4151	0.4714	0.452	0.3521	0.3438	0.3554	0.4109	0.372	0.2203	0.226	0.2205	0.2316	0.2493	0.4552	0.3783	0.3752	0.3703	0.3837	0.3854	0.2793	0.3282	0.3245	0.2905	0.2958	0.3648
Mn2+	0.0544	0.0572	0.0443	0.0312	0.0091	0.0097	0.0161	0.012	0.0082	0.0093	0.0084	0.0079	0.0095	0.0176	0.0169	0.0208	0.0202	0.0229	0.0176	0.0091	0.0081	0.0075	0.0076	0.0067	0.0099
Fe2+	1.3249	1.3963	1.3267	1.2439	1.0268	1.038	1.2036	1.1092	0.8844	0.8697	0.8636	0.8798	0.9113	1.267	1.1998	1.19	1.182	1.1805	1.1778	0.8468	0.8973	0.8965	0.8602	0.8737	0.9923
Fe3+	1.0752	0.9147	1.0196	1.1886	0.8456	0.8362	0.8484	0.9927	0.9379	0.9511	0.9623	0.9187	0.932	0.8834	0.942	0.9143	0.9582	0.9034	0.942	0.7632	0.7591	0.7717	0.7743	0.7778	0.8758
Total	3.0001	2.9999	2.9999	2.9998	3.0001	3.0001	3	2.9999	3.0001	3	2.9999	3	2.9999	3	3.0001	3	3	3	3.0001	3	3	2.9999	3	2.9998	2.9999

Ti-mag	14m	14m	14p	14p	14p	14v	14v	38a	38a	38a	38a	38a	38a
Na2O	0.16	0.16	0.03	0	0.03	0.25	0	0	0	0.05	0	0.05	0.03
MgO	6.68	5.8	8.54	7.9	7.98	8.54	8.42	8.42	9.14	9.14	8.69	8.37	9.32
Al2O3	9.69	8.74	13.67	12.3	12.69	16.03	15.77	14.01	13.87	14.28	14.36	13.91	14.77
SiO2	0.16	0.11	0.05	0.08	0.05	0.05	0.14	0.68	0.03	0.03	0.14	0.19	0.08
K2O	0.05	0.04	0.04	0.05	0.05	0.04	0.05	0.05	0.04	0.04	0.04	0.04	0.05
CaO	0	0.01	0	0	0	0	0	0.04	0	0	0	0	0
TiO2	14	13.97	14.76	13.73	14.01	12.29	12.16	14.73	15.03	14.97	14.14	14.17	14.77
MnO	0.35	0.43	0.23	0.29	0.29	0.29	0.27	0.18	0.32	0.29	0.32	0.37	0.32
FeO	65.37	67.7	60.91	62.97	62.1	59.91	59.96	57.08	59.18	59.27	59.77	59.63	57.38
Total	96.46	96.96	98.23	97.32	97.2	97.4	96.77	95.19	97.61	98.07	97.46	96.73	96.72
recalc	99.9	100.52	101.23	100.58	100.37	100.63	99.89	97.75	100.51	100.98	100.41	99.67	99.5
Na+	0.0121	0.0122	0.0022	0	0.0022	0.0174	0	0	0	0.0035	0	0.0035	0.0022
Mg2+	0.3843	0.3372	0.4612	0.4389	0.4415	0.4617	0.4587	0.4613	0.4926	0.4894	0.4701	0.4577	0.502
Al3+	0.4411	0.402	0.584	0.5409	0.5555	0.6854	0.6798	0.6071	0.5915	0.6049	0.6147	0.6019	0.6292
Si4+	0.0063	0.0042	0.0017	0.0029	0.0018	0.0017	0.0051	0.025	0.0011	0.0011	0.005	0.0071	0.0028
K+	0.0023	0.0019	0.0017	0.0022	0.0022	0.0017	0.0022	0.0022	0.0017	0.0017	0.0017	0.0018	0.0022
Ca2+	0	0.0005	0	0	0	0	0	0.0015	0	0	0	0	0
Ti4+	0.4064	0.4099	0.4022	0.3849	0.3911	0.3353	0.3344	0.4074	0.4087	0.4045	0.3861	0.3909	0.4014
Mn2+	0.0114	0.0143	0.007	0.0092	0.0091	0.0089	0.0083	0.0055	0.0098	0.0089	0.0098	0.0115	0.0098
Fe2+	2.1102	2.2096	1.846	1.9637	1.9282	1.8177	1.8334	1.7551	1.7899	1.7807	1.8148	1.8296	1.7338
Total	3.3741	3.3918	3.306	3.3427	3.3316	3.3298	3.3219	3.2651	3.2953	3.2947	3.3022	3.304	3.2834
Na+	0.0108	0.0108	0.002	0	0.002	0.0157	0	0	0	0.0032	0	0.0032	0.002
Mg2+	0.3417	0.2982	0.4185	0.3939	0.3976	0.416	0.4143	0.4238	0.4485	0.4456	0.4271	0.4156	0.4587
Al3+	0.3922	0.3556	0.5299	0.4854	0.5002	0.6175	0.6139	0.5578	0.5385	0.5508	0.5584	0.5465	0.5749
Si4+	0.0056	0.0037	0.0015	0.0026	0.0016	0.0015	0.0046	0.023	0.001	0.001	0.0045	0.0064	0.0026
K+	0.002	0.0017	0.0015	0.002	0.002	0.0015	0.002	0.002	0.0015	0.0015	0.0015	0.0016	0.002
Ca2+	0	0.0004	0	0	0	0	0	0.0014	0	0	0	0	0
Ti4+	0.3613	0.3626	0.365	0.3454	0.3522	0.3021	0.302	0.3743	0.3721	0.3683	0.3508	0.3549	0.3668
Mn2+	0.0101	0.0126	0.0064	0.0083	0.0082	0.008	0.0075	0.0051	0.0089	0.0081	0.0089	0.0104	0.009
Fe2+	0.9892	1.0303	0.9346	0.9422	0.94	0.8453	0.8805	0.9631	0.9126	0.9058	0.9166	0.9252	0.8937
Fe3+	0.887	0.9241	0.7405	0.8202	0.7963	0.7924	0.7752	0.6495	0.7169	0.7156	0.7321	0.7361	0.6905
Total	2.9999	3	2.9999	3	3.0001	3	3	3	3	2.9999	2.9999	2.9999	3.0002

Cumulates - Ti-magnetite analyses

ilmenite	14a centre	14a centre	14b	14b	14f	38b	38b	38b	38b	38b	38b	38b	14e	14i	14u	14w	38f	38f	38f	38f	38f	14j	38g (1.17V)	38g	38a
Na2O	0	0.03	0.1	0	0	0.08	0	0.03	0.08	0.08	0	0.05	0.03	0	0.05	0.08	0.03	0.08	0	0	0.03	0	0.03	0	0
MgO	1.39	1.36	1.84	1.79	1.21	1.79	1.85	1.74	1.74	1.71	1.68	1.8	2.02	2.03	1.75	2.1	1.45	1.86	2.48	1.86	1.86	6.09	3.67	3.38	8.01
Al2O3	0.11	0.16	0.13	0.13	0.29	0.21	0.21	0.16	0.13	0.21	0.13	0.24	0.19	0.16	0.16	0.21	0.18	0.13	0.18	0.29	0.11	1.06	0.59	0.62	1.06
SiO2	0	0.02	0	0	0	0	0	0	0	0	0	0	0	0	0	0	0	0	0	0	0	0	0	0	0
K2O	0.04	0.04	0.04	0.05	0.04	0.04	0.05	0.04	0.05	0.04	0.05	0.05	0.04	0.06	0.04	0.05	0.06	0.04	0.08	0.06	0.05	0.05	0.04	0.05	0.05
CaO	0.01	0.18	0	0	0	0	0	0	0	0.01	0.06	0	0	0	0	0	0.05	0	0	0.1	0.01	0	0	0.02	0
TiO2	47.22	46.56	45.39	45.39	48	44.64	44.24	44.41	44.13	44.18	46.31	45.99	43.11	46.69	48.99	43.98	47.65	47.38	49.35	51.15	49.24	47.37	42.05	41.8	46.42
MnO	2.54	2.51	1.47	1.5	0.87	1.55	1.44	1.45	1.49	1.54	1.48	1.6	0.94	1.02	1.58	1.03	1.83	1.61	1.52	1.38	1.58	0.33	0.8	0.84	0.23
FeO	46.84	46.27	49.22	49.12	43.51	50.04	50.13	50.02	50.02	49.98	50.41	50.89	51.42	48.94	47.36	51.15	47.23	46.86	45.59	43.43	47.52	43.76	49.27	50.64	41.33
Total	98.15	97.13	98.19	97.98	93.92	98.35	97.92	97.85	97.64	97.75	100.12	100.62	97.75	98.9	99.93	98.6	98.48	97.96	99.2	98.27	100.4	98.66	96.45	97.35	97.1
recalc	99.21	98.23	99.72	99.44	94.31	100.03	99.62	99.51	99.36	99.46	101.62	102.26	99.69	100.21	100.86	100.48	99.5	99.04	100.02	98.54	101.34	100.05	98.57	99.58	98.69
Na+	0	0.0016	0.0051	0	0	0.0041	0	0.0016	0.0042	0.0042	0	0.0025	0.0016	0	0.0025	0.0041	0.0016	0.0041	0	0	0.0015	0	0.0016	0	0
Mg2+	0.0542	0.0535	0.0723	0.0705	0.0484	0.0705	0.0733	0.069	0.0693	0.0679	0.0649	0.0691	0.0806	0.0786	0.0665	0.0828	0.0563	0.0723	0.0942	0.0705	0.0703	0.2285	0.1469	0.1347	0.3025
Al3+	0.0035	0.0051	0.0041	0.0041	0.009	0.0067	0.0067	0.0051	0.0042	0.0067	0.004	0.0074	0.0061	0.005	0.0049	0.0067	0.0056	0.0041	0.0055	0.0086	0.0034	0.0315	0.0187	0.0196	0.0317
Si4+	0	0.0005	0	0	0	0	0	0	0	0	0	0	0	0	0	0	0	0	0	0	0	0	0	0	0
K+	0.0013	0.0013	0.0013	0.0016	0.0013	0.0013	0.0016	0.0013	0.0016	0.0013	0.0016	0.0016	0.0013	0.0019	0.0012	0.0016	0.0019	0.0013	0.0025	0.0018	0.0015	0.0015	0.0013	0.0016	0.0015
Ca2+	0.0003	0.0051	0	0	0	0	0	0	0	0.0003	0.0017	0	0	0	0	0	0.0014	0	0	0.0028	0.0003	0	0	0.0006	0
Ti4+	0.9292	0.9259	0.9002	0.9019	0.9699	0.8877	0.8845	0.8883	0.8857	0.8852	0.9015	0.8923	0.8679	0.9131	0.9398	0.8749	0.9322	0.9301	0.9459	0.9792	0.94	0.8974	0.8494	0.8411	0.8844
Mn2+	0.0563	0.0563	0.0328	0.0335	0.0199	0.0346	0.0324	0.0326	0.0337	0.0347	0.0325	0.035	0.0214	0.0225	0.0342	0.023	0.0403	0.0356	0.0328	0.0298	0.034	0.0071	0.0182	0.019	0.0049
Fe2+	1.0249	1.0233	1.0854	1.0853	0.9777	1.1067	1.1145	1.1127	1.1165	1.1137	1.0912	1.098	1.1514	1.0642	1.0105	1.1316	1.0274	1.023	0.9717	0.9246	1.0088	0.9217	1.1067	1.1331	0.8756
Total	2.0697	2.0726	2.1012	2.0969	2.0262	2.1116	2.113	2.1106	2.1152	2.114	2.0974	2.1059	2.1303	2.0853	2.0596	2.1247	2.0667	2.0705	2.0526	2.0173	2.0598	2.0877	2.1428	2.1497	2.1006
Na+	0	0.0015	0.0049	0	0	0.0039	0	0.0015	0.004	0.004	0	0.0024	0.0015	0	0.0024	0.0039	0.0015	0.004	0	0	0.0015	0	0.0015	0	0
Mg2+	0.0524	0.0516	0.0688	0.0672	0.0478	0.0668	0.0694	0.0654	0.0655	0.0642	0.0619	0.0656	0.0757	0.0754	0.0646	0.0779	0.0545	0.0698	0.0918	0.0699	0.0683	0.2189	0.1371	0.1253	0.288
Al3+	0.0034	0.0049	0.0039	0.0039	0.0089	0.0063	0.0063	0.0048	0.004	0.0063	0.0038	0.007	0.0057	0.0048	0.0048	0.0063	0.0054	0.004	0.0054	0.0085	0.0033	0.0302	0.0175	0.0182	0.0302
Si4+	0	0.0005	0	0	0	0	0	0	0	0	0	0	0	0	0	0	0	0	0	0	0	0	0	0	0
K+	0.0013	0.0013	0.0012	0.0015	0.0013	0.0012	0.0015	0.0012	0.0015	0.0012	0.0015	0.0015	0.0012	0.0018	0.0012	0.0015	0.0018	0.0013	0.0024	0.0018	0.0015	0.0014	0.0012	0.0015	0.0014
Ca2+	0.0003	0.0049	0	0	0	0	0	0	0	0.0003	0.0016	0	0	0	0	0	0.0014	0	0	0.0028	0.0003	0	0	0.0006	0
Ti4+	0.8979	0.8935	0.8568	0.8602	0.9574	0.8408	0.8372	0.8418	0.8375	0.8375	0.8596	0.8474	0.8148	0.8757	0.9126	0.8236	0.9021	0.8984	0.9217	0.9708	0.9127	0.8597	0.7928	0.7825	0.842
Mn2+	0.0544	0.0543	0.0312	0.032	0.0196	0.0328	0.0307	0.0309	0.0319	0.0328	0.031	0.0332	0.0201	0.0216	0.0332	0.0217	0.039	0.0344	0.032	0.0295	0.033	0.0068	0.017	0.0177	0.0047
Fe2+	0.7883	0.7773	0.7441	0.7578	0.8875	0.7311	0.734	0.74	0.7289	0.73	0.7619	0.7411	0.714	0.7753	0.8077	0.7131	0.8006	0.7839	0.793	0.8652	0.8053	0.631	0.633	0.6364	0.5464
Fe3+	0.2021	0.2102	0.289	0.2773	0.0776	0.3171	0.3209	0.3144	0.3268	0.3236	0.2786	0.3017	0.367	0.2454	0.1736	0.3521	0.1936	0.2043	0.1538	0.0515	0.1742	0.252	0.3999	0.4178	0.2873
tot	2.0001	2	1.9999	1.9999	2.0001	2	2	2	2.0001	1.9999	1.9999	1.9999	2	2	2.0001	2.0001	1.9999	2.0001	2.0001	2	2.0001	2	2	2	2

Cumulates - ilmenite analyses

ilmenite	38a	38a	38a	38a	38a	14s centre
Na2O	0	0.1	0	0.02	0	0.03
MgO	7.96	8.34	8.23	8.35	8.11	1.79
Al2O3	1.25	1.25	1.17	1.28	1.2	0.13
SiO2	0	0	0	0	0	0
K2O	0.03	0.04	0.04	0.04	0.04	0.04
CaO	0	0	0.01	0.01	0.01	0
TiO2	46.12	47.56	47.4	47.7	46.89	45.88
MnO	0.17	0.24	0.3	0.32	0.31	1.56
FeO	40.68	41.01	41.14	40.74	41.17	50.11
Total	96.21	98.54	98.29	98.46	97.73	99.54
recalc	97.73	100.09	99.81	99.94	99.27	101.09
Na+	0	0.0048	0	0.0009	0	0.0016
Mg2+	0.3025	0.3086	0.3058	0.3089	0.3034	0.0695
Al3+	0.0377	0.0367	0.0345	0.0376	0.0356	0.0041
Si4+	0	0	0	0	0	0
K+	0.0009	0.0012	0.0012	0.0012	0.0012	0.0013
Ca2+	0	0	0.0003	0.0003	0.0003	0
Ti4+	0.8846	0.8882	0.8887	0.8905	0.8855	0.8986
Mn2+	0.0037	0.0051	0.0063	0.0067	0.0066	0.0344
Fe2+	0.8677	0.8518	0.8579	0.8457	0.8645	1.0914
Total	2.0971	2.0964	2.0947	2.0918	2.0971	2.1009
Na+	0	0.0046	0	0.0009	0	0.0015
Mg2+	0.2885	0.2944	0.292	0.2953	0.2894	0.0662
Al3+	0.036	0.035	0.0329	0.0359	0.034	0.0039
Si4+	0	0	0	0	0	0
K+	0.0009	0.0011	0.0011	0.0011	0.0011	0.0012
Ca2+	0	0	0.0003	0.0003	0.0003	0
Ti4+	0.8436	0.8474	0.8485	0.8514	0.8445	0.8554
Mn2+	0.0035	0.0049	0.006	0.0064	0.0063	0.0327
Fe2+	0.5497	0.5367	0.5478	0.5453	0.5467	0.7508
Fe3+	0.2778	0.2759	0.2713	0.2633	0.2778	0.2882
tot	2	2	1.9999	1.9999	2.0001	1.9999

Cumulates - ilmenite analyses

spin-herc	14d	14h	14h	14l	14l	14v	14v	38a	38a	38a	38a	38e	38e	38e	38e
Na2O	0.1	0.08	0.08	0.02	0.02	0.3	0.04	0.02	0	0.06	0.02	0.04	0	0.06	0.04
MgO	14.6	14.65	14.33	13.76	14.34	14.42	14.22	15.39	15.47	15.19	15.36	13.04	12.75	13.31	13.01
Al2O3	47.56	48.72	49.2	45.97	47.72	47.58	46.03	48.94	49.94	49.4	50.07	47.46	46.62	47.82	47.75
SiO2	0.15	0.06	0.06	0.06	0.06	0.15	0.12	0.09	0.06	0.09	0.09	0	0.06	0.06	0.03
K2O	0.03	0.05	0.03	0.03	0.03	0.03	0.03	0.05	0.03	0.03	0.03	0.03	0.05	0.05	0.03
CaO	0	0	0	0	0	0	0.07	0	0	0	0	0	0	0	0
TiO2	2.16	2.15	2.1	2.69	2.24	2.28	2.53	2.03	2.14	2.09	2.02	1.47	1.49	1.46	1.51
MnO	0.2	0.22	0.17	0.18	0.16	0.21	0.18	0.14	0.2	0.14	0.24	0.27	0.25	0.17	0.22
FeO	35.05	33.4	33.48	36.81	35.64	35.08	35.63	31.2	31.57	31.58	31.85	36.87	37.74	35.9	36.49
Total	99.85	99.33	99.45	99.52	100.21	100.05	98.85	97.86	99.41	98.58	99.68	99.18	98.96	98.83	99.08
recalc	101.64	100.96	101.02	101.33	101.97	101.89	100.65	99.4	100.91	100.1	101.2	101.01	100.83	100.6	100.85
Na+	0.0055	0.0045	0.0045	0.0011	0.001	0.0166	0.0021	0.001	0	0.0034	0.001	0.0021	0	0.0035	0.0021
Mg2+	0.6261	0.6257	0.6107	0.5991	0.614	0.6176	0.6201	0.6602	0.6527	0.6471	0.647	0.5687	0.5604	0.5792	0.5665
Al3+	1.6134	1.6461	1.6586	1.5831	1.6163	1.6121	1.5877	1.6607	1.6667	1.6649	1.6682	1.6373	1.6212	1.6463	1.6445
Si4+	0.0043	0.0017	0.0017	0.0018	0.0017	0.0043	0.0035	0.0026	0.0017	0.0026	0.0025	0	0.0018	0.0018	0.0009
K+	0.001	0.0017	0.001	0.0011	0.001	0.001	0.0011	0.0017	0.001	0.001	0.001	0.0011	0.0018	0.0018	0.0011
Ca2+	0	0	0	0	0	0	0.0021	0	0	0	0	0	0	0	0
Ti4+	0.0468	0.0463	0.0452	0.0591	0.0484	0.0493	0.0556	0.0439	0.0456	0.0449	0.043	0.0324	0.0331	0.032	0.0332
Mn2+	0.0048	0.0053	0.0041	0.0044	0.004	0.0052	0.0044	0.0035	0.0048	0.0034	0.0058	0.0067	0.0062	0.0042	0.0054
Fe2+	0.8435	0.8006	0.8007	0.8992	0.8562	0.8431	0.8719	0.751	0.7474	0.755	0.7528	0.9024	0.9311	0.8769	0.8916
Total	3.1454	3.1319	3.1265	3.1489	3.1426	3.1492	3.1485	3.1246	3.1199	3.1223	3.1213	3.1507	3.1556	3.1457	3.1453
Na+	0.0052	0.0043	0.0043	0.001	0.001	0.0158	0.002	0.001	0	0.0033	0.001	0.002	0	0.0033	0.002
Mg2+	0.5972	0.5993	0.586	0.5708	0.5861	0.5883	0.5909	0.6339	0.6276	0.6218	0.6219	0.5415	0.5328	0.5524	0.5403
Al3+	1.5388	1.5768	1.5915	1.5082	1.543	1.5357	1.5128	1.5945	1.6026	1.5997	1.6034	1.559	1.5413	1.57	1.5685
Si4+	0.0041	0.0016	0.0016	0.0017	0.0016	0.0041	0.0033	0.0025	0.0016	0.0025	0.0024	0	0.0017	0.0017	0.0009
K+	0.001	0.0016	0.001	0.001	0.001	0.001	0.001	0.0016	0.001	0.001	0.001	0.001	0.0017	0.0017	0.001
Ca2+	0	0	0	0	0	0	0.002	0	0	0	0	0	0	0	0
Ti4+	0.0446	0.0444	0.0434	0.0563	0.0462	0.047	0.053	0.0421	0.0438	0.0431	0.0413	0.0309	0.0315	0.0305	0.0317
Mn2+	0.0046	0.0051	0.0039	0.0042	0.0038	0.005	0.0042	0.0034	0.0046	0.0033	0.0056	0.0064	0.0059	0.004	0.0052
Fe2+	0.4347	0.43	0.4446	0.4784	0.4543	0.4242	0.4535	0.4021	0.4113	0.412	0.4126	0.4766	0.4907	0.4658	0.4808
Fe3+	0.3698	0.3369	0.3237	0.3783	0.363	0.379	0.3773	0.319	0.3074	0.3134	0.3109	0.3826	0.3945	0.3705	0.3696
Total	3	3	3	2.9999	3	3.0001	3	3.0001	2.9999	3.0001	3.0001	3	3.0001	2.9999	3

Cumulates - spinel-hercynite (pleonaste) analyses

amphibole	14c	14c	38b	38b	38b	14e	14e	14i	14u	14u	14u	14w	14w	38f	38f	38f	38f	38f	38f	14j	14j	14n	14n	38e	38e
			xeno			centre	centre	centre	centre	centre		centre	centre							centre	a edge a	centre			
Na2O	2.44	2.46	2.61	2.46	2.57	2.97	2.93	2.9	3	3	2.78	2.78	2.77	2.84	3	2.87	2.86	2.73	2.93	2.41	2.3	2.37	2.55	2.63	2.6
MgO	7.7	7.56	10.73	10.9	10.83	11.91	11.32	10.54	11.72	11.33	8.72	9.98	11.58	8.18	8.67	9.95	9.68	9.2	8.32	12.31	12.18	11.54	11.67	12.75	12.72
Al2O3	11.1	10.58	14.2	14.11	13.94	12.26	12.49	12.27	12.75	12.92	11.91	12.58	14.22	11.56	11.87	11.9	12.56	11.45	12.01	14.45	14.68	13.84	14.05	14.43	14.21
SiO2	39.43	38.75	38.35	38.62	37.25	40.39	40.28	40.55	39.58	39.71	39.77	39.79	38.56	39.3	38.36	39.51	38.58	39.88	37.8	38.62	38.8	38.88	38.71	38.83	39.02
K2O	1.73	1.73	1.19	1.14	1.15	1.08	1.11	1.05	1.23	1.2	1.47	1.26	1.25	1.46	1.28	1.26	1.35	1.54	1.17	0.87	0.91	0.99	0.98	1.07	0.99
CaO	10.77	10.61	11.5	11.62	11.36	11.18	11.26	11.01	11.2	11.21	11.04	11.08	11.36	10.85	10.83	11.14	11.19	10.9	10.88	11.55	11.58	11.45	11.56	11.33	11.18
TiO2	3.51	3.33	5.34	5.46	5.39	5.58	5.28	5.01	5.55	5.56	4.35	4.77	5.69	4.2	4.69	4.74	4.86	4.4	4.87	6.69	5.7	5.63	5.4	4.6	4.84
MnO	0.91	0.8	0.22	0.19	0.2	0.24	0.3	0.3	0.27	0.27	0.43	0.36	0.19	0.5	0.52	0.43	0.4	0.4	0.44	0.04	0.12	0.14	0.09	0.07	0.19
FeO	20.1	19.65	11.37	12.87	12.19	12.11	13.03	14.38	12.39	13.2	18.2	15.84	12.09	18.96	17.77	15.72	15.77	17.59	17.68	10.74	11.05	12.35	12.15	11.18	11.21
Total	97.69	95.47	95.51	97.37	94.88	97.72	98	98.01	97.69	98.4	98.67	98.44	97.71	97.85	96.99	97.52	97.25	98.09	96.1	97.68	97.32	97.19	97.16	96.89	96.96
Na+	0.7367	0.7596	0.77	0.7166	0.769	0.857	0.8477	0.8422	0.8698	0.8662	0.8209	0.8122	0.8022	0.8488	0.9021	0.8473	0.8481	0.8071	0.8896	0.6915	0.6623	0.6876	0.7401	0.7616	0.7517
Mg2+	1.7856	1.7937	2.4334	2.4396	2.4887	2.6426	2.5163	2.3521	2.612	2.5144	1.9774	2.2385	2.5772	1.8802	2.0036	2.2582	2.2087	2.0929	1.9399	2.7136	2.6964	2.5759	2.6058	2.8398	2.8299
Al3+	2.0362	1.986	2.5477	2.4983	2.5332	2.1524	2.1955	2.1667	2.2481	2.2674	2.1355	2.2322	2.5036	2.1017	2.1694	2.1356	2.2666	2.0599	2.2155	2.5207	2.5705	2.4445	2.4815	2.5434	2.5008
Si4+	6.1347	6.1695	5.8362	5.8008	5.7437	6.0134	6.0068	6.0719	5.9185	5.9128	6.0501	5.9892	5.7583	6.0604	5.9492	6.0161	5.9057	6.0871	5.9157	5.7124	5.7632	5.8233	5.8004	5.8035	5.8249
K+	0.344	0.3521	0.2304	0.2184	0.2261	0.2058	0.2115	0.1998	0.2354	0.2273	0.2852	0.2424	0.2387	0.2873	0.2535	0.2452	0.2631	0.299	0.2332	0.1635	0.1732	0.189	0.1873	0.2048	0.1884
Ca2+	1.795	1.81	1.8756	1.8701	1.8772	1.7838	1.7994	1.7663	1.7943	1.7887	1.8	1.7872	1.818	1.7931	1.7995	1.8172	1.8352	1.7829	1.8243	1.831	1.8431	1.8379	1.8557	1.8141	1.7886
Ti4+	0.4104	0.3989	0.6109	0.6164	0.6254	0.6244	0.5923	0.5642	0.6245	0.6228	0.4973	0.54	0.6389	0.4874	0.547	0.5426	0.5593	0.5053	0.5736	0.7439	0.6364	0.6345	0.6087	0.5173	0.5436
Mn2+	0.1197	0.1081	0.0283	0.0244	0.0259	0.0304	0.0376	0.0378	0.0341	0.034	0.0558	0.0461	0.0242	0.0649	0.068	0.0558	0.0515	0.0514	0.0583	0.0053	0.0152	0.018	0.0117	0.009	0.0242
Fe2+	2.6149	2.6165	1.4467	1.6165	1.5724	1.5074	1.6256	1.8005	1.549	1.6437	2.3156	1.9943	1.5102	2.4455	2.3046	2.002	2.0192	2.2452	2.3142	1.3288	1.3727	1.5472	1.5226	1.3974	1.3993
Total	15.9772	15.9944	15.7792	15.8011	15.8616	15.8172	15.8327	15.8015	15.8857	15.8773	15.9378	15.8821	15.8713	15.9693	15.9969	15.92	15.9574	15.9308	15.9643	15.7107	15.733	15.7579	15.8138	15.8909	15.8514
Alvi	0.1709	0.1555	0.3839	0.2991	0.2769	0.1658	0.2023	0.2386	0.1666	0.1802	0.1856	0.2214	0.2619	0.1621	0.1186	0.1517	0.1723	0.147	0.1312	0.2331	0.3337	0.2678	0.2819	0.3469	0.3257

amphibole	38e	38e	38e	38e	38g	38g	38g	38g	38g	38h	38h	38h	14h	14h	14h	14h	14m	14m	38a	38a	38a
													in glass	in glass	in glass	in glass	centre	centre			
Na2O	2.79	2.52	2.7	2.52	2.79	2.79	2.7	2.75	2.82	2.59	2.52	2.59	2.01	2.17	2.41	2.55	2.37	1.61	2.18	2.32	2.33
MgO	10.79	12.64	12.61	12.51	10.79	10.8	10.83	10.83	10.79	11.22	11.03	10.83	12.04	11.99	13.51	12.56	12.51	12.56	12.62	12.63	12.66
Al2O3	12.92	14.22	14.41	14.26	12.92	12.82	13.23	13.35	12.47	13.69	14.24	13.59	15.54	15.53	14.12	14.68	14.34	14.07	14.8	14.73	14.84
SiO2	37.95	37.28	37.91	38.49	37.95	39.12	38.82	38.44	38.61	38.45	37.92	37.51	36.42	37.6	38.38	37.98	38.48	38.11	37.43	36.89	37.52
K2O	1.04	1	1.07	0.95	1.04	1.14	1.05	1.03	1.17	1.12	1.27	1.13	1.36	1.31	1.1	1.13	1.3	1.4	1.28	1.27	1.17
CaO	11.32	11.24	11.05	11.31	11.32	11	11.22	11.21	11.05	11.38	11.54	11.4	11.57	11.27	11.56	11.86	11.57	11.58	11.63	11.63	11.6
TiO2	5.24	5.02	4.78	5.46	5.24	4.86	5.37	5.37	4.84	5.35	5.37	5.27	6.91	6.22	6.27	6.81	5.98	5.8	6.21	6.08	6.15
MnO	0.32	0.07	0.16	0.12	0.32	0.31	0.32	0.28	0.28	0.2	0.18	0.22	0.16	0.11	0.05	0.08	0.11	0.07	0.08	0.07	0.1
FeO	13.84	11.04	11.22	11	13.84	14.03	13.87	13.83	14.24	13.08	12.88	13.13	10.19	10.06	9.19	10.08	10.22	10.39	9.81	9.87	9.95
Total	96.21	95.03	95.91	96.62	96.21	96.87	97.41	97.09	96.27	97.08	96.95	95.67	96.2	96.26	96.59	97.73	96.88	95.59	96.04	95.49	96.32
Na+	0.829	0.7474	0.7931	0.7328	0.829	0.8208	0.7906	0.8082	0.838	0.7581	0.7397	0.7717	0.5872	0.6307	0.6962	0.7316	0.6851	0.4723	0.6366	0.6818	0.6782
Mg2+	2.4648	2.8787	2.8441	2.7934	2.4648	2.4434	2.4354	2.4447	2.4642	2.5236	2.4862	2.4793	2.7058	2.6795	2.9986	2.7725	2.7825	2.8295	2.8302	2.8547	2.8318
Al3+	2.334	2.5619	2.5721	2.5188	2.334	2.2947	2.3538	2.3846	2.2524	2.4357	2.5389	2.4608	2.7619	2.7444	2.4787	2.5634	2.5234	2.507	2.6259	2.6341	2.6262
Si4+	5.8175	5.6968	5.7382	5.766	5.8175	5.9374	5.8572	5.8224	5.9165	5.8026	5.7348	5.7616	5.4922	5.6374	5.7153	5.6261	5.7426	5.7607	5.6324	5.5955	5.6312
K+	0.2026	0.1947	0.2074	0.1818	0.2026	0.2207	0.2013	0.1984	0.2284	0.2158	0.2453	0.2215	0.261	0.2505	0.2094	0.2136	0.2475	0.2707	0.246	0.2461	0.2237
Ca2+	1.8596	1.8402	1.7918	1.8158	1.8596	1.7885	1.8143	1.8194	1.8141	1.8399	1.8701	1.8765	1.8694	1.8109	1.8443	1.8825	1.8499	1.8757	1.8754	1.8904	1.865
Ti4+	0.6042	0.5767	0.5439	0.6149	0.6042	0.5545	0.6093	0.6116	0.558	0.6076	0.6106	0.6092	0.7838	0.701	0.7024	0.7583	0.6707	0.6595	0.7026	0.6936	0.6944
Mn2+	0.0414	0.0092	0.0209	0.0153	0.0414	0.0401	0.0408	0.0355	0.0359	0.0254	0.0227	0.0286	0.0208	0.0144	0.0063	0.0098	0.0143	0.0091	0.0099	0.0091	0.0126
Fe2+	1.774	1.4113	1.4207	1.3783	1.774	1.7812	1.7499	1.7521	1.8251	1.6504	1.6293	1.6864	1.2849	1.2614	1.1445	1.2488	1.2751	1.3135	1.2343	1.2524	1.2491
Total	15.9271	15.9169	15.9322	15.8171	15.9271	15.8813	15.8526	15.8769	15.9326	15.8591	15.8776	15.8956	15.767	15.7302	15.7957	15.8066	15.7911	15.698	15.7933	15.8577	15.8122
Alvi	0.1515	0.2587	0.3103	0.2848	0.1515	0.2321	0.211	0.207	0.1689	0.2383	0.2737	0.2224	0.2541	0.3818	0.194	0.1895	0.266	0.2677	0.2583	0.2296	0.2574

Cumulates - amphibole analyses

25analys. each is mean of:	88/14a glass 4	88/14b glass 3	88/14c glass 4	88/14e glass 4	88/14s glass 4	88/14u glass 4	88/14w glass 2
SiO2	68.11	67.77	64.36	64.68	69.11	64	63.26
TiO2	0.42	0.55	0.35	0.43	0.42	0.49	0.61
Al2O3	16.02	16.34	18.57	18.68	16.34	19.31	19.28
Fe2O3T	3.71	3.72	2.39	2.87	2.79	2.9	3.36
MnO	0.22	0.09	0.05	0.06	0.13	0.09	0.09
MgO	0.33	0.66	0.07	0.32	0.3	0.26	0.52
CaO	1.04	1.45	0.39	1.21	1.16	1.08	2.01
Na2O	4.96	4.35	4.44	6.21	4.82	6.9	5.97
K2O	5.19	5.08	9.38	5.54	4.94	4.98	4.91
Total	100	100.01	100	100	100.01	100.01	100.01

Cumulates - interstitial glass analyses

feldspar	14a centre n	14a hwce n	14a edge x	14a hwce x	14a centre x	14a hwce x	14b edge a	14b centre a	14b hwce a		14b centre b	14b edge b	14b centre	14b centre	14c centre c	14c edge c	14c centre d	14c edge d	14c edge e	14c centre e	14c faredge e	14c	14c	14f centre	14f centre k
Na2O	7.63	7.69	7.75	7.67	7.74	7.99	8	7.49	7.66	7.62	7.47	7.9	7.49	7.23	8.14	8.18	8	8.26	7.8	7.28	8.25	6.82	7.34	6.93	4.41
MgO	0.02	0.02	0.02	0	0.02	0	0.02	0.02	0.02	0	0.02	0.04	0.02	0	0.02	0.02	0.02	0.02	0	0	0.02	0.02	0	0.06	0
Al2O3	20.41	20.85	20.57	20.88	20.92	21.21	22.84	24.44	23.47	23.45	23.98	23.41	24.19	24.46	22.26	22.43	23.19	22.27	20.93	24.44	22.02	25.11	24.3	21.08	27.97
SiO2	63.05	63.44	63.45	63.29	64.07	62.34	62.26	60.47	61.2	61.39	60.34	61.48	60.67	60.04	63.16	62.99	62.52	62.55	62.54	60.2	63.35	58.89	60.5	64.36	53.44
K2O	3.71	3.85	3.99	3.74	3.42	2.56	1.33	0.91	1.05	1.1	0.97	1.15	0.94	0.84	1.69	1.64	1.41	1.86	3.91	0.92	1.82	0.75	0.93	3.76	0.37
CaO	2.68	2.62	2.5	2.69	2.98	3.47	4.46	5.89	5.23	5.07	5.76	5.07	5.88	6.31	3.64	3.87	4.44	3.5	2.17	5.99	3.5	6.94	5.85	2.37	10.75
TiO2	0.07	0.02	0.06	0.08	0.04	0.04	0.02	0.04	0.02	0.02	0.04	0.04	0.04	0.02	0.06	0.04	0.06	0.06	0.02	0.02	0.02	0.04	0.04	0.04	0.06
MnO	0.01	0	0	0	0.05	0.01	0	0	0	0	0.01	0.01	0.01	0.01	0.01	0.01	0	0.03	0.01	0	0	0	0.01	0.01	0
FeO	0.19	0.17	0.23	0	0.17	0.16	0.39	0.23	0.25	0.26	0.17	0.26	0.23	0.23	0.2	0.26	0.26	0.22	0.19	0.23	0.2	0.25	0.22	0.25	0.2
Total	97.77	98.66	98.57	98.35	99.41	97.78	99.32	99.49	98.9	98.91	98.76	99.36	99.47	99.14	99.18	99.44	99.9	98.77	97.57	99.08	99.18	98.82	99.19	98.86	97.2
Na+	0.6758	0.6752	0.6818	0.6747	0.6734	0.7062	0.6945	0.6505	0.668	0.664	0.6533	0.6864	0.6506	0.6305	0.706	0.7085	0.6902	0.7208	0.6927	0.6347	0.7158	0.5976	0.6389	0.6038	0.3963
Mg2+	0.0014	0.0013	0.0014	0	0.0013	0	0.0013	0.0013	0.0013	0	0.0013	0.0027	0.0013	0	0.0013	0.0013	0.0013	0.0013	0	0	0.0013	0.0013	0	0.004	0
Al3+	1.0992	1.1131	1.1003	1.1168	1.1067	1.1399	1.2056	1.2907	1.2445	1.2424	1.2752	1.2367	1.2776	1.297	1.1739	1.1813	1.2164	1.1816	1.1301	1.2957	1.1617	1.3379	1.2861	1.1168	1.5281
Si4+	2.8801	2.8727	2.8788	2.8715	2.8749	2.8419	2.7876	2.7087	2.7525	2.7588	2.7217	2.755	2.718	2.7004	2.8252	2.8139	2.7818	2.8151	2.8644	2.7071	2.8348	2.6615	2.716	2.8922	2.4765
K+	0.2162	0.2224	0.231	0.2165	0.1958	0.1489	0.076	0.052	0.0602	0.0631	0.0558	0.0657	0.0537	0.0482	0.0964	0.0935	0.08	0.1068	0.2285	0.0528	0.1039	0.0432	0.0533	0.2156	0.0219
Ca2+	0.1312	0.1271	0.1215	0.1308	0.1433	0.1695	0.214	0.2827	0.252	0.2441	0.2784	0.2434	0.2823	0.3041	0.1745	0.1852	0.2117	0.1688	0.1065	0.2886	0.1678	0.3361	0.2814	0.1141	0.5338
Ti4+	0.0024	0.0007	0.002	0.0027	0.0013	0.0014	0.0007	0.0013	0.0007	0.0007	0.0014	0.0013	0.0013	0.0007	0.002	0.0013	0.002	0.002	0.0007	0.0007	0.0007	0.0014	0.0014	0.0014	0.0021
Mn2+	0.0004	0	0	0	0.0019	0.0004	0	0	0	0	0.0004	0.0004	0.0004	0.0004	0.0004	0.0004	0	0.0011	0.0004	0	0	0	0.0004	0.0004	0
Fe2+	0.0073	0.0064	0.0087	0	0.0064	0.0061	0.0146	0.0086	0.0094	0.0098	0.0064	0.0097	0.0086	0.0087	0.0075	0.0097	0.0097	0.0083	0.0073	0.0086	0.0075	0.0094	0.0083	0.0094	0.0078
Total	5.014	5.0189	5.0255	5.013	5.005	5.0143	4.9943	4.9958	4.9886	4.9829	4.9939	5.0013	4.9938	4.99	4.9872	4.9951	4.9931	5.0058	5.0306	4.9882	4.9935	4.9884	4.9858	4.9577	4.9665

feldspar	14f edge k	14f centre l	14f edge l	14f centre m	14f edge m	14f centre	14f centre	14f centre	14f centre	14s centre o	14s edge o	14s centre	14s centre p	14s edge p	14s centre q	14s edge q	38b centre	38b	38b	38b	38b	38b	14e centre f	14e edge f	14e centre g
Na2O	7.1	7.82	7.34	7.5	7.53	7.11	7.36	7.35	7.08	7.2	7.84	7.72	7.67	7.82	8.15	7.74	7.38	7.36	7.22	7.91	8.14	7.95	7.79	8.06	5.23
MgO	0.06	0.04	0	0	0	0.21	0	0	0.04	0.02	0.04	0.02	0.02	0	0.04	0	0.02	0.19	0.08	0.08	0.02	0.02	0.02	0.02	0.04
Al2O3	20.93	23.17	22.55	23.17	21.9	20.63	21.36	23.78	20.96	24.86	23.49	24.24	24.02	23.65	23.34	23.78	23.43	23.75	24.57	22.99	22.59	22.37	23.41	22.95	28.18
SiO2	63.82	61.53	60.81	60.81	63.18	64.76	64.09	61.41	64.08	59.91	61.52	60.6	61.9	61.56	62.2	60.58	61.06	60.98	59.75	62.03	61.36	59.15	61.84	61.53	53.95
K2O	3.93	1.32	1.33	1.25	2.03	4.41	3.33	1.14	3.68	0.92	1.23	1.01	1.1	1.09	1.42	1.09	1.1	1.15	0.9	1.3	1.38	1.24	0.9	0.96	0.31
CaO	2.36	4.96	4.71	4.76	3.54	2.14	2.73	5.42	2.5	6.45	5.11	5.76	5.24	5.2	4.47	5.4	5.35	5.38	6.2	4.82	4.27	4.66	5.05	4.67	10.41
TiO2	0.06	0.06	0.06	0.04	0.02	0.04	0.06	0.06	0.04	0.08	0.06	0.06	0.06	0.04	0.02	0.02	0.04	0.02	0.06	0.04	0.02	0.02	0.04	0.04	0.08
MnO	0.03	0.01	0	0.01	0.01	0.05	0	0	0.01	0	0.01	0.04	0.04	0	0.01	0.03	0.01	0	0.15	0	0	0.01	0	0.03	0
FeO	0.33	0.2	0.29	0.23	0.26	0.29	0.23	0.23	0.2	0.23	0.56	0.27	0.3	0.32	0.3	0.35	0.29	0	0	0.29	0.32	0.29	0.3	0.48	0.27
Total	98.62	99.11	97.09	97.77	98.47	99.64	99.16	99.39	98.59	99.67	99.86	99.72	100.35	99.68	99.95	98.99	98.68	98.83	98.93	99.46	98.1	95.71	99.35	98.74	98.47
Na+	0.622	0.6811	0.6512	0.6609	0.6572	0.6173	0.6399	0.6376	0.619	0.6253	0.6791	0.6699	0.6594	0.6772	0.7038	0.6762	0.645	0.6417	0.6309	0.6862	0.716	0.7184	0.6752	0.704	0.4647
Mg2+	0.004	0.0027	0	0	0	0.014	0	0	0.0027	0.0013	0.0027	0.0013	0.0013	0	0.0027	0	0.0013	0.0127	0.0054	0.0053	0.0014	0.0014	0.0013	0.0013	0.0027
Al3+	1.1149	1.227	1.2164	1.2415	1.1621	1.0891	1.1291	1.2543	1.1143	1.3128	1.2372	1.279	1.2555	1.2453	1.2255	1.2632	1.2451	1.2591	1.3055	1.2127	1.2082	1.2291	1.2338	1.2188	1.5225
Si4+	2.8837	2.7639	2.7824	2.7637	2.8438	2.8998	2.8737	2.7474	2.8896	2.6835	2.7485	2.7122	2.7445	2.7495	2.7703	2.7297	2.7523	2.7421	2.6929	2.7754	2.7837	2.7566	2.7645	2.7718	2.4725
K+	0.2265	0.0756	0.0776	0.0725	0.1166	0.2519	0.1905	0.0651	0.2117	0.0526	0.0701	0.0577	0.0622	0.0621	0.0807	0.0627	0.0633	0.066	0.0517	0.0742	0.0799	0.0737	0.0513	0.0552	0.0181
Ca2+	0.1143	0.2387	0.2309	0.2318	0.1707	0.1027	0.1312	0.2598	0.1208	0.3096	0.2446	0.2762	0.2489	0.2489	0.2133	0.2607	0.2584	0.2592	0.2994	0.2311	0.2076	0.2327	0.2419	0.2254	0.5112
Ti4+	0.002	0.002	0.0021	0.0014	0.0007	0.0013	0.002	0.002	0.0014	0.0027	0.002	0.002	0.002	0.0013	0.0007	0.0007	0.0014	0.0007	0.002	0.0013	0.0007	0.0007	0.0013	0.0014	0.0028
Mn2+	0.0011	0.0004	0	0.0004	0.0004	0.0019	0	0	0.0004	0	0.0004	0.0015	0.0015	0	0.0004	0.0011	0.0004	0	0.0057	0	0	0.0004	0	0.0011	0
Fe2+	0.0125	0.0075	0.0111	0.0087	0.0098	0.0109	0.0086	0.0086	0.0075	0.0086	0.0209	0.0101	0.0111	0.012	0.0112	0.0132	0.0109	0	0	0.0109	0.0121	0.0113	0.0112	0.0181	0.0103
Total	4.981	4.9989	4.9717	4.9809	4.9613	4.9889	4.975	4.9748	4.9674	4.9964	5.0055	5.0099	4.9864	4.9963	5.0086	5.0075	4.9781	4.9815	4.9935	4.9971	5.0096	5.0243	4.9805	4.9971	5.0048

feldspar	14e edge g	14e centre h	14e edge h	14i centre	14i centre i	14i edge i	14i centre	14u centre r	14u edge r	14u centre s	14u edge s	14u centre t	14u edge t	14w centre u	14w edge u	14w centre v	14w edge v	14w centre	14w centre w	14w edge w	38f	38f	38f	38f	38f
Na2O	5.36	7.26	8.3	4.5	6.01	6.46	4.07	5.73	5.89	5.58	8.09	6.52	6.37	7.01	7.53	6.83	5.77	6.75	5.43	6.04	8.46	6.53	7.2	7.74	6.42
MgO	0.04	0.02	0.02	0.02	0.04	0.04	0.04	0.04	0.02	0.02	0.04	0	0.04	0.02	0.04	0.02	0.02	0.04	0	0.02	0.02	0.02	0	0.02	0.02
Al2O3	27.89	24.75	22.95	29.3	26.8	25.74	30.02	27.53	27.48	27.76	23.39	26.49	26.33	25.05	24	25.22	27.32	25.76	28.1	27.1	22.25	26.33	25.11	23.79	25.7
SiO2	54.72	59.32	62.88	52.9	56.9	58.09	52.28	56.85	56.57	55.81	63.17	57.52	58.09	59.49	61.67	58.73	56.78	59.03	54.89	56.7	64.27	57.79	59.21	60.44	56.2
K2O	0.33	0.65	1.12	0.29	0.49	0.57	0.21	0.46	0.49	0.41	1.33	0.61	0.59	0.78	1.09	0.72	0.5	0.75	0.41	0.53	1.73	0.55	0.72	0.95	0.56
CaO	10.16	6.49	4.23	11.57	8.78	7.7	12.37	9.02	9.08	9.71	4.26	7.97	7.96	6.77	5.35	7.01	9.03	7.16	9.93	8.85	3.47	7.97	6.7	5.5	7.99
TiO2	0.06	0.04	0.04	0.09	0.06	0.04	0.08	0.06	0.06	0.08	0.04	0.02	0.04	0.06	0.06	0.06	0.08	0.08	0.08	0.06	0.04	0.06	0.06	0.02	0.06
MnO	0.01	0	0.01	0	0.01	0	0.01	0.03	0	0.04	0	0	0.01	0	0	0.01	0	0	0	0.05	0	0.01	0	0.01	0.01
FeO	0.25	0.25	0.33	0.26	0.25	0.26	0.29	0.13	0.27	0.16	0.17	0.17	0.29	0.22	0.35	0.25	0.29	0.25	0.33	0.38	0.23	0.17	0.17	0.19	0.17
Total	98.82	98.78	99.88	98.93	99.34	98.9	99.37	99.85	99.86	99.57	100.49	99.3	99.72	99.4	100.09	98.85	99.79	99.82	99.17	99.73	100.47	99.43	99.17	98.66	97.13
Na+	0.474	0.6358	0.7152	0.399	0.5264	0.5664	0.3599	0.4988	0.5138	0.4887	0.6925	0.5704	0.5545	0.6104	0.6491	0.5986	0.5032	0.5859	0.4785	0.5279	0.7242	0.5702	0.6286	0.6776	0.5748
Mg2+	0.0027	0.0013	0.0013	0.0014	0.0027	0.0027	0.0027	0.0027	0.0013	0.0013	0.0026	0	0.0027	0.0013	0.0027	0.0013	0.0013	0.0027	0	0.0013	0.0013	0.0013	0	0.0013	0.0014
Al3+	1.4995	1.318	1.2024	1.5796	1.4272	1.3722	1.6141	1.4572	1.4574	1.4783	1.2173	1.4091	1.3936	1.3263	1.2579	1.3439	1.4488	1.3596	1.5055	1.4401	1.1582	1.398	1.3329	1.2664	1.399
Si4+	2.4955	2.6794	2.7945	2.4191	2.5702	2.6268	2.3843	2.5525	2.5449	2.521	2.7886	2.5953	2.6079	2.6718	2.7416	2.6546	2.554	2.6427	2.4945	2.5558	2.8376	2.6027	2.666	2.729	2.5949
K+	0.0192	0.0375	0.0635	0.0169	0.0282	0.0329	0.0122	0.0263	0.0281	0.0236	0.0749	0.0351	0.0338	0.0447	0.0618	0.0415	0.0287	0.0428	0.0238	0.0305	0.0974	0.0316	0.0414	0.0547	0.033
Ca2+	0.4965	0.3141	0.2014	0.5669	0.425	0.3731	0.6045	0.4339	0.4377	0.47	0.2015	0.3853	0.3829	0.3258	0.2548	0.3395	0.4352	0.3435	0.4835	0.4274	0.1642	0.3846	0.3232	0.2661	0.3953
Ti4+	0.0021	0.0014	0.0013	0.0031	0.002	0.0014	0.0027	0.002	0.002	0.0027	0.0013	0.0007	0.0014	0.002	0.002	0.002	0.0027	0.0027	0.0027	0.002	0.0013	0.002	0.002	0.0007	0.0021
Mn2+	0.0004	0	0.0004	0	0.0004	0	0.0004	0.0011	0	0.0015	0	0	0.0004	0	0	0.0004	0	0	0	0.0019	0	0.0004	0	0.0004	0.0004
Fe2+	0.0095	0.0094	0.0123	0.0099	0.0094	0.0098	0.0111	0.0049	0.0102	0.006	0.0063	0.0064	0.0109	0.0083	0.013	0.0095	0.0109	0.0094	0.0125	0.0143	0.0085	0.0064	0.0064	0.0072	0.0066
Total	4.9994	4.9969	4.9923	4.9959	4.9915	4.9853	4.9919	4.9794	4.9954	4.9931	4.985	5.0023	4.9881	4.9906	4.9829	4.9913	4.9848	4.9893	5.001	5.0012	4.9927	4.9972	5.0005	5.0034	5.0075

feldspar	38f	14j centre	14j centre	14j centre	14j centre	14n centre	14n centre	14n centre	14n centre j	14n edge j	38e	38e	38e	38e	38e	38e	38e	38g	38g	38g	38g	38g	38g	38h	38h
Na2O	6.4	2.71	1.91	2.92	2.2	4.06	3.94	4.9	3.8	3.79	3.04	3.09	2.41	3.48	2.88	2.25	2.23	4.66	4.67	4.65	6.11	5.59	5.36	4.3	4.23
MgO	0.02	0	0.15	0.06	0.04	0	0.1	0.17	0.09	0.19	0.08	0.11	0.13	0.13	0.11	0.08	0.08	0.08	0.06	0.04	0.08	0.08	0.02	0.06	0.04
Al2O3	26.32	32.52	32.78	31.06	32.58	28.8	29.29	29.14	29.8	29.89	30.79	30.45	31.96	30.28	30.68	32.11	31.79	28.61	28.32	27.96	25.92	26.59	26.91	28.85	29.17
SiO2	54.67	47.88	47.82	50.45	47.79	50.44	50.44	52.59	52.29	51.81	48.39	49.57	48.21	50.14	48.59	46.81	46.23	52.56	53.22	50.67	56.39	54.88	53.73	52.24	51.48
K2O	0.53	0.13	0.13	0.22	0.14	0.27	0.24	0.26	0.21	0.23	0.19	0.21	0.14	0.24	0.18	0.13	0.13	0.35	0.37	0.36	0.6	0.5	0.45	0.32	0.31
CaO	8.04	15.91	15.98	14.13	15.92	11.98	12.32	12	12.78	12.55	14.45	14.16	15.61	13.39	14.67	15.58	15.6	11.49	11.07	11.18	8.38	9.47	9.93	11.86	12.24
TiO2	0.04	0.04	0.06	0.04	0.06	0.09	0.08	0.09	0.09	0.09	0.04	0.02	0.02	0.08	0.06	0.04	0.02	0.08	0.06	0.08	0.06	0.06	0.06	0.06	0.08
MnO	0	0	0	0	0	0.01	0.01	0	0	0	0	0.03	0.04	0	0.03	0.01	0	0	0.01	0	0.03	0.03	0	0	0.01
FeO	0.17	0.45	0.38	0.54	0.45	0.43	0.36	0.43	0.42	0.45	0.42	0.46	0.49	0.45	0.45	0.46	0.42	0.35	0.43	0.32	0.33	0.41	0.35	0.54	0.46
Total	96.19	99.64	99.21	99.42	99.18	96.08	96.78	99.58	99.48	99	97.4	98.1	99.01	98.19	97.65	97.47	96.5	98.18	98.21	95.26	97.9	97.61	96.81	98.23	98.02
Na+	0.5796	0.2423	0.171	0.2595	0.1973	0.3721	0.3586	0.4337	0.336	0.3368	0.2769	0.2788	0.2164	0.3131	0.2617	0.2054	0.2057	0.4171	0.4171	0.4295	0.5434	0.5005	0.4846	0.3851	0.3803
Mg2+	0.0014	0	0.0103	0.0041	0.0028	0	0.007	0.0116	0.0061	0.013	0.0056	0.0076	0.009	0.009	0.0077	0.0056	0.0057	0.0055	0.0041	0.0028	0.0055	0.0055	0.0014	0.0041	0.0028
Al3+	1.4493	1.7682	1.784	1.6784	1.7762	1.6048	1.6209	1.5684	1.6023	1.6151	1.7051	1.6707	1.7448	1.6566	1.695	1.7821	1.7832	1.557	1.5378	1.5701	1.4016	1.4476	1.4792	1.5709	1.5946
Si4+	2.5536	2.2082	2.2075	2.3124	2.2099	2.3841	2.3677	2.4009	2.3848	2.3747	2.273	2.307	2.2325	2.3268	2.277	2.2037	2.1996	2.4263	2.4512	2.4136	2.5865	2.5342	2.5051	2.4128	2.387
K+	0.0316	0.0076	0.0077	0.0129	0.0083	0.0163	0.0144	0.0151	0.0122	0.0134	0.0114	0.0125	0.0083	0.0142	0.0108	0.0078	0.0079	0.0206	0.0217	0.0219	0.0351	0.0295	0.0268	0.0189	0.0183
Ca2+	0.4024	0.7862	0.7904	0.694	0.7888	0.6067	0.6197	0.587	0.6245	0.6164	0.7273	0.7061	0.7746	0.6658	0.7366	0.7859	0.7953	0.5683	0.5463	0.5706	0.4119	0.4686	0.4961	0.5869	0.6081
Ti4+	0.0014	0.0014	0.0021	0.0014	0.0021	0.0032	0.0028	0.0031	0.0031	0.0031	0.0014	0.0007	0.0007	0.0028	0.0021	0.0014	0.0007	0.0028	0.0021	0.0029	0.0021	0.0021	0.0021	0.0021	0.0028
Mn2+	0	0	0	0	0	0.0004	0.0004	0	0	0	0	0.0012	0.0016	0	0.0012	0.0004	0	0	0.0004	0	0.0012	0.0012	0	0	0.0004
Fe2+	0.0066	0.0174	0.0147	0.0207	0.0174	0.017	0.0141	0.0164	0.016	0.0172	0.0165	0.0179	0.019	0.0175	0.0176	0.0181	0.0167	0.0135	0.0166	0.0127	0.0127	0.0158	0.0136	0.0209	0.0178
Total	5.0259	5.0313	4.9877	4.9834	5.0028	5.0046	5.0056	5.0362	4.985	4.9897	5.0172	5.0025	5.0069	5.0058	5.0097	5.0104	5.0148	5.0111	4.9973	5.0241	5	5.005	5.0089	5.0017	5.0121

feldspar	38h	38h
Na2O	4.32	4.11
MgO	0.06	0.04
Al2O3	28.83	28.67
SiO2	51.99	51.1
K2O	0.31	0.32
CaO	11.94	12
TiO2	0.08	0.09
MnO	0.01	0
FeO	0.59	0.43
Total	98.13	96.76
Na+	0.3877	0.3739
Mg2+	0.0041	0.0028
Al3+	1.5731	1.5859
Si4+	2.4062	2.3976
K+	0.0183	0.0192
Ca2+	0.5921	0.6033
Ti4+	0.0028	0.0032
Mn2+	0.0004	0
Fe2+	0.0228	0.0169
Total	5.0075	5.0028

Cumulates - feldspar analyses (continued)

carbonate	14a	14a	14b	14b	14b	14f	14f	14s	14s	14s	14e	14e	14n	14n	14v	14v	14v	14v	14d	14l	14l	14l	14l	14m	14f
Na2O	0	0	0.07	0.02	0.14	0	0	0.02	0.02	0.02	0.02	0.02	0	0	0	0	0	0.1	0.24	0	0.05	0	0	0	0.2
MgO	7.21	27.72	12.57	13.94	14.93	19.76	18.07	14.16	13.82	14.38	11.48	10.56	13.34	14.24	14.22	12.3	12.08	10.92	11.49	12.34	9.74	10.25	15.02	0.6	12.76
Al2O3	0.05	0	0.03	0	0	0	0.11	0.03	0.05	0	0.03	0.05	0.05	0	0	0.03	0	0	0	0	0	0	0.03	0.11	0.08
SiO2	0	0.03	0.1	0	0	0.03	0	0	0.03	0.05	0	0.03	0	0	0.03	0	0.08	0	0.03	0	0	0.13	0.05	0.07	0.48
K2O	0.04	0.05	0.04	0.04	0.03	0.03	0.03	0.04	0.04	0.03	0.04	0.04	0.03	0.02	0.03	0.03	0.04	0.03	0.03	0.03	0.03	0.04	0.03	0.04	0.04
CaO	6.01	4.42	5.06	6.12	6.02	4.54	4.58	6.96	6	6.88	7.71	7.83	5.1	3.9	3.38	4	3.66	3.64	3.48	2.97	2.84	2.57	2.89	60.47	25.44
TiO2	0.08	0.03	0.05	0.02	0.05	0.02	0.02	0.02	0.02	0.03	0.02	0.02	0.03	0	0.05	0.03	0.02	0.02	0.08	0.02	0.03	0.02	0.02	0	0.15
MnO	0.69	1.4	0.61	0.6	0.6	1.54	1.58	1.04	0.87	0.96	0.37	0.35	0.26	0.24	0.09	0.1	0.16	0.13	0.12	0.12	0.09	0.1	0.16	0.76	0.84
FeO	44.78	19.57	38.47	35.49	34.48	29.64	31.37	34.09	35.88	34.05	36.87	38.03	39.34	39.06	39.61	41	41.75	43.61	43.2	42.67	45.66	45.87	39.43	0.3	13.06
CO2	41.14	46.78	43	43.77	43.75	44.44	44.24	43.64	43.27	43.6	43.46	43.07	41.85	42.54	42.59	42.51	42.21	41.55	41.33	41.85	41.56	41.02	42.37	37.65	46.95
Total-CO2	58.86	53.22	57	56.23	56.25	55.56	55.76	56.36	56.73	56.4	56.54	56.93	58.15	57.46	57.41	57.49	57.79	58.45	58.67	58.15	58.44	58.98	57.63	62.35	53.05
Na+	0	0	0.0047	0.0013	0.0092	0	0	0.0013	0.0013	0.0013	0.0013	0.0013	0	0	0	0	0	0.0068	0.0164	0	0.0034	0	0	0	0.0124
Mg2+	0.3842	1.2945	0.6434	0.7038	0.7511	0.9715	0.8954	0.7143	0.7015	0.7251	0.5855	0.5425	0.6899	0.7299	0.7288	0.6351	0.6264	0.5732	0.603	0.6427	0.5141	0.543	0.7697	0.0316	0.608
Al3+	0.0021	0	0.0012	0	0	0	0.0043	0.0012	0.002	0	0.0012	0.002	0.002	0	0	0.0012	0	0	0	0	0	0	0.0012	0.0046	0.003
Si4+	0	0.0009	0.0034	0	0	0.001	0	0	0.001	0.0017	0	0.001	0	0	0.001	0	0.0028	0	0.0011	0	0	0.0046	0.0017	0.0025	0.0153
K+	0.0018	0.002	0.0018	0.0017	0.0013	0.0013	0.0013	0.0017	0.0017	0.0013	0.0017	0.0018	0.0013	0.0009	0.0013	0.0013	0.0018	0.0013	0.0013	0.0013	0.0014	0.0018	0.0013	0.0018	0.0016
Ca2+	0.2303	0.1484	0.1862	0.2221	0.2177	0.1605	0.1632	0.2524	0.219	0.2494	0.2827	0.2892	0.1896	0.1437	0.1245	0.1485	0.1364	0.1374	0.1313	0.1112	0.1078	0.0979	0.1065	2.2901	0.8715
Ti4+	0.0022	0.0007	0.0013	0.0005	0.0013	0.0005	0.0005	0.0005	0.0008	0.0005	0.0005	0.0008	0	0.0013	0.0008	0.0005	0.0021	0.0005	0.0008	0.0005	0.0008	0.0005	0.0005	0	0.0036
Mn2+	0.0209	0.0372	0.0177	0.0172	0.0172	0.043	0.0445	0.0298	0.0251	0.0275	0.0107	0.0102	0.0076	0.007	0.0026	0.0029	0.0047	0.0039	0.0036	0.0036	0.0027	0.003	0.0047	0.0228	0.0227
Fe2+	1.3391	0.5128	1.1051	1.0055	0.9734	0.8178	0.8723	0.9651	1.0221	0.9635	1.0553	1.0963	1.1417	1.1235	1.1392	1.1879	1.2148	1.2845	1.2723	1.2471	1.3523	1.3635	1.1339	0.0089	0.3492
C4+	2.0085	2.0014	2.0165	2.0244	2.0164	2.0018	2.0083	2.017	2.0123	2.0141	2.0307	2.027	1.9829	1.9977	1.9998	2.0108	2.0051	1.998	1.9873	1.9969	2.0096	1.9907	1.9892	1.817	2.0495
Total-C4+	1.9806	1.9965	1.9648	1.9521	1.9712	1.9956	1.9815	1.9663	1.9742	1.9706	1.9389	1.9448	2.0329	2.005	1.9987	1.9777	1.9874	2.0076	2.0311	2.0064	1.9825	2.0143	2.0195	2.3623	1.8873

Cumulates - carbonate analyses

Appendix D

Sr-isotope determination

All analyses were made in the Age and Isotope Laboratory at Oxford University, Dept. of Earth Sciences, under the supervision of Dr. P. Taylor and Mr. R. Goodwin.

D.1 Strontium extraction

The quantity of rock powder needed for isotope-determination depends on its Sr-content i.e. 0.05g powder with 1000ppm Sr, 0.4g powder with 5ppm Sr. The powder was weighed out into a Teflon beaker and 10cm^3 HF added, plus a few drops of HNO_3. This was evaporated dry, then 8cm^3 6M HCl added. The solution was put back under the heating lamps to evaporate to incipient crystallisation *only* (to prevent the formation of insoluble anhydrous $FeCl_3$), then 4cm^3 of 2.5M HCl were added, ensuring that all the solids had redissolved. This solution was transferred to centrifuge tubes and centrifuged for 10mins at 2000rpm to remove solid residues and to prevent their introduction into the cation exchange resin columns. The resin used was Dowex X8, which was cleaned with 6M HCl, de-ionised H_2O, then 6M HCl again, and finally 2.5M HCl.

1cm^3 of solution was taken from the top of the centrifuge tube and washed into the resin using two 1cm^3 2.5M HCl washes, taking care to run them down the side of the column to pick up any of the specimen. 35cm^3 of 2.5M HCl were then passed completely, during which the Fe in the specimen usually emerged, appearing as a yellow colour in the HCl. 11cm^3 of the same acid was then passed and collected in the Teflon beakers; this contained the strontium as $SrCl_2$. It was left to evaporate until only a drop remained and then transferred to a quartz microbeaker. After evaporation to dryness a few drops of aqua regia (75% HCl + 25% HNO_3) were added to remove organic carbon. Finally, after complete evaporation, the microbeaker was covered and labelled.

Samples with < 20ppm Sr caused some problems, with too little being extracted to detect even with the Isomass 54E spectrometer. Three separate extractions were therefore made and added together. The results were sometimes variable, with relatively large errors remaining on the Sr-isotope measurements, but they were often useful nevertheless.

D.2 Measurement of the Sr-isotope ratio

The sample was transferred to a tantalum filament by the following method:

a) A drop of 0.25M H_3PO_4 was put on the filament.

b) The specimen was picked up with a drop of quartz-distilled water and added to the drop of acid.

c) The filament was gently heated to dry it, then briefly degassed at dull red-heat.

Six filaments were mounted in a turret and put in the specimen chamber of the mass spectrometer - a VG Aldermaston Micromass 30. Blocks of 12 readings were taken, and the standard error recorded. The run was usually ended after at least five blocks, and when the standard error fell below 2.5×10^{-5}. Corrections were made for mass fractionation, and for Rb contamination of the sample.

The system was semi-automated and controlled by in-house software running on an Amstrad PC-1640 HD20. Results were corrected to the Eimer & Amend international standard (0.70800) which was run periodically to gauge machine drift. The reproducible value for the MM30 was 0.708200.

Samples with low Sr (< 50ppm) were run in the fully automated Isomass 54E mass spectrometer, using the Eimer & Amend and NBS 987 standards.

D.3 Measurement of Rb and Sr concentrations

Rb and Sr were measured on pressed powder pellets using the Phillips XRF (described in Appendix C). Samples with Sr < 100ppm, and very high Rb/Sr clearly have large errors on Rb/Sr, and this problem is discussed in section 5.8.1.

D.4 Calculation of $(^{87}Sr/^{86}Sr)_{initial}$

This section is based on Faure (1986). For each specimen the Rb/Sr is known, the age is either known accurately from K-Ar dating or can be estimated to within 2Ma, and the present $^{87}Sr/^{86}Sr$ has

been measured. The isotopic abundance of ^{87}Rb [Ab(^{87}Rb)] and the atomic mass of natural Rb [WRb] have been determined by Catanzaro *et al* (1969):

$$\begin{aligned} Ab(^{87}Rb) &= 0.278346 \\ WRb &= 85.46776 \text{ g mole}^{-1} \end{aligned}$$

and it is necessary to determine:

$$\begin{aligned} Ab(^{86}Sr) &= \text{isotopic abundance of } ^{86}Sr \text{ in the sample} \\ WSr &= \text{atomic mass of Sr in the sample} \end{aligned}$$

To calculate Ab(^{86}Sr):

			abundances
$^{84}Sr/^{88}Sr$	=	0.006756	Ab(^{84}Sr) = 1/b × 0.006756
$^{86}Sr/^{88}Sr$	=	0.1194	Ab(^{86}Sr) = 1/b × 0.1194
$^{88}Sr/^{88}Sr$	=	1.0000	Ab(^{88}Sr) = 1/b
$^{87}Sr/^{88}Sr$	=	($^{87}Sr/^{86}Sr$) × ($^{86}Sr/^{88}Sr$) = a	Ab(^{87}Sr) = a/b
		sum = b	sum = 1.0000

and to calculate WSr:

		atomic weight of isotope	
Ab(^{84}Sr)	×	83.9134	+
Ab(^{86}Sr)	×	85.9092	+
Ab(^{88}Sr)	×	87.9056	+
Ab(^{87}Sr)	×	86.9088	= WSr

It is then possible to determine:

$$\left(\frac{^{87}Rb}{^{86}Sr}\right) = \left(\frac{Rb}{Sr}\right) \times \frac{Ab\left(^{87}Rb\right) \times WSr}{Ab\left(^{86}Sr\right) \times WRb}$$

which gives:

$$\left(\frac{^{87}Sr}{^{86}Sr}\right)_{initial} = \left(\frac{^{87}Sr}{^{86}Sr}\right)_{present} - \left(\frac{^{87}Rb}{^{86}Sr}\right)\left(e^{\lambda t} - 1\right)$$

where:

t = age in years

$\lambda = 1.42 \times 10^{-11}$ yr^{-1} Steiger and Jäger (1977)

The results of applying this sequence of calculations are given in Tables D.1, D.2 and D.3.

Specimen number	Sr ppm	Rb ppm	Rb/Sr	$^{87}Rb/^{86}Sr$	err. %	$^{87}Sr/^{86}Sr$	St.Dev. ($x10^{-6}$)	Eimer & Amend	$^{87}Sr/^{86}Sr$ corrected	age Ma		error Ma	$^{87}Sr/^{86}Sr$ initial	error ($x10^{-6}$)	
F84/17	7.2	186.6	25.916667	75.079920	5	0.720884	186	0.708039	0.720845	12.90	*	0.20	**0.707091**	1284	F84/17
F84/36	815.4	42.1	0.051631	0.149319	1	0.703617	27	0.708200	0.703417	8.00		1.00	**0.703400**	56	F84/36
F84/39	773.4	56.2	0.072666	0.210154	1	0.703665	27	0.708200	0.703465	8.00		1.00	**0.703441**	57	F84/39
F84/40b	853.3	61.1	0.071604	0.207087	1	0.703890	25	0.708200	0.703690	10.50	*	0.30	**0.703659**	51	F84/40b
F84/43	760.7	46.5	0.061128	0.176783	1	0.703380	11	0.708039	0.703341	8.00		1.00	**0.703321**	25	F84/43
SH86/15	37.4	171.1	4.574866	13.234555	1	0.706395	24	0.708003	0.706392	12.60	*	0.20	**0.704024**	110	SH86/15
SH86/27	945.0	178.3	0.188677	0.545679	1	0.703786	13	0.708039	0.703747	12.00		1.00	**0.703654**	35	SH86/27
SH86/32	4.8	335.8	69.958333	203.025379	10	0.738958	181	0.708039	0.738919	8.00		1.00	**0.715854**	5840	SH86/32
SH86/33	181.2	202.5	1.117550	3.232091	1	0.703901	25	0.708200	0.703701	8.50	*	0.20	**0.703311**	63	SH86/33
SH86/37	242.5	254.8	1.050722	3.039464	1	0.706079	23	0.708200	0.705879	8.20	*	0.20	**0.705525**	58	SH86/37
SH86/47	1329.6	96.8	0.072804	0.210550	1	0.703500	27	0.708200	0.703300	8.15	*	0.20	**0.703276**	55	SH86/47
SH86/49	636.4	50.3	0.079038	0.228582	1	0.703637	24	0.708200	0.703437	8.00		1.00	**0.703411**	52	SH86/49
SH86/52	786.5	64.1	0.081500	0.235703	1	0.703677	24	0.708200	0.703477	8.00		1.00	**0.703450**	52	SH86/52
SH86/54	52.3	177.0	3.384321	9.789056	1	0.704979	46	0.708039	0.704940	7.00	*	0.50	**0.703967**	172	SH86/54
SH86/56	1150.9	89.7	0.077939	0.225405	1	0.703572	8	0.708039	0.703533	8.05	*	0.20	**0.703507**	17	SH86/56
SH86/58	886.0	94.0	0.106095	0.306837	1	0.703800	24	0.708200	0.703600	8.00		1.00	**0.703565**	53	SH86/58
SH86/63	517.6	43.8	0.084621	0.244726	1	0.703549	24	0.708200	0.703349	8.00		1.00	**0.703321**	52	SH86/63
SH87/11	1791.4	105.6	0.058948	0.170486	1	0.703953	25	0.708200	0.703753	12.60	*	0.20	**0.703722**	51	SH87/11
SH87/13	179.0	221.3	1.236313	3.575810	1	0.704395	25	0.708003	0.704392	13.30	*	0.20	**0.703717**	67	SH87/13
SH87/21	931.8	44.7	0.047972	0.138737	1	0.703601	19	0.708200	0.703401	8.00		1.00	**0.703385**	40	SH87/21
SH87/24	4.3	225.8	52.511628	152.384538	10	0.738321	35	0.708003	0.738318	8.00		1.00	**0.721006**	4182	SH87/24
SH87/29	866.1	58.2	0.067198	0.194338	1	0.703536	25	0.708200	0.703336	7.95	*	0.15	**0.703314**	51	SH87/29
SH87/30	493.5	138.9	0.281459	0.814002	1	0.703751	25	0.708200	0.703551	11.00		1.00	**0.703424**	63	SH87/30
SH87/31	454.6	194.7	0.428289	1.238739	1	0.704522	19	0.708200	0.704322	11.00		1.00	**0.704128**	58	SH87/31
SH87/33	540.2	199.3	0.368937	1.067049	1	0.704266	25	0.708200	0.704066	11.00		1.00	**0.703899**	67	SH87/33
SH87/43	733.1	71.5	0.097531	0.282083	1	0.704301	29	0.708200	0.704101	8.00		1.00	**0.704069**	62	SH87/43
SH87/48	89.2	351.4	3.939462	11.395637	1	0.705903	24	0.708200	0.705703	7.70	*	0.20	**0.704457**	93	SH87/48
SH87/49	791.1	29.6	0.037416	0.108207	1	0.703470	23	0.708200	0.703270	9.70	*	1.00	**0.703255**	48	SH87/49
SH87/51	888.9	130.3	0.146586	0.423937	1	0.703714	24	0.708200	0.703514	8.70	*	0.30	**0.703462**	50	SH87/51
SH87/55	5.6	312.6	55.821429	161.545535	10	0.710233	9	0.708003	0.710230	6.50	*	0.20	**0.695319**	2014	SH87/55
SH87/61	256.5	173.6	0.676803	1.957444	1	0.703984	15	0.708039	0.703945	7.70	*	0.15	**0.703731**	36	SH87/61
SH87/65a	22.6	314.6	13.920354	40.289380	2	2 runs used	23		0.711320	13.00		1.00	**0.703882**	778	SH87/65a
SH87/70	908.9	155.0	0.170536	0.493203	1	0.703734	26	0.708200	0.703534	11.10	*	0.20	**0.703456**	54	SH87/70
SH87/74	962.6	120.3	0.124974	0.361444	1	0.704001	25	0.708200	0.703801	11.00		1.00	**0.703745**	56	SH87/74
SH87/75	965.5	75.9	0.078612	0.227351	1	0.703702	19	0.708200	0.703502	8.00		1.00	**0.703476**	42	SH87/75
SH87/76	11.9	247.6	20.806723	60.226945	4	0.712462	14	0.708039	0.712423	8.20	*	0.15	**0.705410**	442	SH87/76
SH87/8	1249.9	78.9	0.063125	0.182562	1	0.703729	25	0.708200	0.703529	8.60	*	0.20	**0.703507**	51	SH87/8
SH88/16	1674.1	188.0	0.112299	0.324786	1	0.704001	23	0.708200	0.703801	10.80	*	0.50	**0.703751**	49	SH88/16
SH88/17	187.4	166.4	0.887940	2.568385	1	0.705310	21	0.708200	0.705110	9.00	*	0.30	**0.704782**	56	SH88/17
SH88/30	1040.1	70.7	0.067974	0.196585	1	0.703495	8	0.708003	0.703492	8.60	*	0.20	**0.703468**	17	SH88/30

Table D.1. $^{87}Sr/^{86}Sr$ data for 40 Velay lavas. An asterisk after the age means that it has been measured by K-Ar. Other ages have been estimated.

Specimen number	Sr ppm	Rb ppm	Rb/Sr	$^{87}Rb/^{86}Sr$	err. %	$^{87}Sr/^{86}Sr$	St.Dev. ($x10^{-6}$)	Eimer & Amend	$^{87}Sr/^{86}Sr$ corrected	age Ma		error Ma	$^{87}Sr/^{86}Sr$ initial	error ($x10^{-6}$)	
SH86/38a	262.2	16.8	0.064073	0.185303	1	0.703699	25	0.708200	0.703499	8.50		0.20	**0.703477**	51	SH86/38a
SH88/14a	807.4	47.7	0.059079	0.170872	1	0.704383	19	0.708200	0.704183	8.50		0.20	**0.704162**	39	SH88/14a
SH88/14b	916.5	63.0	0.068740	0.198816	1	0.704509	19	0.708200	0.704309	8.50	*	0.20	**0.704285**	39	SH88/14b
SH88/14g	94.1	14.2	0.150903	0.436429	1	0.703892	28	0.708200	0.703692	8.50		0.20	**0.703639**	58	SH88/14g

Table D.2. Rb/Sr and $^{87}Sr/^{86}Sr$ data for cumulate specimens.

Specimen number	Sr ppm	Rb ppm	Rb/Sr	$^{87}Rb/^{86}Sr$	err. %	$^{87}Sr/^{86}Sr$	St.Dev. ($x10^{-6}$)	Eimer & Amend	$^{87}Sr/^{86}Sr$ corrected	
F85/2	504.0	131.4	0.260714	0.754612	1	0.711974	24	0.708200	**0.711774**	F85/2
SH86/23	42.8	395.9	9.250000	27.087979	1	0.831984	9	0.708003	**0.831981**	SH86/23
SH86/62	327.9	188.4	0.574565	1.664522	1	0.721179	24	0.708200	**0.720979**	SH86/62
SH87/52	282.1	167.7	0.594470	1.722157	1	0.720842	13	0.708039	**0.720803**	SH87/52
SH88/2a	130.4	247.0	1.894172	5.494574	1	0.734487	29	0.708200	**0.734287**	SH88/2a
SH88/8	134.0	217.2	1.620896	4.700597	1	0.731535	9	0.708003	**0.731532**	SH88/8

Table D.3. Rb/Sr and $^{87}Sr/^{86}Sr$ data for Velay basement specimens.

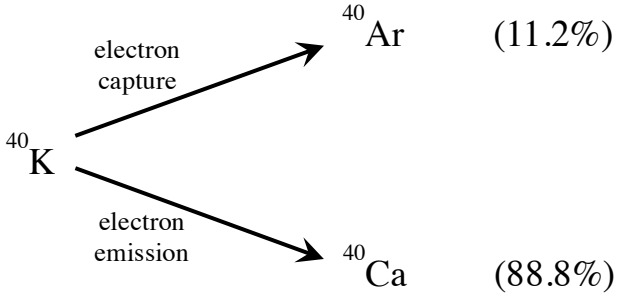
Appendix E

K-Ar age determination

This work was carried out at the Geochronology Laboratory, University of Clermont-Ferrand II, France, under the supervision of Mr. Jean-Marie Cantagrel.

E.1 Theory

The technique used was that of measuring the absolute amount of argon produced within whole rock samples of lavas due to decay of radiogenic ^{40}K. This section is based on Faure (1986).



This breakdown gives:

$$^{40}Ar^{*} + {}^{40}Ca^{*} = {}^{40}K(e^{\lambda t} - 1)$$

where: $^{40}Ar^{*}$, $^{40}Ca^{*}$ = moles of *radiogenic* ^{40}Ar, ^{40}Ca (as opposed to ^{40}Ar, ^{40}Ca already present in sample)

t = time elapsed since ^{40}Ar began to accumulate

Which can be separated into:

$$^{40}Ar^{*} = \left(\frac{\lambda_e}{\lambda}\right) {}^{40}K\left(e^{\lambda t} - 1\right) \qquad \textit{(equation E1)}$$

where: λ_e = decay constant for ^{40}Ar production,

λ = total decay constant.

Values used were:

$\lambda_e = 0.581 \times 10^{-10}\ yr^{-1}$

$\lambda = 5.543 \times 10^{-10}\ yr^{-1}$ Steiger and Jäger (1977)

^{40}K natural abundance = 0.01167% ±0.0004% Garner *et al* (1975)

$^{40}Ar_{atmospheric} = 99.60\%$

$^{38}Ar_{atmospheric} = 0.063\%$

$^{36}Ar_{atmospheric} = 0.337\%$ Nier (1950)

The values for atmospheric argon were needed both for calibrating the spectrometer and for determining absolute atmospheric contamination of the samples, which if left uncorrected could give large errors on the age.

E.2 Potassium determination

Atomic absorption spectrophotometry, using a Perkin-Elmer 303 spectrophotometer, was used to determine potassium concentration.

The specimen was first crushed to 0.5mm chips and split into two piles. The pile for K-determination was then reground to pass through a 100-mesh. 0.1g of this powder was taken, and dissolved in $1cm^3$ HNO_3 (65 - 69% conc.) + $3cm^3$ HF (48 - 51% conc.) in a Teflon container at 75˚C. This was evaporated dry for 24hrs at 100˚C, then redissolved in $2cm^3$ HNO_3, evaporated dry again, and dissolved in $5cm^3$ HCl 6M in deionised water. It was then evaporated dry again, before being dissolved in $2cm^3$ HCl 2.5M. This solution was put in a vial and made up precisely to $100cm^3$ with deionised water.

$5cm^3$ of the resulting solution was diluted to give roughly 2 $x10^{-6}$g K cm^{-3}, estimating K concentration from rock type. Enough CsCl (2%) solution was added during the manufacture of this solution to give 0.1% CsCl in the final mixture. This was to reduce the effect of unwanted ions on the measurement. The amount of the dilution was recorded. Two separate solutions from the original powder were made for each specimen, to act as a check on the procedure.

Each solution was then fed into the butane-air flame of the spectrophotometer, and the narrow waveband light source aimed to pass through this flame. The detector was set to the characteristic wavelength of absorption (766.5nm) of K. The degree of absorption has a linear relationship with K concentration, and absolute concentration was determined by bracketing the sample between two standard solutions 0.5% K apart and interpolating. Both solutions of each specimen were measured at least three times and only if they gave similar values was the mean of all six measurements was used as the K content of the rock.

E.3 Argon determination

Argon was determined by isotope dilution, with the stable isotope ^{38}Ar used as the spike.

E.3.1 Specimen preparation

An amount X of the 0.5mm-grade crushed sample was weighed into an aluminium foil pot, so that:

$$X = P/KR$$

where: K = potassium content %
P = mass of $^{40}Ar^*$ in the sample
R = value of ($^{40}Ar^*$/K) derived from estimated age

P was roughly the same as the mass of the spike to give a measured ratio as near as possible to 1:1 for accuracy. The final weight of the specimen was recorded, and the aluminium pot was then closed and perforated. Great care was taken to avoid losing any of the rock fragments, as this would have affected the result.

The foil-wrapped specimens were finally loaded into the specimen arm of the argon extraction line (see Figures E.1 and E.3) and their order recorded on a sketch.

E.3.2 Argon extraction

The extraction line (Figure E.1) was welded shut and tested with a high voltage ionisation probe to ensure that there were no leaks. The crucible was heated initially to 1400˚C to degass it, then the whole extraction line was baked out to a high vacuum (< $2x10^{-8}$ torr) overnight, with the specimens kept at 120˚C to get rid of adsorbed gases. The charcoal collectors were also heated to "activate" them.

The first specimen was loaded using a magnet to slide it into the crucible (see Figure E.3). The gas traps were all set to the correct temperature (see section below), and the system isolated from the vacuum pumps. The spike was released into the system (see section below) and allowed to equilibrate.

Heating was started slowly, to allow time for the gas traps to lower the pressure as the rock released gases. When the specimen reached maximum temperature (1400-1300˚C, depending on melt viscosity, hence rock type) at about 4.8kV, it was left for 15 minutes, before turning the heater down. At this point the path to the charcoal collectors and the Ti-furnace was opened, and the Ti-furnace

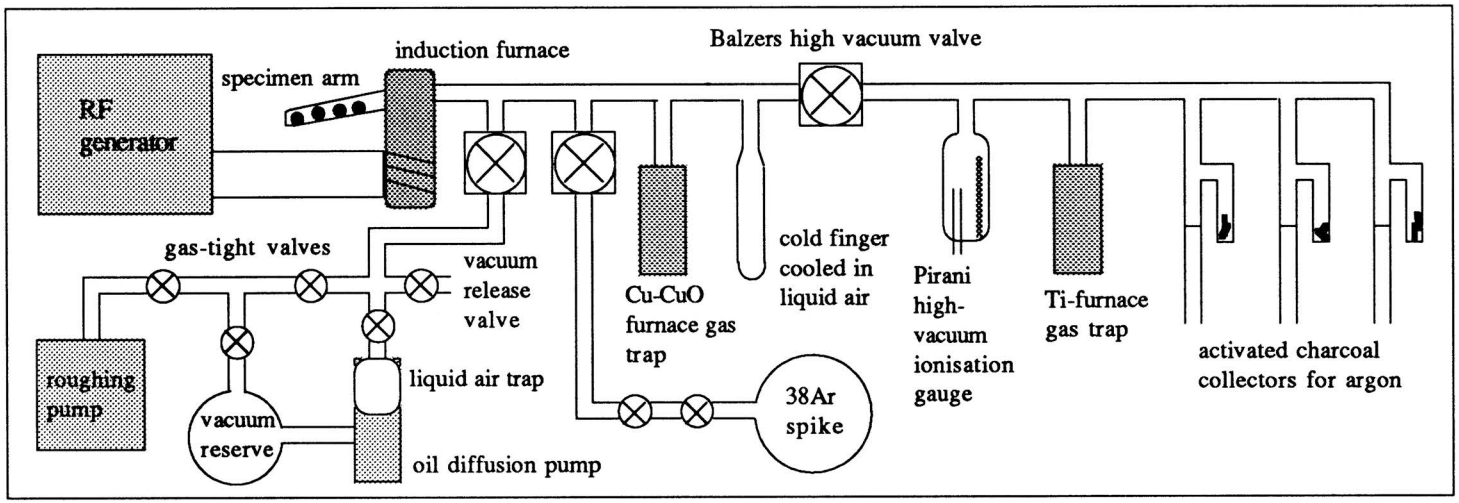


Figure E.1. Schematic layout of argon extraction line.

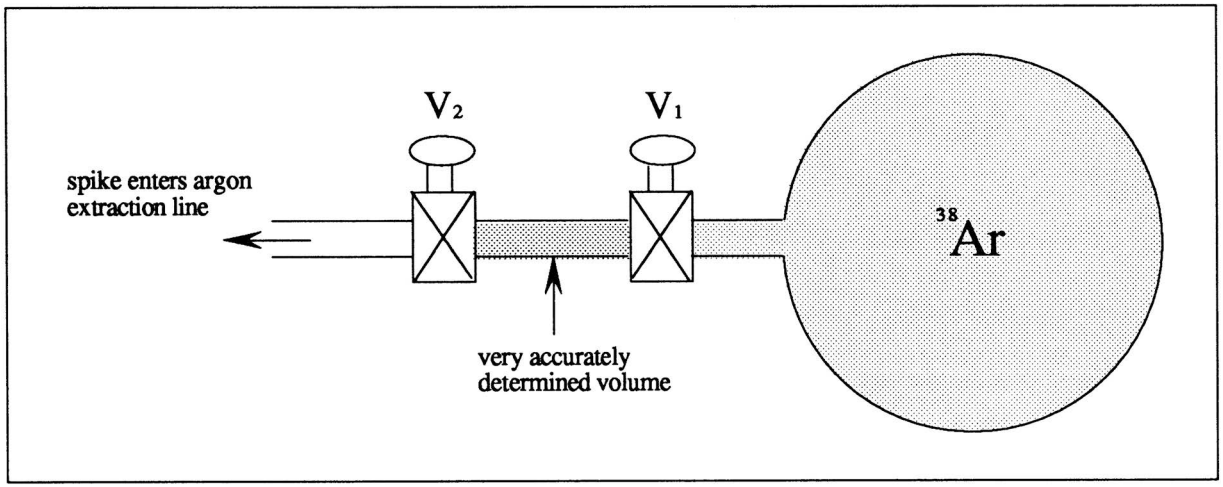


Figure E.2. Arrangement of valves and spike reservoir. V_1 and V_2 are greased glass rotary valves with mercury seals.

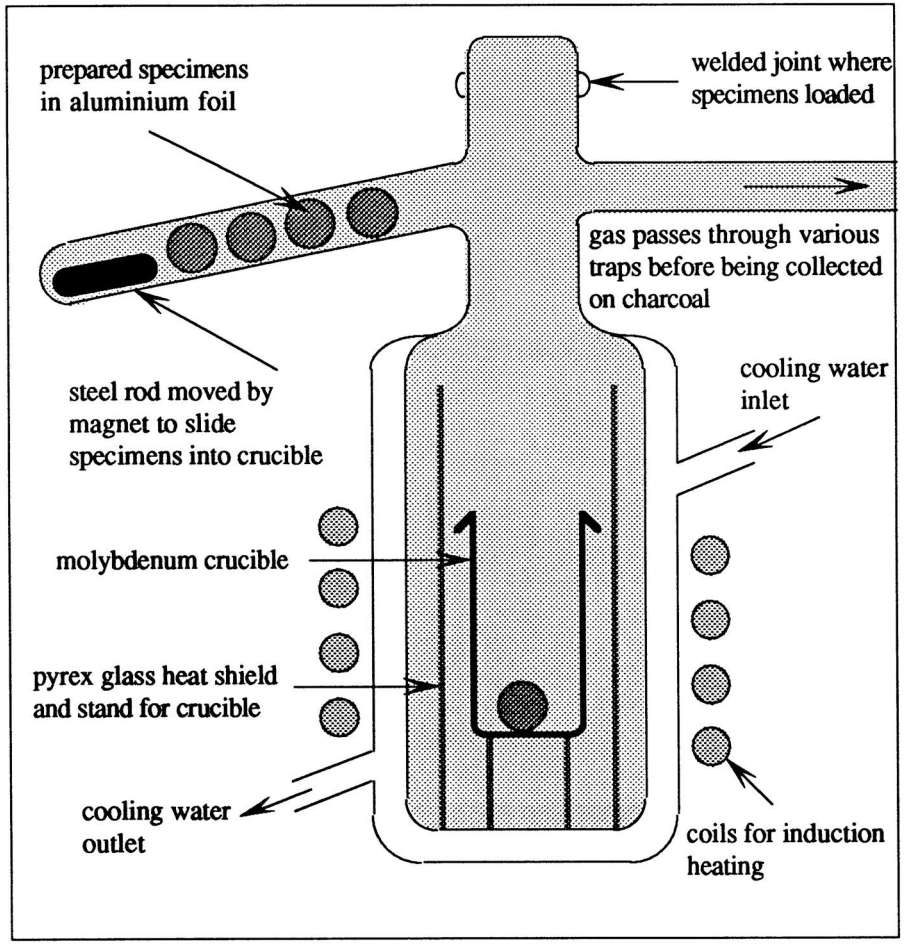


Figure E.3. Induction furnace used for fusion of K-Ar specimens.

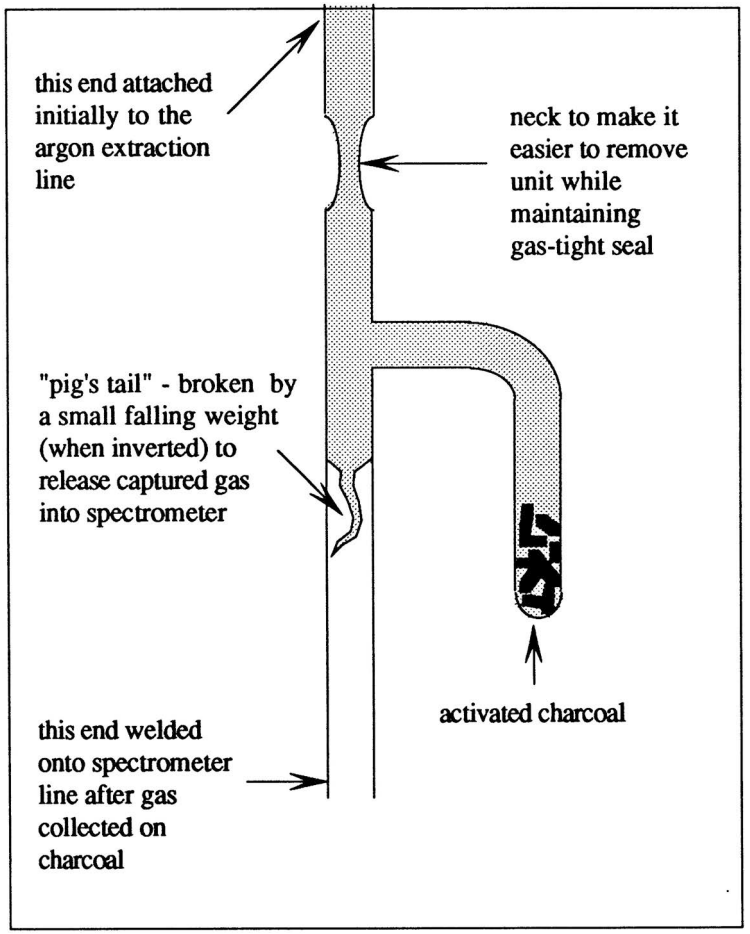


Figure E.4. Activated charcoal collector for Argon.

allowed to cool to 350-400°C over about 10 minutes. The remaining gas, consisting only of argon and trace impurities, was then collected on the charcoal by cooling the spur (see Figure E.4) by immersion in liquid air for 15 minutes.

When the gas had been collected, the charcoal tube was cut off with a blowtorch, taking care to keep the line sealed against the atmosphere. The system was then pumped down for the next extraction.

Gas traps

Fusion of lavas produces H_2O, CO_2, CO, N_2, H_2, O_2, Ar and other minor species. To remove all but the argon from the mixture, various traps were used in the extraction line:

1) CuO-Cu oven at 500°C $\quad CuO + CO \Rightarrow CO_2 + Cu$

$\qquad\qquad\qquad\qquad\qquad\qquad\quad CuO + H_2 \Rightarrow H_2O + Cu$

$\qquad\qquad\qquad\qquad\qquad\qquad\quad 2Cu + O_2 \Rightarrow 2CuO$

2) liquid air finger at -190°C freezes H_2O, CO_2, Kr, Xe

3) Ti-getter absorbs all other non-inert gases at 850°C, and H_2 at 350-430°C.

This leaves only He, Ne, Rn and Ar, and of these only Ar is present in significant amounts.

Spike

In order to provide a supply of spike gas, a flask of ^{38}Ar-enriched argon was obtained, the volume and gas pressure (at standard temperature) of which were known very accurately. Measurement of the isotopic ratios of the gas allowed the calculation of its atomic mass. A known volume (that between V_1 and V_2 in Figure E.2) could then be extracted to spike the specimen gas for the isotope dilution, and the number of spikes removed was recorded to determine the gradual decrease in pressure in the flask. The pressure, once calculated, was used to determine the mass of argon in the spike. The isotopic composition of the spike was also regularly measured to allow correction for its slow contamination by atmospheric argon.

Figure E.2 shows the arrangement of the spike flask and its valves. When the first valve (V_1) was opened equilibration was allowed for 5 minutes. Then V_1 was shut and V_2 opened to release the spike into the system.

E.3.3 Isotopic measurement

Isotopic ratios were measured using a MS-10 (AEI) mass spectrometer running in static mode, controlled by a computer running an in-house programme written in turbo Pascal. Calibration was achieved by measurement of known atmospheric argon ratios.

The charcoal collector containing the extracted argon mixture from the specimen was welded onto the spectrometer gas line, and the whole system checked for leaks. Baking out overnight, with vacuum pumps operating to obtain hard vacuum, ensured minimal contamination by atmospheric argon. At the same time the charcoal collectors were heated to release their stored sample gas.

An initial blank run was made to check the system was clear, then the "pigs-tail" of one of the collectors (see Figure E.4) was broken using a small weight, with the valve to the spectrometer closed. This valve was then slowly opened to release the sample gas into the spectrometer chamber until there was enough for measurement, but not enough to cause saturation. Eleven sweeps across the masses 40, 38, 36 were made and all data recorded and analysed by the computer, which calculated the corrected values of ^{40}Ar/ ^{38}Ar, and ^{38}Ar/ ^{36}Ar.

The specimen tube was then melted off and the whole line pumped to a hard vacuum for the next specimen.

E.4 Age calculation
Data needed:

$^{40}Ar/^{38}Ar$, and $^{36}Ar/^{38}Ar$	for:	specimen gas mixture
		spike
		atmosphere
K content (%) of specimen		
specimen weight in grams		
spike mass in nanograms (10^{-9}g)		
atomic masses of pure ^{40}Ar, ^{38}Ar, ^{36}Ar in grams per mole		

In the calculations that follow:

$Ar_{subscript}$	= number of moles of $Ar_{subscript}$ in specimen, spike or atmosphere
$M_{subscript}$	= atomic mass of $Ar_{subscript}$ in specimen, spike or atmosphere
mass $Ar_{subscript}$	= mass of $Ar_{subscript}$ in specimen, spike or atmosphere

Using the atomic masses of pure ^{40}Ar (39.9623), ^{38}Ar (37.963) and ^{36}Ar (35.968), the atomic masses of the spike (M_{spike}) and atmospheric (M_{atmos}) argon isotopic mixes can be calculated. The mass proportion of ^{40}Ar in the atmosphere, H, is obtained as follows:

$$\frac{M_{^{40}Ar} \times \left(^{40}Ar/Ar_{total}\right)_{atmos}}{M_{atmos}} = H \qquad \textit{(equation E2)}$$

The first Ar isotopic ratio for the specimen gas mixture gives:

$$\left(\frac{^{36}Ar}{^{38}Ar}\right)_{mixture} = \frac{\left(^{36}Ar/Ar_{total}\right)_{atmos} \times \left(Ar_{atmos}\right) + \left(^{36}Ar/Ar_{total}\right)_{spike} \times \left(Ar_{spike}\right)}{\left(^{38}Ar/Ar_{total}\right)_{atmos} \times \left(Ar_{atmos}\right) + \left(^{38}Ar/Ar_{total}\right)_{spike} \times \left(Ar_{spike}\right)} \qquad \textit{(equation E3)}$$

which, after insertion of all known values, gives:

$$\frac{\left(Ar_{atmos}\right)}{\left(Ar_{spike}\right)} = Q$$

Combining the results from equations E2 and E3 gives:

$$\text{mass}\left(^{40}Ar_{atmos}\right) = Q \times H \times \left(M_{atmos}/M_{spike}\right) \times \text{spike mass} \qquad \textit{(equation E4)}$$

The second Ar isotopic ratio for the specimen gas mixture gives:

$$\left(\frac{^{40}Ar}{^{38}Ar}\right)_{mixture} = \frac{\left(^{40}Ar/Ar_{total}\right)_{atmos} \times \left(Ar_{atmos}\right) + \left(^{40}Ar/Ar_{total}\right)_{spike} \times \left(Ar_{spike}\right) + \left(^{40}Ar^{*}\right)}{\left(^{38}Ar/Ar_{total}\right)_{atmos} \times \left(Ar_{atmos}\right) + \left(^{38}Ar/Ar_{total}\right)_{spike} \times \left(Ar_{spike}\right)}$$

(equation E5)

which after the insertion of all known values, including that of Q from equation E3, gives:

$$\left(\frac{^{40}\mathrm{Ar}^{*}}{\mathrm{Ar}_{\mathrm{spike}}}\right)_{\mathrm{mixture}} = \mathrm{W} \qquad \textit{(equation E6)}$$

so that the mass of radiogenic argon in the specimen gas mixture is:

$$\mathrm{mass}\,^{40}\mathrm{Ar}^{*} = \mathrm{W} \times \left(\mathrm{M}_{^{40}\mathrm{Ar}}/\mathrm{M}_{\mathrm{spike}}\right) \times \mathrm{mass\ of\ spike} \qquad \textit{(equation E7)}$$

and the mass proportion of radiogenic ^{40}Ar in the specimen is:

$$\mathrm{mass}\,^{40}\mathrm{Ar}^{*}/\mathrm{mass\ of\ specimen} = \mathrm{Z} \qquad \textit{(equation E8)}$$

Using equation E8, the mass ratio of radiogenic argon to potassium for the specimen gas mixture (R), can be determined (with appropriate conversion for units):

$$\mathrm{R} = \frac{\mathrm{Z}}{\mathrm{K}\%} \times 10^{-7} \qquad \textit{(equation E9)}$$

The next stage is to calculate the ratio of radiogenic argon to ^{40}K in the specimen:

$$\left(\frac{^{40}\mathrm{Ar}^{*}}{^{40}\mathrm{K}}\right) = \mathrm{R} \times \frac{\mathrm{M}_{\mathrm{K}_{\mathrm{natural}}}}{0.0001167 \times \mathrm{M}_{^{40}\mathrm{Ar}}} = \mathrm{D} \qquad \textit{(equation E10)}$$

where 0.0001167 is the natural abundance of ^{40}K, given in section E.1.

The age (t) is calculated by rearranging equation E1:

$$\mathrm{t} = \left(\frac{1}{\lambda}\right)\ln\left[\left(\frac{\lambda}{\lambda_{e}}\right)\mathrm{D} + 1\right] \qquad \textit{(equation E11)}$$

and the percentage atmospheric argon (M) is found using the result of equation E4:

$$\frac{\mathrm{mass}\left(^{40}\mathrm{Ar}\right)_{\mathrm{atmos}}}{\mathrm{mass}\left(^{40}\mathrm{Ar}_{\mathrm{atmos}} + ^{40}\mathrm{Ar}^{*}\right)} \times 100 = \mathrm{M} \qquad \textit{(equation E12)}$$

The estimated error on the age (E_t) is calculated using the equation given by Dalrymple and Lanphere (1969):

$$E_t = [(E_K)^2 + (E_s)^2 + (E_a)^2 M^2 (100 - M)^{-2} + (E_b)^2 \times 10^4 \times (100 - M)^{-2}]^{1/2} \qquad \textit{(equation E13)}$$

where:

E_K = error on K	1.0%
E_s = error on spike mass/mass of specimen	1.5%
E_a = error on (^{36}Ar/^{38}Ar) of final mixture	1.0%
E_b = error on (^{40}Ar/^{38}Ar) of final mixture	0.2%

and this simplifies to:

$$E_t = [3.25 + (M^2 + 400)/(100 - M^2)]^{1/2} \qquad \textit{(equation E14)}$$

In addition a sample of phonolite from Mt. Mézenc in the Velay oriental was repeatedly analysed to check accuracy. A value of 7.70Ma was taken to be the most accurate, and all ages were corrected to agree with this value.

VELAY ORIENTAL

Simplified Geological Map

Northern sheet

1 : 50 000

Based on the available BRGM 1:50 000 geological maps marked on this map (Le Puy, Burzet and Lamastre) and Mergoil (1980)

Volcanic Rocks

Velay oriental

- Basalt, basanite, hawaiite, mugearite and benmoreite - Miocene
- Phonolite, trachyte and rare quartz-trachyte - Miocene
- Deves basalt - Villafranchian
- Bas-Vivarais basalt - Quaternary

Basement

- Velay anatectic granite, with cordierite and biotite

Sedimentary Rocks

- Puy basin - Eocene-Oligocene
- Lacustrine sediments - Miocene

- Maars and sites of phreatomagmatic explosions
- Basement faults, dashed where uncertain
- Basaltic vents
- x 86/20 Specimen locations

N

Crapponne-sur-Arzon sheet

Monistrol-sur-Loire sheet

Le Puy sheet

Yssingeaux sheet

St Agreve sheet

Solignac-sous-Roche

Beauzac

Retournac

Beaux

Yssingeaux

Rosieres

Bessamorel

Le Pertuis

St Hostien

Queyrieres

St Germain Laprade

St Julien Chapteuil

Boussoulet

Le Chambon-sur-Lignon

Mazet St Voy

Lantriac

la Dent

la Madeleine

Miaune

Roche-en-Régnier

Suc de Chaumont

Mt Gerbizon

Suc de Bartou

Suc d'Emeral (Mt. Orcher)

Suc d'Orsier

Veyrines

Suc d'Antreuil

la Plaine

Suc de Jalore

Suc de Fialet

Suc d'Eyme

Pied de Glavenas

Suc de Charbonnière

Suc de Rougeac

Suc de Jorance

Riou Frait

Mont Losegal

Huche Pointue

Huche Plate

Suc de Mialaure

Suc d'Ardemeze

Suc de Saugear

Suc de Piou

Suc de Champblanc

Suc de Bessac

Suc de Bellecombe

Suc d'Achon

Pat à Cuard

Mont Fracelier

Mont Pidgier

Mt Chiroux

le Rand

la Mezère

le Devès

le Montvernoux

Suc de l'Eglise

Mont Chanis

Mont Rouge

Mt Chabrier

Montagne du Meygal

le Mounier

le Testaouaire

Pic du Lizieux

la Chau de Carle

la Chaud de la Croix

Mont de la Tortue

Mont Peylenc

Mont Peynastre

Mont Plaux

St Pierre Eynac

Suc de Monac

Peyre de Bard

Suc de Sauvagnac

Suc de Monac

Suc de Jorance

Suc de Mialaure

Suc de Bellecombe

Suc de l'Eglise

Suc de Champblanc

Suc de Bessac

Suc de Piou

Suc de Sauvagnac

Suc d'Achon

Suc d'Ardemeze

Suc de Charbonnière

Suc de Fialet

Suc de Jalore

Suc de Monac

Suc de Rougeac

Suc de Bartou

Suc d'Orsier

Suc d'Antreuil

Suc de Chaumont

Suc de Pertuis

Suc de Monac

Suc de Sauvagnac

Suc de Piou

Suc de Champblanc

Suc de Bessac

Suc de Bellecombe

Suc de l'Eglise

Suc de Monac

Suc de Jorance

Suc de Mialaure

Suc de Rougeac

Suc de Bartou

Suc d'Orsier

Suc d'Emeral (Mt. Orcher)

VELAY ORIENTAL
Simplified Geological Map
Southern sheet
1 : 50 000

For key see northern sheet

N

le Monastier-sur-Gazeille sheet

Lamastre sheet

45°00'

44°55'

44°50'

4°00'

4°05'

4°10'

4°15'

4°20'

Gourgouras

Clauzelles

St Julien Boutières

Laussonne

St Front

Fay-sur-Lignon

les Roches

Aubépin

Le Monastier-sur-Gazeille

Freycenet-la-Tour

Meyzoux

Vacheresse

Gazelle basalt section

Roche du Bachat

Chaudeyrolles

Mont Signon

Rocher d'Aiglet

St Clément

Orselas Bas

St Martin de Valamas

Mont d'Alambre

La Roche Pointue (Dents de Mézenc)

Mont Mézenc

Les Estables

Rechausseyre

Rocher Tourte

Clabrières

Roche de Borée

Rocher de Pialoux

Rocher de Soutron

Borée

Arcens

Suc de Touron

Suc de la Veine

Serre du Grésier

Rocher des Pradoux

Suc de Sara

Ribefaite

St Martial

Lestrat

Sommet de la Farre

Col de Joux

Dornas

Suc de Taupernas

Suc de la Lauzière

Suc de Montfol

Suc de Séponet

le Séponet

Le Béage

Gerbier de Jonc

le Coux

le lac d'Issarlès

Lachamp Raphaël

Suc de Montivernoux

Ray-Pic

Mézilhac

Burzet sheet

Privas sheet